



Cumhuriyet Science Journal
Faculty of Science, Cumhuriyet University
58140 - Sivas - Türkiye
Phone: +90(346) 487 13 72
Fax: +90(346) 219 11 86
e-mail: csj@cumhuriyet.edu.tr
<http://csj.cumhuriyet.edu.tr/en>
<http://dergipark.org.tr/en/pub/csaj>

Cumhuriyet Science Journal Vol: 44 No: 4 Year 2023

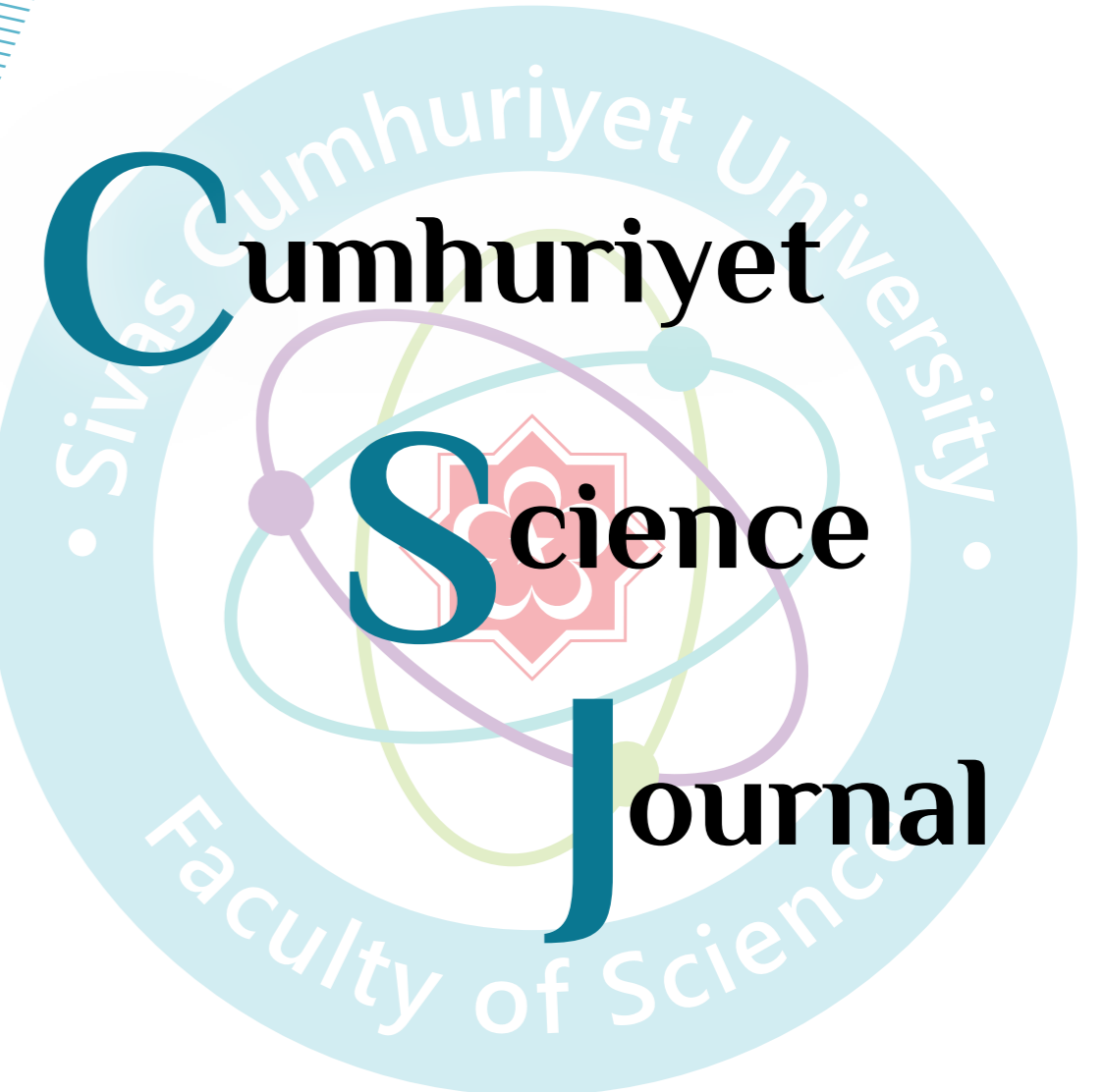


Sivas Cumhuriyet University

ISSN : 2680-2587

e-ISSN : 246-2587X

dergipark.org.tr/tr/pub/csaj
e-mail: csj@cumhuriyet.edu.tr



Cumhuriyet Science Journal (CSJ) is an official publication of Sivas Cumhuriyet University, Science Faculty. The high quality research papers related to the natural sciences are published as online four times a year. CSJ is an open access, free of charge journal and all articles in CSJ have undergone peer review and upon acceptance are immediately and permanently free for everyone to read and download.

Volume: 44

Number: 4

Year: 2023



ISSN: 2587-2680
e-ISSN: 2587-246X
Period: Quarterly
Founded: 2002

Publisher: Sivas Cumhuriyet University

Cumhuriyet Science Journal (CSJ)

Journal Previous Name: Cumhuriyet Üniversitesi Fen-Edebiyat Fakültesi Fen Bilimleri Dergisi

Old ISSN: 1300-1949

Editor in Chief

Prof. Dr. İdris ZORLUTUNA (Sivas Cumhuriyet University)

Managing Editor

Prof. Dr. Adil ELİK (Sivas Cumhuriyet University)

Editors

Prof. Dr. Baki KESKİN

bkeskin@cumhuriyet.edu.tr

Subjects: Mathematics and Statistics

Institution: Sivas Cumhuriyet University

Prof. Dr. Adil ELİK

elik@cumhuriyet.edu.tr

Subjects: Chemistry and Chemical Engineering,
Environmental Sciences, Basic Sciences (General)

Institution: Sivas Cumhuriyet University

Prof. Dr. Nilüfer TOPSAKAL

ntopsakal@cumhuriyet.edu.tr

Subjects: Applied Mathematics

Institution: Sivas Cumhuriyet University

Prof. Dr. Serkan AKKOYUN

sakkoyun@cumhuriyet.edu.tr

Subjects: Physics and Physical Engineering

Institution: Sivas Cumhuriyet University

Prof. Dr. Halil İbrahim ULUSOY

hiulusoy@cumhuriyet.edu.tr

Subjects: Chemistry, Analytical Chemistry, Drug Analysis, Pharmacy

Institution: Sivas Cumhuriyet University

Prof. Dr. Fatih UNGAN

funGAN@cumhuriyet.edu.tr

Subjects: Optics, Phonotics and Fiber optics

Institution: Sivas Cumhuriyet University

Prof. Dr. Nail ALTUNAY

naltunay@cumhuriyet.edu.tr

Subjects: Bioanalytical Chemistry, Chemometric Analysis

Institution: Sivas Cumhuriyet University

Section Editors

Prof. Dr. Natalia BONDARENKO

bondarenkonp@info.sgu.ru

Subjects: Applied Mathematics and Physics

Institution: Samara University

Prof. Dr. Marcello LOCATELLI

marcello.locatelli@unich.it

Subjects: Analytical Chemistry

Institution: University "G. d'Annunzio" of Chieti-Pescara

Prof. Dr. Konstantin P. KATIN

kpkatin@yandex.ru

Subjects: Theoretical Chemistry, Computational design of nanostructures, nanodevices and nanotechnologies

Institution: National Research Nuclear University

Prof. Dr. Duran KARAKAŞ

dkarakas@cumhuriyet.edu.tr

Subjects: Inorganic Chemistry, Theoretical Chemistry

Institution: Sivas Cumhuriyet University

Assoc. Prof. Dr. Yaşar ÇAKMAK

ycakmak@cumhuriyet.edu.tr

Subjects: Applied Mathematics

Institution: Sivas Cumhuriyet University

Prof. Dr. Sevgi DURNA DAŞTAN

sdurna@cumhuriyet.edu.tr

Subjects: Molecular Biology

Institution: Sivas Cumhuriyet University

Assist. Prof. Dr. Yener ÜNAL

uyener@cumhuriyet.edu.tr

Subjects: Statistics

Institution: Sivas Cumhuriyet University

Abstracted&Indexing

ULAKBİM TR-Dizin

Clarivate Analytics Zoological Record

Crossref

WorldCat

Akademik Dizin

Arastirmax Bilimsel Yayın İndeksi

Bielefeld Academic Search Engine (BASE)

Research Gate

Google Scholar

Idealonline

Editorial Board

Prof. Dr. Sezai ELAGÖZ (ASELSAN)
Prof. Dr. Mustafa SOYLAK (Erciyes University)
Prof. Dr. Chuan Fu Yang (Nanjing University of Science and Technology)
Prof. Dr. Münevver SÖKMEN (KGTU)
Prof. Dr. Hüseyin MERDAN (TOBB ETU)
Prof. Dr. Mehmet AKKURT (Erciyes University)
Prof. Dr. Mustafa KAVUTÇU (Gazi University)
Prof. Dr. Francois VOS (The University of Queensland)
Prof. Dr. Abuzar KABIR (International Forensic Research Institute)
Prof. Dr. Mustafa TÜZEN (GOP University)
Prof. Dr. Songül KAYA MERDAN (METU)
Prof. Dr. Jose Javier Valiente-Dobon (INFN-LNL, Padova University)
Prof. Dr. Yeşim SAĞ AÇIKEL (Hacettepe University)
Prof. Dr. Mehmet ŞİMŞİR (Sivas Cumhuriyet University)
Prof. Dr. Atalay SÖKMEN (KGTU)
Prof. Dr. Ricardo I. JELDRES (Universitat de Antofagasta)
Prof. Dr. Mustafa YILDIRIM (Sivas Cumhuriyet University)
Prof. Dr. Ali DELİCEOĞLU (Erciyes University)
Prof. Dr. Tuncay BAYRAM (Karadeniz Technical University)
Prof. Dr. Gökhan KOÇAK (Erciyes University)
Prof. Dr. Nadjet Laouet (Freres Mentouri Constantine-1 University)
Assoc. Prof. Dr. Savaş KAYA (Sivas Cumhuriyet University)

Layout Editors:

Assist. Prof. Dr. Yener ÜNAL
Lecturer Aykut HASBEK

Copyeditors:

Assist. Prof. Dr. Doğa Can SERTBAŞ
Assist. Prof. Dr. Hacı Ahmet KARADAŞ
Research Assistant Özgür İNCE

Proofreader:

Lecturer Aykut HASBEK

Publication Type: Peer Reviewed Journal

Cite Type: Cumhuriyet Sci. J.

Contact Information

Faculty of Science Cumhuriyet University
58140 Sivas- TURKEY
Phone: +90 (346) 487 13 72
Fax: +90 (346) 219 11 86
e-mail: csj@cumhuriyet.edu.tr
<http://dergipark.gov.tr/csj>

CONTENTS		PAGES
1	A Novel Triazolopyrimidinone Derivative: A Portable Electrochemical Approach to Investigate DNA Interactions Arif Engin ÇETİN	<i>Research Article</i> 617 - 624
2	Design, Synthesis and Evaluation of Pyrrol-thiazole Derivatives as AChE and BuChE Inhibitory and Antioxidant Activities Ulviye ACAR ÇEVİK Tugba ERCETİN	<i>Research Article</i> 625 - 628
3	Hydroxychloroquine Modulates m6A RNA Methylation in Prostate Cancer Cells Sevinc YANAR Merve Gülsen BAL ALBAYRAK	<i>Research Article</i> 629 - 634
4	Evaluation of the Antitumor Activity of Omipalisib, a PI3K/AKT/MTOR Pathway Inhibitor, on Burkitt Lymphoma Cell Line Zekeriya KESKİN Fatih YULAK Hatice TERZİ Merve İNANIR	<i>Research Article</i> 635 - 639
5	Unraveling the Role of Apoptosis in the Antiproliferative Activity of β -Glucan on A549 Cells Ziad JOHA Mustafa ERGÜL	<i>Research Article</i> 640 - 644
6	Investigation of the Effect of Indatraline on Oxidative Damage Induced by Hydrogen Peroxide in C6 Glioma Cell Line Fatih YULAK Bünyamin ÜNGÜR	<i>Research Article</i> 645 - 649
7	Evaluation of the Interactions of Cabozantinib with Topoisomerase Enzymes by in vitro Enzyme Activity Assays, and its Effects on Cancer Cell Proliferation Feyza OFLAZ Naz ÜNAL Burcin GUNGOR Pakize CANTÜRK	<i>Research Article</i> 650 - 655
8	Investigation of Electrospun Polyacrylonitrile and Cellulose Acetate Smart Nanofibers Doped with Expanded Graphite for the Structure and Photothermal Effect Özgül GÖK	<i>Research Article</i> 656 - 664
9	Investigation of the Effect of Main Components of Wild Thyme on Covid-19 by Computational Methods Serpil KAYA Sultan ERKAN Duran KARAKAŞ	<i>Research Article</i> 665 - 670
10	Green Synthesis of CuO Nanoparticles Using Tragopogon porrifolius and Their Antioxidant and Photocatalytic Applications Gamze TOPAL CANBAZ	<i>Research Article</i> 671 - 677
11	Synthesis and Characterization of Novel 2,4-Diaryloctahydro-2H-Chromene Derivatives with Four Stereocenters Hayreddin GEZEGEN	<i>Research Article</i> 678 - 686
12	MW Assisted Synthesis of New 4,6-diaryl-3,4-Dihydropyrimidines-2(1H)-thione Derivatives: Tyrosinase Inhibition, Antioxidant, and Molecular Docking Studies Seda FANDAKLI Tayyibe Beyza YÜCEL Elif ÖZTÜRK Uğur UZUNER Burak BARUT Fatih Mehmet ATEŞ Nurettin YAYLI	<i>Research Article</i> 687 - 696
13	Efficient Methanol Electro-oxidation on Ni, S Dual Doped Reduced Graphene Layer Catalyst Rukan SUNA Sedef KAPLAN	<i>Research Article</i> 697 - 702
14	Preparation and Characterization of Tung Oil Loaded Melamine Formaldehyde Microcapsules Tülin GÜRKAN POLAT Ahmet GENÇER Meltem ASİLTÜRK Yılmaz AKSU	<i>Research Article</i> 703 - 709
15	Spectrophotometric Determination of Atorvastatin Based on Charge Transfer Reaction with Quinalizarin Fatih YİĞİT Nurettin TARKAN Mehmet AKDENİZ Figen EREK Işıl AYDIN	<i>Research Article</i> 710 - 715
16	Simultaneously HPLC Analysis of B1, B9 and B12 Vitamins at Trace Levels via Cloud Point Extraction Halil İbrahim ULUSOY İpek Nur YİĞİT Ümmügülsüm POLAT Esra DURGUN Aslıhan GÜRBÜZER Songül ULUSOY	<i>Research Article</i> 716 - 722

17	Investigation of Antiviral Activities of Nickel and Copper Complexes with Macrocyclic Ligands against Crimean-Congo Hemorrhagic Fever by In Silico Calculations Sultan ERKAN Niyazi BULUT Duran KARAKAŞ	<i>Research Article</i>	723 - 732
18	On Directed Length Ratios in the Lorentz-Minkowski Plane Abdulaziz AÇIKGÖZ	<i>Research Article</i>	733 - 740
19	Application of Formable Transform for Solving Growth and Decay Problems, Logistic Growth Model and Prey-Predator Model Nihan GÜNGÖR	<i>Research Article</i>	741 - 752
20	On Deferred Statistical and Strong Deferred Cesàro Convergences of Sequences With Respect to A Modulus Function Cemal BELEN Mustafa YILDIRIM	<i>Research Article</i>	753 - 757
21	New Midpoint-type Inequalities of Hermite-Hadamard Inequality with Tempered Fractional Integrals Tuba TUNÇ Ayşe Nur ALTUNOK	<i>Research Article</i>	758 - 767
22	Predictions on Flexible CdTe Solar Cell Performances by Artificial Neural Networks Sevinj GANBAROVA Serkan AKKOYUN Vusal MAMEDOV Huseyn MAMEDOV	<i>Research Article</i>	768 - 774
23	The Slab Critical Thickness Problem with Reflecting Boundary Condition for the Anlı-Güngör Scattering Function Demet GÜLDEREN R. Gökhan TÜRECI	<i>Research Article</i>	775- 784
24	Study on Electrical, Thermal, Magnetic Properties and Microstructure for η -Al, η -Al ₂ Cu, ω -Al ₇ Cu ₂ Fe Phases in Al-32.5 wt. % Cu-1 wt. % Fe Ternary Alloy Canan ALPER BİLLUR Buket SAATÇI	<i>Research Article</i>	785 - 792
25	A Study on The Optical Properties of Long-Infrared Intraband Transitions of Quadruple Gaas/Alxga1-Xas Quantum Well Under Applied Electric Field Didem ALTUN	<i>Research Article</i>	793 - 798
26	Development of Image Processing Based Line Tracking Systems for Automated Guided Vehicles with ANFIS and Fuzzy Logic Ahmet YÜKSEK Ahmet Utku ELİK	<i>Research Article</i>	799 - 815
27	Determining Efficiency of 15 OECD Countries Coping with Covid-19 using Data Envelopment Analysis after 2 Years of Pandemic Esra POLAT	<i>Research Article</i>	816 - 824

A Novel Triazolopyrimidinone Derivative: A Portable Electrochemical Approach to Investigate DNA Interactions

Arif Engin Çetin^{1,a,*}¹ İzmir Biomedicine and Genome Center, İzmir, Türkiye.

*Corresponding author

Research Article

History

Received: 17/08/2023

Accepted: 28/10/2023

Copyright

©2023 Faculty of Science,
Sivas Cumhuriyet University

ABSTRACT

In this study, a novel triazolopyrimidinone derivative, 2-(2-chlorophenyl)-5-(morpholinomethyl)-[1,2,4]triazolo[1,5-a]pyrimidin-7(3H)-one, abbreviated as CPD-1, was synthesized as a drug candidate. By employing electrochemical techniques, we analyzed the electrochemical behavior of this compound and its interactions with both single-stranded DNA (ssDNA) and double-stranded DNA (dsDNA). Experimental parameters such as pH, concentration, scan rate, immobilization time were studied using Differential Pulse Voltammetry (DPV) and Cyclic Voltammetry (CV) to obtain the most precise analytical signals. We present an innovative approach to evaluate the toxicity effect of this drug candidate on DNA. We also propose a simplified equation to quantify toxicity effects based on changes in electrochemical signals, specifically peak current of guanine bases, before and after drug-DNA interactions. Our methodology contributes to the burgeoning field of electrochemical toxicity assessment and holds promise for advancing drug development and safety evaluation. Furthermore, stability tests for the drug candidate were conducted on different days. Notably, our investigation revealed significant alterations in guanine bases upon the interaction of CPD-1 with both ssDNA and dsDNA, underscoring the potential impact of these compounds on DNA structure. Based on our experimental data, we conclude that this molecule can be utilized as a drug due to its effects on DNA.

Keywords: Drug candidate, Pencil graphite electrodes, Drug-DNA interaction, Triazolopyrimidinone.^a arif.engin.cetin@gmail.com^{id} <https://orcid.org/0000-0002-0788-8108>

Introduction

Heterocyclic compounds, which encompass nitrogen-containing aryl substituents with five- and six-membered rings, have garnered significant interest due to the discovery of their effects in chemistry and various applications [1]. Triazolopyrimidinone, a fused pyrimidinone-triazole heterocyclic compound, has been extensively studied in diverse fields. It consists of a fused structure with a triazole and pyrimidinone ring. The unique structure of this compound imbues it with intriguing and potentially valuable properties, rendering it a subject of keen interest across diverse research domains, such as medicinal chemistry and drug discovery. These compounds have demonstrated a wide range of activities, including antibacterial, antifungal, antiviral, anticancer, herbicidal, antitumor, and antioxidant properties [2,3]. Some triazolopyrimidinones derivatives have demonstrated promising antimicrobial activity against a range of bacterial and fungal strains. These compounds could potentially serve as leads for the development of new antibiotics [4]. Certain triazolopyrimidinones have shown cytotoxic effects against cancer cell lines. They may interfere with cellular processes and pathways that are crucial for cancer cell survival and proliferation. Triazolopyrimidinones have also exhibited antiviral activity against certain viruses [5]. They may inhibit viral replication and entry into host cells,

making them potential candidates for antiviral drug development. Besides their antimicrobial, anticancer, and antiviral properties, triazolopyrimidinones have been investigated for other activities, including anti-inflammatory and antioxidant effects [6-8].

Deoxyribonucleic acid (DNA) is the most popular pharmacological target of many drugs. The interaction between drugs and DNA is crucial for modern medicine, impacting both therapy and adverse effects. Understanding this interplay is key to developing effective treatments and safer drugs. By comprehending how drugs interact with DNA at the molecular level, scientists can tailor medications to target specific genetic factors, optimize treatment outcomes, and minimize potential side effects. Studying the mechanisms underlying drug-DNA interactions is of paramount importance, offering insights into drug actions and paving the way for innovative DNA-targeted drug design. A variety of techniques, spanning optical and infrared spectroscopy, nuclear magnetic resonance (NMR), circular and linear dichroism, viscosity assays, mass spectrometry (MS), molecular docking, and electrochemical methods, are employed to unravel the intricate nature of DNA-drug interactions [9-12]. This multifaceted approach empowers researchers to decipher the complex interplay between drugs and DNA, fostering advancements across the

spectrum of biomedical and pharmaceutical research. Exploring drug-DNA interactions holds pivotal significance, especially in the realm of electrochemical methods. These techniques, ranging from CV to DPV, offer a unique window into the dynamic interrelationship between drugs and DNA molecules. By harnessing the power of electron transfer processes, electrochemical methods unveil valuable insights into binding affinities, structural alterations, and even potential toxicity. This sophisticated approach not only enhances our understanding of drug mechanisms but also propels the development of cutting-edge DNA-targeted therapeutics. They are commonly favored for their rapidity, simple operation, and portability. Their high selectivity ensures accurate identification of target analytes even in complex samples, while their sensitivity allows for the detection of trace concentrations.

Furthermore, the interplay between drugs and DNA holds significant importance in both the pharmaceutical industry and the realm of biomedicine. This interaction offers numerous critical advantages and applications, including drug screening, optimizing drug delivery, personalized medicine, and genetic research. This knowledge forms the bedrock for advancing our comprehension of diseases and enhancing patient outcomes. Comprehending the intricate dance of drugs with DNA can pave the way for the development of precisely targeted therapies. Specifically tailored drugs that interact with DNA can be engineered to target particular genes or sequences linked to diseases, such as cancer. Many chemotherapeutic agents operate by engaging with DNA, thereby inhibiting cell division or triggering programmed cell death. Profound insights into these interactions are essential for crafting chemotherapy drugs that are more effective and less toxic. Delving into the nuances of how drugs interact with DNA also yields insights into their potential toxic effects, which is vital for evaluating the safety of pharmaceutical compounds. For example, certain antibiotics like quinolones function by engaging with bacterial DNA, impeding replication, and ultimately causing bacterial cell demise. This understanding underpins the development of antibiotics and is indispensable for ensuring their efficacy and safety.

In our research, we explored the electrochemical characteristics of 2-(2-chlorophenyl)-5-(morpholinomethyl)-[1,2,4]triazolo[1,5-a]pyrimidin-7(3H)-one (abbreviated as CPD-1) a triazolopyrimidinone derivative and its interactions with both single-stranded DNA (ssDNA) and double-stranded DNA (dsDNA) through DPV and CV. Specifically, we directed our attention to the novel potential drug candidate CPD-1, distinguished by its triazolopyrimidinone structure, and conducted an examination of its electrochemical properties. Various experimental parameters such as pH, concentration, scan rate, and immobilization time were systematically investigated using DPV. Additionally, we determined the

detection limit, reproducibility, precision, linearity, as well as the limits of detection (LOD) and quantification (LOQ). The binding constant (K) was quantified at $7.4 \times 10^1 \text{ M}^{-1}$, indicating the weak strength of the interaction. In terms of toxicity, the values recorded were 31% for ssDNA and 26% for dsDNA, highlighting the varying impact on these DNA types. Moreover, the calculations involving Gibbs free energy (G°) resulted in a value of -10.66 kJ/mol . This insightful calculation offers additional insights into the thermodynamic aspects of the interaction, contributing to a deeper understanding of CPD-1's behavior and its potential applications. To assess the stability of CPD-1, comprehensive tests were conducted under optimal storage conditions (a dark room at 25°C) on specific days (day 0, day 1, day 3, day 7, and day 30). DPV was employed before and after the interaction process to uncover the mechanism of CPD-1's interaction with both ssDNA and dsDNA. Notably, CPD-1's interaction with ssDNA and dsDNA led to significant alterations in guanine bases, emphasizing the crucial nature of these findings.

Our study introduces CPD-1, an entirely novel compound characterized as a "tri-azolo-pyrimidinone derivative." This constitutes a substantial innovation, as the synthesis of novel compounds frequently yields unique properties and prospective applications within the domain of pharmaceutical development. Such compounds often possess distinctive structural attributes and latent pharmacological functionalities that remain relatively unexplored within the extant body of literature. The study elucidates "significant modifications in guanine bases" consequent to the interaction between CPD-1 and DNA, thereby accentuating the conceivable influence of this compound on the structural integrity of DNA. This discernment represents an unprecedented discovery, which may bear implications for comprehending the mechanistic underpinnings of CPD-1's mode of action. CPD-1 could potentially exhibit a distinctive mechanism of action or a heightened affinity for DNA binding, avenues worthy of further exploration for potential therapeutic applications [13-15].

Materials and Methods

Apparatus

The SimpliAmp™ Thermal Cycler (Thermo Fisher Scientific, Waltham, MA) was utilized to generate two distinct single-stranded DNA (ssDNA) strands. DPV and CV measurements were performed using a PalmSens4 potentiostat/galvanostat/impedance analyzer. The PalmSens4 was connected to a computer via a USB cable and operated using PSTrace 5.8 software. The three-electrode system included a pencil graphite electrode (PGE) as the working electrode, an Ag/AgCl reference electrode, and a platinum wire counter electrode. A Rotring T 0.5 mm pencil (Rotring, Germany) served as the holder for the graphite lead. HB pencil leads (Tombo,

Japan) measuring 60 mm in length and 0.5 mm in diameter were obtained from a local bookstore.

PGEs are frequently employed in electrochemical sensors and biosensors due to their excellent electrical conductivity, stability, and ease of functionalization for specific analytes. PGEs represent a category of carbon-based electrodes known for their affordability, simplicity, wide availability, adaptability, and disposability. Graphite is an excellent conductor of electricity, which makes pencil graphite electrodes suitable for various electrochemical processes. They can efficiently transfer electrical energy to the reaction medium, enabling precise control over the process. Graphite is chemically inert, which means it does not react with most chemicals or substances. This property makes PGEs compatible with a wide range of chemical reactions and environments. PGEs typically exhibit low polarization characteristics, meaning they can facilitate electrochemical reactions with minimal energy loss due to overpotential. This can result in more efficient and cost-effective processes. They are relatively strong and can endure mechanical stress and pressure, which is advantageous in industrial applications where electrodes may experience mechanical wear and tear. These characteristics make PGEs a desirable choice for electrochemical sensing applications, particularly due to their distinct advantage of being disposable, setting them apart from other commonly employed carbon-based electrodes. Additionally, PGEs, being mechanically robust, offer ease of customization and miniaturization [16,17].

The active surface area of a pencil graphite electrode can be estimated using the Randles-Sevcik equation, which relates the peak current of an electrochemical reaction to the diffusion coefficient, concentration, and active surface area of the electrode. By measuring the peak current of a well-characterized electroactive species, such as ferrocyanide, and using its known diffusion coefficient and concentration, the active surface area of the pencil graphite electrode was calculated as 0.255 cm², as demonstrated in our previous study [18].

Chemicals

Ethanol absolute (99.9%), and glacial acetic acid were purchased from Isolab Chemicals. Double-stranded salmon sperm DNA (dsDNA) was sourced from Sigma Chemical Co. (St. Louis, USA), and all other chemicals were of high purity, obtained from Merck (Darmstadt, Germany), Tokyo Chemical Industry Co. Ltd. (Tokyo, Japan). All solvents used were of high analytical grade and were employed without further purification. Buffers, including 0.5 M Acetate (ACB) at pH levels of 3.8, 4.8, and 5.6, 0.05 M Phosphate (PBS) at pH 7.4, 0.1 M sodium borate (BBS) at pH 8.1, along with 0.02 M NaCl and 0.05 M Tris-EDTA (TE) buffer at pH 8.0, were utilized in the experiments. Stock solution of CPD-1 was prepared in Dimethylformamide (DMF) and stored in a dark room at 4°C to prevent degradation.

The salmon sperm DNA used in this experiment (Sigma Aldrich, purity ≥ 98%) was dissolved in deionized water to prepare stock solutions. 3-amino-5-(methylthio)-4H-1,2,4-triazole (Merck, purity ≥ 97%) and chloroform (Alfa Aesar-Acros Organics, purity ≥ 99%) were used as received without further purification. The buffers were prepared using analytical grade chemicals from various different companies as Carlo Erba, Alfa Thermo Fisher Scientific, and Isolab.

Experimental

Candidate Drug Molecules

Triazolopyrimidinones can be synthesized through various chemical reactions, including cycloaddition reactions, condensation reactions, and cyclization reactions. The compound 2-(2-chlorophenyl)-5-(morpholinomethyl)-[1,2,4]triazolo[1,5-a]pyrimidin-7(3H)-one was synthesized following literature procedures at the Department of Pharmaceutical Chemistry, Faculty of Pharmacy, Izmir Katip Celebi University, and generously provided [19].

Pre-treatment of PGE

Before activation, the pencil graphite electrodes (PGEs) were trimmed to a length of 3 cm. Subsequently, all PGEs underwent activation by applying a potential of +1.4 V for 30 seconds in acetate buffer (ACB) at pH 4.8, aiming to minimize background current. The electrochemically pre-treated PGEs were then utilized as working electrodes for subsequent experiments.

To cleanse and activate the electrode surface, we initially applied a predetermined voltage for a specific duration to activate the electrodes. Following the immobilization of DNA or drug molecules, we subsequently rinsed the electrodes with buffer solutions to eliminate any unbound substances.

Interaction

CPD-1's electrochemical behavior on PGEs was studied using DPV, considering both the presence and absence of ssDNA and dsDNA. The interaction of CPD-1 with ssDNA. After a 1-minute heating step of dsDNA at 95°C and cooling on ice of CPD-1 was added, and ssDNA was immobilized on PGEs. In our experiment, there was no drying step performed before the measurements. DPV measurements were conducted following this step. In the subsequent stage, CPD-1's interaction with dsDNA was examined. Solutions containing dsDNA and CPD-1 were agitated at 45°C and 600 rpm for 30 minutes. Interaction solutions were then analyzed using DPV.

Measurement

DPV and CV measurements were carried out in the range of + 0.4 to + 1.4 V at 50 mV/s of scan rate. The experimental procedure is shown in Figure 1.

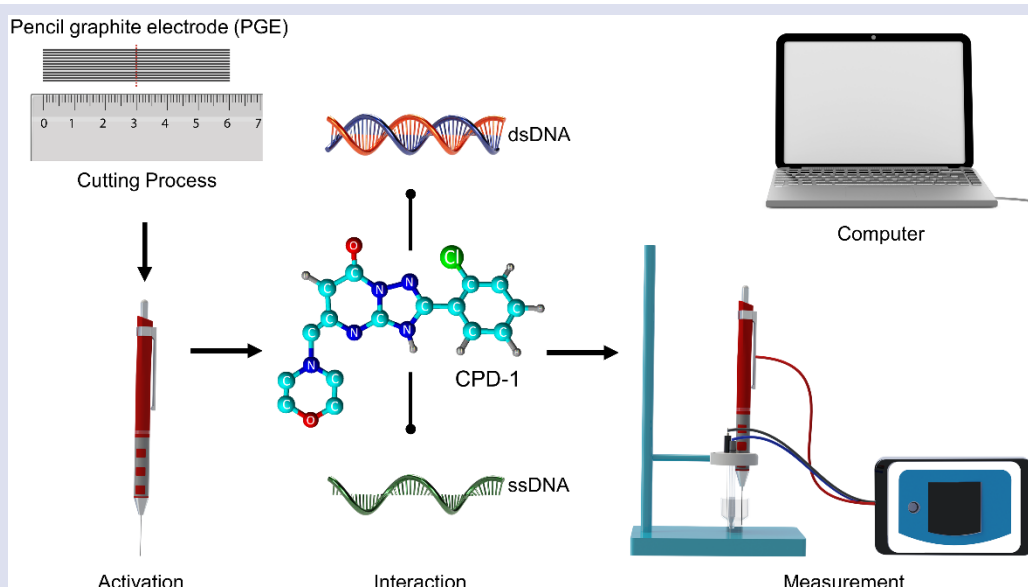


Figure 1. Experimental steps: activation of PGE with ACB; CPD-1 interaction with ssDNA and dsDNA; DPV measurements.

Results and Discussion

Investigation of Electrochemical Properties of Compounds

In this section, the electrochemical behaviors of the drug candidate molecules were investigated using DPV. To begin, the impact of pH on the electrochemical oxidation signals of the drug candidates was assessed, and the corresponding results are presented in Figure 2. Notably, pH plays a pivotal role in drug metabolism and therapeutic efficacy. For the pH study, a range spanning from 3.8 to 9.8 was examined using DPV. The investigation aimed to identify the optimal pH conditions that yield significant changes in peak current and peak potential for the drug candidates. The outcomes revealed that CPD-1 exhibited stable responses, with the most prominent peak observed at pH 5.6. Consequently, a pH of 5.6 was selected for the dilution buffer. This meticulous pH exploration provides essential insights into the electrochemical behavior of the drug candidates and informs their potential therapeutic applications [20]. As an additional point of clarification, in our study, we achieved consistent and reproducible current signals through rigorous optimization of experimental parameters. Therefore, we did not explore the influence of different supporting electrolytes by testing various electrodes.

The subsequent phase of the study focused on establishing the analytical concentration ranges of the drug candidates through DPV measurements conducted at a scan rate of 50 mV/s.

Calibration plots, depicted in Figure 3, were constructed across varying concentrations of the drug candidate. Notably, the resulting calibration graph exhibited a linear relationship between current response and concentrations. Notably, the resulting calibration graph showcased a linear relationship between the current response and the concentrations studied.

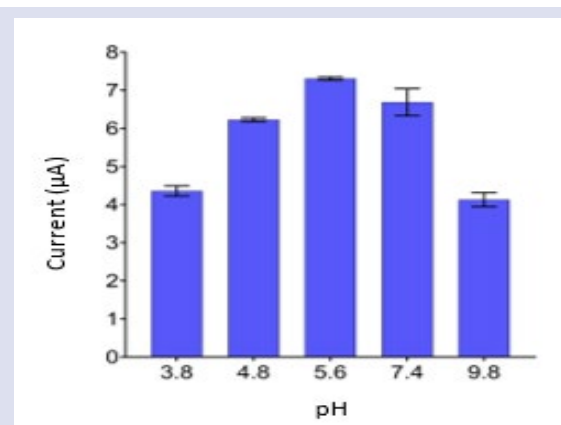


Figure 2. The effect of pH on peak current and peak potential. The bar graph showcases the behavior of the CPD-1 drug molecule across various pH values spanning from 3.8 to 9.8. Notably, the highest peak currents for CPD-1 were observed at pH 5.6.

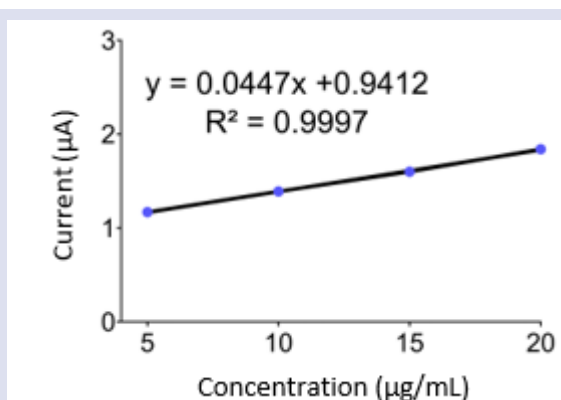


Figure 3. Calibration graph of CPD-1 was obtained by plotting drug concentrations against the current peaks. DPV measurements were performed at 50 mV/s of scan rate with different concentrations from 5 µg/mL to 20 µg/mL.

Specifically, the calibration plot for CPD-1 exhibited a slope of 0.0447 and a correlation coefficient of 0.9997 (as depicted in Figure 3). These outcomes distinctly emphasize the precision and reliability inherent in the developed methodology for quantifying CPD-1's concentrations. Such robust findings augment the analytical potential of the electrochemical approach utilized in this study.

Calibration graph played a pivotal role in calculating the Limit of Detection (LOD) and Limit of Quantification (LOQ) for the CPD-1 drug molecule. The formulas for calculating LOD and LOQ depend on the specific method used, but generally, LOD is calculated as 3 times the standard deviation of the response divided by the slope of the calibration curve ($LOD = 3s/m$), while LOQ is calculated as 10 times the standard deviation of the response divided by the slope of the calibration curve ($LOQ = 10s/m$) [21],[22]. Specifically, the

concentrations 5, 10, 15, and 20 $\mu\text{g/mL}$ were employed for the determination of LOD and LOQ for CPD-1. The calculated values for CPD-1 unveiled a LOD of 0.48 $\mu\text{g/mL}$ and a LOQ of 1.59 $\mu\text{g/mL}$, respectively.

By varying the scan rate, valuable insights can be gained into the kinetics and mechanism of electrochemical reactions. Adjusting the scan rate allows researchers to probe different reaction pathways, investigate the reversibility of redox processes, and analyze the overall electrochemical behavior of compounds. Therefore, the study of scan rate provides a comprehensive understanding of the underlying processes and aids in the design and optimization of electrochemical detection methods and sensor devices. In the last part of the study the influence of scan rate (V) on peak current (I_p) values was explored utilizing CV, covering a scan rate range from 25 mV/s to 150 mV/s.

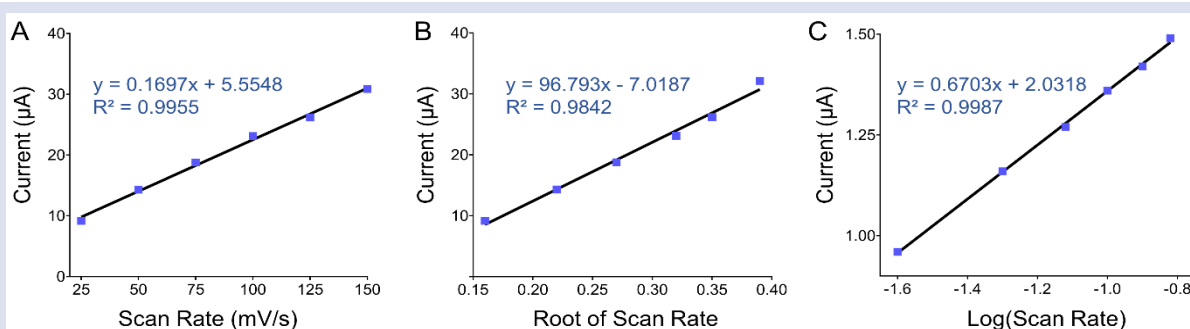


Figure 4. Effect of scan rate on peak current (A), effect of scan rate root on peak current (B), effect of scan rate on the log of peak current of drugs (C).

As shown in Figure 4A, the anodic peak currents (I_{p_a}) is well linear to scan rates (v) and the linear equation is expressed as:

$$I_{p_a}(\mu\text{A}) = 0.01697v + 5.5548 \quad (R^2 = 0.9955) \quad (1)$$

The relationship between I_{p_a} and the root of the scan rate ($v^{1/2}$) also possesses a linear behavior (Figure 4B) and the linear equation is as follows:

$$I_{p_a}(\mu\text{A}) = 96.793v^{(1/2)} - 7.0187 \quad (R^2 = 0.9842) \quad (2)$$

Such linear behavior was also determined between $\log(I_{p_a})$ and $\log(v)$ within the scan rate range between 25 mV/s and 150 mV/s (Figure 4C):

$$\log I_{p_a} = 0.6703\log v + 2.0318 \quad (R^2 = 0.9987) \quad (3)$$

Considering the insights from the literature, these obtained slope values closely align with theoretical expectations, particularly in the case of a value close to 0.5. This alignment suggests the prevalence of diffusion-controlled processes. In contrast, a theoretical value of 1 indicates processes influenced by adsorption [23]. For Equation 3, the determined slopes were calculated as 0.6703. This result distinctly implies that the electrochemical oxidation of CPD-1 diffusion-controlled processes.

Interaction

The electrochemical behaviors of CPD-1 on PGEs were examined using DPV in the presence and absence of both ss-DNA and dsDNA. We begin by conducting a test to assess the interaction of CPD-1 with ssDNA. To facilitate this, a common method involving physical denaturation of dsDNA fragments was employed, as detailed in a referenced study [24]. In this process, a stock solution of dsDNA was initially prepared, and subsequently, 100 μL of dsDNA was aliquoted and sealed in centrifuge tubes. Following this, all samples were subjected to a 1-minute heating step at 95°C in a thermal cycler, followed by cooling on ice for 10 minutes. After adding 10 $\mu\text{g/mL}$ of CPD-1, the resulting ssDNA was immobilized onto pre-treated PGEs for 30 minutes through adsorption. Subsequent to this immersion, DPV measurements were carried out to evaluate the outcomes of the interaction.

In the second stage, the interaction of CPD-1 with ssDNA was examined. Solutions were prepared by mixing 50 $\mu\text{g/mL}$ of dsDNA and 10 $\mu\text{g/mL}$ of the CPD-1 drug candidate in ACB. Following this, these solutions underwent thermal agitation at 45°C and 600 rpm using a thermal shaker for 30 minutes. Subsequently, 100 μL of the resultant interaction solution was carefully transferred into tubes. The Pencil Graphite Electrodes (PGEs) were then submerged in the interaction solutions for a duration of 30 minutes. After this immersion, DPV measurements were carried out to evaluate the outcomes of the interaction.

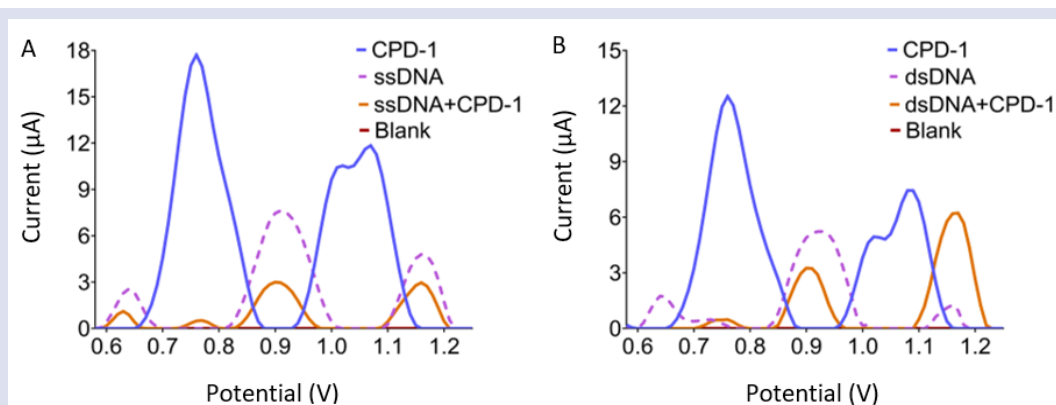


Figure 5. Impact of CPD-1 interaction on ssDNA and dsDNA. Differential pulse voltammograms presenting guanine oxidation currents for ssDNA (A) and dsDNA (B) following interaction with CPD-1.

In Figure 5A, two distinct oxidation signals associated with ssDNA in ACB (pH: 5,6) were obtained at +0.91 V and +1.15 V, respectively. After the interaction with CPD-1, the peak potential of dsDNA shifted to +0.90 V and +1.14 V, respectively. On the other hand, In the presence of CPD-1, the oxidation potentials of dsDNA exhibited a negative shift. (Figure 5B). One of the peak potentials of dsDNA underwent a negative shift, transitioning from +0.93 V to +0.90 V. Similarly, the other peak experienced a shift from +1.16 V to +1.15 V.

In this context, variations in peak potential—whether they are positive or negative—offer insights into the interaction mechanism between the drug candidate CPD-1 and DNA. Positive shifts in peak potential commonly signify intercalative binding, whereas negative shifts are indicative of electrostatic binding [25]. In the scope of our investigation, the observed negative shift in peak potential could be attributed to an irreversible electrode process. This phenomenon might be elucidated by electrostatic binding occurring between CPD-1 and DNA.

The value of the binding constant ($K_{dsDNA-CPD-1}$) was determined using the following Equation 4:

$$\log(1/[DNA]) = \log K + \log (I_{H-G}/I_G - I_{H-G}) \quad (4)$$

where K is the apparent binding constant, I_G and I_{H-G} are the peak current of the free guest (G ; here free CPD-1) and the host-guest complex ($H-G$; CPD-1 intercalated into ss-DNA), respectively. In general, binding constants (K) can range from very low values (indicating weak or transient interactions) to high values (indicating strong, stable interactions). Typical binding constants for drug-DNA interactions can fall within the range of 10^2 to 10^7 M^{-1} , but these values can differ significantly based on the system being studied. A high K value indicates intercalation-based interactions, while a low value indicates electrostatic or groove interactions [26]. Based on changes in current response (I) intensity caused by DNA binding to CPD-1, the binding constant was calculated as $7,4 \times 10^1$ M^{-1} . In the literature, the binding of Doxorubicin (an anthracycline antibiotic) to DNA yields a K value of 3.1×10^5 M^{-1} , Ethidium bromide (a DNA

intercalator) binding to DNA results in a K value of 1.0×10^6 M^{-1} , and Hoechst 33258 (a DNA minor groove binder) binding to DNA exhibits a K value of 2.0×10^7 M^{-1} .

The Gibbs free energy (G°) values provide insights into the thermodynamic favorability of a reaction or interaction. In the context of drug interactions, Gibbs free energy provides insights into the spontaneity and feasibility of a given reaction or binding process. Specifically, in the realm of drug design and development, Gibbs free energy is often utilized to assess the thermodynamic stability of drug molecules when binding to their target biomolecules, such as proteins or DNA. The binding affinity between a drug and its target molecule can be influenced by the change in Gibbs free energy during the binding process. Negative G° values indicate that the interaction is thermodynamically favorable, meaning that the binding process is spontaneous and releases energy [26]. Positive G° values suggest that the interaction is not favorable, requiring an input of energy to occur. A lower Gibbs free energy change (ΔG°) corresponds to a higher K value indicating a tighter binding between the drug and its target. The change in Gibbs free energy (G°) was calculated using Equation 5:

$$\Delta G^\circ = -RT \ln K \quad (5)$$

where R is the universal gas constant (8.31 $J K^{-1} mol^{-1}$), T is the absolute temperature and K is the binding constant. The ΔG° for CPD-1 calculated as $-10,66$ kJ/mol .

In general, the calculation of toxicity effects involves quantifying the change in electrochemical response, such as peak current or potential, caused by the interaction of the drug with DNA. The exact equation will depend on the specific parameters being measured and the data analysis approach chosen. In order to investigate the toxicity effects of CPD-1 on ssDNA and dsDNA, guanine peak changes were calculated before and after interaction. Here's a simplified example of an equation that could be used to calculate the percentage change in peak current as an indicator of toxicity:

$$\text{Toxicity (\%)} = \frac{\text{Peak Current (after interaction)} - \text{Peak Current (before interaction)}}{\text{Peak Current (before interaction)}} \times 100\%$$

This equation provides a percentage value that indicates how much the electrochemical response has changed due to the drug-DNA interaction. A higher percentage change may suggest a higher degree of toxicity. In our study, this value was calculated as 31 % for ssDNA and 26 % for dsDNA.

Stability

Assessing the stability of a drug is of paramount importance in gauging its effectiveness over time. In our study, we scrutinized the stability of CPD-1 by subjecting freshly prepared solutions to controlled storage conditions within a light-protected environment at a constant temperature of 25°C. This scrutiny was carried out over distinct time intervals, specifically on day 0, day 1, day 3, day 7, and day 30. Temporal changes in the peak currents of the drug were meticulously observed. To delve into the stability aspect further, drug solutions were meticulously formulated using ACB (pH: 5.6) at specific concentrations. Swift DPV measurements were executed by immersing Pencil Graphite Electrodes (PGEs) into these solutions immediately post-preparation and at various intervals thereafter (0, 1, 3, 7, and 30 days). The investigation of drug stability occurred under identical molar concentrations using DPV, encompassing a potential range from 0 to +1.4 V, and a scan rate of 100 mV/s. This comprehensive approach allowed us to gain valuable insights into CPD-1's stability profile over the designated timeframes.

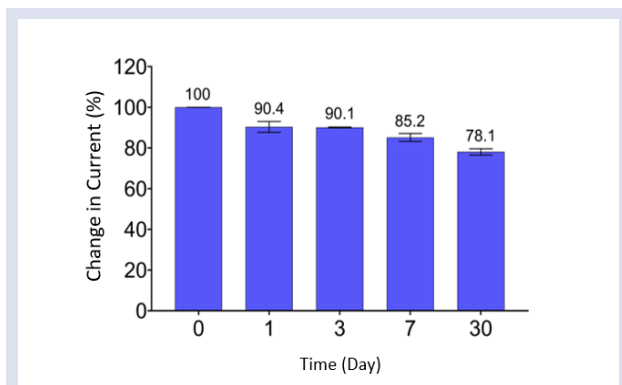


Figure 6. Change in current for CPD-1 examined at 25 °C for different days, e.g., 0, 1, 3, 7, and 30. The current value of the drug candidate was about 78 % by the end of 30 days.

Here, CPD-1 exhibited good stability for 30 days of storage without significant percentage changes in current values, e.g. At the end of day 30, the percentage of the current value for CPD-1 was determined as 78.1%. These findings provide substantial evidence of the stock solutions' stability for a duration of 30 days, with the notable exception of CPD-1. This observation underscores the potential advantages of prolonged utilization, as the majority of the drug candidates retained their vital pharmaceutical attributes over the extended timeframe.

Conclusion

In conclusion, our study delved into the electrochemical properties of triazolopyrimidinone derivative, CPD-1 and its intricate interaction with single-stranded DNA (ssDNA) and double-stranded DNA (dsDNA), employing DPV and CV. This endeavor contributes to the ongoing pursuit of novel therapeutic agents. Our investigation centered on the newly identified drug candidate, CPD-1 characterized by its triazolopyrimidinone structure, and systematically probed its electrochemical behavior. Through meticulous DPV experimentation, we systematically assessed diverse parameters including pH, concentration, scan rate, and immobilization time. The ensuing determination of key parameters such as detection limits, reproducibility, precision, linearity, and limits of detection and quantification (LOD and LOQ) further enriched our understanding. In the quest for stability, comprehensive assessments were conducted under optimal storage conditions, shedding light on the compounds' resilience on specific days. Employing DPV before and after interaction revealed substantial modifications in guanine bases upon the interaction of CPD-1 with dsDNA, thereby highlighting the pivotal role of our research findings. Our endeavor underscores the intricate interplay between electrochemistry, drug candidate, and DNA, underscoring the potential for innovative drug development and therapeutic advancement in the field of biomedicine.

The synthesis and characterization of CPD-1 as a potential drug candidate represent a pivotal advancement in drug development. This innovative compound holds promise as a cornerstone for the formulation of medications engineered to establish specific interactions with DNA, thereby potentially yielding more precisely targeted and efficacious therapies across a spectrum of diseases. The proposed simplified equation for the quantitative assessment of toxicity effects, rooted in alterations in electrochemical signals, constitutes a pragmatic instrument for both researchers and pharmaceutical entities. It furnishes a systematic means of gauging the influence of nascent drug candidates on DNA, thereby rationalizing the drug development process and bolstering safety appraisals. The profound modifications observed in guanine bases within our study, consequent to the interaction of CPD-1 with both single-stranded DNA (ssDNA) and double-stranded DNA (dsDNA), constitute pivotal discoveries. These findings illuminate the potential ramifications of CPD-1 and analogous compounds on DNA architecture, providing indispensable insights for the comprehensive evaluation of the safety and efficacy of these prospective drug candidates.

Conflicts of interest

There are no conflicts of interest in this work.

References

- [1] Singh P.K., Choudhary S., Kashyap A., Verma H., Kapil S., Kumar M., Arora M., Silakari O., An exhaustive compilation on chemistry of triazolopyrimidine: A journey through decades, *Bioorg. Chem.*, *88* (2019) 102919.
- [2] Aliwaini S., Abu Thaher B., Al-Masri I., Shurrab N., El-Kurdi S., Schollmeyer D., Qeshta B., Ghunaim M., Csuk R., Laufer S., Kaiser L., Deigner H.P., Design, synthesis and biological evaluation of novel pyrazolo [1, 2, 4] triazolopyrimidine derivatives as potential anticancer agents, *Molecules*, *26*(13) (2021) 4065.
- [3] Bailey B.L., Nguyen W., Ngo A., Goodman C.D., Gancheva M.R., Favuzza P., Sanz L.M., Gamo F.J., Lowes K.N., McFadden G.I., Wilson D.W., Laleu B., Brand S., Jackson P.F., Cowman A.F., Sleebs B.E., Optimisation of 2-(N-phenyl carboxamide) triazolopyrimidine antimalarials with moderate to slow acting erythrocytic stage activity, *Bioorg. Chem.*, *115* (2021) 105244.
- [4] Ortiz Zacarías N.V., van Veldhoven J.P., den Hollander L.S., Dogan B., Openy J., Hsiao Y.Y., Lenselink E.B., Heitman L.H., IJzerman, A.P., Synthesis and pharmacological evaluation of triazolopyrimidinone derivatives as noncompetitive, intracellular antagonists for CC chemokine receptors 2 and 5, *J. Med. Chem.*, *62*(24) (2019) 11035-11053.
- [5] Abd Al Moaty M.N., El Ashry E.S.H., Awad L.F., Ibrahim N.A., Abu-Serie M.M., Barakat A., Altowyan M.S., Teleb M., Enhancing the Anticancer Potential of Targeting Tumor-Associated Metalloenzymes via VEGFR Inhibition by New Triazolo [4, 3-a] pyrimidinone Acyclo C-Nucleosides Multitarget Agents, *Molecules*, *27*(8) (2022) 2422.
- [6] Brockman R.W., Sparks C., Hutchison D.J., Skipper H.E., A mechanism of resistance to 8-azaguanine I. Microbiological studies on the metabolism of purines and 8-azapurines, *Cancer Res.*, *19*(2) (1959) 177.
- [7] Gigante A., Gómez-SanJuan A., Delang L., Li C., Bueno O., Gamo A.M., Priego E.M., Camarasa M.J., Jochmans D., Leyssen P., Decroly E., Coutard B., Querat G., Neyts J., Pérez-Pérez M.J., Antiviral activity of [1, 2, 3] triazolo [4, 5-d] pyrimidin-7 (6H)-ones against chikungunya virus targeting the viral capping nsP1, *Antiviral Res.*, *144* (2017) 216-222.
- [8] Harrison D., Bock M.G., Doedens J.R., Gabel C.A., Holloway M.K., Lewis A., Scanlon J., Sharpe A., Simpson I.D., Smolak P., Wishart G., Watt A.P., Discovery and Optimization of Triazolopyrimidinone Derivatives as Selective NLRP3 Inflammasome Inhibitors, *ACS Med. Chem. Lett.*, *13*(8) (2022) 1321-1328.
- [9] Chung S., Sugimoto Y., Huang J., Zhang M., Iron oxide nanoparticles decorated with functional peptides for a targeted siRNA delivery to glioma cells, *ACS Appl Mater Interfaces*, *15*(1) (2022) 106-119.
- [10] Sabir A., Majeed M.I., Nawaz H., Rashid N., Javed M.R., Iqbal M.A., Shahid Z., Ashfaq R., Sadaf N., Fatima, R., Sehar A., Surface-enhanced Raman spectroscopy for studying the interaction of N-propyl substituted imidazole compound with salmon sperm DNA, *Photodiagnosis Photodyn Ther.*, *41* (2023) 103262.
- [11] Sharifi-Rad A., Amiri-Tehranizadeh Z., Talebi A., Nosrati N., Medalian M., Pejhan M., Hamzkanloo N., Saberi M.R., Mokaberi P., Chamani J., Multi spectroscopic and molecular simulation studies of propyl acridone binding to calf thymus DNA in the presence of electromagnetic force, *BiolImpacts: BI*, *13*(1) (2023) 5.
- [12] Zhang J., Wang D., Chen H., Yuan X., Jiang X., Ai, L., He J., Chen F., Xie S., Cui C., Tan W., A pH-Responsive Covalent Nanoscale Device Enhancing Temporal and Force Stability for Specific Tumor Imaging, *Nano Lett.*, *22*(23) (2022) 9441-9449.
- [13] Congur G., Electrochemical Biosensors for Monitoring of Drug-DNA Interactions, *Curr. Top. Med. Chem.*, *23*(4) (2023) 316-330.
- [14] Topkaya S.N., Gelatin methacrylate (GelMA) mediated electrochemical DNA biosensor for DNA hybridization Biosensors and Bioelectronics, *64* (2015) 456-461.
- [15] Beitollahi H., Dehghannoudeh G., Moghaddam H.M., Forootanfar H., A Sensitive Electrochemical DNA Biosensor for Anticancer Drug Topotecan Based on Graphene Carbon Paste Electrode, *J. Electrochem. Soc.*, *164*(12), (2017) H812.
- [16] Kawde A.N., Baig N., Sajid M., Graphite pencil electrodes as electrochemical sensors for environmental analysis: a review of features, developments, and applications, *RSC Adv.*, *6* (2016), 91325-91340
- [17] Srinivas S., Kumar A.S., Surface-Activated Pencil Graphite Electrode for Dopamine Sensor Applications: A Critical Review, *Biosens.* *13*(3) (2023) 353.
- [18] Topkaya S.N., Ozyurt V.H., Cetin A.E., Otlés S., Nitration of Tyrosine and Its Effect on DNA Hybridization, *Biosens. Bioelectron.*, *102* (2018) 464-469.
- [19] Istanbulu H., Bayraktar G., Ozturk I., Coban G., Saylam M., Design, synthesis and bioactivity studies of novel triazolopyrimidinone compounds, *J. Res. Pharm.*, *26*(1) 2022.
- [20] Deng P., Xu Z., Kuang Y., Electrochemically reduced graphene oxide modified acetylene black paste electrode for the sensitive determination of bisphenol A, *J. Electroanal. Chem.*, *707* (2013). 7-14.
- [21] Brunetti B., About estimating the limit of detection by the signal to noise approach, *Pharm. Anal. Acta.*, *6*(4) (2014) e2014007.
- [22] Armbruster D.A., Pry T., Limit of blank, limit of detection and limit of quantitation. *Clin. Biochem. Rev.*, *29*(Suppl 1) (2008) S49-52.
- [23] Buleandra M., Popa D.E., David I.G., Bacalum E., David V., Ciucu A.A., Electrochemical behavior study of some selected phenylurea herbicides at activated pencil graphite electrode. Electrooxidation of linuron and monolinuron, *Microchem. J.*, *147* (2019) 1109-1116.
- [24] Wang X., Lim H.J., Son A., Characterization of denaturation and renaturation of DNA for DNA hybridization, *Environ. Health. Toxicol.*, *29* (2014) e2014007.
- [25] Sirajuddin M., Ali S., Badshah A., Drug-DNA interactions and their study by UV-Visible, fluorescence spectroscopies and cyclic voltametry, *J. Photochem. Photobiol. B, Biol.*, *124* (2013) 1-19.
- [26] Ramotowska S., Ciesielska A., Makowski M., What can electrochemical methods offer in determining DNA-drug interactions?, *Molecules*, *26*(11) (2021) 3478.

Design, Synthesis and Evaluation of Pyrrol-thiazole Derivatives as AChE and BuChE Inhibitory and Antioxidant Activities

Ulviye Acar Çevik^{1,a,*}, Tuğba Erçetin^{2,b}¹ Department of Pharmaceutical Chemistry, Faculty of Pharmacy, Anadolu University, Eskişehir 26470, Türkiye.² Department of Pharmacognosy, Eastern Mediterranean University, Cyprus.

*Corresponding author

Research Article

History

Received: 24/02/2023


Accepted: 14/11/2023

Copyright

©2023 Faculty of Science,
Sivas Cumhuriyet University

ABSTRACT

Thiazole rings are one of the most frequently used heterocyclic moieties and are found in a wide variety of biologically active chemicals. In this research project, we report the synthesis and biological activities of some new thiazole derivatives (2a-2c) as potent anti-Alzheimer's agents. These final compounds' structures were characterized by spectral (¹H NMR, ¹³C NMR, and MS spectra) analyses. The highest inhibitory activity against AChE was demonstrated by compound 2c (23.73 ± 0.018 %) with chloro substitution at the *meta* and *para* positions of the phenyl ring, while the highest inhibitory activity against BuChE was produced by compound 2a (28.87 ± 0.003 %) with cyano substitution at the *f* position of the phenyl ring. Ferrous ion-chelating and DPPH techniques were also used to assess the compounds' antioxidant properties. Compound 2a showed antioxidant effect according to the DPPH method with an IC₅₀ value of 27.18 ± 0.009 μM.

Keywords: Thiazole, Imidazole, AChE, BuChE, Antioxidant. uacar@anadolu.edu.tr <https://orcid.org/0000-0003-1879-1034> tugba.ercetin@emu.edu.tr <https://orcid.org/0000-0001-7774-7266>

Introduction

Alzheimer's disease (AD) is a neurological condition that progresses and is characterized by a permanent loss of memory. Although the etiology of the disease is not fully known, many factors seem to play a role. These; decline in acetylcholine (ACh) levels (cholinergic theory), the β -amyloid peptide (A β) deposition, hyperphosphorylated tau-protein deposition and the increase in oxidative stress [1]. According to the cholinergic theory, the death of cholinergic neurons in AD causes a deficiency of acetylcholine (ACh) in particular brain regions, which causes severe memory impairments and irreversible cognitive function impairment [2, 3]. The two main cholinesterase isoenzymes that break down ACh and stop its activities are acetylcholinesterase (AChE) and butyrylcholinesterase (BuChE). AChE hydrolyzes the bulk of ACh in the brain under physiologically normal conditions. As a result, the most popular methods for treating AD have focused on raising acetylcholine levels by decreasing the activity of the AChE enzyme [4-7]. AChE's sister enzyme, BChE, has recently drawn more attention due to a potential connection to Alzheimer's disease [8]. Inhibiting BuChE is a promising method for treating advanced AD, according to numerous research [9].

The European and American regulatory authorities have now approved tacrine, memantine, galantamine, and donepezil as four commonly used medications for the treatment of Alzheimer's disease (Figure 1) [10].

Thiazole nuclei are one of the most frequently used heterocyclic moieties and are found in a wide variety of biologically active chemicals [11, 12]. Thiazole is an

essential structural component of many commercially marketed medications, including as bacitracin, penciling, and ritonavir [8].

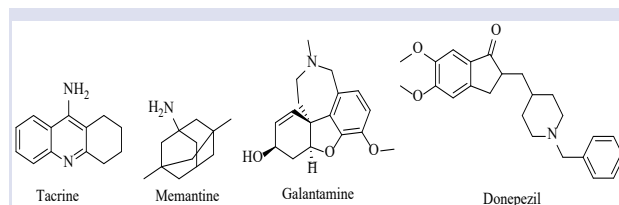


Figure 1. Chemical structure of drugs used for Alzheimer's disease

One of the first and most important pathophysiologies of AD is oxidative stress, according to several researchers. Oxidative stress also plays a significant part in the development of AD. By the deterioration of biological molecules like DNA, proteins, and lipids, it contributes to neurodegeneration. Antioxidant-active substances therefore appear to be helpful for the treatment of AD [13].

In this study, we synthesized new pyrrol-thiazole derivatives and their structures were elucidated by ¹H-NMR, ¹³C-NMR and HRMS. With the purpose of treating Alzheimer's disease, the AChE and BuChE inhibitory activities of these recently synthesized compounds was examined. In addition, the antioxidant effects of the compounds were evaluated by Ferrous ion-chelating and DPPH methods.

Materials and Methods

Chemistry

Synthesis of 2-((1H-pyrrol-2-yl)methylene)hydrazine-1-carbothioamide (1): 1H-pyrrol-2-carbaldehyde and thiosemicarbazide are dissolved in ethanol. After that, it undergoes 3 hours of reflux stirring. The mixture is chilled in an ice bath after the conclusion of the reaction. It is filtered to remove the precipitated product [18].

Synthesis of Target Compounds (2a-c): In ethanol, 2-((1H-pyrrol-2-yl)methylene)hydrazine-1-carbothioamide (1) and its derivative, 2-bromoacetophenone, are dissolved. After that, it is stirred for 4 hours of reflux. The mixture is chilled in an ice bath after the conclusion of the reaction. It is filtered to remove the precipitated product. From ethanol, it is crystallized and dried [18].

4-(4-Cyanophenyl)-2-(2-((1H-pyrrol-2-yl)methylene)hydrazineyl)thiazole (2a):

Yield: 75 %, M.P.= 194.7 °C. ¹H-NMR (300 MHz, DMSO-d₆): δ: 7.74-7.75 (1H, m, Aromatic CH), 7.81-7.82 (2H, m, Aromatic CH), 7.91 (1H, s, Aromatic CH), 8.11-8.15 (5H, m, Aromatic CH, CH=N), 13.22 (1H, s, NH). ¹³C-NMR (75 MHz, DMSO-d₆): δ= 115.40, 116.78 (CN), 123.65, 125.65, 126.40, 127.28, 127.90, 128.78, 131.05, 133.28, 138.78, 139.41 (CH=N). HRMS (m/z): [M+H]⁺ calcd for C₁₅H₁₁N₅S: 294.0808; found: 294.0814.

4-([1,1'-biphenyl]-4-yl)-2-(2-((1H-pyrrol-2-yl)methylene)hydrazineyl)thiazole (2b):

Yield: 78 %, M.P.= 179.2 °C. ¹H-NMR (300 MHz, DMSO-d₆): δ: 7.38-7.41 (1H, m, Aromatic CH), 7.46-7.51 (3H, m, Aromatic CH), 7.59 (1H, s, Aromatic CH), 7.72-7.77 (5H, m, Aromatic CH), 7.81-7.82 (1H, m, Aromatic CH), 7.96-7.98 (2H, m, Aromatic CH), 8.14 (1H, s, CH=N), 13.17 (1H, s, NH). ¹³C-NMR (75 MHz, DMSO-d₆): δ= 123.56, 123.76, 125.69, 126.09, 126.56, 127.21, 127.37, 127.73, 128.04, 128.89, 130.25, 131.09, 132.06, 135.33, 141.62 (CH=N), 148.20. HRMS (m/z): [M+H]⁺ calcd for C₂₀H₁₆N₄S: 345.1168; found: 345.1181.

4-(3,4-Dichlorophenyl)-2-(2-((1H-pyrrol-2-yl)methylene)hydrazineyl)thiazole (2c):

Yield: 74 %, M.P.= >350 °C. ¹H-NMR (300 MHz, DMSO-d₆): δ: 7.57-7.62 (3H, m, Aromatic CH), 7.74 (1H, s, Aromatic CH), 7.80-7.84 (3H, m, Aromatic CH), 8.14 (1H, s, CH=N), 13.11 (1H, s, NH). ¹³C-NMR (75 MHz, DMSO-d₆): δ= 123.06, 127.14, 127.43, 127.59, 128.93, 130.38, 130.81, 131.96, 133.49, 135.07, 138.10, 139.84 (CH=N), 144.32, 147.24. HRMS (m/z): [M+H]⁺ calcd for C₁₄H₁₀N₄SCl₂: 337.0076; found: 337.0091.

Cholinesterase Enzymes Inhibition Assay

The ability of each of the initially produced substances to obstruct AChE and BChE enzymes was evaluated. Using a modified version of Ellman's spectrophotometric technique, the compounds' AChE and BChE inhibitory activities were assessed [14].

Antioxidant Activity

Ferrous ion-chelating effect

By using the Chua et al. approach, the ferrous ion-chelating effect of each extract and the reference was calculated (2008). In a nutshell, different concentrations of the ethanol (80%)-dissolved extracts were incubated with a 200 L solution of 2 mM FeCl₂. 800 L of 5 mM ferrozine (Sigma, St. Louis, MO, USA) was added to the mixture to start the reaction, which was then given 10 minutes to stand at room temperature. With ethanol (80%) serving as a blank, the reaction mixture's absorbance was measured at 562 nm using a spectrophotometer (Varioskan Fast, Thermo Scientific, USA). The following formula was used to determine the ratio of inhibition of ferrozine-Fe²⁺ complex formation:

$$I\% = [(A_{\text{blank}} - A_{\text{sample}}) / A_{\text{blank}}] \times 100$$

where A_{sample} is the absorbance of the extracts/reference, and A_{blank} is the absorbance of the control reaction (consisting solely of ferrozine and FeCl₂). In this test, rutin served as the reference, while butylated hydroxytoluene (BHT) was purchased from Sigma Aldrich (USA). The findings of the analyses were presented as average values with standard error of the mean (S.E.M.) [15, 16].

DPPH radical scavenging activity

The 2,2-diphenyl-1-picrylhydrazyl (DPPH) radical scavenging activity was screened using Blois' UV technique. The reference molecule (gallic acid) and the compound concentrations of 40 M and 100 M were created using this approach in 20 L of methanol. Each solution received 180 L of a 0.15 mM DPPH solution in methanol. The amount of residual DPPH was measured at 520 nm following a 20-minute incubation at room temperature (Varioskan Flash, Thermo Scientific, USA). Using the following formula, the % DPPH radical scavenging activity was determined;

$$I\% = [(A_{\text{control}} - A_{\text{sample}}) / A_{\text{control}}] \times 100,$$

A_{control}: absorbance of the control reaction

A_{sample}: absorbance of the extracts/reference

The findings of the experiments were reported as average values with S.E.M. (standard error mean) [17]. The experiments were carried out in triplicate.

Results and Discussion

In this study, three new compounds with pyrrol-thiazole structure were synthesized. The synthetic strategy for target compounds 2a-c was depicted in Figure 2. The synthesis of the planned compounds was carried out in two steps. First of all, in the first step, 1H-pyrrol-2-carbaldehyde compound was reacted with thiosemicarbazide and thiosemicarbazone compound was obtained. In the second step, the thiosemicarbazone compound obtained in the first step was reacted with 2-bromoacetophenone derivative compounds and thiazole derivative compounds were obtained.

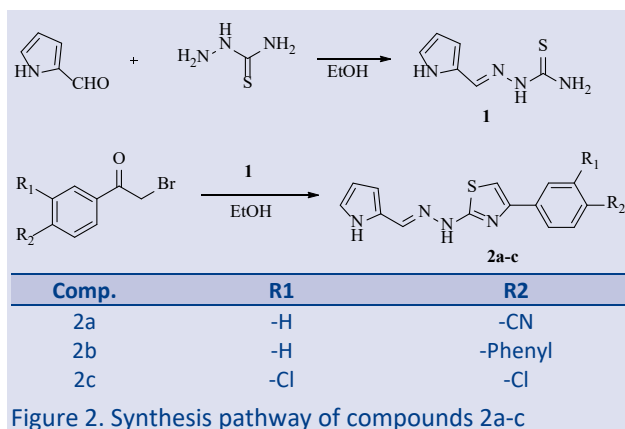
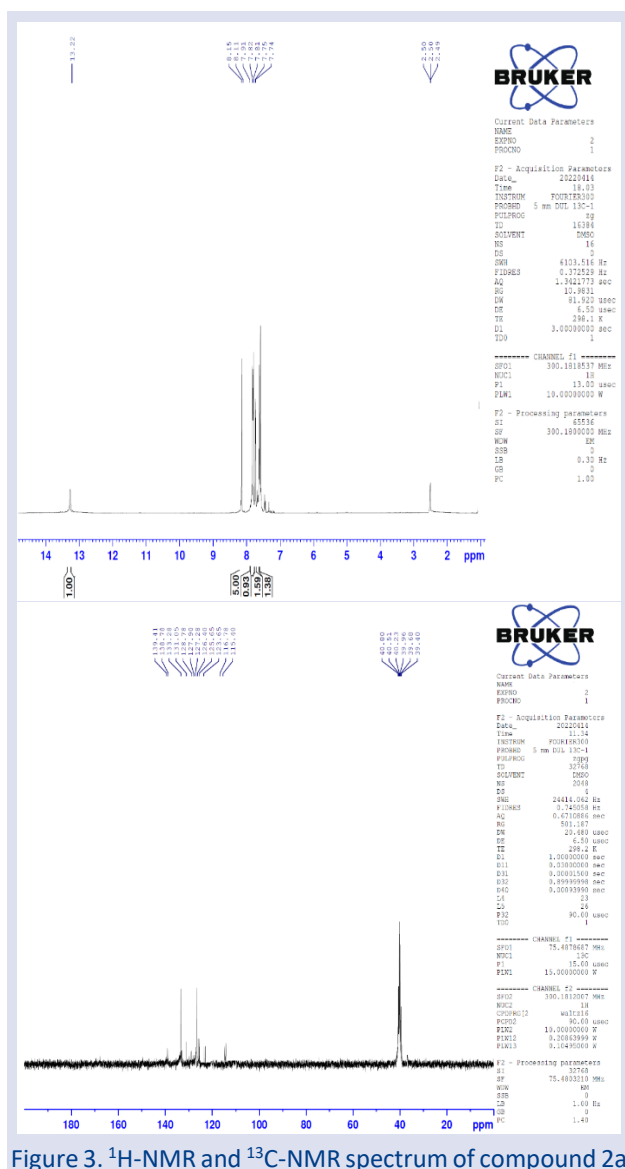


Figure 2. Synthesis pathway of compounds 2a-c

Using $^1\text{H-NMR}$, $^{13}\text{C-NMR}$, and HRMS, the structures of all compounds were clarified. The $^1\text{H-NMR}$ spectrum of final compounds show singlet in the range of 13.11-13.22 ppm, which was attributed to the NH group. Aromatic protons appeared as multiplets in the range of 7.57-8.15 ppm. The predicted chemical changes were followed by the appearance of the $^{13}\text{C-NMR}$ signals. The bulk of the produced compounds included M+1 peaks.

Figure 3. $^1\text{H-NMR}$ and $^{13}\text{C-NMR}$ spectrum of compound 2a

The Ellman technique was used to assess the inhibitory effects of compounds 2a–c against AChE and BuChE *in vitro*. Galantamine was used as a reference drug. The % inhibition values of compounds and reference drug at 50 μM concentration are shown in Table 1. The results showed that all substances had an inhibitory effect on the AChE enzyme, with a range of 7.22-23.73 %. According to the results, the inhibitory effect of all compounds against the BuChE enzyme ranged between 0.25-28.87 %. Compound 2a having cyano group at *para* position on phenyl ring were found to be the most active compound for BuChE among the series. Compound 2c having dichloro group at *para* and *meta* position on phenyl ring were found to be the most active for AChE among the series. Increased inhibition of compound 2c may be caused by the aryl ring's electron-withdrawing -Cl moiety.

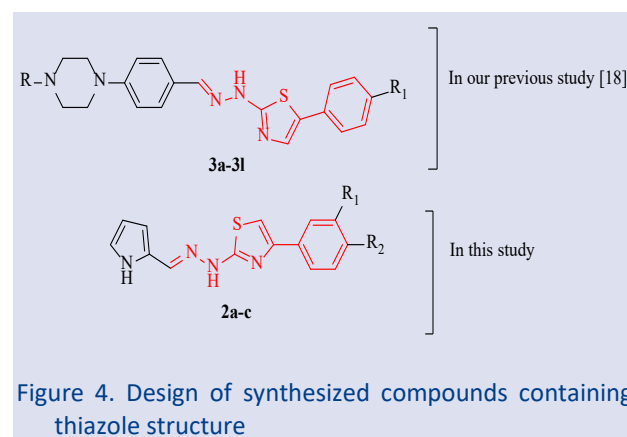


Figure 4. Design of synthesized compounds containing thiazole structure

In our previous study, compounds containing thiazole rings were synthesized and their effects against AChE and BuChE enzymes were examined [18]. As a result of the study, promising values were obtained. In this study, a smaller pyrrole ring was used instead of the piperazine-phenyl ring. However, as a result of the study, it was determined that the activity decreased with the introduction of the pyrrole ring.

Table 1. Inhibitory activity results of synthesized derivatives (2a-c) against AChE and BuChE enzymes

Comp.	% Inhibition (AChE) 50 μM	% Inhibition (BuChE) 50 μM
2a	7.22 \pm 0.006	28.87 \pm 0.003
2b	17.01 \pm 0.014	0.25 \pm 0.001
2c	23.73 \pm 0.018	6.26 \pm 0.008
Gal HBr	97.89 \pm 0.01	62.48 \pm 0.01

Table 2 shows the antioxidative activity results for produced compounds from Ion Chelating and DPPH methods. Among the compounds, compound 2a was found to be more effective than the reference drug gallic acid, with a value of 71.90 \pm 0.004 μM . Compound 2b, on the other hand, was found to have an antioxidant effect close to the reference drug.

Table 2. DPPH and Ion Chelating results of the synthesized compounds

Comp.	IC ₅₀ μM (DPPP)	DPPH	ION CHELATING
2a	27.18 ± 0.009	71.90 ± 0.004	4.26 ± 0.001
2b	31.91 ± 0.011	64.69 ± 0.011	10.20 ± 0.018
2c	> 60 μM	NA	NA
RUTIN 50 μM	-	-	13.21 ± 0.007
RUTIN 100 μM	-	-	28.14 ± 0.011
BHT 50 μM	-	-	2.57 ± 0.004
BHT 50 μM	-	-	7.06 ± 0.009
GALLIC ACID	-	70.29 ± 0.005	-

Conclusion

In this study, three new compounds with pyrrole-thiazole structure were synthesized and their structures were elucidated by spectroscopic methods. The activities of the compounds against AchE and BuChE enzymes were evaluated. In addition, since oxidative stress is known to be effective in Alzheimer's disease, the antioxidant effects of the compounds were evaluated with two different methods. When the activity results were evaluated, it was found that compound 2a was the most effective compound against both BuChE enzyme in the series. In addition, it is seen that this compound shows more effective antioxidant activity than the reference drug according to the DPPH method.

Conflicts of interest

The authors declare that there are no conflicts of interest.

References

- [1] Han C., Wei B.B., Shang P.P., Guo X.Y., Bai L.G., & Ma Z.Y., Design, synthesis and evaluation of 2-(2-oxoethyl) pyrimidine-5-carboxamide derivatives as acetylcholinesterase inhibitors, *Bioorg. Med. Chem. Lett.*, 72 (2022) 128873.
- [2] Messaad M., Dhouib I., Abdelhedi M., & Khemakhem B., Synthesis, bioassay and molecular docking of novel pyrazole and pyrazolone derivatives as acetylcholinesterase inhibitors, *J. Mol. Struct.*, 1263 (2022) 133105.
- [3] Mishra D., Fatima A., Kumar P., Munjal N.S., Singh B.K., Singh R., Synthesis of Benzothiazole Linked Triazole Conjugates and Their Evaluation Against Cholinesterase Enzymes, *Chem. Select.*, 7 (2022) e202203060.
- [4] Faghih Z., Khabnadideh S., Sakhteman A., Shirazi A.K., Yari H.A., Chatraei A., Rezaei Z., Sadeghian S., Synthesis, biological evaluation and molecular modeling studies of novel carbazole-benzylpiperazine hybrids as acetylcholinesterase and butyrylcholinesterase inhibitors, *J. Mol. Struct.*, 1272 (2023) 134209.
- [5] Aggarwal N., Jain S., Chopra N., Hybrids of thiazolidin-4-ones and 1, 3, 4-thiadiazole: Synthesis and biological screening of a potential new class of acetylcholinesterase inhibitors, *Biointerface Res. Appl. Chem.*, 12 (2022) 2800-2812.
- [6] Baréa P., dos Santos Yamazaki D.A., de Souza Lima D., Seixas F.A.V., da Costa W.F., de Freitas Gauze G., & Sarraggiotto M.H., Design, synthesis, molecular docking and biological evaluation of β-carboline derivatives as cholinesterase inhibitors, *J. Mol. Struct.*, 1273 (2023) 134291.
- [7] Khan Y., Rehman W., Hussain R., Khan S., Malik A., Khan M., Liaqat A., Rasheed L., Begum F., Fazil S., Khan I., Abdellatif M.H., New biologically potent benzimidazole-based-triazole derivatives as acetylcholinesterase and butyrylcholinesterase inhibitors along with molecular docking study, *J. Heterocyc. Chem.*, 59 (2022) 2225-2239.
- [8] Ullah H., Jabeen M., Rahim F., Hussain A., Khan F., Perviaz M., Sajid M., Uddin I., Khan M.U., Nabi M., Synthesis, acetylcholinesterase and butyrylcholinesterase inhibitory potential and molecular docking study of thiazole bearing thiourea analogues, *Chem. Data Collect.*, 44 (2023) 100988.
- [9] Zhou S., & Huang G., Synthesis and inhibitory activities of inhibitors for the treatment of Alzheimer's disease, *Chem. Biol. Drug Des.*, 99 (2022) 727-735.
- [10] Silalai P., Jaipea S., Tocharus J., Athipornchai A., Suksamrarn A., & Saeeng R., New 1,2,3-Triazole-genipin Analogues and Their Anti-Alzheimer's Activity, *ACS omega.*, 7 (2022) 24302-24316.
- [11] Khan S., Ullah H., Taha M., Rahim F., Sarfraz M., Iqbal R., Iqbal N., Hussain R., Shah S.A.A., Ayub K., Albalawi M.A., Abdelaziz M.A., Alatawi F.S., Khan K.M., Synthesis, DFT Studies, Molecular Docking and Biological Activity Evaluation of Thiazole-Sulfonamide Derivatives as Potent Alzheimer's Inhibitors, *Molecules*, 28 (2023) 559.
- [12] Hussain R., Ullah H., Rahim F., Sarfraz M., Taha M., Iqbal R., Rehman W., Khan S., Shah S.A.A., Hyder S., Alhomrani M., Alamri A.S., Abdulaziz O., Abdelaziz M.A., Multipotent Cholinesterase Inhibitors for the Treatment of Alzheimer's Disease: Synthesis, Biological Analysis and Molecular Docking Study of Benzimidazole-Based Thiazole Derivatives, *Molecules*, 27 (2022) 6087.
- [13] Kilic B., Bardakkaya M., Sagkan R. I., Aksakal F., Shakila S., & Dogruer D.S., New thiourea and benzamide derivatives of 2-aminothiazole as multi-target agents against Alzheimer's disease: Design, synthesis, and biological evaluation, *Bioorg. Chem.*, 131 (2023) 106322.
- [14] Ellman G.L., Courtney K.D., Andres Jr V., & Featherstone R.M., A new and rapid colorimetric determination of acetylcholinesterase activity, *Biochem. Pharmacol.*, 7 (1961) 88-95.
- [15] Dinis T.C.P., Madeira V.M.C., Almeida L.M., Action of phenolic derivatives (acetaminophen, salicylate, and 5-aminosalicylate) as inhibitors of membrane lipid peroxidation and peroxy radical scavengers, *Arch. Biochem. Biophys.*, 315 (1994) 161-169.
- [16] Ercetin T., Senol F.S., Orhan I.E. and Toker G., Comparative assessment of antioxidant and cholinesterase inhibitory properties of the marigold extracts from *Calendula arvensis* L. and *Calendula officinalis* L, *Ind. Crops. Prod.*, 36 (2012) 203-208.
- [17] Blois M.S., Antioxidant determinations by the use of a stable free radical, *Nature*, 181 (1958) 1199-1200.
- [18] Işık A., Çevik U.A., Celik I., Erçetin T., Koçak A., Özkay Y., & Kaplancıklı Z.A., Synthesis, characterization, molecular docking, dynamics simulations, and in silico absorption, distribution, metabolism, and excretion (ADME) studies of new thiazolyldiazole derivatives as butyrylcholinesterase inhibitors, *Z. Naturforsch. C.*, 77 (2022) 447-457.

Hydroxychloroquine Modulates m6A RNA Methylation in Prostate Cancer Cells

Sevinc Yanar ^{1,2,a,*}, Merve Gulsen Bal Albayrak ^{1,b}

¹ Department of Medical Biology, Faculty of Medicine, Kocaeli University, Kocaeli, Türkiye.

² Department of Histology and Embryology, Faculty of Medicine, Sakarya University, Sakarya, Türkiye.

*Corresponding author

Research Article

History

Received: 30/05/2023

Accepted: 21/11/2023

Copyright




©2023 Faculty of Science,
Sivas Cumhuriyet University


ABSTRACT

Prostate cancer ranks as the second most prevalent cancer in men globally. One of the evolving subjects of investigation in prostate cancer is the role of N6-methyladenosine (m6A) modifications. Hydroxychloroquine (HCQ), an autophagy inhibitor, was shown to be promising in enhancing the response to chemotherapy in prostate cancer. The interplay between autophagy and m6A is an emerging area of research. However, the relationship between m6A modifications and HCQ remains unclear. The objective of this study was to examine the effect of HCQ on the regulation of m6A methylation in prostate cancer. Initially, the cytotoxic effect of HCQ on LNCaP and PC3 cells was evaluated. The IC₅₀ values for each cell were calculated. Finally, m6A levels in HCQ-treated and untreated cells were determined using m6A RNA methylation quantification kit. HCQ showed a significant dose- and time-dependent reduction in cell viability. Following HCQ treatment, a statistically significant decrease in m6A levels was observed: from 0.050±0.001% to 0.013±0.02% in PC3 cells and from 0.039±0.001% to 0.016±0.01% in LNCaP cells. The study unveils for the first time that HCQ affects m6A methylation in prostate cancer. The impact of autophagy inhibitor HCQ on m6A modifications introduces a novel dimension to its potential mechanisms of action.

Keywords: Prostate cancer, Hydroxychloroquine, Autophagy, RNA modifications, N6-methyladenosine (m6A).

 sevincsecer@gmail.com

 <https://orcid.org/0000-0002-6438-7385>

 mervegulsenbal@gmail.com

 <https://orcid.org/0000-0003-2444-4258>

Introduction

Prostate cancer is the second most common type of cancer in men worldwide, after lung cancer. The global incidence and mortality rates of prostate cancer display a correlation with advancing age, with the average age at diagnosis exceeding fifty [1]. Androgen receptor (AR) signaling plays pivotal roles in prostate development, maintenance, and the progression of prostate cancer. The standard treatment for advanced prostate cancer involves a combination of androgen deprivation therapy with anti-androgens and the administration of docetaxel. In most cases, androgen deprivation therapy may lose effectiveness, ultimately leading to the emergence of a life-threatening form of prostate cancer known as castration-resistant prostate cancer [2].

N6-methyladenosine (m6A) modifications represent the most prevalent type of modification in mammalian mRNAs when compared to other forms of RNA modifications. These modifications have been shown to play significant roles in tissue development, cell regeneration, differentiation, DNA damage response, and the development of cancer [3]. m6A modifications in mRNA or some non-coding RNAs such as long non-coding RNA (lncRNA) also play an important role in many cellular processes such as spermatogenesis, T-cell homeostasis, pluripotency and reprogramming [4,5]. In RNAs, m6A is typically located in stop codons, 3'UTR regions, and internal long exons. Following the discovery that m6A is the primary substrate of the fat mass and obesity-

associated protein (FTO) in a dynamic and reversible manner, m6A modifications have garnered considerable attention [4,5].

m6A modifications in mammals are subject to dynamic and reversible regulation by a group of regulatory proteins. These modifications are introduced to RNA by the methyltransferases METTL3 and METTL14 ("writers") and removed by FTO or ALKBH5 ("erasers"). The recognition of m6A occurs in the nucleus through YTHDC1, HNRNPA2B1, and IGF2BP1/2/3, while in the cytoplasm, it is facilitated by YTHDF1/2/3, YTHDC2, eIF3, and IGF2BP1/2/3 ("readers") [6]. Dysregulation of these regulator proteins has been linked to a number of pathophysiological processes in many disorders, including cancer [7]. METTL14 has been shown to suppress the metastatic potential of cancer cells in hepatocellular carcinoma [8]. Alterations in m6A writer and eraser proteins have been shown to be crucial for self-renewal and tumorigenesis in glioblastoma stem cells [9]. In addition, it has been suggested that FTO may have an oncogenic function by affecting the expression of tumor suppressor genes and oncogenes in AML and squamous cell lung cancer [10]. The prevalence of m6A-related genes is high in prostate cancer. These genes have been shown to play multiple roles in the development, progression, and metastases of prostate cancer [11,12]. Several research studies have also suggested that the regulation

of m6A could be a mechanism of resistance in the treatment of metastatic prostate cancer [13,14].

Hydroxychloroquine (HCQ) is a lysosomotropic amine traditionally used in the treatment of malaria and rheumatoid arthritis. As a derivative of chloroquine (CQ), HCQ has demonstrated the capability to inhibit autophagy. It has emerged as one of the most widely used autophagy inhibitors in both preclinical and clinical settings [15,16]. Although HCQ and CQ differ by only one hydroxyl group, the addition of this hydroxyl group results in a significant reduction in toxicity [17]. The inhibition of autophagy by HCQ enhances the response to chemotherapy in the majority of cases among prostate cancer patients [18,19]. The combination of HCQ with other agents could increase the cytotoxicity in cancer cells [20]. Autophagy levels rise due to castration resistance, but HCQ treatment has been found to reduce it [21]. Numerous clinical studies have been conducted and continue to explore the effects of using HCQ alone or in combination with other anticancer agents in various types of cancer [22–25]

The significance of m6A in prostate cancer and the highly effective nature of HCQ in this cancer type underscore the need for a study that delves into the connection between these two factors. Upon conducting a literature search, it became apparent that no such study currently exists. Consequently, we have devised a research plan aimed at investigating the impact of HCQ on m6A levels in prostate carcinoma cells LNCaP and PC3.

Materials and Method

Cell Culture and Preparation of Hydroxychloroquine

The human prostate cancer cell lines PC3, LNCaP, and healthy prostate cell line PNT1A were purchased from the American Type Culture Collection (ATCC, Rockville, MD, USA). The cells were grown in Roswell Park Memorial Institute-1640 medium (RPMI-1640, Thermo Fisher Scientific, MA, USA) containing high glucose, supplemented with 10% fetal bovine serum (FBS, Thermo Fisher Scientific, MA, USA) and 100 U/mL penicillin (Sigma-Aldrich, St Louis, MO, USA), and 100 µg/mL streptomycin (Sigma-Aldrich, St Louis, MO, USA). The cultures were maintained at 37 °C in a humidified incubator (Thermoscientific, MA, USA) with 5% CO₂.

In order to create a stock solution of 5 mM HCQ (TRC, Toronto, Canada), 5 mg of the compound was dissolved in 2300 µL of water. Subsequent dilutions for use in the experiments were prepared using RPMI-1640 (Thermo Fisher Scientific, MA, USA).

Cell Viability Assay

The effect of HCQ on the viability of prostate cancer cells PC3 and LNCaP, as well as normal prostate cells PNT1A, was assessed through the WST-1 assay (Roche Applied Science, Indianapolis, IN, USA). In brief, PC3, LNCaP, and PNT1A cells were seeded in 96-well culture plates at a density of 5×10^3 cells per well. Once the cells adhered, they were exposed to increasing concentrations

of HCQ for 24, 48, and 72 hours. Subsequently, 10 µL of WST-1 reagent (Roche Applied Science, Indianapolis, IN, USA) was added to each well at the end of each time point, and the cells were incubated at 37°C for 2 hours in the dark. After incubation, the cells were analyzed using a microplate reader at a wavelength of 450 nm (Thermoscientific, MA, USA). The half-maximal inhibitory concentration (IC₅₀) value of HCQ for each cancer cell line was determined using the linear regression model. Each experiment was conducted three times for each cell line.

Isolation of Total RNA

Total RNA from PC3 and LNCaP cells treated and untreated with IC₅₀ of HCQ was extracted using RNeasy Mini Kit (Qiagen, Valencia, CA, USA). The isolation procedure was carried out following the manufacturer's instructions. In summary, the cells were pelleted in a centrifuge and subsequently treated with the provided kit buffers in the specified sequence. The samples were then processed through the column and treated with deoxyribonuclease I. After a series of washing steps, the RNAs were collected in a sterile microcentrifuge tube using the elution solution. The purity and concentration of the RNAs were determined using Nanodrop (Thermoscientific, MA, USA). To assess RNA quality, the samples were electrophoresed on a 1% formaldehyde agarose gel, and the quality was confirmed by observing the presence of distinct 18S and 28S bands.

Determination of m6A Level

The commercial m6A RNA methylation quantification kit (Abcam, USA) was used in accordance with the manufacturer's instructions to measure the level of m6A in the total RNAs of treated and untreated cells. Briefly, 200 ng of RNA were seeded into each well, then a capture antibody solution was added to capture m6A RNAs. After the washing steps, a detection antibody solution was used to obtain signals. The colorimetric measurement of the m6A levels was then performed by reading each well's absorbance at a wavelength of 450 nm using a microplate reader (Thermoscientific, USA).

Statistical Analysis

GraphPad Prism 9.1.0 (La Jolla, CA, ABD) was utilized to perform statistical analysis. The data were displayed as the mean standard deviation of three independent experiments. Statistical differences between groups were analyzed considering sample distribution. m6A test results were analyzed by Student's t-test. Two-way analysis of variance (ANOVA) followed by Tukey's test was carried out for multiple comparisons of WST-1 data.

Results

Effect of HCQ on Cell Proliferation

Increasing HCQ concentrations (10, 20, 40, 60, 80 and 100 µM) were administered to LNCaP and PC3 cells for 24, 48 and 72 hours to examine the sensitivity of each cell type to the growth-inhibiting effects of HCQ. The data from WST-1 assay indicated that HCQ inhibited the growth of LNCaP and PC3 cells in a dose- and time-dependent

manner. For PC3 cells, the viability of cells was statistically significantly reduced ($p < 0.05$) at 80 μM and 100 μM of HCQ after 24 hours incubation, whereas significantly reduced viability was observed at 40 μM and higher concentrations for 48 hours treatment. Concentrations above 20 μM statistically significantly decreased the viability when treated for 72 hours (Figure 1a). Regarding LNCaP cells, cellular viability was statistically significantly decreased ($p < 0.05$) at 40 μM and higher concentrations during 24 and 48-hour treatments. All HCQ concentrations statistically significantly reduced viability when applied for 72 hours (Figure 1b). The cytotoxic effect of HCQ on healthy cells was determined using PNT1A normal prostate epithelial cells. The results of the WST-1 assay revealed that HCQ did not have a statistically significant effect on viability up to 100 μM treatment for 48 and 72 hours (Figure 1c).

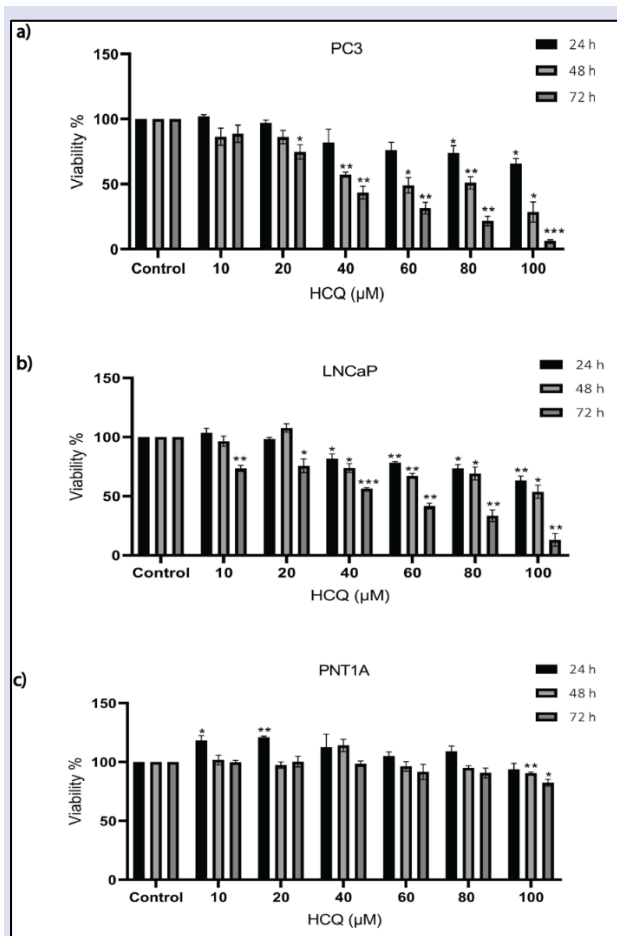


Figure 1: Effects of hydroxychloroquine on a) PC3, b) LNCaP, and c) PNT1A cell viability (* $P < 0.05$, ** $P < 0.01$, *** $P < 0.005$)

Based on the outcomes of the cell viability assay by WST-1, the IC_{50} value of HCQ for each cancer cell line was calculated to determine the concentration at which the drug would be applied to cells in the m6A assay. The calculation was carried out using the linear regression model. IC_{50} values for each time point and cell line were given in Table 1. Subsequent experiments were conducted utilizing the determined IC_{50} values. PNT1A

cells were exclusively employed for evaluating the cytotoxicity of HCQ.

Table 1: IC_{50} values of hydroxychloroquine for PC3 and LNCaP cells

	IC_{50} (μM)	
	PC3	LNCaP
24hr	284,7	133,2
48hr	67,9	105,7
72hr	44,9	52,0

Alteration in m6A Levels Following HCQ Treatment

The purity and quality of the isolated RNAs from PC3 and LNCaP cells were verified by the presence of distinct 28S and 18S ribosomal RNA (rRNA) bands, as observed on a 1% agarose gel. These bands were quantified using the ImageJ software program to analyze their intensities and served as internal RNA standards. The presence of these distinct rRNA bands, which are major components, validated and confirmed the integrity of the RNA samples and ensured that there was no degradation of the products. Additionally, our results achieved the generally accepted 28S:18S rRNA ratio of 2:1 for mammalian rRNA, indicating good RNA quality [26]. To assess the change in m6A levels in the samples, a commercial m6A RNA methylation quantification kit was employed. The cells were treated with the IC_{50} concentrations of the drug for 72 hours. Thus, PC3 cells were treated with 44,9 μM of HCQ whereas LNCaP cells were treated with 52 μM of HCQ. Following the m6A quantification assay and the determination of optical densities, m6A% values were calculated in accordance with the manufacturer's protocol. Statistical analysis of the data demonstrated that the m6A level of both PC3 and LNCaP cells was statistically significantly reduced upon treatment with HCQ ($p < 0.05$) (Figure 2). The m6A level of PC3 cells, which was $0.050 \pm 0.001\%$ in the control group, decreased to $0.013 \pm 0.02\%$ in the HCQ-treated group. On the other hand, the m6A level of LNCaP cells, which was $0.039 \pm 0.001\%$ in the control group, reduced to $0.016 \pm 0.01\%$ in the HCQ-treated group. This represented a 2.4-fold decrease in m6A levels for LNCaP cells and a 3.9-fold decrease for PC3 cells.

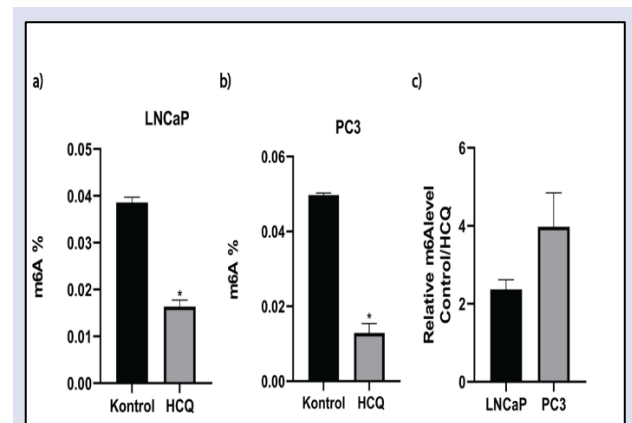


Figure 2: m6A percentage in a) PC3 and b) LNCaP cells after treatment with hydroxychloroquine (* $P < 0.0001$). c) Relative m6A level of control cells to PC3 and LNCaP cells after hydroxychloroquine treatment

Discussion

Given the absence of evidence regarding the relationship between HCQ and m6A, it was aimed to investigate this association using two distinct subtypes of prostate carcinoma cells. Androgen dependency is a crucial characteristic of prostate carcinoma that significantly influences treatment outcomes [2]. In this study, PC3 and LNCaP cell lines were employed, representing androgen-independent and androgen-dependent human prostate cancer cell lines, respectively. PC3 cells are derived from bone metastases and display highly aggressive behavior, which contrasts with the behavior seen in most clinical cases of prostate cancer. Conversely, LNCaP cells originate from lymph node metastases and exhibit a biologically slower behavior, consistent with most cases observed in clinical settings [27,28]. Because of these differences and the varying effects of drugs on the subtypes, both cell lines were used in this study to provide a comprehensive approach.

Over the past few decades, Hydroxychloroquine (HCQ) has emerged as a compelling candidate for cancer therapy, showcasing its remarkable capacity to impede the process of autophagy. This unique characteristic has brought HCQ to the forefront of research in the field of oncology, where it has garnered significant attention for its potential anti-cancer properties across a range of cancer types, including prostate cancer [15,16]. It influences how lysosomes break down proteins by altering the pH level and encourages the accumulation of LC3 and P62 proteins in autophagy bodies [29,30]. The inhibition of autophagy by HCQ has been shown to sensitize tumors to previously resistant treatment regimens or enhance the response to existing treatments [18,19]. In a study investigating the effect of the combination of HCQ with an apoptosis inhibitor on prostate cancer cells, it was shown that the combination of the drugs increased cytotoxicity in prostate cancer *in vitro* and *in vivo*. The modulation of reactive oxygen species was suggested as a potential mechanism for the increased cytotoxicity due to autophagy inhibition [20]. In an *in vivo* study, researchers have shown that HCQ also inhibits autophagy in castration-resistant prostate cancer cells and stated that cellular apoptosis is induced as a result of inhibition [21]. Numerous investigations have delved into the potential applications of HCQ in the realm of cancer, with a particular emphasis on its connection to the intricate autophagy process. However, despite the substantial body of research in this area, there remains a notable dearth of studies scrutinizing the interplay between HCQ and the m6A mechanisms, which are critical in the regulation of gene expression and post-transcriptional modifications [4,5]. Considering this research gap, our study aimed to investigate this effect in prostate cancer cells. At first, the effect of HCQ on cellular proliferation was investigated and the concentration to be used for the m6A test was determined. WST-1 assay data revealed that HCQ had dose- and time-dependent anti-proliferative effects on both PC3 and LNCaP cells. Importantly, it was

found to have no toxic effect on normal prostate cells, indicating that HCQ could be safely used in the study. The IC₅₀ concentration of the drug was determined for both cell lines and found to be fairly close to each other as, 44,9 μ M for PC3 and 52 μ M for LNCaP cells when treated for 72 hours. Consequently, these concentrations of HCQ were applied to the cells for the specified time period before conducting the m6A assay.

Within the context of prostate cancer, the study of m6A-related genes has gained substantial attention, primarily due to their pivotal roles in numerous aspects of cancer, encompassing the initiation of the disease, its relentless progression, and the critical influence they exert on responses to therapeutic interventions. [11–13,31]. Dysregulated m6A modification machinery has been found to impact the expression of genes associated with cell migration, invasion, epithelial-to-mesenchymal transition, leading to enhanced metastatic potential, and genes linked to drug metabolism, DNA repair, and cellular survival, contributing to resistance to therapeutic interventions [11,12]. Furthermore, altered m6A modifications in genes regulating AR expression and activity can influence AR mRNA stability and translation efficiency, thereby affecting AR signaling and contributing to prostate cancer progression. Studies have shown that m6A methylases METTL3 and METTL14 are upregulated in prostate cancer, and their overexpression promotes cancer cell proliferation and invasion. Additionally, the downregulation of the demethylase FTO has been observed, correlating with increased tumor growth and aggressiveness [13,14]. Altered expression of the m6A reader YTHDF2 has also been reported, with its loss being associated with poor patient survival. These findings suggest that m6A levels are elevated in prostate cancer. These findings collectively point to a pronounced elevation in m6A levels within the context of prostate cancer [11,12]. This emerging understanding underscores the complexity of the m6A regulatory network and its profound impact on the clinical landscape, offering a promising avenue for further investigations into the molecular intricacies of the disease and the development of potential therapeutic strategies. When LNCaP and PC3 cells were treated with HCQ, a decrease in the total m6A level was observed. Specifically, the m6A level exhibited a 2.4-fold decrease in LNCaP cells, while a 3.9-fold decline was observed in PC3 cells. This outcome implies that one of the anti-carcinogenic mechanisms of action of HCQ in prostate cancer may involve the disruption of m6A regulations. It's even conceivable that the m6A modification machinery is more dysregulated in PC3 cells compared to LNCaP cells. The fact that HCQ had a more pronounced effect on PC3 cells may suggest that it interferes with m6A modifications in genes associated with cell movement, invasion, DNA repair, or cell survival, as opposed to genes controlling AR regulation.

Autophagy and m6A (N6-methyladenosine) are two distinct biological processes that play important roles in cellular function and regulation. Intriguingly, the interface between autophagy and m6A has garnered attention, as

various m6A writers and erasers have been identified as pivotal players in regulating autophagy-related processes [32,33]. For example, several m6A writers and erasers have been found to regulate autophagy-related processes. Inhibition of the m6A writer METTL3 was shown to promote autophagy and enhance cellular response to nutrient deprivation [34,35], while the inhibition or downregulation of the m6A erasers ALKBH5 and FTO were found to inhibit autophagy under specific conditions [36,37]. m6A modification on specific mRNAs such as ATG5 or ATG7 can affect their stability and translation, thereby modulating the levels of autophagy-related proteins [36]. Additionally, m6A modification has been linked to the regulation of the autophagy-related kinase ULK1, a key initiator of the autophagy process [38,39]. The intricate crosstalk between autophagy and m6A modifications continues to be an evolving area of research, with the precise underlying mechanisms still unraveling [32,33]. Although the precise mechanisms underlying the interplay between autophagy and m6A are still being elucidated, these findings suggest that m6A modification can influence autophagy and, in turn, autophagy-related processes can impact the m6A landscape.

HCQ, in this context, emerges as a notable player. HCQ has demonstrated considerable promise as an autophagy inhibitor, a property that has been substantiated in preclinical studies and some clinical trials [22–25]. However, it has not been extensively explored in the context of m6A modifications until now. This dual role of HCQ, as an autophagy modulator and its potential connection to m6A modifications, exemplifies the multifaceted nature of this drug and its significance in the broader landscape of cancer and cellular regulation research. As the exploration of these interrelated processes unfolds, it promises to open up novel avenues for therapeutic interventions and a deeper understanding of the intricate biology governing both normal and diseased cellular states. Our results reveal that the m6A level in prostate cancer cells is significantly reduced when treated with HCQ. This observation could suggest that autophagy is inhibited due to m6A modifications, or it could mean that the m6A level changes because of autophagy inhibition. In either case, these findings hint at a new dimension for research involving HCQ. It's crucial to recognize that the field of m6A research is continuously evolving. To gain a comprehensive understanding of the intricate connection between HCQ and m6A modification in cancer biology, extensive research, including investigations into m6A regulatory proteins, is necessary. These studies will provide insights into the magnitude and functional implications of this relationship, offering valuable contributions to cancer research.

Conflicts of Interest

There are no conflicts of interest in this work.

References

- [1] Rawla P., Epidemiology of Prostate Cancer, *World J. Oncol.*,10(2) (2019) 63–89.
- [2] Kyprianou N., English H.F., Isaacs J.T., Programmed cell death during regression of PC-82 human prostate cancer following androgen ablation, *Cancer Res.*, 50(12) (1990) 3748–53.
- [3] Xiang Y., Laurent B., Hsu C.H., Nachtergaele S., Lu Z., Sheng W., Xu C., Chen H., Ouyang J., Wang S., Ling D., Hsu P.H., Zou L., Jambhekar A., He C., Shi Y., Corrigendum: RNA m6A methylation regulates the ultraviolet-induced DNA damage response, *Nature*, 552(7685) (2017) 430.
- [4] Aguilo F., Zhang F., Sancho A., Fidalgo M., Cecilia S.D., Vashisht A., Lee D.F., Chen C.H., Rengasamy M., Andino B., Jahouh F., Roman A., Krig S.R., Wang R., Zhang W., Wohlschlegel J.A., Wang J., Walsh M.J., Coordination of m(6)A mRNA Methylation and Gene Transcription by ZFP217 Regulates Pluripotency and Reprogramming, *Cell Stem Cell.*, 17(6) (2015) 689–704.
- [5] [5] Lin Z., Hsu P.J., Xing X., Fang J., Lu Z., Zou Q., Zhang K.J., Zhang X., Zhou Y., Zhang T., Zhang Y., Song W., Jia G., Yang X., He C., Tong M.H., Mettl3-/Mettl14-mediated mRNA N6-methyladenosine modulates murine spermatogenesis, *Cell Res.*, 27(10) (2017) 1216–30.
- [6] Luo J., Liu H., Luan S., He C., Li Z., Aberrant Regulation of mRNA m6A Modification in Cancer Development, *Int. J. Mol. Sci.*, 19(9) (2018) 2515.
- [7] Fitzsimmons C.M., Batista P.J., It's complicated... m6A-dependent regulation of gene expression in cancer, *Biochimica Et Biophysica Acta Bba - Gene Regul Mech.*, 1862(3) (2019) 382–93.
- [8] Ma J., Yang F., Zhou C., Liu F., Yuan J., Wang F., Wang T., Xu Q., Zhou W., Sun S., METTL14 suppresses the metastatic potential of hepatocellular carcinoma by modulating N6-methyladenosine-dependent primary MicroRNA processing, *Hepatology.*, 65(2) (2017) 529–43.
- [9] Cui Q., Shi H., Ye P., Li L., Qu Q., Sun G., Sun G., Lu Z., Huang Y., Yang C.G., Riggs A.D., He C., Shi Y., m6A RNA Methylation Regulates the Self-Renewal and Tumorigenesis of Glioblastoma Stem Cells, *Cell Reports*, 18(11) (2017) 2622–34.
- [10] Li Z., Weng H., Su R., Weng X., Zuo Z., Li C., Huang H., Nachtergaele S., Dong L., Hu C., Qin X., Tang L., Wang Y., Hong G.M., Huang H., Wang X., Chen P., Gurbuxani S., Arnovitz S., Li Y., Li S., Strong J., Neilly M.B., Larson R.A., Jiang X., Zhang P., Jin J., He C., Chen J., FTO Plays an Oncogenic Role in Acute Myeloid Leukemia as a N 6-Methyladenosine RNA Demethylase, *Cancer Cell*, 31(1) (2017) 127–41.
- [11] Li J., Xie H., Ying Y., Chen H., Yan H., He L., Xu M., Xu X., Liang Z., Liu B., Wang X., Zheng X., Xie L., YTHDF2 mediates the mRNA degradation of the tumor suppressors to induce AKT phosphorylation in N6-methyladenosine-dependent way in prostate cancer, *Mol. Cancer*, 19(1) (2020) 152.
- [12] Chen Y., Pan C., Wang X., Xu D., Ma Y., Hu J., Chen P., Xiang Z., Rao Q., Han X., Silencing of METTL3 effectively hinders invasion and metastasis of prostate cancer cells, *Theranostics*, 11(16) (2021) 7640–57.
- [13] Cotter K.A., Gallon J., Uebersax N., Rubin P., Meyer K.D., Piscuoglio S., Jaffrey S.R., Rubin M.A., Mapping of m6A and Its Regulatory Targets in Prostate Cancer Reveals a METTL3-Low Induction of Therapy Resistance, *Mol Cancer Res.*, 19(8) (2021) 1398–411.

- [14] Zhang F., Chen F., Wang C., Zhou F., The functional roles of m6A modification in prostate cancer, *Proteom Clin Appl.*, (2023) e2200108.
- [15] Farrow J.M., Yang J.C., Evans C.P., Autophagy as a modulator and target in prostate cancer, *Nat. Rev. Urol.*, 11(9) (2014) 508–16.
- [16] Sotelo J., Briceño E., López-González M.A., Adding chloroquine to conventional treatment for glioblastoma multiforme: a randomized, double-blind, placebo-controlled trial, *Ann Intern Med.*, 144(5) (2006) 337–43.
- [17] Ben-Zvi I., Kivity S., Langevitz P., Shoenfeld Y., Hydroxychloroquine: From Malaria to Autoimmunity, *Clin. Rev. Allerg. Immu.*, 42(2) (2012) 145–53.
- [18] Carew J.S., Kelly K.R., Nawrocki S.T., Autophagy as a target for cancer therapy: new developments, *Cancer Management Res.*, 4 (2012) 357–65.
- [19] Levy J.M.M., Thompson J.C., Griesinger A.M., Amani V., Donson A.M., Birks D.K., Morgan M.J., Mirsky D.M., Handler M.H., Foreman N.K., Thorburn A., Autophagy Inhibition Improves Chemosensitivity in BRAFV600E Brain Tumors, *Cancer Discov.*, 4(7) (2014) 773–80.
- [20] Saleem A., Dvorzhinski D., Santanam U., Mathew R., Bray K., Stein M., White E., DiPaola R.S., Effect of dual inhibition of apoptosis and autophagy in prostate cancer, *Prostate*, 72(12) (2012) 1374–81.
- [21] Ling S.T., Deng C.L., Huang L., Yao Q.S., Liu C., Sun C.T., Wang L., Yang Y., Gong X.X., Chen C.B., Hydroxychloroquine Blocks Autophagy and Promotes Apoptosis of the Prostate after Castration in Rats, *Urol Int.*, 104(11–12) (2019) 968–74.
- [22] Rosenfeld M.R., Ye X., Supko J.G., Desideri S., Grossman S.A., Brem S., Mikkelsen T., Wang D., Chang Y.C., Hu J., McAfee Q., Fisher J., Troxel A.B., Piao S., Heitjan D.F., Tan K.S., Pontiggia L., O'Dwyer P.J., Davis L.E., Amaravadi R.K., A phase I/II trial of hydroxychloroquine in conjunction with radiation therapy and concurrent and adjuvant temozolomide in patients with newly diagnosed glioblastoma multiforme, *Autophagy*, 10(8) (2014) 1359–68.
- [23] Rangwala R., Leone R., Chang Y.C., Fecher L.A., Schuchter L.M., Kramer A., Tan K.S., Heitjan D.F., Rodgers G., Gallagher M., Piao S., Troxel A.B., Evans T.L., DeMichele A.M., Nathanson K.L., O'Dwyer P.J., Kaiser J., Pontiggia L., Davis L.E., Amaravadi R.K., Phase I trial of hydroxychloroquine with dose-intense temozolomide in patients with advanced solid tumors and melanoma, *Autophagy*, 10(8) (2014) 1369–79.
- [24] Vogl D.T., Stadtmauer E.A., Tan K.S., Heitjan D.F., Davis L.E., Pontiggia L., Rangwala R., Piao S., Chang Y.C., Scott E.C., Paul T.M., Nichols C.W., Porter D.L., Kaplan J., Mallon G., Bradner J.E., Amaravadi R.K., Combined autophagy and proteasome inhibition, *Autophagy*, 10(8) (2014) 1380–90.
- [25] Mahalingam D., Mita M., Sarantopoulos J., Wood L., Amaravadi R.K., Davis L.E., Mita A.C., Curiel T.J., Espitia C.M., Nawrocki S.T., Giles F.J., Carew J.S., Combined autophagy and HDAC inhibition, *Autophagy*, 10(8) (2014) 1403–14.
- [26] Tuma R.S., Beaudet M.P., Jin X., Jones L.J., Cheung C.Y., Yue S., Singer V.L., Characterization of SYBR Gold Nucleic Acid Gel Stain: A Dye Optimized for Use with 300-nm Ultraviolet Transilluminators, *Anal Biochem.*, 268(2) (1999) 278–88.
- [27] Horoszewicz J.S., Leong S.S., Kawinski E., Karr J.P., Rosenthal H., Chu T.M., Mirand E.A., Murphy G.P., LNCaP model of human prostatic carcinoma, *Cancer Res.*, 43(4) (1983) 1809–18.
- [28] Bokhoven A.V., Varella-Garcia M., Korch C., Johannes W.U., Smith E.E., Miller H.L., Nordeen S.K., Miller G.J., Lucia M.S., Molecular characterization of human prostate carcinoma cell lines, *Prostate*, 57(3)(2003)205–25.
- [29] Solomon V.R., Lee H., Chloroquine and its analogs: A new promise of an old drug for effective and safe cancer therapies, *Eur. J. Pharmacol.*, 625(1–3) (2009) 220–33.
- [30] Kumano M., Furukawa J., Shiota M., Zardan A., Zhang F., Beraldi E., Wiedmann R.M., Fazli L., Zoubeidi A., Gleave M.E., Cotargeting Stress-Activated Hsp27 and Autophagy as a Combinatorial Strategy to Amplify Endoplasmic Reticular Stress in Prostate Cancer, *Mol. Cancer Ther.*, 11(8) (2012) 1661–71.
- [31] Eide T., Ramberg H., Glackin C., Tindall D., Taskén K.A., TWIST1, A novel androgen-regulated gene, is a target for NKX3-1 in prostate cancer cells, *Cancer Cell Int.*, 13(1) (2013) 4–4.
- [32] Liang J., Sun J., Zhang W., Wang X., Xu Y., Peng Y., Zhang L., Xiong W., Liu Y., Liu H., Novel Insights into The Roles of N6-methyladenosine (m6A) Modification and Autophagy in Human Diseases, *Int. J. Biol. Sci.*, 19(2) (2023) 705–20.
- [33] Jo H., Shim K., Jeoung D., Roles of RNA Methylations in Cancer Progression, Autophagy, and Anticancer Drug Resistance, *Int. J. Mol. Sci.*, 24(4) (2023) 4225.
- [34] Lin Z., Niu Y., Wan A., Chen D., Liang H., Chen X., Sun L., Zhan S., Chen L., Cheng C., Zhang X., Bu X., He W., Wan G., RNA m6 A methylation regulates sorafenib resistance in liver cancer through FOXO3-mediated autophagy, *Embo J.*, 39(12) (2019) e103181.
- [35] Liu S., Li Q., Li G., Zhang Q., Zhuo L., Han X., Zhang M., Chen X., Pan T., Yan L., Jin T., Wang J., Lv Q., Sui X., Xie T., The mechanism of m6A methyltransferase METTL3-mediated autophagy in reversing gefitinib resistance in NSCLC cells by β -elemene, *Cell Death Dis.*, 11(11) (2020)
- [36] Wang X., Wu R., Liu Y., Zhao Y., Bi Z., Yao Y., Liu Q., Shi H., Wang F., Wang Y., m 6 A mRNA methylation controls autophagy and adipogenesis by targeting Atg5 and Atg7. *Autophagy.*, 16(7) (2019) 1221–35.
- [37] Xu Y., Zhou J., Li L., Yang W., Zhang Z., Zhang K., Ma K., Xie H., Zhang Z., Cai L., Gong Y., Gong K., FTO-mediated autophagy promotes progression of clear cell renal cell carcinoma via regulating SIK2 mRNA stability, *Int. J. Biol. Sci.*, 18(15) (2022) 5943–62.
- [38] Jin S., Zhang X., Miao Y., Liang P., Zhu K., She Y., Wu Y., Liu D.A., Huang J., Ren J., Cui J., m6A RNA modification controls autophagy through upregulating ULK1 protein abundance, *Cell Res.*, 28(9) (2018) 955–7.
- [39] Zhang Y., Gao L., Wang W., Zhang T., Dong F., Ding W., M6A demethylase fat mass and obesity-associated protein regulates cisplatin resistance of gastric cancer by modulating autophagy activation through ULK1, *Cancer Sci.*, 113(9) (2022) 3085–96.

Evaluation of the Antitumor Activity of Omipalisib, a PI3K/AKT/MTOR Pathway Inhibitor, on Burkitt Lymphoma Cell Line

Zekeriya Keskin^{1,a,*}, Fatih Yulak^{2,b}, Hatice Terzi^{3,c}, Merve İnanır^{4,d}

¹ Department Of Internal Medicine, Faculty Of Medicine, Cumhuriyet University, Sivas, Türkiye.

² Department Of Physiology, Faculty Of Medicine, Cumhuriyet University, Sivas, Türkiye.

³ Department Of Hematology, Faculty Of Medicine, Cumhuriyet University, Sivas, Türkiye.

⁴ Department Of Pharmacology, Faculty Of Pharmacy, Cumhuriyet University, Sivas, Türkiye.

*Corresponding author

Research Article

History

Received: 16/08/2023

Accepted: 02/12/2023

Copyright





©2023 Faculty of Science,
Sivas Cumhuriyet University


ABSTRACT


There are many challenges in the treatment of Burkitt lymphoma, especially in immunocompromised individuals, elderly patients, and patients with relapsed or refractory disease. Therefore, there is a need for new and less toxic therapeutic agents. The aim of this study was to determine the antitumoral activity of omipalisib, a PI3K/AKT/mTOR pathway inhibitor, in the Burkitt lymphoma. Raji cell line was used in the study. Omipalisib was administered to the cell line and then the cytotoxic effect of omipalisib on Raji cells was evaluated by the XTT test. The IC50 value was calculated according to the results of the XTT test. Apoptosis and cell cycle experiments were studied with the calculated IC50 value. The flow cytometric method was used to determine the effect of omipalisib on apoptosis and cell death. The results of the study showed a statistically significant cytotoxic effect of increasing concentrations of omipalisib on Raji cells. The apoptosis experiment performed revealed that omipalisib strongly induced apoptosis. The cell cycle experiment showed that omipalisib stimulated the cell cycle arrest at the G0/G1 phase. It was concluded that omipalisib exhibited antitumoral activity on Burkitt lymphoma cells with its cytotoxic effect and induced apoptosis and cell cycle arrest. Considering this effect, targeting the PI3K/AKT/mTOR pathway with omipalisib can be a new treatment option.


Keywords: Apoptosis, Cell cycle, Omipalisib, Raji cells, XTT.


 zekeriyakeskinsh@gmail.com


 <https://orcid.org/0000-0003-3623-9892>


 fatihyulak@gmail.com

 <https://orcid.org/0000-0003-3708-6752>

 dr.terzi@hotmail.com

 <https://orcid.org/0000-0003-3471-1305>

 ecz.merveinanir@gmail.com

 <https://orcid.org/0000-0003-4661-8087>

Introduction

Burkitt lymphoma (BL) is a highly aggressive type of Non-Hodgkin Lymphoma (NHL). It arises from mature germinal or post-germinal center B cells. BL causes c-Myc overexpression and is the fastest growing human tumor with a 24-48 hour doubling time [1]. There are 3 different clinical types of BL: sporadic BL, endemic BL, commonly seen in African children (EBV has been detected in the vast majority of such patients), and immunodeficiency-related BL, usually seen in HIV-infected individuals. It is most commonly seen in young adults and children [2]. Bone marrow and central nervous system involvement are also common [3]. About 70% of patients have an advanced stage at the time of diagnosis [2]. BL is characterized by a high proliferation index and high turnover due to a high apoptosis rate [4].

The PI3K/AKT/mTOR pathway is highly correlated with the development and function of normal lymphocytes. Activation of the PI3K/AKT pathway is associated with BL lymphomagenesis and modulates cellular processes such as cell growth, cell proliferation, survival, and increased cell migration, as well as dysregulated apoptosis and oncogenesis [5-7]. Activation of the PI3K/AKT/mTOR pathway is associated with many solid tumors and

hematological malignancies [8]. Omipalisib (GSK2126458) is a very potent and selective inhibitor of PI3K and mTOR and has been clinically tested in many different solid tumors, which has been demonstrated to target the PI3K/AKT/mTOR pathway. Inhibition of these signals stimulates apoptosis in tumor cells and disrupts biochemical processes of the cell such as oxidative phosphorylation and cellular respiration. Activation of this pathway and key substrates in this pathway plays a role in the prevention of cell death. These signals are highly active in many types of cancer, and PI3K/AKT pathway genetic mutations are implicated in the pathogenesis of different human cancers [9]. This agent has been studied in many different solid tumors and lymphomas and is expected to be beneficial in different cancer types by inhibiting the PI3K/AKT/mTOR pathway [10].

The aim of this study was to evaluate the cytotoxic effect of omipalisib, which inhibits the PI3K/AKT/mTOR pathway, on Burkitt lymphoma cells as well as its effects on the cell cycle with its apoptosis-inducing effect, thus demonstrating the antitumoral activity of this drug and revealing the benefits it can add to the treatment of Burkitt lymphoma.

Materials and Methods

Cell Culture Techniques

CCL-86 coded Human Burkitt lymphoma Raji cell line obtained from ATCC (American Type Cell Collection) was used in the research. The approval for the conduct of the study was obtained from the Ethics Committee of Non-Invasive Clinical Researches of Sivas Cumhuriyet University with the number of 2021-08/11 and date 19.08.2021.

Raji cells were grown by passage when they reached 80% density in 25 cm² flasks using cell culture medium mixtures obtained by adding 10% fetal bovine serum and 1% penicillin-streptomycin into a RPMI 1640 medium. Cell culture studies were carried out at 37°C in a humidified atmosphere with 5% CO₂.

XTT Cell Viability Assay

The effect of Omipalisib, which has been shown to affect the PI3-Kinase and mTOR pathway, on the viability of Raji cells was investigated by the XTT (2,3-bis (2-methoxy-4-nitro-5-sulfophenyl)-5-[(phenylamino) carbonyl]-2H-tetrazolium hydroxide) assay (Roche Diagnostic, Germany). The method is based on the principle that metabolically active cells reduce XTT, a tetrazolium salt, to orange formazan components. Although the dye formed is water-soluble, the dye density can be read at the given wavelengths with the help of a spectrophotometer. The dye intensity (orange color) is proportional to the number of metabolically active cells.

For cytotoxicity, 10x10³ cells were first placed in each well and planted in a sterile 96-well microplate. Afterward, omipalisib was administered alone to Raji cells at 50, 25, 12.5, 1, 0.1, 0.01 μM concentrations and incubated for 24 hours. At the end of 24 hours, 50 μl of XTT solution was added to each well and incubated for 4 hours in a CO₂ oven. At the end of the incubation period, the optical density (OD) value was read with a microplate reader at 450 nm, and the cell viability rate of the control group was considered 100%; the half-inhibitory concentration (IC₅₀) value was calculated using the following formula: % cell viability = (Concentration OD/Control OD) x 100. Apoptosis and cell cycle experiments were studied over the obtained IC₅₀ values.

Flow Cytometric Analysis of Apoptosis and Cell Death

Annexin V is a calcium-dependent and phospholipid-binding protein with a high affinity to phosphatidylserine residues. In the early stages of apoptosis, phosphatidylserine residues translocate to the outer surface of the outer membrane so that they can be stained with annexin V dye. In our study, the Muse™ Cell Analysis System and the Muse™ Annexin V & Cell death kit (Merck, Millipore, USA), which is compatible with this system, were used to detect apoptosis and cell death. This kit not only stains phosphatidylserine residues of apoptotic cells with Annexin V dye but also

evaluates the structural integrity of the cell membrane with a 7-ADD stain. The protocol is based on the direct detection of early apoptotic cells in culture. The final concentration of cells was adjusted to 2x10⁴-1x10⁵ cells/well (or 1x10⁵ to 5x10⁵ cells/mL) for optimal results. The PI3K/mTOR inhibitor omipalisib at IC₅₀ concentration was administered to Raji cells used in the study and incubated for 24 hours. At the end of 24 hours, the cells were centrifuged at 1000 x rpm for 5 minutes to obtain a cell pellet. Approximately 20 minutes after Annexin V dye was added to the pellet, it was read by the device.

Cell Cycle Analysis

Disturbances in cell cycle regulation are a characteristic feature of tumor cells, and mutations in genes under cell cycle control are extremely common in cancer formation. For these reasons, cell cycle analysis is very important to understand the mechanisms of action of anti-cancer compounds and to examine the mechanisms of cell division. In the present study, cell cycle analysis was performed using the Muse™ Cell Cycle Kit (Merck, Millipore, USA) in accordance with the kit procedure. Propidium iodide (PI) and RNAase A reagents intercalating to DNA were used for the analysis. In the presence of RNAase, the PI reagent distinguishes the different stages of the cell cycle depending on the difference in the DNA content of the cell. Cells at rest (G0/G1) contain two copies of each chromosome. When cells begin their division cycle, they synthesize chromosomal DNA (S phase). The fluorescence intensity from PI increases until all chromosomal DNA is doubled (G2/M phase). At this stage, cells in the G2/M stage fluoresce twice the intensity of the G0/G1 population. G2/M cells eventually divide into two cells. The test gives the percentage of cells in each cell cycle phase (G0/G1, S, and G2/M) separately thanks to PI-based staining of the DNA content. In this study, PI3K/mTOR inhibitor omipalisib at IC₅₀ concentration was administered to Raji cells and incubated for 24 hours. At the end of 24 hours, the cells were centrifuged at 1000 x rpm for 5 minutes to obtain a cell pellet. Cells were fixed and prepared for analysis in accordance with the kit procedure. The cell pellet was resuspended with Muse Cell Cycle Kit™ reagent and then incubated for 30 minutes at room temperature by protecting from light. Cell population distribution at different stages of the cell cycle was determined using the Muse™ Cell Analyzer (Merck, Millipore, USA).

Statistical Analysis

Statistical analysis of the study data was carried out using the SPSS software package. One-way ANOVA (Analysis of Variance) test was used for normally distributed data, while the non-parametric Kruskal-Wallis and Mann-Whitney U tests were used for non-normally distributed data. A p-value<0.05 was considered significant in all analyses.

Results

Cytotoxic Effect of Omipalisib on Raji Cells

Omipalisib was administered to BL Raji cells at concentrations of 50, 25, 12.5, 1, 0.1, and 0.01 μM . The cytotoxic effect of these doses was evaluated at 24 hours. Omipalisib was observed to have a strong cytotoxic effect in a concentration-dependent manner. The IC_{50} value produced by omipalisib at 24 hours was calculated to be 3.04 μM . A strong cytotoxic effect was observed at 1, 12.5, 25, and 50 μM concentrations ($p < 0.01$). Although the omipalisib concentrations of 0.01 and 0.1 μM had cytotoxic effects, no statistically significant difference was observed ($p > 0.05$). The cytotoxic effect of omipalisib was dose-dependent and stronger at increasing concentrations. Although significant cytotoxic effects were observed at 1 μM and subsequent doses, the cytotoxic effect became stronger, especially at 12.5 μM and later doses ($p < 0.01$) (Figure 1).

Apoptotic Effect of Omipalisib on Raji Cells

The flow cytometric method was used to evaluate the apoptotic effects of omipalisib on Burkitt lymphoma Raji cells. There was a significant increase in apoptotic cells at IC_{50} concentration compared to the control group at 24 hours. Compared with the control group (4.34%), there was a significant increase in late apoptotic cells (31.35%), with a viable cell rate of 92.05% in the control group, while it was 63.02% in the omipalisib-treated group, with a statistically significant decrease ($p < 0.01$). There was also an increase in the number of dead cells, but it was not statistically significant. While the rate of dead cells was 0.96% in the control group, it was 3.24% in the omipalisib group ($p > 0.05$). A decrease was observed in the rate of early apoptotic cells, but it was not statistically significant. While the rate of early apoptotic cells was 2.65% in the control cell group, it was 2.39% in the omipalisib-treated cell group ($p > 0.05$) (Figures 2 and 3). Omipalisib was found to induce apoptosis in Raji cells, and this property was shown to play an important role in its antitumoral activity.

Effect of Omipalisib on Cell Cycle of Raji Cells

The effect of Omipalisib on the cell cycle of Raji cells was investigated. Cells were treated with the IC_{50} concentration of omipalisib, and the effect was evaluated at 24 hours. The cell population accumulated in the G0/G1 phase in the omipalisib group, with a statistically significant difference with the control group ($p < 0.01$) (Figure 4). Thus, it was determined that cell cycle arrest by omipalisib in the G0/G1 phase is another mechanism of action of its antitumoral activity.

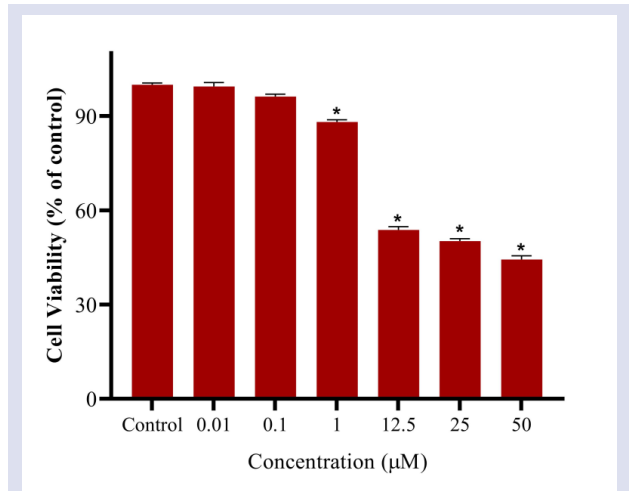


Figure 1. Evaluation of the Cytotoxic Effect of Omipalisib on Raji Cells at 24 Hours

* Statistically significant difference with the control ($p < 0.01$).

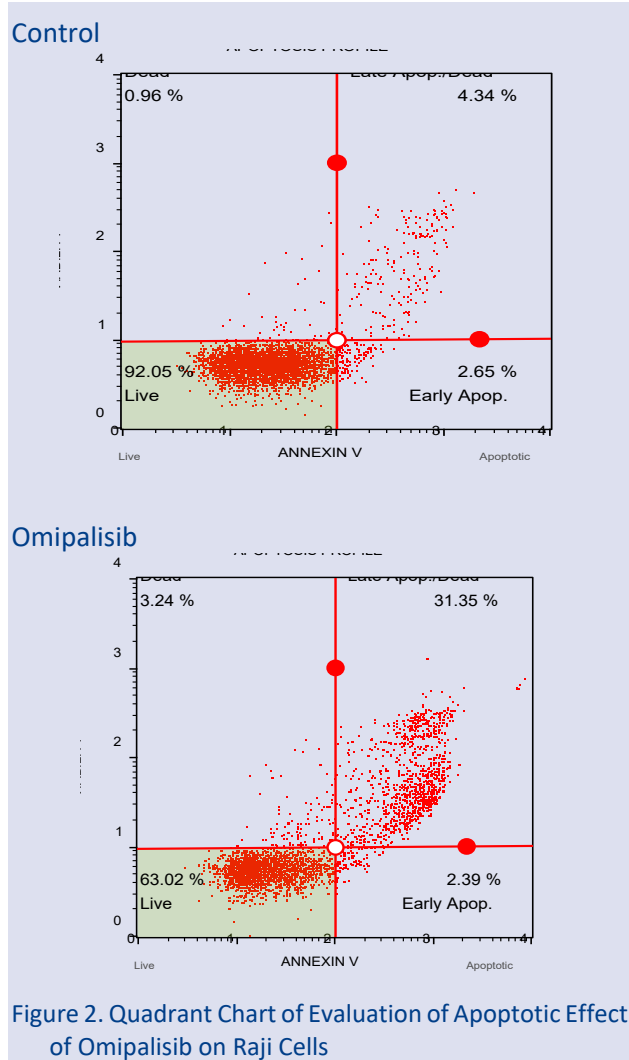


Figure 2. Quadrant Chart of Evaluation of Apoptotic Effect of Omipalisib on Raji Cells

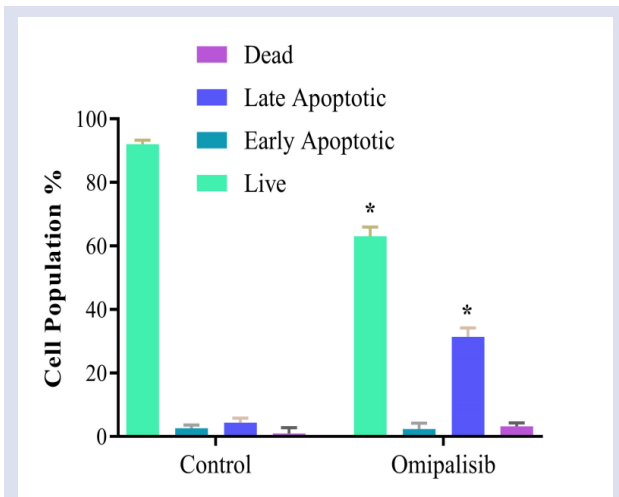


Figure 3. Bar Plot of Evaluation of Apoptotic Effect of Omipalisib on Raji Cells

* Statistically significant difference with the control (p<0.01).

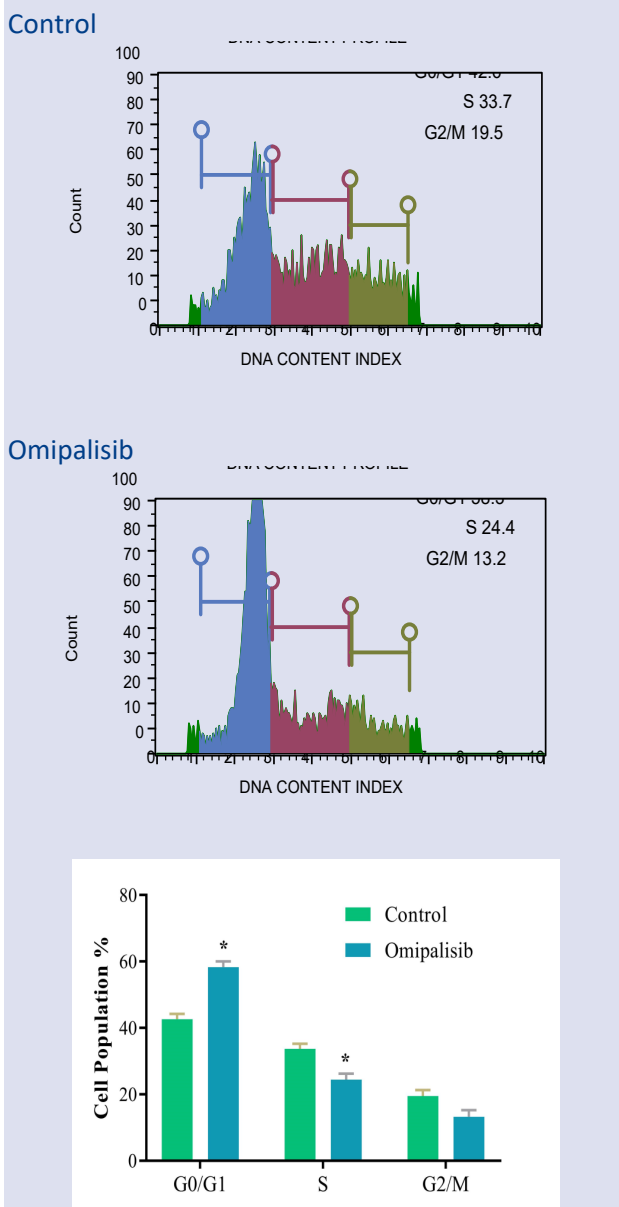


Figure 4. Evaluation of the Effect of Omipalisib on Cell Cycle of Raji Cells.

* Statistically significant difference with the control (p<0.01).

Discussion

Although BL is a very aggressive and fast-growing tumor, it is potentially curable with the use of combination chemotherapy regimens [11]. Regimes such as R-hyperCVAD, CODOX-M/IVAC, DA-EPOCH-R, and LMB are most commonly used for the treatment of BL [12]. Patients with relapsed/refractory BL have a very poor prognosis and often fail to achieve recovery with regimens [13,14]. With the emergence of new genomic findings for the treatment of BL, many new therapeutic agents have been under study. Activation of the PI3K/AKT/mTOR pathway is associated with the BL pathogenesis and poor prognosis in aggressive B-cell NHLs [5]. Ippolito et al. investigated the in vitro and in vivo activity of omipalisib in chemotherapy-sensitive and resistant BL cell culture models. They exposed BL cells to omipalisib for 24-72 hours and observed significant induction of apoptosis in chemosensitive cells after 72 hours; however, higher concentrations were required to induce apoptosis for treatment-resistant cells. G1 cell cycle arrest occurred 72 hours after omipalisib administration to all cell lines. However, cell cycle arrest occurred at higher concentrations of G2/M in chemotherapy-resistant Raji cells. An in vivo study on mice showed slower tumor progression in mice treated with omipalisib compared to the control group. The present study demonstrated in vivo and in vitro that omipalisib inhibited the PI3K/AKT/mTOR pathway, inducing apoptosis and impairing BL cell proliferation [15]. Bhatti et al. administered the molecule named MK-2206, which inhibits the PI3K/AKT/mTOR pathway, to the BL cell line. They showed in a preclinical study with BL cell lines that MK-2206 was not effective alone, but existing chemotherapeutic agents (doxorubicin +/- dexamethasone combination) increased its efficacy [5]. Another study by Li et al. treated the BL cell lines with NVP-BE235, a dual PI3K/mTOR inhibitor. The study revealed the inhibitory effect of NVP-BE235 on the proliferation of BL cells, reporting that the anti-apoptotic activity of the agent was dose and time-dependent [16]. There are various studies in the literature on the efficacy of omipalisib for different solid tumors. These studies have shown both its efficacy alone and synergistic effect with combined treatments. It is therefore believed that PI3K/mTOR inhibitors can be a therapeutic option for such cancers [9,17,18,19].

Considering such studies in the literature and the present study, it is suggested that omipalisib and other PI3K/AKT/mTOR inhibitors have antitumoral activities on BL cells with mechanisms such as cytotoxic effect, induction of apoptosis, and cell cycle arrest.

Conclusion

In conclusion, omipalisib has the potential to be a new treatment option, especially for patients with relapsed/refractory BL and intolerance to intensive chemotherapy. Moreover, inhibition of the PI3K/AKT/mTOR pathway is very important in the

treatment of BL since the inhibition of this pathway results in an antitumoral effect. However, the number of studies investigating the effect of omipalisib on BL is limited. Therefore, there is a need for more studies both in vitro and in vivo with omipalisib alone and with combination treatments. Furthermore, more clinical studies are needed to evaluate its efficacy, side-effect profile, effect on survival, and permanent response of patients.

Acknowledgments

This study was supported by Sivas Cumhuriyet University Scientific Research Projects (CUBAP) with the project number of T-896. The authors thank Sivas Cumhuriyet University Medical Faculty Research Center-CUTFAM for supplying the required facilities for the conduct of this study.

Conflicts of interest

There are no conflicts of interest in this work.

References

- [1] Saleh K., Michot J. M., Camara C.V., Vassetsky Y., Ribrag V., Burkitt and Burkitt-Like Lymphomas: a Systematic Review, *Curr. Oncol. Rep.*, 22(4) (2020) 33.
- [2] Ishizawa K., JSH Practical Guidelines for Hematological Malignancies, 2018: II. Lymphoma-6. Burkitt Lymphoma (BL), *Int. J. Hematol.*, 110 (3) (2019) 265–271.
- [3] Linch D. C., Burkitt Lymphoma in Adults, *Br. J. Haematol.*, 156(6) (2012) 693–703.
- [4] Dunleavy K., Little R. F., Wilson W. H., Update on Burkitt Lymphoma, *Hematol. Oncol. Clin. North. Am.*, 30(6) (2016) 1333–1343.
- [5] Bhatti M., Ippolito T., Mavis C., Gu J., Cairo M. S., Lim M. S., Francisco H.I., Matthew J. B., Pre-clinical Activity of Targeting the PI3K/Akt/mTOR Pathway in Burkitt Lymphoma, *Oncotarget.*, 30(6) (2018)1333–1343.
- [6] Markman B., Atzori F., Pérez-García J., Tabernero J., Baselga J., Status of PI3K Inhibition and Biomarker Development in Cancer Therapeutics, *Ann. Oncol.*, 21(4) (2009) 683–691.
- [7] Porta C., Paglino C., Mosca A., Targeting PI3K/Akt/mTOR Signaling in Cancer, *Front. Oncol.*, 4(2014) 1-11.
- [8] Janku F., Yap T. A., Meric B. F., Targeting the PI3K Pathway in Cancer: Are We Making Headway?, *Nat. Rev. Clin. Oncol.*, 15(5) (2018) 273–291.
- [9] Liu T., Sun Q., Li Q., Yang H., Zhang Y., Wang R., et al., Dual PI3K/Mtor Inhibitors, GSK2126458 and PKI-587, Suppress Tumor Progression and Increase Radiosensitivity in Nasopharyngeal Carcinoma, *Mol. Cancer Ther.*, 14 (2) (2015) 429–439.
- [10] Knight S.D., Adams N.D., Burgess J.L., Chaudhari A.M., Darcy M.G., Donatelli C.A., Luengo J.I., Newlander K.A., Parrish C.A., Ridgers L.H., Sarpong M.A., Schmidt S.J., Van Aller G.S., Carson J.D., Diamond M.A., Elkins P.A., Gardiner C.M., Garver E., Gilbert S.A., Gontarek R.R., Jackson J.R., Kershner K.L., Luo L., Raha K., Sherk C.S., Sung C.M., Sutton D., Tummino P. J., Wegrzyn R. J., Auger K.R., Dhanak D., Discovery of GSK2126458, a Highly Potent Inhibitor of PI3K and the Mammalian Target of Rapamycin, *ACS Med. Chem. Lett.*, 1(1) (2010) 39–43.
- [11] Bociek R.G., Adult Burkitt's Lymphoma, *Clin. Lymphoma.*,6 (2005) 11–20.
- [12] Zayac A.S., Olszewski A. J., Burkitt Lymphoma: Bridging the Gap Between Advances in Molecular Biology and Therapy, *Leuk. Lymphom.*, 61(8) (2020) 1784–1796.
- [13] Short N. J., Kantarjian H.M., Ko H., Khoury J.D., Ravandi F., Thomas D.A.,Garcia M.G., Khouri M., Cortes J. E., Wierda W.G., Verstovsek S., Estrov Z., Ferrajoli A., Thompson P. A., Pierce S.A., O'Brien S.M., Jabbour E., Outcomes of Adults with Relapsed or Refractory Burkitt and High-Grade B-cell Leukemia/Lymphoma, *Am. J. Hematol.*, 92(6) (2017) 114–117.
- [14] Sweetenham J. W., Pearce R., Taghipour G., Biase D., Gisselbrecht C., Goldstone A.H., Adult Burkitt's and Burkitt-like non-Hodgkin's lymphoma - Outcome for patients treated with high-dose therapy and autologous stem-cell transplantation in first remission or at relapse: Results from the European group for blood and marrow transplantation, *J. Clin. Oncol.*, 14(9) (1996) 2465–2472.
- [15] Ippolito T, Mavis C, Gu J, Hernandez-Ilizaliturri F. J, Barth M. J. Omipalisib (GSK458), a Dual an-PI3K/mTOR Inhibitor, Exhibits in Vitro and In Vivo Activity in Chemotherapy-Sensitive and -Resistant Models of Burkitt Lymphoma, *Blood.*, 132 (2018) 2951–2951.
- [16] Li C, Xin P, Xiao H, Zheng Y, Huang Y, Zhu X. The dual PI3K/mTOR inhibitor NVP-BE2235 Inhibits Proliferation and Induces Apoptosis of Burkitt Lymphoma Cell, *Cancer Cell Int.*, 15 (2015) 1–9.
- [17] Munster P, Aggarwal R, Hong D, Schellens J.H.M., Van Der Noll R., Specht J., Witteveen P.O., Werner T.L., Dees E.C., Bergsland E., Agarwal N., Kleha S.F., Durante M., Adams L., Smith D.A., Lampkin T.A., Morris S.R., Kurzrock R., First-in-Human Phase I Study of GSK2126458, an Oral Pan-Class I Phosphatidylinositol-3-Kinase Inhibitor, in Patients with Advanced Solid Tumor Malignancies., *Clin. Cancer Res.*, 22 (2016) 1932–1939.
- [18] Wong K., Di Cristofano F., Ranieri M., De Martino D., Di Cristofano A., PI3K/mTOR Inhibition Potentiates and Extends Palbociclib Activity in Anaplastic Thyroid Cancer, *Endocr. Relat. Cancer.*, 26 (2018) 425–436.
- [19] Zhu D.S, Dong J.Y, Xu Y.Y, Zhang X.T, Fu S.B, Liu W., Omipalisib Inhibits Esophageal Squamous Cell Carcinoma Growth Through Inactivation of Phosphoinositide 3-Kinase (PI3K)/AKT/Mammalian Target of Rapamycin (mTOR) and ERK Signaling, *Med. Sci. Monit.*, 26(2020) e927106.

Unraveling the Role of Apoptosis in the Antiproliferative Activity of β -Glucan on A549 Cells

Ziad Joha ^{1,a,*}, Mustafa Ergül ^{2,b}

¹ Department of Pharmacology, Faculty of Pharmacy, Sivas Cumhuriyet University, Sivas, Türkiye.

² Department of Biochemistry, Faculty of Pharmacy, Sivas Cumhuriyet University, Sivas, Türkiye.

*Corresponding author

Research Article

History

Received: 01/08/2023

Accepted: 02/12/2023

Copyright




©2023 Faculty of Science,
Sivas Cumhuriyet University


ABSTRACT


Previous studies have reported the anticancer properties of β -glucan on various cancer cells. The objective of this research was to investigate the involvement of apoptosis in the cytotoxic action of β -glucan on the A549 cells. The cytotoxic impact of this drug on A549 cells was examined by subjecting them to various quantities of the substance, and the XTT assay was utilized to determine cell survival. Flow cytometry was performed to investigate apoptosis. A statistically significant and dose-dependent cytotoxic impact on A549 cells was observed upon treatment with β -glucan. The calculated IC50 value of β -glucan for A549 cells after a 24-hour treatment period was discovered to be 82.16 μ g/mL. Further investigations carried out using the IC50 dose of β -glucan revealed a significant increase in the late apoptotic cells percentage. The capacity of β -glucan to trigger apoptosis is thought to be the cause of its cytotoxic action on lung cancer. The revelation of this discovery emphasizes the promising possibilities of β -glucan as an effective therapeutic choice.

Keywords: Anticancer, β -glucan, Apoptosis, A549.

 zead-geha@hotmail.com

 <https://orcid.org/0000-0001-8520-3760>

 mergul@cumhuriyet.edu.tr

 <https://orcid.org/0000-0003-4303-2996>

Introduction

According to incidence and cancer-related mortality rates worldwide, lung cancer is among the most widespread kind of malignant tumor [1]. It is still an incurable disease considering significant advancements in our knowledge of disease pathophysiology and the creation of cutting-edge treatments. Small- and non-small-cell lung cancers are the two main kinds of diverse illnesses known as lung cancer [2]. The A549 cell line is a cancerous cell line originating from human lung carcinoma. The lungs consist of various structures, including the respiratory bronchioles, and alveoli. Type I and type II pneumocytes are the two cell types that line the alveoli. Large, flat cells known as type I pneumocytes cover a sizable portion of the alveolar surface. Type I cells cannot divide and are extremely vulnerable to harm from many toxic substances, in contrast to type II pneumocytes. On the other hand, type II pneumocytes are smaller, cuboidal cells typically located at the alveolar septal junctions. These cells have the ability to replicate within the alveoli and play a crucial role in replacing damaged type I pneumocytes. A549 cells share several essential characteristics with type II pneumocytes, making them an ideal model for research purposes. They can be easily cultured due to their human origin and are widely used to study type II pneumocyte behavior and properties. Because of these advantageous features, the A549 cell line was selected for the present study [3]. A physiological mechanism called apoptosis results in cell death. In the organism, it serves as a crucial protective mechanism by eliminating damaged cells or cells that

have overproliferated as a result of an incorrect mitotic stimulus. Cytoplasmic shrinkage, a lack of cell-cell connections, and active membrane blebbing are some of the early morphological changes in apoptotic cells. In recent years, the discovery of anticancer drugs has focused on the production of apoptosis, and an antitumor treatment that specifically induces apoptosis in tumor cells may be the best option [4,5]. Throughout history, natural components have been widely utilized as remedies for medical purposes, mainly due to the perception that they pose minimal adverse effects. Consequently, understanding the processes through which these natural substances can potentially provide health benefits is crucial for civilizations of humanity [6]. β -Glucans, which are plentiful in barley and oats, are a specific type of polysaccharide characterized by their location within the cell wall [7]. β -Glucans exhibit diverse properties that contribute to their beneficial effects in preventing and treating various illnesses. These properties, such as bile acid trapping and immune activation, have been found to be particularly helpful in conditions such as cancer, infectious diseases, diabetes, hyperlipidemia, and obesity [8]. β -Glucan therapy has demonstrated effectiveness in combating numerous types of cancers [9]. The anti-cancer properties of β -glucans are mediated through two essential receptors, receptor 3 (CR3) and lactosylceramide. These receptors are essential for immune system stimulation, cancer prevention, and direct suppression of tumor growth, all contributing to the overall anti-cancer effects of β -glucan

[10]. Numerous studies have showcased the anti-cancer properties of β -glucans on various cancer cell lines [9]. However, the specific mechanisms responsible for the anti-cancer effects of β -glucan against lung carcinoma, particularly on the A549 cell line, remain to be fully understood and require further investigation. This research aimed to explore the role of apoptosis in the cytotoxic action of β -glucan on the A549 cells.

Materials and Methods

Cell Culture

The American Type Culture Collection, a research institution with headquarters in the US, provided the A549 lung cancer cell line (CCL-185) for use in research. The A549 lung cancer cell line was cultured for cell culture purposes using Dulbecco's modified Eagle's medium (DMEM) and kept at a temperature of 37°C. The cells were grown in a humidified atmosphere with the addition of 15% CO₂. In this research, the culture medium used comprised 10% fetal bovine serum (FBS), 1% L-glutamine, and 1% penicillin/streptomycin. The substance of interest, β -glucan, was first dissolved in dimethyl sulfoxide (DMSO) and then further diluted in the culture medium. Before treating the cells, significant care was taken to ensure that the culture medium's DMSO concentration did not exceed 0.1%. All materials utilized in the experiment, with the exception of the cells, were acquired from Sigma-Aldrich.

Cell Viability Assay

The XTT test was employed to evaluate how β -glucan affected the A549 cell line's viability. Some experimental works used the XTT test to measure the cell proliferation [11,12]. Before commencing the experiment, the cells were first seeded at a density of 1×10^4 cells per well and left to incubate for 24 hours. The A549 cells were then treated with β -glucan at different doses (10, 25, 50, 100, 200, and 400 $\mu\text{g}/\text{mL}$). There was also a control group made up of untreated cells. Following the incubation period, a 50 μL XTT mixture was introduced to each well, and the cells were further incubated for 4 hour. Fisher Scientific, based in Altrincham, United Kingdom, provided a microplate reader for use in measuring the absorbance at 450 nm after the cells had been incubated. To assure accuracy and reliability, the experiment was performed three times. By quantifying the proportion of living cells in comparison to the control cells that were not treated, the viability of the cells was evaluated [13,14]. Beta glucan does not interact with the chemicals used in cell culture studies. Since beta glucan containing solutions are removed from the wells before the XTT test and the wells are washed three times with buffer solution, it does not cause any color interference in the XTT test. The XTT test has been frequently used to measure cell proliferation.

Annexin V Binding Assay

A total of around 5×10^5 A549 cells were placed in 6-well plates and given full night to adhere. The next day, the A549 cells were exposed to β -glucan at dose of 82.16 $\mu\text{g}/\text{mL}$ (IC₅₀) and incubated for an additional 24 hours. Following the duration of incubation, the cells were detached using trypsin, gathered, and resuspended in PBS containing at least 1% FBS. Following the manufacturer's directions, the cell suspension was then mixed with an equivalent volume of Annexin V & Dead Cell reagent (Merck, Millipore). To quantify the various cell types, including dead, live, early apoptotic, and late apoptotic cells, the Muse Cell Analyzer (Millipore) was employed [15].

Statistical Analysis

The laboratory results were reported as the mean \pm standard error. The XTT assay results were analyzed using one-way analysis of variance (ANOVA), followed by post-hoc Tukey tests for multiple comparisons. The Student's t-test was used to assess the flow cytometry results. To identify statistically significant modifications, $p < 0.05$ was utilized as the significance threshold. Version 22.3 of the SPSS Statistics Program was used to conduct the statistical analysis.

Results and Discussion

The Antiproliferative Activity of β -glucan in A549 Cells

The A549 cells were subjected to various amounts of β -glucan ranging from 10 to 400 $\mu\text{g}/\text{mL}$ for a duration of 24 hours. The XTT assay was used to examine the total amount of cells that survived. β -glucan did not demonstrate any significant effect at quantities of 10, 25, and 50 $\mu\text{g}/\text{mL}$. However, at quantities of 100, 200, and 400 $\mu\text{g}/\text{mL}$, β -glucan displayed a dose-dependent antiproliferative action on A549 cells ($p < 0.001$; Fig. 1). The IC₅₀ value of β -glucan, identified using GraphPad Prism, was determined to be 18.47 $\mu\text{g}/\text{mL}$.

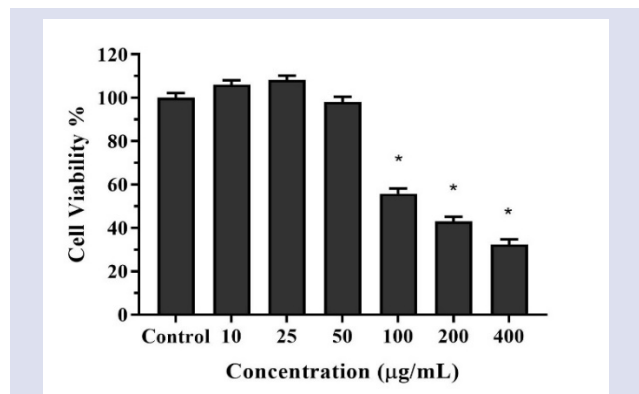


Figure 1: The cytotoxicity activity of β -glucan in A549 cells. The outcomes are expressed as the mean \pm SEM of six samples.

* $p < 0.001$ as compared to the control group.

The apoptotic impact of β -glucan on A549 Cells

The apoptosis profile of β -glucan in A549 lung cancer cells was assessed using a flow cytometry device along with suitable kits. The control group had a late apoptotic cell percentage of 5.67%. However, in the group treated with β -glucan, there was a remarkable and statistically significant increase in late apoptotic cells, with the percentage measuring 14.78%. The percentage of early apoptotic cells did not significantly differ between the two groups. Based on our findings, it was observed that the percentage of dead cells showed an increase from 1.93% in the control group to 6.06% in the β -glucan group. Conversely, there was a considerable reduction in the percentages of live cells, declining from 90.03% to 77.47% after treatment with β -glucan ($p < 0.05$ Fig. 2). The findings indicate that β -glucan significantly contributes to the induction of apoptosis in A549 lung cancer cells, resulting in a remarkable reduction in cell proliferation.

In recent times, β -glucan has attracted considerable interest as a conceivable nominee for cancer cure. While scientists are working to confirm its cancer-fighting abilities, they are still committed to figuring out the particular pathways by which it exerts its effects. In this particular investigation, our focus was on assessing the influences of β -glucans on proliferation and apoptosis using in vitro models. For our experiments, we employed the A549 cell line, which originates from a type II pneumocyte lung tumor. Initially, XTT test was conducted to assess the dose-dependent cytotoxicity of β -glucan on A549 cells. The findings from the experiments demonstrated a notable decrease in the growth of A549 cells, indicating that β -glucan's impact was related to its concentration. After a 24-hour exposure to β -glucan, the IC_{50} value was discovered to be 82.16 μ g/mL. In line with our results, earlier research has demonstrated that β -glucan reduces MCF-7 cell survival in a way that depends on concentration [16]. Furthermore, Kim et al. reported that β -glucan induced cell death in colon cancerous cells [17]. The proliferation of B16 melanoma cells was inhibited by β -glucans extracted from *S. Cerevisiae* [18]. According to Sadeghi et al., the isolated β -glucan demonstrated a substantial cell death in both the sphere and parental cells [19]. Upadhyay's study revealed a remarkable deceleration in the multiplication of the HeLa cancer cells following a 24-hour treatment with different quantities of β -glucan [20]. In our earlier investigation, we observed a concentration-dependent suppression of SH-SY5Y cell reproduction by β -glucan, with a value for the IC_{50} of 94.6 g/mL following 24 hours. Concerns regarding the toxicity of antiproliferative agents on normal cells remain a significant limitation in treatment options. Therefore, during our previous investigation, we looked at how β -glucan affected non-cancerous L929 cells. The findings showed that β -glucan had no detectable cytotoxic consequences on L929 cells [21]. Cell development and proliferation are significantly regulated by the process of apoptosis, which is a type of controlled cell death. When cells receive specific signals triggering apoptosis, they activate internal mechanisms leading to distinct physiological modifications. The alterations involve several processes, including the external presentation of phosphatidylserine (PS) on the outer layer of cells, the breaking down of certain cellular proteins through fragmentation and cleavage, the condensation and fragmentation of nuclear chromatin, and eventually, the deterioration of membrane integrity during later stages [22]. Annexin V is a protein with a selective affinity for phosphatidylserine (PS), a phospholipid mainly situated on the inner surface of the cell membrane. In the early stages of apoptosis, PS molecules are relocated to the external surface of the cell membrane, making them accessible for Annexin V binding. Due to its capability to attach to externalized PS molecules on the cell membrane surface, Annexin V is commonly used as a marker to detect apoptotic cells [23]. Apoptosis is widely recognized as a pivotal factor in the molecular progression of cancer and exerts a

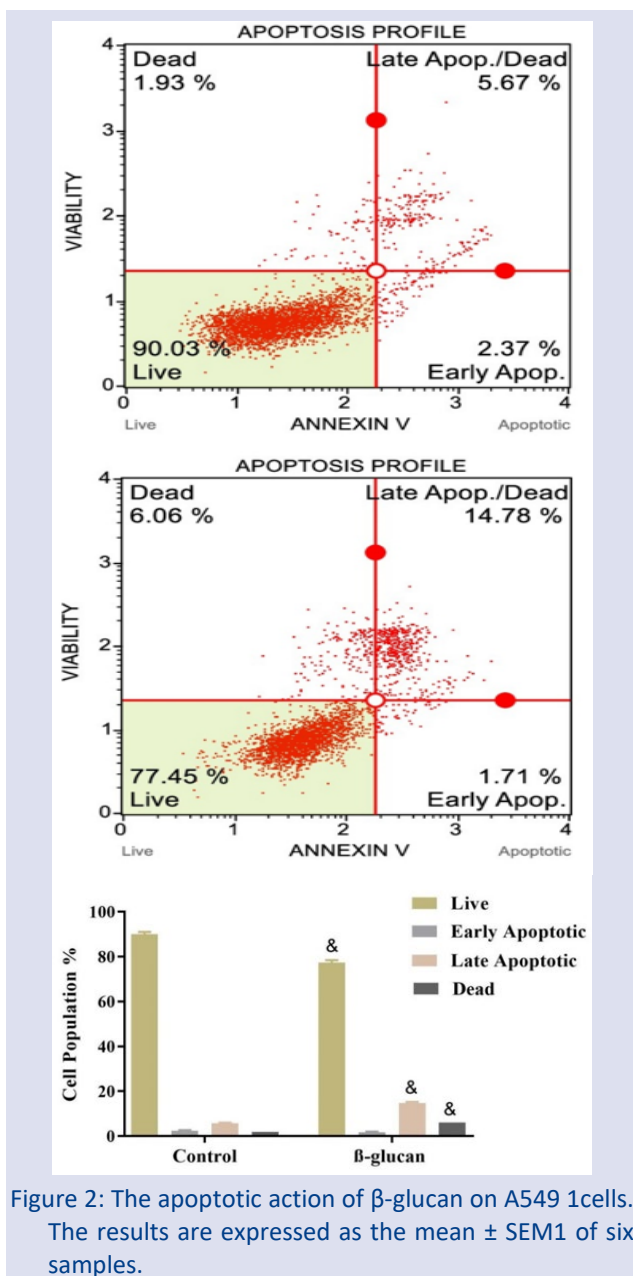


Figure 2: The apoptotic action of β -glucan on A549 1cells. The results are expressed as the mean \pm SEM1 of six samples.

& $p < 0.05$ as compared to the control group.

substantial influence on the efficacy of chemotherapy and radiation remedies [24]. In this investigation, we conducted a flow cytometry-based experiment to analyze the potential induction of apoptosis by β -glucan exposure. Our results demonstrated a significant increase in Annexin V binding of A549 cells following β -glucan treatment, indicating that β -glucan treatment effectively triggered apoptosis in these cells. Consistent with our findings, a study demonstrated that β -glucan exhibited a notable suppression rate of 75% on the viability of S-180 cells [25]. Notably, this inhibition rate surpassed that of the positive control, cytoxan, which recorded a 54% inhibition rate. β -glucan enhanced the immune cell recruitment towards cancerous tumors, leading to subsequent cell apoptosis and suppression of cell survival. Moreover, β -glucan induced an increase in the expression of pro-apoptotic proteins Bax and caspase 3/9, as well as the tumor suppressor p53, while concurrently reducing the levels of the anti-apoptotic protein Bcl-2 in cancer cells [25]. The β -glucan compound effectively inhibited the proliferation of C6 glioma cells through several mechanisms. It induced apoptosis, disrupted the cell cycle, and notably augmented the number of cells in the G0/G1 stage, accompanied by a reduction in the proportion of cells in the S-stage [26]. In a separate study, the efficacy of (1-6,1-3)- β -glucan was observed in combination with oxaliplatin in Hep-G2 cells (human hepatocyte carcinoma) implanted in mice with H22 tumors (mouse hepatoma). The results revealed synergistic effects, as the combination treatment effectively inhibited the expression of NF- κ B, STAT3, and survivin in the cancer cells [27]. Treatment with (1-6,1-3)- β -glucan induces programmed cell death and autophagy in human osteosarcoma cells [26]. This effect is achieved by up-regulating miR-340 expression and inhibiting the MAPK/ERK signaling pathway in MG63 cells. Moreover, (1-6,1-3)- β -glucan treatment leads to reduced levels of cyclin D1, while increasing the levels of Beclin-1, LC3B-II/LC3B-I, and caspase-3, -9 in these cells [28]. In our previous study, we observed a noteworthy effect of β -glucan treatment on pro-apoptotic factors, including increased expressions of Bax, cleaved caspase 3, and cleaved PARP proteins. These findings strongly suggest that apoptosis plays a vital role in the drug's ability to inhibit cell proliferation [21]. However, it is thought that performing apoptosis experiments in 200 and 400 μ g/mL beta glucan may provide more comprehensive results

In summary, our research showed that treatment with β -glucan suppressed the proliferation of A549 cells in a way that was dependent on concentration. This inhibitory impacts was associated with notable programmed cell death. These promising results suggest that β -glucan could hold promise as a therapeutic agent for lung cancer treatment. Nevertheless, it is crucial to emphasize that additional validation through in vivo and clinical investigations is required to corroborate these results and comprehensively evaluate the safety and efficacy of β -glucan as a potential treatment option.

Acknowledgments

The Sivas Cumhuriyet University, School of Medicine, CUTFAM Research Center, Sivas, Turkey, provided the necessary tools and infrastructure for the execution of this examination, for which the authors are grateful.

References

- [1] Roudi R., Mohammadi S.R., Roudbary M, Mohsenzadegan M., Lung cancer and β -glucans: review of potential therapeutic applications, *Investigational New Drugs*, 35 (2017) 509–17.
- [2] Peymaeei F., Sadeghi F., Safari E., Khorrami S., Falahati M., Mohammadi S.R., et al., Candida albicans Beta-Glucan Induce Anti- Cancer Activity of Mesenchymal Stem Cells against Lung Cancer Cell Line: An In-Vitro Experimental Study, *Asian Pacific Journal of Cancer Prevention*, 21 (2020) 837.
- [3] Koparal A.T., Zeytinoglu M., Effects of carvacrol on a human non-small cell lung cancer (NSCLC) cell line, A549, *Cytotechnology*, 43 (2003) 149–54.
- [4] Tong X., Tang R., Xiao M., Xu J., Wang W., Zhang B., et al., Targeting cell death pathways for cancer therapy: recent developments in necroptosis, pyroptosis, ferroptosis, and cuproptosis research, *Journal of Hematology & Oncology*, 15 (2022) 1–32.
- [5] Castro-Cruz A., Echeverría O.M., Juárez-Chavero S., Sánchez-Sánchez L., Torres-Ramírez N., Vázquez-Nin G.H., et al., Transcriptional activity and splicing factors are preserved during physiological apoptosis, *Journal of Structural Biology*, 214 (2022) 107884.
- [6] Liu Y., Chen Y., Lin L., Li H., Gambogic acid as a candidate for cancer therapy: A review, *International Journal of Nanomedicine*, 15 (2020) 10385–99.
- [7] Thomas S., Rezoagli E., Abidin I.Z., Major I., Murray P., Murphy E.J., β -Glucans from Yeast—Immunomodulators from Novel Waste Resources, *Applied Sciences*, 12 (2022) 5208.
- [8] Karimi R., Homayoonfal M., Malekjani N., Kharazmi M.S., Jafari S.M., Interaction between β -glucans and gut microbiota: a comprehensive review, *Critical Reviews in Food Science and Nutrition*, (2023) 1-32.
- [9] Sima P., Richter J., Vetvicka V., Glucans as New Anticancer Agents, *Anticancer Research*, 39 (2019) 3373–8.
- [10] Ikewaki N., Dedeepiya V.D., Raghavan K., Rao K.S., Vaddi S., Osawa H., et al. β -glucan vaccine adjuvant approach for cancer treatment through immune enhancement (B-VACCIEN) in specific immunocompromised populations (Review), *Oncology Reports*, 47 (2022) 1–9.
- [11] Ergul M., Bakar-Ates F., A specific inhibitor of polo-like kinase 1, GSK461364A, suppresses proliferation of Raji Burkitt's lymphoma cells through mediating cell cycle arrest, DNA damage, and apoptosis, *Chemico-Biological Interactions*, 332 (2020) 109288.
- [12] Ergul M., Bakar-Ates F., Investigation of molecular mechanisms underlying the antiproliferative effects of colchicine against PC3 prostate cancer cells, *Toxicology in Vitro*, 73 (2021) 105138.
- [13] Çiltaş A.Ç., Gündoğdu S., Yulak F., Levetiracetam Protects Against Glutamate-Induced Excitotoxicity in SH-SY5Y Cell Line, *International Journal of Nature and Life Sciences*, 6 (2022) 142–50.

- [14] Bilal .S, Handan G., Aysegül O., Investigation of the mechanisms involved in anticancer effect of glucosamine sulfate on SH-SY5Y cell line, *Bratislavské Lekárske Listy*, 123 (2022) 366–71.
- [15] Taskiran A.S., Ergül M., Gunes H., Ozturk A., Sahin B., Ozdemir E., The Effects of Proton Pump Inhibitors (Pantoprazole) on Pentylentetrazole-Induced Epileptic Seizures in Rats and Neurotoxicity in the SH-SY5Y Human Neuroblastoma Cell Line, *Cellular and Molecular Neurobiology*, 41 (2021) 173–83.
- [16] Maimon Y., Karaush V., Yaal-Hahoshen N., Ben-Yosef R., Ron I., Vexler A., et al., Effect of Chinese Herbal Therapy on Breast Cancer Adenocarcinoma Cell Lines, *Journal of International Medical Research*, 38 (2010) 2033–9.
- [17] Kim M.J., Hong S.Y., Kim S.K., Cheong C., Park H.J., Chun H.K., et al., β -Glucan enhanced apoptosis in human colon cancer cells SNU-C4, *Nutrition Research and Practice*, 3 (2009) 180–4.
- [18] Vetvicka V., Vetvickova J., Glucans and Cancer: Comparison of Commercially Available β -glucans – Part IV, *Anticancer Research*, 38 (2018) 1327–33.
- [19] Sadeghi F., Peymaeei F., Falahati M., Safari E., Farahyar S., Roudbar Mohammadi S, et al., The effect of Candida cell wall beta-glucan on treatment-resistant LL/2 cancer cell line: in vitro evaluation, *Molecular Biology Reports*, 47 (2020) 3653–61.
- [20] Upadhyay T.K., Trivedi R., Khan F., Al-Keridis L.A., Pandey P., Sharangi A.B., et al., In vitro elucidation of antioxidant, antiproliferative, and apoptotic potential of yeast-derived β -1,3-glucan particles against cervical cancer cells, *Frontiers in Oncology*, 12 (2022) 942075.
- [21] Filiz A.K., Joha Z., Yulak F., Mechanism of anti-cancer effect of β -glucan on SH-SY5Y cell line, *Bangladesh Journal of Pharmacology*, 16 (2021) 122–8.
- [22] D’Arcy M.S., Cell death: a review of the major forms of apoptosis, necrosis and autophagy, *Cell Biology International*, 43 (2019) 582–92.
- [23] Van Heerde W.L., De Groot P.G., Reutelingsperger C.P.M., The complexity of the phospholipid binding protein annexin V, *Thrombosis and Haemostasis*, 73 (1995) 172–9.
- [24] Chen Z., Zhang B., Gao F., Shi R., Modulation of G2/M cell cycle arrest and apoptosis by luteolin in human colon cancer cells and xenografts, *Oncology Letters*, 15 (2018) 1559–65.
- [25] Xu H., Zou S., Xu X., Zhang L., Anti-tumor effect of β -glucan from *Lentinus edodes* and the underlying mechanism, *Scientific Reports*, 6 (2016) 1–13.
- [26] Atiq A., Parhar I., Anti-neoplastic Potential of Flavonoids and Polysaccharide Phytochemicals in Glioblastoma, *Molecules*, 25 (2020) 4895.
- [27] Zhang Y., Li Q., Wang J., Cheng F., Huang X., Cheng Y., et al., Polysaccharide from *Lentinus edodes* combined with oxaliplatin possesses the synergy and attenuation effect in hepatocellular carcinoma, *Cancer Letters*, 377 (2016) 117–25.
- [28] Xu H.L., Dai J.H., Hu T., Liao Y.F., Lentinan up-regulates microRNA-340 to promote apoptosis and autophagy of human osteosarcoma cells, *International Journal of Clinical and Experimental Pathology*, 11 (2018) 3876.

Investigation of the Effect of Indatraline on Oxidative Damage Induced by Hydrogen Peroxide in C6 Glioma Cell Line

Fatih Yulak ^{1,a,*}, Bünyamin Üngür ^{2,b}

¹ Department of Physiology, School of Medicine, Sivas Cumhuriyet University, Sivas, Türkiye.

² School of Medicine, Sivas Cumhuriyet University, Sivas, Türkiye.

*Corresponding author

Research Article

History

Received: 10/08/2023

Accepted: 12/12/2023

Copyright



©2023 Faculty of Science,
Sivas Cumhuriyet University

fatihyulak@gmail.com

<https://orcid.org/0000-0003-3708-6752>

ungurbunyamin@gmail.com

<https://orcid.org/0009-0003-7635-6820>

ABSTRACT

Oxidative stress is defined as an imbalance between the generation of reactive oxygen species (ROS) and their scavenging. Indatralin, which has serotonin reuptake inhibitory activity, has not yet been studied for its ability to prevent oxidative damage. Our research's objective was to find out how indatraline defends against oxidative damage. C6 cells were used in the study and four different cell groups were created. The control group received no therapy at all. For 24 hours, cells in the H₂O₂ group were exposed to 0.5 mM H₂O₂. The indatraline group received indatraline treatments for 24 hours at various doses (0.5, 1, 2.5, 5 and 10 µM). For one hour, indatraline was administered to the indatraline + H₂O₂ group at various concentrations (0.5, 1, 2.5, 5 and 10 µM) before the group was subjected to 0.5 mM H₂O₂ for 24 hours. Following the occurrence of oxidative damage, total antioxidant status (TAS) and total oxidant status (TOS) levels were determined. Cell viability was also evaluated using the XTT assay. As a result, after hydrogen peroxide-induced oxidative damage, indatraline at doses of 10, 5, and 2.5 µM showed a protective effect by significantly enhanced cell survival in C6 cells (p < 0.001). Additionally, indatraline boosted the lowered TAS level while decreasing the elevated TOS levels following hydrogen peroxide-induced oxidative damage (p < 0.001).

Keywords: Oxidative damage, Hydrogen Peroxide (H₂O₂), Indatraline, C6 Glioma.

Introduction

Hydrogen peroxide (H₂O₂), superoxide anions (O₂⁻), and hydroxyl radicals (OH⁻), which are generated in minute quantities during regular oxygen metabolism, are known as reactive oxygen species (ROS). In the dismutation reaction of superoxide, two superoxide molecules receive two protons to produce hydrogen peroxide and molecule oxygen. Because non-radical products are produced in this process, either naturally or as a result of the enzyme superoxide dismutase (SOD), it is known as the dismutation reaction. In addition, ROS play a crucial role for these cells[1] in crucial signal transduction processes including secondary messenger systems[1]. Free radicals are extremely harmful to cells and maintain homeostasis by interacting harmoniously with the antioxidant system[2]. Disruption of the oxidant/antioxidant balance causes the formation of free radicals, damaging important cell structures such DNA[3], lipids[4], proteins[5], and carbohydrates[6]. Cells lose their ability to function and finally perish as a result of genetic damage brought on by an excessive increase in H₂O₂ production [7,8]. Lipid peroxidation is the primary mechanism of ROS-induced oxidative damage[9]. Due to the brain's high lipid content and heightened sensitivity to ROS, many neurodegenerative disorders are caused by increased oxidative stress [10–12]. Long-term

potentiation (LTP), a key process for learning, synaptic transmission, and neural plasticity, has been demonstrated to be dramatically reduced by elevated ROS concentrations[13,14]. Glial cells like microglia and astrocytes are the principal producers of ROS[15]. Therefore, lowering oxidative stress by regulating ROS generation in glial cells is crucial for the treatment of neurodegenerative disorders.

A strong inhibitor of serotonin (5-HT) reuptake is indatraline. By inhibiting 5-HT reuptake, serotonin reuptake medications boost serotonin transmission and have antidepressant effects by reducing the number and sensitivity of post synaptic receptors[16], [17]. Numerous psychiatric medications, including serotonin reuptake inhibitors, have been shown in studies to have neuroprotective benefits[18,19]. One study suggested that indatralin may slow the progression of various neurodegenerative disorders, including Alzheimer's disease, by inducing autophagy.[20]. Its effects on oxidative damage in C6 glioma cells, however, have not yet been studied and are still unknown. In this study, we looked at how indatraline affected the production of ROS and the viability of C6 glioma cells under an oxidative damage scenario generated by H₂O₂.

Material And Methods

Cell Culture

C6 Glioma (CRL107) cell lines were acquired from the American Type Culture Collection and cultured in DMEM (Thermo Fisher Scientific, Altrincham, UK) containing 10% Fetal Bovine Serum (FBS) (Sigma-Aldrich Co., St Louis, MO, USA), 1% L-glutamine (Sigma-Aldrich Co., St Louis, MO, USA), and 1% penicillin/streptomycin. The cells were kept at 37°C in a 5% CO₂ humidified environment. Before treatment, stock solutions were made by dissolving indatraline and H₂O₂ (Sigma-Aldrich Co., St. Louis, MO, USA) in DMEM.

Cell Viability Assay

The Roche Diagnostic, Massachusetts, USA, XTT assay was employed to measure cell viability. Prior to indatraline treatment, C6 glioma cells were seeded in 96-well plates at a density of 1x10⁴ cells per well in 100 mL of DMEM. Four cell groups were set up the following day to assess indatraline's protective effects. The control group did not receive any care. For 24 hours, cells in the H₂O₂ group were exposed to 0.5 mM H₂O₂. For 24 hours, cells in the indatraline group were exposed to indatraline at different concentrations (10, 5, 2.5, 1 ve 0.5 µM). For 24 hours, cells in the indatraline group were exposed to indatraline at different concentrations (10, 5, 2.5, 1 ve 0.5 µM). The indatraline + H₂O₂ group's cells had an hour of pretreatment with varying doses of indatraline (10, 5, 2.5, 1 or 0.5 µM) before being exposed to 0.5 mM H₂O₂ for 24 hours. After incubation, the medium was taken out, and phosphate buffered saline was used to wash the wells twice. The plates were then kept at 37°C for 4 hours after the last step of adding 100 µL of DMEM without phenol red and 50 µL of XTT labeling solution to each well. The plates were shaken, and an ELISA microplate reader (Thermo Fisher Scientific, Altrincham, UK) was used to measure the absorbance at 450 nm. The cell viability was determined by comparing the percentage of viable cells to the control, or untreated cells, in each experiment three times (Figure 1).

Preparation of Cells Homogenates

Sterilized tubes were used to collect the cells for each group. They underwent a 10-minute centrifugation at 2000 rpm. Supernatants were eliminated. PBS (pH: 7.4) is used to thin the cell suspension to a cell concentration of roughly 1 million cells per milliliter. This component of the cells that are in the under the tubes, suspended. Through numerous freeze-thaw cycles, the cells were destroyed in order to release the internal components. They underwent a 10-minute, 4°C, 4000 rpm centrifugation process. Then, using TAS and TOS commercial kits (Rel Assay Kit Diagnostics, Antep, Turkey), the supernatants were collected for biochemical examination of total antioxidant status (TAS) and total oxidant status (TOS). The total protein levels in samples were determined using

a Bradford protein assay kit (Merck Millipore, located in Darmstadt, Germany)[21].

Measurement of TAS and TOS

An automated test technique that Erel had previously created was used to measure the TAS concentrations in the cell supernatants [22]. The technique is based on detecting the absorbance of colored diacidly radicals during free radical reactions, starting with the generation of hydroxyl radicals in the Fenton reaction, in order to track the reaction rate of free radicals. According to their quantities, antioxidants in the tissue samples should decrease coloring[22]. Micromolar Trolox equivalents per milligram of tissue protein (mol Trolox Eq/mg protein) were used to express the results. Using Erel's automated test approach, tissue TOS concentrations in cell supernatants were measured[23]. The method enables the measurement of tissue ferric ion levels using xylenol orange in order to quantify TOS levels because ferrous ion is converted to ferric ion when sufficient amounts of oxidants are present in the medium. The calibration of the assay was done using hydrogen peroxide[23]. In micromolar hydrogen peroxide equivalents per milligram tissue protein (µmol H₂O₂ Eq/mg protein), the assay's results were expressed.

Statistical Analysis

The results were expressed as a mean ± standard error of the mean (SEM). The data analyses were performed with SPSS Version 23.0 for Windows. The data were evaluated using a one-way analysis of variance (ANOVA) and a postdoc Tukey test was utilized to identify the differences between the experimental groups, and a value of p < 0.05 was accepted as statistically significant.

Results

Effects of Indatraline on Cell Viability in C6 Glioma Cells Induced Oxidative Damage by H₂O₂

To assess the neuroprotective effects of indatraline on C6 glioma cell toxicity by, an XTT cell viability experiment was carried out. Our work employed the 0.5 mM H₂O₂ IC₅₀ value that was discovered in earlier research on C6 glioma cells[24]. According to Figure 1, continuous H₂O₂ (0.5 mM) concentration significantly reduced cell viability when compared to control (*P<0.001, Figure 1). At concentrations of 10, 5, and 2.5 µM, indatraline treatment significantly boosted the viability of H₂O₂-induced C6 glioma cells (αP<0.001, Figure 1). Additionally, there was no discernible difference between the control group and the C6 glioma cells treated with various amounts of indatraline in cells not treated with H₂O₂ (P>0.05).

Groups (XTT)	Cell Viability (% of control)	SEM
Control	100	0
H ₂ O ₂	52.73	± 0.81
Ind 10 µM + H ₂ O ₂	78.64	± 1.57
Ind 5 µM + H ₂ O ₂	72.53	± 0.91
Ind 2.5 µM + H ₂ O ₂	67.34	± 1.93
Ind 1 µM + H ₂ O ₂	53.53	± 1.74
Ind 0.5 µM + H ₂ O ₂	55.63	± 1.82
Ind 10 µM	105.52	± 1.42
Ind 5 µM	104.42	± 2.53
Ind 2.5 µM	103.56	± 2.41
Ind 1 µM	100.11	± 1.11
Ind 0.5 µM	99.22	± 2.12

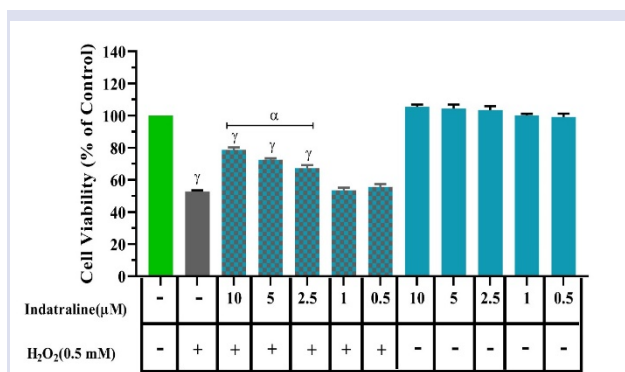


Figure 1. Effects of indatraline on C6 glioma cells' ability to survive after being subjected to H₂O₂-induced oxidative damage. Results are shown as the mean ± SEM (^γP<0.001, ^αP<0.001).

Evaluation of the Effect of Indatraline on TAS and TOS in C6 Glioma Cells Induced Oxidative Damage by H₂O₂

Using commercial kits, TAS and TOS were evaluated in C6 glioma cells. H₂O₂-treated cells had considerably lower TAS levels than control cells in C6 glioma cells (^γP<0.001, Figure 2). The TAS level in the H₂O₂ + indatraline group was considerably higher than that in the H₂O₂ group (^αP<0.001, figure 2). In H₂O₂-treated cells compared to control, TOS level was considerably higher (^γP<0.001, Figure 2). When compared to the H₂O₂ group, the TOS level was considerably lower in the H₂O₂ + indatraline group (^αP<0.001, Figure 2).

Groups (TAS)	mol Trolox Eq/mg protein	SEM
Control	0.76	± 0.041
H ₂ O ₂ (0.5 mM)	0.49	± 0.022
Ind 10 µM + H ₂ O ₂	0.72	± 0.025
Ind 10 µM	0.75	± 0.017

Groups (TOS)	µmol H ₂ O ₂ Eq/mg protein	SEM
Control	1.54	± 0.085
H ₂ O ₂ (0.5 mM)	4.01	± 0.094
Ind 10 µM + H ₂ O ₂	2.54	± 0.076
Ind 10 µM	1.55	± 0.083

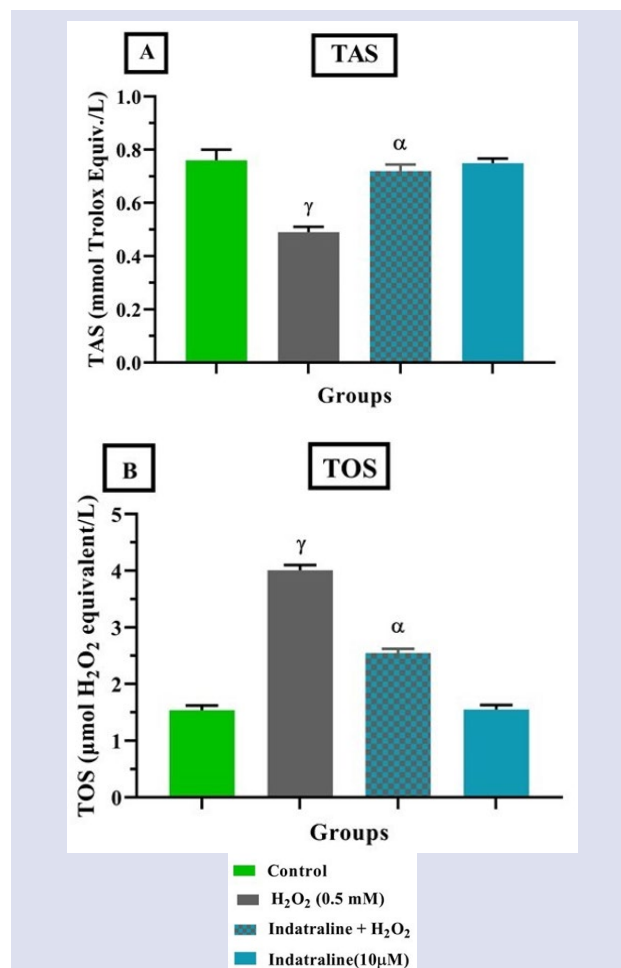


Figure 2. Effects of indatraline on TAS and TOS following H₂O₂ treatment in C6 glioma cells. Values are presented as mean ± SEM (^γP<0.001, ^αP<0.001).

Discussion

Numerous mechanism can cause oxidative stress, which can cause cell death and brain dysfunction [25]. As a result, it may increase the risk of developing neurodegenerative illnesses like Alzheimer's, Parkinson's, Huntington, and others [26,27], with ROS and H₂O₂ in general, which are the main causes of oxidative stress, contributing to the underlying causes of these conditions [28]. Indatraline's ability to protect C6 glioma cells from oxidative damage brought on by hydrogen peroxide was assessed in this work for the first time. Here, indatraline significantly shielded C6 cells from the toxicity brought on by hydrogen peroxide. Additionally, indatraline pretreatment demonstrated a strong protective effect by raising TAS level and lowering TOS level against hydrogen peroxide-induced oxidative damage in C6 cells.

Numerous antidepressants, including indatraline, have been demonstrated in prior research to shield the brain from oxidative stress. In vitro research done concurrently with our findings revealed that indatraline greatly increased cell viability in HT-22 hippocampus cells subjected to glutamate-induced toxicity[29]. Indatraline

may mitigate various neurodegenerative illnesses marked by the buildup of fibrillary tangles, according to another in vivo study[20]. According to yet another study, serotonin reuptake inhibitors like indatraline exhibit brain-protective effects via boosting the brain's production of neurotrophic factor[30], [31]. Indatraline shown a neuroprotective effect against neuropathic pain in another trial of the condition[32]. Salam et al. demonstrated, in accordance with our findings, that serotonin reuptake medications boosted the antioxidant system and decreased oxidative stress by raising TAS levels in the brain and liver[33]. In a comparable manner it was demonstrated in a comparable in vivo investigation using the serotonin reuptake inhibitor fluvoxamine that elevated TAS levels lowered oxidative stress by activating the antioxidant system[34].

Our results support earlier research and demonstrate that indatraline protects against oxidative damage by enhancing the antioxidant system and suppressing the oxidant system in glial cells and makes a major contribution to their survival. In the pathophysiology of several neurodegenerative illnesses, glial cells are crucial. Consequently, in the treatment of such disorders, indatraline might function as a protective agent. However, further research is required in this area.

This article has some limitations. Instead of primary glial cells, glioma cells, a secondary cell line, were used for this study. The techniques used are insufficient to explain indatraline's protective effects. More methodologies and mechanisms need to be studied, such as measurement of oxidative stress parameters including ROS levels and lipid peroxidation.

Conclusion

The results of this investigation demonstrated that indatraline decreased the oxidative damage caused by hydrogen peroxide in C6 glial cells. These effects are most likely brought about by the antioxidant system being stimulated, which lowers oxidative stress. Indatraline may therefore have a calming impact on the central nervous system. To clarify this, more study is necessary.

Acknowledgment

This study was supported by TUBITAK as a 2209-A project (1919B012109251). The authors would like to thank TUBITAK and the management of Sivas Cumhuriyet University, Faculty of Medicine, CÜTFAM Research Center, Sivas, Turkey for providing the necessary facilities to conduct this study.

Conflict of Interest

The authors declare that they have no conflict of interest.

References

- [1] H. J. Forman, Use and abuse of exogenous H₂O₂ in studies of signal transduction, *Free Radic. Biol. Med.*, vol. 42(7) (2007) 926–932.
- [2] Karabulut H., Şükrü Gülay M., Serbest Radikaller., *MAKÜ Sag. Bil. Enst. Derg.*, 4(41) (2016) 50–59.
- [3] Kuraoka B., Robins P., Masutani C., Hanaoka F., Gasparutto D., Harbiyeli J., Ahsap RD., Lindahl T., Oxygen free radical damage to DNA. Translesion synthesis by human DNA polymerase ϵ and resistance to exonuclease action at cyclopurine deoxynucleoside residues., *J. Biol. Chem.*, 276(52) (2001) 49283–49288.
- [4] Devasagayam T. P. A., Bloor K. K., and Ramasarma T., Methods for estimating lipid peroxidation: an analysis of merits and demerits., *Indian J. Biochem. Biophys.*, 40(5) (2003) 300–308.
- [5] Bengal W., Free Radicals and Their Role in Different Clinical Conditions : An Overview, 1(3) (2010) 185–192.
- [6] Devasagayam T. P. A., Tilak J. C., Bloor K. K., Sane K. S., Ghaskadbi S. S., and Lele R. D., Free radicals and antioxidants in human health: current status and future prospects., *J. Assoc. Physicians India*, 52(10) (2004) 794–804.
- [7] Gandhi S. and Abramov A. Y., Mechanism of Oxidative Stress in Neurodegeneration, *Oxid. Med. Cell. Longev.*, 2012 (2012) 428010. doi: 10.1155/2012/428010.
- [8] Coyle J. T. and Puttfarcken P., Oxidative Stress, Glutamate, and Neurodegenerative Disorders, *Science.*, 262(5134) (1993)689–695.
- [9] Shirley R., Ord E. N. J., and Work L. M., Oxidative Stress and the Use of Antioxidants in Stroke., *Antioxidants*, 3(3) (2014) 472–501.
- [10] Dias V., Junn E., and Mouradian M. M., The role of oxidative stress in Parkinson's disease., *J. Parkinsons. Dis.*, 3(4) (2013) 461–491.
- [11] Gella A. and Durany N., Oxidative stress in Alzheimer disease., *Cell Adh. Migr.*, 3(1) (2009) 88–93.
- [12] Jelinek M., Jurajda M., and Duris K., Oxidative Stress in the Brain: Basic Concepts and Treatment Strategies in Stroke., *Antioxidants*, vol. 10(12) (2021) 1886.
- [13] Knapp L. T. and Klann E., Role of reactive oxygen species in hippocampal long-term potentiation: contributory or inhibitory?, *J. Neurosci. Res.*, 70(1) (2002) 1–7.
- [14] Zhuo M., Small S. A., Kandel E. R., and Hawkins R. D., Nitric oxide and carbon monoxide produce activity-dependent long-term synaptic enhancement in hippocampus., *Science*, 260(5116) 1946–1950.
- [15] Rodrigo R., Fernández-Gajardo R., Gutierrez R., Matamala J.M., Carrasco R., Miranda-Merchak A., Feuerhake W., Oxidative stress and pathophysiology of ischemic stroke: novel therapeutic opportunities., *CNS Neurol. Disord. Drug Targets*, 12(5) (2013) 698–714.
- [16] Bøgesø K. P., Christensen A. V., Hyttel J., and Liljefors T., 3-Phenyl-1-indanamines. Potential antidepressant activity and potent inhibition of dopamine, norepinephrine, and serotonin uptake., *J. Med. Chem.*, 28(12) (1985) 1817–1828.
- [17] Hyttel J. and Larsen J. J., Neurochemical profile of Lu 19-005, a potent inhibitor of uptake of dopamine, noradrenaline, and serotonin., *J. Neurochem.*, 44(5) (1985) 1615–1622.
- [18] Hunsberger J., Austin D. R., Henter I. D., and Chen G., The neurotrophic and neuroprotective effects of psychotropic

- agents., *Dialogues Clin. Neurosci.*, 11(3) (2009) 333–348.
- [19] Young L. T., Neuroprotective effects of antidepressant and mood stabilizing drugs., *Journal of psychiatry & neuroscience : JPN*, 27(1) (2002) 8–9.
- [20] Cho Y. S., Yen C., Shim J. S., Kang D. H., and Kang S. W., Antidepressant indatraline induces autophagy and inhibits restenosis via suppression of mTOR / S6 kinase signaling pathway, *Nat. Publ. Gr.*, 6(5) (2016) 1–9.
- [21] Kruger N. J., The Bradford Method for Protein Quantitation BT - The Protein Protocols Handbook, Ed. Totowa, NJ: Humana Press, (2002)15–21.
- [22] Erel O., A novel automated method to measure total antioxidant response against potent free radical reactions, *Clin. Biochem.*, 37(2) (2004) 112–119.
- [23] Erel O., A new automated colorimetric method for measuring total oxidant status, *Clin. Biochem.*, 38(12) (2005) 1103–1111.
- [24] Ergül M. and Taşkıran A. Ş., Thiamine protects glioblastoma cells against glutamate toxicity by suppressing oxidative/endoplasmic reticulum stress, *Chem. Pharm. Bull.*, 69(9) (2021) 832–839.
- [25] Armstrong R. W. and Wu C. C., Lattice Misorientation and Displaced Volume for Microhardness Indentations in MgO Crystals, *J. Am. Ceram. Soc.*, 61(3–4) (1978) 102–106.
- [26] Rao A. V and Balachandran B., Role of oxidative stress and antioxidants in neurodegenerative diseases., *Nutr. Neurosci.*, 5(5) (2002) 291–309.
- [27] Niedzielska E., Smaga I., Gawlik M., Moniczewski A., Stankowicz P., Pera J., Filip M., Oxidative Stress in Neurodegenerative Diseases., *Mol. Neurobiol.*, 53(6) (2016) 4094–4125.
- [28] Li J., O W., Li W., Jiang Z.-G., and Ghanbari H. A., Oxidative stress and neurodegenerative disorders., *Int. J. Mol. Sci.*, 14(12) (2013) 24438–24475.
- [29] Maher P. and Davis J. B., The role of monoamine metabolism in oxidative glutamate toxicity., *J. Neurosci. Off. J. Soc. Neurosci.*, 16(20) (1996) 6394–6401.
- [30] Nibuya M., Morinobu S., and Duman R. S., Regulation of BDNF and trkB mRNA in rat brain by chronic electroconvulsive seizure and antidepressant drug treatments., *J. Neurosci. Off. J. Soc. Neurosci.*, 15(11) (1995) 7539–7547.
- [31] Lindén A. M., Väisänen J., Lakso M., Nawa H., Wong G., and Castrén E., Expression of neurotrophins BDNF and NT-3, and their receptors in rat brain after administration of antipsychotic and psychotropic agents., *J. Mol. Neurosci.*, 14(1–2) (2000) 27–37.
- [32] Hacısüleyman L., Saraç B., and Joha Z., Analgesic Effects of Vilazodone, Indatraline, and Talsupram in a Rat Model of Neuropathic Pain., *Turkish J. Pharm. Sci.*, 19(3) (2021) 336–342.
- [33] Abdel-Salam O. M. E., Morsy S. M. Y., and Sleem A. A., The effect of different antidepressant drugs on oxidative stress after lipopolysaccharide administration in mice., *EXCLI J.*, 10 (2011) 290–302.
- [34] Severcan S. M., Severcan C., Tazehkand M. N., and Oz Z. S., Evaluation of Oxidant-Antioxidant Status of Fluvoxamine on Human Lymphocyte Cell Culture, 8(1) (2021) 79–83.

Evaluation of the Interactions of Cabozantinib with Topoisomerase Enzymes by *in vitro* Enzyme Activity Assays, and its Effects on Cancer Cell Proliferation

FeYZa OfIaz ^{1,a}, Naz Unal ^{2,b}, Burcin Gungor ^{2,c}, Pakize Canturk ^{3,d,*}

¹ Department of Physiology, Faculty of Medicine, Sivas Cumhuriyet University, 58140, Sivas, Türkiye

² Department of Biochemistry, Faculty of Pharmacy, Yeditepe University, 34755, Istanbul, Türkiye

³ Department of Pharmaceutical Biotechnology, Faculty of Pharmacy, Sivas Cumhuriyet University, 58140, Sivas, Türkiye

*Corresponding author

Research Article

History

Received: 16/10/2022

Accepted: 15/12/2023

Copyright





©2023 Faculty of Science,
Sivas Cumhuriyet University


ABSTRACT


The discovery of many drugs in recent years provides a definitive solution in the treatment of various diseases, but today, despite the discovery of many effective anticancer drugs, there are various types of cancer that have limitations in treatment and are still not completely curable. Since most of these limitations are due to cancer cells gaining resistance or compounds only being effective in certain types of cancer cells, the search for more effective anticancer drugs that are also effective in these types of cancer is inevitable. Cabozantinib is in medical use as a highly effective anticancer drug in various types of cancer, such as medullary thyroid cancer and kidney cancer. The anticancer properties of the Cabozantinib compound have attracted more attention in recent years, however, more studies are needed to define the anticancer activities of this compound. In our study, the interactions of Cabozantinib with topoisomerase enzymes, were demonstrated through *in vitro* enzyme activity tests, and the anti-proliferative effect of Cabozantinib was studied on MCF7, A549 and PC3 cell lines. By analyzing the interactions of the Cabozantinib with topoisomerases, the action mechanisms of the compound at the molecular level was evaluated.


Keywords: Topoisomerase enzymes, Cancer, Cabozantinib, Tyrosine kinase inhibitor, DNA damage.

 feyza1994@gmail.com


 <https://orcid.org/0000-0002-2131-6982>


 burcin.gungor@yeditepe.edu.tr

 <https://orcid.org/0000-0001-7725-5835>

 nazunal2012@gmail.com

 <https://orcid.org/0009-0000-3327-0428>

 pcanturk@cumhuriyet.edu.tr

 <https://orcid.org/0000-0001-8623-784X>

Introduction

DNA topoisomerase enzymes play one of the most critical roles in the intact transmission of DNA, our hereditary material, to new generations. How these roles are fulfilled has been explained in detail through extensive research, based on the functions of topoisomerase enzymes in intracellular events such as replication and transcription, and therefore they are primarily targeted in anti-cancer drug development research [1]. Topoisomerase enzymes are divided into two groups according to their ability to create breaks on DNA. In contrast to Topoisomerase I enzymes, which relax DNA by creating single-strand breaks in DNA, Topoisomerase II enzymes simultaneously break double-stranded DNA molecules and allow another double-stranded DNA molecule to pass through them, creating temporary breaks in DNA [2, 3]. Breaks in these DNA strands are reversible unless prevented by an inhibitor, are stabilized according to intracellular mechanisms, and topoisomerase enzymes recombine the strands in a controlled manner. By restricting or inhibiting the activities of these enzymes, uncontrolled and excessive breaks can be created on the DNA. Thus, in light of the knowledge that cancer cells divide rapidly and uncontrollably, aiming to increase the amount of DNA breaks that will disrupt the DNA integrity of these cells is a competent anticancer approach [4–7]. The reasons for targeting topoisomerase I are the remarkable findings

that rapidly dividing cancer cells with high topoisomerase I levels are highly sensitive to topoisomerase I inhibitors. Cancer cells become more sensitive to Topoisomerase I-mediated therapies due to overexpression of the topoisomerase I enzyme and associated impairment of DNA repair mechanisms [8, 9].

Clinical Topoisomerase I inhibitors derived from Camptothecin (such as Irinotecan and Topotecan) appear to be highly effective in treating many types of cancer, including colon, ovarian, pancreatic and small cell lung cancers [10-13], whereas Camptothecin analogues Belotecan and Topotecan for sensitive-relapsed small-cell lung cancer (SCLC)[14]. However, some of these cancer types cannot be defeated because they develop drug resistance that reduces the treatment potential of these inhibitors [10-12]. These topoisomerase I-targeting derivatives stabilize topoisomerase I enzymes to form DNA-drug-enzyme complexes and are called enzyme poisons. Because of the fact that the more numerous targets a drug has, the more toxic that drug is, compounds that target too many molecules, such as Camptothecins, create toxicity that must be avoided. However, it is still very reasonable to use less toxic derivatives or combinations of these compounds, since topoisomerase enzymes, whose expression increases in parallel with the rapidly increasing replication of the cancer cell population, will be selectively poisoned by these drugs.

Because of this poisoning mechanism, DNA breaks begin to form early in replication, and although this is a reversible reaction, the DNA breaks reach the amount required to destroy cancerous cells [12, 15]. Moreover, Topoisomerase I and Topoisomerase II enzymes are both involved in DNA metabolism, so targeting both of these enzymes can impair resistance resulting from downregulation of the target enzyme and compensatory upregulation of the other topoisomerase enzyme [3, 10, 16].

One of the factors that cause cell death triggered by apoptosis is DNA-damaging compounds that induce many different DNA lesions. It has been stated that DNA damage can be defined as many different DNA modifications that can activate apoptosis, and overexpression of repair proteins involved in DNA repair pathways has a negative effect on cells. The mechanisms by which DNA lesions trigger apoptosis also vary depending on how DNA damage occurs and the cell's reaction to it [17]. Tyrosine kinases regulate DNA damage signaling pathways to orchestrate cell cycle, growth, proliferation, differentiation and survival, while DNA damage response proteins (DDR) alarmed by DNA lesions or chromatin alterations, manipulates the DNA repair system to keep the genome intact [17, 18]. Receptor tyrosine kinases (RTKs) perform functions such as cell proliferation, survival and differentiation, and are targeted for these functions in cancer treatment.

Several tyrosine kinase inhibitors (TKIs) have been approved by the FDA for targeted therapy, and combination therapies with other anticancer drugs or TKIs show promising synergistic effects [19, 20]. Cabozantinib (CBZ) is an orally available and bioavailable small molecule receptor tyrosine kinase (RTK) inhibitor antineoplastic agent. Approved by the US Food and Drug Administration (FDA), CBZ is a drug produced by EXELIS for patients with renal carcinoma, medullary thyroid cancer and kidney cancer [21, 22]. Cabozantinib has been proposed as a compound for the treatment of cases of resistance to drugs that are ABCG2 substrates. As the researchers reported, CBZ sensitized ABCG2-overexpressing cells to the drugs mitoxantrone, SN-38, and topotecan at non-toxic concentrations, thus suggesting Cabozantinib as a compound for treatments of drug resistance that is an ABCG2 substrate [23].

In our study, in order to elucidate one of the molecular mechanisms of how Cabozantinib's anticancer drug properties occur, we investigated the interactions of topoisomerase enzymes with Cabozantinib *in vitro* by performing enzyme activity tests. Whether Cabozantinib has a toxic effect on cancer cells was analyzed by viability assays in different types cancer cell lines for which there is limited data and for the cancer types that have not yet received FDA approval for Cabozantinib treatment.

Methods

All of the compounds used in our experiments were purchased in lyophilized form. Cabozantinib (AdooQ,

Irvine, CA, USA), Etoposide (Sigma-Aldrich, St. Louis, MO, USA) were dissolved in 100% Dimethyl Sulfoxide (Sigma-Aldrich, St. Louis, MO, USA). A549 (CCL-185) and PC3 (CRL-1435) cell lines were obtained from ATCC and MCF7 cell line was kindly gifted by Prof Dilek Telci Temeltas, Genetics and Bioengineering Department of Yeditepe University.

Investigation of Topoisomerase-DNA Interactions Enzyme Activity Tests

The reaction products were runned by horizontal electrophoresis (5V/cm) in 1xTAE buffer on a 1% agarose gel. Relaxation assay substrats were runned in the absence of EtBr on agarose gel, while decatenation substrates were runned in the presence of EtBr. Cabozantinib (CBZ) and control compound Etoposide (ETP) were dissolved in 100% DMSO.

Supercoiled DNA Relaxation Assays

Relaxation of supercoiled plasmid DNA was performed in a total of 20 μ L volume of buffer (72 mM KCl, 5 mM $MgCl_2$, 5 mM DTT, 5 mM spermidine and 0.1% bovine serum albumin), with 0.5 μ g of supercoiled DNA (Takara, Shiga, Japan) and 1 unit of human topoisomerase I enzyme (Topogen, CO, USA). The definition of one unit of topoisomerase enzyme is the amount of enzyme that relaxes 0.5 μ g of supercoiled DNA in 30 minutes at 37°C. Compared to the leading bands of supercoiled DNA on the gel, supercoiled DNA, which is less supercoiled by the DNA relaxation activity of the enzyme, appears further back on the gel [24, 25].

Decatenation Assays

In the analysis of decatenation activity reactions, human topoisomerase II (Topogen, CO, USA) enzyme was applied with catenated DNA (kDNA) substrates for 30 minutes at 37 °C in the presence and absence of the test compound [25, 26]. In the assays, 0.2 μ g kDNA substrate, and 1 unit of human topoisomerase II enzyme, were interacted in a total of 20 μ l final volume in the reaction buffer (50 mM Tris-Cl pH 8.0, 120 mM KCl, 10 mM $MgCl_2$, 0.5 mM ATP, 0.5 mM Dithiothreitol). Enzyme activity was terminated using topoisomerase II stop buffer (5% sarcosyl, 0.0025% bromphenol blue, 25% glycerol).

The Cell Viability Assay

The effect of the CBZ was examined by 3-(4,5-dimethylthiazol-2-yl)-2,5-diphenyl tetrazoliumbromide (MTT) (Sigma-Aldrich, St. Louis, MO, USA) assay against breast cancer cell line (MCF7), non-small lung cancer cell line (A549) and prostate cancer cell line (PC3). Each cell line was grown and maintained in DMEM (Gibco, Thermo Fisher Scientific, MA, USA) medium containing 10% (v/v) heat-inactivated fetal bovine serum (FBS) (Gibco, Thermo Fisher Scientific, MA, USA), 2mM L-glutamine (Gibco, Thermo Fisher Scientific, MA, USA) and 50 units/mL penicillin-streptomycin (Invitrogen, Thermo Fisher Scientific, MA, USA). 1mg/mL of MTT was applied to the cells. When MTT is applied to living cells, it transforms into

a blue-violet, water-insoluble reduced form, formazan. Determination of viable cell number was calculated by determining the color intensity obtained after dissolving formazan in alcohol by photometric measurements. To investigate the effect of CBZ on MCF7, A549 and PC3 cell viability, CBZ was applied at 5 different concentrations (1.25-20 μ M). The cells were seeded at a density of 3500 cells/well a day before treatment with the sample. Subsequently, different concentrations of CBZ were administered to cells. After 72 hours of incubation, formazan formation was determined for each concentration and formazan crystals were dissolved by addition of 150 μ L isopropanol. The percentage of viable cells was calculated based on the values acquired by colorimetric methods using Ascent spectrophotometer at 570 nm. Cell group which was not treated with CBZ considered as 100% viable (control group) and its cytotoxic effect calculated as follows: (Compound Abs-Blank Abs)*100/(Control Abs-Blank Abs). Each condition was studied in five replicates.

Results

Supercoiled DNA Relaxation Assays

Before performing the enzyme activity tests, it was analyzed whether CBZ had DNA intercalation activity and it was determined that there was no intercalative formation between DNA and CBZ under the assay conditions. The supercoiled DNA and CBZ bands remained in the lane similar to the band of supercoiled DNA (Figure 1). When CBZ was applied together with supercoiled DNA, the distance of supercoiled DNA running in the gel was the same as the distance of DNA running in the lane where only supercoiled DNA was loaded. The relaxed DNA bands seen in the remaining part of the gel were DNA structures that were physically formed due to the experimental conditions and they ran at a similar distance to each other in the experiment, therefore they were not taken into consideration for examining the effect of DNA intercalation.

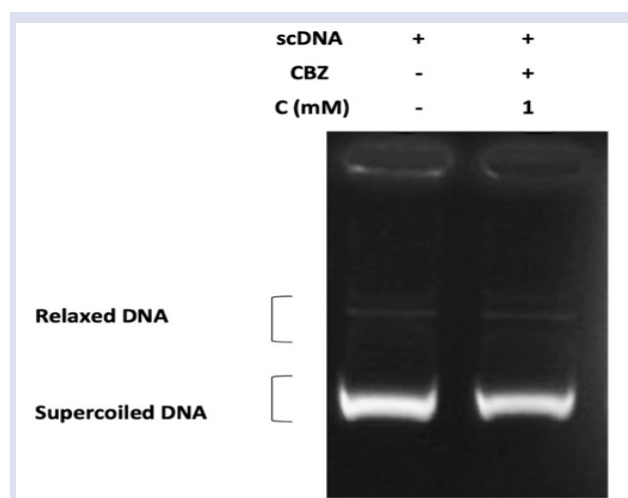


Figure 1. DNA intercalation test. Line 1; 0.5 μ g supercoiled DNA, line 2; 0.5 μ g supercoiled DNA and 1mM CBZ.

With the interaction of supercoiled DNA and topoisomerase I enzyme, DNA bands relaxed and ran behind in the gel (Figure 2, lane 2). However, due to the inhibition activity that occurred when CBZ was added, the DNA bands appeared to run the same distance as the control supercoiled DNA. According to the results of supercoiled DNA relaxation tests, the CBZ compound inhibited the topoisomerase I enzyme in the concentration range of 1- 5 mM (Figure 2, lane 5).

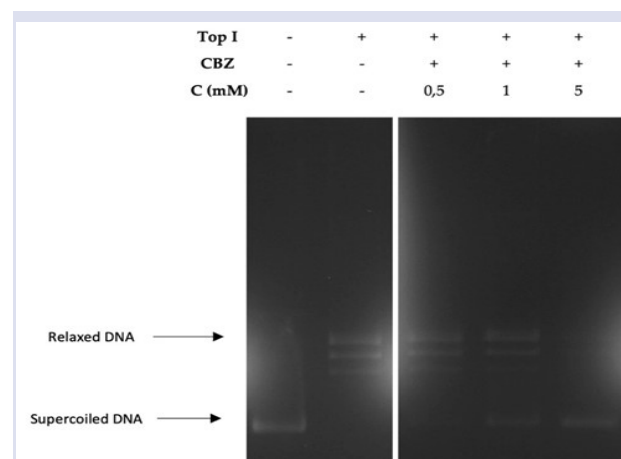


Figure 2. Cabozantinib inhibited topoisomerase I enzyme. Left panel: Line 1; 0.5 μ g supercoiled DNA, line 2; 0.5 μ g supercoiled DNA and Topoisomerase I enzyme. Right panel: All in the presence of 0.5 μ g supercoiled DNA and Topoisomerase I enzyme, line 1; 0.5mM CBZ, line 2; 1 mM CBZ, line 3; 5mM CBZ.

Decatenation Assays

As seen in the gel, catenated DNA was able to come out of the gel by the interaction of Topoisomerase II enzyme (Figure 3, lane 2).

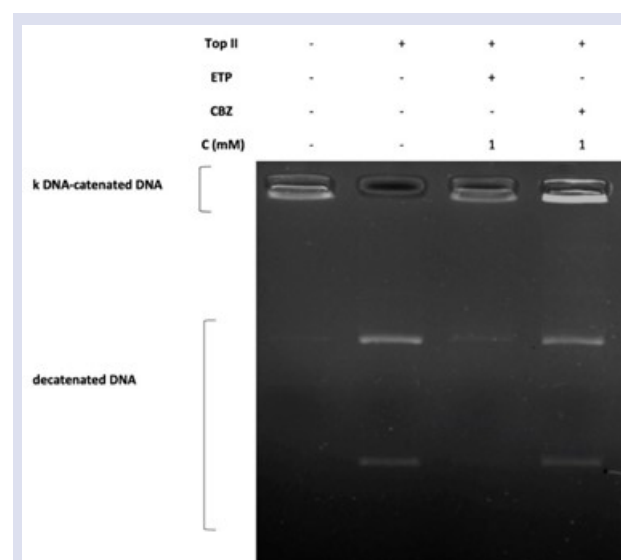
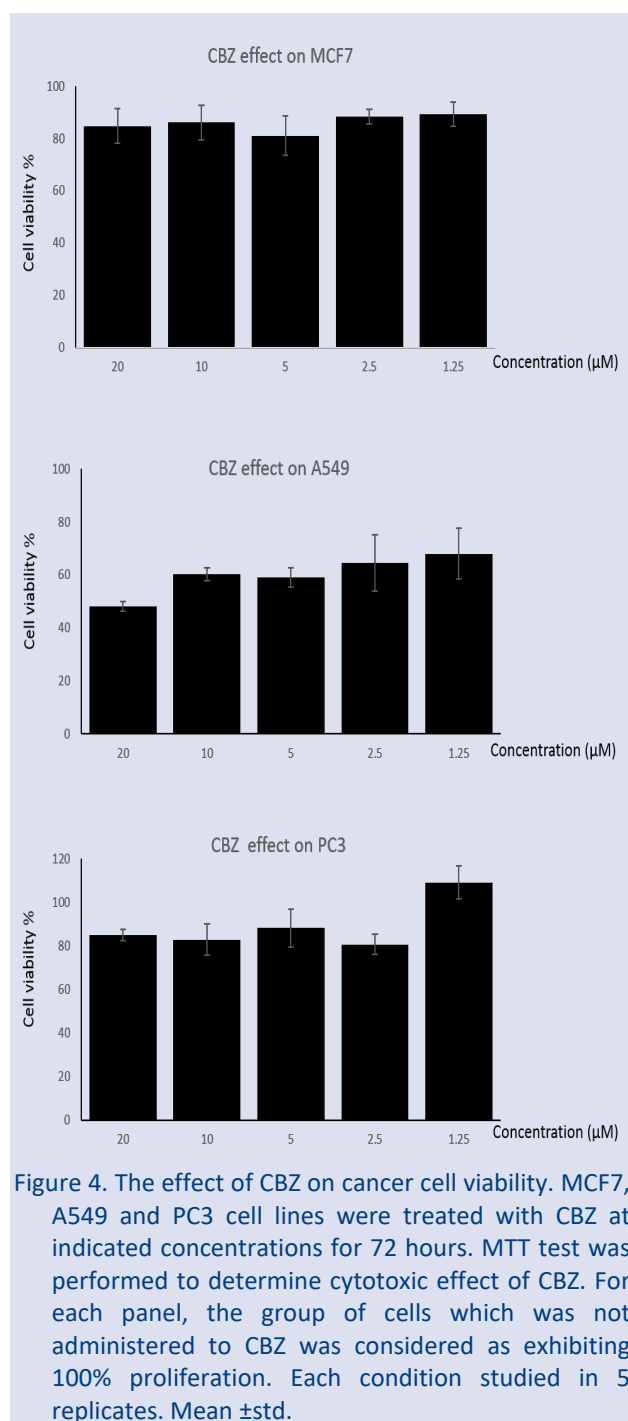


Figure 3. Topoisomerase II decatenation test. Line 1; k-DNA in the absence of topoisomerase II, 2; k-DNA in the presence of topoisomerase II, 3; k-DNA in the presence of topoisomerase II and ETP at 1mM concentration, 4; k-DNA in the presence of topoisomerase II and CBZ at 1mM concentration.

When Etoposide (ETP) added, catenated DNA (kDNA) could not run in the gel because enzyme activity was lost (Figure 3, lane 3), but CBZ compound at 1mM concentration (Figure 3, line 4) did not show an inhibitory effect similar to ETP (Figure 3, lane 4).

The Cell Viability Assay

The anti-proliferative effect of CBZ was studied on MCF7, A549 and PC3 cell lines. Each cell line grown in 96 well plate, was exposed to CBZ's five different concentrations (1.25-20 μM) for 72 hours. MTT assay results demonstrated that there is no concentration dependent inhibitory effect of CBZ (Figure 4) on cell lines, studied.



Discussion

By preferring anticancer molecules that cause breaks in DNA to rapidly proliferating cancer cells, many intracellular pathways can be blocked and rapid destruction of cancer cells can occur [27, 28]. With the mentioned inhibitory activity, the cell's ability to relieve the stress provided by topoisomerases is prevented, and a sad drama occurs in the cancerous cell, in which the DNA strands are torn into pieces and the cell is dragged into apoptosis [29, 30]. Protein kinases have important roles in cell signaling and help destroy cancer cells through apoptosis. The majority of cancers are known to rapidly develop resistance to kinase inhibitors administered alone; therefore, a molecule that interacts with more than one kinase appears critical to be a successful anticancer drug. Depending on the signal transmission received in the cell, they change the enzyme activity in the target protein and its interactions with other proteins [21, 22]. In terms of frequency and appropriateness of use in clinical practice, most of the approved and recommended TKIs have not yet achieved significant clinical success. Among the highlights, it is noteworthy that combination treatments provide successful results. It is suggested that checkpoint inhibitors and epigenetic modifiers combined with TKI may show significant effectiveness in many types of cancer, including lymphoma cells [31, 32]. For the targeted treatment of unresectable HCC, Lenvatinib, Cabozantinib, Ramucirumab and Regorafenib have been approved [33].

Cabozantinib is a multi-targeted small-molecule TKI, which targets VEGFR, MET and AXL and it has gained importance that Cabozantinib is effective after Sorafenib administration in the treatment of HCC (Cabometyx[®] brand). The effectiveness of this compound under another brand, for the treatment of "unresectable locally advanced" or "metastatic Medullary thyroid cancer (MTC)", has also come to the fore (Cometriq[®] brand). Because the Cabometyx[®] is formed as a tablet and Cometriq[®] formed as a capsule, it has been reported that their formulation can not be fully equal indeed [20, 32]. A phase II study expected to reveal the efficacy of Cabozantinib in the treatment of patients with incurable, refractory, germ cell tumors, including ovarian germ cell tumors, have started in May 2021 (NCT04876456). However, in cases where the response to immunotherapy in ovarian cancer is unfortunately low, the effectiveness of Cabozantinib in this type of cancer has become a matter of possibility [32]. According to a phase II study reported in recent years, the effectiveness of Cabozantinib in the second- and third-line treatments of clear cell ovarian, fallopian tube or primary peritoneal carcinoma was limited to a minimal level [34]. In addition to all these promising results, CBZ has also been proven to have an effect on other types of cancer cells. When administered in combination with Erlotinib and Cabozantinib, antitumor effects against non-small cell lung cancer cells have been demonstrated in both *in vitro* and *in vivo* models [35].

In our study, the interactions of this compound with topoisomerase I and topoisomerase II enzymes was investigated by subjecting it to *in vitro* topoisomerase enzyme activity assays and cell viability tests. According to the results, Cabozantinib did not have a significant concentration-dependent inhibitory effect on MCF7, A549 and PC3 cell lines. However, Cabozantinib inhibits human topoisomerase I enzyme but not human topoisomerase II enzyme *in vitro* conditions, providing a *bona fide* information about the pathways through which the compound acts. Further analyzes are needed to answer questions such as whether this chemical will give successful results when applied alone to different cancer cell types and whether its effectiveness will increase with combination applications.

Acknowledgments

This research was supported by the Scientific and Technological Research Council of Turkiye (TUBITAK)/BIDEP 2209-A program (1919B011701745).

Conflicts of Interest

The authors declare no conflict of interest.

References

- Wang J.C., Cellular roles of DNA topoisomerases: a molecular perspective, *Nat Rev Mol Cell Biol.*, 3 (2002) 430-440.
- Carey J.F., Schultz S.J., Sisson L., Fazio T.G., Champoux J.J., DNA relaxation by human topoisomerase I occurs in the closed clamp conformation of the protein, *Proc Natl Acad Sci USA*, 100 (10) (2003) 5640-5645.
- Skok Ž., Zidar N., Kikelj D., Ilaš J., Dual Inhibitors of Human DNA Topoisomerase II and Other Cancer-Related Targets, *J Med Chem.*, 63 (2020) 884-904.
- Nitiss J.L., Investigating the biological functions of DNA topoisomerases in eukaryotic cells, *Biochim Biophys Acta*, 1400 (1-3) (1998) 63-81.
- Bjornsti M.A., Osheroff N., Introduction to DNA Topoisomerases, *Methods Mol Biol.*, 94 (1999) 1-8.
- Pommier Y., Leo E., Zhang H., Marchand C., DNA topoisomerases and their poisoning by anticancer and antibacterial drugs, *Chem Biol.* 17 (2010) 421-433.
- Swedan H.K., Kassab A.E., Gedawy E.M., Elmeligie S.E., Topoisomerase II inhibitors design: Early studies and new perspectives, *Bioorg Chem.* 136 (2023) 106548.
- Champoux J.J., DNA Topoisomerases: Structure, Function, and Mechanism, *Annu Rev Biochem.* 70 (2001) 369-413.
- Cinelli M.A., Topoisomerase II inhibitors: Over a half-century of drug leads, clinical candidates, and serendipitous discoveries, *Med Res Rev.* 39 (2019) 1294-1337.
- Baglini E., Salerno S., Barresi E., Robello M., Da Settimo F., Taliani S., Marini A.M., Multiple Topoisomerase I (TopoI), Topoisomerase II (TopoII) and Tyrosyl-DNA Phosphodiesterase (TDP) inhibitors in the development of anticancer drugs, *Eur J Pharm Sci.*, 156 (2021) 105594.
- Madkour M.M., Ramadan W.S., Saleh E., El-Awady R., Epigenetic modulations in cancer: predictive biomarkers and potential targets for overcoming the resistance to topoisomerase I inhibitors, *Ann Med.* 55 (1) (2023) 2203946
- Pommier Y., Thomas A., New Life of Topoisomerase I Inhibitors as Antibody-Drug Conjugate Warheads, *Clin. Cancer Res.*, 29 (2023) 991-993.
- Syrios J., Kouroussis C., Kotsakis A., Kentepozidis N., Kontopodis E., Kalbakis K., Vardakis N., Hatzidaki D., Polyzos A., Georgoulas V., Combination of weekly topotecan and gemcitabine as a salvage treatment in patients with recurrent ovarian cancer: a phase I study, *Minerva Ginecol.*, 71 (3) (2019) 182-190.
- Kang J.H., Lee K.H., Kim D.W., Kim S.W., Kim H.R., Kim J.H., Choi J.H., An H.J., Kim J.S., Jang J.S., Kim B.S., Kim H.T., A randomised phase 2b study comparing the efficacy and safety of belotecan vs. topotecan as monotherapy for sensitive-relapsed small-cell lung cancer, *Br J Cancer*, 124 (2021) 713-720.
- Bax B.D., Murshudov G., Maxwell A., Germe T., DNA Topoisomerase Inhibitors: Trapping a DNA-Cleaving Machine in Motion, *J Mol Biol.*, 431 (2019) 3427-3449.
- Martin-Encinas E., Selas A., Palacios F., Alonso C., The design and discovery of topoisomerase I inhibitors as anticancer therapies, *Expert Opin Drug Discov.*, 17 (2022) 581-601.
- Roos W.P., Kaina B., DNA damage-induced cell death: From specific DNA lesions to the DNA damage response and apoptosis, *Cancer Lett.* 332 (2013) 237-248.
- Mahajan K., Mahajan N.P., Cross talk of tyrosine kinases with the DNA damage signaling pathways, *Nucleic Acids Res.*, 43 (2015) 10588-10601.
- Yang P.W., Liu Y.C., Chang Y.H., Lin C.C., Huang P.M., Hua K.T., Lee J.M., Hsieh M.S., Cabozantinib (XL184) and R428 (BGB324) Inhibit the Growth of Esophageal Squamous Cell Carcinoma (ESCC), *Front Oncol.*, 9 (2019) 1138.
- Esteban-Villarrubia J., Soto-Castillo J.J., Pozas J., Román-Gil M.S., Orejana-Martín I., Torres-Jiménez J., Carrato A., Alonso-Gordoa T., Molina-Cerrillo J., Tyrosine kinase receptors in oncology, *Int J Mol Sci.*, 21 (2020) 1-48.
- Lyseng-Williamson K.A., Cabozantinib as first-line treatment in advanced renal cell carcinoma: a profile of its use, *Drugs Ther Perspect.*, 34 (2018) 457-465.
- Karmacharya U., Guragain D., Chaudhary P., Jee J.G., Kim J.A., Jeong B.S., Novel pyridine bioisostere of cabozantinib as a potent c-met kinase inhibitor: Synthesis and anti-tumor activity against hepatocellular carcinoma, *Int J Mol Sci.*, 22 (18) (2021) 9685.
- Zhang G.N., Zhang Y.K., Wang Y.J., Barbuti A.M., Zhu X.J., Yu X.Y., Wen A.W., Wurpel J.N.D., Chen Z.S., Modulating the function of ATP-binding cassette subfamily G member 2 (ABCG2) with inhibitor cabozantinib, *Pharmacol Res.*, 119 (2017) 89-98.
- Senarisoy M., Canturk P., Zencir S., Baran Y., Topcu Z., Gossypol Interferes with Both Type I and Type II Topoisomerase Activities Without Generating Strand Breaks, *Cell Biochem Biophys.*, 66 (2013) 199-204.
- Nitiss J.L., Topoisomerase Assays, *Curr Protoc Pharmacol.*, 3 (3-1) (1998) 1934-8282
- Canturk P., Kucukoglu K., Topcu Z., Gul M., Gul H.I., Effect of Some Bis Mannich Bases and Corresponding Piperidinols on DNA Topoisomerase I, *Arzneimittelforschung*, 58 (12) (2008) 686-691.
- Liang X., Wu Q., Luan S., Yin Z., He C., Yin L., Zou Y., Yuan Z., Li L., Song X., He M., Lv C., Zhang W., A comprehensive review of topoisomerase inhibitors as anticancer agents in the past decade, *Eur J Med Chem.*, 171 (2019) 129-168.

- [28] Pommier Y., Nussenzweig A., Takeda S., Austin C., Human topoisomerases and their roles in genome stability and organization, *Nat Rev Mol Cell Biol.*, 23 (2022) 407-427.
- [29] Capranico G., Binaschi M., DNA sequence selectivity of topoisomerases and topoisomerase poisons, *Biochim Biophys Acta.*, 1400 (1998) 185-194.
- [30] Xu J., Higgins M.J., Tolaney S.M., Come S.E., Smith M.R., Fournier M., Mahmood U., Baselga J., Yeap B.Y., Chabner B.A., Isakoff S.J., A Phase II Trial of Cabozantinib in Hormone Receptor-Positive Breast Cancer with Bone Metastases, *Oncologist*, 25 (2020) 652-660.
- [31] Piccaluga P.P., Cascianelli C., Inghirami G., Tyrosine kinases in nodal peripheral T-cell lymphomas, *Front Oncol.*, 13 (2023) 1099943.
- [32] Maroto P., Porta C., Capdevila J., Apolo A.B., Viteri S., Rodriguez-Antona C., Martin L., Castellano D., Cabozantinib for the treatment of solid tumors: a systematic review, *Ther Adv Med Oncol.*, 14 (2022) 17588359221107112.
- [33] Rizzo A., Brandi G., Biochemical predictors of response to immune checkpoint inhibitors in unresectable hepatocellular carcinoma, *Cancer Treat Res Commun.*, 27 (2021) 100328.
- [34] Konstantinopoulos P.A., Brady W.E., Farley J., Armstrong A., Uyar D.S., Gershenson D.M., Phase II study of single-agent cabozantinib in patients with recurrent clear cell ovarian, primary peritoneal or fallopian tube cancer (NRG-GY001), *Gynecol Oncol.*, 150 (2018) 9-13.
- [35] Alhazzani K., Alsahli M., Alanazi A.Z., Algahtani M., Alenezi A.A., Alhoshani A., Alqinyah M., Alhamed A.S., Alhosaini K., Augmented antitumor effects of erlotinib and cabozantinib on A549 non-small cell lung cancer: In vitro and in vivo studies, *Saudi Pharm J.*, 31 (2023) 101756.

Investigation of Electrospun Polyacrylonitrile and Cellulose Acetate Smart Nanofibers Doped with Expanded Graphite for the Structure and Photothermal Effect

Özgül Gök^{1,a,*}

¹ Veterinary Medicine Department, Çölemerik VHS, Hakkari University, Hakkari, Türkiye.

*Corresponding author

Research Article

History

Received: 06/04/2023

Accepted: 28/10/2023

Copyright



©2023 Faculty of Science,
Sivas Cumhuriyet University

ozgulgok@hakkari.edu.tr

<https://orcid.org/0000-0001-5443-2843>

ABSTRACT

In this study, photothermal effect by doping expanded graphite (EG) to smart nanofibers produced by electrospinning method was investigated. Fourier transform infrared (FT-IR) spectroscopy was exploited for chemical characterization. Thermal analysis experiments were carried out by heating and cooling curves. Surface morphology of the produced materials was investigated through scanning electron microscope (SEM). Contact angle was determined through contact angle measurement device. The appearance of the peak of the characteristic cyano group in the structure of Polyacrylonitrile (PAN) at 2237.02 cm⁻¹ in the nanofibers having different percentages synthesized with EG and PAN was accepted as the evidence of PAN nanofibers formation. The temperature platforms in the heating/cooling curves exhibited that the temperature of the PAN and cellulose acetate (CA) nanofibers mixed with different EG percentage have higher than pristine nanofibers. The surfaces of the EG@PAN and EG@CA nanofibers were homogeneously distributed fibrous, excessive EG heterogeneously dispersed or electrospayed in shape. The maximum contacts angles were measured as 67.96° and 52.88° for nanofibers synthesized with EG@CA and EG@PAN, respectively. As the result, the temperature of the nanofibers mixed EG at different percentages increased resulting from having the higher thermal conductivity of EG. Main goal of the study is both investigating photothermal effect in PAN and CA electrospun nanofibers doped with EG of activating heat accumulation property of the produced smart nanofibers for heat energy production from the solar. Thus, it will be possible to develop a new promising method in the production of the smart textile products that have the storage capacity of the solar energy.

Keywords: Solar energy, Photothermal effect, Electrospinning, Smart nanofibers, Expanded graphite.

Introduction

In recent years, energy conservation is getting important as energy production. Studies on the efficient use of existing energy provide very important contributions to energy sector all over the world.

Energy requirement supplied by fossil fuels such as oil, coal, and natural gas. As a result of the oil crisis people faced in the 1970s and the detection of the ozone hole which caused by CFCs (chlorofluorocarbons), they turned to environmentally friendly, clean and renewable energy sources such as fuel cells, wind energy and solar energy [1-3]. In conventional energy production systems, energy is obtained in three stages. In the first stage, thermal energy is obtained as a result of the combustion of the fuel. The heat produced in the second stage is converted into mechanical energy. In the final stage, electrical energy is obtained from mechanical energy. All these conversion steps cause energy loss. Energy storage systems prevent this loss and ensure that the needed energy is used more efficiently [4, 5]. These renewable energy sources can be stored and used via thermal energy storage methods when energy is needed. With this method, two types of storage can be made as short-term (day and night) and long-term (summer-winter). Thus, by ensuring the sustainability of energy, both energy

efficiency increased and the damage caused by fossil fuels to the environment is reduced [6].

Thermal energy is the sum of the kinetic and potential energies of the atoms and/or molecules that make up a substance. It is formed as a result of atomic or molecular vibration [7,8]. The transfer of thermal energy occurs with the heat flow caused by the temperature difference [9]. Thermal energy can be stored as sensible heat, latent heat, thermochemical heat or a combination of all these. The latent heat storage method is performed by storing the latent heat generated by phase change as a result of a significant change in the internal energy of the thermal energy storage (TES) material [7, 10]. Compared with other heat storage methods, the required storage volume for the latent heat storage method is smaller, the heat storage capacity of this method is high, and this method is suitable for constant temperature heat storage. The heat storage materials used in latent heat storage methods are called phase change material (PCM). In recent years, many applications have been carried out where solar energy is stored in PCMs in the form of latent heat storage and then this stored heat is released by the PCM. Here, there is usually a solid-liquid phase change [7, 8, 11].

Moreover, PCMs have been used to produce thermostable textiles for garments that provide thermal comfort [12,13]. The use of PCM containing fibres or fabrics in home textile products such as bed linen, furniture fabrics, curtains is becoming increasingly common, besides garments. It is seen that PCM products are applied especially after microencapsulation into the polymer structure, in many textile studies [14-16]. Nowadays, the use of nanofibers produced by electrospinning method and that can store thermal energy are becoming increasingly common [17-19]. Production of bicomponent nanowebs, composed of Polyacrylonitrile (PAN) and PCM (polyethylene glycols (PEG), polyethylene glycol methyl ethers (PEGME)) and paraffin waxes (n-alkane) were carried out via coaxial electrospinning method. Özmen et al. (2020) produced nanofibers with heat storage/releasing properties composed of PCM (fatty acid) and polymethylmethacrylate (PMMA) by using a coaxial electrospinning method [20]. In the literature, it is seen that there are some studies thermo-active smart fibres are used in the applications such as drug release, separation processes, energy storage and conversion etc. [21]. Liu et al. (2023) reported to synthesize the flexible phase change nonwovens (GB-PCN) by wet-spinning hybrid graphene boron nitride (GB) fibre and subsequent impregnating paraffins such as eicosane and octadecane. [22]. A very small amount of the energy released from the sun reaches the earth's surface. Solar energy coming to the earth's surface, at various wavelengths consists of radiation. Recently, the studies were carried out to develop multifunctional hybrid polymeric materials that allow solar energy to be stored as thermal energy. [23-25].

PAN is a thermoplastic polymer obtained as a result of polymerization of acrylonitrile monomers. This polymer, which has strong secondary interactions thanks to polar acrylonitrile groups, has superior properties such as good mechanical properties and thermal resistance. Thanks to these superior properties, PAN has become a highly demanded polymer by the fibre industry [26].

Cellulose acetate (CA) natural polymer with a wide range of properties and is used most of industrial applications such as membrane technologies, textiles and energy storage materials [27-29].

In this study, photothermal effect in PAN and CA electrospun nanofibers doped with EG was investigated, and heat accumulation property of the produced smart nanofibers were carried out. It will help to validate them for heat energy production from the solar. The produced structures and their energy harvesting properties were proven by FT-IR spectroscopy, photolytic heating measurements, SEM analysis and contact angle measurements.

Materials and Methods

Materials

CA was purchased from Across Organics. PAN was obtained AKSA Akrilik Kimya Sanayii A.Ş. Expanded Graphite (EG, thermal conductivity: 4.26 W/mK) was obtained from the Fluka Company. N, N-Dimethylformamide (DMF) (Merck) was used as a solvent. These chemicals were not further purified prior to use. These chemicals were not further purified prior to use due to their analytical purity percentages of 99 % and plus.

Synthesis of Nanofiber by Electrospinning

PAN and CA based smart nanofibers with EG were prepared by electrospinning of their DMF solutions. They are so called EG@PAN and EG@CA in this article. They are 8 different nanofibers as single matrix polymers and EG imparted composites at different weight ratios. The smart nanofibers produced using electrospinning instrument (Nano WEB electrospin 100 instrument) were having photothermal property. In Table 1, the produced smart nanofibers were shown. 5 ml syringe with a 21 G blunt tip needle was used for pumping the solution at a rate of 1.5 ml/hr. The syringe tip to collector distance was set to determine optimum distance between the needle and Al pad which was found as 18 cm and the optimum voltage between the needle tip to an aluminium foil covered collector was determined as 18 kV voltage. Application time to produce the smart nanofibers was found as 4 hours. The obtained nanofiber mats were collected and conserved at 25 °C temperature before characterization tests.

Table 1. The expanded graphite-polymer mixtures weight/weight (w/w) ratios in electrospinning solutions

Smart nanofiber sample	The expanded graphite-polymer (w/w) ratios (%)	
	EG (%)	Polymer, PAN, CA weight percentages (%)
PAN nanofiber	0	(PAN) 100
EG@PAN 10/90 nanofiber	10	(PAN) 90
EG@PAN 15/85 nanofiber	15	(PAN) 85
EG@PAN 20/80 nanofiber	20	(PAN) 80
EG@PAN 25/75 nanofiber	25	(PAN) 75
CA nanofiber	0	(CA) 100
EG@CA 10/90 nanofiber	10	(CA) 90
EG@CA 15/85 nanofiber	15	(CA) 85
EG@CA 20/80 nanofiber	20	(CA) 80
EG@CA 25/75 nanofiber	25	(CA) 75

Characterization

Chemical analysis

The chemical analysis of the smart nanofiber samples was carried out by using a Fourier transform infrared (FT-IR) spectrometry instrument (JASCO FT/IR-4700) with an

attenuated total reflection accessory. FT-IR spectra were recorded between 4000 cm^{-1} and 400 cm^{-1} at a total of 16 scans.

Thermal analysis

Heating and cooling curves were drawn for the smart nanofibers samples with help of a 100 Watt lamp placed approximately 20 cm above as photothermal energy source (General Electric 100W E27 R95 INFRARED) in the closed system. Temperature data were recorded for constant periods of time during light on (heating) and during dark (cooling) by using a data-logger (Nova 5000) device.

Morphological analysis

Surface morphology investigation of the produced nanofibers samples were performed by using a scanning electron microscope (SEM) instrument (TESCAN MIRA3 XMU). The nanofibers samples surfaces were coated with

a conducting paint including gold prior to the measurements.

Contact angle analysis

The Contact angles of the nanofibers were determined through contact angle measurement instrument (Terra Lab Attension Theta Lite Optical Contact Angle Measurement Device).

Results and Discussion

In Table 2, the properties of the similar electrospun fibers used for thermocomfortable and thermoregulated textile productions were compared to the properties of the EG@PAN AND EG@CA nanofibers. It was seen that the surfaces of the nanofibers were smooth and homogeneously distributed fibrous in shape, when examined by SEM instrument.

Table 2. The properties of the electrospun fibers used for thermocomfortable textile products

Electrospun Fibers	Melting Temperature (°C)	Surface Morphology	Contact Angle	Reference
EG@PAN nanofiber	-	homogeneously distributed fibrous	52.88°	-
EG@CA nanofiber	-	homogeneously distributed fibrous	67.96°	-
Superhydrophobic–superoleophilic fibrous *PVDF membranes	-	smooth and homogeny surface	$\geq 153^\circ$	[16]
*PEG 1000-PVA nanofiber	28°C	homogenic surface	-	[17]
*PMMA16-KA-GA nanofiber	35.1°C	smooth and homogeny surface	-	[20]
*PMMA16-LA-GA nanofiber	49.7°C	smooth and homogeny surface	-	[20]
*PMMA16-MA-GA nanofiber	63.4°C	smooth and homogeny surface	-	[20]

*PVDF:

*PEG 1000-PVA:

*PMMA-KA-GA: polymethylmethacrylate-capric acid-graphene

*PMMA-LA-GA: polymethylmethacrylate-lauric acid-graphene

*PMMA-MA-GA: polymethylmethacrylate- myristic acid-graphene

Chemical Properties of the EG@PAN and EG@CA Nanofibers

The FT-IR spectra of the EG@PAN nanofibers and the EG@CA nanofibers were showed in Figures 1 and 2, respectively.

In the FT-IR spectrum of PAN nanofiber the peak appeared at 2237.02 cm^{-1} attributed from the characteristic $\text{C}\equiv\text{N}$ group in the structure of PAN. The peak observed at 2925.48 cm^{-1} is due to the aliphatic

methylene (CH_2) group [26, 30]. The peak appeared at 1232.29 cm^{-1} is attributed by the C-O-C vibrations of vinyl acetate in the PAN nanofiber structure in Figure 1 [26, 31].

In the FT-IR spectrum of CA nanofiber, the peaks appeared at 1734.66 cm^{-1} related to C=O stretching and 1366.32 cm^{-1} related to C-H bending. In addition, the peaks seen in 1216.86 cm^{-1} and 1034.62 cm^{-1} wave numbers are associated with C-O stretching in Figure 2 [32, 33].

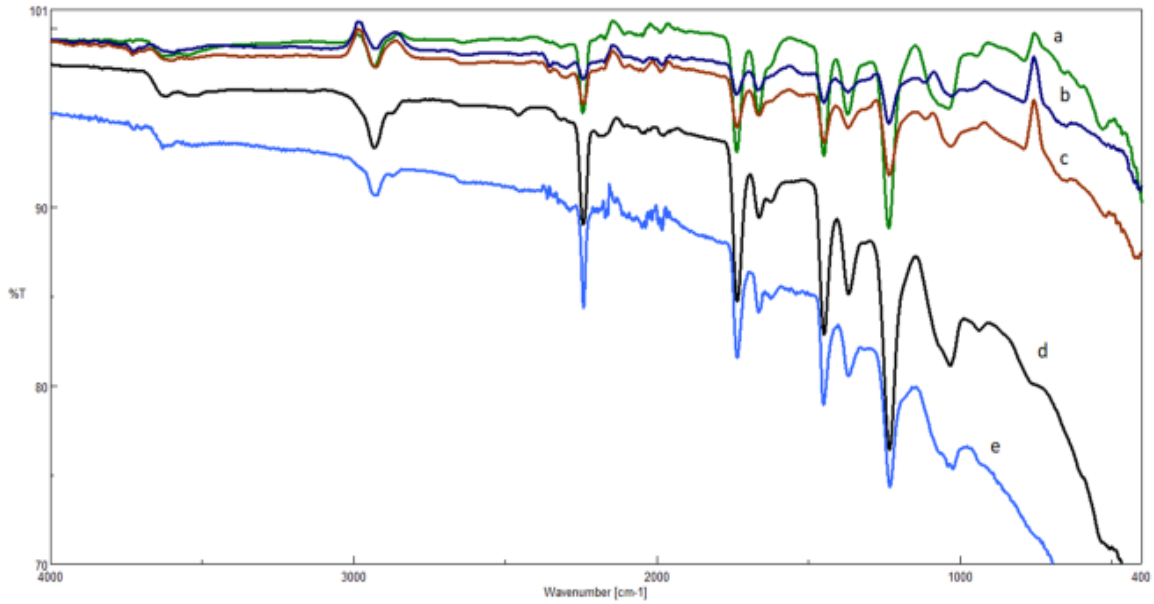


Figure 1. The FT-IR spectra of the EG@PAN nanofibers at different EG weight percentages (a: Pristine PAN nanofiber; b: 10 % EG + 90 % PAN; c: 15 % EG + 85 % PAN; d: 20 % EG + 80 % PAN; e: 25 % EG + 75 % PAN)

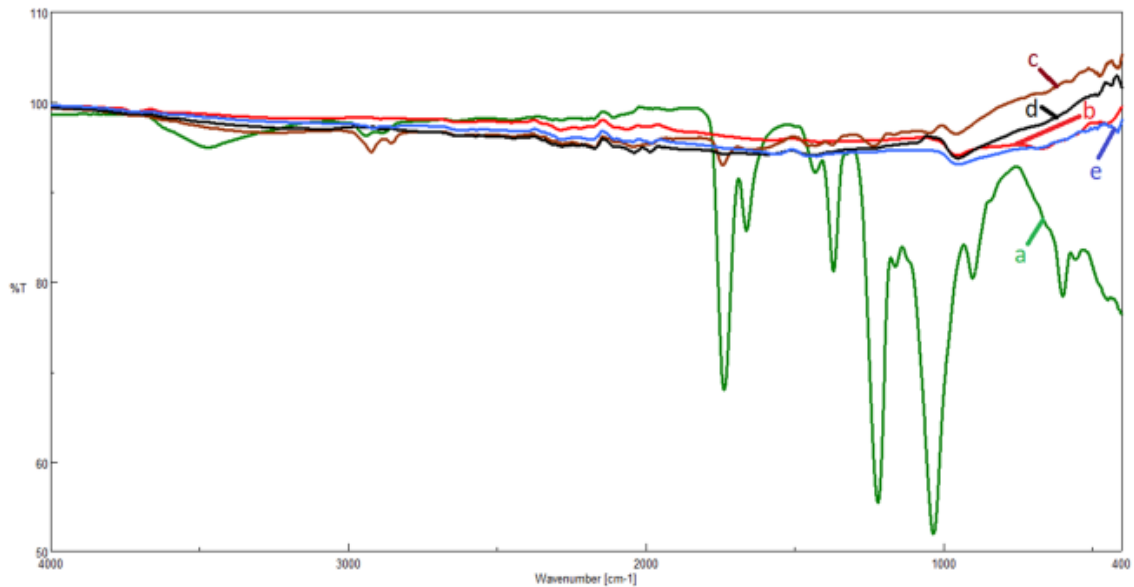


Figure 2. The FT-IR spectra of the EG@CA nanofibers at different EG weight percentages (a: Pristine CA nanofiber; b: 10 % EG + 90 % CA; c: 15 % EG + 85 % CA; d: 20 % EG + 80 % CA; e: 25 % EG + 75 % CA)

Thermal Properties of the EG@PAN and EG@CA Nanofibers

The thermal properties of the nanofibers were investigated by determining the heating and cooling curves. The photothermal energy source was used in the closed system. The heating and cooling curves of the EG@PAN and EG@CA smart nanofibers having different percentages were showed in Figures 3 and 4, respectively.

The temperature platforms in the heating/cooling curves exhibit heat storage/release process in these figures. The temperature converts slowly during the heating/cooling process. As seen in Figures 3 and 4, the temperature of the nanofibers mixed EG at different percentages is always highest. The reason is that EG has high thermal conductivity which is helpful for the heating/cooling process.

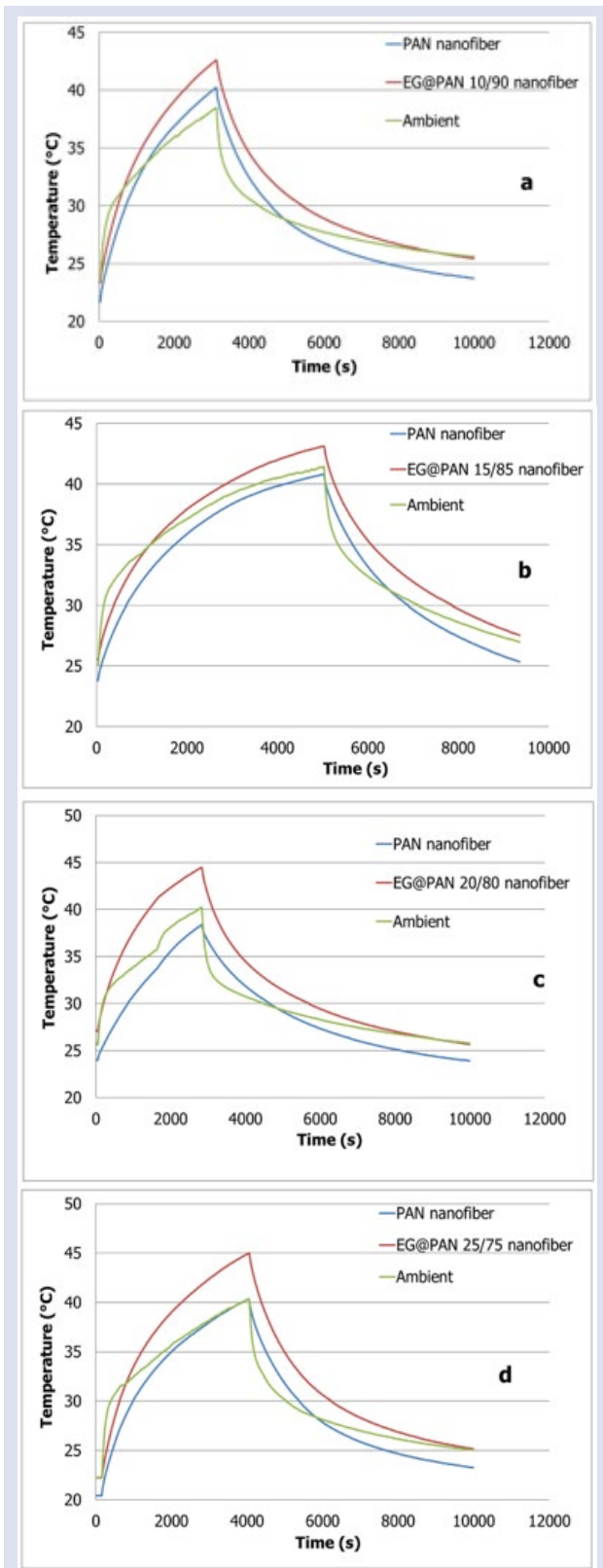


Figure 3. The Heating and cooling curves of the EG@PAN nanofibers at different EG weight percentages (a: 10 % EG + 90 % PAN; b: 15 % EG + 85 % PAN; c: 20 % EG + 80 % PAN; d: 25 % EG + 75 % PAN)

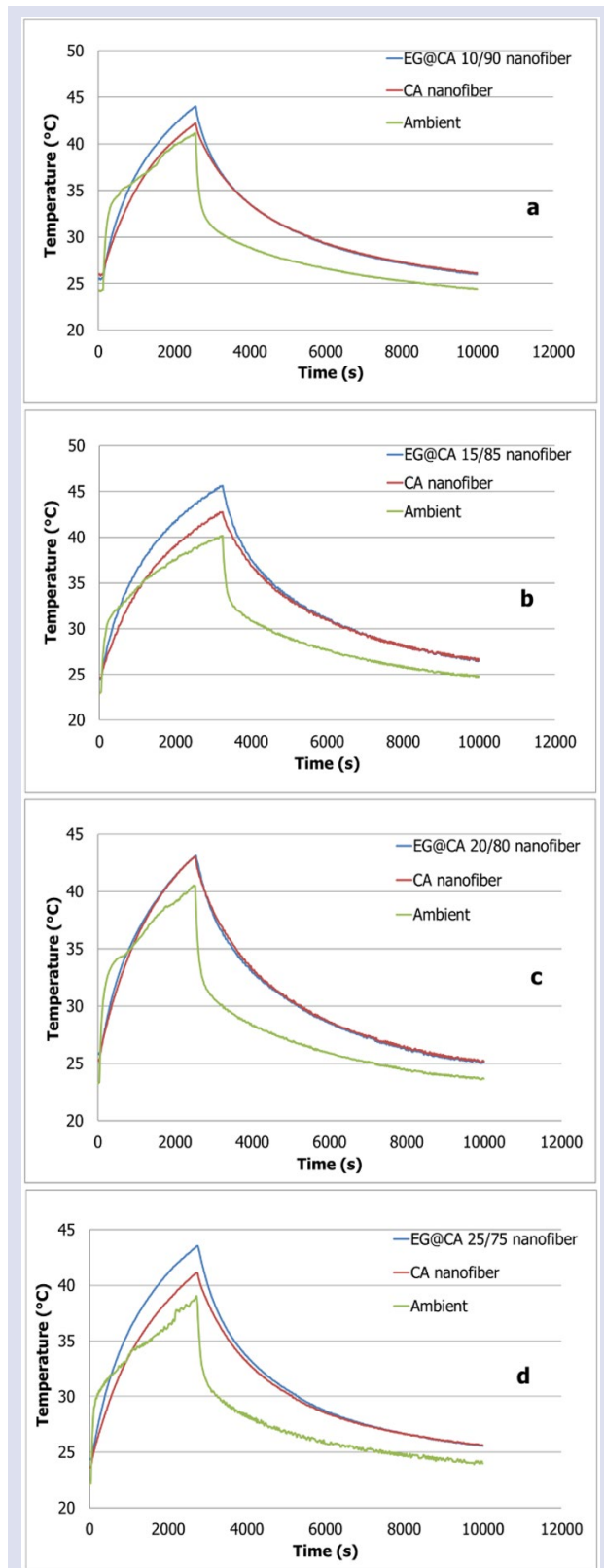


Figure 4. The Heating and cooling curves of EG@CA nanofibers at different EG weight percentages (a: 10 % EG + 90 % CA; b: 15 % EG + 85 % CA; c: 20 % EG + 80 % CA; d: 25 % EG + 75 % CA)

Morphological Properties of the EG@PAN and EG@CA Nanofibers

The SEM images of the matrices PAN and CA nanofibers, and EG@PAN and EG@CA composite nanofibers at different percentages of EG were given in Figures 5 and 6, respectively. According to the SEM images, the surfaces of the EG@PAN and EG@CA nanofibers were homogeneously distributed fibrous, excessive EG heterogeneously dispersed or electrospayed in shape. The surface morphology of the nanofibers was a coated by the polymer structure, and light reached through the host polymer to bear photothermal effect [34]. EG has a better dispersion in nanofibers synthesized with PAN and, consequently, it greatly improves the overall performance of the nanofibers.

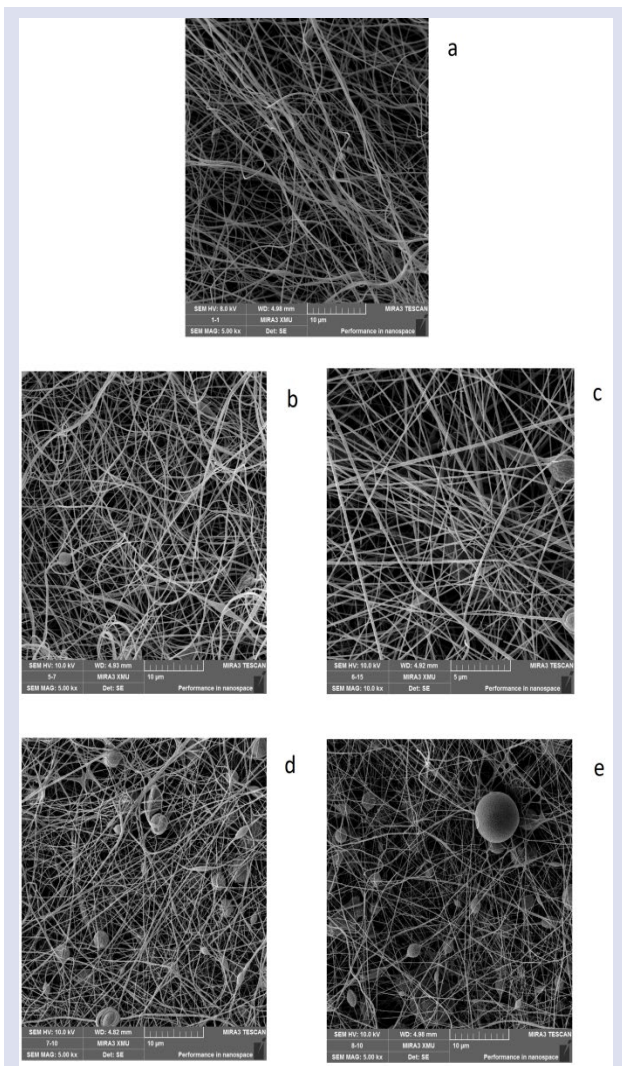


Figure 5. The SEM images of the EG@PAN nanofibers at different EG weight percentages (a: Pristine PAN nanofiber; b: 10 % EG + 90 % PAN; c: 15 % + 85 % PAN; d: 20 % + 80 % PAN; e: 25 % + 75 % PAN)

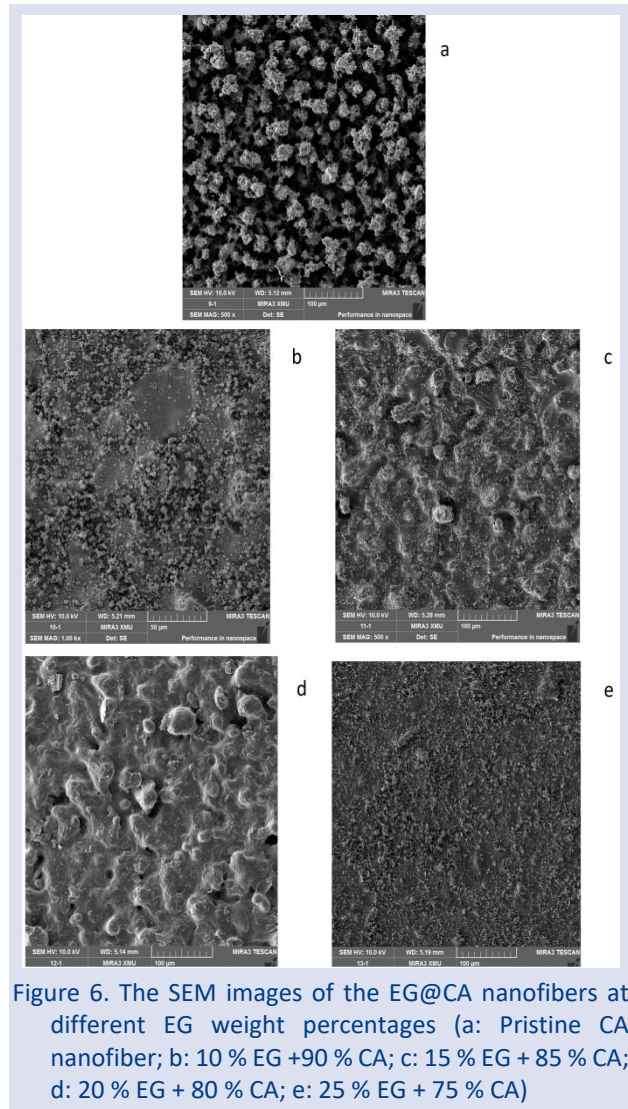


Figure 6. The SEM images of the EG@CA nanofibers at different EG weight percentages (a: Pristine CA nanofiber; b: 10 % EG + 90 % CA; c: 15 % EG + 85 % CA; d: 20 % EG + 80 % CA; e: 25 % EG + 75 % CA)

Contact Angle Measurements of the EG@PAN and EG@CA Nanofibers with Water

The contact angle measurements images of the EG@PAN and EG@CA nanofibers which have different percentages were given in Figures 7 and 8, respectively. As seen in Figures 7 and 8, while the water contacts angle of the nanofibers synthesized with EG and CA at different percentages increase, the water contacts angle of the EG@PAN nanofibers at different percentages decrease. The increase in the contact angles of the EG@CA nanofibers indicated the wettability decreased. The maximum contacts angles were measured as 67.96° and 52.88° for EG@CA nanofibers and EG@PAN nanofibers, respectively. The surface morphology of the EG@PAN and EG@CA nanofibers has played a crucial role in the hydrophobicity of the resulting ultrathin fibrous nanofibers. In the experimental study it has been seen that the water contact angles of electrospun EG@PAN nanofibers are lower than those of EG@CA nanofibers.

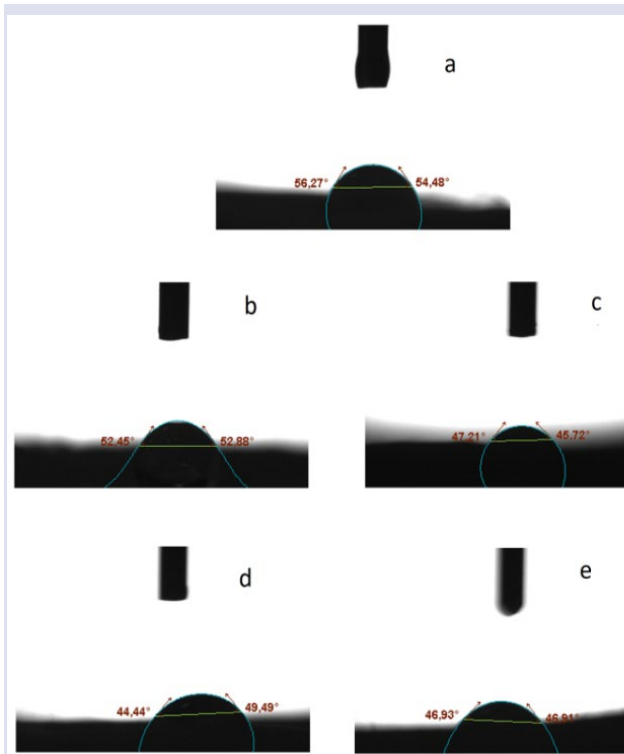


Figure 7. The contact angle images of the EG@PAN nanofibers at different EG weight percentages (a: Pristine PAN nanofiber; b: 10 % EG + 90 % PAN; c: 15 % EG + 85 % PAN; d: 20 % EG + 80 % PAN; e: 25 % EG + 75 % PAN)

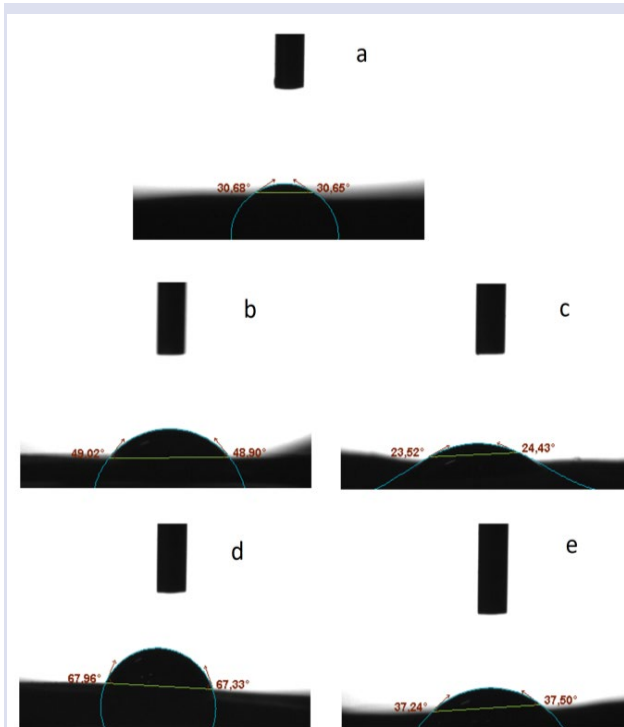


Figure 8. The contact angle images of the EG@CA nanofibers at different EG weight percentages (a: Pristine CA nanofiber; b: 10 % EG + 90 % CA; c: 15 % EG + 85 % CA; d: 20 % EG + 80 % CA; e: 25 % EG + 75 % CA)

Conclusions

EG as a photothermal effect agent was embedded into nanofiber matrices of CA and PAN polymers by electrospinning in DMF solution in order to have smart fabrics with energy harvesting property.

Characterization by FT-IR spectroscopy revealed the copresence of the polymers and expanded graphite together in the smart fabric structures. The appearance of the peak of the characteristic $\text{-C}\equiv\text{N}$ group in the structure of PAN at 2237.02 cm^{-1} in the nanofibers synthesized with EG and PAN at different percentages was accepted as the evidence of PAN nanofibers formation. At 1734.66 cm^{-1} related to $\text{C}=\text{O}$ stretching in the nanofibers synthesized with EG and CA at different percentages was appeared. The temperature platforms in the heating/cooling curves exhibit that the temperature of the PAN and CA nanofibers mixed with different EG percentage have higher than pristine PAN and CA nanofibers. The surfaces of the EG@PAN and EG@CA nanofibers were homogeneously distributed fibrous, excessive EG heterogeneously dispersed or electrospayed in shape. This is evidence of the increase in surface area which is very important for energy harvesting property of the smart fabrics. Therefore, they will interact to light much more. It was determined that the temperature of the nanofibers including EG in the matrices at different weight percentages was increasing when subjected to light. Thermal conductivity increment by the expanded graphite content was also helpful for energy harvesting property at the proposed level. When examined by SEM instrument, PAN nanofibers with expanded graphite showed some seepage at high expanded graphite contents whereas CA nanofibers resulted in compatible but not fibrous structures applicable for energy harvesting applications. The maximum contacts angles were measured as 67.96° and 52.88° for nanofibers synthesized with EG and CA and nanofibers synthesized with EG and PAN, respectively. It has been seen that the water contact angles of electrospun EG@CA nanofibers are higher than those of EG@PAN nanofibers and have higher hydrophobicity as a result of the measurements of the contact angles.

Conflicts of interest

There are no conflicts of interest in this work.

Acknowledgments

The author gratefully acknowledges Professor Cemil Alkan from Polymer Research Laboratory of Chemistry Department in Science and Letter Faculty of Tokat Gaziosmanpaşa University in Turkey. The study was produced during a visiting researcher period in his laboratory.

References

- [1] Yaman Y., Enerji tasarrufu ve yenilenebilir enerji kaynakları. 1st Ed. İstanbul: Birsen Yayınevi, (2007) 17-20.
- [2] Dinçer İ. and Rosen M.A., Thermal Energy Storage, Systems and Applications, 1st Ed. England: John Wiley & Sons, (2002) 23-26.
- [3] Konuklu Y., Ersoy O., Paksoy H.Ö., Evcimen S., Çelik S. and Toraman Ö.Y., Termal enerji depolama materyali olarak diatomit/faz değıştiren madde kompozitlerinin üretilmesi, *Ömer Halisdemir Üniversitesi Mühendislik Bilimleri Dergisi*, 6 (1) (2017) 238-243.
- [4] Lucia U., Overview on fuel cells, *Renewable and Sustainable Energy Reviews*, 30 (2014) 164-169.
- [5] Alkan, C., Thermal energy storage methods. In: Pielichowska K. and Pielichowski K. (Eds). Multifunctional Phase Change Materials. 1st ed. Amsterdam: Woodhead Publishing-Elsevier, (2023) 1-93.
- [6] Gök Ö., Alkan C. and Konuklu Y., Developing a polyethylene glycol (PEG)/cellulose phase change composite for cooling application, 14th International Conference on Energy Storage-ENERSTOCK2018, Adana-Turkey, 2018, 999-1005.
- [7] Strith U., Zavrl E. and Paksoy H.O., Energy analysis and carbon saving potential of a complex heating system with solar assisted heat pump and phase change material (PCM) thermal storage in different climatic conditions, *European Journal of Sustainable Development Research*, 3 (1) (2019) Article No: em0067.
- [8] Abhat A., Low temperature latent heat thermal energy storage: Heat storage materials, *Solar Energy*, 30 (4) (1983) 313-332.
- [9] Zalba B., Marin J.M., Cabeza L.F. and Mehling H., Review on thermal energy storage with phase change: materials, heat transfer analysis and applications, *Applied Thermal Engineering*, 23 (3) (2003) 251-283.
- [10] Crespo A., Fernández C., Vérez D., Tarragona J., Borri E., Frazzica A., Cabeza L.F. and de Gracia A., Thermal performance assessment and control optimization of a solar-driven seasonal sorption storage system for residential application, *Energy*, 263 (2023) 125382.
- [11] Navarro M., Diarce G., Lázaro A., Rojo A. and Delgado M., Comparative study on bubbling and shearing techniques for the crystallization of xylytol in TES systems, *Results in Engineering*, 17 (2023) 100909.
- [12] Saraç E.G., Isıl düzenleme özelliđi gösteren akıllı tekstil ürünlerinin geliştirilmesi ve performans özelliklerinin incelenmesi, PhD Thesis, Marmara University, Graduate School of Natural and Applied Sciences, 2020.
- [13] Kuru A., Alay Aksoy S., Faz değıştiren maddeler ve tekstil uygulamaları, *Journal of Textiles and Engineer*, 19 (86) (2012) 41-48.
- [14] Tözüm M.S., Alkan C. and Alay Aksoy S., Developing of thermal energy storing visual textile temperature indicators based on reversible color change, *Journal of Industrial Textiles*, 51 (2S) (2022) 1964S-1988S.
- [15] Tözüm M.S., Alay Aksoy S. and Alkan C., Manufacturing surface active shell and bisphenol A free thermochromic acrylic microcapsules for textile applications, *International Journal of Energy Research*, 45 (2021) 7018-7037.
- [16] Zhou Z., Wu X.F., Electrospinning superhydrophobic-superoleophilic fibrous PVDF membranes for high-efficiency water-oil separation, *Materials and Letters*, 160 (2015) 423-427.
- [17] Gök Ö., Alkan C., Polivinil alkol (PVA) ile poli(etilen glikol) (PEG) 1000 karışımının elektro eğirilmiş lif oluşumunun incelenmesi ve ısıl enerji depolama uygulamalarında faz değışim maddesi (FDM) olarak kullanılması, 5th International Fiber and Polymer Research Symposium, İstanbul-Turkey, 2019, 44-45.
- [18] Karatepe U.Y., Ozdemir T., Improving mechanical and antibacterial properties of PMMA via polyblend electrospinning with silk fibroin and polyethyleneimine towards dental applications, *Bioactive Materials*, 5 (2020) 510-515.
- [19] Boz Noyan E.C., The development of heat storing nanocomposite nanofibers, Master Thesis, İstanbul Technical University (İTÜ), Graduate School of Science Engineering and Technology, 2015.
- [20] Özmen G. and Alay Aksoy S., Eş eksenli elektro lif çekim yöntemi ile termal enerji depolama özellikli kompozit nanolif üretimi üzerine bir araştırma, *Journal of Engineering Sciences and Design*, 8 (4) (2020) 1248-1259.
- [21] Liguori A., Pandini S., Rinoldi C., Zaccheroni N., Pierini F., Focarete M.L. and Gualandi C., Thermoactive smart electrospun nanofibers, *Macromolecular Rapid Communications*, (2022) 2100694.
- [22] Liu H., Zhou F., Shi X., Sun K., Kou Y., Das P., Li Y., Zhang X., Mateti S., Chen Y., Wu Z.S., Shi Q., A thermoregulatory flexible phase change nonwoven for all-season high-efficiency wearable thermal management, *Nano-Micro Letters*, 15 (29) (2023) 1-12.
- [23] Li Z. and Yuan J., Phase change microcapsules with high encapsulation efficiency using Janus silica particles as stabilizers and their application in cement, *Construction and Building Materials*, 307 (2021) 124971.
- [24] Taş C.E., Hybrid polymeric materials comprising clay nanotubes, photothermal agents and phase change materials for food, water and energy applications, PhD Thesis, Sabancı University, Graduate School of Engineering and Natural Sciences, 2021.
- [25] Li M., Wu Z. and Tan J., Heat storage properties of the cement mortar incorporated with composite phase change material, *Applied Energy*, 103 (2013) 393-399.
- [26] Okay Z., Poliakrilonitril liflerin kimyasal modifikasyonu ve modifiye edilmiş liflere gümüş parçacıkları çöktürülerek bazı özelliklerinin incelenmesi, Master Thesis, Ankara University, Graduate School of Natural and Applied Sciences, 2018.
- [27] Puls J., Wilson S.A. and Hölter D., Degradation of cellulose acetate-based materials: A review, *Journal of Polymers and the Environment*, 19 (2011) 152-165.
- [28] Wsoo M.A., Shahir S., Bohari S.P.M., Nayan N.H.M. and Abd Razak S.I., A review on the properties of electrospun cellulose acetate and its application in drug delivery systems: A new perspective, *Carbohydrate Research*, 491 (2020) 107978.
- [29] Vatanpour V., Pasaoglu M.E., Barzegar H., Teber O.O., Kaya R., Bastug M., Khataee A. and Koyuncu I., Cellulose acetate in fabrication of polymeric membranes: A review, *Chemosphere*, 295 (2022) 133914.
- [30] Ouyang Q., Cheng L., Wang H. and Li K., Mechanism and kinetics of the stabilization reactions of itaconic acid-modified polyacrylonitrile, *Polymer Degradation and Stability*, 93 (8) (2008) 1415-1421.
- [31] Voronko Y., Eder G. C., Knausz M., Oreski G., Koch T. and Berger K. A., Correlation of the loss in photovoltaic module performance with the ageing behaviour of the backsheets used, *Progress in Photovoltaics: Research and Applications*, 23 (11) (2015) 1501-1515.

- [32] Keun S.W., Ho Y.J., Seung L.T. and Ho P.W., Electrospinning of ultrafine cellulose acetate fibers: Studies of a new solvent system and deacetylation of ultrafine cellulose acetate fibers, *J Polym Sci Phys*, 42 (2004) 5-11.
- [33] Dudak F.C., Resveratrol yüklü selüloz asetat liflerinin karakterizasyonu, *GIDA The Journal of Food*, 44 (5) (2019) 810-818.
- [34] Demirbağ Genç S., Alay Aksoy S. and Alkan C., A smart cotton fabric with adaptive moisture management through temperature sensitive poly(2-hydroxyethyl-6-(vinyl amino) hexanoate) finishing, *Cellulose*, 30 (2023) 2467-2481.

Investigation of the Effect of Main Components of Wild Thyme on Covid-19 by Computational Methods

Serpil Kaya ^{1,a}, Sultan Erkan ^{1,b}, Duran Karakaş ^{1,c,*}

¹ Chemistry Department, Science Faculty, Sivas Cumhuriyet University, Sivas, Türkiye.

*Corresponding author

Research Article

History

Received: 17/07/2023

Accepted: 08/11/2023

Copyright



©2023 Faculty of Science,
Sivas Cumhuriyet University

ABSTRACT

Aromatic plant species of the genus thymus have an important role as they have therapeutic properties such as antirheumatic, antiseptic, antispasmodic, antimicrobial, cardiac, carminative, diuretic and expectorant. It is also known that such plants strengthen the immune system and help cope with infectious diseases such as colds and flu. In this study, the effects of thymol, p-cymene, γ -terpinene, bornyl acetate, borneol, carvacrol, thymol methyl ether, thymol acetate, which are the main components of wild thyme (*thymus serpyllum L.*), on Covid-19 were investigated at the molecular level. Optimizations and molecular docking were done in Docking Server with the MMFF94 method. Major components of wild thyme were docked separately against 6LU7 protein representing the first gene form of Covid-19 and 7KDL protein representing the mutated form. Docking poses and binding energies between target proteins and wild thyme components were calculated. The results were compared with favipiravir, an antiviral drug developed against influenza virus and also used in the treatment of Covid-19. It was found that the thymol molecule, one of the main components of wild thyme, has the highest biological activity against both 6LU7 and 7KDL protein chains of Covid-19.

Keywords: *Thymus serpyllum L.*, Covid-19, Molecular docking.

^a sersude@hotmail.com

^b <https://orcid.org/0000-0003-3360-4735>

^c dkarakas@cumhuriyet.edu.tr

^c <https://orcid.org/0000-0002-6770-3726>

^b sultanerkan@cumhuriyet.edu.tr

^d <https://orcid.org/0000-0001-6744-929X>

Introduction

Studies continue to develop appropriate treatment strategies to reduce the symptoms and deaths caused by Covid-19, which causes a serious pandemic in the world. Drugs that have been tried against other viruses, such as favipiravir, are also being tried against Covid-19. Unfortunately, complete success has not been achieved due to the rapid mutation of the virus. New vaccine and drug development studies continue in this area [1].

As in the past, viruses are still an important cause of morbidity and mortality worldwide. Viruses such as influenza, acquired immune deficiency syndrome (AIDS), Ebola, severe acute respiratory syndrome (SARS) and Covid-19 can still be lethal. It may be a good choice to use plants to discover new antiviral agents and to treat viral diseases.

It is frequently discussed that herbal products can be protective and therapeutic against the Covid-19 virus [2]. Black elderberry (*Sambucus nigra*) is one of the most widely used plants known to have antiviral effects. This herb has been used for medicinal purposes for thousands of years by Native Americans [3] and people of the Mediterranean region [4]. Licorice root (*Glycyrrhiza glabra*) is an antiviral medicinal plant known since ancient times and used in viral respiratory infections such as dry cough and hoarseness [5-7]. Another plant with antiviral activity is echinacea (*Echinacea purpurea*). Echinacea extract was found to be as effective as the neuraminidase inhibitor oseltamivir in the treatment of influenza by Rauş

et al. [8]. Ginger (*Zingiber officinale Roscoe*) has antiviral activity against human respiratory syncytial virus (HRSV). Chang et al found that ginger inhibited HRSV-induced plaque formation in both HEp-2 and A549 cell lines [9]. Rosehip extract (*Cistus incanus*) has been found to exhibit potent antiviral activity in A549 or MDCK cell cultures infected with different influenza strains [10]. Studies were also conducted to find the components responsible for the antiviral activity of garlic (*Allium sativum*), and thiosulfates were found as virucidal active components in fresh garlic extract [11]. The antiviral effects of green tea catechins (*Green Tea Catechins*) have been the subject of many studies and have been found to have antiviral activity against many viruses such as HBV, HSV, HIV, HCV, influenza, enterovirus and rotavirus. The mechanisms of their antiviral effects against many viruses have also been described [12]. In the literature, natural compounds of procyanidin A2, procyanidin B1 and cinnamtannin B1 isolated from cinnamon cortex (*Cinnamomi Cortex*) have been found to inhibit SARSCoV infection [13]. It is known that the curcumin molecule in turmeric has antiviral activity and is effective against viruses such as influenza, hepatitis C, HIV, and SARS-CoV [14,15].

The aerial parts and volatile components of thyme (*thymus*) are used as herbal tea, condiment and spice [16]. The aerial parts of thyme species have been reported to have activities such as tonic, carminative, digestive, antispasmodic, antimicrobial, antioxidant, antiviral, anti-inflammatory and expectorant [17]. The chemical

composition, antimicrobial, antioxidant and antitumor activities of thyme were investigated by Nikolic et al. [18]. It has been found that there are three species of thymus, *thymus serpyllum L*, *thymus algeriensis* and *thymus vulgaris L*, and there are approximately 48 different components in each of these species. The main components in *thymus serpyllum L* are thymol (38.5%), p-cymene (8.9%), γ -terpinene (7.2%), bornyl acetate (7.0%), borneol (6.0%), carvacrol (4.7%), thymol methyl ether (3.8%) and thymol acetate (2.8%). Other ingredients are low in quantity.

The aim of this study is to examine the biological activities of *thymus serpyllum L* essential components against 6LU7 and 7KDL protein of Covid-19. For this purpose, the main components of *thymus serpyllum L* will be docked against the aforementioned cell lines, docking poses and binding energies will be calculated. The results will be compared with favipiravir, an antiviral drug developed against influenza and also used for the treatment of Covid-19 at the beginning of the coronavirus pandemic, and an activity ranking will be obtained.

Materials and Methods

The molecular structures of thymol, p-cymene, γ -terpinene, bornyl acetate, borneol, carvacrol, thymol methyl ether, thymol acetate, which are the main components of *thymus serpyllum L*, were obtained from the PubChem website, which is an open chemistry

database [19]. These molecules were docked against the protein (PDB ID: 6LU7) representing the unmutated form of Covid-19 [20] and the protein representing the first mutated form (PDB ID: 7KDL) [21]. The three-dimensional crystal structure of the 6LU7 and 7KDL proteins was retrieved from the Protein Data Bank. Docking Server was used for docking process [22]. Geometry optimization of essential components of *thymus serpyllum L* on the docking server was performed again with the MMFF94 method [23]. The Gasteiger partial load calculation method was chosen [24]. pH = 7.0 was taken. Grid maps were created using 90 \times 90 \times 90 Å grid points and 0.2 Å spacing. Lamarckian genetic algorithm was used for insertion simulations [22]. The population size was set to 150. The 5 Å quaternion and torsion steps were applied for the studied ligands to search for the appropriate region of the target protein.

Findings and Discussion

Molecular Structures

The molecular structures of the main components of wild thyme (*thymus serpyllum L*) were obtained from the PubChem website, which is an open chemistry database. The three-dimensional molecular structures of these compounds and favipiravir are given in Figure 1.

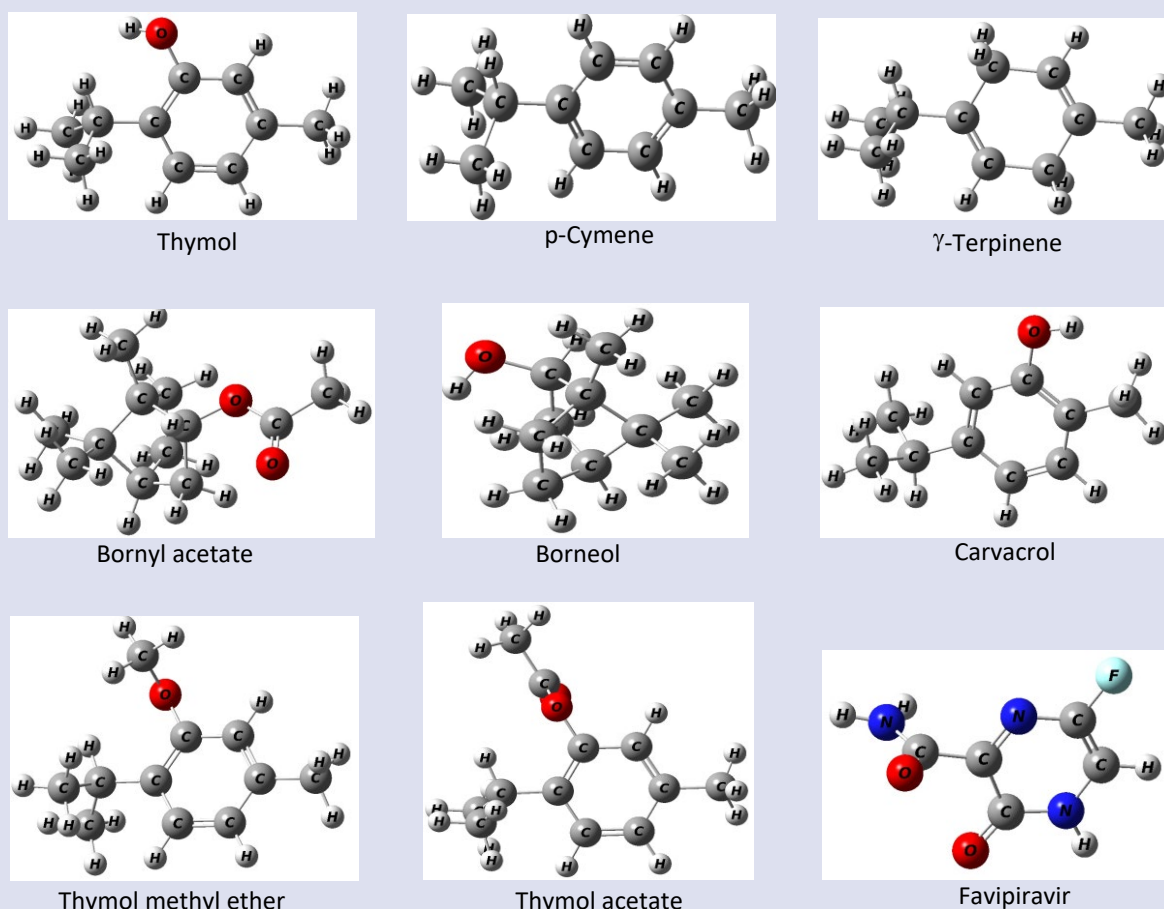


Figure 1. Molecular structures of the main components of *thymus serpyllum L*. and favipiravir

As seen in Figure 1, thymol, borneol and carvacrol have OH⁻, bornyl acetate and thymol acetate have CH₃COO⁻, thymol methyl ether has CH₃O⁻ and p-cymene and γ -terpinene have C=C functional groups.

Determination of the Active Component on Covid-19

Drug research and development is an extensive, expensive, and time-consuming process. In drug research and development, new technologies are being developed to shorten the research time and reduce the cost. Molecular docking (MD) is one of the computer aided drug designs (CADD) technologies [25]. Various MD approaches and tools have been developed today [26]. The MD process allows to examine the biological activities of molecules at the molecular level and is one of the popular techniques used in the identification and development of drug candidate molecules.

The MD process provides the opportunity to calculate the interactions between the cell lines' minimized protein structure at the molecular level and the drug candidate molecule. In this way, the binding energies, binding modes and types of secondary chemical interactions between the target protein and the molecule under investigation can be determined [27-30].

In this study, molecular docking process was used to determine the components that are effective on Covid-19 in wild thyme. Molecular docking was done with the Docking Server program. The main components of *thymus serpyllum L.* and favipiravir used as a Covid-19 drug were docked to target proteins with PDB codes 6LU7 and 7KDL. The docking poses between the main components of *thymus serpyllum L.* and the 6LU7 protein are given in Figure 2 and the docking poses between the 7KDL protein are given in Figure 3.

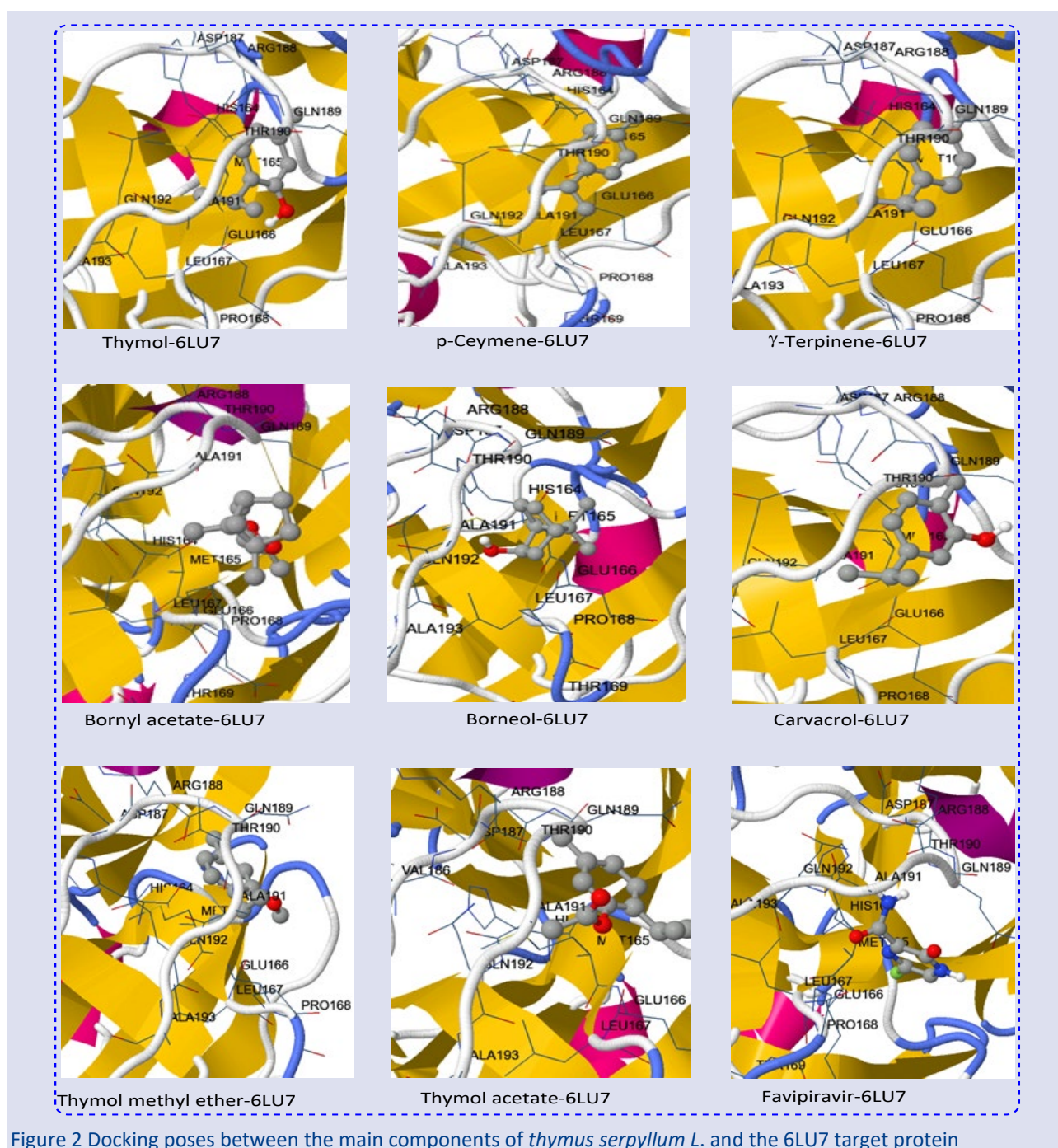


Figure 2 Docking poses between the main components of *thymus serpyllum L.* and the 6LU7 target protein

Table 1 Binding energies between major components of *thymus serpyllum L.* and proteins 6LU7 and 7KDL

Molecules	6LU7	7KDL
Thymol	-4.61	-4.61
p-Cymene	-4.37	-3.84
γ - Terpinene	-4.23	-3.70
Bornyl acetate	-4.40	-4.28
Borneol	-4.42	-4.03
Carvacrol	-4.45	-3.96
Thymol methyl ether	-4.26	-3.85
Thymol acetate	-4.44	-4.07
Favipiravir	-4.39	-4.27

Energies are in kcal/mol

As seen in Table 1, the binding energy between favipiravir used as a Covid-19 drug and 6LU7 representing the unmutated form of Covid-19 was calculated as -4.39 kcal/mol. It can be said that ligands with lower absolute binding energies than these values have lower inhibition efficiency against 6LU7 cell line than favipiravir. When Table 1 is examined, the binding energies of p-cymene, γ -terpinene and thymol methyl ether ligands are lower than those of favipiravir. Therefore, it can be said that the main components of *thymus serpyllum L.* p-cymene, γ -terpinene and thymol methyl ether are not active against the 6LU7 cell line. As seen in Figure 1, the molecular structures of p-cymene and γ -terpinene are composed of carbon and hydrogen atoms and contain only the C=C functional group. On the other hand, although thymol methyl ether contains CH₃O functional group, its binding energy is low. Therefore, it can be said that thymol methyl ether cannot be an active ingredient against 6LU7. The order of biological activity against 6LU7 according to the binding energies of the ligands is as follows.

γ -Terpinene < Thymol methyl ether < p-Cymene < Favipiravir < Bornyl acetate < Borneol < Thymol acetate < Carvacrol < Thymol

According to this order, it can be said that the molecules on the left of favipiravir are inactive against the 6LU7 cell line, while the molecules on the right are active. Considering the binding energies of 6LU7 and components, the component with the highest biological activity is thymol.

A similar interpretation can be made according to the binding energies between the main components of *thymus serpyllum L.* and the 7KDL cell line. The order of biological activity between the main components of *thymus serpyllum L.* and the 7KDL cell line according to their binding energies is as follows.

γ -Terpinene < p-Cymene < Thymol methyl ether < Carvacrol < Borneol < Thymol acetate < Favipiravir < Bornyl acetate < Thymol

According to this order, it can be said that only bornyl acetate and thymol are active against the 7KDL cell line, and other ligands are inactive.

As a result, the inhibition efficiency of bornyl acetate, borneol, thymol acetate, carvacrol and thymol against the

6LU7 target protein of Covid-19, and of bornyl acetate and thymol against the 7KDL protein is higher than favipiravir. It is seen that the biological activity of the thymol molecule, which is the highest amount in wild thyme, is high against the examined cell lines. According to the results obtained, it is thought that the thymol molecule and its derivatives may be a molecule that should be considered in drug development against Covid-19.

Conclusions

In this study, the antiviral effects of thymol, p-cymene, γ -terpinene, bornyl acetate, borneol, carvacrol, thymol methyl ether, thymol acetate, which are the main components of wild thyme, on Covid-19 were investigated. Molecules were docked to the 6LU7 and 7KDL target protein of Covid-19. Docking poses and binding energies between target proteins and molecules were calculated. The results were compared with favipiravir, an antiviral drug developed against influenza virus and also used in the treatment of Covid-19. It was predicted that the thymol molecule, one of the main components of wild thyme, has antiviral activity against Covid-19 and should be considered in drug development.

Conflicts of interest

There are no conflicts of interest among the authors of this study.

References

- [1] Chintagunta A. D., Kumar M., Sampath Kumar N. S., Jeevan Kumar S. P., Differential diagnosis and possible therapeutics for coronavirus disease 2019, *In Diagnostic Strategies for COVID-19 and other Coronaviruses*, (2020) 51-71.
- [2] Islam M. T., Sarkar C., El-Kersh D. M., Jamaddar S., Uddin S. J., Shilpi J. A., Mubarak M. S., Natural products and their derivatives against coronavirus: A review of the non-clinical and pre-clinical data, *Phytotherapy Research*, 34(10) (2020) 2471-2492.
- [3] Ulbricht C., Basch E., Cheung L., Goldberg H., Hammerness P., Isaac R., Wortley J., An evidence-based systematic review of elderberry and elderflower (*Sambucus nigra*) by the Natural Standard Research Collaboration, *Journal of dietary supplements*, 11(1) (2014) 80-120.
- [4] Valles J., Bonet M. A., Agelet A., Ethnobotany of *Sambucus nigra L.* in catalonia (Iberian Peninsula): The integral exploitation of a natural resource in mountain regions, *Economic botany*, 58(3) (2004) 456-469.
- [5] Armanini D., Fiore C., Mattarello M. J., Bielenberg J., Palermo M., History of the endocrine effects of licorice, *Experimental and clinical endocrinology & diabetes*, 110(06) (2002) 257-261.
- [6] Fiore C., Eisenhut M., Krause R., Ragazzi E., Pellati D., Armanini D., Bielenberg J., Antiviral effects of Glycyrrhiza species, *Phytotherapy Research: An International Journal Devoted to Pharmacological and Toxicological Evaluation of Natural Product Derivatives*, 22(2) (2008) 141-148.
- [7] Fiore C., Eisenhut M., Ragazzi E., Zanchin G., Armanini D., A history of the therapeutic use of liquorice in Europe, *Journal of ethnopharmacology*, 99(3) (2005) 317-324.

- [8] Raus K., Pleschka S., Klein P., Schoop R., Fisher P., Effect of an Echinacea-based hot drink versus oseltamivir in influenza treatment: a randomized, double-blind, double-dummy, multicenter, noninferiority clinical trial, *Current Therapeutic Research*, (77) (2015) 66-72.
- [9] San Chang J., Wang K. C., Yeh C. F., Shieh D. E., Chiang L. C., Fresh ginger (*Zingiber officinale*) has anti-viral activity against human respiratory syncytial virus in human respiratory tract cell lines, *Journal of ethnopharmacology*, 145(1) (2013) 146-151.
- [10] Ehrhardt C., Hrinčius E. R., Korte V., Mazur I., Droebner K., Poetter A., Ludwig S., A polyphenol rich plant extract, CYSTUS052, exerts anti influenza virus activity in cell culture without toxic side effects or the tendency to induce viral resistance, *Antiviral research*, 76(1) (2007) 38-47.
- [11] Weber N. D., Andersen D. O., North J. A., Murray B. K., Lawson L. D., Hughes B. G., In vitro virucidal effects of *Allium sativum* (garlic) extract and compounds, *Planta medica*, 58(05) (1992) 417-423.
- [12] Xu J., Xu Z., Zheng W., A review of the antiviral role of green tea catechins, *Molecules*, 22(8) (2017) 1337.
- [13] Zhuang M., Jiang H., Suzuki Y., Li X., Xiao P., Tanaka T., Hattori T., Procyanidins and butanol extract of *Cinnamomi Cortex* inhibit SARS-CoV infection, *Antiviral research*, 82(1) (2009) 73-81.
- [14] Praditya D., Kirchhoff L., Brüning J., Rachmawati H., Steinmann J., Steinmann E., Anti-infective properties of the golden spice curcumin, *Frontiers in microbiology*, (10) (2019) 912.
- [15] Wen C. C., Kuo Y. H., Jan J. T., Liang P. H., Wang S. Y., Liu H. G., Yang N. S., Specific plant terpenoids and lignoids possess potent antiviral activities against severe acute respiratory syndrome coronavirus, *Journal of medicinal chemistry*, 50(17) (2007) 4087-4095.
- [16] Stahl-Biskup E., Essential oil chemistry of the genus *Thymus*—a global view. In *Thyme* (2002) 89-138, CRC Press.
- [17] Nickavar B., Mojab F., Dolat-Abadi R., Analysis of the essential oils of two *Thymus* species from Iran, *Food chemistry* (2005) 90(4) 609-611.
- [18] Nikolic M., Glamoclija J., Ferreira I. C., Calhella R. C., Fernandes A., Markovic T., Sokovic M., Chemical composition, antimicrobial, antioxidant and antitumor activity of *Thymus serpyllum* L., *Thymus algeriensis* Boiss. and *Reut* and *Thymus vulgaris* L. essential oils, *Industrial Crops and Products*, (52) (2014) 183-190.
- [19] Kim S., Thiessen P. A., Cheng T., Yu B., Shoemaker B. A., Wang J., Bryant S. H., Literature information in PubChem: associations between PubChem records and scientific articles, *Journal of cheminformatics*, 8(1) (2016) 1-15.
- [20] Hatada R., Okuwaki K., Mochizuki Y., Handa Y., Fukuzawa K., Komeiji Y., Tanaka S., Fragment molecular orbital-based interaction analyses on COVID-19 main protease–inhibitor N3 complex (PDB ID: 6LU7), *Journal of chemical information and modeling*, 60(7) (2020) 3593-3602.
- [21] Verkhivker G. M., Agajanian S., Oztas D., Gupta G., Computational analysis of protein stability and allosteric interaction networks in distinct conformational forms of the SARS-CoV-2 spike D614G mutant: Reconciling functional mechanisms through allosteric model of spike regulation. *Journal of Biomolecular Structure and Dynamics*, (2021) 1-18.
- [22] Bikadi Z., Hazai E., Application of the PM6 semi-empirical method to modeling proteins enhances docking accuracy of AutoDock. *Journal of cheminformatics*, 1(1) (2009) 1-16.
- [23] Halgren T. A., Merck molecular force field. I. Basis, form, scope, parameterization, and performance of MMFF94. *Journal of computational chemistry*, 17(5-6) (1996) 490-519.
- [24] Gasteiger J., Marsili M., Iterative partial equalization of orbital electronegativity—a rapid access to atomic charges, *Tetrahedron*, 36(22) (1980) 3219-3228.
- [25] Tang Y., Zhu W., Chen K., Jiang H., New technologies in computer-aided drug design: Toward target identification and new chemical entity discovery, *Drug discovery today: technologies*, 3(3) (2006) 307-313.
- [26] Kuntz I. D., Blaney J. M., Oatley S. J., Langridge R., Ferrin T. E., A geometric approach to macromolecule-ligand interactions, *Journal of molecular biology*, 161(2) (1982) 269-288.
- [27] Onodera K., Satou K., Hirota H., Evaluations of molecular docking programs for virtual screening, *Journal of chemical information and modeling*, 47(4) (2007) 1609-1618.
- [28] Kaya S., Erkan S., Karakaş D., Computational design and characterization of platinum-II complexes of some Schiff bases and investigation of their anticancer-antibacterial properties, *Applied Organometallic Chemistry*, (36) (2022) e6805.
- [29] Kaya S., Erkan S., Karakaş D. Computational investigation of molecular structures, spectroscopic properties and antitumor-antibacterial activities of some Schiff bases, *Spectrochimica Acta Part A: Molecular and Biomolecular Spectroscopy*, (244) (2021) 118829.
- [30] Erkan, S., Karakaş, D. Computational investigation of structural, nonlinear optical and anti-tumor properties of dinuclear metal carbonyls bridged by pyridyl ligands with alkyne unit, *Journal of Molecular Structure*, (1199) (2020) 127054.

Green Synthesis of CuO Nanoparticles Using *Tragopogon porrifolius* and Their Antioxidant and Photocatalytic Applications

Gamze Topal Canbaz^{1,a,*}

¹ Department of Chemical Engineering, Engineering Faculty, Sivas Cumhuriyet University, 58140 Sivas, Türkiye.

*Corresponding author

Research Article

History

Received: 18/07/2023

Accepted: 08/11/2023

Copyright



©2023 Faculty of Science,
Sivas Cumhuriyet University

gtopal@cumhuriyet.edu.tr

<https://orcid.org/0000-0001-7615-7627>

ABSTRACT

Copper oxide nanoparticles (CuO NPs) were produced by green synthesis method which is a cheap, easy and effective method using *Tragopogon porrifolius* extract. The shape, bond and crystal structure of the nanoparticles were determined by Fourier transform infrared spectroscopy (FTIR), scanning electron microscopy (SEM), energy dispersive X-ray (EDX) and X-ray diffractometer (XRD) analysis methods. SEM analysis showed that the particles were spherical and EDX analysis showed the elemental composition of Cu and O as Cu 58.17 % and O 32.73 %. Cu-O bond structure was identified in FTIR analysis. In XRD analysis, peaks defining CuO NPs were observed. The antioxidant and photocatalytic activity of the synthesized CuO NPs were investigated. Antioxidant capacities were examined in the range of 50-500 µg/mL. The free radical scavenging activity of the nanoparticles was determined as 70.75 % at a concentration of 500 µg/mL. In photocatalytic studies, Reactive Red 120 (RR 120) dye degradation was investigated. The degradation time was calculated as 76 % in 30 min.

Keywords: Copper oxide nanoparticles, *Tragopogon porrifolius*, Biogenic synthesis, Antioxidant, Photocatalytic.

Introduction

One of the most significant areas of study in material science is nanotechnology. As significant research is done, this sector of science and engineering is noted for its quick growth [1]. The fact that it takes place in most of human life in daily life has made it one of the leading research areas of our age [2]. Nanotechnology produces and studies materials in the range of 1-100 nm, either by increasing the size of atoms/molecules to nano-size (bottom-up methods) or by size reduction of macroscopic materials (top-down methods) [3]. Among nanostructured materials, nanoparticles provide the link between macroscopic materials and atomic structures. While macroscopic materials show constant properties independent of their size and mass, the properties of nanoparticles depend on their size [4]. Due to their thermal characteristics, surface areas, particle sizes, and electrical conductivity, nanomaterials play a significant role in many different fields [5]. There is an increasing interest in the production of nanomaterials, which have many applications in industry such as biomedical [6], pharmaceutical [7], cosmetic [8], food [9] and catalyst [10].

Most of the methods applied for nanoparticle synthesis are physical and chemical methods. Most of these methods are expensive and often require the use of toxic solvents. This is potentially dangerous for the environment and living organisms. These negative effects in the synthesis of nanoparticles have led researchers to use environmentally friendly methods. For this purpose, a green synthesis method has emerged that aims to

produce nanoparticles that are economical, easily applicable and of high purity. In comparison to chemical and physical synthesis methods, biosynthesis of nanoparticles utilizing bio-green technologies has a lot of advantages in terms of effectiveness, cleanliness, simplicity, non-toxicity, low cost, and sustainability [11]. Environmentally safe fungi [12], bacteria [13] and plants [14] are used as reductants in green synthesis to produce nanoparticles. Synthesis using microorganisms is slower, more expensive and more complex than synthesis using plant extracts. Furthermore, aseptic conditions are required during the process and the waste products that can be generated are hazardous to the environment.

Recently, studies on CuO NPs are available in the literature due to their widespread applications in different scientific fields. The use of CuO NPs in many application areas has increased due to their cheap and abundant compared to gold and silver metals [15]. CuO NPs have been used in the production of optical [16], electronic [17], catalytic [1], medical [18], dental [19], nanofluid [20], antibacterial [18] and antioxidant [21] agents.

In this study, CuO NPs were synthesized by green synthesis method. In the biosynthesis of nanoparticles, *Tragopogon porrifolius* plant extract, which is consumed raw or cooked as food, was used as a reductant. As far as we know, this plant has not been used in particle synthesis before. The structure and morphology of the particles were determined by characterization analysis. The antioxidant activity of the synthesized CuO NPs and their photocatalytic activity for the azo class toxic Reactive Red 120 dye were investigated.

Materials and Methods

Materials

"Tragopogon porrifolius" plant was collected from Sivas Cumhuriyet University campus. $\text{CuSO}_4 \cdot 5\text{H}_2\text{O}$ (Sigma-Aldrich) was used as starting metal and Reactive Red 120 (Sigma-Aldrich, CAS No: 61951-82-4) was used in photocatalytic experiments. pH adjustments were made with concentrated and dilute H_2SO_4 and NaOH.

Preparation of Tragopogon Porrifolius Extract

Tragopogon porrifolius plant was washed to remove dust and impurities and dried until the moisture was completely removed. After drying, 5 g of dry plant was extracted by boiling in 100 ml of water for 15 minutes. The extract cooled to room temperature was filtered with Whatman No. 1 filter paper and stored at +4 °C for use in metal nanoparticle synthesis.

Determination of Total Phenolic Compounds by Folin-Ciocalteu Method

The total phenolic compounds of the extracts was determined according to the described method using 2 N Folin-Ciocalteu phenol reagent [22]. 2 N 100 μL Folin-Ciocalteu phenol reagent, 100 μL extract, 100 μL standard gallic acid solutions, 2.3 mL distilled water and 1 mL 7 % aqueous sodium carbonate solution were mixed and kept at room temperature for 2 h. Absorbance at 750 nm wavelength was measured in a spectrophotometer. The results are expressed as gallic acid equivalent (GAE).

CuO NPs synthesis

Tragopogon porrifolius extract was used as a reducing agent to produce CuO NPs by green synthesis method. $\text{CuSO}_4 \cdot 5\text{H}_2\text{O}$ was used to prepare the metal solution. 10 mL of plant extract was added dropwise to 50 mL of 0.2 M $\text{CuSO}_4 \cdot 5\text{H}_2\text{O}$ solution and stirred in a magnetic stirrer for 2 hours. The pH of the resulting solution was adjusted to 10. After 2 hours of stirring, a color change was observed indicating the formation of CuO NPs and CuO NPs were separated by centrifugation at 10,000 rpm for 15 minutes. The synthesized CuO NPs were dried in an oven at 50°C.

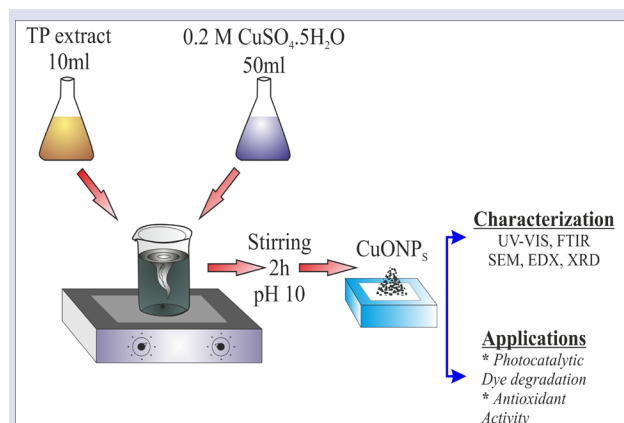


Figure 1. Schematic diagram of the green synthesis of CuO NPs

CuO NPs characterization

Using Tragopogon porrifolius extract as the starting material, CuO NPs were synthesized and then characterized using UV-Vis, FTIR, XRD, SEM and EDX.

FT-IR analysis in the range of 400–4000 cm^{-1} was performed to determine the possible functional groups present in the structure of CuO NPs. The crystal structure of CuO NPs was determined by XRD. SEM analysis was performed for the morphology of the particles and EDX analysis was performed to determine the elemental composition.

Antioxidant Assay

In vitro DPPH radical scavenging assay

Using the method given by Sathiskumar [23] the ability of CuO NPs, an extract of Tragopogon porrifolius, to scavenge free radicals, was evaluated.

Ascorbic acid (as a positive control) and different quantities (50-500 g/mL) of CuONPs, Tragopogon porrifolius extract, and DPPH % solution in ethanol (0.1 mM) were also combined. 30 minutes were given for the mixtures to sit in the dark before the absorbance at 517 nm was determined.

The following equation 1 was used to determine the DPPH% inhibition percentage:

$$\% \text{Inhibition} = \left[\frac{(A_{\text{control}} - A_{\text{sample}})}{A_{\text{control}}} \right] \times 100 \quad [1]$$

where A_{sample} is the absorbance of DPPH/ sample solution and A_{control} is the absorbance of DPPH % solution without including the sample.

Photocatalytic Degradation

The photocatalytic activity of CuO NPs produced by green synthesis method was evaluated by analyzing the degradation of Reactive Red 120 dye. Photocatalytic activity experiments were carried out under UV-C (254 nm) lamp in dark environment. The studies were carried out in a reactor with constant stirring speed to ensure homogeneous dispersion of the nanoparticles. The samples obtained from the photocatalytic reactions were analyzed by UV-vis spectroscopy (Shimadzu UV-2600) at $\lambda = 530$ nm [24].

The photodegradation efficiency of RR 120 dye was determined using the following equation (Eq. 2):

$$\% \text{Degradation} = \left[\frac{(C_o - C_t)}{C_o} \right] \times 100 \quad [2]$$

where C_o : The initial concentration of the RR 120 dye. C_t : The residual concentration of the RR 120 dye.

Results and Discussion

Determination of Total Phenolic Compound

The total amount of phenolic compounds in *Tragopogon porrifolius* extract was determined according to Folin-Ciocalteu method. In this method, when a marker is added to the extract, the color of the extract turns blue, indicating the presence of polyphenols in it.

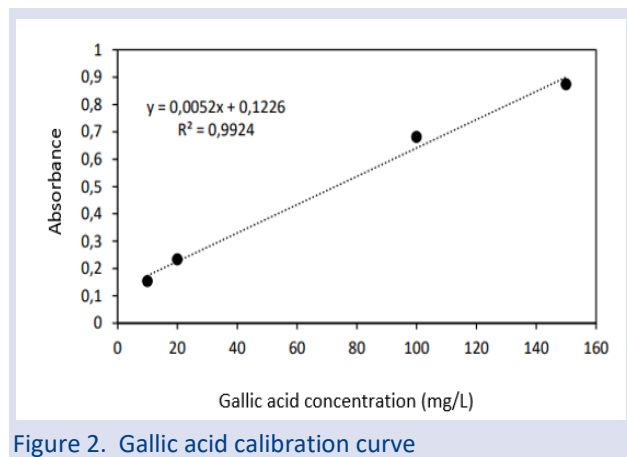


Figure 2. Gallic acid calibration curve

The amount of phenolic compounds in the extract was determined with the help of the standard curve, which is the equivalent of the absorbance value read at 750 nm in terms of gallic acid. With the help of the gallic acid standard curve given in Figure 2 the total amount of phenolic compound in *Tragopogon porrifolius* was determined as 43.27 mg/L.

UV-Vis Result

UV-Vis spectroscopy is among the analyses used to characterize and validate metal nanoparticles. Since the method is easily applicable, it is used as the first step in the verification of nanoparticle synthesis. UV-Vis absorption spectroscopy of the synthesized CuO NPs was examined in the range of 400-800 nm. UV-Vis absorption spectroscopy of CuO NPs synthesized by green synthesis method using TP extract and extract is given in Figure 3. No peak was observed in the absorption spectroscopy of TP extract. The absorption band of CuO nanoparticles observed at 461 nm confirms the synthesis of CuO NPs. The obtained results show that the UV-Vis absorption results are in agreement with the literature [25].

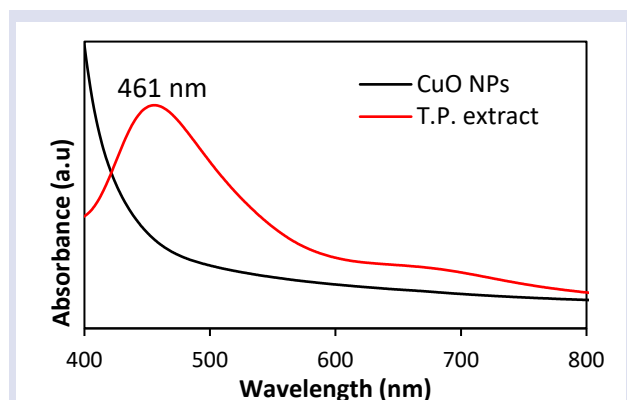


Figure 3. UV-Vis UV-vis spectroscopy absorbance results of TP extract and CuO NPs

The optical energy band gap of CuO NPs synthesized by green synthesis method was determined by Tauc plot obtained by plotting $(\alpha h\nu)^2$ versus $h\nu$ [26–28].

$$(\alpha h\nu)^2 = B(h\nu - E_g) \quad [3]$$

- α : absorption coefficient
- h : Planck's constant
- ν : frequency of the photon
- E_g : optical energy band gap
- B : constant

Figure 4 shows the data obtained from the transmittance values and the plot of $(\alpha h\nu)^2$ versus photon energy ($h\nu$). The optical band gap of CuO NPs was found to be 2.25 eV.

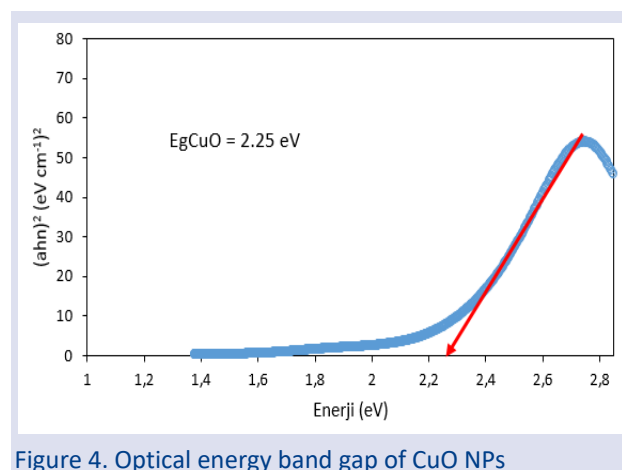


Figure 4. Optical energy band gap of CuO NPs

FTIR Result

FTIR analysis was performed to characterize the chemical composition and bond structure of CuO NPs. FTIR analysis was performed by ATR method in the range of 400-4000 cm^{-1} (Fig. 5).

CuO exhibits a characteristic peak in the IR spectrum between 400 and 600 cm^{-1} [14, 29]. The peaks at 599 cm^{-1} and 424 cm^{-1} observed in the spectrum define the Cu-O bond structure.

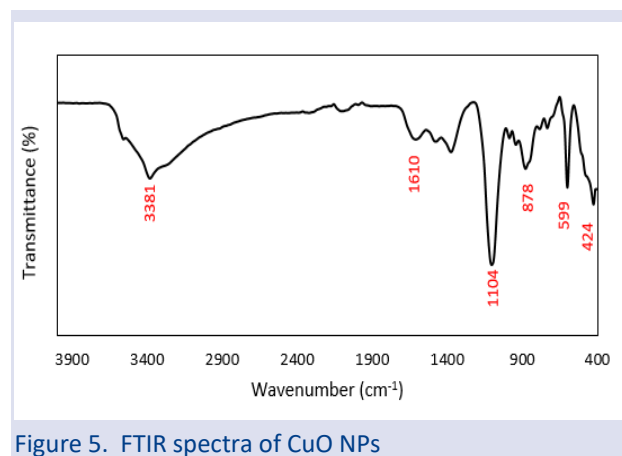


Figure 5. FTIR spectra of CuO NPs

Peaks between 900-700 cm^{-1} define the aromatic bending vibration of the C-H group and the peak observed at 878 cm^{-1} in the spectrum corresponds to the aromatic bending vibration of the C-H group [30]. The peak observed at 1104 cm^{-1} corresponds to O-H bending of

phenol and alcoholic compounds (alcohols) [31]. The peak observed at 3381 cm^{-1} corresponds to amide N-H stretching and the peak observed at 1628 cm^{-1} corresponds to C=C stretching (alkene) [31].

SEM Result

The morphology of the nanoparticles produced by green synthesis method was analyzed by SEM. SEM images were obtained by "Au coating". Images showing the morphological structure of CuO NPs taken with 100 kx are given in Figure 6. It is clearly seen from the SEM image that the particles are spherical in shape. In many studies investigating the production of CuO NPs by green synthesis, it was determined that CuO NPs synthesized with TP extract yielded similarly shaped spherical particles [32–34]. It is seen that the particle sizes in the measured area vary between 235 nm and 350 nm. With the average of 20 measurements taken, the average particle size in the measured area was calculated as 288 nm.

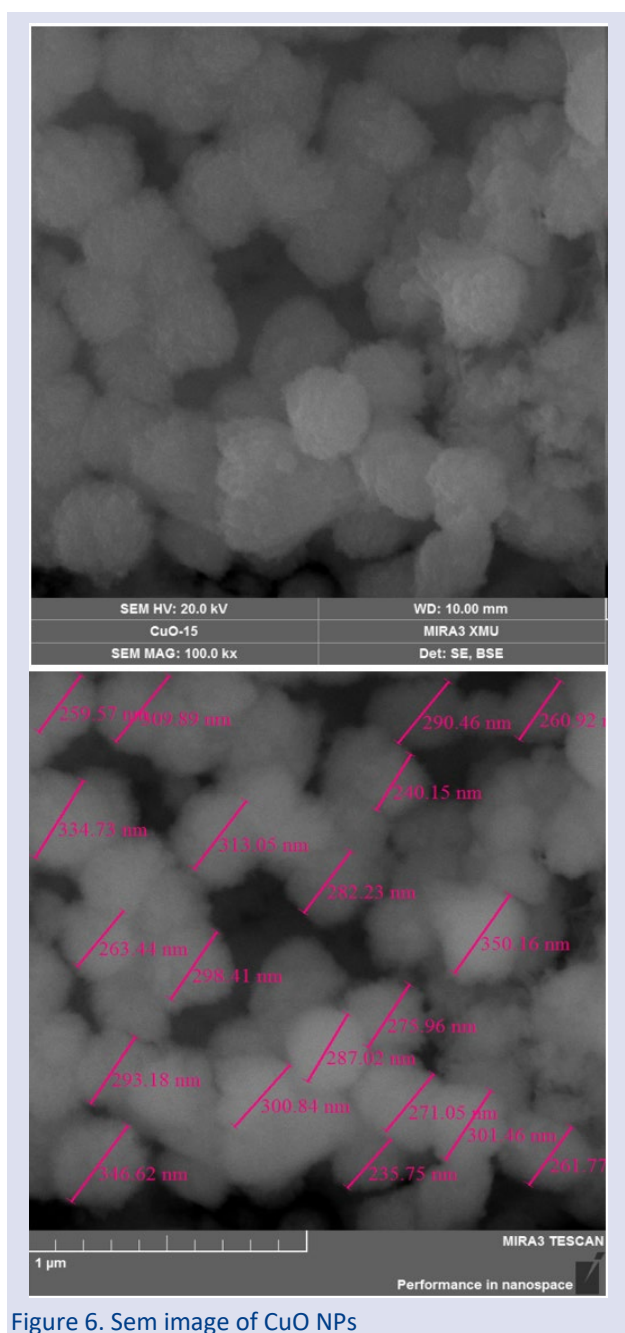


Figure 6. Sem image of CuO NPs

EDX Result

The EDX spectrum of CuO NPs is given in Figure 7. The strong peaks due to Cu and O elements observed in the spectrum prove the CuO structure. Cu and O incorporation ratios were determined as 58.17 % (w.t.) and 32.73 % (w.t.), respectively. There are weak peaks belonging to C and S in the spectrum. C peak is due to the organic compounds in the structure of TP extract and S is due to the metal salt [14, 35].

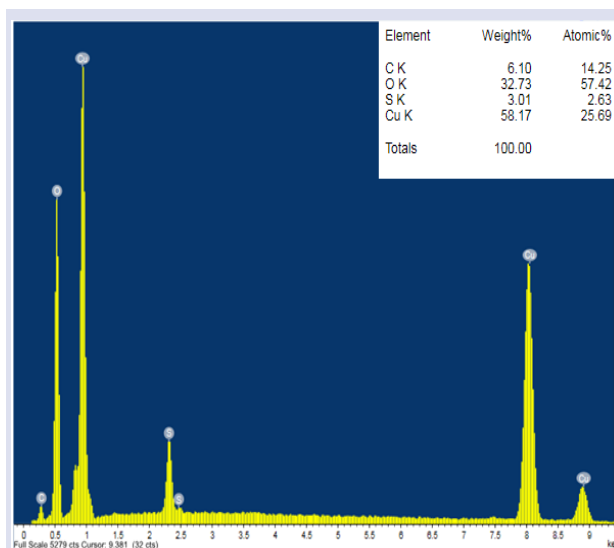


Figure 7. EDX spectrum of the CuO NPs

XRD Result

XRD analysis result of CuO NPs synthesized by green synthesis method using TP extract is given in Figure 8. XRD analysis was performed at a scanning speed of $2^\circ/\text{min}$. The presence of XRD peaks at 2θ value of 31.92° , 35.7° , 38.6° , 48.82° , 52.84° , 58.06° , 61.4° corresponds to the (1 1 0), (1 1 1), (2 0 0), (2 0 2), (0 2 0), (0 2 1), (1 1 3) crystal planes, respectively. This result confirms the formation of CuO NPs [36, 37]. The obtained XRD pattern clear and well-defined CuO reflections indicate that the produced nanoparticles have a high degree of crystallinity.

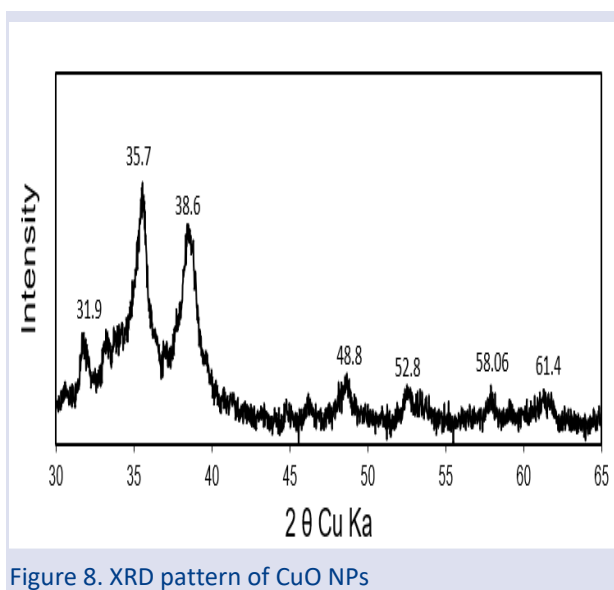


Figure 8. XRD pattern of CuO NPs

Antioxidant Activity

Antioxidants are substances used to reduce the damage caused by free radicals. Different chemical entities known as free radicals have one or more unpaired electrons. These free radicals are very unstable and try to stabilize themselves by attacking other molecules and taking their electrons. They form within the system and are highly reactive. This makes them potentially damaging for short-lived chemical species. These radicals are continuously produced in the human body because they are essential for detoxification, energy supply and immune function [38]. The redox properties of phenolic compounds, which are crucial in absorbing and neutralizing free radicals, are what give them their antioxidant activity [39, 40].

The antioxidant capacity of biosynthesized CuONPs was examined in this study using the DPPH technique. The principle of DPPH analysis is that the intense purple color of a freshly made DPPH solution tends to fade or disappear when an antioxidant sample is present in the solution. As a result, antioxidant molecules aim to quench DPPH free radicals, converting them into a colorless product. Analyses are performed by absorbance measurement at 517 nm.

The antioxidant capacity of CuO NPs synthesized with TP extract was investigated in the concentration range of 50-500 $\mu\text{g}/\text{mL}$ (Fig. 9). Ascorbic acid was used as a positive control in the study.

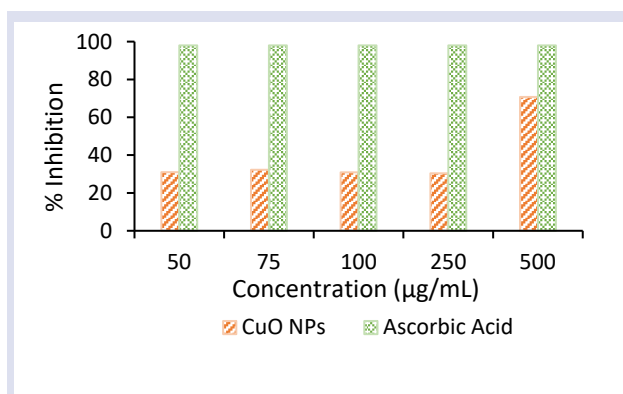


Figure 9. DPPH radical scavenging activity of CuO NPs and ascorbic acid

The results obtained showed that CuO NPs have antioxidant activity. In the concentration range of 50-250 $\mu\text{g}/\text{mL}$, the % inhibition values of CuO NPs ranged between 30-32 %. The % inhibition value of CuO NPs at 500 $\mu\text{g}/\text{mL}$ concentration was calculated as 70.75 %. The decrease in the concentration of CuO NPs resulted in a decrease in antiradical capacity.

Photocatalytic Activity

The time dependent absorbance spectra and % removal of RR 120 dye as a result of photocatalytic degradation with CuO NPs produced by green synthesis method using TP extract are given in Figure 10 and Figure 11, respectively. In the experiment for the degradation of RR 120 dye, 50 ppm dye concentration, 0.04 g adsorbent

amount and natural pH (pH= 7.98) of the dye solution were studied. The degradation of RR 120 was studied for up to 45 minutes and measurements were taken at 5 minute intervals for the first 30 minutes.

As seen in Figure 11, 55 % RR 120 degradation occurred in the first 5 minutes of photocatalytic degradation. RR 120 dye degradation occurred in approximately 30 minutes and the removal efficiency was calculated as 76 %.

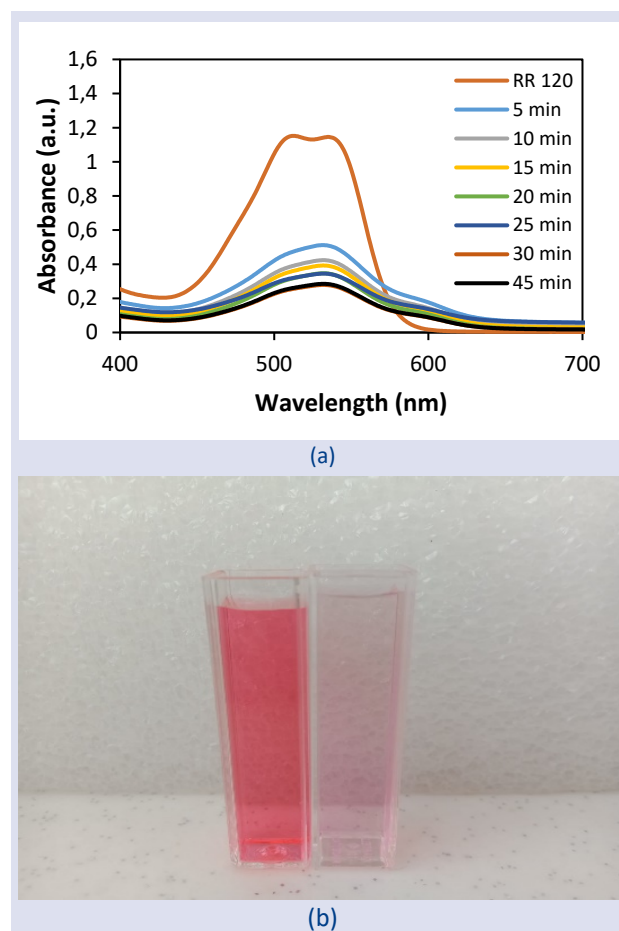


Figure 10. Time dependent absorbance spectra of RR 120 (a), before and after the UV light induced degradation

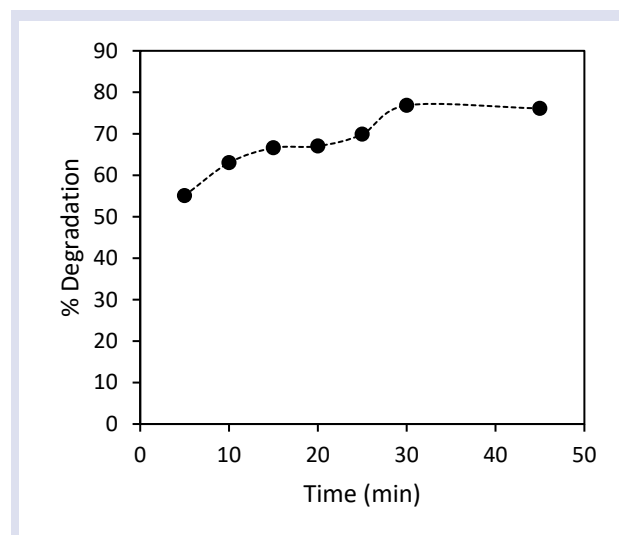


Figure 11. % Degradation-time graph for RR 120

Conclusion

CuO NPs were produced by green synthesis method using *Tragopogon porrifolius* extract as reducing agent. In the SEM analysis of the nanoparticles, it was determined that the nanoparticles had a spherical structure and the average particle size of the particles within the measured area was 288 nm. In EDX analysis, Cu and O ratios were determined as 58.17 % and 32.73 %, respectively. The synthesis of CuO NPs was confirmed by peaks obtained from XRD and FTIR analysis.

Antioxidant and photocatalytic activity of the synthesized CuO NPs were investigated. The free radical scavenging activity of CuO NPs synthesized with TP extract was investigated in the concentration range of 50-500 µg/mL. Free radical scavenging activity was determined as 70.75 % for 500 µg/mL CuO. The free radical scavenging activity of ascorbic acid was calculated as 98 %. In antioxidant activity studies, CuO NPs were found to have antioxidant activity.

In the photocatalytic study, the degradation of azo dye and toxic Reactive Red 120 dye was investigated. The study was carried out at a concentration of 50 ppm and at the natural pH of the solution. The catalyst amount of CuO NPs was used as 2 g/L. RR 120 degradation was calculated as 76 % in about 30 minutes. In the first 5 minutes, 55 % RR 120 degradation was realized. These results showed that CuO NPs synthesized with TP extract were highly effective in RR 120 degradation.

Acknowledgement

This study was supported by Sivas Cumhuriyet University Scientific Research Projects Coordination Unit (CÜBAP) with the project number M-796.

Conflict of interest

The authors declare that they have no competing interests.

References

- [1] Dulta, K., Koşarsoy Ağçeli, G., Chauhan, P., Jasrotia, R., Chauhan, P. K., Ighalo, J. O., Multifunctional CuO nanoparticles with enhanced photocatalytic dye degradation and antibacterial activity, *Sustainable Environment Research*, 32 (1) (2022) 1-15.
- [2] Sudha, A., Jeyakanthan, J., Srinivasan, P., Green synthesis of silver nanoparticles using *Lippia nodiflora* aerial extract and evaluation of their antioxidant, antibacterial and cytotoxic effects, *Resource-Efficient Technologies*, 3 (4) (2017) 506-515.
- [3] Chaudhuri, S. K., & Malodia, L., Biosynthesis of zinc oxide nanoparticles using leaf extract of *Calotropis gigantea*: characterization and its evaluation on tree seedling growth in nursery stage, *Applied Nanoscience*, 7 (8) (2017) 501-512.
- [4] Abdullah, J. A. A., Eddine, L. S., Abderrhmane, B., Alonso-González, M., Guerrero, A., & Romero, A., Green synthesis and characterization of iron oxide nanoparticles by *Phoenix dactylifera* leaf extract and evaluation of their antioxidant activity, *Sustainable Chemistry and Pharmacy*, 17 (2020) 100280.
- [5] Ighalo, J. O., Sagboye, P. A., Umenweke, G., Ajala, O. J., Omoarukhe, F. O., Adeyanju, C. A., Adeniyi, A. G., CuO nanoparticles (CuO NPs) for water treatment: A review of recent advances, *Environmental Nanotechnology, Monitoring & Management*, 15 (2021) 100443.
- [6] McNamara, K., Tofail, S. A., Nanoparticles in biomedical applications, *Advances in Physics: X*, 2 (1) (2017) 54-88.
- [7] De Jong, W. H., Borm, P. J., Drug delivery and nanoparticles: applications and hazards, *International Journal of Nanomedicine*, 3 (2) (2008) 133-149.
- [8] Paiva-Santos, A. C., Herdade, A. M., Guerra, C., Peixoto, D., Pereira-Silva, M., Zeinali, M., Veiga, F., Plant-mediated green synthesis of metal-based nanoparticles for dermatopharmaceutical and cosmetic applications, *International Journal of Pharmaceutics*, 597 (2021) 120311.
- [9] Chen, Z., Han, S., Zhou, S., Feng, H., Liu, Y., Jia, G., Review of health safety aspects of titanium dioxide nanoparticles in food application, *NanoImpact*, 18 (2020) 100224.
- [10] Zhang, Q., Yin, Y., Nanomaterials engineering and applications in catalysis, *Pure and Applied Chemistry*, 86 (1) (2014) 53-69.
- [11] Thandapani, G., Arthi, K., Pazhanisamy, P., John, J. J., Vinothini, C., Rekha, V., Sekar, V., Green synthesis of copper oxide nanoparticles using *Spinacia oleracea* leaf extract and evaluation of biological applications: Antioxidant, antibacterial, larvicidal and biosafety assay, *Materials Today Communications*, 34 (2023) 105248.
- [12] Khan, A. U., Malik, N., Khan, M., Cho, M. H., Khan, M. M., Fungi-assisted silver nanoparticle synthesis and their applications. *Bioprocess and biosystems engineering*, 41 (2018) 1-20.
- [13] Tsekhmistrenko, S. I., Bityutskyy, V. S., Tsekhmistrenko, O. S., Horalskiy, L. P., Tymoshok, N. O., Spivak, M. Y., Bacterial synthesis of nanoparticles: A green approach, *Biosystems Diversity*, 28 (1) (2020) 9-17.
- [14] Topal Canbaz, G., Keskin, Z. S., Yokuş, A., Aslan, R., Biofabrication of copper oxide nanoparticles using *Solanum tuberosum* L. var. Vitelotte: characterization, antioxidant and antimicrobial activity, *Chemical Papers*, 77 (8) (2023) 4277-4284.
- [15] Bezza, F. A., Tichapondwa, S. M., Chirwa, E. M., Fabrication of monodispersed copper oxide nanoparticles with potential application as antimicrobial agents, *Scientific Reports*, 10 (1) (2020) 16680.
- [16] Dang, T. M. D., Le, T. T. T., Fribourg-Blanc, E., Dang, M. C., Synthesis and optical properties of copper nanoparticles prepared by a chemical reduction method, *Advances in Natural Sciences: Nanoscience and Nanotechnology*, 2 (1) (2011) 015009.
- [17] Zhou, Y., Wu, S., Liu, F., High-performance polyimide nanocomposites with polydopamine-coated copper nanoparticles and nanowires for electronic applications, *Materials Letters*, 237 (2019) 19-21.
- [18] Maliki, M., Ifijen, I. H., Ikhuoria, E. U., Jonathan, E. M., Onaiwu, G. E., Archibong, U. D., Ighodaro, A., Copper nanoparticles and their oxides: optical, anticancer and antibacterial properties, *International Nano Letters*, 12 (4) (2022) 379-398.
- [19] Xu, V. W., Nizami, M. Z. I., Yin, I. X., Yu, O. Y., Lung, C. Y. K., & Chu, C. H., Application of copper nanoparticles in dentistry, *Nanomaterials*, 12 (5) (2022) 805.

- [20] Gurav, P., Naik, S. S., Ansari, K., Srinath, S., Kishore, K. A., Setty, Y. P., Sonawane, S., Stable colloidal copper nanoparticles for a nanofluid: Production and application, *Colloids and Surfaces A: Physicochemical and Engineering Aspects*, 441 (2014) 589-597.
- [21] Liu, H., Wang, G., Liu, J., Nan, K., Zhang, J., Guo, L., Liu, Y., Green synthesis of copper nanoparticles using *Cinnamomum zelanicum* extract and its applications as a highly efficient antioxidant and anti-human lung carcinoma, *Journal of Experimental Nanoscience*, 16 (1) (2021) 410-423.
- [22] Singleton, V. L., Rossi, J. A., Colorimetry of total phenolics with phosphomolybdic-phosphotungstic acid reagents, *American journal of Enology and Viticulture*, 16 (3) (1965) 144-158.
- [23] Sathishkumar, G., Jha, P. K., Vignesh, V., Rajkuberan, C., Jeyaraj, M., Selvakumar, M., Sivaramakrishnan, S., Cannonball fruit (*Couroupita guianensis*, Aubl.) extract mediated synthesis of gold nanoparticles and evaluation of its antioxidant activity, *Journal of Molecular Liquids*, 215 (2016) 229-236.
- [24] Cho, I. H., Zoh, K. D., Photocatalytic degradation of azo dye (Reactive Red 120) in TiO₂/UV system: Optimization and modeling using a response surface methodology (RSM) based on the central composite design, *Dyes and Pigments*, 75 (3) (2007) 533-543.
- [25] Nabila, M. I., Kannabiran, K., Biosynthesis, characterization and antibacterial activity of copper oxide nanoparticles (CuO NPs) from actinomycetes, *Biocatalysis and agricultural biotechnology*, 15 (2018) 56-62.
- [26] Zhao, J., Ge, S., Pan, D., Shao, Q., Lin, J., Wang, Z., Guo, Z., Solvothermal synthesis, characterization and photocatalytic property of zirconium dioxide doped titanium dioxide spinous hollow microspheres with sunflower pollen as bio-templates, *Journal of colloid and interface science*, 529 (2018) 111-121.
- [27] Keiteb, A. S., Saion, E., Zakaria, A., Soltani, N., Structural and optical properties of zirconia nanoparticles by thermal treatment synthesis, *Journal of nanomaterials*, 2016 (2016) 1-7.
- [28] Nazim, M., Khan, A. A. P., Asiri, A. M., Kim, J. H., Exploring rapid photocatalytic degradation of organic pollutants with porous CuO nanosheets: synthesis, dye removal, and kinetic studies at room temperature, *ACS omega*, 6 (4) (2021) 2601-2612.
- [29] Suramwar, N. V., Thakare, S. R., Khaty, N. T., Synthesis and catalytic properties of nano CuO prepared by soft chemical method, *International Journal of Nano Dimension*, 3 (1) (2012) 75-80.
- [30] Padil, V. V. T., Černík, M., Green synthesis of copper oxide nanoparticles using gum karaya as a biotemplate and their antibacterial application, *International Journal Of Nanomedicine*, 8 (2013) 889-898.
- [31] Sepasgozar, S. M. E., Mohseni, S., Feizyadeh, B., Morsali, A., Green synthesis of zinc oxide and copper oxide nanoparticles using *Achillea Nobilis* extract and evaluating their antioxidant and antibacterial properties, *Bulletin of Materials Science*, 44 (2021) 1-13.
- [32] Zaman, M. B., Poolla, R., Singh, P., Gudipati, T., Biogenic synthesis of CuO nanoparticles using *Tamarindus indica* L. and a study of their photocatalytic and antibacterial activity, *Environmental Nanotechnology, Monitoring & Management*, 14 (2020) 100346.
- [33] Vinothkanna, A., Mathivanan, K., Ananth, S., Ma, Y., Sekar, S., Biosynthesis of copper oxide nanoparticles using *Rubia cordifolia* bark extract: characterization, antibacterial, antioxidant, larvicidal and photocatalytic activities, *Environmental Science and Pollution Research*, 30 (15) (2023) 42563-42574.
- [34] Ssekatawa, K., Byarugaba, D. K., Angwe, M. K., Wampande, E. M., Ejobi, F., Nxumalo, E., Kirabira, J. B., Phyto-mediated copper oxide nanoparticles for antibacterial, antioxidant and photocatalytic performances, *Frontiers in Bioengineering and Biotechnology*, 10 (2022) 820218.
- [35] Ali, D., Ismail, M., Hashem, M. A., Akl, M. A., Antibacterial activity of eco friendly biologically synthesized copper oxide nanoparticles, *Egyptian Journal of Chemistry*, 64 (8) (2021) 4099-4104.
- [36] Varughese, A., Kaur, R., Singh, P., Green synthesis and characterization of copper oxide nanoparticles using *Psidium guajava* leaf extract, In *IOP Conference Series: Materials Science and Engineering*, 961 (1) (2020) 012011.
- [37] Ganesan, K., Jothi, V. K., Natarajan, A., Rajaram, A., Ravichandran, S., Ramalingam, S., Green synthesis of Copper oxide nanoparticles decorated with graphene oxide for anticancer activity and catalytic applications, *Arabian Journal of Chemistry*, 13 (8) (2020) 6802-6814.
- [38] Gülçin, İ., The antioxidant and radical scavenging activities of black pepper (*Piper nigrum*) seeds, *International journal of food sciences and nutrition*, 56 (7) (2005) 491-499.
- [39] Rehana, D., Mahendiran, D., Kumar, R. S., Rahiman, A. K., Evaluation of antioxidant and anticancer activity of copper oxide nanoparticles synthesized using medicinally important plant extracts, *Biomedicine & Pharmacotherapy*, 89 (2017) 1067-1077.
- [40] Javanmardi, J., Stushnoff, C., Locke, E., Vivanco, J. M., Antioxidant activity and total phenolic content of Iranian *Ocimum* accessions, *Food chemistry*, 83 (4) (2003) 547-550.

Synthesis and Characterization of Novel 2,4-Diaryloctahydro-2H-Chromene Derivatives with Four Stereocenters

Hayreddin Gezegen^{1,a,*}¹ Department of Nutrition and Dietetics, Faculty of Health Sciences, Sivas Cumhuriyet University, 58140 Sivas, Türkiye.

*Corresponding author

Research Article

History

Received: 11/08/2023

Accepted: 13/11/2023

Copyright

©2023 Faculty of Science,
Sivas Cumhuriyet University

ABSTRACT

Chromene derivatives are among the natural compounds and they can also be easily obtained synthetically. They are one of the most commonly used skeletons in heterocyclic chemistry. Chromene derivatives are used in the cosmetic and pigment industries as well as having a wide spectrum of biological activity. Synthesis of chromene derivatives and their application areas is a current topic. In this study, it is aimed to synthesis and characterization of new chromene derivatives by catalysis of molecular iodine starting from 1,5-diol derivatives with chiral centers. In this context, 8 new 2,4-diaryloctahydro-2H-chromene derivatives were synthesized in high yields and their structure determinations were made by spectroscopic methods (1H-NMR, 13C-NMR, 2D-NMR, GCMS and FTIR) and their stereochemistry was determined.

Keywords: Chalcone, 1,5-Diol, Chromene, Iodine.gezegenh@cumhuriyet.edu.tr<https://orcid.org/0000-0003-3602-7400>

Introduction

Today, many synthetic or natural compounds, which used as drugs in medical therapy, are in the class of heterocyclic compounds. Among heterocyclic compounds, the six-membered oxygen-containing heterocyclic compound adjacent to the benzene ring is known as chroman (benzodihydropyran or 3,4-dihydro-2H-chromene) (I) [1]. The chroman ring is a pharmacologically important structural unit and it is found in the structure of e vitamins and some drugs that are troglitazone used as an antidiabetic [2], ormeloxifene used as a selective estrogen receptor [3] and nebivolol used in the treatment of high blood pressure and heart failure [4].

Chromene derivatives are obtained by the placement of various functional groups in different positions on the chromane skeleton (I).

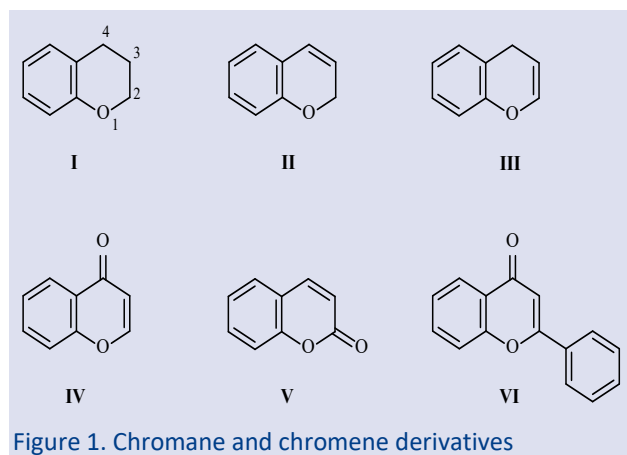


Figure 1. Chromane and chromene derivatives

2H-Chromene derivatives (II) are formed by the double bond between of carbons 3 and 4, 4H-chromene derivatives (III) are formed by the double bond between of carbons 2 and 3 on this skeleton, and 4H-chromen-4-one derivatives (IV) are formed with the carbonyl group in the 4 position. In addition, coumarin (V) and flavonoid (VI) derivatives have this basic skeleton (Figure 1) [5].

Chromene derivatives are widely found in nature and can be easily obtained by synthesis. Due to their bioactive potential, they are one of the most commonly used skeletons in heterocyclic chemistry. It is known that chromene derivatives have a wide spectrum of biological activity [6]. While some chromene derivatives act as sex pheromones [7], some are used as drugs especially as antifungal [8] and antimicrobial agents [9]. In addition, chromene derivatives are also used in the cosmetics and pigment industries [10]. When the studies on the activity of chromene derivatives are examined, it is seen that these compounds have important biological activities such as antimalarial, antituberculosis [11], anti-cancer [12], potassium channel opener [13], anti-HIV activity [14] and antioxidant [15]. Synthesis and application areas of chromene derivatives is a current and interesting subject and there are many studies in the literature, and new ones are added to these studies every day.

Molecular iodine, which is used as an effective catalyst in various organic synthesis reactions, stands out as a clean and non-toxic Lewis acid catalyst compared to metallic catalysts [16]. In addition to being a cheap and easily available compound, its use in reactions and its removal from the reaction medium are carried out by

uncomplicated simple methods [17]. Iodine catalyzes C-C, C-N, C-O and C-S bond formations, allowing the synthesis of heteroatom-containing polyfunctional compounds and the formation of molecular diversity [16], [18], [19]. Molecular iodine, which is widely used especially in Michael addition reactions also plays an important role in condensation, cycloaddition, esterification, etherization and production of cyclic ethers [20], [21].

In the light of this information, here in this study, first time molecular iodine-catalyzed synthesis of new 2,4-diaryloctahydro-2*H*-chromene derivatives with four stereo centers (Figure 2) was carried out over 1,5-diols that we synthesized in our previous studies [22], [23]. The method we used and the reaction we performed are capable of guiding and giving ideas to researchers working in this field in the design and synthesis of various functional new compounds.

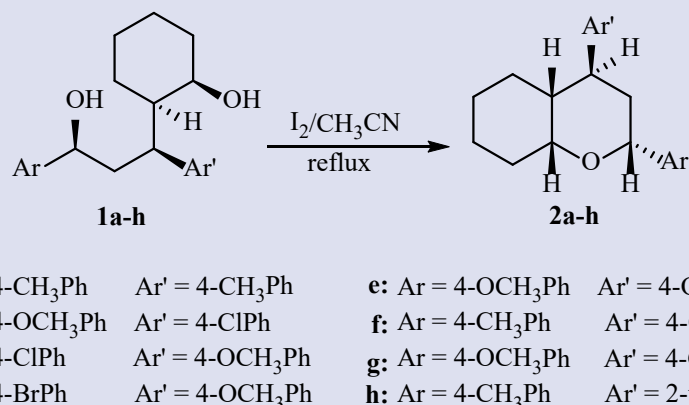


Figure 2. The general route for the preparation of 2,4-diaryloctahydro-2*H*-chromene derivatives (2a-h)

Material and Methods

¹H-NMR, ¹³C-NMR and 2D-NMR spectra were measured on a Bruker Avance DPX-400 NMR (Nuclear Magnetic Resonance, 400 MHz) instrument in CDCl₃ and (D₆)DMSO at 25 °C. δ in ppm relative to Me₄Si (δ 0.00) for ¹H-NMR, CDCl₃ (δ 77.0) and (D₆)DMSO (δ 39.5) for ¹³C-NMR spectra as internal standards, *J* in Hz. GC-MS (Gas chromatography-mass spectrometry) spectra were measured on a PerkinElmer Clarus 500 instrument. All the FTIR (Fourier Transform Infra-Red) spectra were measured on a JASCO FT/IR-430 spectrometer.

General Procedure for the Synthesis of Chromene Derivatives

The synthesis of 1,5-diols, which are used as starting compounds in the synthesis of chromene derivatives, has been reported in our previous studies [22], [23].

To a solution of 1,5-diol derivative (1 mmol) (1a-h) in CH₃CN (10 mL) was added molecular iodine (I₂, 10% mole) and the mixture was refluxed for 6 hours. At the end of the reaction, the mixture was taken into a separatory funnel and sodium thiosulfate solution (10%) was added, and the organic phase was separated by extraction with CHCl₃ (3x20 mL). After drying over Na₂SO₄ and removing the solvent, the crude product was purified on a silica gel column eluting with CHCl₃/n-hexane (3:7).

rel-(2*R*,4*S*,4*aR*,8*aR*)-2,4-di-*p*-tolyl-octahydro-2*H*-chromene (2a): Yield 84%, yellow viscous liquid. ¹H NMR (400 MHz, Chloroform-*d*) δ 7.26 (d, *J* = 8.1 Hz, 2H), 7.12 (d, *J* = 8.2 Hz, 2H), 7.10 (s, 4H), 4.82 (dd, *J* = 11.6, 2.4 Hz, 1H), 4.14 (dt, *J* = 12.4, 4.8 Hz, 1H), 3.16 (td, *J* = 12.2, 3.7 Hz, 1H), 2.31 (s, 6H), 2.26 – 2.19 (m, 1H), 1.96 (ddd, *J* = 13.2, 3.7,

2.5 Hz, 1H), 1.87 (dt, *J* = 5.6, 3.5 Hz, 1H), 1.78 (dd, *J* = 25.0, 12.2 Hz, 2H), 1.49 – 1.38 (m, 1H), 1.33 – 1.24 (m, 5H). ¹³C-NMR (100 MHz, DMSO-*d*₆, ppm): δ 141.5, 140.9, 136.3, 135.4, 129.4 (2C), 128.9 (2C), 127.6 (2C), 126.2 (2C), 75.5, 71.4, 43.3, 40.7, 38.6, 26.9, 25.5, 25.4, 21.1, 21.0, 20.2. IR (KBr, cm⁻¹): 3018, 2931, 2856, 1513, 1450, 1375, 1139, 1085, 1029, 981, 811, 721, 572, 514. GC/MS (*m/z*) (%): 321 (M⁺, 2.1), 302 (4.9), 228 (32.8), 185 (28.7), 131 (41.2), 118 (100.0), 105 (82.5), 91 (44.6).

rel-(2*R*,4*S*,4*aR*,8*aR*)-4-(4-chlorophenyl)-2-(4-methoxyphenyl)octahydro-2*H*-chromene (2b): Yield 80%, colorless viscous liquid. ¹H-NMR (400 MHz, CDCl₃, ppm): δ 7.34 (d, *J* = 8.8 Hz, 2H), 7.30 (d, *J* = 8.4 Hz, 2H), 7.19 (d, *J* = 8.4 Hz, 2H), 6.90 (d, *J* = 8.4 Hz, 2H), 4.83 (d, *J* = 11.6 Hz, 1H), 4.18 (dt, *J* = 12.4, 4.8 Hz, 1H), 3.81 (s, 3H), 3.22 (td, *J* = 12.2, 3.4 Hz, 1H), 2.21 (bd, *J* = 12.4 Hz, 1H), 2.02-1.91 (m, 3H), 1.80-1.73 (m, 3H), 1.44-1.27 (m, 4H). ¹³C-NMR (100 MHz, CDCl₃, ppm): δ 158.9, 142.7, 135.2, 131.9, 128.8 (2C), 128.7 (2C), 127.2 (2C), 113.7 (2C), 76.1, 71.5, 55.3, 42.7, 40.6, 39.0, 26.8, 25.5, 25.4, 20.3. IR (KBr, cm⁻¹): 2998, 2935, 2856, 1614, 1513, 1490, 1450, 1367, 1301, 1245, 1174, 1139, 1087, 1029, 1012, 827, 549, 522. GC/MS (*m/z*) (%): 359 (M⁺, 1.6), 258 (16.4), 205 (18.4), 151 (20.6), 134 (100.0), 121 (73.3), 108 (55.2), 91 (31.9), 77 (34.8).

rel-(2*R*,4*S*,4*aR*,8*aR*)-2-(4-chlorophenyl)-4-(4-methoxyphenyl)octahydro-2*H*-chromene (2c): Yield 84%, yellow viscous liquid. ¹H-NMR (400 MHz, CDCl₃, ppm): δ 7.37 (d, *J* = 8.4 Hz, 2H), 7.34 (d, *J* = 8.4 Hz, 2H), 7.18 (d, *J* = 8.4 Hz, 2H), 6.90 (d, *J* = 8.8 Hz, 2H), 4.88 (d, *J* = 11.6 Hz, 1H), 4.24-4.19 (m, 1H), 3.82 (s, 3H), 3.23-3.19 (m, 1H), 2.39 (bd, *J* = 12.4 Hz, 1H), 2.05-1.91 (m, 3H), 1.79-1.73 (m, 3H), 1.51 (bd, *J* = 12.4 Hz, 1H), 1.37-1.31 (m, 3H). ¹³C-NMR (100

MHz, CDCl₃, ppm): δ 158.2, 141.9, 136.1, 132.8, 128.4 (2C), 128.3 (2C), 127.3 (2C), 113.9 (2C), 76.3, 71.5, 55.2, 43.1, 40.8, 38.6, 26.8, 25.5, 25.4, 20.3. IR (KBr, cm⁻¹): 2996, 2933, 2856, 1610, 1511, 1490, 1450, 1375, 1247, 1178, 1083, 1037, 1014, 827, 561, 530. GC/MS (m/z) (%): 358 (M⁺, 5.0), 259 (20.8), 201 (13.4), 147 (37.1), 134 (100.0), 121 (91.4), 91 (31.4), 77 (21.2).

rel-(2*R*,4*S*,4*aR*,8*aR*)-2-(4-bromophenyl)-4-(4-methoxyphenyl)octahydro-2*H*-chromene (2d): Yield 81%, colorless viscous liquid. ¹H-NMR (400 MHz, CDCl₃, ppm): δ 7.48 (d, *J* = 8.6 Hz, 2H), 7.30 (d, *J* = 8.6 Hz, 2H), 7.17 (d, *J* = 8.6 Hz, 2H), 6.89 (d, *J* = 8.6 Hz, 2H), 4.85 (dd, *J* = 11.4, 1.8 Hz, 1H), 4.20 (td, *J* = 8.6, 4.8 Hz, 1H), 3.81 (s, 3H), 3.18 (td, *J* = 12.0, 3.6 Hz, 1H), 2.25 (bd, *J* = 11.4 Hz, 1H), 2.02-1.91 (m, 3H), 1.78-1.71 (m, 3H), 1.51 (bd, *J* = 11.4 Hz, 1H), 1.35-1.25 (m, 3H). ¹³C-NMR (100 MHz, CDCl₃, ppm): δ 158.2, 142.4, 136.1, 131.3 (2C), 128.8 (2C), 127.7 (2C), 120.1, 113.9 (2C), 76.3, 71.5, 55.3, 43.1, 40.8, 38.6, 26.8, 25.5, 25.4, 20.3. IR (KBr, cm⁻¹): 2996, 2933, 2856, 1610, 1511, 1486, 1450, 1247, 1178, 1085, 1072, 1035, 1010, 827, 559, 530. GC/MS (m/z) (%): 403 (M⁺, 2.5), 303 (17.7), 201 (22.3), 147 (46.8), 134 (100.0), 121 (94.3), 91 (37.9), 77 (30.4).

rel-(2*R*,4*S*,4*aR*,8*aR*)-2,4-bis(4-methoxyphenyl)octahydro-2*H*-chromene (2e): Yield 73%, yellow viscous liquid. ¹H-NMR (400 MHz, CDCl₃, ppm): δ 7.34 (d, *J* = 8.4 Hz, 2H), 7.17 (d, *J* = 8.8 Hz, 2H), 6.90-6.86 (m, 4H), 4.83 (dd, *J* = 11.2, 2.0 Hz, 1H), 4.17 (dt, *J* = 12.4, 4.6 Hz, 1H), 3.81 (s, 3H), 3.18 (td, *J* = 12.0, 3.4 Hz, 1H), 2.27-2.22 (m, 1H), 2.00-1.91 (m, 3H), 1.82-1.72 (m, 3H), 1.48 (bd, *J* = 12.0 Hz, 1H), 1.35-1.28 (m, 3H). ¹³C-NMR (100 MHz, CDCl₃, ppm): δ 158.8, 158.0, 136.3, 135.4, 128.3 (2C), 127.2 (2C), 113.9 (2C), 113.7 (2C), 75.8, 71.7, 55.3, 55.2, 42.9, 40.9, 38.6, 26.8, 25.5, 25.4, 20.3. IR (KBr, cm⁻¹): 2996, 2933, 2856, 1612, 1511, 1463, 1450, 1375, 1301, 1247, 1176, 1139, 1083, 1035, 1012, 829, 738, 565, 528. GC/MS (m/z) (%): 353 (M⁺, 2.5), 244 (52.0), 201 (23.8), 147 (33.0), 134 (100.0), 121 (90.3), 91 (32.9), 77 (18.5).

rel-(2*R*,4*S*,4*aR*,8*aR*)-4-(4-methoxyphenyl)-2-(*p*-tolyl)octahydro-2*H*-chromene (2f): Yield 79%, yellow viscous liquid. ¹H-NMR (400 MHz, DMSO-*d*₆, ppm): δ 7.27 (d, *J* = 8.0 Hz, 2H), 7.13 (d, *J* = 8.4 Hz, 2H), 7.10 (d, *J* = 8.0 Hz, 2H), 6.85 (d, *J* = 8.4 Hz, 2H), 4.78 (d, *J* = 11.2 Hz, 1H), 4.06-4.02 (m, 1H), 3.68 (s, 3H), 3.16-3.10 (m, 1H), 2.24 (s, 3H), 2.19-2.09 (m, 2H), 1.84 (bd, *J* = 12.4 Hz, 1H), 1.78-1.76 (m, 1H), 1.68-1.52 (m, 2H), 1.33-1.11 (m, 5H). ¹³C-NMR (100 MHz, DMSO-*d*₆, ppm): δ 158.1, 141.0, 136.4, 136.2, 128.9 (2C), 128.5 (2C), 126.1 (2C), 114.2 (2C), 75.6, 71.5, 55.2, 43.5, 40.9, 38.3, 26.8, 25.5, 25.4, 21.1, 20.2. IR (KBr, cm⁻¹): 3027, 2996, 2933, 2856, 1610, 1511, 1450, 1375, 1247, 1178, 1083, 1037, 829, 813, 563, 520. GC/MS (m/z) (%): 338 (M⁺, 0.7), 239 (16.4), 228 (58.0), 201 (30.5), 147 (59.0), 134 (100.0), 121 (91.6), 105 (45.4), 91 (55.9), 77 (16.7).

rel-(2*R*,4*S*,4*aR*,8*aR*)-2-(4-methoxyphenyl)-4-(*p*-tolyl)octahydro-2*H*-chromene (2g): Yield 82%, yellow viscous liquid. ¹H-NMR (400 MHz, CDCl₃, ppm): δ 7.35 (d, *J* = 8.4 Hz, 2H), 7.16 (s, 4H), 6.90 (d, *J* = 8.4 Hz, 2H), 4.84 (d, *J* = 11.2 Hz, 1H), 4.18 (dt, *J* = 12.4, 4.8 Hz, 1H), 3.82 (s, 3H), 3.20 (td, *J* = 12.0, 3.6 Hz, 1H), 2.36 (s, 3H), 2.30-2.28 (m, 1H), 2.00-1.91 (m, 2H), 1.88-1.74 (m, 3H), 1.49 (bd, *J* = 12.4 Hz, 1H), 1.35-1.26 (m, 4H). ¹³C-NMR (100 MHz, CDCl₃, ppm): δ 158.8, 141.2, 135.8, 135.4, 129.2 (2C), 127.4 (2C), 127.2 (2C), 113.7 (2C), 76.3, 71.7, 55.3, 42.8, 40.7, 39.1, 26.9, 25.5, 25.4, 21.0, 20.3. IR (KBr, cm⁻¹): 3004, 2933, 2857, 1612, 1511, 1450, 1301, 1245, 1174, 1083, 1035, 815, 736, 551, 524. GC/MS (m/z) (%): 338 (M⁺, 0.6), 244 (34.0), 201 (20.5), 185 (32.3), 135 (63.1), 118 (100.0), 105 (54.6), 91 (43.0), 77 (20.7).

rel-(2*R*,4*S*,4*aR*,8*aR*)-4-(thiophen-2-yl)-2-(*p*-tolyl)octahydro-2*H*-chromene (2h): Yield 70%, yellow viscous liquid. ¹H-NMR (400 MHz, CDCl₃, ppm): δ 7.33 (d, *J* = 8.0 Hz, 2H), 7.22-7.18 (m, 3H), 6.98 (dd, *J* = 4.8, 3.6 Hz, 1H), 6.89 (d, *J* = 3.2 Hz, 1H), 4.87 (d, *J* = 10.4 Hz, 1H), 4.20 (dt, *J* = 12.4, 4.6 Hz, 1H), 3.60 (td, *J* = 12.0, 3.2 Hz, 1H), 2.37 (s, 3H), 2.25-2.17 (m, 1H), 2.00-1.85 (m, 2H), 1.79-1.65 (m, 4H), 1.41-1.35 (m, 4H). ¹³C-NMR (100 MHz, CDCl₃, ppm): δ 148.3, 139.9, 137.0, 129.0 (2C), 126.5, 125.8 (2C), 123.6, 122.8, 76.2, 71.9, 44.2, 42.6, 35.1, 26.9, 25.5 (2C), 21.1, 20.3. IR (KBr, cm⁻¹): 3023, 2933, 2856, 1513, 1448, 1367, 1265, 1247, 1135, 1085, 1039, 813, 740, 694, 563. GC/MS (m/z) (%): 314 (M⁺, 0.7), 227 (43.1), 177 (17.1), 134 (31.5), 110 (100.0), 97 (53.9), 91 (31.3), 79 (19.1).

Results and Discussion

In our previous study, we synthesized 1,5-diols starting from chalcones [22], [23]. In this study, we carried out the synthesis of eight new chromene derivatives that have four stereogenic centers. The 2,4-diaryloctahydro-2*H*-chromene derivatives (2a-h) were obtained by reaction of 1,5-diols (1a-h) with molecular iodine in CH₃CN at reflux condition in high yields. The synthesized new compounds and their structures are shown in Table 1.

The mechanism of the transformation of 1,5-diols to 2,4-diaryloctahydro-2*H*-chromene derivatives in the presence of iodine can be explained as shown Figure 3. As a result of the interaction of iodine with the oxygen atom in the benzylic position, a polarization occurs on the 1,5-diol. Thus generating an electron-deficient centre (δ^+). Through the transition state, the electron-rich oxygen atom (δ^-) in the structure attacks the benzylic position and realized the cyclisation. Meanwhile, the hydroxyl group in the benzylic position takes the hydrogen and leaves as a water molecule [24]. The resulting cyclization yields new 2,4-diaryloctahydro-2*H*-chromene derivatives with four stereocenters (2a-h).

Table 1. Synthesized 2,4-diaryloctahydro-2H-chromene derivatives (2a-h)

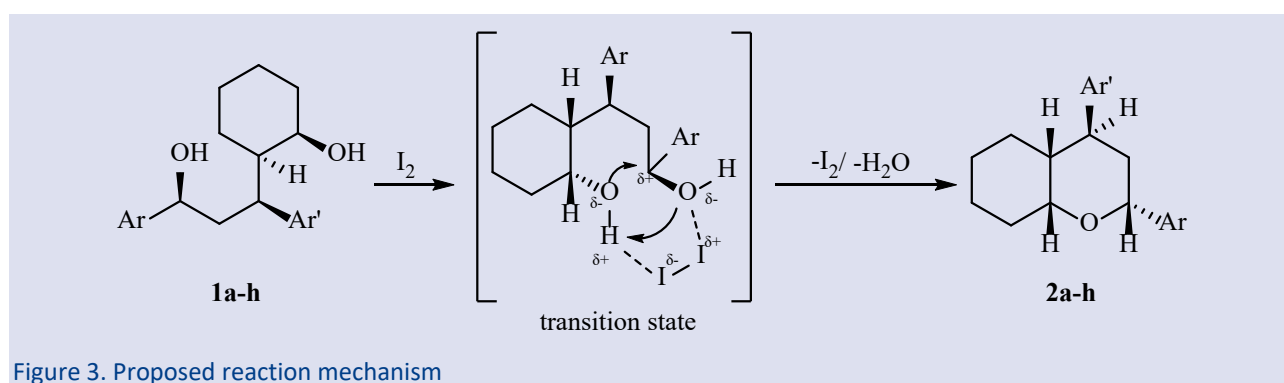
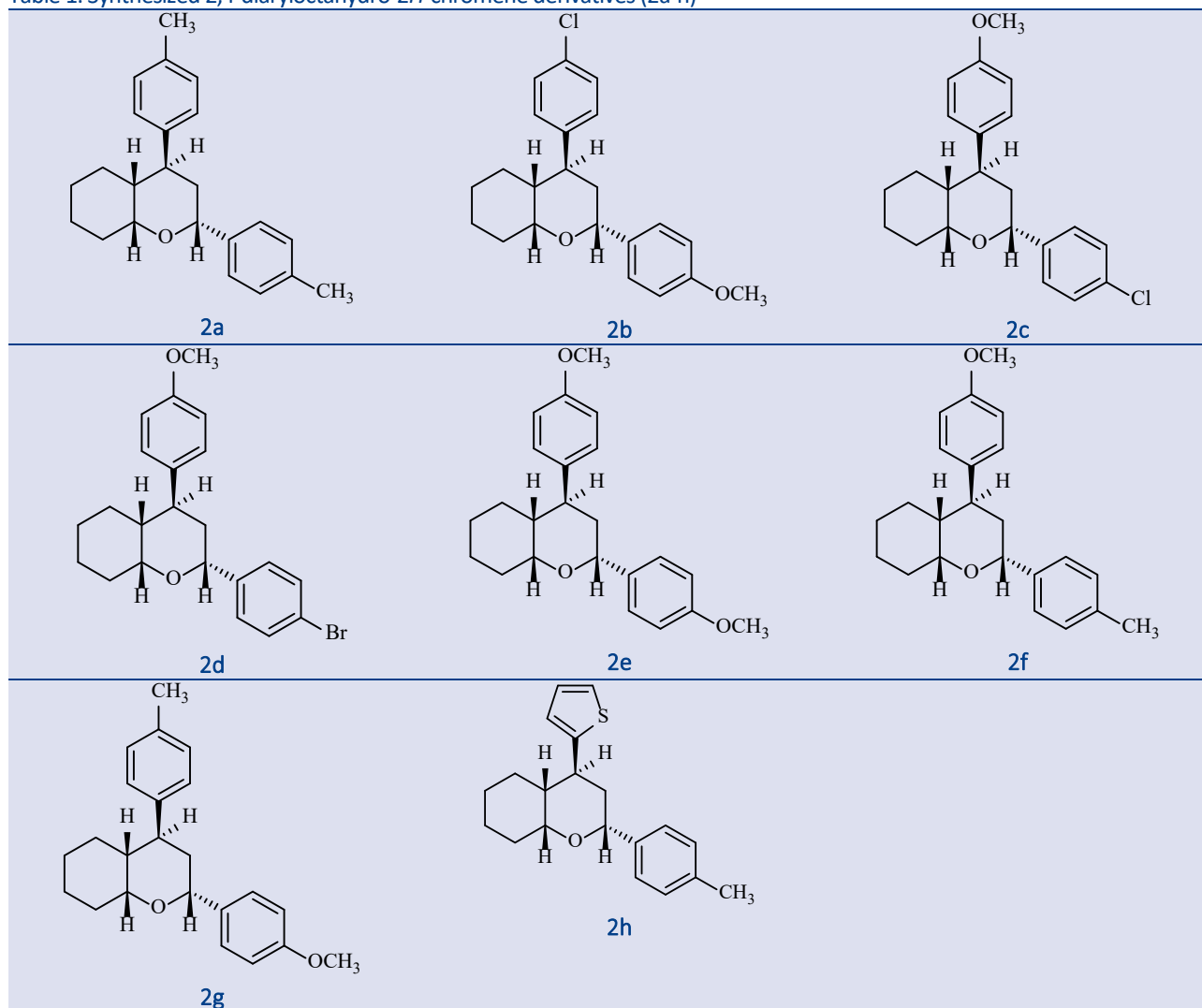


Figure 3. Proposed reaction mechanism

The structures of the synthesized new chromenes were determined by spectroscopic analysis studies (1H -NMR, ^{13}C -NMR, 2D-NMR, FTIR and GC/MS). The full analysis of 1H -NMR, ^{13}C -NMR, COSY and HETCOR spectra of 2a confirmed the presence of chromene structure (Figure 4, Figure 5, Figure 6 and Figure 7). Moreover, the stereochemistry of 2a was predicted from NOESY analysis. In the NOESY spectrum of compound 2a, a strong correlations between the H-C4 signal at 2.23 ppm and the H-C1 signal at 4.82 ppm was observed. In addition, a strong correlation between the H-C4 signal at 2.23 ppm

and the H-C5 signal at 4.15 ppm was observed (Figure 8). In the 1H -NMR spectrum of 2a, the H-C1 proton gave a doublet of doublets at 4.82 ($J = 11.6, 2.4$ Hz) ppm. Additionally the signals of the H-C5, H-C3 and H-C4 protons of 2a in the spectrum were observed as doublet of triplets at 4.14 ($J = 12.4, 4.8$ Hz), triplet of doublets at 3.16 ($J = 12.2, 3.7$ Hz) and multiplet 2.27-2.20 ppm respectively. The methylene protons in the structure resonate by giving an AB spin system. The A part of the AB system gave doublet of doublets of doublets at 1.96 ($J = 13.2, 3.7, 2.5$ Hz) ppm, while the B part gave doublet of

doublets at 1.78 ($J = 25.0, 12.2$ Hz) ppm respectively. All the aliphatic and aromatic signals in the spectrum were consistent with the structure of 2a (Figure 4). In the ^{13}C -NMR spectrum, it is seen that the C1 and C5 etheric carbons in the chromene structure resonate at 72.0 ppm and 76.3 ppm respectively, and the other aliphatic and aromatic signals are in full harmony with the structure (Figure 5).

The absorption bands seen at $3014\text{--}2856\text{ cm}^{-1}$ in the FTIR spectrum of 2a result from the stretching vibration of

the aliphatic and aromatic C-H units in the structure. Aromatic C-C stretch bands arising from aromatic rings in the structure are seen at 1513 and 1450 cm^{-1} in the spectrum. The asymmetric stretch band of the C-O-C bridge, which indicates the presence of the chromene ring, is located at 1085 cm^{-1} in the spectrum, while the symmetric stretch band is seen as a weak peak at 890 cm^{-1} . The band seen at 811 cm^{-1} in the spectrum proves that the substituents in the aromatic rings are in the para position (Figure 9).

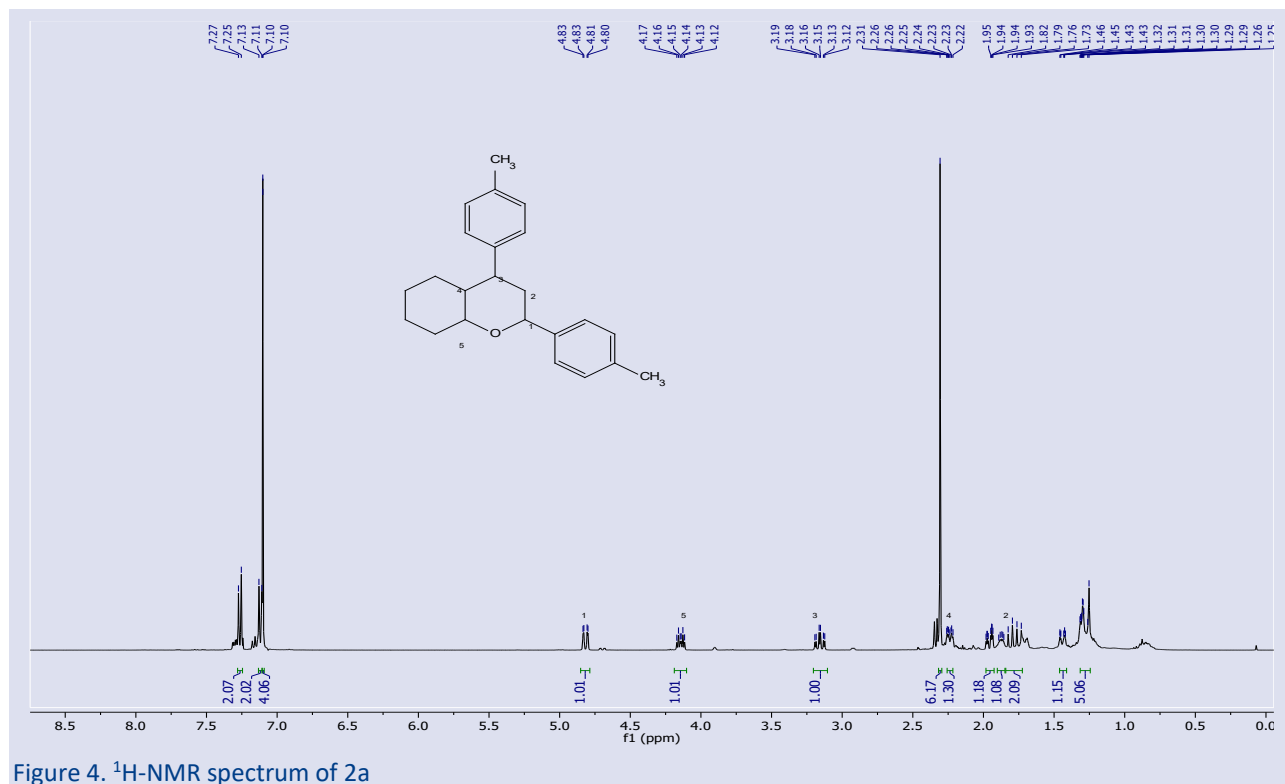


Figure 4. ^1H -NMR spectrum of 2a

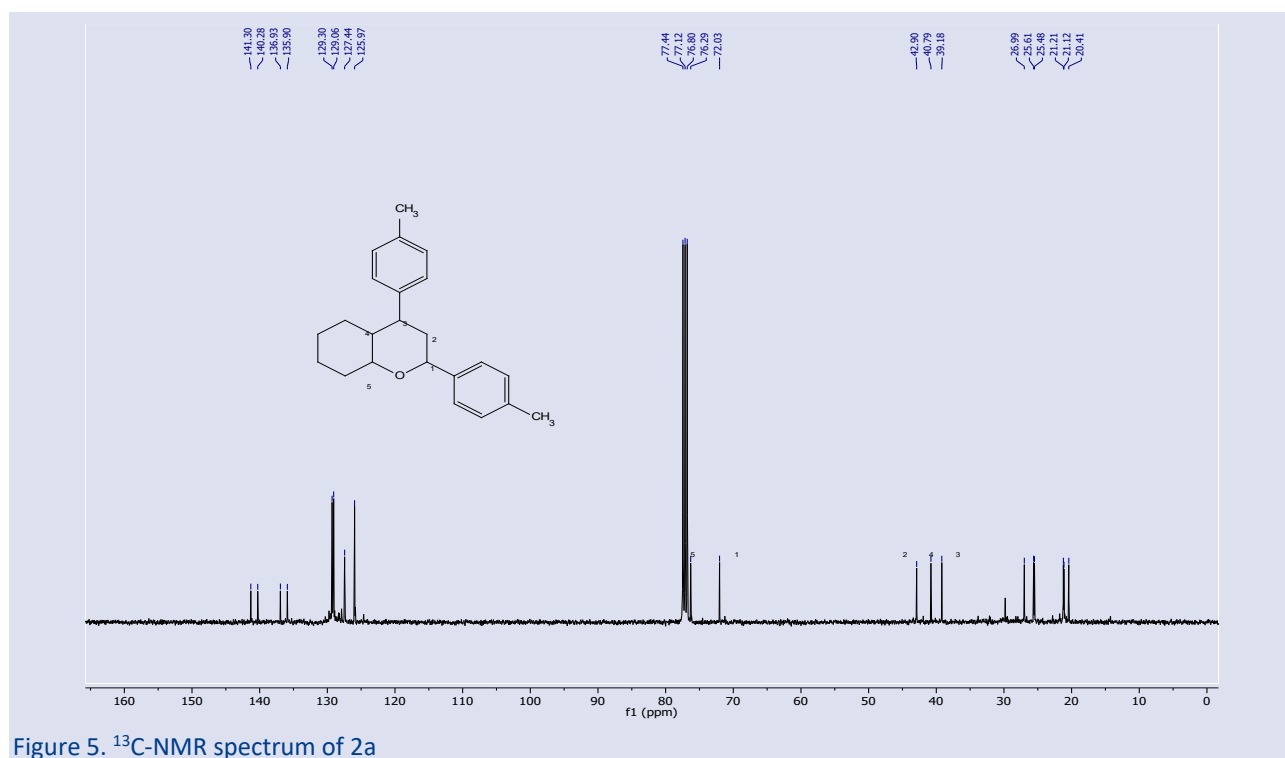


Figure 5. ^{13}C -NMR spectrum of 2a

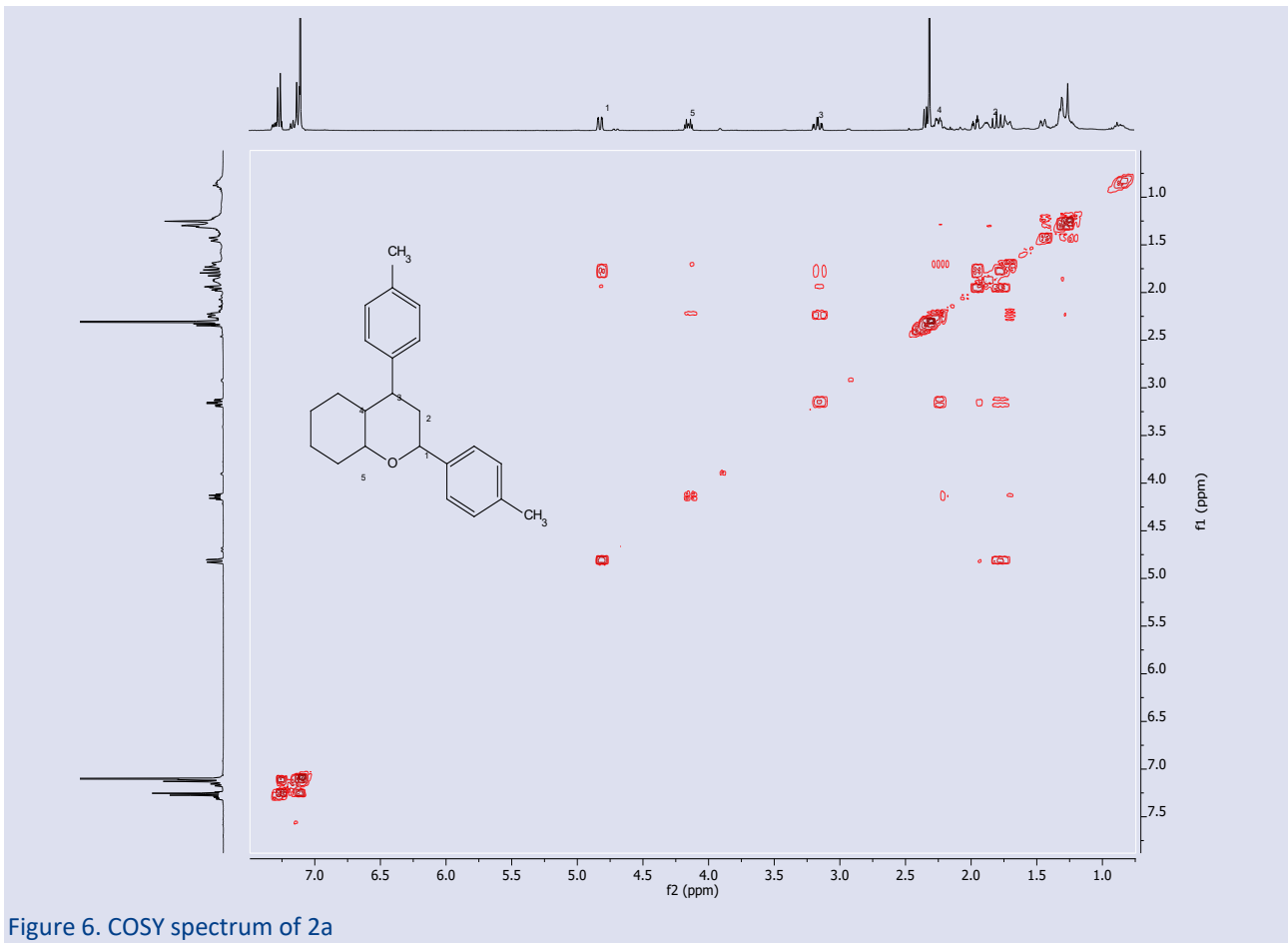


Figure 6. COSY spectrum of 2a

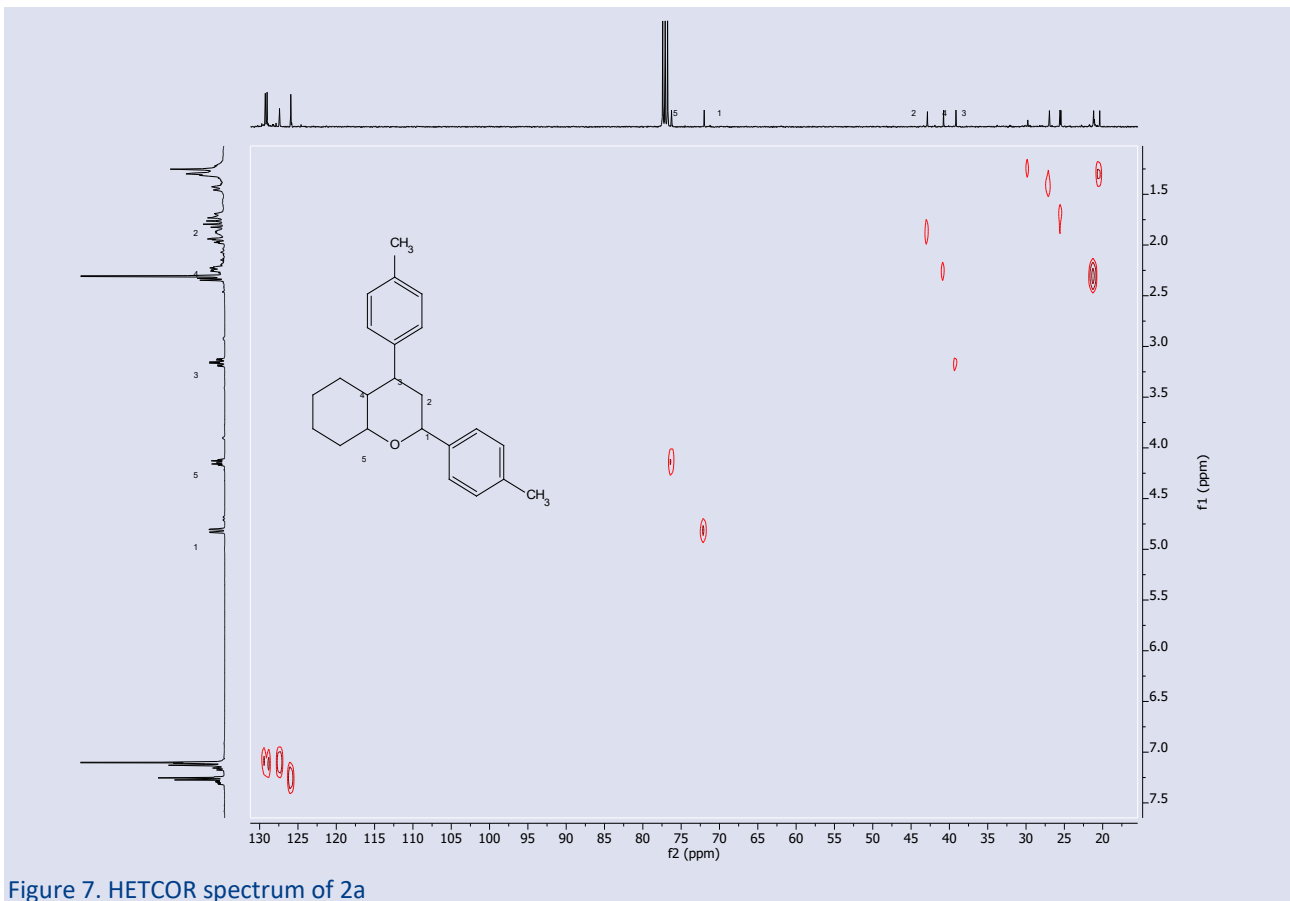
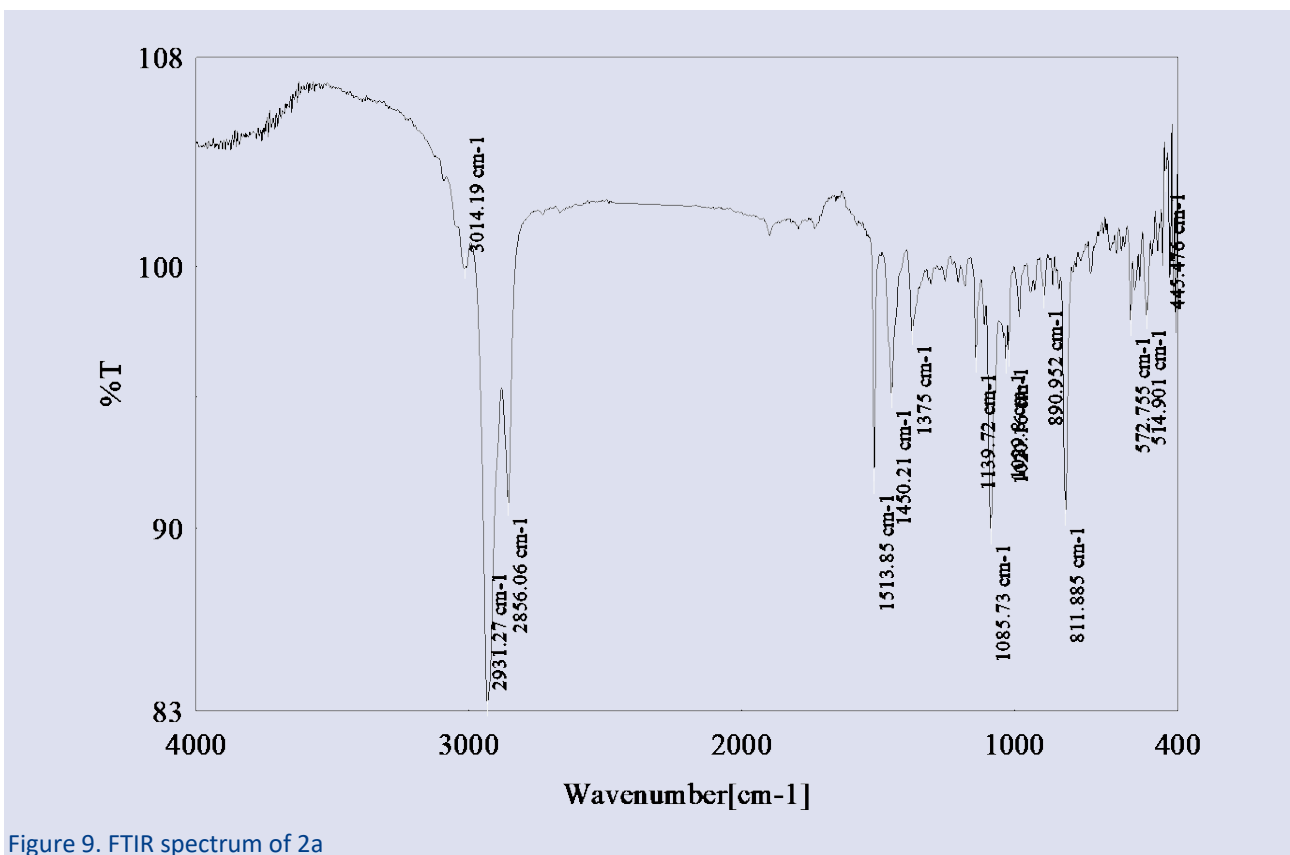
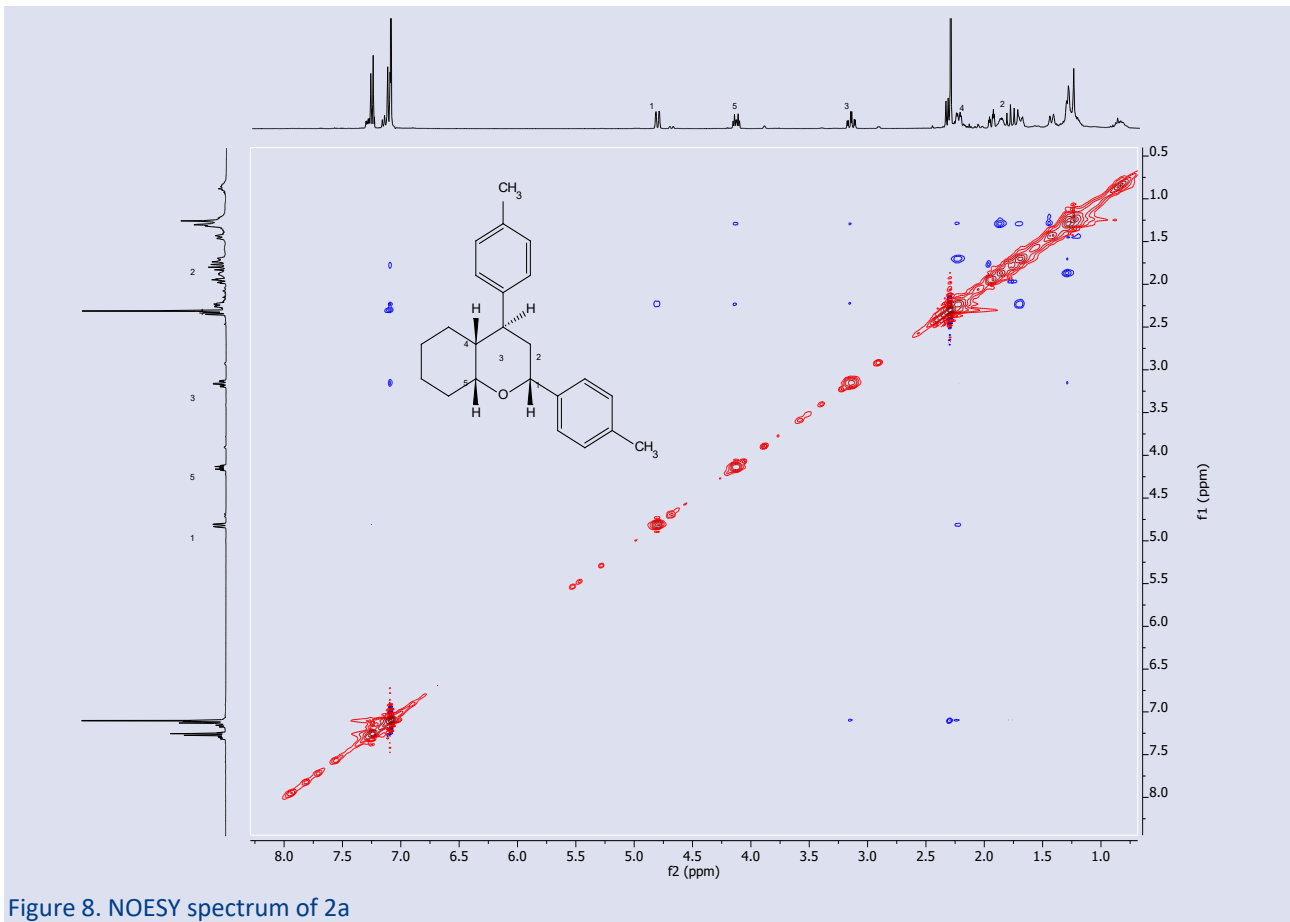


Figure 7. HETCOR spectrum of 2a



Conclusion

It is known that chromene derivatives are compounds with high biological activity potential as well as being

natural compounds [6]. At the same time, chromene derivatives are among the important compounds that are used in industry [25]. In this respect, the synthesis and application areas of chromene derivatives is a current issue that attracts the attention of researchers. In the present study, eight novel 2,4-diaryloctahydro-2H-chromene derivatives (2a-h) were synthesized from molecular iodine catalysed cyclization of 1,5-diols (1a-h) that we synthesized in our previous studies [22], [23]. The chemical structures of the synthesized new compounds were determined by spectroscopic methods ($^1\text{H-NMR}$, $^{13}\text{C-NMR}$, 2D-NMR, FT-IR, and GC-MS). Although various chromene derivatives and various synthesis methods are reported in the literature, there is no study on the synthesis of iodine-catalyzed chromene derivatives over 1,5-diols. This study demonstrated a route for converting 1,5-diols to cyclic ethers under mild conditions in high yield with iodine. The synthesized compounds are new chiral chromene derivatives with four different stereocenters and are not included in the literature. The 2D-NMR analyzes performed support the proposed configurations of the compounds. The method used can be useful and applicable in synthesizing and developing new chiral compounds with high bioactive potential and multifunctionality. In this respect, this study will make an important contribution to the literature.

Conflicts of interest

There are no conflicts of interest in this work.

Acknowledgements

The authors are indebted to the Gaziosmanpaşa University (Grant BAP-201194) for financial support of this work.

References

- [1] Eicher T., Hauptmann S. & Speichcr, A., *The Chemistry of Heterocycles: Structure, Reactions, Synthesis and Applications*. 2nd ed. Weinheim (2004) 341-345.
- [2] Wen Z., Yang K.-C., Deng J.-F. & Chen L., Advancements in the preparation of 4H-chromenes: an overview, *Advanced Synthesis & Catalysis*, 365 (2023) 1290-1331.
- [3] Singh M. M., Centchroman, a selective estrogen receptor modulator, as a contraceptive and for the management of hormone-related clinical disorders, *Medicinal Research Reviews*, 21 (2001) 302-347.
- [4] Hilar O. & Ezzo D., Nebivolol (bystolic), a novel beta blocker for hypertension, *Pharmacy and Therapeutics*, 34(4) (2009) 188-192.
- [5] Mamaghani M., Nia H. R., Tavakoli F. & Jahanshahi P., Recent Advances in the MCRs Synthesis of Chromenes: A Review, *Current Organic Chemistry*, 22(17) (2018) 1704 - 1769.
- [6] Raj V. & Lee J., 2H/4H-Chromenes-a versatile biologically attractive scaffold, *Frontiers in Chemistry*, 8(623) (2020) 1-23.
- [7] Bianchi G. & Tava, A., Synthesis of (2R)-(+)-2,3-Dihydro-2,6-dimethyl-4H-pyran-4-one, a Homologue of Pheromones of a Species in the Hepialidae Family, *Agricultural and Biological Chemistry*, 51 (1987) 2001-2002.
- [8] Tangmouo J. G., Meli A. L., Komguem J., Kuete V., Ngounou F. N., Lontsi D., Beng V. P., Houdhary M. L. & Sondengam B. L., Crassiflorone, a new naphthoquinone from *Diospyros crassiflora* (Hien), *Tetrahedron Letter*, 47 (2006) 3067-3070.
- [9] Kitamura R. O. S., Romoff P., Young M. C. M., Kato M. J. & Lago J. H. G., Chromenes from *Peperomia serpens* (Sw.) Loudon (Piperaceae), *Phytochemistry*, 67 (2006) 2398-2402.
- [10] Ellis G. P., The Chemistry of Heterocyclic Compounds. In: Weissberger, A. & Taylor, E. C. (Eds). *Chromenes. Chromanes and Chromones*. 2nd ed. New York and London: John Wiley and Sons. (1977) Chapter 11, 11-139.
- [11] McCracken S. T., Kaiser M., Boshoff H. I., Boyd P. D. W. & Copp B. R., Synthesis and antimalarial and antituberculosis activities of a series of natural and unnatural 4-methoxy-6-styryl-pyran-2-ones, dihydro analogues and photo-dimers, *Bioorganic & Medicinal Chemistry*, 20 (2012) 1482-1493.
- [12] Mohareb R. M. & Schatz J., Anti-tumor and anti-leishmanial evaluations of 1,3,4-oxadiazine, pyran derivatives derived from cross-coupling reactions of β -bromo-6H-1,3,4-oxadiazine derivatives, *Bioorganic & Medicinal Chemistry*, 19 (2011) 2707-2713.
- [13] Press J. B., McNally J. J., Sanfilippo P. J., Addo M. F., Loughney D., Giardino E., Katz L. B., Falotico R. & Haertlein B. J., Novel thieno[2,3-b]- and [3,4-b]pyrans as potassium channel openers, Thiophene systems-XVII, *Bioorganic & Medicinal Chemistry*, 1 (1993) 423-435.
- [14] Tummino P. J., Prasad J. V. N. V., Ferguson D., Nouhan C., Graham N., Domagala J. M., Ellsworth E., Gajda C., Hagen S. E., Lunney E. A., Para K. S., Tait B. D., Pavlovsky A., Erickson J. W., Gracheck S., McQuade T.J. & Hupe D.J., Discovery and optimization of nonpeptide HIV-1 protease inhibitors, *Bioorganic & Medicinal Chemistry*, 4 (1996) 1401-1410.
- [15] Jayaprakasha G. K., Rao L. J. & Sakariah K. K., Antioxidant activities of flavidin in different in vitro model systems, *Bioorganic & Medicinal Chemistry*, 12 (2004) 5141-5146.
- [16] Yusubov M.S. & Zhdankin V. V., Iodine catalysis: A green alternative to transition metals in organic chemistry and technology, *Resource-Efficient Technologies*, 1 (2015) 49-67.
- [17] Prajapati D. & Gohain M., Iodine a Simple, Effective and Inexpensive Catalyst for the Synthesis of Substituted Coumarins, *Catalysis Letters*, 119 (2007) 59-63.
- [18] Zhang H., Wang H., Jiang Y., Cao F., Gao W., Zhu L., Yang Y., Wang X., Wang Y., Chen J., Feng Y., Deng X., Lu Y., Hu X., Li X., Zhang J., Shi T. & Wang Z., Recent Advances in Iodine-Promoted C-S/N-S Bonds Formation, *Chemistry-A European Journal*, 26 (2020) 17289-17317.
- [19] Samanta S. & Mondal S., Iodine-Catalyzed or -Mediated Reactions in Aqueous Medium, *Asian Journal of Organic Chemistry*, 10 (2021) 2503-2520.

- [20] Breugst M. & von der Heiden D., Mechanisms in Iodine Catalysis, *Chemistry-A European Journal*, 24 (2018) 9187-9199.
- [21] Kasashima Y., Fujimoto H., Mino T., Sakamoto M., Fujita T., An Efficient Synthesis of Five-membered Cyclic Ethers from 1,3-Diols Using Molecular Iodine as a Catalyst, *Journal of Oleo Science*, 57 (2008) 437-443.
- [22] Gezegen H., Tutar U., & Ceylan M., Synthesis and antimicrobial activity of racemic 1,5-diols: 2-(1,3-diaryl-3-hydroxypropyl)cyclohexan-1-ol derivatives, *Helvetica Chimica Acta*, 99 (2016) 608-616.
- [23] Çelik İ., Akkurt M., Gezegen H., Üremiş M. M. & Duteanu N., 2-[1-(4-Bromophenyl)-3-hydroxy-3-(4-methoxyphenyl)propyl]cyclohexanol, *Acta Crystallographica Section E*, E69 (2013) o1091-o1092.
- [24] Jereb M. & Vrazic D., Iodine-catalyzed Transformation of Aryl-substituted Alcohols Under Solvent-free and Highly Concentrated Reaction Conditions, *Acta Chimica Slovenica*, 64 (2017) 747-762.
- [25] El-Sayed R., Mohamed K.S. & Fadda A. A., Synthesis and evaluation of some chromene derivatives as antioxidant with surface activity, *Afinidad Journal of Chemical Engineering Theoretical and Applied Chemistry*, 75 (2018) 581, 66-75.

MW Assisted Synthesis of New 4,6-diaryl-3,4-Dihydropyrimidines-2(1H)-thione Derivatives: Tyrosinase Inhibition, Antioxidant, and Molecular Docking Studies

Seda Fandaklı ^{1,a,*}, Tayyibe Beyza Yücel ^{2,b}, Elif Öztürk ^{3,c}, Ugur Uzuner ^{4,d}, Burak Barut ^{1,e}, Fatih Mehmet Ateş ^{5,f}, Nurettin Yaylı ^{1,g}

¹Faculty of Pharmacy, Karadeniz Technical University, Trabzon, Türkiye

²Health Services Vocational School, Giresun University, Giresun, Türkiye

³Faculty of Health Sciences, Karadeniz Technical University, Trabzon, Türkiye

⁴Department of Molecular Biology and Genetics, Faculty of Science, Karadeniz Technical University, Trabzon, Türkiye

⁵Occupational Health and Safety, Vocational School of Technical Sciences, Bayburt University, Bayburt, Türkiye

*Corresponding author

Research Article

History

Received: 24/05/2023

Accepted: 14/11/2023

Copyright





©2023 Faculty of Science,
Sivas Cumhuriyet University


ABSTRACT

A number of new methoxy-substituted 4,6-diaryl-3,4-dihydropyrimidine-2(1H)-thiones (DH-Pyr-S, 17-28) were designed and synthesized by the reaction of methoxy-substituted chalcones (1–14) with thiourea using solid-phase microwave method (MW) in view of the structural requirements as suggested in the pharmacophore model for tyrosinase inhibition (TI). Synthesized compounds were assessed for their *in vitro* TI potential and compounds 16, 17, and 21 exhibited notable tyrosinase inhibitory properties at the concentrations of $31.86 \pm 2.45 \mu\text{M}$, $44.58 \pm 0.46 \mu\text{M}$, and $48.47 \pm 0.66 \mu\text{M}$, respectively. Compounds (16, 17, and 21) were exhibited experimentally more potent TI than the standard used in terms of the IC_{50} value (Kojic acid, $55.38 \pm 2.30 \mu\text{M}$; $p < 0.0001$). Additionally, DPPH activity of 15-28 were evaluated and compound 17 showed the moderate DPPH activity ($45.64 \pm 0.34\%$). Binding affinities of synthesized molecules to the tyrosinase catalytic core were further investigated through *in silico* molecular docking studies using AutoDock Vina (version 1.2.5), discovery studio accelrys (BIOVIA, Dassault Systèmes) and predicting small-molecule pharmacokinetic properties using graph-based signatures (pkCSM) programs were used for ADMET calculations. Among synthesized compounds 15, 21, and 24 revealed high binding affinity to tyrosinase active site with lowest binding free energy (ΔG) values of -7.9 kcal/mol , thereby outperformed kojic acid affinity. In conclusion most modeling results were in agreement with their experimental data, suggesting the TI potential of lead compounds.

Keywords: Dihydropyrimidine-2(1H)-thione, Tyrosinase inhibition, DPPH, ADMET, Molecular docking.

^a  sedaf_84@hotmail.com

^c  elifyayli@ktu.edu.tr

^e  burakbarut@ktu.edu.tr

^g  yayli@ktu.edu.tr


^{id} <https://orcid.org/0000-0002-8199-3336>


^{id} <https://orcid.org/0000-0002-0809-6145>

^{id} <https://orcid.org/0000-0002-7441-8771>

^{id} <https://orcid.org/0000-0003-4174-3014>

^b  beyza.yucel@giresun.edu.tr

^d  uguruzuner@ktu.edu.tr

^f  fmehmetates@bayburt.edu.tr

^{id} <https://orcid.org/0000-0002-2632-8325>

^{id} <https://orcid.org/0000-0002-5308-3730>

^{id} <https://orcid.org/0000-0002-7497-2211>

Introduction

Heterocycles play a role in different fields, inclusive of medicinal chemistry, biochemistry, and others. Pharmaceuticals, agrochemicals, and veterinary items are the main applications of heterocyclic compounds [1]. Pyrimidine is the one of the general names of nitrogenous heterocyclic aromatic organic compounds in the structure of nucleic acids, some coenzymes, and vitamins. Pyrimidine and its derivatives, found in many natural products, are essential for the synthesis of pharmaceutical compounds [2], antitumor, antitubercular, antileukemia, antileishmanial, analgesic, anticonvulsant, anticancer, antifungal, and anti-inflammatory [3]. Pyrimidine derivatives known to be effectively used in the cosmetic sector for wrinkle treatment, strengthening hair roots, and strengthening the epidermis layer to prevent gray hair formation. Many methods have been employed to synthesize 3,4-dihydropyrimidine-2-one/thione compounds, e.g., the condensation reaction of malonate derivatives and urea in a basic medium, the cyclocondensation reaction of aldehyde, dicarbonyl compound, and urea/thiourea in one step with the Biginelli reaction [4], α,β -unsaturated esters by the

Michael addition reaction [5], condensation of carbonyls with diamines, and the condensation reaction of chalcones with urea, thiourea, and guanidine derivatives [6]. Chalcones are the most used and attractive bioactive starting materials to synthesize various heterocyclic compounds, such as pyrimidine, pyrazoline [7]. Substituted chalcones and thiourea can easily react under basic conditions according to the 1,4-Michael addition reaction to yield DH-Pyr-S compounds [8].

Some of the drugs used as azathioprine (immunosuppressive), zidovudine, erlotinib, and 5-fluorouracil (anticancer), sulfadiazine and minoxidil (antibacterial), lamivudine (anti-HIV), etravirine (antiviral), and moxonidine (antihypertensive) have pyrimidine structure [9]. In this context, to treat over pigmentation in human bodies, there is a strong urge to find out new and efficient tyrosinase inhibition (TI). Several TI have been reported, but a few of these inhibitors have been commercially in use [10]. There are a few sulfurs containing tyrosinase inhibitors in the literature. It is well known that oxidation resulted by reactive oxygen species is a major cause of melanogenesis

[11]. Sulfur containing compounds possess good antimelanogenic and antioxidant activities, which shows their capacity to affect key redox enzymes. Literature work have shown that small molecules which has sulfur resulted a key role in a wide range of various biological activities [12]. Thus, these finding attracted many scientists to find out new S analogs for the prevention and therapy. Some substances such as kojic acid and arbutin have been well described as TI. However, some of these compounds possess undesirable side effects like carcinogenicity and cytotoxicity [13].

Due to the above problems, we tried to develop new safer and more effective tyrosinase inhibitors. Literature revealed that some thioxo pyrimidine compounds, including compound 15, showed good antiparasitic activity but low cytotoxicity against L1210 and B16 cells [14]. The insecticidal activity of a series of methoxy and various halo-substituted thiopyrimidine compounds, including compound 16, has been studied in the literature [14, 15]. Moreover, the binding affinities of 17 and 21 to the tyrosinase catalytic core (2Y9X) were studied by molecular docking studies [16-18]. The current research focuses on synthesizing methoxy DH-Pyr-S derivatives from the reaction of methoxy chalcones with thiourea and tested their TI, DPPH activity, and molecular docking studies.

Materials and Methods

Materials and Equipment

2-/4-methoxyacetophenone, 2-/3-/4-methoxybenzaldehyde, 2,3-/2,5-dimethoxybenzaldehyde, 2,3,4-trimethoxybenzaldehyde, benzaldehyde and thiourea were of Merck, Fluka, Lancaster, and Sigma-Aldrich brands and they are in analytical purity. Solvents, including ethanol, chloroform, ethyl acetate, and *n*-hexane used in synthesis, purification, and analysis in instrumental devices were purified by fractional distillation. The NMR solvent was CDCl₃ (Merck, 99.8%). The NMR spectra were recorded on a Varian Mercury 200 MHz and Bruker 400 MHz NMR instruments, UV spectra were taken on a Unicam UV2-100 spectrophotometer, FT-IR spectra were acquired on a Perkin-Elmer 1600 (ATR, 4000-400 cm⁻¹) spectrophotometer, mass spectra were recorded using an Agilent LC-QTOF-MS spectrophotometer. Melting points were found with a Thermovar device attached to the microscope. The reactions of the synthesized compounds were performed on a laboratory microwave device (Milestone).

Synthesis

Synthesis of 1–14

The preparation of known 1,3-diaryl-2-propene-1-one derivatives (1–14) was carried out in line with the procedure described in the literature [19-20]. The stirring of the equimolar quantities of substituted acetophenone (10 mmol), benzaldehyde (10 mmol), and NaOH (40%, 4 mL) in ethanol (10 mL) was carried out at a temperature of 0-5 °C for half an hour. Reaction mixture was stirred for

a period of 12 h at room temperature and the reactions were terminated after TLC monitoring. The reaction mixture was acidified with 6 N HCl and poured into crushed ice. The precipitated solid filtrated and washed with cold water and crystallized from ethanol to provide white or yellow products or they were purified by column chromatography when required. Structure of synthesized chalcones (1-14) were confirmed by their NMR data (¹H and ¹³C/APT) and by comparing them with data reported in the literature [19-20].

Synthesis of 15-28

Basic alumina (5 g) was added in a successive way to a solution of 1,3-diaryl-2-propene-1-one (1-14) (4 mmol) and thiourea (4 mmol), and chloroform (15 mL) in a round bottom flask (100 mL), and the reaction mixture was carefully mixed and dried on the rotary evaporator. The material adsorbed on basic silica was transferred to a Pyrex tube (2 cm diameter, 30 mL) and inserted inside the MW oven (Milestone) and heated using a fixed power of 600 W for 5-6 min at 85 °C. The reaction mixture was solved in methanol and neutralized with 2N HCl solution. The solvent was evaporated, and the residue was dissolved in water (50 mL) then extracted with chloroform (20 mL x 3). Then they were purified by column chromatography (Silica gel) using *n*-hexane (50 mL) and a *n*-hexane-ethyl acetate solvent mixture (4:1, 4:2, and 1:1; 100 mL each). After the TLC control, corresponding pure products (DH-Pyr-S, 15-28) were obtained in the range of 60-80% yields, respectively. The structures of 15-28 were identified by their spectral properties (¹H and ¹³C/APT-NMR, FT-IR, LC-QTOF-MS) and comparison of the data reported in the literature [14-15].

4-(2-Methoxyphenyl)-6-phenyl-3,4-dihydropyrimidine-2(1H)-thione (17)

Yield: 75%, mp = 221-223 °C, Rf: 0.67 (*n*-hexane-ethyl acetate, 1:1); FTIR (ATR, cm⁻¹): 3149 (-NH), 3026(=CH), 2900, 2974 (-CH), 1573 (C=C, aromatic ring), 1245 (-OCH₃), 1270 (C=S); UV-vis λ nm (log): 284 (0.229); ¹H-NMR (400 MHz, CDCl₃, δ, ppm), 3.92 (s, 3H, -OCH₃), 5.15-5.16 (m, 1H, H₆), 5.29-5.30 (m, 1H, H₅), 6.94-6.96 (m, 1H, H₃), 7.28-7.32 (m, 2H, H₄/H_{4'}), 7.32-7.42 (m, 6H, H₅/H₆/H₂'/H₃'/H₅'/H₆'), 6.84, 8.20 (s, 2H, -NH). ¹³C/APT-NMR (100 MHz, CDCl₃, δ, ppm): 55.77 (-OCH₃), 58.41 (C₆), 102.37 (C₅), 111.32 (C₃'), 121.14 (C₅'), 121.22 (C₁'), 126.99 (C₂'/C₆''), 129.14 (C₃''/C₅''), 128.55 (C₆'), 129.36 (C₄'), 130.91 (C₄''), 133.17 (C₄), 142.55 (C₂'), 156.60 (C₁''), 174.56 (C₂]). LC-QTOF-MS: (*m/z*) (%) [M+Na]⁺: 319.0877 (100), calc. 319.0879.

4,6-Bis(2-methoxyphenyl)-3,4-dihydropyrimidine-2(1H)-thione (18)

Yield: 78%, mp = 194-195 °C, Rf: 0.68 (*n*-hexane-ethyl acetate, 1:1); FTIR (ATR, cm⁻¹): 3168 (-NH), 3005,3073(=CH), 2835, 2965 (-CH), 1562 (C=C, aromatic ring), 1242 (-OCH₃), 1261 (C=S); UV-vis λ nm (log): 212 (3.754), 276 (0.624); ¹H-NMR (400 MHz, CDCl₃, δ, ppm), 3.90, 3.92 (s, 6H, -OCH₃), 5.23-5.24 (m, 1H, H₆), 5.65-5.66 (m, 1H, H₅), 7.28-7.41 (m, 4H, H₃/H₄/H₃'/H₅''), 7.42-7.44 (m, 4H, H₅/H₆/H₄'/H₆''), 6.98, 8.06 (s, 2H, -NH). APT-NMR (100 MHz, CDCl₃ δ, ppm): 50.86, 55.44 (-OCH₃), 55.57 (C₆), 100.59 (C₅), 110.45 (C₃''), 111.33 (C₃'), 121.03 (C₅'), 121.15 (C₆'), 127.72 (C₄'), 122.04 (C₁'), 129.52 (C₁''), 129.53 (C₄''),

129.70 (C_{6''}), 130.84 (C_{5''}), 134.27 (C₄), 156.21 (C_{2'}), 156.56 (C_{2''}), 174.70 (C₂), LC-QTOF-MS: (*m/z*) (%) [M+Na]⁺: 349.0992 (60), calc. 349.0993.

4-(2-Methoxyphenyl)-6-(3-methoxyphenyl)-3,4-dihydropyrimidine-2(1H)-thione (19)

Yield: 73%, mp = 170-171 °C, Rf: 0.69 (*n*-hexane–ethyl acetate, 1:1); FTIR (ATR, cm⁻¹): 3149 (-NH), 3102(=CH), 2835, 2937 (-CH), 1577, 1602 (C=C, aromatic ring), 1241 (-OCH₃), 1271 (C=S); UV-vis λ nm (log): 243 (0.433), 282 (0.425); ¹H-NMR (400 MHz, CDCl₃, δ, ppm), 3.84, 3.91 (s, 6H, -OCH₃), 5.14-5.15 (m, 1H, H₆), 5.26-5.27 (m, 1H, H₅), 6.94-6.98 (m, 4H, H₃/H₄/H₅/H_{4''}), 7.32-7.35 (m, 4H, H₆/H_{2''}/H_{5''}/H_{6''}), 6.84, 8.19 (s, 2H, -NH). ¹³C/APT-NMR (100 MHz, CDCl₃, δ, ppm): 55.36, 55.77 (-OCH₃), 57.17 (C₆), 102.26 (C₅), 111.31 (C_{4''}), 112.59 (C_{2''}), 113.94 (C_{3'}), 119.20 (C_{5'}), 121.15 (C_{6''}), 121.70 (C_{1'}), 129.37 (C_{6''}), 130.21 (C_{4'}), 130.93 (C_{5''}), 133.26 (C₄), 144.05 (C_{1''}), 156.59 (C_{2'}), 160.20 (C_{3''}), 174.55 (C₂). LC/ MS-TOF: (*m/z*) (%) [M+23]⁺: 349.0995 (100), calc. 349.0992. LC-QTOF-MS: (*m/z*) (%) [M+Na]⁺: 349.0972 (60), calc. 349.0975.

4-(2-Methoxyphenyl)-6-(4-methoxyphenyl)-3,4-dihydropyrimidine-2(1H)-thione (20)

Yield: 79%, mp = 161-162 °C, Rf: 0.71 (*n*-hexane–ethyl acetate, 1:1); FTIR (ATR, cm⁻¹): 3175 (-NH), 2835, 2971 (-CH), 1575, 1601 (C=C, aromatic ring), 1241 (-OCH₃), 1265 (C=S); UV-vis λ nm (log): 223 (3.620), 276 (0.510); ¹H-NMR (400 MHz, CDCl₃, δ, ppm), 3.83, 3.92 (s, 6H, -OCH₃), 5.13 (s, 1H, H₆), 5.26 (s, 1H, H₅), 6.95-6.96 (m, 1H, H_{3'}), 7.28-7.33 (m, 4H, H₄/H₅/H_{3''}/H_{5''}), 7.33-7.35 (m, 3H, H_{2''}/H_{6''}/H₆), 6.60, 8.14 (s, 2H, -NH). ¹³C/APT-NMR (100 MHz, CDCl₃, δ, ppm): 55.39, 55.78 (-OCH₃), 56.76 (C₆), 102.59 (C₅), 111.31 (C_{3'}), 114.44 (C_{3''}/C_{5''}), 121.16 (C_{5'}), 121.74 (C_{1'}), 128.34 (C_{2'/} C_{6''}), 129.35 (C_{6'}), 130.90 (C_{4'}), 134.81 (C₄), 133.08 (C_{1''}), 156.58 (C_{2'}), 159.80 (C_{4''}), 174.37 (C₂). LC-QTOF-MS: (*m/z*) (%) [M+Na]⁺: 349.0982 (100), calc. 349.0980.

4-(2-Methoxyphenyl)-6-(2,3-dimethoxyphenyl)-3,4-dihydropyrimidine-2(1H)-thione (21)

Yield: 70%, mp = 175-176 °C, Rf: 0.65 (*n*-hexane–ethyl acetate, 1:1); FTIR (ATR, cm⁻¹): 3177 (-NH), 2835, 2979 (-CH), 1570 (C=C, aromatic ring), 1241 (-OCH₃), 1271 (C=S); UV-vis λ nm (log): 224 (3.723), 275 (0.798); ¹H-NMR (400 MHz, CDCl₃, δ, ppm), 3.89, 3.92 (s, 9H, -OCH₃), 5.19-5.21 (m, 1H, H₆), 5.63-5.64 (m, 1H, H₅), 6.93-6.95 (m, 3H, H₃/H₄/H_{5''}), 7.07-7.08 (m, 2H, H₄/H_{6''}), 7.35-7.36 (m, 2H, H₅/H₆), 6.80, 8.12 (s, 2H, -NH). ¹³C/APT-NMR (100 MHz, CDCl₃, δ, ppm): 51.24, 55.76, 55.90 (-OCH₃), 61.07 (C₆), 101.37 (C₅), 111.32 (C_{4''}), 112.54 (C_{3'}), 119.61 (C_{6''}), 121.13 (C_{5'}), 121.90 (C_{1'}), 124.56 (C_{6'}), 129.34 (C_{4'}), 130.82 (C_{5''}), 133.70 (C_{1''}), 135.54 (C₄), 145.76 (C_{2'}), 152.56 (C_{2''}), 156.55 (C_{3''}), 174 (C₂). LC-QTOF-MS: (*m/z*) (%) [M+Na]⁺: 379.1076 (100), calc. 379.1077.

4-(2-Methoxyphenyl)-6-(2,5-dimethoxyphenyl)-3,4-dihydropyrimidine-2(1H)-thione (22)

Yield: 72%, mp = 148-151 °C, Rf: 0.72 (*n*-hexane–ethyl acetate, 1:1); FTIR (ATR, cm⁻¹): 3262 (-NH), 3000,3070(=CH), 2835, 2963 (-CH), 1561,1600 (C=C, aromatic ring), 1242 (-OCH₃), 1259, 1273 (C=S); UV-vis λ nm (log): 244 (0.425), 283 (0.412); ¹H-NMR (400 MHz,

CDCl₃, δ, ppm), 3.79, 3.91 (s, 9H, -OCH₃), 5.19 (s, 1H, H₆), 5.62 (s, 1H, H₅), 6.84-7.03 (m, 5H, H₃/H₅/H_{3''}/H_{4''}/H_{6''}), 7.36-7.41 (m, 2H, H₄/H₆), 8.08 (s, 2H, -NH). ¹³C/APT-NMR (100 MHz, CDCl₃, δ, ppm): 50.81, 55.75 (-OCH₃), 55.82 (C₆), 100.28 (C₅), 111.35 (C_{4''}), 111.38 (C_{6''}), 113.33 (C_{3'}), 114.48 (C_{3''}), 120.58 (C_{1'}), 121.13 (C_{5'}), 129.30 (C_{6'}), 130.66 (C_{1''}), 130.84 (C_{4'}), 134.47 (C₄), 150.41 (C_{2''}), 153.91 (C_{5''}), 156.67 (C_{2'}), 174.77 (C₂). LC-QTOF-MS: (*m/z*) (%) [M+Na]⁺: 379.1077 (100), calc. 379.1077.

4-(2-Methoxyphenyl)-6-(2,3,4-trimethoxyphenyl)-3,4-dihydropyrimidine-2(1H)-thione (23)

Yield: 80%, mp = 210-211 °C, Rf: 0.66 (*n*-hexane–ethyl acetate, 1:1); FTIR (ATR, cm⁻¹): 3263 (-NH), 3098 (=CH), 2827, 2951 (-CH), 1599,1569 (C=C, aromatic ring), 1238 (-OCH₃), 1263 (C=S); UV-vis λ nm (log): 231 (3.623), 274 (1.205), 283 (1.041); ¹H-NMR (400 MHz, CDCl₃, δ, ppm), 3.87, 3.88 (s, 12H, -OCH₃), 5.52 (s, 1H, H₅), 5.17 (s, 1H, H₆), 6.68-6.78 (m, 2H, H₅/H_{5''}), 6.95-6.98 (m, 2H, H₃/H_{6''}), 7.36-7.39 (m, 2H, H₄/H₆), 7.10, 8.09 (s, 2H, -NH). ¹³C/APT-NMR (100 MHz, CDCl₃, δ, ppm): 51.12, 55.76, 56.06, 60.84 (-OCH₃), 61.22 (C₆), 101.25 (H₅), 107.23 (C_{5''}), 111.33 (C_{3'}), 121.15 (C_{6''}), 121.15 (C_{1''}), 122.42 (C_{5'}), 127.67 (C_{1'}), 129.29 (C_{6'}), 130.82 (C_{4'}), 133.86 (C₄), 141.86 (C_{3''}), 150.68 (C_{2''}), 153.93 (C_{4''}), 156.55 (C_{2'}), 174.48 (C₂). LC-QTOF-MS: (*m/z*) (%) [M+Na]⁺: 409.1206 (100), calc., 409.1205.

4-(4-Methoxyphenyl)-6-(2-methoxyphenyl)-3,4-dihydropyrimidine-2(1H)-thione (24)

Yield: 69%, mp = 233-234 °C, Rf: 0.65 (*n*-hexane–ethyl acetate, 1:1); FTIR (ATR, cm⁻¹): 3159 (-NH), 3010(=CH), 2841, 2961 (-CH), 1553,1611 (C=C, aromatic ring), 1240 (-OCH₃), 1273 (C=S); UV-vis λ nm (log): 241 (0.620), 276 (0.615), 283 (0.524); ¹H-NMR (400 MHz, CDCl₃, δ, ppm), 3.85, 3.90 (s, 6H, -OCH₃), 5.19-5.20 (s, 1H, H₆), 5.63-5.65 (m, 1H, H₅), 6.92-7.01 (m, 2H, H_{3''}/H_{5''}), 6.94 (d, 2H, J=8 Hz, H_{3'/}H_{5'}), 7.01-7.04 (m, 2H, H_{4''}/H_{6''}), 7.42 (d, 2H, J=8 Hz, H₂/H₆), 7.28, 7.63 (s, 2H, -NH). ¹³C/APT-NMR (100 MHz, CDCl₃, δ, ppm): 55.42, 55.87 (-OCH₃), 55.46 (C₆), 97.46 (C₅), 110.52 (C_{3''}), 114.36 (C_{3'/}C_{5'}), 121.04 (C_{2'/}C_{6'}), 126.03 (C_{1''}), 126.52 (C_{4''}), 127.54 (C_{6''}), 129.67 (C_{1'}), 129.67 (C_{5''}), 134.76 (C₄), 156.20 (C_{2''}), 160.53 (C₄), 175.40 (C₂). LC-QTOF-MS: (*m/z*) (%) [M+Na]⁺: 349.0972 (100), calc. 349.0975.

4-(4-Methoxyphenyl)-6-(3-methoxyphenyl)-3,4-dihydropyrimidine-2(1H)-thione (25)

Yield: 60%, mp = 155-156 °C, Rf: 0.70 (*n*-hexane–ethyl acetate, 1:1); FTIR (ATR, cm⁻¹): 3200 (-NH), 3102 (=CH), 2838, 2971 (-CH), 1566,1606 (C=C, aromatic ring), 1247 (-OCH₃), 1268 (C=S); UV-vis λ nm (log): 226 (4.345), 268 (2.212); ¹H-NMR (400 MHz, CDCl₃, δ, ppm), 3.74, 3.75 (s, 6H, -OCH₃), 5.06-5.07 (m, 1H, H₆), 5.13-5.14 (m, 1H, H₅), 6.77-6.90 (m, 5H, H₃/H₅/H_{2''}/H_{4''}/ H_{6''}), 7.22-7.26 (m, 1H, H_{5''}), 7.39-7.41 (m, 2H, H₂/H₆), 8.89, 9.36 (s, 2H, -NH). ¹³C/APT-NMR (100 MHz, CDCl₃, δ, ppm) : 55.30, 55.41, 55.45 (-OCH₃), 64.17 (C₆), 99.48 (C₅), 112.64 (C_{2''}), 112.94 (C_{4''}), 113.97 (C_{3'/}C_{5'}), 118.90 (C_{6''}), 126.10 (C_{1'}), 127.37 (C_{2'/}C_{6'}), 129.95 (C_{5''}), 134.40 (C₄), 145.85 (C_{1''}), 155.58 (C_{4'}), 156.78 (C_{3''}), 175.40 (C₂). LC-QTOF-MS: (*m/z*) (%) [M+Na]⁺: 349.0995 (100), calc. 349.0993.

4-(4-Methoxyphenyl)-6-(2,3-dimethoxyphenyl)-3,4-dihydropyrimidine-2(1H)-thione (26)

Yield: 73%, mp = 102-103 °C, Rf: 0.69 (*n*-hexane–ethyl acetate, 1:1); FTIR (ATR, cm⁻¹): 3197 (-NH), 3002, 3100 (=CH), 2833, 2963 (-CH), 1599, 1607 (C=C, aromatic ring), 1252 (-OCH₃), 1282 (C=S); UV-vis λ nm (log): 227 (4.182), 264 (3.542); ¹H-NMR (400 MHz, CDCl₃, δ, ppm), 3.70-3.91 (m, 9H, -OCH₃), 5.15 (s, 1H, H₆), 5.60 (s, 1H, H₅), 6.90-7.10 (m, 5H, H₄"/H₅"/ H₆"/H₃/ H₅'), 7.28-7.38 (m, 2H, H₂/H₆'), 6.90, 7.84 (s, 2H, -NH). ¹³C/APT-NMR (100 MHz, CDCl₃, δ, ppm): 51.31, 55.45, 55.93 (-OCH₃), 61.13 (C₆), 98.40 (C₅), 112.58 (C₄"'), 114.34 (C₃'/C₅'), 119.47 (C₆"'), 124.62 (C₅"'), 126.59 (C₂'/C₆'), 125.95 (C₁"'), 134.14 (C₁''), 135.60 (C₄), 145.78 (C₂"'), 152.63 (C₃"'), 160.51 (C₄'), 175.48 (C₂). LC/ MS-TOF: (*m/z*) (%) [M+Na]⁺: 379.1085 (100), calc. 379.1087.

4-(4-Methoxyphenyl)-6-(2,5-dimethoxyphenyl)-3,4-dihydropyrimidine-2(1H)-thione (27)

Yield: 74%, mp = 241-242 °C, Rf: 0.68 (*n*-hexane–ethyl acetate, 1:1); FTIR (ATR, cm⁻¹): 3127 (-NH), 2835, 2959 (-CH), 1599, 1608 (C=C, aromatic ring), 1244 (-OCH₃), 1271 (C=S); UV-vis λ nm (log): 242 (0.425), 275 (0.410); ¹H-NMR (400 MHz, CDCl₃, δ, ppm), 3.78, 3.86 (s, 9H, -OCH₃), 5.17 (s, 1H, pyrimidine-H₅), 5.61 (s, 1H, H₆), 6.84-6.99 (m, 5H, H₃"/H₄"/ H₆"/H₃/ H₅'), 7.41-7.43 (m, 2H, H₂/H₆'), 7.62, 8.12 (s, 2H, -NH), ¹³C/APT-NMR (100 MHz, CDCl₃, δ, ppm): 50.87, 55.41 (-OCH₃), 55.84 (C₆), 97.19 (C₅), 111.34 (C₄"'), 113.27 (C₆"'), 114.33 (C₃"'), 114.37 (H₃/H₅'), 126.55 (H₂/H₆'), 126.55 (C₁"'), 130.85 (C₁''), 135.11 (C₄), 150.38 (C₂"'), 154.04 (C₂"'), 160.55 (C₄'), 175.58 (C₂). LC-QTOF-MS: (*m/z*) (%) [M+Na]⁺: 379.1063 (40), calc. 379.1067.

4-(4-Methoxyphenyl)-6-(2,3,4-trimethoxyphenyl)-3,4-dihydropyrimidine-2(1H)-thione (28)

Yield: 61%, mp = 124-125 °C, Rf: 0.70 (*n*-hexane–ethyl acetate, 1:1); FTIR (ATR, cm⁻¹): 3192 (-NH), 2850, 2920 (-CH), 1557, 1599 (C=C, aromatic ring), 1247 (-OCH₃), 1283 (C=S); UV-vis λ nm (log): 309 (0.426), 327 (0.315); ¹H-NMR (400 MHz, CDCl₃, δ, ppm), 3.85-3.99 (m, 12H, -OCH₃), 5.11-5.14 (m, 1H, H₆), 5.51-5.52 (m, 1H, H₅), 6.69 (m, 1H, H₄"'), 6.68 (d, 1H, *J*=8 Hz, H₆"'), 6.94 (d, 2H, *J*=8 Hz, H₃/H₅'), 7.45 (d, 2H, *J*=8 Hz, H₂/H₆'), 6.86, 7.59 (s, 2H, -NH). ¹³C/APT-NMR (100 MHz, CDCl₃, δ, ppm): 51.20, 55.42, 56.06, 60.85 (-OCH₃), 61.23 (C₆), 98.05 (C₅), 107.19 (C₅"'), 114.37 (C₃'/C₅'), 122.23 (C₆"'), 125.96 (C₁"'), 126.47 (C₂'/C₆'), 127.53 (C₁''), 134.34 (C₄), 141.90 (C₃"'), 150.71 (C₂"'), 154.01 (C₄"'), 160.53 (C₄'), 175.22 (C₂). LC-QTOF-MS: (*m/z*) (%) [M+Na]⁺: 409.1192 (100), calc. 409.1199.

Tyrosinase Inhibition Assay of 15-28

The tyrosinase inhibitory impacts of the compounds were assayed in line with our previous research with slight modifications [21]. Kojic acid was utilized as a standard compound, whereas DMSO (1%) was used as a negative control. The solutions were newly prepared in phosphate buffer (100 mM, pH 6.8). The compounds (12.5-250 μM) in wells were treated with tyrosinase from mushroom (Sigma-Aldrich, T3824) (250 U/mL, 20 μL). The incubation of the mixtures was done for a period of 15 min at room temperature. After incubation, 3,4-dihydroxy-L-phenylalanine (*L*-DOPA) (Sigma-Aldrich, D9628) was

added to the wells with the objective of starting the enzymatic reaction, and the incubation of the mixture was performed for a 15 min period at room temperature. Optical density was found to be 475 nm with a microplate reader. The IC₅₀ values were computed with the formula below; % inhibition: (A-B) × 100 / A, where A refers to the activity of tyrosinase without the compounds, and B denotes tyrosinase activity with the compounds [21].

DPPH Radical Scavenging Assay of 15-28

The DPPH radical scavenging properties of the compounds were assayed following our previous research [21]. Ascorbic acid was used as a standard compound, whereas DMSO (1%) was utilized as a negative control. DPPH solution (0.2 mM) (Sigma-Aldrich, D9132) was prepared in methanol. DPPH solution, and the compounds (100 μM) were added to each other in wells. The incubation of the mixtures was carried out for 30 min at room temperature in the dark. Optical density (OD) was found to be 517 nm with a microplate reader. The IC₅₀ values were computed with the formula above [22].

Molecular Docking**Protein Preparation**

The 3D structure of the *Agaricus bisporus* tyrosinase enzyme (PDB ID: 2Y9X) was retrieved from the Protein Data Bank (<https://www.rcsb.org/>). Water molecules, bound ligand compounds and metal ion groups were simply excluded from the structure. The protonation states of 2Y9X were calculated by Propka 3.1 software [16-17] at pH=7.0. For the receptor protein, all basic amino acids were positively charged, while acidic amino acids were negatively charged by employing the Kollman charges embedded within AutoDock software. The 3D structures of ligand compounds were also prepared before molecular docking studies. OpenBabel software was utilized to build specific pdbqt files for each compound [18]. Each compound was also charged by executing the Gasteiger charges in AutoDock Vina. The prepared ligands and target protein structures were eventually used as input files during the execution of AutoDock Vina-based molecular docking.

Statistical analysis

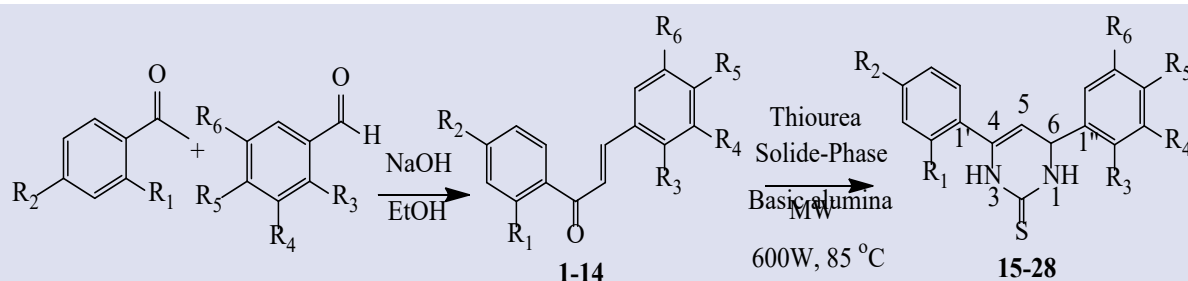
GraphPad Prism 5.0 was utilized to analyze the data. The results are presented as mean ± standard deviation (*n* = 3). The differences between the compounds and standard compound were studied by conducting a one-way analysis of variance (ANOVA), followed by Tukey's tests.

Results and Discussion**Chemistry**

In order to find a new potential TI, a diverse range of methoxy DH-Pyr-S (15-28) were designed and synthesized in two step. The complete synthetic scheme of target DH-Pyr-S (15-28) is shown in Scheme 1. The first step was the

base-catalyzed condensation of the methoxy acetophenone with methoxy benzaldehydes in ethanol solvent to yield intermediate methoxy chalcones (1-14). The second step was the condensation of methoxy chalcones with thiourea by the solid-phase MW method to give methoxy DH-Pyr-S (15-28) analogous [14-15]. Structure of target DH-Pyr-S (15-28) were identified by their spectroscopic data (^1H NMR, ^{13}C /APT NMR, FT-IR,

UV-vis, and LC-QTOF-MS). The spectral data of already known methoxy chalcones (1-14) [19-20] and compounds 15-16 [14-15] have been reported. However, the spectral data of the all new methoxy DH-Pyr-S (17-28) are given in the experimental part. In the literature, DH-Pyr-S compounds have been synthesized by reflux, and MW methods [7-8, 10-11, 14-15].



No	R ₁	R ₂	R ₃	R ₄	R ₅	R ₆
15	-H	-OCH ₃	-H	-H	-H	-H
16	-H	-OCH ₃	-H	-H	-OCH ₃	-H
17	-OCH ₃	-H	-H	-H	-H	-H
18	-OCH ₃	-H	-OCH ₃	-H	-H	-H
19	-OCH ₃	-H	-H	-OCH ₃	-H	-H
20	-OCH ₃	-H	-H	-H	-OCH ₃	-H
21	-OCH ₃	-H	-OCH ₃	-OCH ₃	-H	-H
22	-OCH ₃	-H	-OCH ₃	-H	-H	-OCH ₃
23	-OCH ₃	-H	-OCH ₃	-OCH ₃	-OCH ₃	-H
24	-H	-OCH ₃	-OCH ₃	-H	-H	-H
25	-H	-OCH ₃	-H	-OCH ₃	-H	-H
26	-H	-OCH ₃	-OCH ₃	-OCH ₃	-H	-H
27	-H	-OCH ₃	-OCH ₃	-H	-H	-OCH ₃
28	-H	-OCH ₃	-OCH ₃	-OCH ₃	-OCH ₃	-H

Figure 2. N₂ adsorption isotherm of the Ni/GCE and Ni@s-rGO/GCE

Biological Activities of Compounds (15-28)

Tyrosinase Inhibition of 15-28

In a continuation of our prior investigations to find out a new TI [22], methoxy DH-Pyr-S were studied for their antityrosinase activity. All the synthetic methoxy DH-Pyr-S (15-28) showed moderate to good inhibition against tyrosinase enzyme (Table 1) [21]. IC₅₀ values of 15-28 and the reference kojic acid (IC₅₀ = 55.38 ± 2.30 μM) are in the table 1. The IC₅₀ values of 15-28 ranged from 31.86 ± 2.45 to 229.77 ± 8.033 μM. Among all the synthesized methoxy DH-Pyr-S, the compound 17 exhibited excellent tyrosinase inhibitory activity with the lowest IC₅₀ = 31.86 ± 2.45 μM. Therefore, compounds 21 (44.58 ± 0.46 μM) and 16 (IC₅₀ = 48.47 ± 0.66 μM) may be useful as a potential lead candidate to cure tyrosinase-mediated hyperpigmentation in the future. In the literature, cytotoxicity of eleven synthesized 1,2,3,4-tetrahydro-2-thioxopyrimidine analogs were reported against the growth of two cancer cell lines (B16 melanoma and L1210

leukemia). It was mentioned that two of those analogs exhibited significant activity (IC₅₀ < 1 μM for L1210 and <10 μM for B16 cells) [23]. Biological activity of 2-thiopyrimidine derivatives had shown that some of the compound gave good antiinflammatory (37.4% at 100 mg/kg) and analgesic activity (75% at 100 mg/kg). Some of the compounds also had shown moderate analgesic (25–75%), protein kinase (CDK-5, GSK-3), and antiinflammatory (5–20%) inhibitory activities (IC₅₀ > 10 μM) [24]. Antiproliferative activities of a fused thiazolo[2,3-b]pyrimidinones were reported against K562 (chronic myelogenous leukemia), HepG2 (hepatocellular carcinoma), MDA-MB-231 (breast cancer), MCF-7 (breast cancer), COLO 205 (colorectal adenocarcinoma) cell lines. Thus, 3,4-dihydropyrimidine-2(1H)-one/thione analogs are highly valuable bioactive compounds [9].

Table 1. Tyrosinase inhibition and DPPH of 15-28

Compounds	Tyrosinase (IC ₅₀ values μ M)	DPPH (%) (at 100 μ M)
15	128.64 \pm 6.70	34.90 \pm 0.26
16	48.47 \pm 0.66*	42.30 \pm 2.50
17	31.86 \pm 2.45*	45.64 \pm 0.34
18	182.64 \pm 4.36	31.87 \pm 1.48
19	229.77 \pm 8.03	34.35 \pm 0.27
20	223.56 \pm 4.06	37.95 \pm 1.68
21	44.58 \pm 0.46*	30.30 \pm 0.63
22	> 250	40.39 \pm 1.93
23	> 250	36.06 \pm 0.34
24	191.22 \pm 3.55	34.22 \pm 0.35
25	125.70 \pm 3.04	33.39 \pm 0.77
26	100.59 \pm 2.49	39.18 \pm 1.36
27	159.35 \pm 2.05	36.68 \pm 0.53
28	> 250	40.27 \pm 0.39
Kojic acid	55.38 \pm 2.30	-
Ascorbic acid	-	86.03 \pm 0.09

*p<0.0001

DPPH Activity of 15-28

In this study, the DPPH radical scavenging impacts of the compounds were investigated, and Table 1 shows the inhibition ratios (%) of the compounds at 100 μ M. Ascorbic acid was utilized as a standard compound. Compound 17 exhibited the best DPPH radical scavenging effect, with 45.64 \pm 0.34%, among the compounds tested [22]. According to the results, these compounds had lower radical scavenging effects than ascorbic acid. Literature revealed that DH-Pyr-S gave significant biological activities such as good response to antimicrobial activity and possessed good antioxidant activities [25]. DPPH of various synthesized pyrimidinones and pyrimidinethiones were mentioned and they showed significant antioxidant activity. Significant anticancer activity of pyrimidines against HeLa and HepG2 cell lines were also reported [26]. Synthetic dihydropyrimidines had shown better activity than other compounds due to presence of the electron withdrawing groups [27]. In another work, 2,3-dihydropyrimidin-2(1H)-one derivatives were clearly indicated that the dihydropyrimidines gave both antioxidant and anti-inflammatory activities. Due to the pharmacologic and antimicrobial activities of synthesized tetrahydropyrimidine derivatives have been evaluated as drug candidates [28]. In a study, synthesized pyrimidine-thiones analogs gave good acetylcholinesterase, and human carbonic anhydrase isoforms I and II activities. The antioxidant activity of the DH-Pyr-S was also reported by DPPH and Fe²⁺ chelating activities. The antioxidant, antiinflammatory and antituberculosis screenings of pyrimidine-2-one was reported. The result of all heterocyclic analogs indicated that they all have significant antioxidant and anti-inflammatory activities when compared to standard drugs used. Moderate antituberculosis activity for the synthesized pyrimidine-2-one compounds were also reported. Thus, 3,4-

dihydropyrimidine-2(1H)-one/thione analogs are highly valuable bioactive compounds. These studies showed that 3,4-dihydropyrimidine-2(1H)-one/thione compounds resulted very different biological activities.

ADMET calculations

Pharmacokinetic and toxicity properties of synthesized DH-Pyr-S molecules including adsorption, distribution, metabolism, excretion, and toxicity predictions (ADMET) were predicted accordingly and (pkCSM) program were used for ADMET (Table 2).

Molecular Docking Data

Binding affinities and TI potentials of newly synthesized DH-Pyr-S molecules were examined by employing AutoDock Vina (version 1.2.5) program and the obtained results were summarized in Table 3 [16-18]. Molecular docking results showed that compounds 15, 21 and 24 share the lowest but identical binding free energies (Δ G: -7.9 kcal/mol) for the 2Y9X tyrosinase catalytic core, whereas compounds 17, 18, 21 and 25 have the potential to form 2 hydrogen bonds with the 2Y9X catalytic residues.

Among newly synthesized DH-Pyr-S molecules, tyrosinase binding affinities of two compounds with the lowest experimental half-maximal inhibitory concentration (IC₅₀) values were investigated in detail to decipher their interaction modes to 2Y9X. For this, 2Y9X-17 and 2Y9X-21 complexes from molecular docking studies were comprehensively studied using the Discovery studio Accelrys program (BIOVIA, Dassault Systèmes). Both compound 17 and compound 21 showed higher binding affinity to the tyrosinase active site than kojic acid, with low binding free energies of -7.6 kcal/mol and -7.9 kcal/mol, respectively (Table 3). Furthermore, the presence of numerous alkyl and pi-alkyl interactions between tyrosinase and compound 21 (2Y9X-21 complex), as well as Pi-sigma and carbon-hydrogen bond interactions, appeared to contribute to the strong TI activity. This suggests that the multiple hydrophobic interactions as well as robust H bonds identified from the 2Y9X-21 complex are able to promote the tyrosinase inhibitory activity of compound 21.

Considering its low IC₅₀ value, the biochemical interaction pattern of compound 17 was also investigated through 2D plot analysis. The descriptive biochemical interaction analysis revealed that compound 17 also forms two close hydrogen bonds with 2Y9X catalytic residues ASN260 and ARG268 (Figure 1A and 1B). This explains the experimentally proved stronger tyrosinase inhibition potential of 17 compared to both 15 and 16 (Figures 1A-B). Furthermore, in-depth intermolecular interaction analysis revealed that the catalytic site of 2Y9X is more accessible for compounds 15, 21, and 24 than compound 17, suggesting that the basic scaffold of these compounds is well suited for catalytic core of 2Y9X (Table 3). On the other hand, molecular docking data also suggested compounds 15 and 24 as promising tyrosinase inhibitors with high binding affinity to 2Y9X with a low

binding free energy of -7.9 kcal/mol. However, *in silico* predictions for these compounds did not correlate well with the experimental IC₅₀ values (Table 3). Taking together, both *in vitro* experimental outputs and *in silico*

molecular docking findings elucidated that among synthesized molecules, 21 is the leading compound for tyrosinase inhibition.

Table 2. ADMET analysis of synthesized DH-Pyr-S molecules

Property	ADMET Properties	15	16	17	18	19	20	21	22	23	24	25	26	27	28
Absorption	Water solubility (log mol/L)	-3.874	-3.991	-3.961	-4.084	-4.084	-4.084	-4.236	-4.236	-4.404	-3.991	-3.991	-4.144	-4.143	-432
	Caco2 permeability (log Papp in 10-6cm/s)	1.797	1.916	1.685	1.803	1.803	1.803	1.144	1.144	1.136	1.916	1.916	1.144	1.144	1.136
	Intestinal absorption (human) (% Absorbed)	90.327	90.435	90.786	90.894	90.894	90.894	91.002	90.787	91.007	90.435	90.435	90.543	90.328	90.548
	Skin Permeability (log Kp)	-2.798	-2.864	-2.804	-2.875	-2.875	-2.875	-2.921	-2.928	-2.943	-2.864	-2.864	-2.905	-2.911	-2.923
	P-glycoprotein substrate	Yes	Yes	No	Yes	Yes	Yes	Yes	Yes	Yes	Yes	Yes	Yes	Yes	Yes
	P-glycoprotein I inhibitor	No	Yes	No	Yes	Yes	Yes	Yes	Yes	Yes	Yes	Yes	Yes	Yes	Yes
	P-glycoprotein II inhibitor	No	No	No	No	No	No	No	No	No	Yes	No	No	No	No
Distribution	VDss (human) (log L/kg)	0.245	0.105	0.305	0.166	0.166	0.166	0.0243	0.0039	0.108	0.105	0.105	0.004	-0,025	-0,172
	Fraction unbound (human) (Fu)	0.091	0.09	0.094	0.092	0.092	0.092	0.089	0.089	0.085	0.09	0.09	0.088	0.088	0.084
	BBB permeability (log BB)	0.297	0.049	0.3	0.053	0.053	0.053	-0,195	-0,195	-0,563	0,049	0,049	-0,199	-0,199	-0,566
	CNS permeability (log PS)	-1.215	-1.277	-1.159	-1.221	-1.221	-1.221	-2.205	-2.194	-2.358	-1.277	-1.277	-2.205	-2.199	-2.363
Metabolism	CYP2D6 substrate	No	No	No	No	No	No	No	No	No	No	No	No	No	No
	CYP3A4 substrate	Yes	Yes	Yes	Yes	Yes	Yes	Yes	Yes	Yes	Yes	Yes	Yes	Yes	Yes
	CYP1A2 inhibitor	Yes	Yes	Yes	Yes	Yes	Yes	Yes	Yes	Yes	Yes	Yes	Yes	Yes	Yes
	CYP2C19 inhibitor	Yes	Yes	Yes	Yes	Yes	Yes	Yes	Yes	Yes	Yes	Yes	Yes	Yes	Yes
	CYP2C9 inhibitor	No	Yes	Yes	Yes	Yes	Yes	Yes	Yes	Yes	Yes	Yes	Yes	Yes	Yes
	CYP2D6 inhibitor	No	No	No	No	No	No	No	No	No	No	No	No	No	No
	CYP3A4 inhibitor	No	No	No	No	No	No	Yes	No	Yes	No	No	No	No	Yes
Excretion	Total Clearance (log ml/min/kg)	-0.222	-0.193	-0.037	0.116	-0.222	0,009	-0,243	0.207	0.325	-0,069	-0,186	0.059	0.023	0.141
	Renal OCT2 substrate	Yes	Yes	Yes	No	No	No	No	No	No	Yes	Yes	Yes	No	No
Toxicity	AMES toxicity	Yes	Yes	Yes	Yes	Yes	Yes	Yes	Yes	Yes	Yes	Yes	Yes	Yes	Yes
	Max. tolerated dose (log mg/kg/day)	-0.046	-0.136	0.009	-0,082	-0,082	-0,082	-0,142	-0,142	-0,159	-0,136	-0,136	-0,195	-0,195	-0,211
	hERG I inhibitor	No	No	No	No	No	No	No	No	No	No	No	No	No	No
	hERG II inhibitor	Yes	Yes	Yes	Yes	Yes	Yes	Yes	Yes	Yes	Yes	Yes	Yes	Yes	Yes
	Oral Rat Acute Toxicity (LD50) (mol/kg)	2.691	2.747	2.741	2.797	2.797	2.797	2.855	2.843	2.908	2.747	2.747	2.803	2.791	2.855
	Oral Rat Chronic Toxicity (LOAEL) (log mg/kg_bw/day)	1.693	1.422	1.713	1.432	1.432	1.432	1.085	1.085	1.055	1.422	1.422	1.138	1.138	1.108
	Hepatotoxicity	Yes	No	No	No	Yes	Yes	Yes	No	No	Yes	No	Yes	No	No
	Skin Sensitisation	No	No	No	No	No	No	No	No	No	No	No	No	No	No
	<i>T.pyrififormis</i> toxicity (log ug/L)	1.849	1.884	1.782	1.827	1.827	1.827	1.718	1.714	1.451	1.884	1.884	1.762	1.757	1.479
	Minnow toxicity (log mM)	0.298	0.349	0.137	0.188	0.188	0.188	0.337	0.337	0.585	0.349	0.349	0.498	0.498	0.745

Table 3. Estimated binding affinity of docked compounds (16, 17, and 21) against *Agaricus bisporus* tyrosinase and the profile of the interacting residues in the binding site

Ligand ID	2Y9X Binding energy (kcal/mol)	H bond number
15	-7.9	1
16	-7.4	NA
17	-7.6	2
18	-7.7	2
19	-7.3	NA
20	-7.4	1
21	-7.9	2
22	-7.4	2
23	-7.2	NA
24	-7.9	1
25	-7.6	2
26	-7.1	NA
27	-7.3	NA
28	-6.9	NA
Kojic acid	-5.7	2

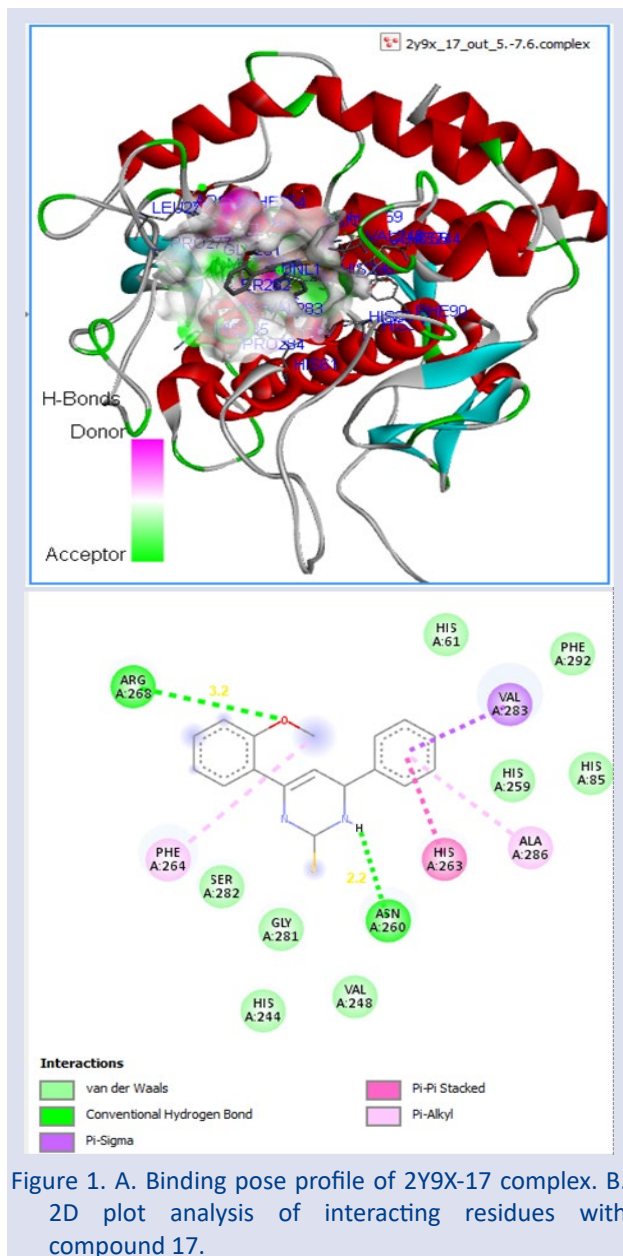


Figure 1. A. Binding pose profile of 2Y9X-17 complex. B. 2D plot analysis of interacting residues with compound 17.

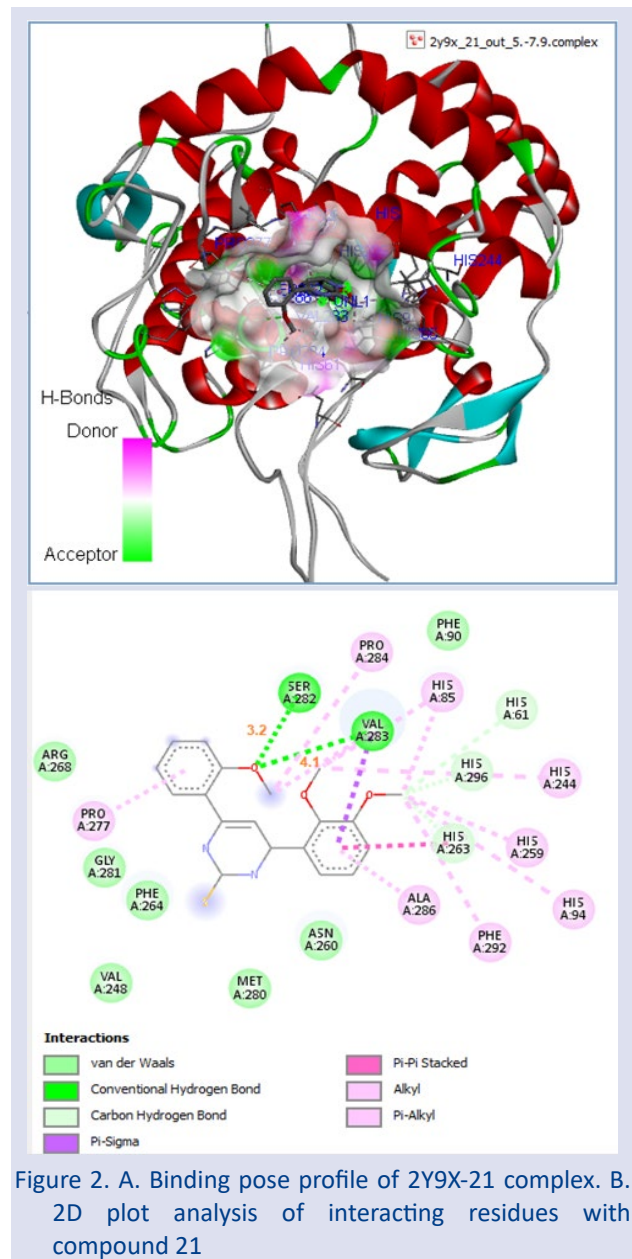


Figure 2. A. Binding pose profile of 2Y9X-21 complex. B. 2D plot analysis of interacting residues with compound 21

In the literature, docking study for the dihydropyrimidine compounds as a potential inhibitors of gyrase enzyme were reported and one of the dihydropyrimidine compound had shown significant inhibition with binding free energies higher than novobiocin that was used as standard [29].

Conclusion

In summary, a series of new methoxy DH-Pyr-S (17-28) were synthesized using known methodologies starting from methoxy acetophenone and methoxy benzaldehydes over two steps reaction. Structure of them were identified by various spectral techniques (NMR, FT-IR, UV, and LC-QTOF-MS). All the target methoxy DH-Pyr-S compounds (17-28) were tested against the tyrosinase enzyme. In order to find activities of methoxy DH-Pyr-S in terms of potent TI, we herein, report that some of the synthetic methoxy DH-Pyr-S analogs are potential new TI.

Among the synthesized methoxy DH-Pyr-S, the new compound 17 exhibited excellent TI with the lowest IC₅₀ value of 31.86 ± 2.45 μM. Furthermore, compounds 21 (IC₅₀ = 44.58 ± 0.46 μM) and 16 (IC₅₀ = 48.47 ± 0.66 μM) may prove to be effective inhibitors against the tyrosinase enzyme. All the synthesized target methoxy DH-Pyr-S (15-28) exhibited weak DPPH activities. A molecular modeling studies of methoxy DH-Pyr-S (16, 17, and 21) were performed against 2Y9X enzyme to find the binding interactions against the target protein. The best binding affinities of these molecules (15, 21, and 24) to the tyrosinase catalytic core were found to be -7.9 kcal/mol. All three compounds showed higher binding affinity to the tyrosinase active site compared to the standard molecule kojic acid. Calculated molecular docking studies of the most active compounds 16, 17, and 21 revealed that they could be considered as TI candidates. Moreover, *in silico* binding analyzes specific to the synthesized molecules revealed that the catalytic core of 2Y9X was more accessible to compounds 15, 21, and 24; however, this suggests that functional groups added to compound 17 can be used to modify these three lead compounds towards the development of more selective tyrosinase inhibitors.

Ultimately, experimental and theoretical analysis results confirmed that DH-Pyr-S molecules could be a good starting point for the development of more selective tyrosinase inhibitors.

Acknowledgment

The current research was supported from the Research Found of Karadeniz Technical University (KTU-BAP-02 FHD5395), Türkiye.

Conflicts of interest

There are no conflicts of interest in this work.

References

- [1] Kabir E., Uzzaman M., A review on biological and medicinal impact of heterocyclic compounds, *Result in Chemistry*, 4 (2022) 100666.
- [2] Lagoja I.M., Pyrimidine as constituent of natural biologically active compounds, *Chem. Biodivers.*, 2(1) (2005) 1-50.
- [3] Borge V.V., Vaze J.A., A comprehensive study of pyrimidine and its medicinal applications, *Heterocycles*. 104(3) 2022 431-445.
- [4] Wang M., Song L.E., Zhao S., Wan X, Synthesis of 3,4-Dihydropyrimidin-2(1H)-ones using Sodium Bisulfate as a Catalyst under Solvent-free Conditions, *Org Prep Proced Int.*, 46 (2014) 457-462.
- [5] Su, G., Formica, M., Yamazaki, K., Hamlin, T. A., & Dixon, D. J., Catalytic Enantioselective Intramolecular Oxa-Michael Reaction to α , β -Unsaturated Esters and Amides, *J. Am. Chem. Soc.*, 145 (23) (2023) 12771–12782.
- [6] Sunduru N., Nishi P., Chauhan P.M.S., Gupta S., Synthesis and antileishmanial activity of novel 2,4,6-trisubstituted pyrimidines and 1,3,5-triazines, *Eur. J. Med. Chem.*, 44 (2009) 2473-2481.
- [7] El-Naggar A.M., Hassan A.M.A., Elkaeed E.B., Alesawy M.S., Al-Karmalawy A.A., Design, synthesis, and SAR studies of novel 4-methoxyphenyl pyrazole and pyrimidine derivatives as potential dual tyrosine kinase inhibitors targeting both EGFR and VEGFR-2, *Bioorg. Chem.*, 123 (2022) 105770.
- [8] Aghayan-Mirza M., Moradi A., Bolourtchion M., Cheap and efficient Protocol for the Synthesis of Tetrahydroquinazolinone, Dihydro pyrimidinone and Pyrimidinone and Pyrimidinone Derivatives, *Synth. Commun.*, 40 (1) (2011) 8-20.
- [9] Kaur R., Chaudhary S., Kumar K., Gupta M.K., Rawal R.K., Recent synthetic and medicinal perspectives of dihydropyrimidinones: A review, *Eur. J. Med. Chem.*, 132 (2017) 108-134.
- [10] Nazir Y., Rafique H., Kausar N., Abbas Q., Ashraf Z., Rachtanapun P., Jantanasakulwong K., Ruksiriwanich W., Methoxy-substituted tyramine derivatives synthesis, computational studies and tyrosinase inhibitory kinetics, *Molecules*, 26 (9) (2021) 2477-2482.
- [11] Obaid R.J., Mughal E.U., Naeem N., Sadiq A., Alsantali R.I., Jassas R.S., Moussa Z., Ahmed S.A., Natural and synthetic flavonoid derivatives as new potential tyrosinase inhibitors: A systematic review, *RSC Adv.*, 11 (36) (2021) 22159-22198.
- [12] Liu P., Shu C., Liu L., Huang Q., Peng Y., Design and synthesis of thiourea derivatives with sulfur-containing heterocyclic scaffolds as potential tyrosinase inhibitors, *Bioorg. Med. Chem.*, 24 (8) (2016)1866-1871.
- [13] Lam K.W., Syahida A., Ul-Haq Z., Rahman M.B.A., Lajis N.H., Synthesis and biological activity of oxadiazole and triazolothiadiazole derivatives as tyrosinase inhibitors, *Bioorg. Med. Chem. Lett.*, 20 (12) (2010) 3755-3759.
- [14] Desta D., Sjöholm R., Lee L., Lee M., Dittenhafer K., Chanche S., Babu B., Chavda S., Dewar C., Yanow S., Best A.A., Lee M., Thiocarbohydrazone and chalcone-derived 3, 4-dihydropyrimidinethione as lipid peroxidation and soybean lipoxygenase inhibitors, *Med Chem. Res.*, 20 (2011) 364-369.
- [15] Upadhyay A., Gopal M., Srivastava C., Pandey N.D., Synthesis and insecticidal activity of 3, 4-dihydropyrimidine-2 (1H)-thiones against the pulse beetle, *Callosobruchus chinensis*, *J. Pestic. Sci.*, 36(4) (2011) 467-472.
- [16] Olsson M.H.M., Søndergaard C.R., Rostkowski M., Jensen J.N., PROPKA3: Consistent Treatment of Internal and Surface Residues in Empirical pKa Predictions, *J. Chem. Theory Comput.* 7 (2011) 525-537.
- [17] Søndergaard C.R., Olsson M.H.M., Rostkowski M., Jensen J.N., Improved Treatment of Ligands and Coupling Effects in Empirical Calculation and Rationalization of pKa Values, *J. Chem. Theory Comput.* 7 (2011) 2284-95.
- [18] Boyle N.M., Banck M., James C.A., Morley C., Vandermeersch T., Hutchison G.R., Open Babel: An open chemical toolbox, *J. Cheminformatics.* 3 (2011) 2-14.
- [19] Albay C., Kahrman N., Iskender N.Y., Karaoglu Ş.A., Yaylı N., Synthesis and antimicrobial activity of methoxy azachalcones and N-alkyl substituted methoxy azachalconium bromides, *Turk. J. Chem.*, 35(3) (2011) 441-454.
- [20] Yaylı N., Küçük M., Üçüncü O., Yaşar A., Yaylı N., Karaoglu Ş.A., Synthesis of methyl (E)-2', 4''-thiazachalcones and their N-alkyl derivatives, photochemistry with theoretical

- calculations and antimicrobial activities, *J. Photochem. and Photobio. A: Chem.*, 188 (2007) 161-168.
- [21] Şöhretoğlu D., Bakır S.D., Barut B., Soral M., Sarı S., Multiple biological effects of secondary metabolites of *Ziziphus jujuba*: isolation and mechanistic insights through in vitro and in silico studies, *Eur. Food Res. Technol.*, 248(4) (2022) 1059-1067.
- [22] Yaylı N., Kılıç G., Kahriman N., Kanbolat Ş., Bozdeveci A., Karaoğlu Ş.A., Aliyazıcıoğlu R., Sellitepe H.E., Doğan İ. S., Aydın A., Tatar G., Synthesis, biological evaluation (antioxidant, antimicrobial, enzyme inhibition, and cytotoxic) and molecular docking study of hydroxy methoxy benzoin/benzil analogs, *Bioorg. Chem.*, 115 (2021) 105183.
- [23] Lee L., Davis R., Vanderham J., Hills P., Mackay H., Brown T., Mooberry S.L., Lee M., Synthesis and antiprotozoal activity of 1, 2, 3, 4-tetrahydro-2-thioxypyrimidine analogs of combretastatin A-4, *Eur. J. Med. Chem.*, 43 (2008) 2011-2015.
- [24] Sondhi S.M., Goyal R.N., Lahoti A.M., Singh N., Shukla R., Raghbir R., Synthesis, and biological evaluation of 2-thiopyrimidine derivatives, *Bioorg. Med. Chem.* 2005 13 (2005)3185-3195.
- [25] Lakshmi H.V., Kumar K.R., Shaik A.B., Synthesis, characterization, and biological evaluation of 3, 4-dihydropyrimidin-2 (1H)-thione derivatives, *Arch. Appl. Sci. Res.* 6(6) (2014)121-127.
- [26] Dinakaran V.S., Jacob D., Mathew J.E., Synthesis and biological evaluation of novel pyrimidine-2(1H)-ones/thiones as potent anti-inflammatory and anticancer agents, *Med. Chem. Res.*, 21(11) (2012) 3598-3606.
- [27] Rao C.M.M.P., Rajeswari T., Parmender K., Yadav S.K., Synthesis, characterization, anti-microbial and antioxidant activity of novel dihydropyrimidines, *Asian J. Pharm. Anal.* 10(1) (2022) 21-28.
- [28] Mahmoud N.F.H., Ghareeb E.A., Synthesis of novel substituted tetrahydropyrimidine derivatives and evaluation of their pharmacological and antimicrobial activities, *J. Heterocycl. Chem.*, 56(1) (2019) 81-91.
- [29] Gondrui R., Peddi S.R., Manga V., Khanapur M., Gali R., Sirassu N., Bavantula R., One-pot synthesis, biological evaluation and molecular docking studies of fused thiazolo[2,3-b]pyrimidinone-pyrazolylcoumarin hybrids, *Mol. Divers.*, 2018 22(4) (2018) 943-956.

Efficient Methanol Electro-oxidation on Ni, S Dual Doped Reduced Graphene Layer Catalyst

Rukan Suna Karatekin ^{1,a,*}, Sedef Kaplan ^{1,b}¹ Science Faculty, Mersin University, Mersin, Türkiye.

*Corresponding author

Research Article

History

Received: 06/04/2023


Accepted: 14/11/2023

Copyright

©2023 Faculty of Science,
Sivas Cumhuriyet University

ABSTRACT

Energy crisis is the most popular issue in the world, which must be overcome with the development of alternative energy sources. Among them, methanol is a promising fuel when used in direct methanol fuel cells. However, the mentioned cell needs highly electroactive and stable anode materials toward MeOH. Ni has gained attention as it is an alternative to noble atoms. In this study, Ni was deposited on reduced graphene layer which functionalized with S atoms via the hydrothermal method. The fabricated sample was characterized by using Scanning Electron Microscopy (SEM), Energy Dispersive X-ray Spectroscopy (EDX), mapping, X-ray Powder Diffraction (XRD), and Brunauer–Emmett–Teller method (BET). Two samples as called Ni/GCE and Ni@s-rGO/GCE were examined for methanol oxidation reaction in alkaline media. For methanol oxidation, due to the higher surface area, and small particle size of Ni, the mass activity of Ni@s-rGO/GCE is two times higher than Ni/GCE

Keywords: Methanol oxidation, s-doped reduced graphene, Ni nanoparticles. rukansuna@mersin.edu.tr <https://orcid.org/0000-0003-3052-1539> kaplansedef33@gmail.com <https://orcid.org/0000-0002-3345-1452>

Introduction

Fuel cells have effective approaches for the conversion of energy due to their high efficiency, low energy consumption, clean, and quick refueling characteristics [1]. Among them, Direct methanol fuel cells (DMFCs) have great attention due to their high energy density, safe storage and transportation, simple operation, and environmental friendliness. Additionally, methanol has a low molecular weight, low cost, high specific energy density, and simplicity of storage [2]. Pt and Pt-group metals have been used as anode materials to improve the methanol oxidation in DMFC. Due to the high cost of these metals and their poisoning property, a new alternative electrode material has been researched.

Nickel is a transition metal that because of its surface oxidation property gain the potential to be used as a catalyst for different electrochemical reaction. It is reported that Ni is an alternative material because it is cheap and abundant, that shows excellent catalytic activity toward methanol oxidation in alkaline media [3]. The oxophilicity of Ni allows the forming OH groups to be active sites at the surface of the catalyst; thereby antipoisoning property of the catalyst increases [4]. For this reason, Ni based catalysts have been used as an alternative to noble metals especially in alkaline medium [5].

It is well known that the catalytic activity of an electrode depends on its morphology, particle size, active surface area, and ability of methanol adsorption. Recently, in some studies, Ni nanoparticles were synthesized on different supporting materials and examined for MOR. For example, Ji et al, deposited Ni on

N-doped carbon frameworks (CFNs) and used this fabricated electrode for MOR. They emphasized that the interactions between Ni and CFNs supported the forming of smaller particle sizes of Ni, and uniform dispersion on CFNs. So, with attended these two effects, the reaction kinetics of methanol oxidation increased [6]. Liu et al., synthesized pure Ni nanocrystalline anchored on rGO and examined it for methanol oxidation reaction (MOR) under alkaline conditions. They reported that due to the synthesis of Ni with ultra-nano size on rGO the active surface area increased and this situation improves the mass activity toward methanol oxidation and antipoisoning property of the catalyst [7].

To obtain uniform and nanosize metal nanoparticles, carbon-based materials have been used commonly. In the last studies, reduced graphene oxide (rGO) has been used as a supporting material for this purpose. Besides, rGO has excellent properties such as conductivity, and higher surface area, when compared to other carbon materials [8, 9]. Furthermore, the properties of rGO such as stability, conductivity, surface area, and catalytic activity enhance with dopant (heteroatoms, anionic or cationic surfactant) loading.

In this study, Ni nanoparticles were synthesized on reduced graphene oxide which functionalized with sodium dodecylbenzene sulfonate (SDBS) via the hydrothermal method. Fabricated Ni@s-rGO electrode was examined for MOR under alkaline conditions. To investigate the supporting material effect on the performance of Ni for MOR, Ni nanoparticles were

synthesized by hydrothermal method without supporting material.

Materials and Methods

S-rGO Synthesis

Firstly, graphene oxide was synthesized by Hummer's method [10]. The other steps were mentioned in our previous study[11]. Briefly, a certain amount of GO was dispersed in 120 mL of bi-distilled water after 1h, and 120 mg SDBS was added to the GO solution for 30 minutes. Then hydrazine solution was added to the homogenous solution and the prepared solution was refluxed for 24 h. This solution is used directly when synthesizing Ni@SrGO.

Ni@S-rGO synthesis

25 mL of as-prepared s-rGO, 118 mg of nickel chloride hexahydrate ($\text{NiCl}_2 \cdot 6\text{H}_2\text{O}$), and 30 mL of ethylene glycol were mixed with a magnetic stirrer. Also, 0.5 g of sodium hydroxide (NaOH) was dissolved in 10 mL of 80% hydrazine (N_2H_4) in a different beaker. This solution was dropped slowly into other solutions and was mixed for 15 minutes. The prepared solution was transferred into a Teflon-lined autoclave at 200 °C for 1 h. After 1h of waiting the cell cooled down and the sample was centrifuged and washed with water and methanol several times. Finally, it was left to dry in the drying oven.

Characterization and Electrochemical Measurement

The X-ray diffraction spectra were obtained by Empyrean, Panalytical, operated in a 2θ scan from 20° to 90° and with $\text{Cu-K}\alpha$ irradiation as an X-ray source (40 kV/30 mA). Quanta 650 field emission microscopy (FESEM) and energy dispersive X-ray spectroscopy (EDS) were used to identify the morphology and elemental composition of the catalysts. In addition, mapping was conducted to observe the dispersion state of the Ni particles. To estimate the BET surface area of the samples was recorded N_2 adsorption isotherms by using a Micromeritics (TriStar-II) instrument.

Electrochemical measurements were performed by using a CHI-660C workstation unit. Pt mesh, Glass carbon electrode, and Ag/AgCl were used as counter electrodes, working electrodes, and reference electrodes, respectively. All measurements were recorded under alkaline conditions at room temperature. The impedance spectrum was performed within the frequency range of 10–1 -105 Hz at constant potential (0.7V). To prepare the catalyst ink, 5 mg of catalyst was dispersed in 100 μL 2-propanol and 5 μL Nafion (was used as a binder agent) solution by ultrasonication for 20 min. Then, 10 μL catalyst ink was dropped onto the GCE and dried at 50 °C.

Results and Discussions

Figures 1a and b illustrate SEM images of powder of Ni and Ni@s-rGO recording with two different magnifications. When looking at the Ni nanoparticles outlook, it was observed that formed like a chain consisting of an oval-like structure. However, after the deposition of Ni on s-rGO, the morphology of particles was changed and their size got smaller. It was concluded that thanks to S-rGO the Ni particles formed with

ultra-nanosize and porous structure. Through EDX measurement, it was understood that the catalysts include Ni, C, S, and O elements (Figure 1c). While S belongs to the SDBS, observed O implies that the deoxygenation process was not completed literally. The mapping result exhibits Ni was deposited on the graphene layer homogeneously (Figure 1d).

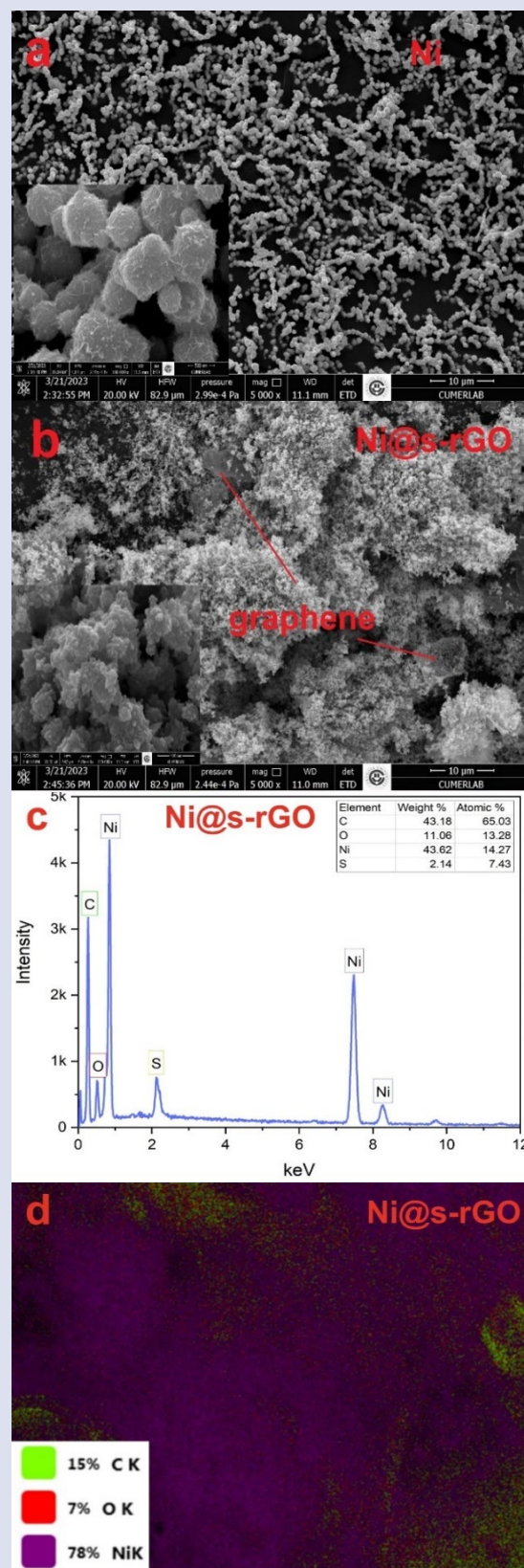


Figure 1. SEM image of a) Ni b) Ni@s-rGO c) EDX spectrum and d) mapping result of Ni@s-rGO

BET analysis

To compare the surface area of samples N_2 adsorption isotherms were recorded as shown in Figure 2. While the quantity adsorbed value for Ni/GCE is 0.4 mmol/g, this value increased to 1.8 mmol/g after being modified with s-rGO. This result exhibits that, the surface area of Ni increased with the contribution of s-rGO.

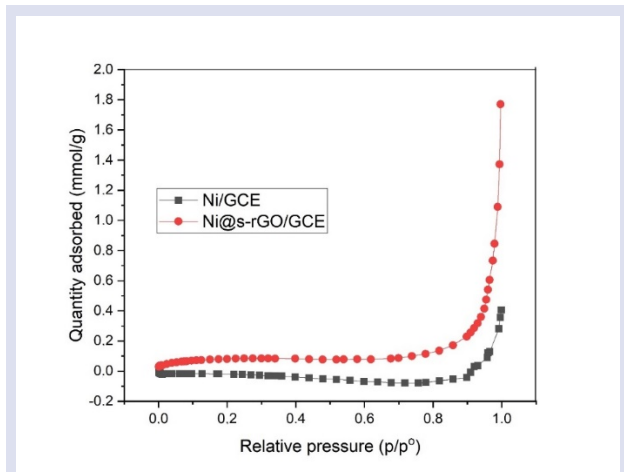


Figure 2. N_2 adsorption isotherm of the Ni/GCE and Ni@s-rGO/GCE

XRD measurement

Figure 3 shows the XRD pattern of Ni/GCE and Ni@s-rGO/GCE in the range of 10° and 90° . In the diffractogram of Ni@s-rGO/GCE, a broader peak was observed at $2\theta=22.3^\circ$ belonging to the S-doped graphene layer. This result is compatible with the earlier study [11].

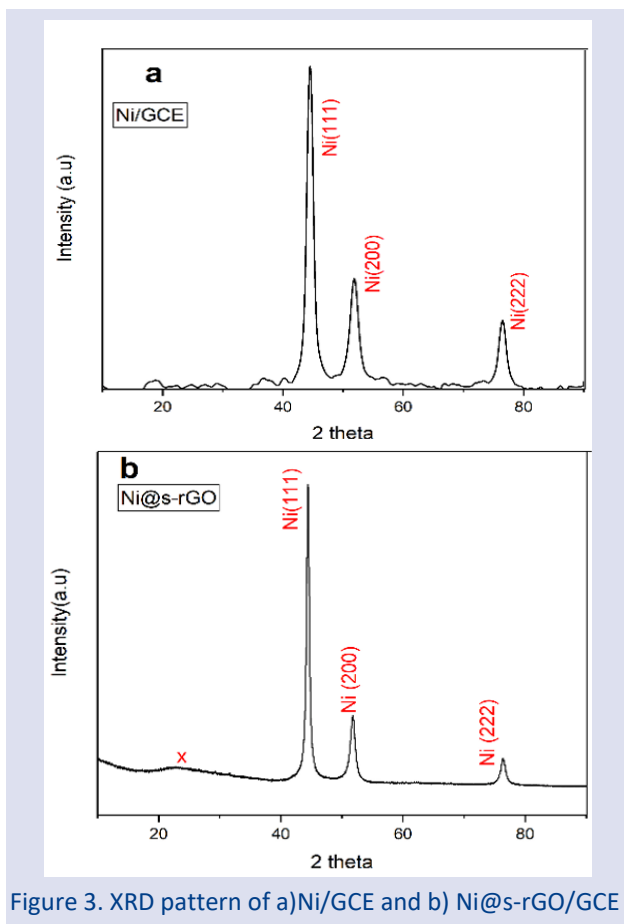


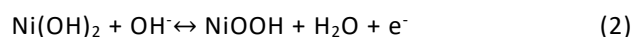
Figure 3. XRD pattern of a) Ni/GCE and b) Ni@s-rGO/GCE

It was concluded that Ni was deposited on both supporting materials with the same crystalline structure is called cubic structure [12]. However, with sharper peak intensity Ni was deposited on s-rGO with a higher density of crystalline form compared to GCE.

The Debye-Scherer equation was used to calculate the average grain size of the samples [13]. From this equation, the average grain size of Ni/GCE and Ni@s-rGO/GCE was calculated as 28 nm and 16 nm, respectively. This result implies that when using s-rGO as a supporting material the particle size of Ni decreased. This result is supported by SEM analysis.

Electrochemical measurement

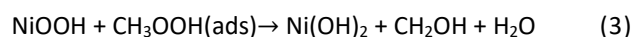
In Figure 4a before the oxygen evolution peak, a pair of redox peaks was observed around 0.2 and 0.45 V, which is attributed to the Ni/Ni(OH)₂ redox couple in Equation [3].



When comparing the peak potential of a pair redox for Ni@GCE and Ni@s-rGO/GCE, the formation of NiOOH on s-rGO occurred at lower potential indicating it needs lower energy.

Figure 4b and 4c show comparing the cyclic voltammograms of Ni/GCE and Ni@s-rGO/GCE with and without MeOH in NaOH. In the presence of methanol, observed a pair of redox peaks disappeared and the current density increased in the anodic region corresponding methanol oxidation. Figure 4d shows that the current density of methanol oxidation of Ni@s-rGO/GCE is higher than Ni/GCE, because of two potential reasons. First, maybe as a result of the synergistic effect between Ni and S formed higher amount of NiOOH that accelerates the decomposed methanol. This conclusion is suggested by Fleischman et al., with the reaction mechanism as follows equations 1 and 2.

The other reason is linked to the adsorption methanol amount which got higher in the presence of S atoms on the graphene layer [14]. In general, recorded CVs for MeOH oxidation reaction include forward peak current and backward current peak belonging to the CO₂ and carbonaceous species (CO_{ad}) which were adsorbed on the catalyst surface, and the adsorbed carbonaceous species were oxidized, respectively [15].



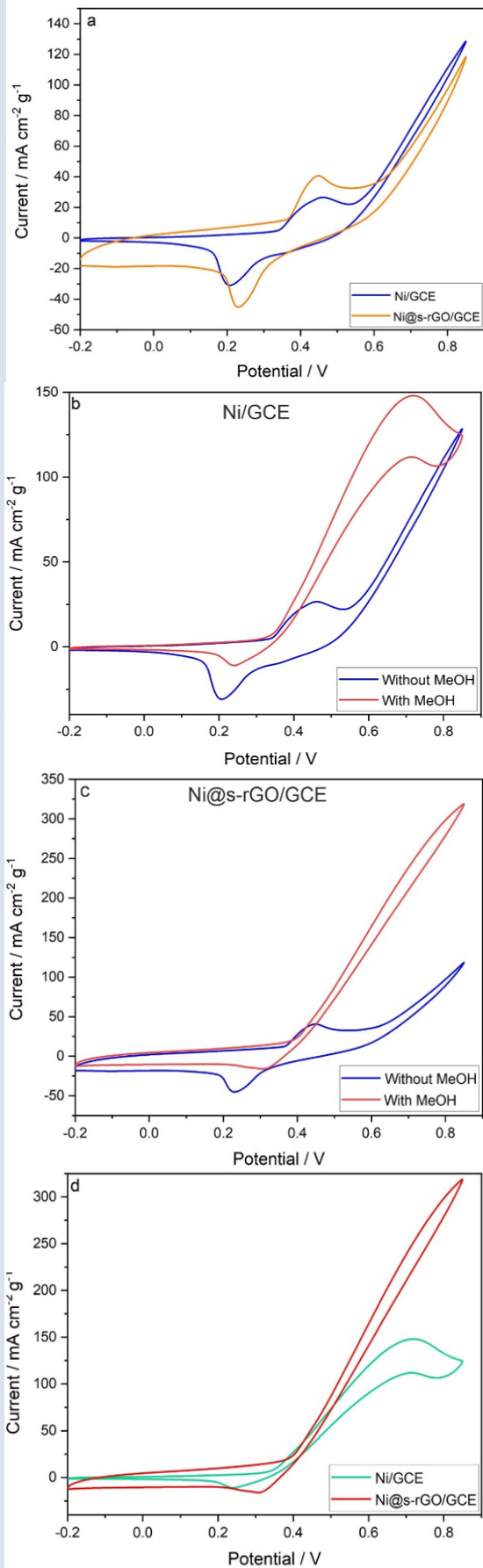


Figure 4. CVs of a) Ni/GCE and Ni@s-rGO/GCE in 0.5 M KOH, b) Ni/GCE, c) Ni@s-rGO/GCE in 0.5 M KOH with and without methanol, and d) Ni/GCE and Ni@s-rGO/GCE in 0.5 M KOH including 0.5 M MeOH.

When looking at the anodic region of CVs for both electrodes, only Ni@GCE CVs include backward peak current. From these observations, it was concluded that poisoning species such as CO, and COOH don't adsorb on Ni@s-rGO/GCE. Therefore it can be said, it has good anti-poisoning properties.

Figure 5a illustrates the cyclic voltammograms of methanol oxidation on the Ni@s-rGO/GCE for different methanol concentrations ranging from 0.1 to 1 M. It was observed that current density increased gradually with methanol concentrations. However, when the concentration reached 1M, the current became constant indicating that the active sites of the electrode were saturated with methanol.

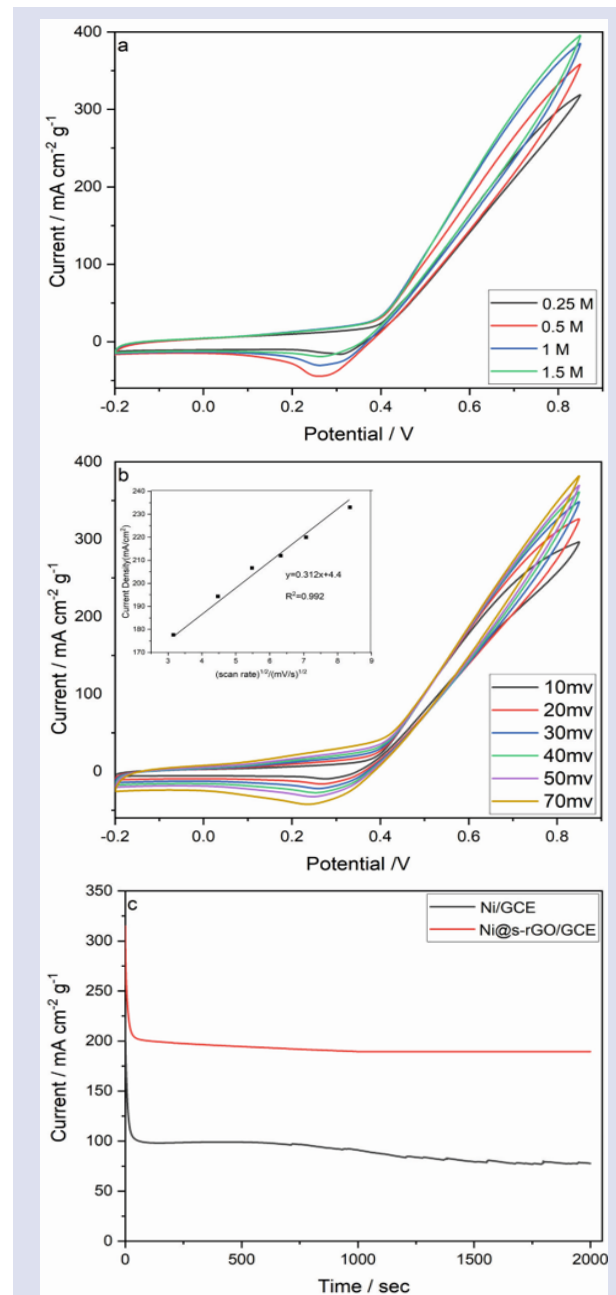


Figure 5. CVs of Ni@s-rGO/GCE a) in 0.5 M KOH including variation concentration of methanol b) at different scan rates in 0.5 M KOH including 0.5 M MeOH c) amperometric measurement of Ni@GCE and Ni@s-rGO/GCE at a constant potential.

The catalytic kinetics of Ni@S-rGO/GCE for the methanol electrooxidation reaction was studied at various scan rates from 10 to 70 mV/s in the presence of 0.5 M methanol in 0.5 M KOH solution. The current density of methanol oxidation increases with the scan rate as shown in Figure 5b. The Inset figure in Figure 5b shows a plot of peak current density versus the square root of the scan rate ($v^{1/2}$). The linear response of the graph shows that the reaction occurred under diffusion-controlled conditions [15].

Figure 5c shows the chronoamperometric measurement of Ni@GCE and Ni@s-rGO/GCE for methanol oxidation in KOH including 0.5 M methanol. Due to the anti-poisoning property and decomposition capability of methanol Ni@s-rGO/GCE exhibits higher current intensity when compared to Ni@GCE. Besides, the current density value of Ni@s-rGO/GCE remains with time. Therefore, from these results, it was concluded that Ni@s-rGO/GCE shows higher stability and good anti-positioning properties for methanol oxidation.

Electrochemical impedance spectroscopy measurement

Two semicircles are observed in the Nyquist diagrams of Ni@GCE and Ni@S-rGO/GCE in Figure 6. While the semicircle diameter in the high-frequency region is associated with the electrical conductivity of the electrode, the semicircle diameter in the low frequency is related to the resistance of charge mobility [16]. From Table 1, Ni@S-rGO/GCE has higher conductivity and charge mobility compared to Ni@GCE. When looking at the CPE1-T values of both electrodes in Table 1, the CPE-T value of Ni@S-rGO/GCE is three times higher than Ni@GCE, associated with depositing the higher amount of methanol on Ni@S-rGO/GCE. From EIS measurement, it was concluded that the catalytic activity of Ni@S-rGO/GCE was higher than Ni@GCE for MOR because it provides active sites for adsorption methanol and enhances charge mobility so the reaction rate.

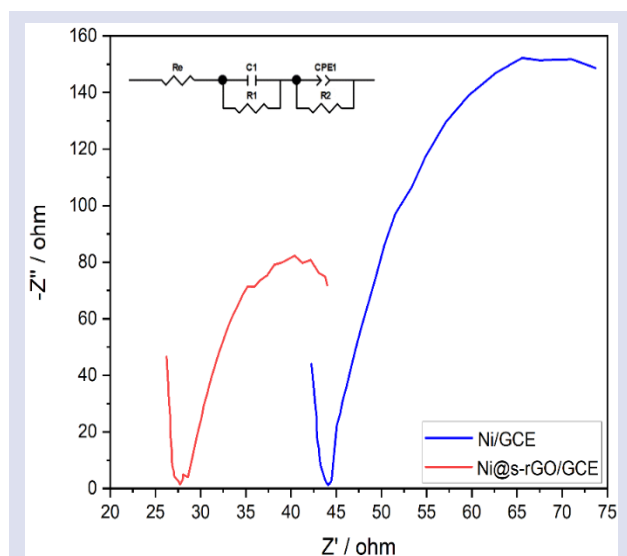


Figure 6. Nyquist diagram of Ni@GCE and Ni@s-rGO/GCE (inset: equivalent circuit for both electrode)

Table 1. Fitting result of EIS measurement of Ni@GCE and Ni@s-rGO/GCE

Electrode	C1(nF)	R1 (Ω)	CPE1-T	CPE1-P	R2 (Ω)
Ni@GCE	5.1	42.68	0.002	0.78	46.4
Ni@S-rGO/GCE	4.73	26	0.006	0.46	29.83

Conclusion

We have presented a facile method for synthesizing Ni with ultra nano-size particles which promote the oxidation of methanol. Ni was fabricated on S-doped reduced graphene oxide. The graphene layer acted as a supporting material for the deposition of Ni homogenously and thanks to S atoms Ni particles formed with smaller size. Due to the synergistic effect between Ni and S, the oxophilicity of Ni enhanced so the number of Nickel oxyhydroxides which are the active sites for methanol oxidation increased. Therefore, comparing the catalytic activity of Ni@rGO and Ni@s-rGO has two times higher mass activity which implies increased the methanol oxidation reaction rate. From the amperometric measurement, it was concluded that after the deposition of Ni on s-rGO, the obtained catalyst became stable against poisoning types. To sum up, with S-doped reduced graphene oxide, Ni nanoparticles show excellent catalytic activity towards methanol oxidation.

Conflicts of interest

There are no conflicts of interest in this work.

References

- Mei J., Hou G., Zhang H., Chen Q., Cao H., Tang Y., Zhang J., Zheng G., Convenient construction of porous dendritic Cu-doped Ni@PPy/stainless steel mesh electrode for oxidation of methanol and urea, *Applied Surface Science*, 623 (2023) 156930.
- Mahapatra S.S., Datta J., Characterization of Pt-Pd/C Electrocatalyst for Methanol Oxidation in Alkaline Medium, *International Journal of Electrochemistry*, (2011) 563495.
- Wu D., Albert M., Soldan A., Pettigrew C., Oishi K., Tomogane Y., Ye C., Ma T., Miller M.I., Mori S., Multi-atlas based detection and localization (MADL) for location-dependent quantification of white matter hyperintensities, *NeuroImage: Clinical*, 22 (2019) 101772.
- Liu C., Yang F., Schechter A., Feng L., Recent progress of Ni-based catalysts for methanol electrooxidation reaction in alkaline media, *Advanced Sensor and Energy Materials*, 2 (2023) 100055.
- Samimi G., Ashrafi H., Tashkhourian J., Haghghi B., rGO@Ni/NiO composite an effective electrocatalyst for methanol oxidation reaction in alkaline media, *Journal of Physics and Chemistry of Solids*, 184 (2024) 111724.
- Wang J., Zhao Q., Hou H., Wu Y., Yu W., Ji X., Shao L. Nickel nanoparticles supported on nitrogen-doped honeycomb-like carbon frameworks for effective methanol oxidation, *RSC Advances*, 7 (2017) 14152–14158.
- Sun H., Ye Y., Liu J., Tian Z., Cai Y., Li P., Liang C., Pure Ni nanocrystallines anchored on rGO present ultrahigh electrocatalytic activity and stability in methanol oxidation, *The Royal Society of Chemistry*, 54 (2018) 1563-1566.

- [8] Raluca Tarcan R., Todor-Boer O., Petrovai I., Leordean C., Astilean S., Botiz I., Reduced graphene oxide today, *The Royal Society of Chemistry*, 8 (2020) 1198-1224.
- [9] Sundaram R.S., Chemically derived graphene, *Graphene. Cambridge: Elsevier*, (2014) 50-80.
- [10] Hummers W.S., Offeman R.E., Preparation of Graphitic Oxide, . *Am. Chem. Soc.*, 80 (1958) 1339.
- [11] Kaplan S., Suna Karatekin R., Kahya Dudukcu M., Avci G., A novel Ni-Fe₃O₄@s-rGO/GCE electrode for electrochemical detection of H₂O₂, *Materials Chemistry and Physics*, 294 (2023) 127051.
- [12] Taghizadeh F., The study of structural and magnetic properties of NiO nanoparticles, *Optics and Photonics Journal*, 6 (2016) 164-169.
- [13] Kumar P R., Prasad N., Veillon F., Prellier W., Raman spectroscopic and magnetic properties of Europium doped nickel oxide nanoparticles prepared by microwave-assisted hydrothermal method, *Journal of Alloys and Compounds*, 858 (2021) 157639.
- [14] Suna Karatekin R., Kaya D., Kaplan S., Kahya Dündükcü M., Effect of the configurations of N and S atoms on electrochemical performance of Pt for methanol oxidation, *Journal of Nanoparticle Research*, 24 (2022) 233.
- [15] Suna Karatekin R., Kaplan S., Ildan Ozmen S., Kahya Dündükcü M., Enhanced methanol oxidation on N-doped reduced graphene oxide/ZnO/nano-Pt catalyst, *Diamond & Related Materials*, 127 (2022) 109145.
- [16] Karazehir T., Electrodeposited Pd nanoparticles on polypyrrole/nickel foam for efficient methanol oxidation, *International Journal of Hydrogen Energy*, 48 (2023) 10493-10506.

Preparation and Characterization of Tung Oil Loaded Melamine Formaldehyde Microcapsules

Tülin Gürkan Polat^{1,a,*}, Ahmet Gençer^{1,b}, Meltem Asiltürk^{2,c}, Yılmaz Aksu^{2,d}

¹ AGT Wood Industry and Trade Co., R&D Center, 07190, Antalya, Türkiye.

² Material Science and Engineering Department, Akdeniz University, Antalya 07070,

*Corresponding author

Research Article

History

Received: 24/05/2023

Accepted: 21/11/2023

Copyright





©2023 Faculty of Science,
Sivas Cumhuriyet University


ABSTRACT


In this study microcapsules were prepared by in-situ polymerization route with melamine formaldehyde as a shell material and tung oil as core material. Melamine formaldehyde (MF), a thermosetting polymer, is one of the most widely used monomers in microencapsulation due to its superior mechanical strength and thermal stability. Tung oil contains unsaturated double bonds that can be oxidized to form a film in air. Tung oil is fast drying and biodegradable, besides it is low cost and does not pollute the environment. Most importantly, tung oil is a versatile substance in industry. Therefore, tung oil is a good choice as core material. The chemical structure of microcapsules were characterized by Fourier Transform Infrared (FTIR) spectroscopy. The surface morphology and particle size and distribution were evaluated by Scanning Electron Microscopy (SEM). The thermal behavior of microcapsules and tung oil were studied by thermogravimetric analysis (TGA). The results showed that the spherical microcapsules (particle size of mostly 4-5 µm) were produced with a filling content of 15.64 wt.%, and a yield of 49.78 wt.%. The microcapsules exhibit a good thermal stability.


Keywords: Microencapsulation, Tung oil, Melamine formaldehyde, In-situ polymerization.


 tulingurkan@gmail.com


 <https://orcid.org/0000-0002-6545-0518>


 meltemasilturk@akdeniz.edu.tr

 <https://orcid.org/0000-0001-8447-5684>

 ahmet88gencer@gmail.com

 <https://orcid.org/0000-0002-4961-966X>

 yilmazaksu@akdeniz.edu.tr

 <https://orcid.org/0000-0003-3687-890X>

Introduction

Microencapsulation is a method in which the solid, liquid or gaseous active core material is covered with the coating material in micro sizes [1]. In recent years, the microencapsulation technique has been used for a wide variety of purposes. It is mainly used to protect the core material from adverse environmental factors (pH, temperature, humidity and, microorganisms) and extend the shelf life [2,3]. In some cases, it can be used to mask undesirable flavor and aroma substances especially in food and cosmetic industries [4-6]. Nano and microcapsules are also interesting and promising option in controlled drug delivery technologies [7,8]. Apart from these, there are studies in areas such as energy storage [9-11], wood modification [12], medicine [13] and agriculture [14]. In the self-healing mechanism with the microencapsulation system, the healing agent is encapsulated with a protective layer (shell). With the formation of scratches or cracks, the capsule breaks and the healing agent emerges and repairs the surface.

In microencapsulation, techniques such as spray-drying [15], spray-chilling and spray-cooling [16], extrusion [17], lyophilisation [18], in-situ polymerization [19] and supercritical fluid technology [20] are used for coating the active substances with the coating material. In this project, in-situ polymerization technique was used in the synthesis of microcapsules. The most commonly used monomers in this technique are urea-formaldehyde, melamine-formaldehyde and urea-melamine

formaldehyde resins. According to this technique, an oil-in-water emulsion is formed first. For this purpose, the filling material to be encapsulated (water-insoluble, oil-phase core material) is emulsified in the water phase, which is mixed at high speed in the presence of surfactant (emulsifier). Prepolymers (e.g. melamine-formaldehyde) are then added to the emulsion. Finally, the polymerization reaction is initiated between the prepolymers by increasing the temperature and/or adjusting the pH. Instead of the prepolymer, melamine and formaldehyde or monomers such as urea and formaldehyde can be used directly.

Chung et al. [21] prepared mechanically and thermally stable polyurea formaldehyde-coated microcapsules containing curing agents and added them to the urea formaldehyde matrix to improve the self-healing surface layers of instrument panels in automobiles. During the synthesis of microcapsules by in-situ emulsion polymerization method, platinum was used as a catalyst. The self-healing efficiency of the material was examined with the help of an optical microscope and it was observed that there was an improvement of 82%. In another study, microcapsules containing linseed oil coated with urea-formaldehyde were synthesized by in-situ polymerization technique to prevent corrosion in metals. 1%, 3% and 5% microcapsule impregnated epoxy resins were coated on the scratched metal surfaces and immersed in NaCl solutions. SEM images of metals showed that metal

containing 3% microcapsule had a great improvement [22]. Jeong et al. [23] stated that an adhesive with energy storage properties can be obtained for wooden flooring application with micro-encapsulated phase change material and epoxy glue.

In this study the tung oil was encapsulated with melamine formaldehyde (MF) as a shell material. In-situ polymerization method was preferred because of its advantages such as high efficiency encapsulation, low cost, and ease of processing. Tung oil used as core material. Tung oil is a triglyceride and used in many areas such as paint, varnish, and printing ink due to its ability to polymerize into a film when in contact with air. Pretzl et al. [24] and Pan et al. [25] stated that the most commonly used coating material in microencapsulation is melamine formaldehyde resin, due to its resistance to water, acids and alkalis, and its price is also very low in industrial applications. Mustapha and his colleagues [26] encapsulated tung oil with a urea-formaldehyde shell using a one-step in situ polymerization technique for use in extrinsic self-healing applications.

Materials and Methods

Materials

Tung oil, used as core material, and melamine and formaldehyde (37 wt.% aqueous solution) which were used as wall material, were obtained from Sigma Aldrich. Tween 80 utilized as surfactant, was purchased from Merck. Acetone which was used for rinsing the microcapsules was obtained from Tekkim. Ammonium chloride used to remove unreacted formaldehyde was purchased from Merck Millipore. Sodium hydroxide and hydrochloric acid, which were used as pH controllers were supplied from Sigma Aldrich. All materials were used without additional purification. Deionized water was used in all experiments.

Synthesis of Microcapsules

In this study, the method proposed by Hwang et al. [27] was used for the synthesis of melamine formaldehyde microcapsules (Figure 1). In the first step, melamine formaldehyde prepolymer was synthesized. For this purpose fifty milliliters of water and 5 g of melamine were taken into a 100 mL reaction flask. After the resulting solution was stirred for a while, 11.4 g of 37% formaldehyde solution was added. Then the pH was adjusted to 9 by adding 10% NaOH solution. The temperature was increased to 70 °C and stirred at 300 rpm under reflux for a certain time. At the end of the reaction period, the pH was reduced to 6.5 and cooled to room temperature. The obtained melamine formaldehyde prepolymer was characterized by FTIR spectroscopy.

In the second step, tung oil loaded melamine formaldehyde microcapsules were synthesized by in-situ polymerization method. Fifty milliliters of water and 0.5 g of Tween 80 were added in a three-necked round-bottomed flask and stirred for 20 minutes at 300 rpm. At the end of this period, 10 g of tung oil was added and the pH value was adjusted to the range of 4-5.

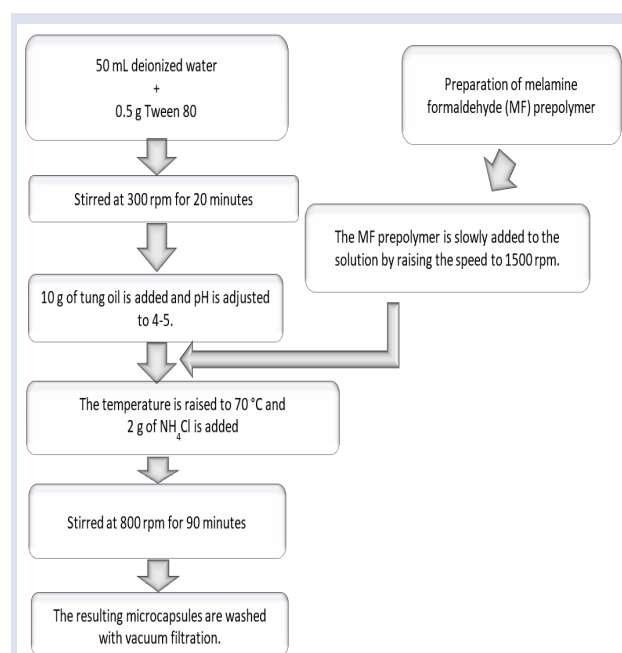


Figure 1. Schematic illustration of the preparation of tung oil loaded MF microcapsules

The stirring rate was increased to 1500 rpm and the previously prepared MF prepolymer was added slowly. After the temperature was increased to 70 °C, 2 g of NH_4Cl was added in order to remove the unreacted formaldehyde and it was mixed for 90 minutes at a stirring speed of 800 rpm. The resulting microcapsules were separated under vacuum using Suction filtration. The microcapsules were washed with deionized water and then air dried. The encapsulation yield calculation for the synthesis made is based on the equation (1) below [28,29].

$$\text{Encapsulation yield\%} = \frac{W_{\text{microcapsule}}}{W_{\text{MF prepolymer}} + W_{\text{tung oil}}} \times 100 \quad (1)$$

$W_{\text{Microcapsules}}$, $W_{\text{MF prepolymer}}$ and $W_{\text{tung oil}}$ stand for weight of microcapsules, MF prepolymer and tung oil, respectively.

FTIR Analysis

FTIR measurements were performed with a Bruker-Alpha II model FTIR spectrometer in the range of 4000-400 cm^{-1} waveform and 4 cm^{-1} resolution and used to obtain information about interactions within the MF prepolymer and microcapsule formulations.

SEM

SEM analyses were conducted using a ZEISS-LEO 1430 scanning electron microscope available at Akdeniz University Electron Microscope Image Analysis Unit (TEMGA). Before the analysis, the microcapsules were coated with gold-palladium under high vacuum using a Polaron brand, SC7620 model coating device in order to impart conductivity to the microcapsules. Images were taken at a magnification between 200x and 10000x. Image-Pro Plus 2D Image Analysis Software was applied to measure constituent microcapsule particles by using SEM images.

TGA

Thermal behavior of microcapsules was carried out by heating from 30 °C to 800 °C at a nitrogen flow of 20 mL/min, with a heating rate of 10 °C/min, using the Perkin Elmer STA-8000 model thermal analyzer. Samples tested were previously dried in a vacuum oven during 24 h at 40 °C to remove the water moisture absorbed. Sample mass was about 8-10 mg.

Tung Oil Content in Microcapsules

A quantity of microcapsules was taken, ground and weighed (m_1). After grinding, they were immersed in acetone and filtered under vacuum. This process was repeated three times to ensure that all core material was washed. The collected microcapsule walls were dried at room temperature and weighed (m_2). The following equation was used to calculate the core content.

$$\text{Tung oil content (\%)} = \frac{m_1 - m_2}{m_1} \times 100 \quad (2)$$

Results and Discussion

Structure Elucidation of Microcapsules

In this study, in situ polymerization technique was used in the synthesis of microcapsules. In the first step, melamine-formaldehyde prepolymer was synthesized. In the second step, microcapsules were obtained by adding melamine-formaldehyde prepolymer to the oil-in-water emulsion. Schematic representation is given in Figure 2.

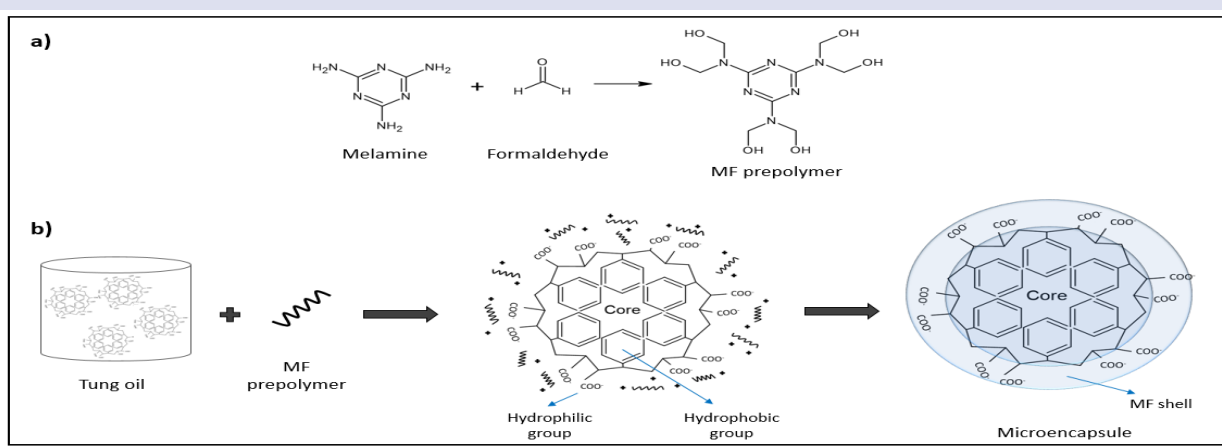


Figure 2. a) MF prepolymer formation mechanism, b) Schematic illustration of the synthesis of microencapsulation of tung oil.

For chemical characterization of prepolymers and microcapsules, FTIR spectroscopy was utilized (Figure 3 and Figure 4). Figure 3a represents characteristic IR absorption bands appear due to melamine. The peaks of -NH_2 stretching vibration occur at 3466, 3415, 3321 and 3119 cm^{-1} . In addition, the absorption peaks at 1631, 1529 and 809 cm^{-1} are assigned to the triazine ring [30,31]. FTIR spectra of formaldehyde is presented in Figure 3b. As can be seen from the Figure 3b, the -CH stretching peak is observed in the 2900-3300 cm^{-1} region. Absorption peak

of -C=O group of aldehyde was recorded at 1636 cm^{-1} and 1429 cm^{-1} . Symmetric stretching vibrations of C-O and =C-O-C are seen at 1272 cm^{-1} and 986 cm^{-1} , respectively [32]. In the FTIR spectra of MF prepolymer (Figure 3c), the absorption peak appeared between 3300 and 3500 cm^{-1} is attributed to the -NH and -OH stretching. The stretching frequency at 1564 cm^{-1} corresponding to the N-H banding, 1376 cm^{-1} corresponding to C-H bending, 994 cm^{-1} corresponding to C-O stretching vibration in $\text{CH}_2\text{-OH}$ and peak at 807 cm^{-1} represents the triazine ring [33,34].

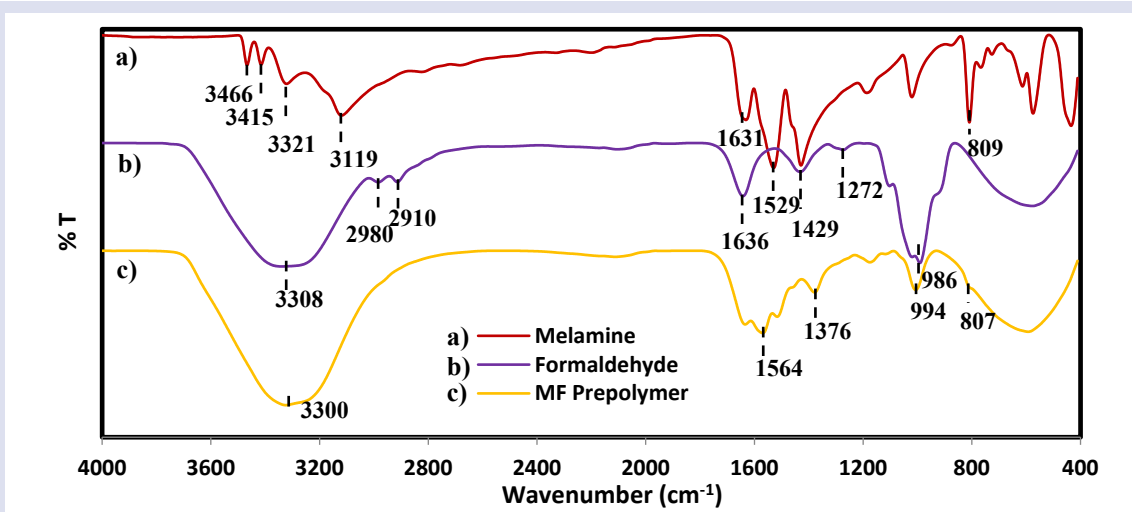
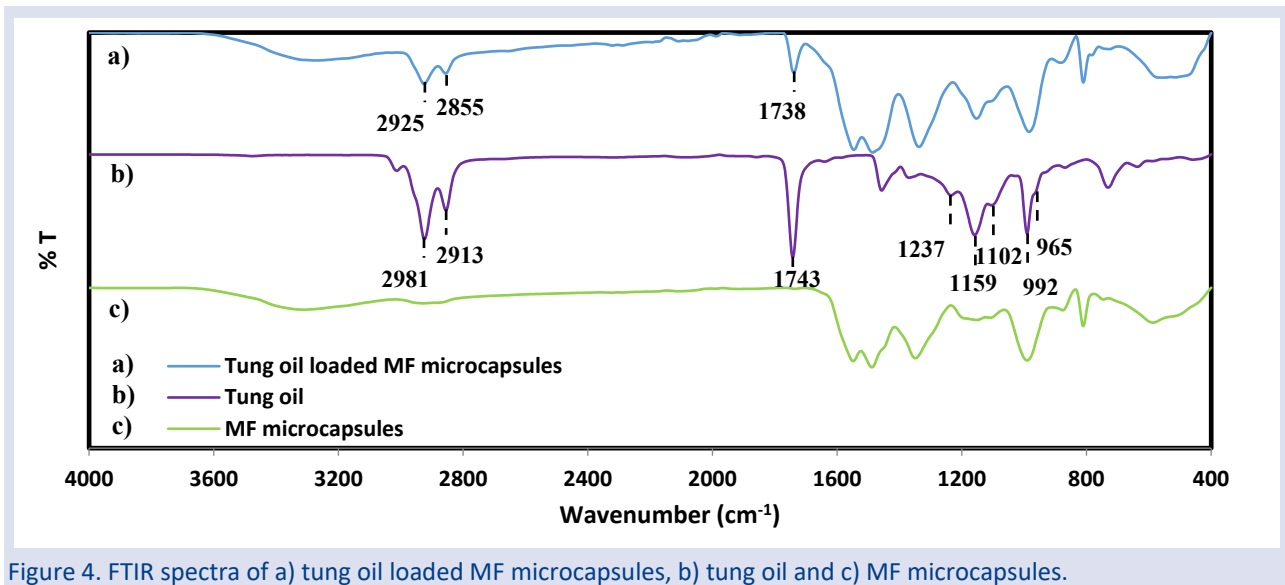


Figure 3. FTIR spectra of a) melamine, b) formaldehyde and c) melamine formaldehyde (MF) prepolymer.



In the FTIR spectra of tung oil given in Figure 4b, absorption peaks arising from symmetrical and asymmetrical -CH stretching vibrations of methyl and methylene groups are seen at 2981 and 2913 cm^{-1} [35, 36]. These vibrations have also occurred in tung oil loaded microcapsules (Figure 4a). While the C=O stretching vibration of tung oil at 1743 cm^{-1} was not observed in the tung oil free microcapsule (Figure 4c), its occurrence at 1738 cm^{-1} in the tung oil loaded microcapsule confirms that tung oil is chemically bonded with the MF shell structure. The strong absorption band at 1159 cm^{-1} and the bands on both sides (1237 and 1102 cm^{-1}) correspond to the asymmetric stretching vibration of the C-O bond of the C-CO-O fragment of aliphatic triglyceride esters. Besides, there are two absorptions at 992 and 965 cm^{-1}

attributed to the C-H swinging vibrations of trans, trans and cis, trans conjugated double bonds.

Morphologies and Particle Size Distribution

The morphology and diameter of microcapsules were observed by scanning electron microscopy (SEM). SEM micrographs taken at different magnifications (3.00 KX, 5.00 KX and 10.00 KX) of MF microcapsules without tung oil and loaded with tung oil are illustrated in Figure 5a-c and Figure 6a-c, respectively. The microcapsules presented compact, regular, smooth outer surface and spherical structures. It appears that MF microcapsules containing tung oil tend to be relatively agglomerated compared to empty microcapsules.

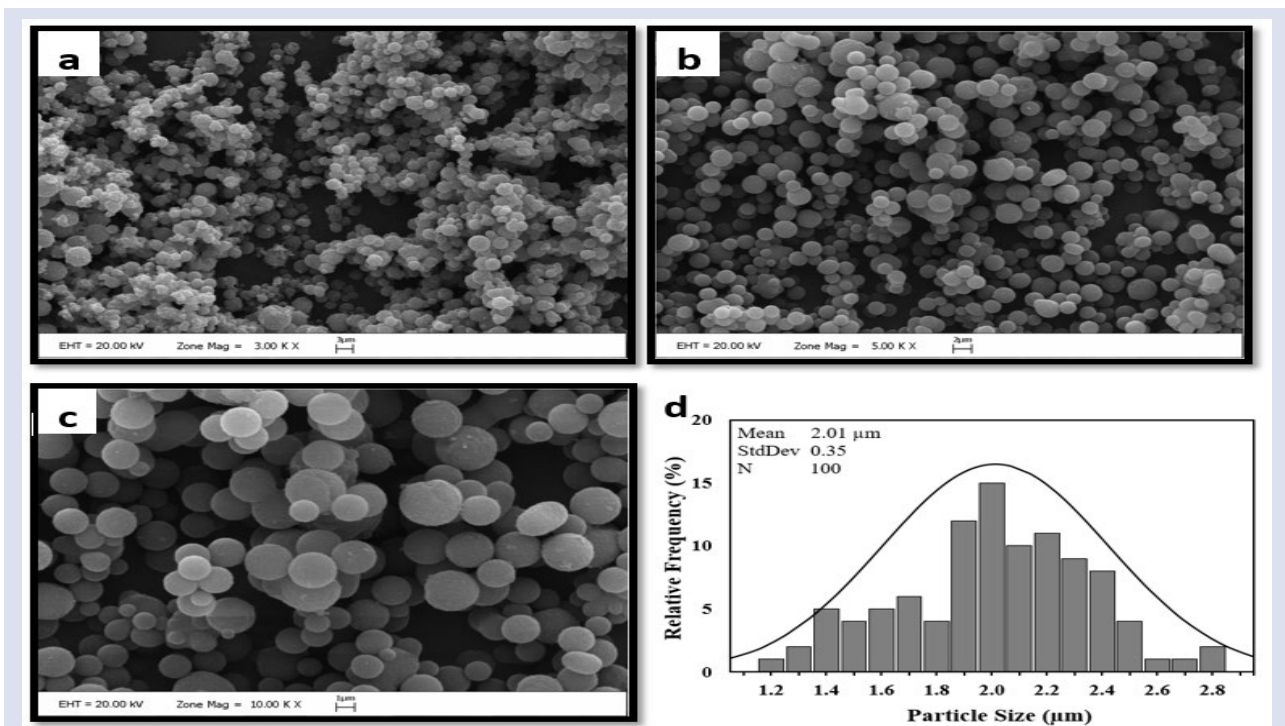


Figure 5. SEM micrographs and size distribution of MF microcapsules (tung oil-free) a) microcapsules magnification: 3.00 KX, b) microcapsules magnification: 5.00 KX, c) microcapsules magnification: 10.00 KX and d) size distribution

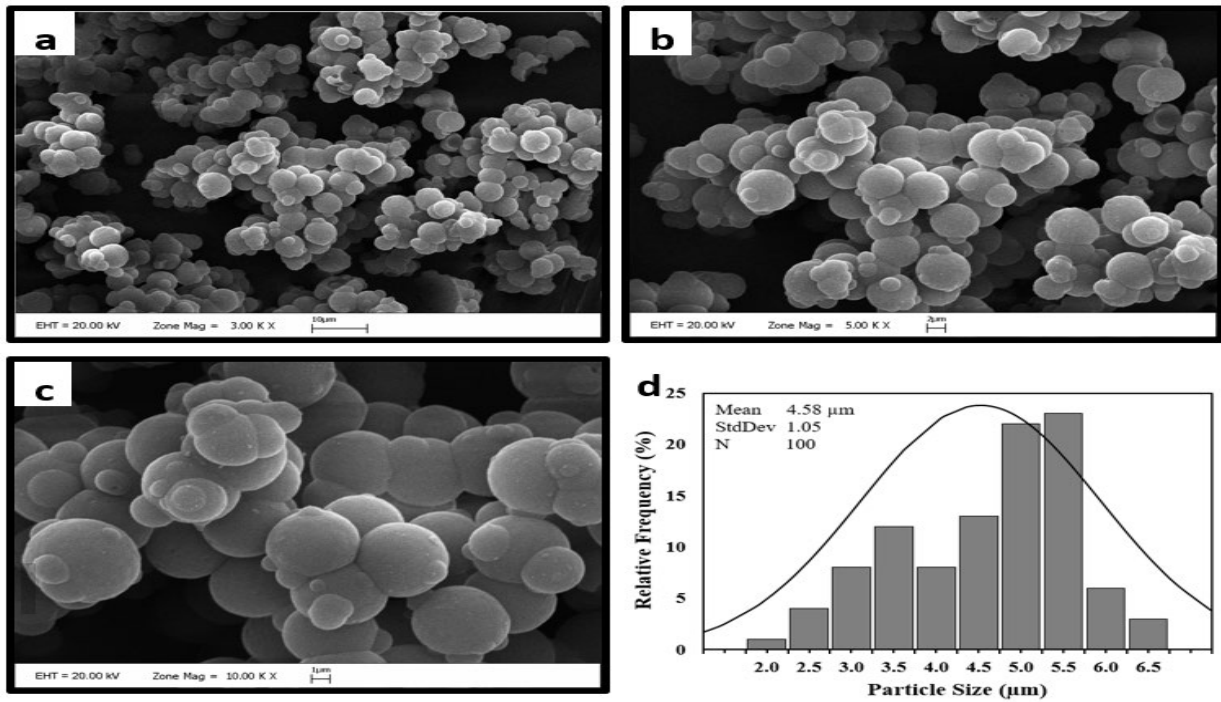


Figure 6. SEM micrographs and size distribution of tung oil loaded microcapsules a) microcapsules magnification: 3.00 KX, b) microcapsules magnification: 5.00 KX, c) microcapsules magnification: 10.00 KX and d) size distribution.

Particle size distribution of the microcapsules are shown in Fig. 5d for MF microcapsules (tung oil-free) and Fig. 6d for tung oil loaded microcapsules. The size of the microcapsules was calculated by measuring 100 individual microcapsules by SEM and the average diameter of the particles was determined as $2.01 \pm 0.35 \mu\text{m}$ and $4.58 \pm 1.05 \mu\text{m}$ for tung oil-free and tung oil loaded microcapsules, respectively. In addition, the microcapsules core content determined as 15.64 wt.% calculated by the acetone extraction method and its yield is approximately 49.78%. In a similar study conducted by Pan et al. [37], it was reported that tung oil-filled urea formaldehyde microcapsules prepared using Tween 80 as a surfactant were obtained with a particle size of 6-15 μm and a spherical morphology.

Thermal Properties of Microcapsules

The thermal behavior of tung oil and microcapsules were studied by TG curves. Figure 7 plotted the weight loss curves of tung oil, MF microcapsules (empty) and tung oil filled MF microcapsules. It was observed that the degradation of tung oil begins at approximately 350 °C. The high decomposition temperature of tung oil is due to its thermally stable structure [38]. MF microcapsules (empty) and tung oil filled MF microcapsules demonstrated almost similar thermal behaviour. Slight loss of both microcapsule systems in the region starting from 100°C and up to 220°C is related to the removal of chemically absorbed water molecules.

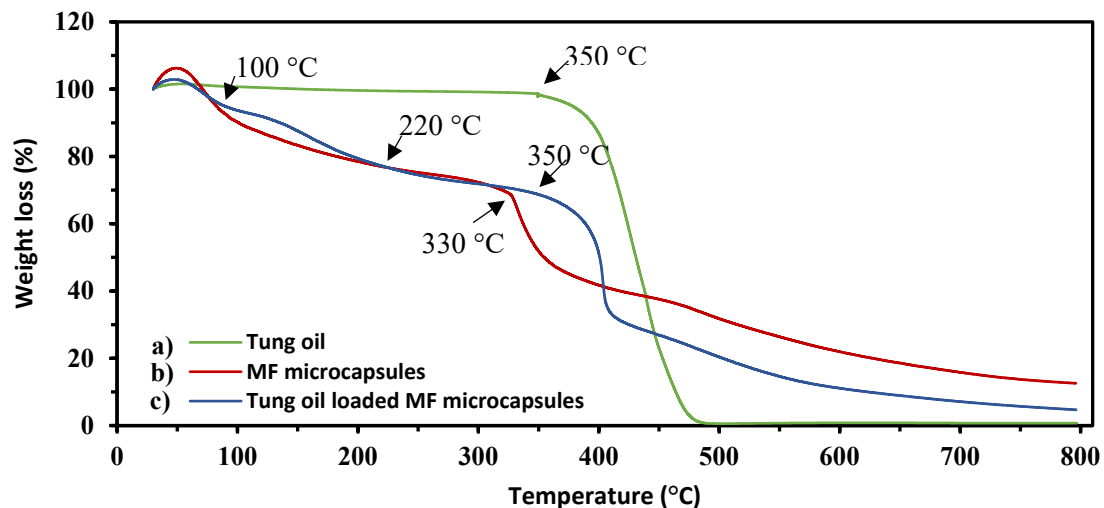


Figure 7. TGA thermograms of a) tung oil, b) MF microcapsules, and c) tung oil loaded MF microcapsules.

The decomposition temperature of MF microcapsules was recorded as 330 °C, while the decomposition temperature of MF microcapsules loaded with tung oil was recorded as 350 C. The residual weight of the MF and tung oil loaded microcapsules at 800 °C was 12.5 and 5.0 wt.%, respectively. Feng et al. [39] prepared tung oil-loaded PU (polyurethane)/PANI (polyaniline) microcapsules by two-step polymerization (interfacial polymerization and in-situ polymerization). In this study TGA thermogram showed that the initial decomposition temperature of the tung oil was about ~350 °C. They reported that tung oil loaded PU/PANI microcapsules have good thermal stability and can be used in the field of anti-corrosion coatings.

Conclusion

Melamine-formaldehyde microcapsules containing tung oil were prepared with in-situ polymerization technique. The obtained microcapsules were evaluated with regard to chemical structure, morphologies, size distribution and thermal properties. It was determined that the prepared microcapsules contained approximately 15.64 wt.% of tung oil and the encapsulation efficiency was 49.78 wt.%. The successful formation of tung oil-loaded microcapsules was confirmed by FTIR spectroscopy. SEM images proved that both tung oil-free and tung oil-loaded MF microcapsules have regular and smooth surface morphologies with diameters of $2.01 \pm 0.35 \mu\text{m}$ and $4.58 \pm 1.05 \mu\text{m}$, respectively. These microcapsules can be used as self-healing anti-corrosion coatings due to their high good thermal stability and the ability to form films on exposure to air of the tung oil they contain.

Acknowledgements

This work was supported by TÜBİTAK TEYDEB 1501-Industry R&D support program (Project Number: 3191369). We would like to thank to Akdeniz University Materials and Science Laboratory for TGA analysis. The authors thank AGT Wood Industry and Trade Co. for technical support.

Conflicts of Interest

The authors stated that did not have conflict of interests.

References

- [1] Snehal D., Swapna R., Manoj M., Chandrakant S., Microencapsulation: A review, *Research Journal of Pharmacy and Technology*, 6 (2013) 954-961.
- [2] Oxley J., Stability and prediction of shelf-life for microencapsulated ingredients, *Agro Food Industry Hi-Tech*, 23 (2012) 60-63.
- [3] Hu M., Guo J., Yu Y., Cao L., Xu Y., Research advances of microencapsulation and its prospects in the petroleum industry, *Materials (Basel, Switzerland)*, 10 (4) (2017) 369.
- [4] Bastos F., Santos L., Encapsulation of cosmetic active ingredients for topical application – a review, *Journal of Microencapsulation*, 33 (2015) 1-17.
- [5] Ayoub A., Sood M., Singh J., Bandral J., Gupta N., Bhat A., Microencapsulation and its applications in food industry, *Journal of Pharmacognosy and Phytochemistry*, 8 (3) (2019) 32-37.
- [6] Mamusa M., Resta C., Sofroniou C., Baglioni P., Encapsulation of volatile compounds in liquid media: Fragrances, flavors, and essential oils in commercial formulations, *Advances in Colloid and Interface Science*, 298 (2021) 102544.
- [7] Singh M.N., Hemant K.S., Ram M., Shivakumar H.G., Microencapsulation: A promising technique for controlled drug delivery, *Research in Pharmaceutical Sciences*, 5 (2) (2010) 65-77.
- [8] Meng Q., Zhong S., He S., Gao Y., Cui X., Synthesis and characterization of curcumin-loaded pH/reduction dual-responsive folic acid modified carboxymethyl cellulose-based microcapsules for targeted drug delivery, *Journal of Industrial and Engineering Chemistry*, 105 (2022) 251-258.
- [9] Konuklu Y., Unal M., Paksoy H.O., Microencapsulation of caprylic acid with different wall materials as phase change material for thermal energy storage, *Solar Energy Materials and Solar Cells*, 120 (2014) 536-542.
- [10] Lin Y., Zhu C., Alva G., Fang G., Microencapsulation and thermal properties of myristic acid with ethyl cellulose shell for thermal energy storage, *Applied Energy*, 231 (2018) 494-501.
- [11] Zou L., Li S., Li L., Ji W., Li Y., Cheng X., Synthesis of TiO₂ shell microcapsule-based phase change film with thermal energy storage and buffering capabilities, *Materials Today Sustainability*, 18 (2022) 100119.
- [12] Can A., Erkan G., Duran H., Sivrikaya H., Microencapsulated di-ammonium hydrogen phosphate (DAHP) with a polyurethane shell: characterization and its properties in wood, *European Journal of Wood and Wood Products*, 79 (2021) 1405-1417.
- [13] Tomaro-Duchesneau C., Saha S., Malhotra M., Kahouli I., Prakash S., Microencapsulation for the therapeutic delivery of drugs, live mammalian and bacterial cells, and other biopharmaceutics: Current status and future directions, *Journal of Pharmaceutics*, 103527 (2013) 1-19.
- [14] Cesari A., Loureiro M., Vale M., Yslas E., Dardanelli M., Marques A.C., Polycaprolactone microcapsules containing citric acid and naringin for plant growth and sustainable agriculture: physico-chemical properties and release behavior, *Science of the Total Environment*, 703 (2020) 1-11.
- [15] Mohammed N.K., Tan C.P., Manap Y.A., Muhialdin B.J., Hussin A.S.M., Spray drying for the encapsulation of oils-A review, *Molecules*, 25 (17) (2020).
- [16] Favaro-Trindade C., Technological challenges for spray chilling encapsulation of functional food ingredients, *Food Technology and Biotechnology*, 51 (2013) 171.
- [17] Seth D., Mishra H.N., Deka S.C., Effect of microencapsulation using extrusion technique on viability of bacterial cells during spray drying of sweetened yoghurt, *International Journal of Biological Macromolecules*, 103 (2017) 802-807.
- [18] Nogueira M., Prestes C., Burkert J., Microencapsulation by lyophilization of carotenoids produced by *Phaffia*

- rhodozyma with soy protein as the encapsulating agent, *Food Science and Technology*, 37 (2017) 1-4.
- [19] Krupa I., Nógellová Z., Janigová I., Boh Podgornik B., Šumiga B., Kleinová A., Karkri M., AlMaadeed M.A., Phase change materials based on high-density polyethylene filled with microencapsulated paraffin wax, *Energy Conversion and Management*, 87 (2014) 400-409.
- [20] Soh S.H., Lee L., Microencapsulation and nanoencapsulation using supercritical fluid (SCF) techniques, *Pharmaceutics*, 11 (2019) 1-17.
- [21] Chung U.S., Min J.H., Lee P.C., Koh W.G., Polyurethane matrix incorporating PDMS-based self-healing microcapsules with enhanced mechanical and thermal stability, *Colloids and Surfaces A: Physicochemical and Engineering Aspects*, 518 (2017) 173-180.
- [22] Thanawala K., Khanna A., Singh R., Development of self-healing coatings based on linseed oil as autonomous repairing agent for corrosion resistance, *Materials*, 7 (2014) 7324-7338.
- [23] Jeong S.G., Jeon J., Seo J., Lee J.H., Kim S., Performance evaluation of the microencapsulated PCM for wood-based flooring application, *Energy Conversion and Management*, 64 (2012) 516-521.
- [24] Pretzl M., Neubauer M., Tekaát M., Kunert C., Kuttner C., Leon G., Berthier D., Erni P., Ouali L., Fery A., Formation and mechanical characterization of aminoplast core/shell microcapsules, *ACS Applied Materials and Interfaces*, 4 (2012) 2940-2948.
- [25] Pan X.M., York D., Preece J.A., Zhang Z.B., Size and strength distributions of melamine-formaldehyde microcapsules prepared by membrane emulsification, *Powder Technology*, 227 (2012) 43-50.
- [26] Mustapha A.N., AlMheiri M., AlShehhi N., Rajput N., Joshi S., Antunes A., AlTeneiji M., The Microencapsulation of Tung Oil with a Natural Hydrocolloid Emulsifier for Extrinsic Self-Healing Applications. *Polymers (Basel)*. 14 (9) (2022) 1907.
- [27] Hwang J.S., Kim J.N., Wee Y.J., Yun J.S., Jang H.G., Kim S.H., Ryu H.W., Preparation and characterization of melamine-formaldehyde resin microcapsules containing fragrant oil, *Biotechnology and Bioprocess Engineering*, 11 (2006) 332-336.
- [28] Huang M., Yang J., Facile microencapsulation of HDI for self-healing anticorrosion coatings, *Journal of Materials Chemistry*, 21 (2011) 11123-11130.
- [29] Haghayegh M., Mirabedini M., Yeganeh H., Microcapsules containing multi-functional reactive isocyanate-terminated polyurethane prepolymer as a healing agent. Part 1: synthesis and optimization of reaction conditions, *Journal of Materials Science*, 51 (2016) 3056-3068.
- [30] Wang D., Preparation and property analysis of melamine formaldehyde foam, *Advances in Materials Physics and Chemistry*, 2 (2012) 63-67.
- [31] Zhu H., Xu S., Preparation and fire behavior of rigid polyurethane foams synthesized from modified urea-melamine-formaldehyde resins, *RSC Advances*, 8 (2018) 17879-17887.
- [32] Mirghani M., Detection of formaldehyde in cheese using FTIR spectroscopy, *International Food Research Journal*, 24 (2017) 496-500.
- [33] Saikia B., Dolui S., Designing semiencapsulation based covalently self-healable poly(methyl methacrylate) composites by atom transfer radical polymerization, *Journal of Polymer Science Part A Polymer Chemistry*, 54 (2016) 1842-1851.
- [34] Weiss S., Urdl K., Mayer H., Zikulnig-Rusch E., Kandelbauer A., IR spectroscopy: Suitable method for determination of curing degree and crosslinking type in melamine-formaldehyde resins, *Journal of Applied Polymer Science*, 141 (2019) 1-10.
- [35] Izzo F.C., Källbom A., Nevin A., Multi-analytical assessment of bodied drying oil varnishes and their use as binders in armour paints, *Heritage*, 4 (2021) 3402-3420.
- [36] Xiao L., Huang J., Wang Y., Chen J., Liu Z., Nie X., Preparation of tung oil-loaded PU/PANI microcapsules and synergetic anti-corrosion properties of self-healing epoxy coatings, *ACS Sustainable Chemistry and Engineering*, 7 (20) (2019) 17344-17353.
- [37] Pan P., Yan X., Peng W., Tung oil microcapsules prepared with different emulsifiers and their effects on the properties of coating film, *Coatings*, 12 (2022) 1166.
- [38] Li H., Cui Y., Wang H., Zhu Y., Wang B., Preparation and application of polysulfone microcapsules containing tung oil in self-healing and self-lubricating epoxy coating, *Colloids and Surfaces A: Physicochemical and Engineering Aspects*, 518 (2017) 181-187.
- [39] Feng Y., Cui Y., Zhang M., Li M., Li H., Preparation of tung oil-loaded PU/PANI microcapsules and synergetic anti-corrosion properties of self-healing epoxy coatings, *Macromolecular Materials and Engineering*, 306 (2) (2020) 2000581.

Spectrophotometric Determination of Atorvastatin Based on Charge Transfer Reaction with Quinalizarin

Fatih Yiğit ^{1,a}, Nurettin Tarkan ^{2,b}, Mehmet Akdeniz ^{2,c}, Figen Erek ^{3,d}, Işıl Aydın ^{4,e}

¹ Bursa Group Chairmanship, The Council of Forensic Medicine, Bursa, 16230, Türkiye.

² Diyarbakir Group Chairmanship, The Council of Forensic Medicine, Diyarbakir, 21070, Türkiye.

³ Department of Chemistry, Faculty of Science, Dicle University, Diyarbakir, 21280, Türkiye.

⁴ Department of Analytical Chemistry, Faculty of Pharmacy, Dicle University, Diyarbakir, 21280, Türkiye.

*Corresponding author

Research Article

History

Received: 24/07/2023

Accepted: 21/11/2023

Copyright



©2023 Faculty of Science,
Sivas Cumhuriyet University

ABSTRACT

An easy and economical spectrophotometric method has been developed for the determination of atorvastatin from tablet formulation. This method is based on the formation of a blue-colored charge transfer complex of Atorvastatin with quinalizarin in methanol medium. The blue colored complex gives maximum absorbance at 573 nm. In order to develop the quantitative analysis method of atorvastatin, several parameters such as the type of solvent, the effect of reagent concentration, and the reaction time and temperature on absorbance of complex were investigated. It was determined that the optimum Quinz solution (0.5×10^{-3} M) was 3 mL and the optimum temperature of the reaction was room temperature. Beer's law range of proposed method is found 10-100 $\mu\text{g} \cdot \text{mL}^{-1}$. LOD and LOQ of the proposed method were found as 1.49 $\mu\text{g} \cdot \text{mL}^{-1}$ and 4.98 $\mu\text{g} \cdot \text{mL}^{-1}$, respectively. As a result, this proposed method can be used in the quantitative analysis of atorvastatin in tablet formulations.

Keywords: Quinalizarin, Atorvastatin, Spectrophotometric determination.

yfatih4478@gmail.com

mehmetakdeniz21@hotmail.com

iaydin@dicle.edu.tr

<https://orcid.org/0009-0000-5822-1699>

<https://orcid.org/0000-0002-4435-4826>

<https://orcid.org/0000-0001-6571-6032>

nurettintarkan@gmail.com

figen.erek@dicle.edu.tr

<https://orcid.org/0009-0006-6494-3085>

<https://orcid.org/0000-0002-2861-5504>

Introduction

Atorvastatin (ATV) is a member of the statins class [1,2]. In addition, it is prevent heart disease, including heart attacks and strokes [3]. There are three different salt forms of Atorvastatin: Atorvastatin Calcium, Atorvastatin Lactone and Atorvastatin Sodium [4]. The molecular formula of Atorvastatin Calcium is $[\text{C}_{33}\text{H}_{35}\text{FN}_2\text{O}_5]_2 \cdot \text{Ca} \cdot 3\text{H}_2\text{O}$ with molecular weight 1209.4 grams/mol. It dissolves in methanol and is slightly soluble in ethanol [5].

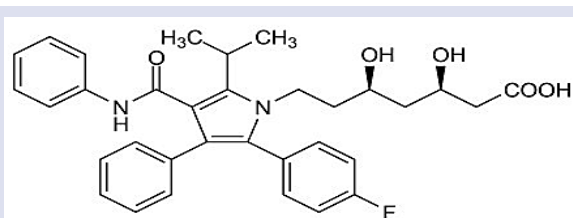


Figure 1. Chemical structure of ATV

Atorvastatin is a synthetic HMG-CoA reductase inhibitor that lowers plasma cholesterol levels and triglyceride levels [6]. Many different techniques have been used for the determination of atorvastatin. These techniques are; HPLC with electrospray tandem mass spectrometry [7-9], extractive spectrophotometry [10], LC-MS [11-16], HPTLC [17], and GC [18] for the determination of the amount of ATV in several samples.

The charge transfer complex (CTC) is formed as a result of the interaction between an electron acceptor and an electron donor. The formation of CTC is often characterized by broad-band absorbance peaks in visible spectrophotometry, however, this spectrum differs from that of both the acceptor and donor moleculars [19-22].

Charge transfer interactions, which were first discovered by Benesi Hildebrand (1949), were developed and their importance increased over time with the explanations of valence bonds and molecular orbitals. These non-covalent interactions are hydrophobic, electrostatic, hydrogen bond interactions. These interactions are the basic steps in molecular recognition in the field of biology and chemistry [23]. Charge transfer interactions are also important from a pharmacological perspective. The activity of pharmacological compounds can be determined [24]. These interactions can also be used in protein-ligand recognition and drug design [25].

Quinalizarin (1,2,5,8-tetrahydroxyanthraquinone) is a chromogenic reagent and one of the tetrahydroxyanthraquinone isomers derived by replacing four hydrogen atoms with four hydroxyl (OH) groups. It is used in the pigment and dye industry and is used as an indicator, being orange in neutral/acidic medium, blue in slightly basic medium and purple in strongly basic medium [26-30].

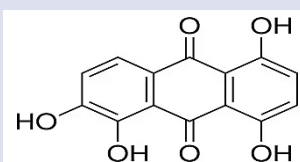


Figure 2. Chemical structure of Quinalizarin

The aim of this study was developed a simple, rapid, economic, validated spectrophotometric method for the determination of ATV in pharmaceutical formulation. The method depends on the reaction between the ATV (π -acceptor group) and quinalizarin (donor group) in the methanol to yield charge transfer complex that is measured at 573nm. In order to optimize the method, parameters such as solvent type, quinalizarin concentration, reaction time and temperature were examined. Once the optimum conditions were determined, the method was validated. Then, the resulting charge transfer complex was characterized.

Material and Methods

Instrumentations

All the absorption spectral measurements were made by using UV-1800 UV/Visible Scanning Spectrophotometer (Shimadzu Ltd) equipped with 1 cm matched quartz cells.

Materials and Reagents

All solvents (methanol, ethanol, acetonitrile, chloroform, acetone) used in this work were of HPLC grade.

The powder used as the atorvastatin reference standard was supplied by Abdi İbrahim Drug Comp.-Turkey. According to the manufacturer's method, its purity was 92.39 %. The Cholvast tablets used (Biofarma product, Turkey), pharmaceutical dosage form of Atorvastatin 10 mg per tablet, were purchased from commercial source with label content. Sigma Aldrich brand Quinalizarin, (1,2,5,8-tetrahydroxy-anthraquinone, Quin) was used without purification.

Stock Solutions

Atorvastatin stock solution was prepared as 500 $\mu\text{g}/\text{mL}$ by dissolving in Methanol. Standard ATV solutions to be used in the analysis were prepared by diluting this stock solution.

$5 \cdot 10^{-4} \text{ molL}^{-1}$ stock solution of quinalizarin, daily, was prepared in 100 mL of methanol.

Determining the Calibration Range of Proposed Method

Standard working solutions in the range of 10-100 $\mu\text{g}/\text{mL}$ were prepared in 10 mL volumetric flasks, then 3 mL ($0.5 \times 10^{-3} \text{ M}$) Quin solution was added to the flasks. The mixture was then shaken well and made up to a final volume of 10 mL with methanol. The flasks were shaken at room temperature for 30 minutes, after which the

absorbance of all solutions was measured at 573 nm against a blank of reagent solutions containing Quin. A linear regression plot was plotted using absorbance data versus atorvastatin concentration.

Test Procedure for Tablets

The colvast tablet formulation containing 10 mg of ATV was purchased from a local pharmacy. 10 tablets were independently weighed (average 152 mg per tablet), then 10 tablets were ground into a glass mortar. A portion of the powder sample equivalent to 10 mg of atorvastatin was transferred to a 50 mL beaker. 20 mL of methanol was added to the beaker and the mixture was shaken. The solution was then kept in an ultrasonic bath for 10 minutes. This solution was filtered, then the solution was transferred into a flask and the volume was made up to 50 mL with methanol. Solutions containing ATV at concentrations within the working range were prepared in 10 mL flask and the recommended method was applied to these solutions. The contents of the tablets were determined from the absorbance of the solutions with the help of the calibration equation. The developed process for the analysis of atorvastatin from the pharmaceutical formulation (Cholvast tablets) was applied.

Results and Discussions

The Effect of the Solvent Nature

The study of the effect of the solvent is the first parameter to be examined. It plays a role in increasing the interaction of the solvent reagent with the drug. It is also important in the stability of the CTC formed [31]. As can be seen in Table 1, the most sensitive result was obtained with methanol. It was decided to use methanol as a solvent in our other studies, probably because of its high capacity to form hydrogen bonds with the quinalizarin [32-34].

Table 1. Effect of the solvent(N=3)

Solvents	Absorbance \pm SD
Methanol	0.512 \pm 0.007
Acetonitrile	0.265 \pm 0.021
Ethanol	0.192 \pm 0.073
Acetone	0.251 \pm 0.025
Chloroform	0.064 \pm 0.008

Effect of Quin Concentration

Since the maximum formation of the complex from the analyte depends on the amount of reagent in the solution and the associated equilibrium, it is an important parameter to examine the concentration of the reagent in the solution(32-34). Studies were conducted by taking the concentration of ATV as 75 $\mu\text{g}/\text{mL}$. 0.5-5mL of Quin solution ($0.5 \times 10^{-3} \text{ M}$) was added to these ATV solutions and completed with methanol to 10 mL. The absorbance of ATV-Quin CTC was measured. Looking at the results in Figure 1, it was seen that the addition of 3 mL of the reagent solution ($0.5 \times 10^{-3} \text{ M}$) was sufficient to bring the color exactly to the desired intensity.

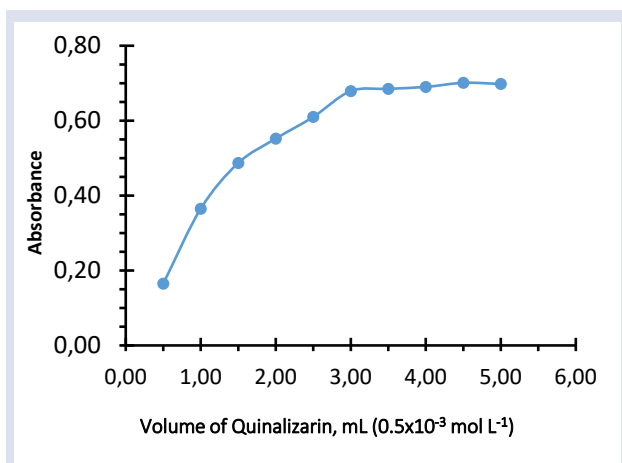


Figure 3. The effect of reagent volume

In Figure 3., a remarkable increase in absorbance continues up to 3 mL, while the amount of reagent added after this point increases the absorbance slightly and after remains constant.

Effect of the Reaction Time and Temperature

The optimum reaction time was determined by constantly monitoring the absorbance of the solution consisting of 75 µg/mL ATV and 0.5×10^{-3} M Quin reagent at different temperatures and at the optimum wavelength. As seen in Figure 4., it was observed that the absorbance of CTC decreased in the range of 30-60 °C over 30 min. The absorbance was measured every 30 minutes from the starting point of the experiment, the decrease in absorbance values continued, and the experiment was terminated here because the decrease in absorbance continued after 150 minutes. It was observed that the absorbance of colored CTC was both most stable and maximum at 25 ± 2 °C (laboratory temperature). Subsequent experiments were carried out at 25 ± 2 °C (laboratory temperature)

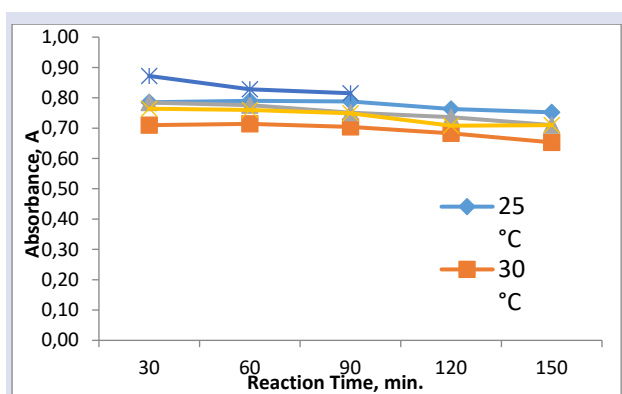


Figure 4. The effect of reaction time and temperature

Stoichiometry of the Charge Transfer Complex

Job's method was used to determine the stoichiometry of ATV-Quinalizarin CTC. Solutions of the studied atorvastatin drug and quinalizarin reagent were prepared in equal concentrations [35]. While changing the concentration ratio of ATV and Quin, the absorbances of

the mixtures, at the optimum wavelength, were measured for each point of the experiment against the prepared blank solution (Figure 5). The molar ratio (ATV:Quin) that provides the best absorbance in the reaction; was 0,7.

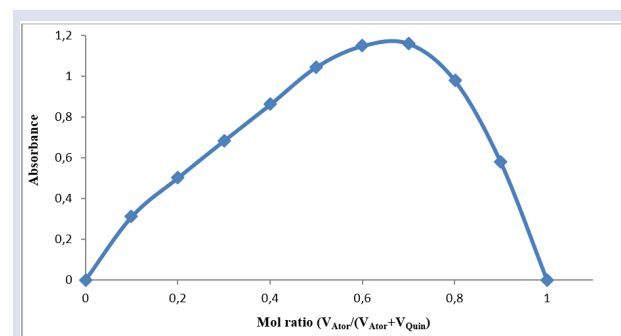


Figure 5. The Stoichiometry of CTC

Quin in methanol showed a maximum absorption band at 490 nm, while a solution of atorvastatin in methanol showed no absorbance in the 400-700 nm range. The CTC obtained by mixing the two solutions formed a new characteristic band at 573 nm.

Validation of Proposed Method

The linear regression equation was obtained by using the International Harmonization Conference resolutions method [36]. In the concentration range indicated for atorvastatin, the method showed that the correlation coefficient was linear. As a result of the linear correlation analysis of the data, the following equation was found.

According to the International Harmonization Conference resolutions method, the process of determining the lowest measurable concentration was calculated as "Detection limit and Detection limit" [36]. As seen in Table 2, LOD and LOQ of the proposed method were found as 1.49 µg/mL and 4.98 µg/mL, respectively.

Table 2. Optimum conditions and analytical parameters

Parameters	Values
λ_{maks} , (nm)	573
Working range (µg/mL)	10-100
Correlation coefficient (r^2)	0.9964
Regression equation	$y=0.0097x+0.0646$
Slope	0.0097
Interception	0.0646
LOD (µg/mL)	1.49
LOQ (µg/mL)	4.98
Molar Absorptivity $L \cdot mol^{-1} \cdot cm^{-1}$	6.05×10^3

The Accuracy of the proposed method

The accuracy of the proposed method was tested by recovery % and t test. As seen in Table 3, the percentage of the relative standard deviation (%RSD) value was less than 1% for the method, indicating that the precision values for the developed method were good [36]. The accuracy of the proposed method was calculated with a percent relative error (RE%) of less than 1% and the value indicates the accuracy of the proposed method [36].

Table 3. The accuracy of the proposed method for ATV

Taken Conc. (µg/mL)	Found Conc. ^a (µg/mL)	±SD	RSD %	RE ^b %	Recovery %
20	20,13	0,092	0,46	0.63	100.63
60	60,39	0,121	0,20	0.65	100.65
100	99,27	0,111	0,11	0.73	99.27

^a Meaning of 10 different values detected. ^b RE – Relative error; SD – Standard deviation; RSD – Relative standard deviation

The proposed method was used for the detection of atorvastatin in pharmaceutical dosage forms and the results are shown in Table 4. Statistical value at 95% confidence level was obtained from the t-test. The fact that the recovery value is high and the t^b value is greater than the t_c value shows that the proposed method is reliable and accurate [36].

Table 4. t-test for pharmaceutical preparation of ATV

Commercial Brand	Found Calculated ±SD
Cholvast 10 mg (ATV)	10,01 ± 0,108
	$t^b = 2,132$ $t_c = 2,017$
	Recovery % = % 101
	b: Theoretical t value to 95% confidence level c: Calculated average value of five determinations.

Ho: $\mu = 10\text{mg}$, $v = n - 1 = 4$
Ho: $\mu \neq 10\text{mg}$ $\alpha = 0,05$

Precision

After the optimum experimental conditions were determined, the test was carried out for the stability of the CTC formed against time. For this, a complex was formed at 3 different concentrations, and the absorbance values in the morning, noon and evening for 3 days are shown in Table 5. As a result of the experiment, it was observed that the decreasing trend in intraday and interday absorbance values continued at all different concentrations. So, it is thought that the structure of the CTC is caused by the deterioration over time.

Table 5. The intra-day and inter-day of the proposed method for ATV (N=3)

Taken Conc. (µg/mL)	Found Conc. (µg/mL)			Found Conc. (µg/mL) Inter-day ±SD
	Intra-day ±SD			
	Day-1	Day-2	Day-3	
20	20.21±0.84	19.22±1.02	18.36±0.67	19.26±0.93
60	60.90±0.79	60.49±1.23	56.57±0.91	59.32±2.39
100	99.53±1.2	96.09±1.42	95.40±1.51	97.01±2.21

Robustness

The robustness of the proposed method was evaluated the effect of small changes in the parameters reaction time (30 ± 5 min), volume of added reagent (3.0 ± 0.1 mL). As seen in Table 6, none of the small changes in these parameters significantly affected the determination of atorvastatin.

Table 6. The effect of small change in Quin volume and reaction temperature on absorbance of CTC.

Changed parameters	Recovery %	±SD	RSD%
Quin Volume (mL)	3,0 + 0.1	99.8	0.02
	3,0 - 0.1	99,9	0.11
Reaction Time (°C)	30 + 5	99.6	0.22
	30 - 5	100.4	0.18

Conclusions

The original goal of this research was to demonstrate the formation of charge transfer (π - π) complex between the important Quin, a π -electron rich aromatic molecule, and an electron deficient aromatic acceptor molecule (ATV). So, the proposed method is based on the easily formed CTC between the atorvastatin and quinalizarin in methanol. The formation of complex was substantiated by UV-visible spectroscopy. In addition, this research has shown that the concept of π - π complex formation is a viable method for the development of ATV and other drugs. The linear working range, detection and quantification limits of the method were found to be 10-100 µg/mL, 1.49 µg/mL and 4.98 µg/mL, respectively. This easy, economical method based on CTC reaction can be easily applied for analysis of atorvastatin drug from pharmaceutical formulations.

Conflict of interest

All authors declared no conflict of interest regarding this paper.

Reference

- [1] Budavari S., *The Merk Index*. 13th ed. Whitehouse Station, N.J. Merk & Co., Inc. (1997), 148.
- [2] Sweetman S.C., Martindale, *The Complete Drug Reference*. 34th ed. London, The Pharmaceutical Press, (2005), 868.
- [3] About Atorvastatine, Available at: <https://www.nhs.uk/medicines/atorvastatin/about-atorvastatin/> Retrieved November 4, 2023
- [4] "Lipitor becomes world's top-selling drug", *Crain's New York Business*, (2011), 12-28
- [5] Wei J., Chen S., Fu H., Wang X., Li H., Lin J., Xu F., Changliang H., Xiaoxia L., Huaqiao T., Gang S., Wei Z., Measurement and correlation of solubility data for atorvastatin calcium in pure and binary solvent systems from 293.15 K to 328.15 K, *Journal of Molecular Liquids*, 324, (2021) 115124.
- [6] Andrew P. Lea and Donna McTavish, Atorvastatin: A Review of its Pharmacology and Therapeutic Potential in the Management of Hyperlipidaemias, *Drugs*, 53, (5) (1997) 828-47
- [7] Jemal M., Ouyang Z., Chen B.C., Teitz D., Quantitation of the acid and lactone forms of atorvastatin and its biotransformation products in human serum by highperformance liquid chromatography with electrospray tandem mass spectrometry, *Rapid Commun Mass Spectrom*, 13 (1999) 1003-1015.
- [8] Miao X.S., Metcalfe C.D., Determination of cholesterol lowering stain dugs in aqueous samples using liquid chromatography-electrospray ionization tandem mass spectrometry, *J Chromatography A*, 998 (2003) 133-41.
- [9] Bullen W.W., Miller R.A., Hayes R.N., Development and validation of a high performance liquid chromatography-tandem mass spectrometry assay for atorvastatin, ortho-hydroxy atorvastatin and para-hydroxy Atorvastatin in human, dog and rat plasma, *J Am Soc Mass Spectrom*, 10 (1999) 55-66.
- [10] Erk N., Extractive spectrophotometric determination of atorvastatin in bulk and pharmaceutical formulations, *Anal Lett.*, 36 (2003) 2699-711
- [11] Altuntas T.G., Erk N., Liquid chromatographic determination of atorvastatin in bulk drug, tablets and human plasma, *J Liq Chromatogr Relat Technol.*, 27 (2004) 83-93.
- [12] Verd J.C., Peris C., Alergret M., Diaz C., Hernandez Z.G., Sanchez R.M., Different effect of simvastatin and atorvastatin on key enzyme involved in VLDL synthesis and catabolism on high fat /cholesterol rabbit, *Br J Pharmacol.*, 127 (1999) 1479-85.
- [13] Erturk S., Aktas E.S, Ersoy L., Ficioglu S., A HPLC method for the determination of atorvastatin and its impurities in bulk drugs and tablets, *J Pharm Biomed Anal.*, 33 (9) (2003) 1017-1023
- [14] Shen H.R., Liz D., Zhong M.K., HPLC assay and pharmacokinetic study of atorvastatin in beagle dog after oral administration of atorvastatin self-micro emulsifying drug delivery system", *Pharmazie*, 61 (2006) 18-20.
- [15] Bleske B.E., Willis R.A., Anthony M., Casselberry N., Datwani M., Uhley V.E., The effect of pravastatin and atorvastatin on coenzyme Q10, *Am Heart J.*, 142 (2001) 262.
- [16] Nirogi R.V., Kandikere V.N., Shukla M., Mudigonda M., Maurya S., Boosi R., Yerramilli A., Simultaneous quantification of atorvastatin and active metabolites in human plasma by LC-MS using rosuvastatin as internal standard, *Biomed Chromatogr.*, 20 (2006). 924-36.
- [17] Yadav S.S., Mhaske D.V., Kakad A.B., Patil B.D., Kadam S.S., Dhaneshwar S.R., Simple and sensitive HPTLC method for determination of content uniformity of atorvastatin calcium tablet, *Indian J Pharm Sci*, 67 (2005) 182-8.
- [18] McKenney J.M., McCormick L.S., Weiss S., Koren M., Kafonek S., Blanck D.M., A randomized trial of the effects of atorvastatin and niacin in patients with combined hyperlipidaemic or isolated hypertriglyceridemia, collaborative atorvastatin study group, *Am J Med.*, 104 (1998)137-43.
- [19] Hassib H.B., Issa Y. M., Conductimetric studies of charge transfer complexes of some benzyldine aniline schiff's bases with substituted-benzoquinones, *Egypt, J. Chem.*, 39 (1996) 329-338.
- [20] Mulliken R. S., Molecular compounds and their spectra. III. The interaction of electron donors and acceptors, *Phys. Chem.*, 56 (1952) 801-822.
- [21] Al-Attas A.S., Habeeb M.M., Al-Raimi D.S., Spectrophotometric determination of some amino heterocyclic donors through charge transfer complex formation with chloranilic acid in acetonitrile, *J. Mol. Liq.*, 148 (2009) 58-66.
- [22] Amano M., Yamamura Y., Sumita M., Yasazuka S., Kawaji H., Atake T., Saito K., Calorimetric and dielectric study of organic ferroelectrics, phenazine-chloranilic acid, and its bromo analog, *J. Chem. Phys.*, 130 (2009) 034503.
- [23] Powell E. , Lee Y.H., Partch R., Dennis D., Morey T., Varshney M., Pi-Pi complexation of bupivacaine and analogues with aromatic receptors: implications for overdose remediation, *Int J Nanomedicine*, 2 (3) (2007) 449-59.
- [24] Yousef T.A., Ezzeldin E., A Abdel-Aziz H., H Al-Agamy M., Mostafa G.A.E., Charge Transfer Complex of Neostigmine with 2,3-Dichloro-5,6-Dicyano-1,4-Benzoquinone: Synthesis, Spectroscopic Characterization, Antimicrobial Activity, and Theoretical Study, *Drug Des Devel Ther.*, 14 (2020) 4115-4129
- [25] Meyer E.A., Castellano R.K., Diederich F. Interactions with Aromatic Rings in Chemical and Biological Recognition, *Angew.Chem.Int.Ed.*, 42 (2003) 1210 - 125.
- [26] Barbosa J., Bosch E., Carrera R., A comparative study of some hydroxyanthraquinones as acid-base indicators, *Talanta*. 32 (11) (1985) 1077- 1081.
- [27] Banerjee N. L. and Sinha B. C., Extraction spectrophotometric method for determination of aluminium in silicates, *Talanta*. 37 (10) (1990) 1017-1020.
- [28] Gouda A. A., Cloud point extraction, preconcentration and spectrophotometric determination of trace amount of manganese(II) in water and food samples, *Spectrochimica Acta Part A: Molecular and Biomolecular Spectroscopy*, 131 (2014) 138-144.
- [29] Amin A. S., El-Sharjawy A.-A. M., Kassem M. A, Determination of thalliumat ultra-trace levels in water and biological samples using solid phase spectrophotometry, *Spectrochimica Acta A: Molecular and Biomolecular Spectroscopy*, 110 (2013) 262- 268.
- [30] Gouda A.A., Malah Z.A., Development and validation of sensitive spectrophotometric method for determination of two antiepileptics in pharmaceutical formulations, *Spectrochimica Acta A: Molecular and Biomolecular Spectroscopy*. 105 (2013) 488-496.

- [31] Ayad M.M., El-Hefnawy G.B., Bahlol G.W., Charge transfer complexes of methylnaphthalene derivatives with TCNE in CCl_4 , *Spectrochimica Acta Part A*, 58 (2002) 161–166.
- [32] Mohamed E.M., Frag Y.Z., Hathoot A.A., Shalaby E.A., Spectrophotometric determination of fenoprofen calcium drug in pure and pharmaceutical preparations. Spectroscopic characterization of the charge transfer solid complexes, *Spectrochimica Acta Part A: Molecular and Biomolecular Spectroscopy*, 189 (2018) 357–365.
- [33] Gouda A.A., Kassem M., Novel spectrophotometric methods for determination of desloratidine in pharmaceutical formulations based on charge transfer react, *Arabian Journal of Chemistry*, 9 (2012) 1712–1720
- [34] Alzoman N. Z., Sultan M. A., Maher H. M., Alshehri M. M., Wani T. A., Darwish I. A. Analytical Study for the Charge-Transfer Complexes of Rosuvastatin Calcium with π -Acceptors, *Molecules*, 18 (2013) 7711-7725.
- [35] Job P., Recherches sur la formation de complexes mineéraux en solution, et sur leur stabilité (Formation and stability of inorganic complexes in solution), *Anal. Chem.*, 9 (1928) 133–203
- [36] ICH-Q2, International Conference on Harmonisation of Technical Requirements for Registration Of Pharmaceuticals For Human Use. Validation of analytical Procedures: Text And Methodology Q2 (R1), Step 4 Version, (2005).

Simultaneously HPLC Analysis of B1, B9 and B12 Vitamins at Trace Levels via Cloud Point Extraction

Halil İbrahim Ulusoy^{1,a}, İpek Nur Yiğit^{1,b}, Ümmügülsum Polat^{1,2,c,*}, Esra Durgun^{3,d}, Aslıhan Gürbüzler^{4,e}, Songül Ulusoy^{5,f}

¹ Department of Analytical Chemistry, Faculty of Pharmacy, Sivas Cumhuriyet University, Sivas, Türkiye.

² Department of Analytical Chemistry, Institute of Health Sciences, Ankara University, Ankara, Türkiye.

³ Department of Analytical Chemistry, Institute of Health Sciences, Erciyes University, Kayseri, Türkiye.

⁴ Department of Plant and Animal Production, Vocational School of Technical Sciences, Sivas Cumhuriyet University, Sivas, Türkiye.

⁵ Department of Pharmacy, Vocational School of Technical Services, Sivas Cumhuriyet University, Sivas, Türkiye.

*Corresponding author

Research Article

History

Received: 16/08/2023

Accepted: 30/11/2023

Copyright



©2023 Faculty of Science,
Sivas Cumhuriyet University

ABSTRACT

An enrichment and determination method based on liquid chromatographically analysis and cloud point extraction (CPE) has been developed for trace levels of B vitamins (B1, B9 and B12) in the proposed study. Vitamin molecules were drawn into the non-ionic surfactant phase of Polyethylene Glycol (PEG-6000) in the presence of pH 9.0 medium. The surfactant-rich phase separated by centrifugation and then dissolved with 700 µL of ethanol. The obtained ethanol phase was filtered by 0.45-micron filter prior to the HPLC analysis. All parameters affecting the CPE method such as pH, buffer volume, incubation time, surfactant and electrolyte concentration, solvent for the surfactant-rich phase and its amount have been individually studied and optimized step by step. After the optimization of all parameters of the CPE process, the detection limits of the developed method for B1, B9 and B12 vitamins were calculated as 1.42 ng mL⁻¹, 7.14 ng mL⁻¹ and 14.28 ng mL⁻¹, respectively. The linear working ranges for three vitamin molecules was obtained in the range of 5.0-500.0 ng mL⁻¹. After CPE procedure, determination of vitamin molecules was carried out by using HPLC system with diode array detector (DAD) at 244 nm for vitamin B1, 285 nm for vitamin B9, and 361 nm for vitamin B12, respectively.

Keywords: Cloud point extraction, HPLC, Vitamin B1, Vitamin B9, Vitamin B12.

^a hiulusoy@cumhuriyet.edu.tr

^b <https://orcid.org/0000-0002-8742-5145>

^c ugulsum@cumhuriyet.edu.tr

^d <https://orcid.org/0000-0001-8393-2396>

^e aslihan@cumhuriyet.edu.tr

^f <https://orcid.org/0000-0002-6753-2808>

^b ipeknuryigit@gmail.com

^d <https://orcid.org/0009-0009-0593-5394>

^d esradurgun2017@gmail.com

^d <https://orcid.org/0009-0009-2613-4019>

^f songululusoy@yahoo.com

^f <https://orcid.org/0000-0003-3640-5416>

Introduction

Vitamins are organic substances that are necessary for the normal occurrence of metabolic events in the body and to maintain a healthy state which cannot be synthesized in the body or are synthesized insufficiently and which taken in small amounts from the environment in foods. Vitamins are an indispensable part of healthy life originate from the Latin word "vita" which means life. It is produced little or not at all in our body and therefore must be taken from outside with food. Vitamins are found in foods in active form or in the form of pro-vitamins that will become active in the body. In fact, each vitamin has its own name but they are referred to with the letters of the alphabet for easy understanding [1].

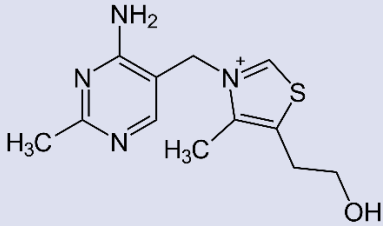
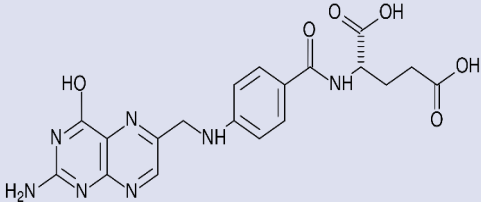
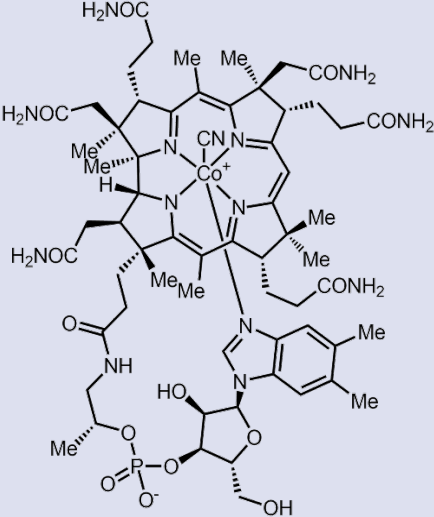
Vitamins are important compounds for the normal functions of the body which take part as coenzymes or enzymes in many vital processes. According to the general view that emerged because of many studies each vitamin has a separate task in the body and the health problem or diseases caused by a vitamin deficiency can't be eliminated with another vitamin. If one or more of the vitamins we take with our daily foods are missing or not in the required density, growth retardation, low productivity, decreased reproductive performance and some similar disorders appear. Essential vitamins are taken with diets and vitamin supplements[2].

Vitamin B1 is very important for body and mental health which is in the group of powerful vitamins called B vitamin complex. Vitamin B1, also known as thiamine, was obtained purely for the first time in 1926 as an anti-beriberi factor. In the following years, it was determined that it took part as a cofactor in important enzyme reactions [3]. Folic acid, also called folacin or folate, is used to describe a family of compounds related to pteric acid. Pteric acid consists of a pteridine ring joined by a para-aminobenzoic acid (PABA) structure, while a variable number of glutamyl structures are linked by peptide bonds[4]. It is slightly soluble in water and completely soluble in alcohol[5,6]. Vitamin B12 is the most complex of the water-soluble vitamin. Its most common form, Cobalamin, which is in the form of red crystals, dissolves in water and alcohol at high temperatures. However, it is insoluble in acetone, ether and chloroform [7,8]. Chemical structures of the studied vitamins were shown in Table 1.

Despite the development of high-precision analytical devices for the analysis of biological, environmental, food and pharmaceutical products, the analytical systems often fail to determine in the complex matrix medium. Therefore, pre-treatment is usually required for the

extraction (separation) and concentration (enrichment) of the analytes from the matrix medium.

Table 1. Molecular structure of the studied vitamins

Chemical Name	Vitamin Name	Molecular Structure
Thiamine	Vitamin B1	
Folic Acid	Vitamin B9	
Cobalamin	Vitamin B12	

Separation and enrichment processes are generally carried out by processes such as distillation, adsorption into a solid surface, and extraction[9]. Extraction processes are mostly applied as liquid-liquid, solid-liquid and solid phase extraction [10]. The cloud point extraction method was first developed by Hiroto Watanabe et al. in 1976. Especially after the 1990s, it has been frequently used by analytical chemists for the enrichment and analysis of organic molecules in the presence of surfactant for separation and enrichment [11].

Sample preparation is one of the most important steps in chemical analysis. A pre-treatment procedure is often required to separate interfering species and to concentrate trace analytes prior to detection[12]. Although new sample preparation methods such as solid phase microextraction (SPME), supercritical fluid

extraction (SFE) and accelerated solvent extraction (ASE) are used more frequently; conventional solid phase extraction (SPE), classical liquid-liquid extraction (LLE) and cloud point extraction (CPE) are still widely used [13] thanks to easy operation[14,15]. Cloud point extraction (CPE) as a pre-concentration method attracts great interest as a green analytical approach by limiting the use of toxic organic solvents[14]. In the CPE experiments, mostly non-ionic surfactants are used and the samples is heated till a certain temperature called as cloud point (CP) temperature. In this point, the solution spontaneously splits into two separate phases. The first phase is the surfactant-rich phase including target molecules and aquatic phases including the other components [16].

Briefly, a new analytical methodology was developed for vitamin B1, B9, and B12 based on CPE combined HPLC-DAD system. Experimental variables of the proposed method were studied and optimized step by step and analytical parameters of method were calculated and presented by means of model solutions.

Experimental

Instruments and Reagents

Shimadzu (Prominence) HPLC (Kyoto, Japan) device was used for all chromatographic measurements. The HPLC device used; It is equipped with LC 20 AD quaternary pump, SPD-M20 A PDA detector, DGU-20A vacuum degasser and CTO-10 AS VP column furnace. All separations and determinations were performed on a reverse phase C18 column (Inertsil ODS-3, 250 mm×4.6 mm, 5 μm). Evaluation of chromatograms was done using LC Solution 2.0 software. A pH meter (pH-2005, JP Selecta, Barcelona, Spain) was used to adjust pH of solutions.

All reagents used during the experiments were of analytical grade and were purchased from Sigma or Merck companies. All solutions used were prepared with ultrapure water with 18.2 mΩ/cm resistance obtained from ELGA Pure Lab Flex III instrument.

pH 1.0-10.0 Britton-Robinson(BR) Buffer Solution: This buffer solution was prepared by dissolving of 2.4732 g H₃BO₃, 2.67 mL of H₃PO₄ and 2.32 mL of acetic acid in 1.0 L of ultrapure water. The desired pH valued of buffer solution was adjusted to appropriate pH ranges according to their acidity constants, and pH was checked with the help of a pH meter, and then protected from light until use.

- **Vitamin B1, B9 and B12 Stock Solution, 500 mg L⁻¹ :** 50 mg of pure vitamins B1, B9 and B12 (Sigma Aldrich) were weighed and taken into a flask, dissolved with methyl alcohol and made up to 100.00 mL, transferred to a dark glass bottle and stored at +4 °C.
- **20 % Polyethyleneglycol (PEG) 6000 Stock Solution:** 20.000 g of analytical grade polyethyleneglycol was weighed and dissolved in water and made up to 100 mL, transferred to a dark glass bottle and stored at +4 °C.
- **20 % Na₂SO₄ Stock Solution:** 20 g of analytical grade sodium sulphate and dissolved by heating with the help of some water in the beaker and completed to 100.00 mL.

HPLC Analysis Conditions for Determination of Vitamins B1, B9 and B12 Molecules

Before proceeding to the CPE experiments, directly determination parameters by HPLC were optimized for vitamin B1, B9 and B12. For this purpose, based on the literature, a C-18 column was chosen as the stationary phase. Many experiments were performed to determine the suitable mobile phases, including methanol, ethanol, acetonitrile, and buffers with different pHs, using isocratic and gradient elution modes. Experiments were continued until ideal peaks were obtained for vitamins B1, B9, and B12. As a result of the experiments, it was determined that the most ideal mobile phase conditions were pH 6.5 phosphate buffer and acetonitrile. The ideal HPLC operating conditions obtained after optimization were given in Table 2.

Table 1. HPLC operating conditions

Parameter Value	
HPLC Mode	Isocratic
Mobil Phases	ACN : pH 6.5 Phosphate Buffer (0.02 M)
Flow Rate	1.0 mL/min
Wavelength in DAD	244 nm for vitamin B1, 285 nm for vitamin B9, 361 nm for vitamin B12
Column	C18- Inertsil ODS-3 (250 mm×4.6, 5.0 μm)
Column Temperature	40°C
Injection Volume	10 μL

Calibration parameters were given in Table 3 under the optimized HPLC conditions. - Chromatogram peaks obtained from standard solutions of vitamin species were given in Figure 4.

Table 2. Direct determination results by HPLC before CPE

Parameter	Vitamin B1	Vitamin B9	Vitamin B12
Retention Time, min	9.70	5.10	11.50
Wavelength in DAD Detector	244 nm	285 nm	361 nm
Calibration Range	1.0-50.0 μg mL ⁻¹	1.0-50.0 μg mL ⁻¹	1.0-50.0 μg mL ⁻¹
Limit of Detections, (LOD)	0.23 μg mL ⁻¹	0.23 μg mL ⁻¹	0.23 μg mL ⁻¹
R ²	0.9986	0.9995	0.9975
The number of repetitions, (N)	3	3	3

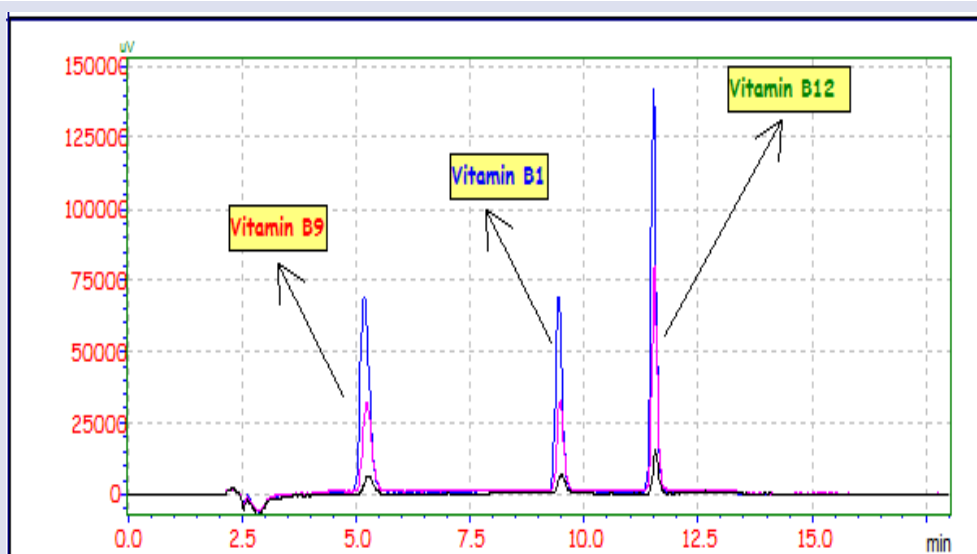


Figure 4. Chromatogram obtained under HPLC Conditions before CPE for B1, B9 and B12 vitamins

The Proposed Method

CPE experiments based on cloud point extraction, parameters such as pH, analyte concentrations, surfactant amount, incubation temperature and time, vortex time were studied and optimized step by step. In the proposed method, 2 mL of sample solution was transferred into tubes and 2.0 mL pH 9.00 BR buffer, 1.0 mL 20% (w/v) Polyethylene glycol (PEG-6000), 10.0 mL 20 % (w/v) Na₂SO₄ were added on this solution. After that, the solution was made up to 15 mL by adding with water and incubated in a water bath at 50°C for 30 minutes in order to increase temperature to cloud point temperature of surfactant. Then the solutions were centrifuged at 4000

rpm for 5 minutes in order to separate the surfactant-rich phase and the aqueous phase. Sample tubes were kept in the refrigerator for 20 minutes to facilitate the separation of the surfactant-rich phase and the aqueous phase. At the end of this period the surfactant phase with a high density was collected in the upper part of the tube and the aqueous phase in the lower part was separated with the help of an injector. The surfactant-rich phase was diluted with 700 μL of ethanol and completely homogenized with the help of a vortex. Then the samples filtered with a 0.45 μm injector-tipped filter were transferred to HPLC bottles. Vitamin contents of enriched samples were determined by HPLC device.

Experimental Studies and Discussion

Basic Approach of Experimental Studies

The developed method based on cloud point extraction and HPLC-DAD detection has been optimized for the determination of target group B vitamins. At the beginning of the experimental studies, preliminary trials were carried out on all parameters that would enable the quantitative transition of the related vitamin molecules to the surfactant-rich phase. B vitamins may be existed as charged or uncharged form depending on the pH of the medium. Therefore, all parameters CPE method such as pH, buffer volume, incubation time, surfactant and electrolyte concentration, solvent for the surfactant-rich phase and its amount, were individually studied and optimized.

Optimization of the Developed Method

pH effect

Ambient pH is very important as it affects both the reactions between the analytes and other species and the enrichment in the next steps. As the pH of the medium moves to the acidic region, the amount of positively charged ions in the medium increases which reduces the activity of the hydrophilic head of the surfactant in the solution medium.

For this purpose, buffers with pH values between 2-10 were used in the presence of PEG-6000, which is used as a non-ionic surfactant in the sample solution. The obtained results were shown in Figure 5, it is seen that the most suitable pH value for the CPE processes is pH 9.00. Therefore, pH 9.00 BR buffer system was used in later studies.

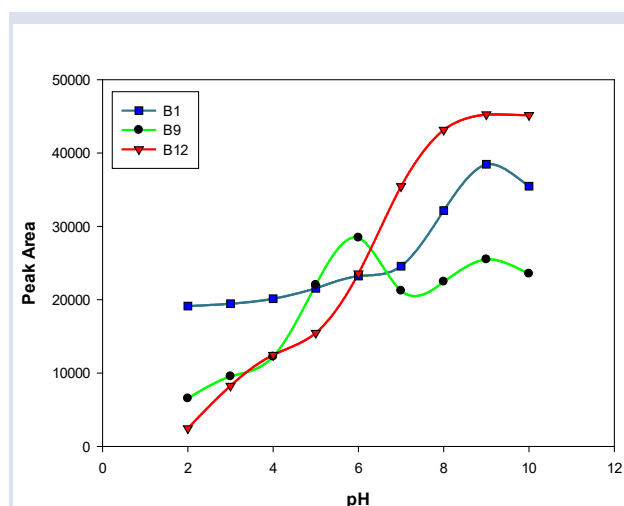


Figure 5. pH effect on the proposed method

After choosing the optimal pH value for the next experimental studies, optimization study was carried out with volume of buffer solution volume. For this purpose, volume of the optimum pH 9.00 BR was scanned between 0-5.00 mL. As can be seen in Figure 6, the highest signals were obtained with 2.0 mL of buffer.

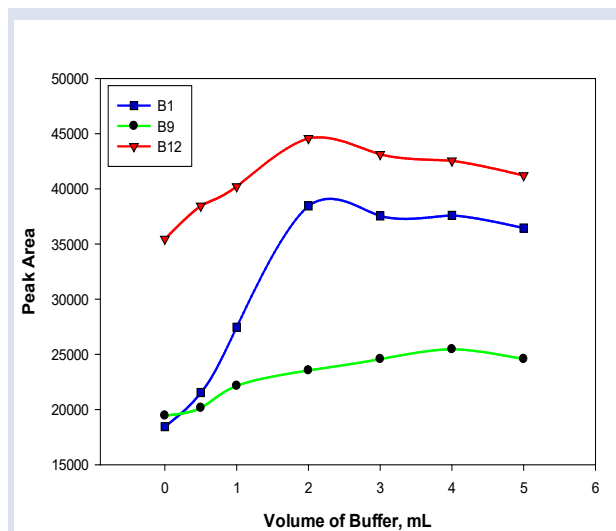


Figure 6. Effect of volume of buffer solution on the proposed method

Effect of non-ionic surfactant concentration

The amount of surfactant in the samples is one of the most important parameters affecting the effectiveness of cloud point extraction. If the surfactant concentration is low, micelle formation is limited and the extraction efficiency decreases. The non-ionic surfactant used for this experiment is Polyethylene glycol 6000 (PEG-6000) and a concentration of 20 % (w/v) surfactant was prepared before the experiments. Concentration of PEG-6000 was studied in the range of 0.4- 2.0 % (w/v). As a result of these procedures, it was seen that the best signal was obtained with 1.1 % (w/v) PEG-6000. Next studies were continued with this value.

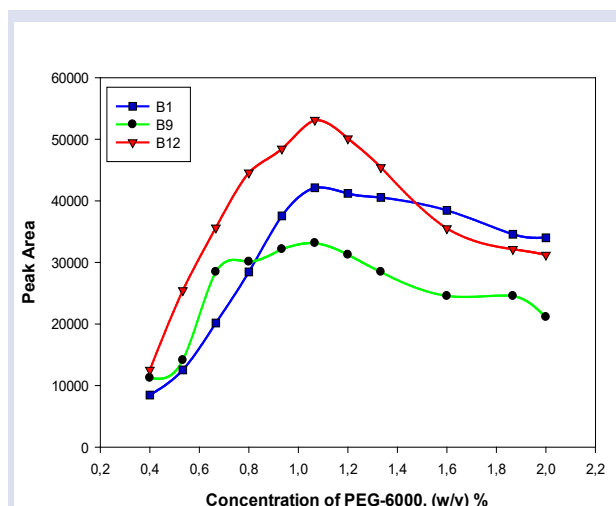


Figure 1. Effect of concentration of non-ionic surfactant

Electrolyte effect on CPE

Surfactants are macromolecules with high molecular mass that can form a micelle structure when a certain concentration and temperature is exceeded. As being proteins, the solubility of surfactants is reduced due to the salt effect. This effect, known as the salting effect, facilitates the separation of surfactant molecules from the

aqueous phase. When the literature is examined, it is seen that strong electrolytes such as NaCl, KCl, KNO₃, Na₂SO₄ or NaNO₃ are used for this aim. In our study, sodium sulphate was preferred to allow the phases to be separated from each other more easily. Concentration of Na₂SO₄ was studied in the range of 5.0-15.0 % (w/v). As can be seen in Figure 8, the best signals were obtained with 11.0 % (w/v).

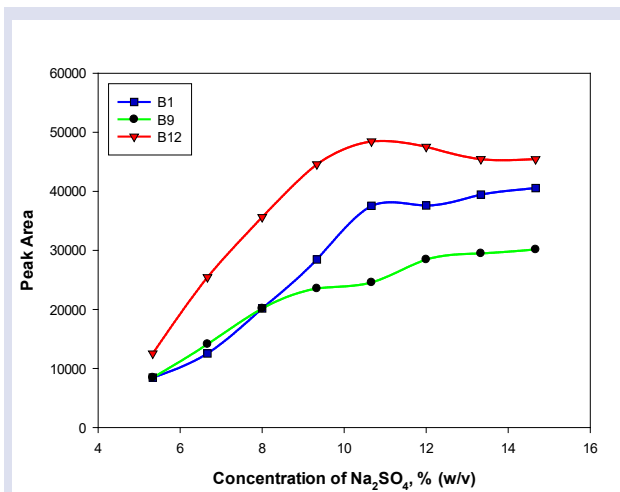


Figure 8. Electrolyte effect on the proposed method

Effect of incubation time

The another studied parameter is the effect of incubation time. Temperature is an important parameter in cloud point extraction and it is important in the formation of micelle structure. In order that optimize the effect of incubation time on cloud point extraction, the samples were place to water bath at 50 °C. The optimization of time was carried out in the rage of 5-90 minutes. As can be seen in Figure 9, 30 min is enough for extraction efficiency. Therefore, in future studies, 30 minutes was used as the incubation time.

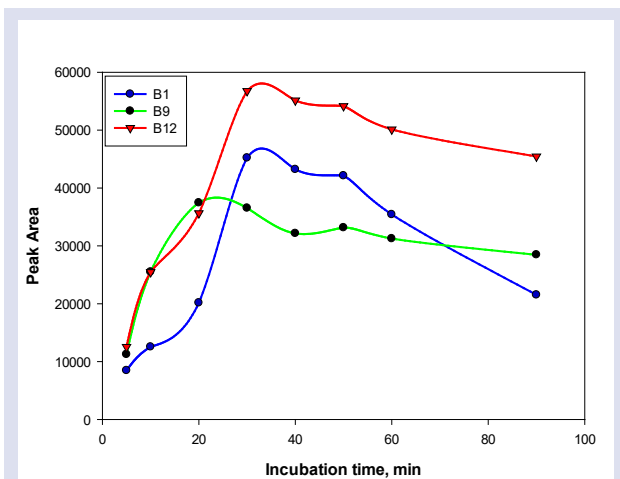


Figure 9. Effect of incubation time on the proposed method

Preparation of surfactant-rich phase for analysis

After centrifugation, the surfactant-rich phase was collected at the top of the tube. In order to facilitate the surfactant-rich phase (SRP) to be easily separated from the aqueous phase, the sample solutions were kept in the refrigerator for a while thus increasing the viscosity of the surfactant-rich phase. At the end of this period, the

aqueous phase was easily separated from the surfactant-rich phase with the help of an injector. After the aqueous phase has been separated, the surfactant-rich phase must be diluted with a suitable solvent before being introduced into the HPLC device. Because the phase with high viscosity is not suitable for injection as such and is not sufficient to receive a signal in the device. For this purpose, various solvents were tried to dissolve the surfactant-rich phase before the analysis. The solvent chosen should both completely dissolve the surfactant-rich phase and not damage the device to be determined.

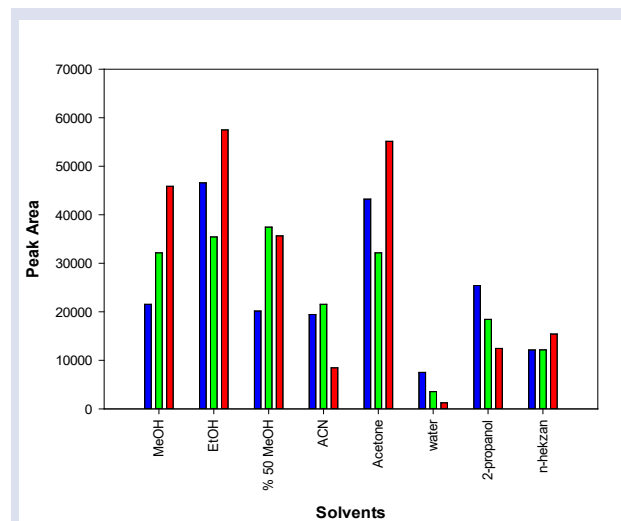


Figure 10. Effect of solvents for SRP

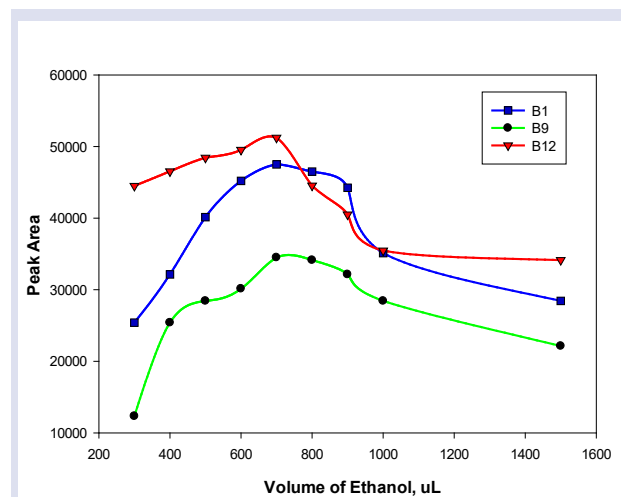


Figure 11. Volume of ethanol used for SRP

While selecting the solvents to be used for this purpose, it is desirable that the HPLC system be suitable for the operating stage and be strong enough to dissolve the SRP quantitatively. As can be seen in Figure 10, the best signal was obtained with ethanol. The surfactant-rich phase was dissolved with this solvent. Since the amount of solvent used to dissolve the surfactant-rich phase will directly affect the enrichment factor, it is important how much solvent volume is taken. To obtain a high enrichment coefficient, the solvent volume must be at the smallest value. The volume of ethanol was optimized in the range of 300-1500 µL of solvent as can be seen in

Figure 11. As a result of this study, the maximum signals were obtained with 700 μL of ethanol and this value was used in further studies.

Analytical Performance of the Developed Method

After each experimental variable of CPE was optimized, analytical merits of the developed method

were studied and calculated. The CPE experiments were applied to vitamin B solutions at different concentrations in order to determine the linear working range. As a results of this study, the signals increase in proportion to the concentration. All analytical parameters of the developed method were presented in Table 4.

Table 4. Analytical parameters of the developed method

Parameter	Before CPE		After CPE	
	B1, B9, B12	B1	B9	B12
Linearity	1.0-50.0 $\mu\text{g mL}^{-1}$	5-500.0 ng mL^{-1}	25.0-500.0 ng mL^{-1}	50.0-500.0 ng mL^{-1}
Limit of Detection	0.23 $\mu\text{g mL}^{-1}$	1.42 ng mL^{-1}	7.14 ng mL^{-1}	14.28 ng mL^{-1}
Limit of Quantification	0.94 $\mu\text{g mL}^{-1}$	4.71 ng mL^{-1}	23.57 ng mL^{-1}	47.14 ng mL^{-1}
Slope of Calibration	1,528	40.3	45.5	58.8
Correlation Coefficient (R^2)	0.9986	0.9945	0.9912	0.9875
Enrichment Factor ^a	-	21,4	21,4	21,4
Pre-concentration Factor ^b	-	26.4	29.8	38.5

^a It was calculated by taking the ratio of the volume initial and final (15 mL and 0.7 mL)

^b It was calculated by taking the ratios of the calibration slopes before and after CPE.

Conclusion

Cloud point extraction (CPE) is a widely used and increasingly common method for the separation and enrichment of both organic and inorganic species, especially in the last two decades. Hundreds of studies were published every year in this area. The CPE covers wide application areas for many different species and sample types. The main factors in finding so many application areas of the method are; It can be listed as simplicity, environmental friendly, low cost and easy applicability in almost every laboratory. All parameters that may have an effect on the method developed described throughout the experimental section of this paper have been optimized one by one. For the CPE process, the most effective CPE conditions were determined for method variables such as ambient pH, type and concentration of nonionic surfactants, electrolyte effect, incubation temperature, selection of suitable solvent for the surfactant-rich phase. After the optimization of a newly developed CPE method was completed and its analytical parameters were determined, it was applied to several model solutions in order to calculate analytical merits. This method can be easily applied for determination of B1, B9 and B12 vitamins simultaneously.

Acknowledgment

This study is graduation thesis of İpek Nur Yiğit who graduated from faculty of pharmacy in 2019. The experimental data was collected and arranged by helping with the other authors. Also, experimental studies of this study has been carried out by using project budgets supported by Cumhuriyet University Scientific Research Projects Commission.

Conflicts of interest

The authors state that did not have conflict of interests.

References

- [1] Brancaccio M., Mennitti C., Cesaro A., Fimiani F., Vano M., Gargiulo B., Caiazza M., Amodio F., Coto I., D'alicandro G., Mazzaccara C., Lombardo B., Pero R., Terracciano D., Limongelli G., Calabrò P., D'argenio V., Frisso G., Scudiero O., The Biological Role of Vitamins in Athletes' Muscle, Heart and Microbiota, *Int. J. Environ. Res. Public Health.*, 19 (2022) 1249.
- [2] Hashim N.H., Osman R., Abidin N.A.Z., N.S.A. Kassim N.A.Z., Recent trends in the quantification of vitamin b, *Malaysian J. Anal. Sci.*, 25 (2021) 466–482.
- [3] Hassan O., M.J. Chee, Sensitivity of UV detection in simultaneous separation and detection of B-vitamins using HPLC, *Malaysian J. Anal. Sci.* 7 (2001) 251–255.
- [4] Chan Y., Bailey R., O'Connor D.B., Advances in Nutrition, Folate 1, (2013) 123–125.
- [5] Aygun B., Açık Y.D., Vitamin B12 and Folic Acid Levels After Iron Therapy in Iron-Deficiency Anemia, *Cukurova Anestezi ve Cerrahi Bilim. Derg.*, 3 (2020) 261–267.
- [6] Ulusoy S., Erdoğan S., Karaslan M. G., Ateş B., Ulusoy H. İ. & Erdemoğlu S. Optimization Of Extraction Parameters For Folic Acid And Antioxidant Compounds From An Edible Plant (*Polygonum Cognatum* Meissn) Using Pressurized Liquid Extraction (PLE) System, *Cumhuriyet Sci. J.*, 39 (2018) 1069–1080.
- [7] Smith A. D., Warren M. J., Refsum, H. Vitamin B12, *Adv. Food Nutr. Res.*, 83 (2018) 215–279.
- [8] Osman D., Cooke A., Young T. R., Deery E., Robinson N. J., Warren M. J. The requirement for cobalt in vitamin B12: A paradigm for protein metalation, *Biochim. Biophys. Acta - Mol. Cell Res.*, 1868 (2021) 118896.
- [9] Ulusoy S., Ulusoy H.İ., Preconcentration and determination of safranin T in environmental water samples, *Environ. Eng. Manag. J.*, 17 (2018) 147–154.

- [10] Halko R., Hagarová I., Andruch V. Innovative approaches in cloud-point extraction, *J. Chromatogr. A*, 1701 (2023) 464053.
- [11] Bezerra M. D. A., Arruda M. A. Z. and Ferreira S. L. Cloud point extraction as a procedure of separation and pre-concentration for metal determination using spectroanalytical techniques: a review, *Applied Spectroscopy Reviews*, 40 (4) (2005) 269-299.
- [12] Karaca E., Ulusoy S., Morgül U., Ulusoy H.I. Development of Analytical Method for Sensitive Determination of Streptozotocin based on Solid Phase Extraction, *Cumhuriyet Sci. J.*, 41 (2020) 826–831.
- [13] Pragst F. Application of solid-phase microextraction in analytical toxicology, *Anal. Bioanal. Chem.*, 388 (2007) 1393–1414.
- [14] Ulusoy H.I., Yilmaz Ö., Gürkan R. A micellar improved method for trace levels selenium quantification in food samples, alcoholic and nonalcoholic beverages through CPE/FAAS, *Food Chem.*, 139 (2013) 1008–1014.
- [15] Ulusoy H.I., Acidereli H., Ulusoy S., Erdoğan S. Development of a New Methodology for Determination of Vitamin B9 at Trace Levels by Ultrasonic-Assisted Cloud Point Extraction Prior to HPLC, *Food Anal. Methods*, 10 (2017) 799–808.
- [16] Ulusoy S., Akçay M. Simultaneous Determination of Vitamins B1 and B2 in Food Samples by Modified Cloud Point Extraction Method and HPLC-DAD, *Food Anal. Methods*, 11 (2018) 260–269.
- [17] Kori S. Cloud point extraction coupled with back extraction: a green methodology in analytical chemistry, *Forensic Sci. Res.*, 6 (2021) 19–33.
- [18] Kojro, G., Rudzki, P. J., Pisklak, D. M. and Giebułtowicz, J. Matrix effect screening for cloud-point extraction combined with liquid chromatography coupled to mass spectrometry: bioanalysis of pharmaceuticals, *Journal of Chromatography A*, 1591 (2019) 44-54.

Investigation of Antiviral Activities of Nickel and Copper Complexes with Macrocyclic Ligands against Crimean-Congo Hemorrhagic Fever by In Silico Calculations

Sultan Erkan ^{1,a,*}, Niyazi Bulut ^{2,b}, Duran Karakaş ^{1,c}¹ Chemistry Department, Science Faculty, Sivas Cumhuriyet University, Sivas, Türkiye² Department of Physics, Faculty of Science, Fırat University, 23119, Elazığ, Türkiye

*Corresponding author

Research Article

History

Received: 16/10/2022

Accepted: 15/12/2023

Copyright

©2023 Faculty of Science,
Sivas Cumhuriyet University

ABSTRACT

For the first time, electronic characteristics of potential drug candidates and their inhibitory activities have been linked thanks to this work. Synthesized copper and nickel complexes with trans-N1,N8-bis(2-cyanoethyl)-2,4,4,9,11,11-hexamethyl-1,5,8,12-tetraazacyclotetradecane (tet-bx) ligand, as well as the proposed hypothetical complexes, were properly examined by the appropriate calculation method in atomic and molecular dimensions. The appropriate calculation level was achieved by using the IR spectroscopic data of the tet-bx ligand. The experimental and calculated bond stretching frequencies were compared for synthesized complexes [Ni(tet-bx)](ClO₄)₂ (1), [Cu(tet-bx)](ClO₄)₂ (2), [Ni(tet-bx)(NCS)₂] (3), and [Ni(tet-bx)(ClO₄)Cl] (5). Some bond stretching frequencies of hypothetical complexes [Cu(tet-bx)(NCS)₂] (4) and [Cu(tet-bx)(ClO₄)Cl] (6) have also been proposed and their molecular structure were determined. To analyze the electronic behavior of the examined complexes at the atomic level, Fukui function indices (nucleophilic *f*⁺ and electrophilic *f*⁻ populations) were determined. Furthermore, antibacterial and antiviral inhibition efficiency of the complexes against Crimean-Congo hemorrhagic fever has been investigated by docking studies.

Keywords: Fukui function indices, Molecular docking, Crimean-Congo.^a sultanerkan58@gmail.com
^c dkarakas@cumhuriyet.edu.tr^{id} <https://orcid.org/0000-0001-6744-929X>
^{id} <https://orcid.org/0000-0002-6770-3726>^b bulut_niyazi@yahoo.com^{id} <https://orcid.org/0000-0003-2863-7700>

Introduction

Macrocyclic ligands and their metal complexes have a wide field of study in coordination chemistry. Tetraazamacrocyclic ligands provide application area with wide perspective thanks to donor nitrogen atoms. Metal ions can bind to the macrocyclic cavity [1,2]. In addition, their electronic behaviour may change by the donor and accepting groups. Complexes with macrocyclic ligands are called chelates. Chelates are of biological importance due to activities of antibacterial, antifungal and antitumor. Therefore, chelates have been evaluated in the pharmacological field [3]. In recent years, they have been used as contrast-enhanced magnetic resonance imaging (MRI) agents and even radio immunotherapeutic agents in the field of radiology [4].

In recent years a number of compounds to be tested can be reduced and the design based on the structure required in treatment can be provided thanks to the in silico (or virtual) compound design [5]. The pharmaceutical industry increasingly uses modern medicinal chemistry methods with molecular modelling [6]. Molecular and structural drug design has been developed with spectroscopic methods. In this way, the three-dimensional protein structure is obtained and provided structural information about drug targets and drug candidates [7]. Drug candidate compounds are

interacted with target proteins representing biological structures with the aid of simulation [8].

Crimean-Congo haemorrhagic fever (CCHFV) is a tick-borne viral disease. The efficacy of therapeutic options has not been proven in clinical trials for viral disease with a high mortality rate [9]. Drug developments that can be the basis of treatment continue [10].

In this study, synthesized and hypothetical complexes are investigated by computational chemistry methods. The appropriate calculation level is determined according to some bond stretching frequencies of tet-bx ligand. IR spectra of previously synthesized complexes (1), (2), (3) and (5) are computed with the appropriate computational level and are compared with the experimental data. IR spectra of the (4) and (6) hypothetical complexes are proposed. The nucleophilic and electrophilic behaviours of the atoms in the studied complexes can be separated by Fukui function indices. Antibacterial properties are examined and detailed with the help of molecular docking. From the docking results of the investigated complexes, their suitability for Crimean-Congo haemorrhagic fever is discussed. In docking studies, the types of interaction between the amino acid residues of target proteins and the atoms in the complexes are examined. The behaviour of the atoms that play an active role in the interaction types of (1) - (6) complexes are

compared with the electronic behaviours obtained from Fukui functions.

Materials and Methods

The complexes structures of (1) - (6) were drawn in the GaussView 6.0.16 program [11]. Optimization and vibration frequency calculations for tet-bx were made at B3LYP, B3PW91 and M062X methods [12-14]. LANL2DZ (for metal atoms) [15] and 6-31G(d) (for other atoms) [16] basis sets used for electron spin selection. All calculations performed in Gaussian 09: AS64L-G09RevD.01 program and no imaginary frequency was obtained [17]. The complexes and proteins examined in MMFF94 method were optimized with DockingServer [18]. Charge calculations were carried out using the Gasteiger method. Neutral medium (pH = 7.0) was used in all calculations. The dimensions of the grid maps were $90 \times 90 \times 90 \text{ \AA}$ (x, y and z) and were calculated by the Solis Wets local search method and Lamarckian genetic algorithm [19].

Result and Discussion

Determination of Calculation Level

One of the spectroscopic analysis methods that may be obtained in depth using computational chemistry approaches is the infrared spectrum. It's also one of the factors that goes into choosing the calculation level [20]. The field of study offers quite a lot of computation levels with many methods and basis sets. Density Functional Theory (DFT) is an approach that gives the most reasonable results. For this purpose, the B3LYP, B3PW91 and M062X methods were chosen for including the DFT. As the basis set, LANL2DZ for metal atoms and 6-31G(d) for other atoms were preferred. The experimental and calculated with different DFT methods some vibrational frequencies and the corresponding regression coefficient (R^2) values are given in Table 1 for the tet-bx ligand and the molecular structure are pictured in Figure 1.

Table 1. Some experimental and calculated stretching frequencies of tet-bx ligand.

	Exp.	B3LYP	B3PW91	M062X
$\nu_{\text{N-H}}$	3271	3448	3434	3300
$\nu_{\text{C-H}}$	2965	2946	2928	2973
ν_{CH_3}	1385	1431	1416	1367
$\nu_{\text{C-C}}$	1141	1236	1217	1179
$\nu_{\text{C}\equiv\text{N}}$	2245	2342	2338	2315
R^2	-	0.9943	0.9941	0.9988

Vibration frequencies are in cm^{-1} unit.

The calculated frequencies listed in Table 1 are the anharmonic frequencies. Anharmonic frequencies are obtained by multiplying the harmonic frequencies with the scale factor suitable for the studying level.

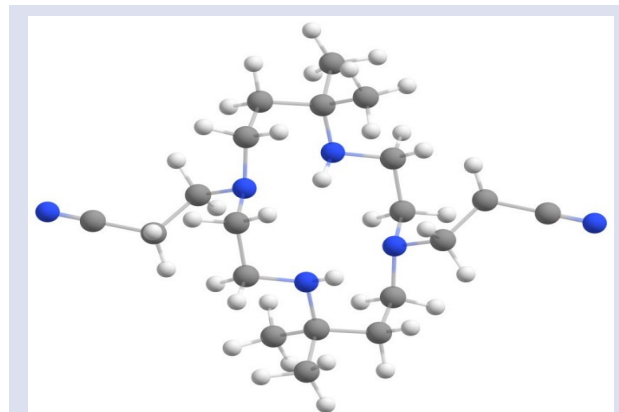


Figure 1. Optimized structure of tet-bx ligand.

The scale factor for B3LYP/6-31g(d) and B3PW91/6-31g(d) levels were taken as 0.991 and 0.986, respectively [21]. The scale factor is selected as 0.9496 for level M062X/6-31G(d) [22]. The N-H bond stretching frequency obtained at the experimental 3271 cm^{-1} was calculated as 3300 cm^{-1} at the M062X/6-31G(d) level. The C-H bond stretching frequency with an experimental value of 2965 cm^{-1} was calculated as 2946 cm^{-1} with B3LYP, 2928 cm^{-1} with B3PW91 and 2973 cm^{-1} with M062X. As seen in Table 1, the closest experimental value for CH_3 bond stretching was obtained as 1367 cm^{-1} at the M062X level. The calculated values of the $\text{C}\equiv\text{N}$ bond stretching are 2342 cm^{-1} for B3LYP, 2338 cm^{-1} for B3PW91 and 2315 cm^{-1} for M062X. As a result, the most suitable level was determined as M062X/6-31G(d) level. According to the simple linear regression analysis, the calculation level with R^2 value close to 1 was used for other calculations.

Optimized Structure

$[\text{Ni}(\text{tet-bx})(\text{ClO}_4)_2]$ (1), $[\text{Cu}(\text{tet-bx})(\text{ClO}_4)_2]$ (2), $[\text{Ni}(\text{tet-bx})(\text{NCS})_2]$ (3) and $[\text{Ni}(\text{tet-bx})(\text{ClO}_4)\text{Cl}]$ (5) complexes were synthesized by Roy et al at 2021 [23]. In addition to nickel complexes, hypothetical copper complexes ($[\text{Cu}(\text{tet-bx})(\text{NCS})_2]$ (4) and $[\text{Cu}(\text{tet-bx})\text{Cl}(\text{ClO}_4)]$ (6)) were also investigated considering the difference in molecular properties of electron-releasing (ClO_4 , NCS) and electron donating (Cl) groups with inductive effect. Figure 2 depicts the optimal structures of the hexamethyl tetraazamacrocyclic ligand, as well as synthetic and hypothesized nickel-copper complexes containing this ligand. These structures were discovered at M062X/LANL2DZ/6-31G(d) in the gas phase.

The molecular properties of these electron-rich structures, which are quite large in volume and difficult to analyze, are quite a struggle at the molecular level. It has been observed that the optimized structures form the six coordinated octahedral nickel (II) and copper (II) complexes by axial addition of the four coordinated square-planar nickel (II) and copper (II) complexes.

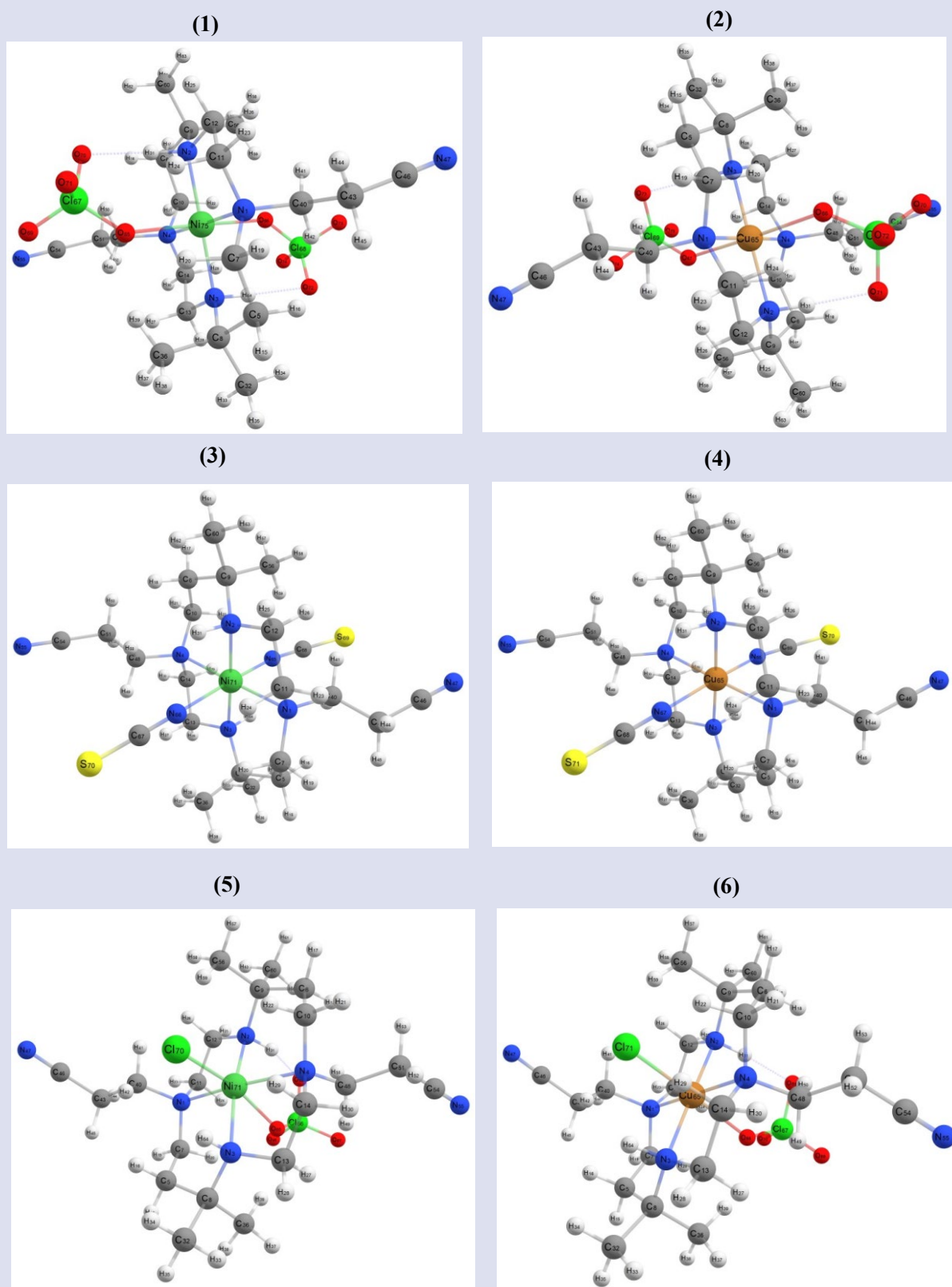


Figure 2. Optimized structure of investigated complexes.

IR Spectra Analysis

IR spectra of the studied complexes were calculated to obtain information about functional groups. For this purpose, IR spectra of the synthesized complexes ((1), (2), (3) and (5)) and hypothetical complexes ((4) and (6)) are

listed in Table 2. The results of the spectrums calculated at the M062X/LANL2DZ/6-31G(d) level were compared with the experimental data. In this analysis, the peaks with the highest intensity were taken into account. In this analysis, labeling was made with the help of the animation, considering the peaks with the highest intensity.

Table 2. IR spectral data of the metal complexes.

Comp.	(1)		(2)		(3)		(4)		(5)		(6)	
Modes	Exp.	Calc.	Exp.	Calc.	Exp.	Calc.	Calc.	Exp.	Calc.	Calc.	Exp.	Calc.
vN-H	3167	3207	3182	3190	3217	3270	3376	3147	3223	3214		
vC-H	2997	3004	2974	2953	2970	2955	2928	2960	2954	2924		
vCH3	1383	1372	1380	1359	1381	1373	1413	1371	1358	1354		
vC-C	1157	1151	1153	1148	1180	1171	1119	1186	1181	1172		
vM-N	532		538	536	540	545	566	522	522	515		
vC≡N	2245	2319	2256	2313	2249	2301	2319	2245	2316	2311		
vCl-O	1087	1053	1087	1084	-	-	-	1095	1068	1066		
vM-N	624	596	-	-	-	-	-	613	577	-		
vM-Cl	-	-	-	-	-	-	-	-	-	873		
vM-O	-	-	1041	976	-	-	-	-	-	-		
vC≡N	-	-	-	-	2063	2063	-	-	-	-		
vCN	-	-	-	-	-	-	1030	-	-	-		
vCS	-	-	-	-	862	773	800	-	-	-		
δNCS	-	-	-	-	478	474	-	-	-	-		

v: stretching, δ: Scissoring

When looking at the data in Table 2, it was discovered that the analyzed complexes peaked at similar frequencies. The designation of frequencies that qualify empirically as other is a specific distinction in this section. Complex (1) has an experimental value of 1087 cm⁻¹, which corresponds to a calculated Cl-O bond stretching frequency of 1053 cm⁻¹. In addition, the experimental frequency at 624 cm⁻¹ was labeled as the metal nitrogen vibration mode at 596 cm⁻¹. Experimental Cl-O bond stretching frequency for complex (2), at 1087 cm⁻¹ was calculated as 1084 cm⁻¹, and M-O bond stretching frequency at 1041 cm⁻¹ was computed as 976 cm⁻¹. The calculated results are quite compatible with the experimental values according to the relevant labeling. In addition, the scissoring mode was experimentally found to be 478 cm⁻¹. In the calculation, it was determined as scissoring mode at 474 cm⁻¹. Scissoring mode for complex (3), has been taken into account as it is a high-intensity peak. Depending on the harmony of the experimental and the calculation results, the bond stretching frequencies of the hypothetical complexes (4) and (6) can be boldly suggested. The bond stretching frequency for complex (4) at 1030 cm⁻¹ was assigned to bond stretching containing the single bond carbon-nitrogen. The frequency at 800 cm⁻¹ is the C-S bond stretching mode. For complex (6), the frequency at 1066 cm⁻¹ was labeled as Cl-O bond stretching with the help of animation.

Chemical Reactivity

Computational chemistry methods allow reactivity analysis of the chemical species under study. The reactivity analysis of a chemical species can be interpreted by the quantum chemical parameters such as hardness (η), softness (σ), chemical potential (μ) and electronegativity (χ). Relevant parameters for reactivity analysis of ligands and complexes were calculated with Equations (1)-(3) and given in Table 3.

$$\mu = -\chi = \left[\frac{\partial E}{\partial N} \right]_{v(r)} = -\left(\frac{I + A}{2} \right) \quad (1)$$

$$\eta = \frac{1}{2} \left[\frac{\partial^2 E}{\partial N^2} \right]_{v(r)} = \frac{I - A}{2} \quad (2)$$

$$\sigma = 1 / \eta \quad (3)$$

Table 3. Quantum chemical parameters of metal complexes.

Compounds	η (eV)	σ (eV ⁻¹)	χ (eV)	μ (eV ⁻¹)
(1)	3.4247	0.2920	4.4656	-4.4656
(2)	5.0838	0.1967	3.8465	-3.8465
(3)	2.8458	0.3514	3.9879	-3.9879
(4)	3.6542	0.2737	2.4558	-2.4558
(5)	3.4247	0.2920	4.4656	-4.4656
(6)	4.7216	0.2118	3.6593	-3.6593

When Table 3 is examined for the reactivity relationship of the complexes, it is noted that the hardness parameter of copper complexes is generally higher. In relation to this parameter, the softness value of complex (3) is the highest. Hard molecules have high energy gap values and softness is the multiplicative inverse of hardness. According to the Maximum Hardness Principle, molecules arrange themselves to be as hard as possible. Therefore, chemical hardness is a measure of stability.

Electronic Behavior of Atoms in the Complexes

The major aim of this part is to investigate the molecular behavioural aspects of atomic locations in pharmacological investigations. In drug design, predicting of the charge of the atoms in complex it can be useful. In this study, Fukui function indices are used to predict the electronic behaviour of atoms in studied complexes. The electronic density of the system against the number of electrons at a constant external potential is used to calculate Fukui functions using the finite difference

approximation of the first derivative. Fukui functions, according to this method, are provided by the following Equations (4)- (6) [24].

$$f_k^+ = q_k(N+1) - q_k(N) \quad (4)$$

$$f_k^- = q_k(N) - q_k(N-1) \quad (5)$$

$$f_k^0 = \frac{1}{2}[q_k(N+1) - q_k(N-1)] \quad (6)$$

From top to bottom, these equations reflect the selectivity of a molecule's nucleophilic, electrophilic, and radical attack sites, respectively. In neutral (N), anionic

(N+1), and cationic (N-1) states, q_k is the atomic charges in the k th atomic region of a molecule. Fukui function indices of the investigated complexes are given Table S1-S3 and Figure S1. The Fukui function indices of the atoms in the complexes are given graphically in Figure 3, except for indices in the range 0-0.01. The f^+ and f^- values are considered while describing donor-receptor interactions. Electronically, the nucleophilic (f^+) and electrophilic (f^-) populations correspond to Fukui function indices of atomic sites. Positive values are denoted by (f^+), whereas negative values are denoted by (f^-). The tendency to donate electrons increases with increasing positive charge.

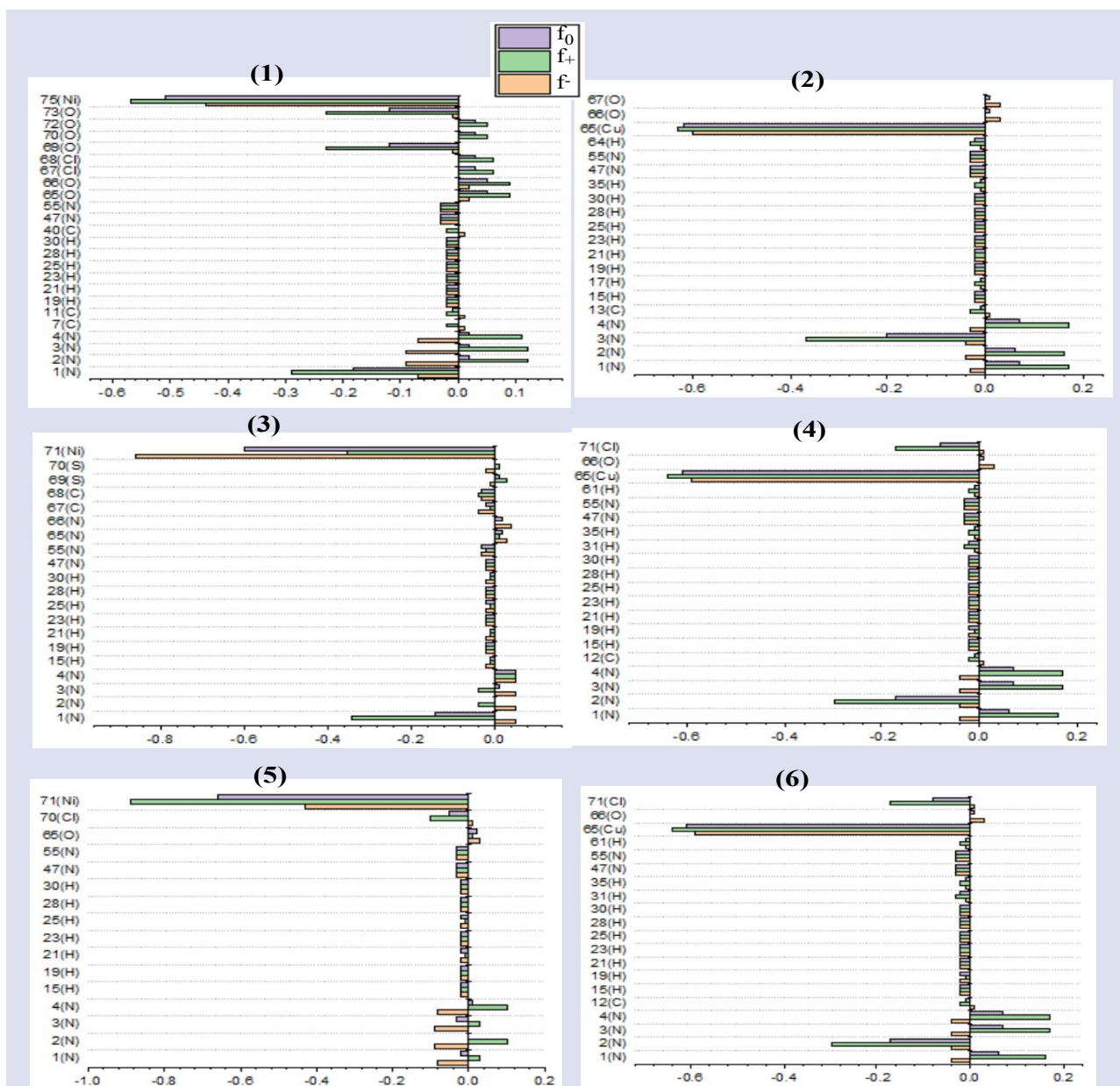


Figure 2. Graphical representation of Fukui function indices for investigated complexes.

With increasing negative charge, the ability of atomic sites to receive electrons increases. Metal atoms in all complexes have the biggest negative peak in terms of Fukui function indices, as seen in Figure 3. The electrical behaviour, on the other hand, varies depending on the type of metal and the ligand connected to it. The electrical

richness of metal complexes is analogous to this condition.

The electrophilic property of the metal atoms in the complexes appears to be more prominent. Furthermore, 73O, 69O and 1N electrophilic, 2N, 3N, 4N, and other

oxygen atoms exhibit nucleophilic activity in complex (1). The 1N and 2N act as electron donors in complex (2), whereas the 3N and 4N act as electron acceptors. Complexes (3) with 7OS and 1N atoms and complex (4) with 71Cl and 2N atoms have a high potential to receive electrons. In complex (5), 1N and 3N atoms have a strong inclination to gain electrons, whereas the 1N, 3N and 4N atoms in complex (6) have a strong inclination to donate electrons.

Molecular Docking Studies

Molecular docking studies allow to examine drug design at the molecular atomic level. Binding energies and interaction types of the drug candidate substances with the proteins can be determined with molecular docking studies. Thus, it can be predicted whether the drug candidate molecule has anticancer, antibacterial, antifungal and antiviral properties. Cellular sized protein structures are obtained from the protein data bank. Amino acid residues in each protein with drug candidate molecules exhibit different types of interaction. It has been stated that the previously synthesized complexes (1), (2), (3) and (5) have antimicrobial activity against *Bacillus cereus*, *Staphylococcus aureus*, *Salmonella typhi* and *Pseudomonas aeruginosa*. Protein codes for these gram-positive bacteria species and gram-negative bacteria species are 5V8E [25], 5YHG [26], 6V4O [27] and 4NX9 [28], respectively.

In addition to docking studies against bacterial cell types, there is still an undeveloped pharmaceutical industry for Crimean Congo haemorrhagic fever. The inhibition efficiency of the complexes examined with the help of docking will be investigated for this viral disease,

which has caused the increase in mortality rates in recent years. There are five different protein structures of the Crimean-Congo haemorrhagic disease determined in the literature. These are Crimean Congo Haemorrhagic Fever Gn zinc finger (PDB ID=2L7X) [29], Structural analysis of a viral OTU domain protease from the Crimean-Congo Haemorrhagic Fever virus in complex with human ubiquitin (PDB ID=3PRP) [30], Envelope glycoprotein from tick-borne encephalitis virus (PDB ID=1SVB) [31], A RNA binding protein from Crimean-Congo haemorrhagic fever virus (PDB ID=3U3I) [32] and The cryo-EM structure of Tick-borne encephalitis virus complexed with Fab fragment of neutralizing antibody (PDB ID=5O6V) [33]. The binding energies and interaction types of synthesized and hypothetical complexes with target proteins determined for antibacterial and antiviral effects were examined. The effective roles of nucleophilic and electrophilic atoms determined by Fukui function indices were investigated.

To test its antibacterial activity, the studied complexes were docked against 5V8E, 5YHG, 6V4O and 4NX9 cell lines, and the molecular docking results are given in Table 3. To estimate the antiviral activity, the studied complexes were docked against the 2L7X, 3PRP, 1SVB, 3U3I and 5O6V cell lines and the results are presented in Table 4. Additionally, the secondary chemical interactions between the amino acid residues of the atoms in the complexes are given in Tables 4 and 5 in terms of antibacterial and antiviral, respectively. Moreover, binding modes of studied complexes with the identified 1SVB target proteins are given in Figures 3. For the reliability of the results, calculations were made with and DockingServer [34].

Table 4. Docking energy results of complexes (1)-(6) for antibacterial effect

Complex	5V8E		5YHG		6V4O		4NX9	
	E_{Bind}	E_s	E_{Bind}	E_s	E_{Bind}	E_s	E_{Bind}	E_s
(1)	-5.06	-5.36	-9.64	-9.63	-5.56	-5.97	-5.40	-5.26
(2)	-5.97	-6.95	-9.47	-9.78	-5.09	-4.58	-5.16	-4.87
(3)	-6.15	-5.94	-9.49	-9.56	-5.53	-5.30	-5.07	-4.87
(4)	-6.34	-6.97	-8.30	-8.82	-5.84	-4.88	-4.99	-4.59
(5)	-6.13	-7.61	-8.76	-9.05	-4.90	-5.89	-4.97	-4.72
(6)	-5.94	-7.86	-7.79	-8.20	-5.26	-4.52	-4.98	-4.90
Ampicillin	-4.72	-4.57	-4.65	-4.17	-4.04	-4.43	-4.50	-4.45

E_{Bind} : Est. Free Energy of Binding (kcal/mol), E_s : vdW + Hbond + desolve Energy (kcal/mol)

With docking studies in the first step, the antibacterial effects of the complexes on gram-positive and gram-negative bacterial species were investigated. The obtained calculation results and experimental data were compared. According to the experimental data, the inhibition efficiency of complex (3) against *Bacillus cereus* bacteria species is higher than complexes (1), (2) and (5) [23]. Docking results are consistent with the experimental findings.

Because the estimated free energy of binding (E_{Bind}) of complex (3) was calculated as -6.15 kcal/mol in the interaction of the investigated complexes with the 5V8E target protein. This value is greater than the estimated free energy of binding of other complexes and reference material. In addition, it was concluded that the complexes (2), (3) and (5) with the same antibacterial effects had different E_{bind} and E_s values according to the docking results.

Table 5. Docking energy results of complexes (1)-(6) for Crimean Congo

Complex	2L7X		3PRP		1SVB		3U3I		5O6V	
	E _{Bind}	E _s	E _{Bind}	E _s	E _{Bind}	E _s	E _{Bind}	E _s	E _{Bind}	E _s
(1)	-4.68	-5.51	+317.06	+312.09	-4.19	-5.44	-4.67	-6.85	-4.01	-4.56
(2)	-5.42	-6.04	+146.59	+139.50	-5.23	-5.59	-5.14	-6.73	-6.03	-6.32
(3)	-5.32	-6.46	+368.02	+365.92	-4.68	-5.17	-5.02	-6.59	-5.79	-6.16
(4)	-5.31	-6.22	+208.49	+206.91	-4.46	-5.21	-5.19	-6.60	-4.80	-5.48
(5)	-5.00	-6.39	+14.74	+12.65	-4.23	-5.66	-4.95	-6.32	-5.23	-6.71
(6)	-5.48	-4.28	+6.40	+3.74	-4.48	-4.75	-5.27	-7.76	-5.35	-5.93
Ribiravin	-4.48	-4.08	-3.65	-4.07	-3.27	-4.39	-3.90	-5.08	-3.22	-3.76

E_{Bind}: Est. Free Energy of Binding (kcal/mol), E_s: vdW + Hbond + desolve Energy (kcal/mol)

The fact that the docking results are highly consistent with the experimental data allows discussing the advantages and disadvantages of all the complexes studied for Crimean-Congo hemorrhagic fever. There are five different protein structures described in the literature for Crimean-Congo hemorrhagic fever. As shown in Table 5, except for 3PRP target protein, Complexes (1) - (6) exhibit higher inhibitory activity than reference Ribiravine. Positive data at E_{Bind} values given in Table 5 indicate that the drug candidate complexes have no inhibitory activity on the related target protein. Negative increase in E_{Bind} values highlights the high inhibitory efficiency of the drug candidate. According to the results from Table 5, in general ClO₄⁻ substituted copper complexes are more biologically active than ClO₄⁻ substituted nickel complexes.

In addition, the inhibition efficiency of nickel complexes with NCS ligands on target proteins is generally higher than copper complexes with NCS ligands.

The secondary chemical interactions between the investigated complexes and the target proteins were investigated. The types of interaction of complexes (1) - (6) with amino acid residues of antibacterial cell proteins are given in Tables S4-S7 in Supplementary Materials. Data including secondary chemical interactions of complexes with amino acid residues of the target proteins of PDB ID: 2L7X, 3PRP, 3U3I and 5O6V representing Crimean-Congo hemorrhagic fever are given in Tables S8-S12 in the Supplementary Materials. In addition, the interaction types between PDB ID: 1SVB with (1) - (6) are given in Table 6.

Table 6. Interaction types between investigated complexes and 1SVB target protein

	Hydrogen Bonds	Polar	Hydrophobic
(1)- 1SVB	N-LYS284 N-GLY28	N-ASN8 N-GLU26 N-LYS284	C-LEU27
(2)- 1SVB	N-ASP46	N-ARG2 N-TRP44 N-LYS284	C-LEU27 C-ALA47 C-HIS282
(3)- 1SVB	N-LEU27	N-LYS284	C-LEU27 C-PRO272 C-VAL273
(4)- 1SVB	N-LEU27	-	C-LEU27 C-PRO272 C-VAL273
(5)- 1SVB	N-ASP46	N-ARG2 N-TRP44 N-ASP46 N-ARG160 N-LYS284	C-LEU27 C-HIS282
(6)- 1SVB	N-VAL273 N-LYS284	N-LYS284	C-LEU27 C-VAL273

According to Table 6, nitrogen atoms of complex (1) formed H-bond with LYS284 and GLY28 amino acid residues of 1SVB protein. Again, the nitrogen atoms of complex (1) are in polar interaction with the ASN8 amino acid residue of the 1SVB protein. In addition, the carbon atom of complex (1) exhibits hydrophobic interaction with

LEU27. The interactions of the other complexes with the amino acid residues of the 1SVB target protein are shown in Table 6. In addition, the mode of binding of the investigated complexes with the 1SVB target protein is given in Figure 4.

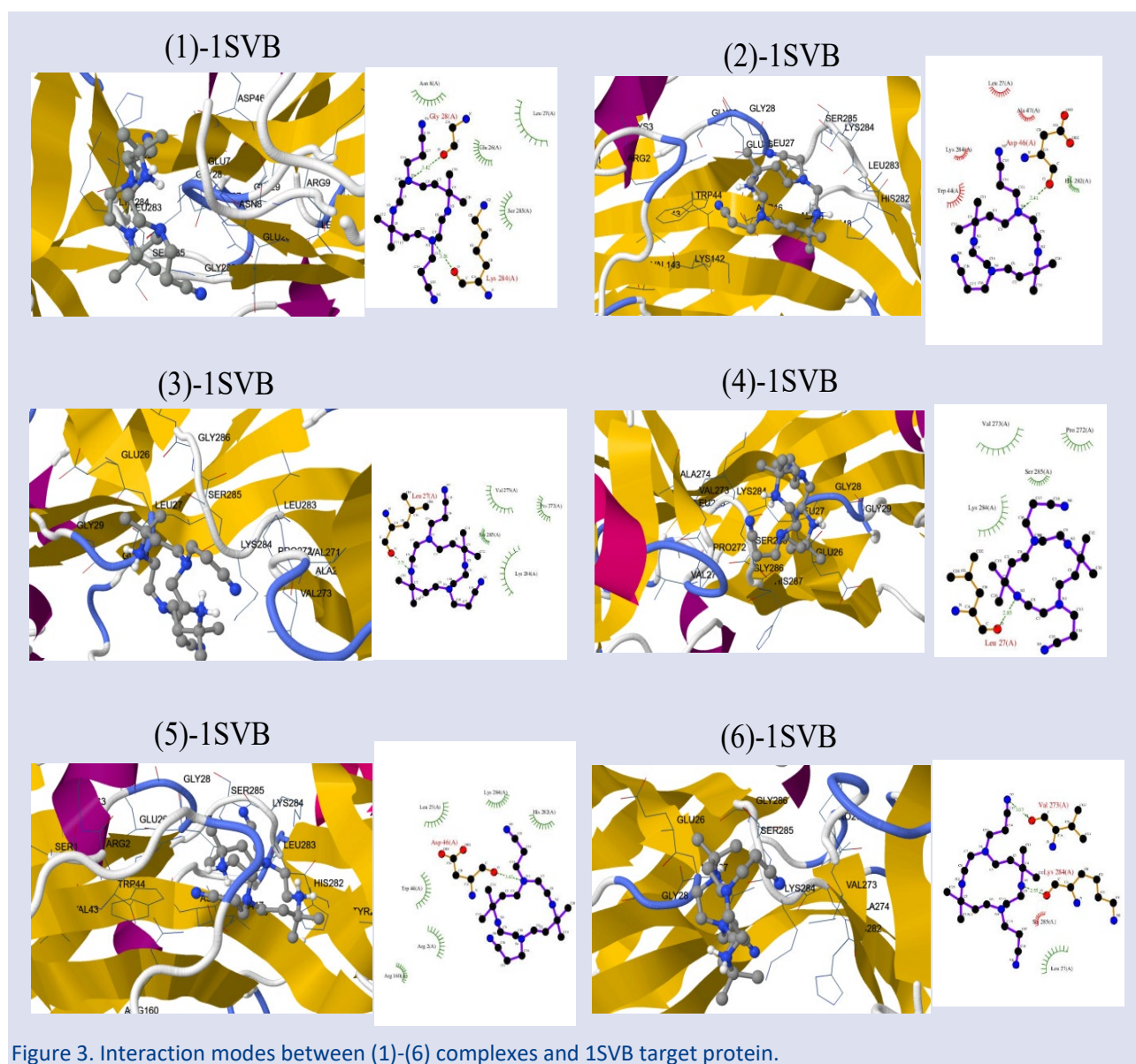


Figure 3. Interaction modes between (1)-(6) complexes and 1SVB target protein.

The investigated interaction results show that the nucleophilic nitrogen atoms obtained from the Fukui functions formed H-bonds with the amino acid residues of the target proteins. Electrophilic nitrogen and carbon atoms determined by Fukui functions exhibit polar interaction and hydrophobic interactions. With this manuscript, which was conducted for the first time in the literature, pioneering approaches for drug development can be presented. Interactions of nucleophilic and electrophilic atoms in drug candidate molecules with target proteins can be predicted in *in silico* studies. In this way, the interactions of the drug studied in drug modelling with target proteins can be improved and their biological activities can be improved.

Conclusion

The vibrational frequencies of the synthesized tet-bx ligand were compared experimentally and using several DFT approaches. The M062X/6-31g(d) level was judged to be the ideal calculation level based on linear regression

coefficients (R^2), and all computational studies were conducted using the M062X approach. Hypothetical complexes (4) and (6) were hypothesized based on the experimentally synthesized complexes (1), (2), (3), and (5). The values calculated with the experimental certain bond stretching frequencies were compared for the complexes (1), (2), (3), and (5), and the experimental and computational data were determined to be comparable according to the comparison results. For the structural investigation of complexes (4) and (6), some needed bond stretching frequencies were provided. Fukui function indices were used to differentiate the nucleophilic and electrophilic characteristics of the atoms in the studied complexes. The biological activities at the molecular level of the complexes whose antibacterial properties were shown to be experimentally high were investigated using docking studies. The complexes' usefulness for the treatment of Crimean-Congo hemorrhagic illness was also studied. The inhibition activities of the complexes on all target proteins in the literature representing the Crimean Congo were investigated. The investigated complexes

yielded higher binding energies compared to the reference Ribiravine with all target proteins except PDB ID: 3PRP. The nucleophilic atoms produced by Fukui functions have been found to have secondary chemical interactions with the target proteins' amino acid residues. Finally, it was determined that the chemical species chosen for drug design against antibacterial and Crimean Congo should have nucleophilic substituent.

Acknowledgments

The numerical calculations reported in this paper were fully/partially performed at TUBITAK ULAKBIM, High Performance and Grid Computing Center (TRUBA resources). NB would like to thank FIRAT University Scientific Research Projects Unit (Project number: FF.20.22).

Conflicts of interest

The authors have made the following contributions to this article. Niyazi Bulut: The calculation of tet-bx ligand and their nickel and copper complexes. Duran Karakaş: Determination of target proteins suitable for antibacterial and Crimean-Congo hemorrhagic fever, creating figures and tables. Sultan Erkan: Design of complexes, the collection and interpretation of all calculation results and writing of the article.

References

- [1] Martell, A. E., Smith, R. M., Critical stability constants, vol 3 Plenum Press. New York, NY, (1977).
- [2] Hassan, M. M., Kinetics and mechanism of complex formation of a pendant arm macrocycle reacting with copper (II) and mercury (II), *J. Saudi Chem. Soc.*, 13(2) (2009) 185-190.
- [3] Shankarwar, S. G., Nagolkar, B. B., Shelke, V. A., Chondhekar, T. K., Synthesis, spectral, thermal and antimicrobial studies of transition metal complexes of 14-membered tetraaza [N4] macrocyclic ligand, *Spectrochim. Acta, Part A*, 145 (2015) 188-193.
- [4] Bernhardt, P. V., Sharpe, P. C., C-substituted macrocycles as candidates for radioimmunotherapy, *Inorg. Chem.*, 39 (18) (2000) 4123-4129.
- [5] Hughes, J. P., Rees, S., Kalindjian, S. B., Philpott, K. L., Principles of early drug discovery, *Br. J. Pharmacol.*, 162 (6) (2011) 1239-1249.
- [6] Lipinski, C. A., Lombardo, F., Dominy, B. W., Feeney, P. J., Experimental and computational approaches to estimate solubility and permeability in drug discovery and development settings, *Adv. Drug Delivery Rev.*, 23(1-3) (1997) 3-25.
- [7] Erkan, S., Activity of the rocuronium molecule and its derivatives: A theoretical calculation, *J. Mol. Struct.*, 1189 (2019) 257-264.
- [8] Kaya, S., Erkan, S., Karakaş, D., Computational investigation of molecular structures, spectroscopic properties and antitumor-antibacterial activities of some Schiff bases, *Spectrochim. Acta, Part A*, 244 (2021) 118829.
- [9] Zivcec, M., Scholte, F. E., Spiropoulou, C. F., Spengler, J. R., Bergeron, É., Molecular insights into Crimean-Congo hemorrhagic fever virus, *Viruses*, 8(4) (2016) 106.
- [10] Guo, Y., Wang, W., Ji, W., Deng, M., Sun, Y., Zhou, H., ... Rao, Z., Crimean-Congo hemorrhagic fever virus nucleoprotein reveals endonuclease activity in bunyaviruses, *Proc. Natl. Acad. Sci. U.S.A.*, 109(13) (2012) 5046-5051.
- [11] Sharifi, A., Amanlou, A., Moosavi-Movahedi, F., Golestanian, S., Amanlou, M., Tetracyclines as a potential antiviral therapy against Crimean Congo hemorrhagic fever virus: Docking and molecular dynamic studies, *Comput. Biol. Chem.*, 70 (2017) 1-6.
- [12] R.D. Dennington, T.A. Keith, J.M. Millam, GaussView 6.0. 16, Semichem. Inc., Shawnee Mission KS, 2016.
- [13] Becke, A. D. Perspective: Fifty years of density-functional theory in chemical physics, *J. Chem. Phys.*, 140(18) (2014) 18A301.
- [14] Lee, C., Yang, W., Parr, R. G., Development of the Colle-Salvetti correlation-energy formula into a functional of the electron density, *Phys. Rev. B*, 37(2) (1988) 785.
- [15] Zhao, Y., Truhlar, D. G., The M06 suite of density functionals for main group thermochemistry, thermochemical kinetics, noncovalent interactions, excited states, and transition elements: two new functionals and systematic testing of four M06-class functionals and 12 other functionals, *Theor. Chem. Acc.*, 120(1-3) (2008) 215-241.
- [16] Check, C. E., Faust, T. O., Bailey, J. M., Wright, B. J., Gilbert, T. M., Sunderlin, L. S., Addition of polarization and diffuse functions to the LANL2DZ basis set for p-block elements, *J. Phys. Chem. A*, 105(34) (2001) 8111-8116.
- [17] Rassolov, V.A., Ratner, M.A., Pople, J.A., Redfern, P.C., Curtiss, L.A., 6-31G* basis set for third-row atoms, *J. Comput. Chem.*, 22 (9) (2001) 976-984.
- [18] Frisch, M.J., Trucks, G.W., Schlegel, H.B., Scuseria, G.E., Robb, M.A., Cheeseman, J.R., ... Nakatsuji, H., Gaussian09 Revision D. 01, Gaussian Inc., Wallingford CT, 2009. <http://www.gaussian.com>.
- [19] Bikadi, Z., Hazai, E., Application of the PM6 semi-empirical method to modeling proteins enhances docking accuracy of AutoDock, *J. Cheminform.*, 1(1) (2009) 1-16. <https://www.dockingserver.com/web>
- [20] Güzel, E., Koçyiğit, Ü. M., Taslimi, P., Erkan, S., Taskin, O. S., Biologically active phthalocyanine metal complexes: Preparation, evaluation of α -glycosidase and anticholinesterase enzyme inhibition activities, and molecular docking studies, *J. Biochem. Mol. Toxicol.*, (2021) e22765.
- [21] Zapata Trujillo, Juan C.; Mckemmish, Laura K. Meta-analysis of uniform scaling factors for harmonic frequency calculations, *Wiley Interdiscip. Rev., Comput. Mol. Sci.*, 12 (2022) 1584.
- [22] Ünal, Y., Nassif, W., Özyaydin, B. C., Sayin, K. Scale factor database for the vibration frequencies calculated in M06-2X, one of the DFT methods, *Vib. Spectrosc.*, 112 (2021) 103189.
- [23] Dey, L., Rabi, S., Hazari, S. K. S., Roy, T. G., Buchholz, A., Plass, W. Copper (II) and nickel (II) complexes of an N-pendent bis-(cyanoethyl) derivative of an isomeric hexamethyl tetraazamacrocyclic ligand: Synthesis, characterization, electrolytic behavior and antimicrobial studies, *Inorg. Chim. Acta*, 517 (2021) 120172.
- [24] R.B. Woodward and R. Hoffmann, *J. Amer. Chem. Soc.*, 87 395 (1965)

- [25] Sychantha, D., Little, D. J., Chapman, R. N., Boons, G. J., Robinson, H., Howell, P. L., Clarke, A. J. PatB1 is an O-acetyltransferase that decorates secondary cell wall polysaccharides, *Nat. Chem. Biol.*, 14(1) (2018) 79.
- [26] Song, L., Zhang, Y., Chen, W., Gu, T., Zhang, S. Y., Ji, Q., Mechanistic insights into staphylopine-mediated metal acquisition, *Proc. Natl. Acad. Sci. U.S.A.*, 115(15) (2018) 3942-3947.
- [27] Madsen, A., Dai, Y. N., McMahon, M., Schmitz, A. J., Turner, J. S., Tan, J., ... Ellebedy, A. H., Human antibodies targeting influenza B virus neuraminidase active site are broadly protective, *Immunity*, 53(4) (2020) 852-863.
- [28] Song, W. S., Yoon, S. I., Crystal structure of FlhC flagellin from *Pseudomonas aeruginosa* and its implication in TLR5 binding and formation of the flagellar filament, *Biochem. Biophys. Res. Commun.*, 444(2) (2014) 109-115.
- [29] Estrada, D. F., De Guzman, R. N., Structural characterization of the Crimean-Congo hemorrhagic fever virus Gn tail provides insight into virus assembly, *J. Biol. Chem.*, 286(24) (2011) 21678-21686.
- [30] Capodagli, G. C., McKercher, M. A., Baker, E. A., Masters, E. M., Brunzelle, J. S., Pegan, S. D., Structural analysis of a viral ovarian tumor domain protease from the Crimean-Congo hemorrhagic fever virus in complex with covalently bonded ubiquitin, *J. Virol.*, 85(7) (2011) 3621-3630.
- [31] Rey, F. A., Heinz, F. X., Mandl, C., Kunz, C., Harrison, S. C., The envelope glycoprotein from tick-borne encephalitis virus at 2 Å resolution, *Nature*, 375(6529) (1995) 291-298.
- [32] Guo, Y., Wang, W., Ji, W., Deng, M., Sun, Y., Zhou, H., ... Rao, Z., Crimean-Congo hemorrhagic fever virus nucleoprotein reveals endonuclease activity in bunyaviruses, *Proc. Natl. Acad. Sci. U.S.A.*, 109(13) (2012) 5046-5051.
- [33] Füzik, T., Formanová, P., Růžek, D., Yoshii, K., Niedrig, M., Plevka, P., Structure of tick-borne encephalitis virus and its neutralization by a monoclonal antibody, *Nat. Commun.*, 9(1) (2018) 1-11.
- [34] Huey, R., Morris, G. M., Olson, A. J., Goodsell, D. S., A semiempirical free energy force field with charge-based desolvation, *J. Comput. Chem.*, 28(6) (2007) 1145-1152.

On Directed Length Ratios in the Lorentz-Minkowski Plane

Abdulaziz Açıkgöz^{1,a,*}

¹ Mathematic, Faculty of Science and Literature, Afyon Kocatepe University, Afyonkarahisar, Türkiye.

*Corresponding author

Research Article

History

Received: 21/06/2022

Accepted: 28/09/2023

Copyright



©2023 Faculty of Science,
Sivas Cumhuriyet University

ABSTRACT

The linear structure of the Lorentz-Minkowski plane is almost the same as Euclidean plane. But, there is one different aspect. These planes have different distance functions. So, it can be interesting to study the Lorentz analogues of topics that include the distance concept in the Euclidean plane. Thus, in this study, we show that the relationship between Euclidean and Lorentz distances is given depending on the slope of the line segment. Following, we investigate Lorentz analogues of Thales' theorem, Angle Bisector theorems, Menelaus' theorem and Ceva's theorem.

Keywords: Lorentz distance, Directed lengths, Angle bisector theorems, Menelaus' theorem, Ceva's theorem.

^a aziz@aku.edu.tr

^{id} <https://orcid.org/0000-0002-4424-4870>

Introduction

Lorentz-Minkowski geometry is created by taking the Lorentz distance function instead of the Euclidean distance function. The basic notions, inner product, metric and vector classification in Lorentz space are given in [1, 3, 5, 6].

Lorentz-Minkowski plane (L^2) is the vector space \mathbb{R}^2 provided with Lorentz inner product

$$\langle x, y \rangle_L = x_1 y_1 - x_2 y_2$$

where $x = (x_1, x_2) \in \mathbb{R}^2$, $y = (y_1, y_2) \in \mathbb{R}^2$. The arbitrary vector $x = (x_1, x_2) \in \mathbb{R}^2$ is classified according to the sign of $\langle x, x \rangle_L$ as follows:

- (i) x is timelike vector if $\langle x, x \rangle_L < 0$,
- (ii) x is spacelike vector if $\langle x, x \rangle_L > 0$ and $x \neq 0$,
- (iii) x is lightlike vector if $\langle x, x \rangle_L = 0$ ve $x \neq 0$.

Let $e = (0, 1)$. A timelike vector $x = (x_1, x_2)$ is future-pointing (past-pointing) if $\langle x, e \rangle_L < 0$ ($\langle x, e \rangle_L > 0$). The norm $\| \cdot \|$ of any $x = (x_1, x_2) \in L^2$ is defined by $\|x\|_L = \sqrt{|\langle x, x \rangle|}$ [1]. Then the distance function between two points is defined by

$$d_L(x, y) = \|x - y\|_L = \sqrt{|(x_1 - y_1)^2 - (x_2 - y_2)^2|}$$

where $x = (x_1, x_2) \in L^2$, $y = (y_1, y_2) \in L^2$.

The Lorentz-Minkowski plane is almost the same as the Euclidean plane since the points and the lines are the same. The angles are measured in the same way. But, the distance function is different. Since the distance function is different, the properties in the Euclidean plane can be

reproduced faithfully in L^2 . A few such topics have been studied by some authors [1, 2, 4, 7, 8] in this plane. So, in this study we show that the relationship between Euclidean and Lorentz distances is given depending on the slope of the line segment. Following, we investigate Lorentz analogues of Thales' theorem, Angle Bisector theorems, Menelaus' theorem and Ceva's theorem

Materials and Methods

In this section, we mention the basic concepts that would be the basis of our study.

Proposition 2.1 Let d_E denote the Euclidean distance function and $P = (x_1, x_2)$ and $Q = (y_1, y_2)$ be two points in the analytical plane and the slope of the line \overline{PQ} be m . Then

- i) $d_E(P, Q) = \sqrt{\frac{1+m^2}{|1-m^2|}} \cdot d_L(P, Q)$, if $|m| \neq 1$ and $m \in \mathbb{R}$,
- ii) $d_E(P, Q) = d_L(P, Q)$, if $m = 0$ or $m \rightarrow \infty$.

Proof:

- i) Let $P = (x_1, x_2)$ and $Q = (y_1, y_2)$ be two points in the analytical plane and the slope of the line \overline{PQ} be m , ($|m| \neq 1$). We will show that

$$d_E(P, Q) = p(m) \cdot d_L(P, Q)$$

where $p(m) = \sqrt{\frac{1+m^2}{|1-m^2|}}$. We can write

$$d_E(P, Q) = |x_1 - y_1| \sqrt{1 + m^2}$$

and

$$d_L(P, Q) = |x_1 - y_1| \sqrt{|1 - m^2|}.$$

From above equations, we obtain that

$$\frac{d_E(P, Q)}{d_L(P, Q)} = \frac{|x_1 - y_1| \sqrt{1 + m^2}}{|x_1 - y_1| \sqrt{|1 - m^2|}}$$

$$d_E(P, Q) = \sqrt{\frac{1 + m^2}{|1 - m^2|}} \cdot d_L(P, Q)$$

$$d_E(P, Q) = p(m) \cdot d_L(P, Q).$$

ii) If $m = 0$ or $m \rightarrow \infty$, it is clear that $d_E(P, Q) = d_L(P, Q)$.

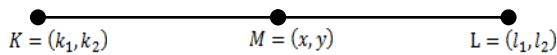
Corollary 2.1 Let P, Q and X be three collinear points in analytical plane. Then, $d_E(P, X) = d_E(Q, X)$ if and only if $d_L(P, X) = d_L(Q, X)$.

Theorem 2.1 Let $K = (k_1, k_2)$ and $L = (l_1, l_2)$ be any two different points in the analytical plane. If $M = (x, y)$ is a point on the line passing through K and L , then we can write

$$\frac{d_E(K, M)}{d_E(M, L)} = \frac{d_L(K, M)}{d_L(M, L)}.$$

That is, the ratios of the Euclidean and Lorentz directed lengths are the same [9].

Proof:



If $K = M$ then both ratios are equal to 0. Therefore without loss of generality, let $K \neq M \neq L$. It is enough to show that

$$\frac{|(k_1 - x)^2 - (k_2 - y)^2|}{|(x - l_1)^2 - (y - l_2)^2|} = \frac{(k_1 - x)^2 + (k_2 - y)^2}{(x - l_1)^2 + (y - l_2)^2}.$$

Let examine the cases of the line \overleftrightarrow{KL} be spacelike, timelike and lightlike separately.

Case 1: If the line \overleftrightarrow{KL} is spacelike, since $|k_1 - x| > |k_2 - y|$ and $|x - l_1| > |y - l_2|$, we obtain

$$\begin{aligned} \frac{(k_1 - x)^2 - (k_2 - y)^2}{(x - l_1)^2 - (y - l_2)^2} &= \frac{(k_1 - x)^2 + (k_2 - y)^2}{(x - l_1)^2 + (y - l_2)^2} \\ \Rightarrow (k_1 - x)^2(x - l_1)^2 + (k_1 - x)^2(y - l_2)^2 - (k_2 - y)^2(x - l_1)^2 - (k_2 - y)^2(y - l_2)^2 \\ &= (k_1 - x)^2(x - l_1)^2 - (k_1 - x)^2(y - l_2)^2 + (k_2 - y)^2(x - l_1)^2 - (k_2 - y)^2(y - l_2)^2 \\ \Rightarrow (k_1 - x)(y - l_2) &= (k_2 - y)(x - l_1) \\ \Rightarrow (k_1 - x)(y - l_2) - (k_2 - y)(x - l_1) &= 0 \end{aligned} \tag{1}$$

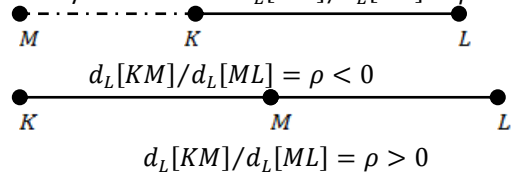
$$\begin{aligned} \Rightarrow k_1 y - k_1 l_2 - xy + xl_2 - k_2 x + k_2 l_1 + yx - yl_1 &= 0 \\ \Rightarrow (k_1 - l_1)y &= (k_2 - l_2)x + k_1 l_2 - k_2 l_1 \\ y &= \frac{k_2 - l_2}{k_1 - l_1} x + \frac{k_1 l_2 - k_2 l_1}{k_1 - l_1}. \end{aligned} \tag{2}$$

Thus, from equation (2), the point M is on the line \overleftrightarrow{KL} . Using this value of y in the equation (1) we get

Definition 2.1 Let $d_L[AB]$ denote the Lorentz directed distance from A to B along the line l in L^2 . We define Lorentz directed distance of the segment $[AB]$ as follows:

$$d_L[AB] = \begin{cases} d_L(A, B), & \text{if } AB \text{ and } l \text{ have same direction,} \\ -d_L(A, B), & \text{if } AB \text{ and } l \text{ have opposite direction.} \end{cases}$$

If K, L, M are points on the same directed line and M is between points K and L , they are denoted KML . If KML then the point M divides the line segment $[KL]$ internally and becomes $d_L[KM]/d_L[ML] = \rho > 0$. If KLM and MKL then the point M divides the line segment $[KL]$ externally and becomes $d_L[KM]/d_L[ML] = \rho < 0$ [9].



$$\begin{aligned}
 & (k_1 - x) \left(\frac{k_2x - l_2x + k_1l_2 - k_2l_1}{k_1 - l_1} - l_2 \right) - \left(k_2 - \frac{k_2x - l_2x + k_1l_2 - k_2l_1}{k_1 - l_1} \right) (x - l_1) = 0 \\
 & (k_1 - x) \left[\frac{k_2x - l_2x + k_1l_2 - k_2l_1 - l_2k_1 + l_2l_1}{k_1 - l_1} \right] - \left[\frac{k_2k_1 - k_2l_1 - k_2x + l_2x - k_1l_2 + k_2l_1}{k_1 - l_1} \right] (x - l_1) = 0 \\
 & (k_1 - x) \left[\frac{x(k_2 - l_2) - l_1(k_2 - l_2)}{k_1 - l_1} \right] - (x - l_1) \left[\frac{k_1(k_2 - l_2) - x(k_2 - l_2)}{k_1 - l_1} \right] = 0 \\
 & \frac{1}{k_1 - l_1} [(k_1 - x)(x - l_1)(k_2 - l_2) - (x - l_1)(k_1 - x)(k_2 - l_2)] = 0.
 \end{aligned}$$

Thus, the equation (1) is satisfied.

Case 2: If the line \overleftrightarrow{KL} is timelike, since $|k_1 - x| < |k_2 - y|$ and $|x - l_1| < |y - l_2|$, we obtain

$$\begin{aligned}
 & \frac{(k_2 - y)^2 - (k_1 - x)^2}{(y - l_2)^2 - (x - l_1)^2} = \frac{(k_1 - x)^2 + (k_2 - y)^2}{(x - l_1)^2 + (y - l_2)^2} \\
 & \Rightarrow (k_2 - y)^2(x - l_1)^2 + (k_2 - y)^2(y - l_2)^2 - (k_1 - x)^2(x - l_1)^2 - (k_1 - x)^2(y - l_2)^2 \\
 & = (k_1 - x)^2(y - l_2)^2 - (k_1 - x)^2(x - l_1)^2 + (k_2 - y)^2(y - l_2)^2 - (k_2 - y)^2(x - l_1)^2 \\
 & \Rightarrow (k_2 - y)(x - l_1) = (k_1 - x)(y - l_2) \\
 & \Rightarrow (k_2 - y)(x - l_1) - (k_1 - x)(y - l_2) = 0 \tag{3}
 \end{aligned}$$

$$\begin{aligned}
 & \Rightarrow k_2x - k_2l_1 - yx + yl_1 - k_1y + k_1l_2 + xy - xl_2 = 0 \\
 & \Rightarrow y(l_1 - k_1) = x(l_2 - k_2) + k_2l_1 - k_1l_2 \\
 & \Rightarrow y = \frac{l_2 - k_2}{l_1 - k_1}x + \frac{k_2l_1 - k_1l_2}{l_1 - k_1} \tag{4}
 \end{aligned}$$

Thus, from equation (4), the point M is on the line \overleftrightarrow{KL} . Using this value of y in the equation (3) we get

$$\begin{aligned}
 & (x - l_1) \left(k_2 - \frac{l_2x - k_2x + k_2l_1 - k_1l_2}{l_1 - k_1} \right) - (k_1 - x) \left(\frac{l_2x - k_2x + k_2l_1 - k_1l_2}{l_1 - k_1} - l_2 \right) = 0 \\
 & (x - l_1) \left[\frac{k_2l_1 - k_2k_1 - l_2x + k_2x - k_2l_1 + k_1l_2}{l_1 - k_1} \right] - (k_1 - x) \left[\frac{l_2x - k_2x + k_2l_1 - k_1l_2 - l_1l_2 + k_1l_2}{l_1 - k_1} \right] = 0 \\
 & (x - l_1) \left[\frac{k_1(l_2 - k_2) - x(l_2 - k_2)}{l_1 - k_1} \right] - (k_1 - x) \left[\frac{x(l_2 - k_2) - l_1(l_2 - k_2)}{l_1 - k_1} \right] = 0 \\
 & \frac{1}{l_1 - k_1} [(x - l_1)(k_1 - x)(l_2 - k_2) - (k_1 - x)(x - l_1)(l_2 - k_2)] = 0
 \end{aligned}$$

Thus, the equation (3) is satisfied.

Case 3: If the line \overleftrightarrow{KL} is lightlike, then $|k_1 - x| = |k_2 - y|$ and $|x - l_1| = |y - l_2|$. Thus, it is obvious.

If the point M divides the line segment $[KL]$ externally, the proof is similar.

Conclusion and Discussion

In this section, we give Lorentz versions of some Euclidean theorems.

Theorem 3.1 (Thales' Theorem) In the Lorentz-Minkowski plane, if we have three or more parallel lines, and they cut the other two lines, then they produce proportional segments.

Proof:

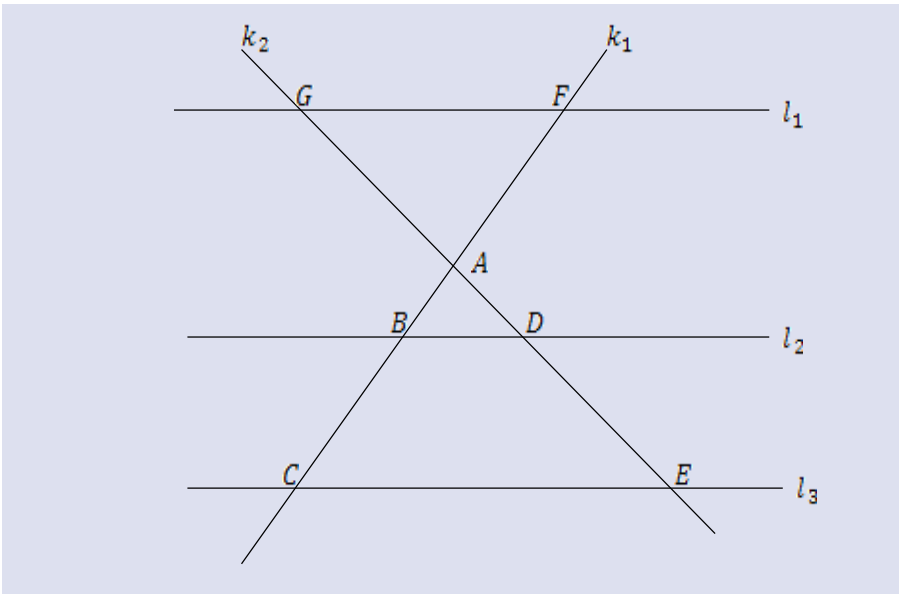


Figure 1. The parallel lines and two other lines intersecting these lines.

Let the lines l_1, l_2, l_3 are parallel and the lines k_1, k_2 cut of them like in the above figure. Since the lines l_1, l_2, l_3 are parallel, the slopes of this lines are same. Thus, let the slopes of the lines l_1, l_2, l_3 be m_1 and the slope of the lines k_1, k_2 be m_2, m_3 , respectively. Then, from Proposition 2.1, we can write that

$$\frac{d_E(A, B)}{d_E(A, C)} = \frac{\sqrt{\frac{1+m_2^2}{|1-m_2^2|}} \cdot d_L(A, B)}{\sqrt{\frac{1+m_2^2}{|1-m_2^2|}} \cdot d_L(A, C)} = \frac{d_L(A, B)}{d_L(A, C)},$$

$$\frac{d_E(A, D)}{d_E(A, E)} = \frac{\sqrt{\frac{1+m_3^2}{|1-m_3^2|}} \cdot d_L(A, D)}{\sqrt{\frac{1+m_3^2}{|1-m_3^2|}} \cdot d_L(A, E)} = \frac{d_L(A, D)}{d_L(A, E)},$$

$$\frac{d_E(B, D)}{d_E(C, E)} = \frac{\sqrt{\frac{1+m_1^2}{|1-m_1^2|}} \cdot d_L(B, D)}{\sqrt{\frac{1+m_1^2}{|1-m_1^2|}} \cdot d_L(C, E)} = \frac{d_L(B, D)}{d_L(C, E)}.$$

Since

$$\frac{d_E(A, B)}{d_E(A, C)} = \frac{d_E(A, D)}{d_E(A, E)} = \frac{d_E(B, D)}{d_E(C, E)},$$

we can obtain as follows

$$\frac{d_L(A, B)}{d_L(A, C)} = \frac{d_L(A, D)}{d_L(A, E)} = \frac{d_L(B, D)}{d_L(C, E)}.$$

Theorem 3.2 (Interior Angle Bisector Theorem) Let interior angle bisector of vertex A of the triangle ΔABC intersects side $[BC]$ at point D , $a_L = d_L(B, C)$, $b_L = d_L(C, A)$, $c_L = d_L(A, B)$, $p_L = d_L(B, D)$, $q_L = d_L(D, C)$ and slopes of sides $[AB]$, $[BC]$, $[AC]$ be m_c, m_a, m_b , respectively, in the Lorentz-Minkowski plane. Then we can write as follows:

- i) $\frac{p_L}{q_L} = \frac{c_L}{b_L} \cdot \left[\frac{1+m_c^2}{|1-m_c^2|} \cdot \frac{|1-m_b^2|}{1+m_b^2} \right]$,
- ii) $\frac{p_L}{q_L} = \frac{c_L}{b_L} \cdot \left[\frac{1+m_c^2}{|1-m_c^2|} \right]$, if $m_b = 0$ or $m_b \rightarrow \infty$,
- iii) $\frac{p_L}{q_L} = \frac{c_L}{b_L} \cdot \left[\frac{|1-m_b^2|}{1+m_b^2} \right]$, if $m_c = 0$ or $m_c \rightarrow \infty$,

where $m_c, m_a, m_b \neq \pm 1$. Here, sides of the triangle ΔABC must be same kinds. That is, three sides of the triangle ΔABC are either spacelike lines or timelike lines.

Proof.

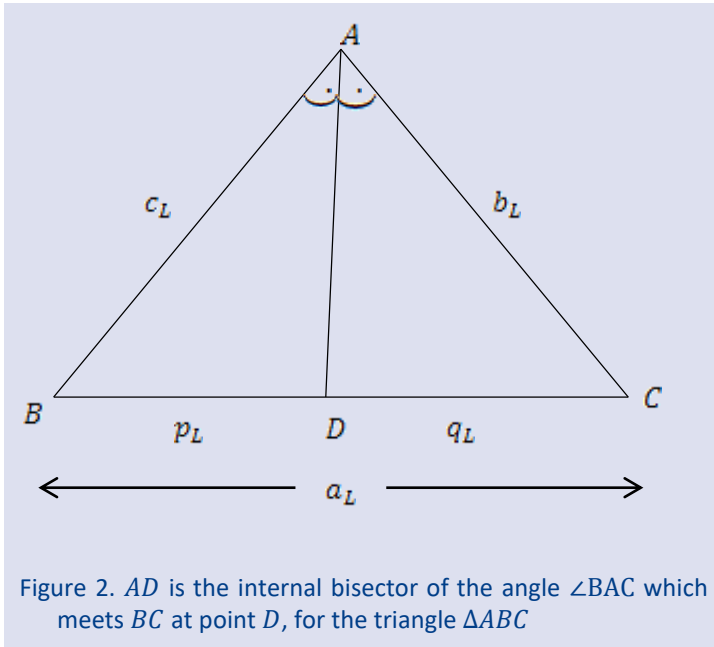


Figure 2. AD is the internal bisector of the angle $\angle BAC$ which meets BC at point D, for the triangle ΔABC

i) Let slopes of sides $[AB], [BC], [AC]$ be m_c, m_a, m_b , respectively. It is clear that,

$$\frac{d_E(A, B)}{d_E(A, C)} = \frac{d_E(B, D)}{d_E(D, C)} \tag{5}$$

is satisfied in the Euclidean plane. According to Proposition 2.1, we obtain that,

$$d_E(A, B) = \sqrt{\frac{1+m_c^2}{|1-m_c^2|}} \cdot c_L, \quad d_E(A, C) = \sqrt{\frac{1+m_b^2}{|1-m_b^2|}} \cdot b_L,$$

$$d_E(B, D) = \sqrt{\frac{1+m_a^2}{|1-m_a^2|}} \cdot p_L, \quad d_E(D, C) = \sqrt{\frac{1+m_a^2}{|1-m_a^2|}} \cdot q_L.$$

If the above values are substituted in the equation (5), we get

$$\frac{\sqrt{\frac{1+m_c^2}{|1-m_c^2|}} \cdot c_L}{\sqrt{\frac{1+m_b^2}{|1-m_b^2|}} \cdot b_L} = \frac{\sqrt{\frac{1+m_a^2}{|1-m_a^2|}} \cdot p_L}{\sqrt{\frac{1+m_a^2}{|1-m_a^2|}} \cdot q_L},$$

$$\frac{p_L}{q_L} = \frac{c_L}{b_L} \cdot \left[\frac{1+m_c^2}{|1-m_c^2|} \cdot \frac{|1-m_b^2|}{1+m_b^2} \right]. \tag{6}$$

ii) It is clear that, for $m_b = 0$ or $m_b \rightarrow \infty$, the equation (6) is obtained that

$$\frac{p_L}{q_L} = \frac{c_L}{b_L} \cdot \left[\frac{1+m_c^2}{|1-m_c^2|} \right].$$

iii) It is clear that, for $m_c = 0$ or $m_c \rightarrow \infty$, the equation (6) is obtained that

$$\frac{p_L}{q_L} = \frac{c_L}{b_L} \cdot \left[\frac{|1-m_b^2|}{1+m_b^2} \right].$$

Theorem 3.3 (Exterior Angle Bisector Theorem) Let exterior angle bisector of vertex A of the triangle ΔABC intersects side \overrightarrow{BC} at point D , $a_L = d_L(B, C)$, $b_L = d_L(C, A)$, $c_L = d_L(A, B)$, $p_L = d_L(B, D)$, $q_L = d_L(D, C)$ and slopes of sides $[AB]$, $[BC]$, $[AC]$ be m_c , m_a , m_b , respectively, in the Lorentz-Minkowski plane. Then we can write as follows:

- i) $\frac{p_L}{q_L} = \frac{c_L}{b_L} \cdot \left[\frac{1+m_c^2}{|1-m_c^2|} \cdot \frac{|1-m_b^2|}{1+m_b^2} \right]$,
- ii) $\frac{p_L}{q_L} = \frac{c_L}{b_L} \cdot \left[\frac{1+m_c^2}{|1-m_c^2|} \right]$, if $m_b = 0$ or $m_b \rightarrow \infty$,
- iii) $\frac{p_L}{q_L} = \frac{c_L}{b_L} \cdot \left[\frac{|1-m_b^2|}{1+m_b^2} \right]$, if $m_c = 0$ or $m_c \rightarrow \infty$,

where $m_c, m_a, m_b \neq \pm 1$. Here, sides of the triangle ΔABC must be same kinds. That is, three sides of the triangle ΔABC are either spacelike lines or timelike lines.

Proof:

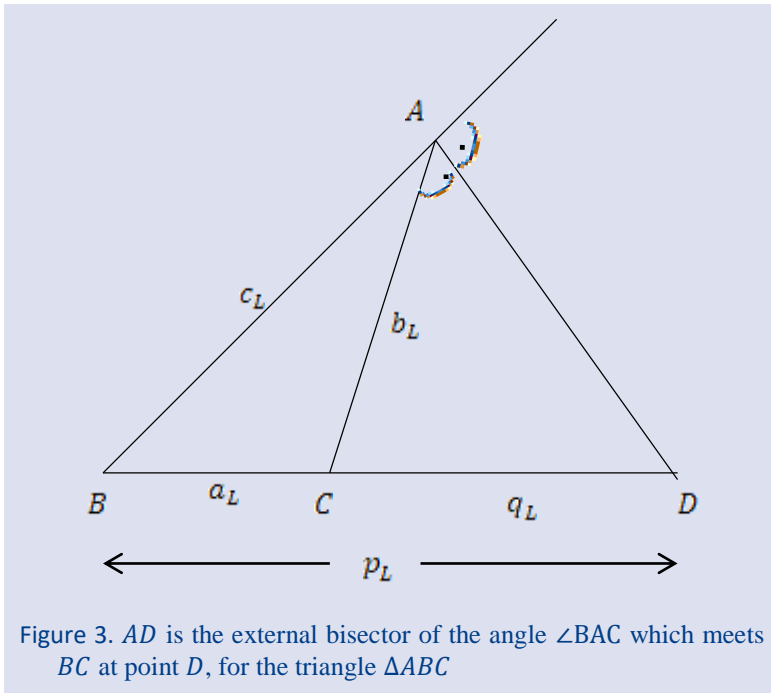


Figure 3. AD is the external bisector of the angle $\angle BAC$ which meets BC at point D , for the triangle ΔABC

i) Let slopes of the sides $[AB]$, $[BC]$, $[AC]$ be m_c , m_a , m_b , respectively. It is clear that,

$$\frac{d_E(A, B)}{d_E(A, C)} = \frac{d_E(B, D)}{d_E(C, D)} \tag{7}$$

is satisfied in the Euclidean plane. According to Proposition 2.1, we obtain that,

$$d_E(A, B) = \sqrt{\frac{1+m_c^2}{|1-m_c^2|}} \cdot c_L, \quad d_E(A, C) = \sqrt{\frac{1+m_b^2}{|1-m_b^2|}} \cdot b_L,$$

$$d_E(B, D) = \sqrt{\frac{1 + m_a^2}{|1 - m_a^2|}} \cdot p_L, \quad d_E(C, D) = \sqrt{\frac{1 + m_a^2}{|1 - m_a^2|}} \cdot q_L.$$

If the above values are substituted in the equation (7), we get

$$\frac{\sqrt{\frac{1 + m_c^2}{|1 - m_c^2|}} \cdot c_L}{\sqrt{\frac{1 + m_b^2}{|1 - m_b^2|}} \cdot b_L} = \frac{\sqrt{\frac{1 + m_a^2}{|1 - m_a^2|}} \cdot p_L}{\sqrt{\frac{1 + m_a^2}{|1 - m_a^2|}} \cdot q_L},$$

$$\frac{p_L}{q_L} = \frac{c_L}{b_L} \cdot \left[\frac{1 + m_c^2}{|1 - m_c^2|} \cdot \frac{|1 - m_b^2|}{1 + m_b^2} \right]. \tag{8}$$

ii) It is clear that, for $m_b = 0$ or $m_b \rightarrow \infty$, the equation (8) is obtained that

$$\frac{p_L}{q_L} = \frac{c_L}{b_L} \cdot \left[\frac{1 + m_c^2}{|1 - m_c^2|} \right].$$

iii) It is clear that, for $m_c = 0$ or $m_c \rightarrow \infty$, the equation (8) is obtained that

$$\frac{p_L}{q_L} = \frac{c_L}{b_L} \cdot \left[\frac{|1 - m_b^2|}{1 + m_b^2} \right].$$

Theorem 3.4 (Menelaus’ Theorem) Let ΔABC be a triangle and P_1, P_2, P_3 be on the lines that contain the sides BC, CA, AB , respectively, in the Lorentz-Minkowski plane. If P_1, P_2, P_3 are collinear, then

$$\frac{d_L[BP_1]}{d_L[P_1C]} \cdot \frac{d_L[CP_2]}{d_L[P_2A]} \cdot \frac{d_L[AP_3]}{d_L[P_3B]} = -1$$

where none of P_1, P_2, P_3 coincide with any of A, B, C . Here, the points P_1, P_2, P_3, A, B, C must be same kinds. That is, all of them are either spacelike or timelike.

Proof:

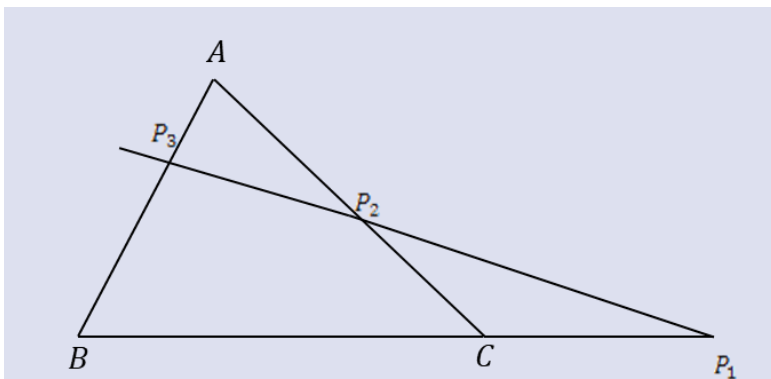


Figure 4. Collinear points P_1, P_2, P_3 on the sides BC, CA, AB , respectively.

Let slopes of the lines $\overrightarrow{AB}, \overrightarrow{BC}, \overrightarrow{CA}$ be m_1, m_2, m_3 , respectively and $m_1, m_2, m_3 \neq \pm 1$. It is clear that

$$\frac{d_E[BP_1]}{d_E[P_1C]} \cdot \frac{d_E[CP_2]}{d_E[P_2A]} \cdot \frac{d_E[AP_3]}{d_E[P_3B]} = -1 \tag{9}$$

is satisfied in the Euclidean plane. According to Proposition 2.1, we obtain that

$$\begin{aligned}
 d_E(B, P_1) &= \sqrt{\frac{1+m_2^2}{|1-m_2^2|}} \cdot d_L(B, P_1), & d_E(P_1, C) &= \sqrt{\frac{1+m_2^2}{|1-m_2^2|}} \cdot d_L(P_1, C) \\
 d_E(C, P_2) &= \sqrt{\frac{1+m_3^2}{|1-m_3^2|}} \cdot d_L(C, P_2), & d_E(P_2, A) &= \sqrt{\frac{1+m_3^2}{|1-m_3^2|}} \cdot d_L(P_2, A) \\
 d_E(A, P_3) &= \sqrt{\frac{1+m_1^2}{|1-m_1^2|}} \cdot d_L(A, P_3), & d_E(P_3, B) &= \sqrt{\frac{1+m_1^2}{|1-m_1^2|}} \cdot d_L(P_3, B).
 \end{aligned}$$

From Definition 2.1, $|BP_1|$ and $|P_1C|$ have opposite direction. If the above values are substituted in the equation (9), we get

$$\frac{d_E[BP_1]}{d_E[P_1C]} \cdot \frac{d_E[CP_2]}{d_E[P_2A]} \cdot \frac{d_E[AP_3]}{d_E[P_3B]} = - \frac{\sqrt{\frac{1+m_2^2}{|1-m_2^2|}} \cdot d_L[BP_1]}{\sqrt{\frac{1+m_2^2}{|1-m_2^2|}} \cdot d_L[P_1C]} \cdot \frac{\sqrt{\frac{1+m_3^2}{|1-m_3^2|}} \cdot d_L[CP_2]}{\sqrt{\frac{1+m_3^2}{|1-m_3^2|}} \cdot d_L[P_2A]} \cdot \frac{\sqrt{\frac{1+m_1^2}{|1-m_1^2|}} \cdot d_L[AP_3]}{\sqrt{\frac{1+m_1^2}{|1-m_1^2|}} \cdot d_L[P_3B]} = -1.$$

Theorem 3.5 (Ceva’s Theorem) Let ΔABC be a triangle and lines l_1, l_2, l_3 pass through the vertices A, B, C , respectively and intersect lines containing the opposite sides at points P_1, P_2, P_3 , in the Lorentz-Minkowski plane. Then the lines l_1, l_2, l_3 are concurrent if and only if

$$\frac{d_L[BP_1]}{d_L[P_1C]} \cdot \frac{d_L[CP_2]}{d_L[P_2A]} \cdot \frac{d_L[AP_3]}{d_L[P_3B]} = 1.$$

Here, none of P_1, P_2, P_3 are of A, B, C . The points P_1, P_2, P_3, A, B, C must be same kinds. That is, all of them are either spacelike or timelike.

Conflict of interests

The authors state that did not have conflict of interests.

References

[1] Birman G.S., Nomizu K., Trigonometry in lorentzian geometry, *The American Mathematical Monthly*, 91 (9) (1984) 543–549.

[2] Catoni F., Boccaletti D., Cannata R., Catoni V., Nichelatti E., Zampetti P., *The Mathematics of Minkowski Space-Time, With an Introduction to Commutative Hypercomplex Numbers*. Berlin, (2008) 27-57.

[3] Duggal, K.L., Bejancu, A., *Lightlike Submanifolds of Semi-Riemannian Manifolds and Applications*. Amsterdam, (1996) 1-5.

[4] Nešović E., Petrović-Torgašev M., Some trigonometric relations in the lorentzian plane, *Kragujevac Journal of Mathematics*, 33 (25) (2003) 219– 225.

[5] O’Neill B., *Semi-Riemannian Geometry, with applications to relativity*. London, (1983) 126-185.

[6] Ratchlife J.G., *Foundations of hyperbolic manifolds*. 2nd ed. New York, (2006) 54-98.

[7] Shonoda, E.N., Classification of conics and Cassini curves in Minkowski space-time plane, *Journal of Egyptian Mathematical Society*, 24 (2016) 270-278.

[8] Yaglom, I.M., *A Simple Non-Euclidean Geometry and Its Physical Basis*. New York, (1979) 174-201.

[9] Ozcan M., Kaya R., On the Ratio of Directed Lengths in the Taxicab plane and Related Properties, *Missouri J. of Math. Sci.*, 14 (2) (2002) 107-117.

Application of Formable Transform for Solving Growth and Decay Problems, Logistic Growth Model and Prey-Predator Model

Nihan Güngör^{1,a,*}

¹Department of Mathematical Engineering, Faculty of Engineering and Naturel Sciences, Gumushane University, Gumushane, Türkiye.

*Corresponding author

Research Article

History

Received: 19/12/2022

Accepted: 15/10/2023

Copyright



©2023 Faculty of Science,
Sivas Cumhuriyet University

ABSTRACT

Integral transforms have become the focus of investigations, because they allow the solution of significant problems in the domains of science and engineering to be accomplished with a minimal number of straightforward calculations. In this study, growth and decay problems, which are crucial in fields such as biology, zoology, physics, chemistry, and economics, are solved utilizing the Formable transform. The Formable transform method is applied to the logistic growth model in population and prey-predator models. The effectiveness and simplicity of the use of the Formable transform in obtaining the solution to these problems are examples.

Keywords: Integral transforms, Formable transform, Growth and decay problem, Logistic growth model, Lotka-Volterra systems.

^anihangungor@gumushane.edu.tr  <https://orcid.org/0000-0003-1235-2700>

Introduction

One of the earliest mathematical models for the dynamic change of populations was provided by Thomas Malthus. The Malthusian model posits that the rate of population growth in a country is directly proportional to its total population, denoted as $\mathcal{P}(t)$ at any given time t . Based on this theory, the growth of the population at a given time is directly proportional to the projected increase in population in the future. From a mathematical perspective, this assumption can be expressed such that κ is a constant of proportionality. The proportionality can be expressed using the following differential equation:

$$\frac{dP(t)}{dt} = \kappa P(t). \quad (1)$$

The mathematical representation of population growth is described as a first-order ordinary linear differential equation,

$$\frac{dP}{dt} = \kappa P$$

with initial condition

$$P(t_0) = P_0$$

where, P represents the population at time t , P_0 indicates the starting population at time t_0 and κ is a real number greater than zero. Mathematically, the decay problem of substances is written as a first-order ordinary linear differential equation

$$\frac{dP}{dt} = -\kappa P \quad (2)$$

with initial condition

$$P(t_0) = P_0$$

where, P represents the population at time t , P_0 represents the initial population at time t_0 and κ is a real number greater than zero. Based on these equations, it can be deduced that the population graph demonstrates exponential growth [1].

Due to limited resources such as food, space, and other factors, competition arises, resulting in a deviation from exponential population growth. As a result, the logistic model serves as a replacement for the Malthus model. The nonlinear biological models encompass a logistic growth model within a population, represented by the equation

$$\frac{dP(t)}{dt} = rP(t) \left(1 - \frac{P(t)}{\kappa}\right) \quad (3)$$

where r is a positive constant and κ is the carrying capacity. The function $P(t)$ denotes the population of the species at time t , while the expression $rP(t) \left(1 - \frac{P(t)}{\kappa}\right)$ represents the per capita growth rate. The non-dimensionalization of equation (3) is achieved by

$$v(\tau) = \frac{P(t)}{\kappa}, \quad \tau = rt$$

which yields

$$\frac{dv}{d\tau} = v(1 - v). \tag{4}$$

If the initial condition is given as $P(0) = P_0$, then $v(0) = \frac{P_0}{\kappa}$. Therefore, the analytical solution of equation (4) is obtained as

$$v(\tau) = \frac{1}{1 + \left(\frac{\kappa}{P_0} - 1\right) e^{-\tau}}. \tag{5}$$

A predator-prey relationship describes the dynamic between two species and how they affect one another. In this case, one species is in fact consuming the other species for food. A predator is an organism that consumes or hunts other organisms for food, while a prey is an organism that is slain by another organism for food. Examples of predators with their prey are the fox and the rabbit, the lion, and the zebra. The concept of predator-prey dynamics extends beyond animals and encompasses plants as well. The relationship between the grasshopper and the leaf serves as an illustrative example in this context. Consider the predator-prey models: Lotka-Volterra systems as an interacting species model to serve as a model for interacting species that are governed by

$$\frac{dN}{dt} = N(a - bP) \tag{6}$$

$$\frac{dP}{dt} = P(cN - d) \tag{7}$$

where a, b, c and d are constants [2]. Here $N = N(t)$ represents the prey population, and $P = P(t)$ represents the population of predators at the time t . The non-dimensionalization of the system (6)-(7) is achieved by

$$w(\tau) = \frac{cN(t)}{d}, \quad v(\tau) = \frac{bP(t)}{a}, \quad \tau = at, \quad \mu = d/a$$

and it turns into

$$\frac{dw}{d\tau} = w(1 - v) \tag{8}$$

$$\frac{dv}{d\tau} = \mu[g(w, v) - v]. \tag{9}$$

Integral transforms are a valuable mathematical tool for solving a wide range of processes and phenomena in the fields of science, engineering, and real-life applications. These transforms allow us to express various complex problems in a mathematical framework, enabling their solution through rigorous mathematical techniques. The Laplace transform is widely recognized as the most commonly used among these various transforms. Many novel integral transformations, such as Laplace-Carson, Sumudu, Aboodh, Elzaki, Mohand, Sawi, Shehu, Sadik,

Anuj, Rishi, Kamal, Kharrat-Toma, and Kashuri-Fundo have been developed in recent years in an effort to help scientists and engineers tackle increasingly complex issues in a variety of fields. Many researchers have analyzed the duality between various integral transforms, particularly the Laplace transform [3-10]. Rao [11] used the ZZ transform to handle natural growth and decay problems. Aggarwal et al. [12-18] applied Laplace, Elzaki, Kamal, Aboodh, Mahgoub, Mohand, Shehu transforms to solve growth and decay problems. Aggarwal and Bhatnagar [19] demonstrated how to use the Sadik transform to resolve growth and decay problems. Singh and Aggarwal [20] investigated population growth and decay problems with the Sawi transform. Verma et al. [21] scrutinized the applications of the Dines Verma Transform for handling population growth and decay problems. Bansal et al. [22] provided examples of applications for the Anuj transform. Pamuk and Soylu [23] utilized the Laplace transform method for logistic population growth and predator models. Additional works on integral transforms can be found in references [23-30].

A novel integral transform, the Formable transform, was described by Saadeh and Ghazal [31]. They proved some properties of this transform for handling both ordinary and partial differential equations. Additionally, they investigated the duality between the new transform and some existing transforms. Güngör [32] utilized Formable transform to solve linear Volterra integral equations of the convolution type. Ghazal et al. [33] introduced the concept of the double Formable transform, demonstrated its characteristics, and used it to solve partial integro-differential equations. Saadeh et al. [34] gave illustrative applications of heat equations via the use of numerical examples. For the purpose of resolving time-fractional partial differential equations, Saadeh et al. [35] used the Formable transform decomposition method. Prajapati and Meher [36] investigated a time-fractional Rosenau-Hyman model based on a KdV-like equation with compacton solutions using a robust homotopy analysis method with a formable transform. The Formable integral transform of the Hilfer-Prabhakar and its regularized variant of the Hilfer-Prabhakar fractional derivative were developed by Khalid and Alha [37].

The aim of this study is to present the concept of Formable transform as a technique that facilitates the solution of linear differential equations through growth and decay models as well as nonlinear differential equations through biological models, specifically those comprising a logistic growth model to study population dynamics and the prey-predator model to analyze ecological interactions.

Materials and Methods

This section will present the definition of the Formable transform, along with an exploration of its properties and its relationship to other widely recognized transforms.

Definition 1. [31] If there exists a positive number M that satisfying

$$|v(t)| \leq Me^{\alpha t}, M > 0, \alpha > 0, \forall t \geq 0$$

then the function $v(t)$ is said to have exponential order on every finite interval in $[0, +\infty)$.

Definition 2. [31] Over the set of functions

$$\mathcal{W} = \{v(t): \exists \gamma, \rho_1, \rho_2 > 0, |v(t)| < \gamma e^{\frac{t}{\rho_i}}, \text{ if } t \in [0, \infty)\},$$

the Formable integral transform of an exponential order function $v(t)$ is described as

$$\mathfrak{R}[v(t)] = \mathcal{V}(s, u) = s \int_0^\infty e^{-st} v(ut) dt. \tag{10}$$

This is equivalent to

$$\mathfrak{R}[v(t)] = \frac{s}{u} \int_0^\infty e^{-\frac{st}{u}} v(t) dt \tag{11}$$

where s and u are the variables of Formable transform.

The expression

$$\mathfrak{R}^{-1}[\mathcal{V}(s, u)] = v(t) = \frac{1}{2\pi i} \int_{c-i\infty}^{c+i\infty} \frac{1}{s} e^{\frac{st}{u}} \mathcal{V}(s, u) ds.$$

denotes the inverse Formable transform of a function $v(t)$.

Theorem 1. (Linearity property) [31] If $v_1(t)$ and $v_2(t)$ are two functions in \mathcal{W} , then $c_1 v_1(t) + c_2 v_2(t) \in \mathcal{W}$ where c_1 and c_2 are arbitrary constants, and

$$\mathfrak{R}[c_1 v_1(t) + c_2 v_2(t)] = c_1 \mathfrak{R}[v_1(t)] + c_2 \mathfrak{R}[v_2(t)].$$

Theorem 2. (Formable transform of the derivative) [31] Let's take the function $v^{(k)}(t)$ is the k -th derivative of the function $v(t)$. If $v^{(k)}(t) \in \mathcal{W}$ for $k = 0, 1, 2, \dots$, then

$$\mathfrak{R}[v^{(k)}(t)] = \frac{s^k}{u^k} \mathcal{V}(s, u) - \sum_{m=0}^{k-1} \left(\frac{s}{u}\right)^{k-m} v^{(m)}(0).$$

The Formal transform and inverse of certain functions are presented below [31]:

$v(t)$	$\mathfrak{R}[v(t)] = \mathcal{V}(s, u)$
1	1
t	$\frac{u}{s}$
$\frac{t^n}{n!}$	$\frac{u^n}{s^n}$
$e^{\beta t}$	$\frac{s}{s - \beta u}$
$\frac{t^n}{n!} e^{\beta t}$	$\frac{su^n}{(s - \beta u)^{n+1}}$
$\sin(\beta t)$	$\frac{\beta su}{s^2 + \beta^2 u^2}$
$\cos(\beta t)$	$\frac{s^2}{s^2 + \beta^2 u^2}$
$\sinh(\beta t)$	$\frac{\beta su}{s^2 - \beta^2 u^2}$
$\cosh(\beta t)$	$\frac{s^2}{s^2 - \beta^2 u^2}$

$\mathcal{V}(s, u)$	$v(t) = \mathfrak{R}^{-1}[\mathcal{V}(s, u)]$
1	1
$\frac{u}{s}$	t
$\frac{u^n}{s^n}$	$\frac{t^n}{n!}$
$\frac{s}{s - \beta u}$	$e^{\beta t}$
$\frac{su^n}{(s - \beta u)^{n+1}}$	$\frac{t^n}{n!} e^{\beta t}$
$\frac{\beta su}{s^2 + \beta^2 u^2}$	$\sin(\beta t)$
$\frac{s^2}{s^2 + \beta^2 u^2}$	$\cos(\beta t)$
$\frac{\beta su}{s^2 - \beta^2 u^2}$	$\sinh(\beta t)$
$\frac{s^2}{s^2 - \beta^2 u^2}$	$\cosh(\beta t)$

The definitions of many integral transforms that can be found in [3-5, 7-10, 12-15, 17, 18, 20, 31] are given in a tabular format below:

Table 1. Definitions of some integral transforms

Integral Transform	Definition
Laplace transform	$\mathcal{L}[v(t)] = \int_0^\infty v(t)e^{-st} dt = F(s)$
Sumudu transform	$\mathcal{S}[v(t)] = \int_0^\infty v(st)e^{-t} dt = G(s)$
Elzaki transform	$E[v(t)] = s \int_0^\infty v(t)e^{-\frac{t}{s}} dt = C(s)$
Natural transform	$\mathcal{N}^+[v(t)](s, u) = \frac{1}{u} \int_0^\infty e^{-\frac{st}{u}} v(t) dt = N(s, u)$
Shehu transform	$\mathcal{S}[v(t)] = \int_0^\infty e^{-\frac{st}{u}} v(t) dt = Q(s, u)$
Aboodh transform	$\mathcal{A}[v(t)] = \frac{1}{s} \int_0^\infty v(t)e^{-st} dt = A(s)$
Kamal transform	$\mathcal{K}[v(t)] = \int_0^\infty v(t)e^{-\frac{t}{s}} dt = H(s)$
Mohand transform	$\mathcal{M}[v(t)] = s^2 \int_0^\infty v(t)e^{-st} dt = I(s)$
Sawi transform	$\mathcal{S}[v(t)] = \frac{1}{s^2} \int_0^\infty v(t)e^{-\frac{t}{s}} dt = J(s)$

Let $\mathcal{V}(s, u)$ be the Formable transform of the function $v(t)$. Hence, the relationships between the Formable transform and other certain integral transforms are illustrated in the following manner:

- *Formable–Laplace duality* [31]: If $F(s)$ is the Laplace transform of the function $v(t)$, then

$$\mathcal{V}(s, 1) = sF(s).$$

Indeed, it is clear that $\mathcal{V}(s, 1) = s \int_0^\infty e^{-st} v(t) dt = sF(s)$ from (10).

- *Formable–Sumudu duality* [31]: If $G(u)$ represents the Sumudu transform of the function $v(t)$, then

$$\mathcal{V}(1, u) = G(u).$$

In fact, it is evident that $\mathcal{V}(1, u) = \int_0^\infty e^{-t} v(ut) dt = G(u)$ from (10).

- *Formable–Elzaki duality* [31]: If $C(u)$ is the Elzaki transform of the function $v(t)$, then

$$\mathcal{V}(1, u) = \frac{1}{u^2} C(u).$$

By using the equation (11), one gets $\mathcal{V}(1, u) = \frac{1}{u} \int_0^\infty e^{-\frac{t}{u}} v(t) dt = \frac{1}{u^2} \left(u \int_0^\infty v(t) e^{-\frac{t}{u}} dt \right) = \frac{1}{u^2} C(u)$.

- *Formable–Natural duality* [31]: If $N(s, u)$ is the Natural transform of the function $v(t)$, then

$$\mathcal{V}(s, u) = sN(s, u).$$

In fact, one obtains $\mathcal{V}(s, u) = \frac{s}{u} \int_0^\infty e^{-\frac{st}{u}} v(t) dt = s \frac{1}{u} \int_0^\infty e^{-\frac{st}{u}} v(t) dt = sN(s, u)$ from (11).

- *Formable–Shehu duality*: If $Q(s, u)$ is the Shehu transform of the function $v(t)$, then

$$\mathcal{V}(s, u) = \frac{s}{u} Q(s, u).$$

It is readily apparent that $\mathcal{V}(s, u) = \frac{s}{u} \int_0^\infty e^{-\frac{st}{u}} v(t) dt = \frac{s}{u} Q(s, u)$ from (11).

- *Formable–Aboodh duality*: If $A(u)$ is the Aboodh transform of the function $v(t)$, then

$$\mathcal{V}(1, u) = \frac{1}{u^2} A\left(\frac{1}{u}\right).$$

Indeed, one gets $\mathcal{V}(1, u) = \frac{1}{u} \int_0^\infty e^{-\frac{t}{u}} v(t) dt = \frac{1}{u^2} u \int_0^\infty e^{-\frac{t}{u}} v(t) dt = \frac{1}{u^2} A\left(\frac{1}{u}\right)$ by using the equation (11).

- *Formable–Kamal duality*: If $H(u)$ is the Kamal transform of the function $v(t)$, then

$$\mathcal{V}(1, u) = \frac{1}{u} H(u).$$

It is clear that $\mathcal{V}(1, u) = \frac{1}{u} \int_0^\infty e^{-\frac{t}{u}} v(t) dt = \frac{1}{u} H(u)$ from (11).

Applying of Formable Transform for Exponential Growth and Decay Model

In this part, the Formable transform is applied to find solutions to the problems of population growth and decay, which are mathematically described by equations by (1) and (2). Taking Formable transform on either side of the equation (1), we find

$$\mathfrak{R} \left[\frac{dP(t)}{dt} \right] = k\mathfrak{R}[P(t)].$$

By implementing the Formable transform of the derivative of the function, we get

$$\frac{s}{u}\mathfrak{R}[P(t)] - \frac{s}{u}P(0) = k\mathfrak{R}[P(t)].$$

Hence, we have

$$\left(\frac{s}{u} - k\right)\mathfrak{R}[P(t)] = \frac{s}{u}P_0$$

$$\mathfrak{R}[P(t)] = \frac{s}{s-ku}P_0. \tag{12}$$

After applying the inverse Formable transform to either side of (12), we can write the result as

$$P(t) = \mathfrak{R}^{-1} \left[\frac{s}{s-ku}P_0 \right]$$

$$P(t) = P_0\mathfrak{R}^{-1} \left[\frac{s}{s-ku} \right]$$

$$P(t) = P_0e^{kt}$$

which represents the desired population at the time t .

Applying the Formable transform on either side of equation (2), we find

$$\mathfrak{R} \left[\frac{dP(t)}{dt} \right] = -k\mathfrak{R}[P(t)].$$

Now, by implementing the Formable transform of the derivative of the function, we obtain

$$\frac{s}{u}\mathfrak{R}[P(t)] - \frac{s}{u}P(0) = -k\mathfrak{R}[P(t)].$$

Therefore, we have

$$\left(\frac{s}{u} + k\right)\mathfrak{R}[P(t)] = \frac{s}{u}P_0$$

$$\mathfrak{R}[P(t)] = \frac{s}{s+ku}P_0. \tag{13}$$

After applying the inverse Formable transform on either side of (13), we get

$$P(t) = \mathfrak{R}^{-1} \left[\frac{s}{s+ku}P_0 \right]$$

$$P(t) = P_0\mathfrak{R}^{-1} \left[\frac{s}{s+ku} \right]$$

$$P(t) = P_0e^{-kt}$$

which represents the desired population at time t .

Applying of Formable Transform for Logistic Growth Model

Take into account the model equation in the form of

$$\frac{dv}{dt} = v - h(v), \quad v(0) = v_0 \tag{14}$$

where h represents a nonlinear function of v . Therefore, we suppose that the solution, v of (14) has a representation in the form of an infinite series

$$v = v(t) = \sum_{n=0}^{\infty} c_n t^n \tag{15}$$

and it fulfills the necessary requirements for the existence of the Formable transform. Once Formable transform is applied to either side of the Equation (14), it is obtained as

$$\mathfrak{R} \left[\frac{dv}{dt} \right] = \mathfrak{R}[v] - \mathfrak{R}[h(v)]$$

$$\frac{s}{u}\mathcal{V}(s, u) - \frac{s}{u}v(0) = \mathcal{V}(s, u) - \mathcal{H}(s, u)$$

where $\mathfrak{R}[v] = \mathcal{V}(s, u)$ and $\mathfrak{R}[h(v)] = \mathcal{H}(s, u)$ are Formable transforms of the functions $v(t)$ and $h(v)$, respectively. By rearranging the terms in the equation, the expression $\mathcal{V}(s, u)$ can be determined as

$$\mathcal{V}(s, u) = v_0 \frac{s}{s-u} - \frac{u\mathcal{H}(s, u)}{s-u}. \tag{16}$$

Therefore, under the assumption that the inverse Formable transform \mathfrak{R}^{-1} exists and applying it to the expression (16), the equation can be expressed as follows:

$$v(t) = v_0 e^t - \mathfrak{R}^{-1} \left[\frac{u\mathcal{H}(s, u)}{s-u} \right].$$

Applying of Formable Transform for Prey-Predator Model

Let us consider the system of non-linear differential equations that determines the predator-prey model.

$$\frac{dw}{dt} = w - h(w, v) \tag{17}$$

$$\frac{dv}{dt} = \mu[g(w, v) - v] \tag{18}$$

with initial conditions

$$w(0) = w_0, v(0) = v_0 \tag{19}$$

where h and g are nonlinear functions of w and v and also μ be a positive constant. It is assumed that the solutions w and v of the system (17)-(18) possess infinite series expansions in the following form:

$$w(t) = \sum_{n=0}^{\infty} a_n t^n, v(t) = \sum_{n=0}^{\infty} c_n t^n. \tag{20}$$

Furthermore, the necessary criteria for the existence of their Formable transforms are satisfied by them. By utilizing the Formable transform for the equations (17)-(18) and utilizing equation (19), we obtain

$$\frac{s}{u} \mathcal{W}(s, u) - \frac{s}{u} w_0 = \mathcal{W}(s, u) - \mathcal{H}(s, u) \tag{21}$$

$$\frac{s}{u} \mathcal{V}(s, u) - \frac{s}{u} v_0 = \mu[G(s, u) - \mathcal{V}(s, u)] \tag{22}$$

where

$\mathfrak{R}[w(t)] = \mathcal{W}(s, u)$, $\mathfrak{R}[h(w(t), v(t))] = \mathcal{H}(s, u)$, $\mathfrak{R}[v(t)] = \mathcal{V}(s, u)$, $\mathfrak{R}[g(w(t), v(t))] = G(s, u)$ are the Formable transforms of the functions $w(t)$, $h(w(t), v(t))$, $v(t)$ and $g(w(t), v(t))$, respectively. By solving the equations (21)-(22) for $\mathcal{W}(s, u)$ and $\mathcal{V}(s, u)$, one gets

$$\mathcal{W}(s, u) = \frac{s}{s-u} w_0 - \frac{u}{s-u} \mathcal{H}(s, u) \tag{23}$$

$$\mathcal{V}(s, u) = \frac{s}{s+\mu u} v_0 + \frac{u\mu}{s+\mu u} G(s, u). \tag{24}$$

Assuming inverse Formable transforms exist and utilizing them to the system, we obtain

$$w(t) = w_0 e^t - \mathfrak{R}^{-1} \left[\frac{u\mathcal{H}(s, u)}{s-u} \right]$$

$$v(t) = v_0 e^{-\mu t} + \mu \mathfrak{R}^{-1} \left[\frac{u}{s+\mu u} G(s, u) \right]$$

desired solutions to the initial value problem (17)-(19).

Applications

This section presents numerical examples to illustrate the efficacy of the Formable transform in problem-solving.

Example 1. The population of a city experiences growth at a rate that is directly proportional to the current number of people living there. Estimate how many people lived in the city at the beginning if the population has doubled after three years and 30000 after four years.

The mathematical model of the mentioned problem can be expressed as

$$\frac{dP(t)}{dt} = kP(t). \tag{25}$$

where k is the constant of proportionality and P represents number of individuals that are currently living in the city at any given time t . Suppose that P_0 represents the beginning population of the city at $t = 0$. By applying

the Formable transform to both sides of equation (25), the following result is obtained:

$$\mathfrak{R} \left[\frac{dP(t)}{dt} \right] = k\mathfrak{R}[P(t)]$$

$$\frac{s}{u} \mathfrak{R}[P(t)] - \frac{s}{u} P(0) = k\mathfrak{R}[P(t)].$$

Substituting the condition $P(0) = P_0$ at $t = 0$, we acquire

$$\left(\frac{s}{u} - k \right) \mathfrak{R}[P(t)] = \frac{s}{u} P_0$$

$$\mathfrak{R}[P(t)] = \frac{s}{s-ku} P_0. \tag{26}$$

Upon applying the inverse Formable transform on either side of (26), we find

$$P(t) = \mathfrak{R}^{-1} \left[\frac{s}{s-ku} P_0 \right]$$

$$P(t) = P_0 \mathfrak{R}^{-1} \left[\frac{s}{s-ku} \right]$$

$$P(t) = P_0 e^{kt}.$$

Since $P = 2P_0$ at $t = 3$, we can write

$$P_0 e^{3k} = 2P_0$$

$$e^{3k} = 2$$

$$k = \frac{1}{3} \ln 2 \cong 0.23104. \tag{27}$$

Now, substituting the value of k found in (27) and using the condition $P = 30000$ at $t = 4$, we have

$$30000 = P_0 e^{4 \cdot \frac{1}{3} \ln 2}$$

$$P_0 \cong 11905$$

which is the required number of people who lived in the city at the beginning.

Example 2. Bacteria in a certain culture increase at a rate proportional to the number present. Estimate the number of bacteria at the beginning of a certain culture after six hours, if the number of bacteria grows from 500 to 1500 in three hours.

The mathematical model of the mentioned problem can be expressed as

$$\frac{dP(t)}{dt} = kP(t). \tag{28}$$

where P denotes the number of bacteria at any time t and k is the constant of proportionality. The result of using the Formable transform on either side of (28) is

$$\frac{s}{u} \mathfrak{R}[P(t)] - \frac{s}{u} P(0) = k\mathfrak{R}[P(t)].$$

Since the initial amount is 500 at $t = 0$, we have

$$\begin{aligned} \left(\frac{s}{u} - k\right) \mathfrak{R}[P(t)] &= 500 \frac{s}{u} \\ \mathfrak{R}[P(t)] &= \frac{s}{s - ku} 500 \end{aligned} \tag{29}$$

Having applied inverse Formable transform on either side of (29), we find

$$\begin{aligned} P(t) &= \mathfrak{R}^{-1} \left[\frac{s}{s - ku} 500 \right] \\ P(t) &= 500 \mathfrak{R}^{-1} \left[\frac{s}{s - ku} \right] \\ P(t) &= 500e^{kt}. \end{aligned}$$

By using the another given condition $P = 1500$ at $t = 3$, we find

$$\begin{aligned} 500e^{3k} &= 1500 \\ e^{3k} &= 3 \\ k &= \frac{1}{3} \ln 3 \cong 0.23104 \end{aligned} \tag{30}$$

We are looking for $t = 6$, so we get the number of bacteria present in a certain culture as

$$P(6) = 500e^{6 \cdot \frac{1}{3} \ln 3} \cong 4500$$

by substituting the value of k found in (30).

Example 3. The decay of a radioactive substance is recognized to occur at a rate that is directly proportional to the quantity of the substance present. Find the half-life of the radioactive substance, if 50 milligrams of the substance are originally present and the radioactive substance has lost 20 percent of its original mass after five hours.

The mathematical model of the mentioned problem can be expressed as

$$\frac{dP(t)}{dt} = -kP(t) \tag{31}$$

where P represents the quantity of radioactive substance at time t and k is the proportionality constant. Suppose that P_0 is the initial amount of the radioactive substance at time $t = 0$. When we apply the Formable transform on either side of (31), we get the following result:

$$\begin{aligned} \mathfrak{R} \left[\frac{dP(t)}{dt} \right] &= -k \mathfrak{R}[P(t)] \\ \frac{s}{u} \mathfrak{R}[P(t)] - \frac{s}{u} P(0) &= -k \mathfrak{R}[P(t)]. \end{aligned}$$

Substituting the condition $P(0) = P_0$ at $t = 0$, we acquire

$$\begin{aligned} \left(\frac{s}{u} + k\right) \mathfrak{R}[P(t)] &= \frac{s}{u} P_0 \\ \mathfrak{R}[P(t)] &= \frac{s}{s + ku} 50. \end{aligned} \tag{32}$$

Having applied the inverse Formable transform on either side of (32), we obtain

$$\begin{aligned} P(t) &= \mathfrak{R}^{-1} \left[\frac{s}{s + ku} 50 \right] \\ P(t) &= 50 \mathfrak{R}^{-1} \left[\frac{s}{s + ku} \right] \\ P(t) &= 50e^{-kt}. \end{aligned} \tag{33}$$

At time $t = 5$, the radioactive substance has lost 20 percent of its original mass of 50 milligrams. Hence $P = 50 - 10 = 40$. By using this in (33), we get

$$\begin{aligned} 40 &= 50e^{-5k}. \\ e^{-5k} &= 0.8 \\ k &= -\frac{1}{5} \ln 0.8 \cong 0.04462 \dots \end{aligned} \tag{34}$$

We required t when $P = \frac{P_0}{2} = 25$. Therefore, we can write

$$25 = 50e^{-kt}$$

from (31). By substituting the value of k from (34), we obtain

$$\begin{aligned} 25 &= 50e^{-0.04462t} \\ e^{-0.04462t} &= 0.5 \\ t &= -\frac{1}{0.04462} \ln 0.5 \\ t &\cong 15.531 \text{ hours} \end{aligned}$$

which is the desired half-time of the radioactive substance.

In Examples 1-3, it is demonstrated that Formable transform successfully determines the solutions to population growth and decay problems solved by other integral transforms studied in [11-22]. Upon individually solving the instances provided in the references, it will be seen that the same results are obtained with the Formable transform.

Example 4. Let us consider the logistic growth model equation (14) where $P_0 = 2$ and $\kappa = 1$. Hence v_0 can be expressed as $v_0 = \frac{P_0}{\kappa} = 2$. We set $h(v) = v^2$ as in (4) so that one finds

$$h(v) = \left(\sum_{n=0}^{\infty} c_n t^n \right)^2 = (c_0 + c_1 t + c_2 t^2 + \dots + c_n t^n + \dots)^2$$

$$= c_0^2 + 2c_0 c_1 t + (2c_0 c_2 + c_1^2) t^2 + (2c_0 c_3 + 2c_1 c_2) t^3 + \dots$$

Implementing Formable transform to each side of the equation

$$\mathfrak{R}[h(v)] = \mathcal{H}(s, u) = c_0^2 + 2c_0 c_1 \frac{u}{s} + (2c_0 c_2 + c_1^2) 2! \frac{u^2}{s^2} + (2c_0 c_3 + 2c_1 c_2) 3! \frac{u^3}{s^3} + \dots$$

One obtains

$$\mathcal{V}(s, u) = v_0 \frac{s}{s-u} - \frac{u \mathcal{H}(s, u)}{s-u}$$

$$= \frac{2s}{s-u} - \left[\frac{u c_0^2}{s-u} + \frac{2c_0 c_1 u^2}{s(s-u)} + 2! \frac{(2c_0 c_2 + c_1^2) u^3}{s^2(s-u)} + 3! \frac{(2c_0 c_3 + 2c_1 c_2) u^4}{s^3(s-u)} + \dots \right]$$

$$= \frac{2s}{s-u} - \left[\left(\frac{s}{s-u} - 1 \right) c_0^2 + \left(\frac{s}{s-u} - 1 - \frac{u}{s} \right) 2c_0 c_1 + 2! \left(\frac{s}{s-u} - 1 - \frac{u}{s} - \frac{u^2}{s^2} \right) (2c_0 c_2 + c_1^2) \right.$$

$$\left. + 3! \left(\frac{s}{s-u} - 1 - \frac{u}{s} - \frac{u^2}{s^2} - \frac{u^3}{s^3} \right) (2c_0 c_3 + 2c_1 c_2) + \dots \right]$$

by using (16). Upon application of the inverse Formable transform to this equation yields

$$c_0 + c_1 t + c_2 t^2 + c_3 t^3 + \dots = 2 \left(1 + t + \frac{t^2}{2!} + \frac{t^3}{3!} + \dots \right)$$

$$- (c_0^2 + 2c_0 c_1 + 4c_0 c_2 + 2c_1^2 + 12c_0^2 2c_0 c_3 + 12c_1 c_2 + \dots) \left(1 + t + \frac{t^2}{2!} + \frac{t^3}{3!} + \dots \right)$$

$$+ (c_0^2 + 2c_0 c_1 + 4c_0 c_2 + 2c_1^2 + 12c_0^2 2c_0 c_3 + 12c_1 c_2 + \dots)$$

$$+ (2c_0 c_1 + 4c_0 c_2 + 2c_1^2 + 12c_0^2 2c_0 c_3 + 12c_1 c_2 + \dots) t$$

$$+ (2c_0 c_1 + c_1^2 + 6c_0^2 2c_0 c_3 + 6c_1 c_2 + \dots) t^2 + (2c_0 c_3 + 2c_1 c_2 + \dots) t^3 + \dots$$

$$= 2 \left(1 + t + \frac{t^2}{2!} + \frac{t^3}{3!} + \dots \right) - c_0^2 t - \left(\frac{c_0^2}{2} + c_0 c_1 \right) t^2 - \left(\frac{c_0^2}{6} + \frac{c_0 c_1}{3} + \frac{2c_0 c_2}{3} + \frac{c_1^2}{3} \right) t^3 - \dots$$

$$= 2 + (2 - c_0^2) t + \left(1 - \frac{c_0^2}{2} - c_0 c_1 \right) t^2 + \left(\frac{1}{3} - \frac{c_0^2}{6} - \frac{c_0 c_1}{3} - \frac{2c_0 c_2}{3} - \frac{c_1^2}{3} \right) t^3 + \dots$$

from (15). When the coefficients of power t are equated, the result is

$$c_0 = 2,$$

$$c_1 = 2 - c_0^2 \Rightarrow c_1 = -2,$$

$$c_2 = 1 - \frac{c_0^2}{2} - c_0 c_1 \Rightarrow c_2 = 3,$$

$$c_3 = \frac{1}{3} - \frac{c_0^2}{6} - \frac{c_0 c_1}{3} - \frac{2c_0 c_2}{3} - \frac{c_1^2}{3} \Rightarrow c_3 = -\frac{13}{3},$$

$$\vdots$$

and so on. Consequently, the solution $v(t)$ is obtained from (15) as follows

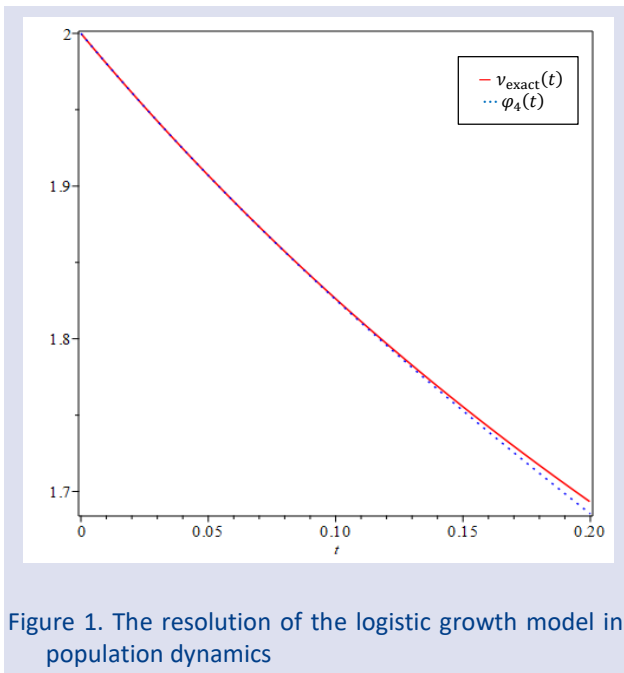
$$v(t) = 2 - 2t + 3t^2 - \frac{13}{3} t^3 + \dots$$

that is the closed form exact solution obtained in (5). This solution is identical to the one discovered in [23].

The n th partial sums of the series (15) is represented by $\varphi_n(t)$ which is equivalent to

$$\varphi_n(t) = \sum_{m=0}^n c_m t^m. \tag{35}$$

Based on the observation of Figure 1, it is evident that a highly accurate approximation of the exact solution for the logistic growth model within the time interval $[0,0.20]$ has been achieved by computing only four terms of the series in (35). This indicates that the rate at which the Formable transform method converges is highly rapid. Furthermore, it is possible to minimize the overall errors and obtain a reasonably accurate estimation of the exact solution for $t \geq 0.2$ by incorporating new terms into the series.



Example 5. Consider the differential equation system that governs the predator and prey model

$$\frac{dw}{dt} = w - wv \tag{36}$$

$$\frac{dv}{d\tau} = wv - v \tag{37}$$

with initial data $w(0) = 1.3, v(0) = 0.6$. Assume that $w(t) = \sum_{n=0}^{\infty} a_n t^n, v(t) = \sum_{n=0}^{\infty} c_n t^n$ be solutions of the system of (36)-(37). Therefore, we have

$$h(w, v) = g(w, v) = wv = \left(\sum_{n=0}^{\infty} a_n t^n\right) \left(\sum_{n=0}^{\infty} c_n t^n\right) = a_0 c_0 + (a_0 c_1 + a_1 c_0)t + (a_0 c_2 + a_1 c_1 + a_2 c_0)t^2 + (a_0 c_3 + a_1 c_2 + a_2 c_1 + a_3 c_0)t^3 + \dots$$

The corresponding Formable transform of these functions are

$$\begin{aligned} \mathfrak{R}[wv] &= a_0 c_0 \mathfrak{R}[1] + (a_0 c_1 + a_1 c_0) \mathfrak{R}[t] + (a_0 c_2 + a_1 c_1 + a_2 c_0) \mathfrak{R}[t^2] + (a_0 c_3 + a_1 c_2 + a_2 c_1 + a_3 c_0) \mathfrak{R}[t^3] + \dots \\ &= a_0 c_0 + (a_0 c_1 + a_1 c_0) \frac{u}{s} + (2a_0 c_2 + 2a_1 c_1 + 2a_2 c_0) \frac{u^2}{s^2} + (6a_0 c_3 + 6a_1 c_2 + 6a_2 c_1 + 6a_3 c_0) \frac{u^3}{s^3} + \dots \end{aligned}$$

Here $\mathcal{H}(s, u) = G(s, u) = \mathfrak{R}[wv]$. From (23) and (24), it is found that

$$\begin{aligned} \mathcal{W}(s, u) &= \frac{s}{s-u} 1.3 - \frac{u}{s-u} \mathcal{H}(s, u) \\ &= \frac{s}{s-u} 1.3 - \frac{u}{s-u} a_0 c_0 - (a_0 c_1 + a_1 c_0) \frac{u^2}{s(s-u)} - (a_0 c_2 + a_1 c_1 + a_2 c_0) \frac{2u^3}{s^2(s-u)} \\ &\quad - (a_0 c_3 + a_1 c_2 + a_2 c_1 + a_3 c_0) \frac{6u^4}{s^3(s-u)} + \dots \\ &= \frac{s}{s-u} 1.3 - a_0 c_0 \left(\frac{s}{s-u} - 1\right) - (a_0 c_1 + a_1 c_0) \left(\frac{s}{s-u} - 1 - \frac{u}{s}\right) \\ &\quad - 2! (a_0 c_2 + a_1 c_1 + a_2 c_0) \left(\frac{s}{s-u} - 1 - \frac{u}{s} - \frac{u^2}{s^2}\right) \\ &\quad - 3! (a_0 c_3 + a_1 c_2 + a_2 c_1 + a_3 c_0) \left(\frac{s}{s-u} - 1 - \frac{u}{s} - \frac{u^2}{s^2} - \frac{u^3}{s^3}\right) + \dots \end{aligned}$$

$$\begin{aligned} \mathcal{V}(s, u) &= \frac{s}{s+u} 0.6 + \frac{u}{s+u} G(s, u) \\ &= \frac{s}{s+u} 0.6 + \frac{u}{s+u} a_0 c_0 + (a_0 c_1 + a_1 c_0) \frac{u^2}{s(s+u)} + (a_0 c_2 + a_1 c_1 + a_2 c_0) \frac{2u^3}{s^2(s+u)} \\ &\quad + (a_0 c_3 + a_1 c_2 + a_2 c_1 + a_3 c_0) \frac{6u^4}{s^3(s+1)} + \dots \\ &= \frac{s}{s+u} 0.6 + a_0 c_0 \left(1 - \frac{s}{s+u}\right) + (a_0 c_1 + a_1 c_0) \left(-1 + \frac{u}{s} + \frac{s}{s+u}\right) \\ &\quad + 2! (a_0 c_2 + a_1 c_1 + a_2 c_0) \left(1 - \frac{u}{s} + \frac{u^2}{s^2} - \frac{s}{s+u}\right) \\ &\quad + 3! (a_0 c_3 + a_1 c_2 + a_2 c_1 + a_3 c_0) \left(-1 + \frac{u}{s} - \frac{u^2}{s^2} + \frac{u^3}{s^3} + \frac{s}{s+u}\right) + \dots \end{aligned}$$

When the inverse Formable transform is applied to these equations, one gets

$$\begin{aligned}
 a_0 + a_1t + a_2t^2 + a_3t^3 + \dots &= 1.3 \left(1 + t + \frac{t^2}{2!} + \frac{t^3}{3!} + \dots \right) - a_0c_0t - (a_0c_0 + a_0c_1 + a_1c_0) \frac{t^2}{2!} \\
 &\quad - (a_0c_0 + a_0c_1 + a_1c_0 + 2a_0c_2 + 2a_1c_1 + 2a_2c_0) \frac{t^3}{3!} - \dots \\
 &= 1.3 + (1.3 - a_0c_0)t + (1.3 - a_0c_0 - a_0c_1 - a_1c_0) \frac{t^2}{2!} \\
 &\quad + (1.3 - a_0c_0 - a_0c_1 - a_1c_0 - 2a_0c_2 - 2a_1c_1 - 2a_2c_0) \frac{t^3}{3!} + \dots
 \end{aligned}$$

and

$$\begin{aligned}
 c_0 + c_1t + c_2t^2 + c_3t^3 + \dots &= 0.6 \left(1 - t + \frac{t^2}{2!} - \frac{t^3}{3!} + \dots \right) - a_0c_0t - (a_0c_0 + a_0c_1 + a_1c_0) \frac{t^2}{2!} \\
 &\quad - (a_0c_0 + a_0c_1 + a_1c_0 + 2a_0c_2 + 2a_1c_1 + 2a_2c_0) \frac{t^3}{3!} - \dots \\
 &= 0.6 + (a_0c_0 - 0.6)t + (0.6 - a_0c_0 + a_0c_1 + a_1c_0) \frac{t^2}{2!} \\
 &\quad + (-0.6 + a_0c_0 - a_0c_1 - a_1c_0 + 2a_0c_2 + 2a_1c_1 + 2a_2c_0) \frac{t^3}{3!} + \dots .
 \end{aligned}$$

If the coefficients are equalized to powers of t , it is found as

$a_0 = 1.3$	$c_0 = 0.6$
$a_1 = 1.3 - a_0c_0$	$c_1 = a_0c_0 - 0.6$
$a_1 = 0.52$	$c_1 = 0.18$
$a_2 = \frac{1}{2!}(1.3 - a_0c_0 - a_0c_1 - a_1c_0)$	$c_2 = \frac{1}{2!}(0.6 + a_0c_1 + a_1c_0 - a_0c_0)$
$a_2 = -0.013$	$c_2 = 0.183$
$a_3 = \frac{1}{3!}(1.3 - a_0c_0 - a_0c_1 - a_1c_0 - 2a_0c_2 - 2a_1c_1 - 2a_2c_0)$	$c_3 = \frac{1}{3!}(-0.6 + a_0c_0 - a_0c_1 - a_1c_0 + 2a_0c_2 + 2a_1c_1 + 2a_2c_0)$
$a_3 = -0.1122$	$c_3 = 0.0469$
\vdots	\vdots

The subsequent terms of the series can be obtained using this method. By substituting these terms into equation (20), we obtain the approximate solutions for the problem described by equations (36)-(37):

$$\begin{aligned}
 w(t) &= 1.3 + 0.52t - 0.013t^2 - 0.1122t^3 - \dots \\
 v(t) &= 0.6 + 0.18t + 0.183t^2 + 0.0469t^3 + \dots .
 \end{aligned}$$

The outcomes we have presently achieved exhibit congruence with the findings derived from the study conducted in reference [23].

Figure 2 shows the approximate solutions to system (36)-(37) which are obtained by Formable transform using

only four terms of the series (20). This system's numerical solutions are shown in Figure 3. The system's numerical solutions are obtained using Ode45, which is a built-in ordinary differential equation solver in MATLAB.

The comparison of the two figures reveals a significant level of closeness between the two solutions for w (prey population) and v (predator population) within the time interval of $[0,2]$. Adding more terms to the series provides an even closer approximation to the numerical answer for $t \geq 1,6$, as previously mentioned in the context of the logistic growth model.

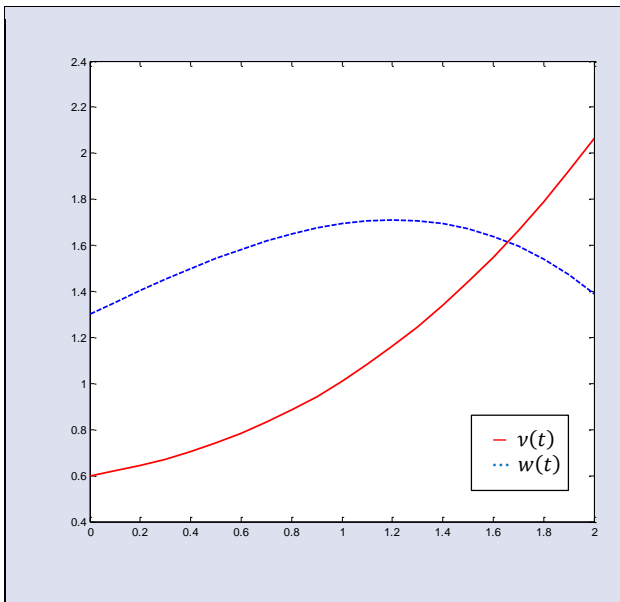


Figure 2. Approximate solutions to the system (36)-(37) by Formable transform method

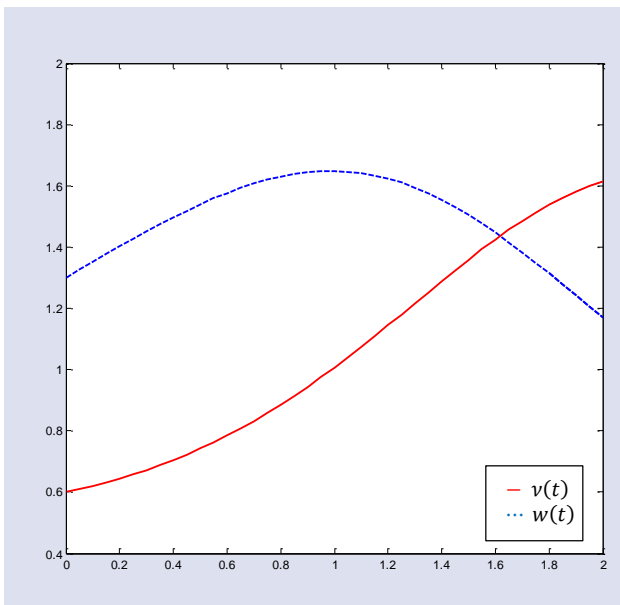


Figure 3. Numerical solutions to the system (36)-(37)

Conclusions

Differential equations are of paramount importance in the development of mathematical models to describe physical phenomena. In this study, we successfully applied the Formable transform to growth and decay problems. We further strengthened its application to growth and decay problems with several numerical examples, showing that the Formable transform is a highly handy approach for solving differential equations. These applications demonstrate how the Formable transform may be used to resolve growth and decay problems without complex calculations. The Formable transform method provides very accurate approximate solutions to nonlinear problems in mathematics, biology, physics, etc. Furthermore, it does not necessitate the process of

linearization or rely on biologically implausible assumptions. As a result of its efficiency and convenience, this transform is a powerful tool for numerically solving a wide variety of interesting mathematical models involving differential equations.

Conflict of interests

The authors state that did not have conflict of interests.

References

- [1] Weiglhofer W.S., Lindsay K.A., Ordinary differential equations & applications: Mathematical methods for applied mathematicians, physicists, engineers and bioscientists, Woodhead (1999).
- [2] Murray J. D., Mathematical Biology, Springer, Berlin (1993).
- [3] Aggarwal S., Gupta, A.R., Dualities between Mohand transform and some useful integral transforms, *International Journal of Recent Technology and Engineering*, 8(3) (2019) 843 -847.
- [4] Aggarwal S., Gupta A.R., Dualities between some useful integral transforms and Sawi transform, *International Journal of Recent Technology and Engineering*, 8(3) (2019), 5978-5982.
- [5] Aggarwal S., Bhatnagar K., Dua A., Dualities between Elzaki transform and some useful integral transforms, *International Journal of Innovative Technology and Exploring Engineering*, 8(12) (2019), 4312-4318.
- [6] Chauhan R., Kumar N., Aggarwal S., Dualities between Laplace-Carson transform and some useful integral transforms, *International Journal of Innovative Technology and Exploring Engineering*, 8(12) (2019) 1654-1659.
- [7] Aggarwal S., Bhatnagar K., Dualities between Laplace transform and some useful integral transforms, *International Journal of Engineering and Advanced Technology*, 9(1) (2019) 936-941.
- [8] Chaudhary R., Sharma S.D., Kumar N., Aggarwal S., Connections between Aboodh transform and some useful integral transforms, *International Journal of Innovative Technology and Exploring Engineering*, 9(1) (2019) 1465-1470.
- [9] Aggarwal S., Sharma N., Chauhan R., Duality relations of Kamal transform with Laplace, Laplace-Carson, Aboodh, Sumudu, Elzaki, Mohand and Sawi transforms, *SN Appl. Sci.*, 2, 135 (2020) doi:10.1007/s42452-019-1896-z.
- [10] Mishra R., Aggarwal S., Chaudhary L., Kumar A., Relationship between Sumudu and some efficient integral transforms, *International Journal of Innovative Technology and Exploring Engineering*, 9(3) (2020) 153-159.
- [11] Rao R.U., ZZ Transform Method for Natural Growth and Decay Problems, *International Journal of Progressive Sciences and Technologies*, 5(2) (2017) 147-150.
- [12] Aggarwal S., Gupta A.R., Singh D.P., Asthana N., Kumar N., Application of Laplace transform for solving population growth and decay problems, *International Journal of Latest Technology in Engineering, Management & Applied Science*, 7(9) (2018) 141-145.
- [13] Aggarwal S., Singh D.P., Asthana N., Gupta A.R., Application of Elzaki Transform for Solving Population Growth and Decay Problems, *Journal of Emerging Technologies and Innovative Research*, 5(9) (2018) 281-284.

- [14] Aggarwal S., Gupta A.R., Asthana N., Singh D.P., Application of Kamal transform for Solving Population Growth and Decay Problems, *Global Journal of Engineering Science and Researches*, 5(9) (2018) 254-260.
- [15] Aggarwal S., Asthana N., Singh D.P., Solution of Population Growth and Decay Problems by Using Aboodh Transform Method, *International Journal of Research in Advent Technology*, 6(10) (2018) 2706-2710.
- [16] Aggarwal S., Pandey M., Asthana N., Singh D.P., Kumar N., Application of Mahgoub Transform for Solving Population Growth and Decay Problems, *Journal of Computer and Mathematical Sciences*, 9(10) (2018) 1490-1496.
- [17] Aggarwal S., Sharma N., Chauhan R., Solution of Population Growth and Decay Problems by Using Mohand Transform, *International Journal of Research in Advent Technology*, 6(11) (2018) 3277-3282.
- [18] Aggarwal S., Sharma S.D., Gupta A.R., Application of Shehu Transform for Handling Growth and Decay Problems, *Global Journal of Engineering Science and Researches*, 6(4) (2019) 190-198.
- [19] Aggarwal S., Bhatnagar K., Sadik Transform for Handling Population Growth and Decay Problems, *Journal of Applied Science and Computations*, 6 (6) (2019) 1212-1221.
- [20] Singh G.P., Aggarwal S., Sawi Transform for Population Growth and Decay Problems, *International Journal of Latest Technology in Engineering, Management & Applied Science*, 8(8) (2019) 157-162.
- [21] Verma D., Singh A.P., Verma S.K., Scrutinize Of Growth and Decay Problems by Dinesh Verma Transform (DVT), *IRE Journals*, 3(12) (2020) 148-153.
- [22] Bansal S., Kumar A., Aggarwal S., Application of Anuj Transform for the Solution of Bacteria Growth Model, *GIS Science Journal*, 9(6) (2022) 1465-1472.
- [23] Pamuk S., Soylu N., Laplace transform method for logistic growth in a population and predator models, *New Trends in Mathematical Sciences*, 8(3) (2020) 9-17.
- [24] Peker H. A., Çuha, F. A., Application of Kashuri Fundo Transform to Decay Problem, *Süleyman Demirel Üniversitesi Fen Bilimleri Enstitüsü Dergisi*, 26 (3) (2022) 546-551.
- [25] Priyanka, Aggarwal S., Solution of the model of the bacteria growth via Rishi transform, *Journal of Advanced Research in Applied Mathematics and Statistics*, 7(1&2) (2022) 5-11.
- [26] Higazy M., Aggarwal S., Nofal T.A., Sawi decomposition method for Volterra integral equation with application, *Journal of Mathematics*, (2020) Article ID 6687134, 13 pages.
- [27] Higazy M., Aggarwal S., Hamed Y.S., Determination of number of infected cells and concentration of viral particles in plasma during HIV-1 infections using Shehu transformation, *Journal of Mathematics*, (2020), Article ID 6624794, 13 pages.
- [28] Kumar R., Chandel J., Aggarwal S., A new integral transform "Rishi Transform" with application, *Journal of Scientific Research*, 14(2) (2022) 521-532.
- [29] Güngör N., Application of Kharrat-Toma Transform for Solving Linear Volterra Integral Equations, *Journal of Universal Mathematics*, 3 (2) (2020) 137-145.
- [30] Oral P., Merdan M., Bekiryazıcı Z., Analysis of a Random Zeeman Heartbeat Model with Differential Transformation Method, *Cumhuriyet Science Journal*, 40 (2) (2019) 285-298. DOI: 10.17776/csj.460984
- [31] Saadeh R.Z., Ghazal B.f., A New Approach on Transforms: Formable Integral Transform and Its Applications, *Axioms*, 10 (332) (2021) 1-21.
- [32] Güngör N., Solution of Convolution Type Linear Volterra Integral Equations with Formable Transform, *International Journal of Latest Technology in Engineering, Management & Applied Science*, 11(12) (2022) 1-4.
- [33] Ghazal B., Saadeh R., Sedeeg A.K., Solving Partial Integro-Differential Equations via Double Formable Transform, *Applied Computational Intelligence and Soft Computing*, (2022) Article ID 6280736, 15 pages.
- [34] Saadeh R., Sedeeg A.K., Ghazal B., Gharih G., Double Formable Integral Transform for Solving Heat Equations, *Symmetry*, 15 (218) (2023).
- [35] Saadeh R., Qazza A., Burqan A., Al-Omari S., On Time Fractional Partial Differential Equations and Their Solution by Certain Formable Transform Decomposition Method, *Computer Modeling in Engineering & Sciences*, 136(3) (2023) 3121-3139.
- [36] Prajapati J.V., Meher R., Solution of Time-Fractional Rosenau-Hyman Model Using a Robust Homotopy Approach via Formable Transform, *Iran J. Sci. Technol. Trans. Sci.*, 46 (2022) 1431-1444.
- [37] Khalid M., Alha S., On Hilfer-Prabhakar derivatives Formable integral transform and its applications to fractional differential equations, *Authorea*, January 24 (2023).

On Deferred Statistical and Strong Deferred Cesàro Convergences of Sequences With Respect to A Modulus Function

Cemel Belen ^{1,a}, Mustafa Yıldırım^{2,b,*}

¹ Department of Mathematics Education, Ordu University, 52200, Ordu, Türkiye.

² Department of Mathematics, Faculty of Science, Sivas Cumhuriyet University, Sivas, Türkiye

*Corresponding author

Research Article

History

Received: 28/07/2023

Accepted: 02/11/2023

Copyright



©2023 Faculty of Science,
Sivas Cumhuriyet University

ABSTRACT

Let f be any modulus function. We prove that the classes of strongly deferred Cesàro convergent sequences defined by f and deferred statistical convergent sequences are equivalent if the sequence is f -deferred uniformly integrable. Some converse inclusions are obtained when the modulus function f is compatible. Finally, for any compatible modulus f , we prove that any sequence is f -strongly deferred Cesàro convergent if and only if it is deferred f -statistically convergent and deferred uniformly integrable.

Keywords: Deferred statistical convergence, Strong deferred convergence, Uniformly integrable sequence, Compatible modulus function.

^a cbelen52@gmail.com

^b <https://orcid.org/0000-0002-8832-1524>

^b yildirim@cumhuriyet.edu.tr

^b <https://orcid.org/0000-0002-8880-5457>

Introduction

Statistical convergence was first introduced by Fast [1] and also independently by Buck [2] and Schoenberg [3] for real and complex sequences, but the rapid developments started after the papers of Šalát [4] and Fridy [5].

Strong Cesàro convergence with respect to a modulus function was introduced by Maddox [6]. Connor [7] extended this idea by replacing Cesàro matrix with a non-negative regular matrix A and proved that A -statistical convergence includes strong A -summability with respect to a modulus and further these notions are equivalent for bounded sequences. Connor also established the relationship between statistical convergence and strong Cesàro convergence [8]: A real sequence is strongly convergent if and only if it is statistical convergent and bounded. Khan and Orhan [9] extended this result by replacing the boundedness condition with a strictly weaker condition so-called uniform integrability.

By using any modulus function f , Aizpuru and coworkers [10] introduced the concept of f -statistical convergence. León-Saavedra et. al. [11] defined the notion of f -strongly convergence by means of modulus functions. They proved that if a sequence is f -strongly convergent then it is f -statistically convergent and uniformly integrable, and the converse statement is true when f is compatible modulus function. Such type of modulus functions are those for which the concepts of statistical convergence and f -statistical convergence are equivalent.

Motivated by Agnew [12], Küçükaslan and Yılmaztürk [13] defined and studied on the the concept of deferred statistical convergence. Later this concept was improved by Gupta and Bhardwaj [14] with the help of modulus

functions. They also introduced the notion of strongly deferred Cesàro convergence of sequences defined by modulus function f and investigated its relation with deferred f -statistical convergence. We refer to [15-22] for additional different works on deferred statistical convergence.

In the present paper, we investigate the relationship between strongly deferred Cesàro convergent sequences defined by a modulus function and deferred statistically convergent sequences. We prove that these two classes are equivalent in the context of f -deferred uniformly integrable sequences. Later we define f -strongly deferred Cesàro convergence of a real sequence and examines its relation with strongly deferred Cesàro convergence. If f is any modulus function, f -strongly deferred Cesàro convergence (deferred f -statistical convergence) implies strongly deferred Cesàro convergence (deferred statistical convergence), but not conversely. We prove that converse statements are true when f is compatible modulus function. Finally, for any compatible modulus f , we prove that any sequence is f -strongly deferred Cesàro convergent if and only if it is deferred f -statistically convergent and deferred uniformly integrable.

Materials and Methods

Let \mathbb{N} be set of positive integers and $x = (x_k)$ be sequence of real numbers. Then x is statistically convergent to the number L (in short $x \in S$) provided for each $\varepsilon > 0$,

$$\lim_{n \rightarrow \infty} \frac{1}{n} |\{k \leq n: |x_k - L| \geq \varepsilon\}| = 0.$$

Suppose that (p_n) and (q_n) are the sequences of non-negative integers with $p_n < q_n$ and $q_n \rightarrow \infty$ (as $n \rightarrow \infty$). We say that (x_k) is strongly deferred Cesàro convergent to L if

$$\lim_{n \rightarrow \infty} \frac{1}{q_n - p_n} \sum_{k=p_n+1}^{q_n} |x_k - L| = 0$$

(see [12]). In this paper we prefer the notation $w_{p,q}$ for the set of all strongly deferred Cesàro convergent sequences.

Any sequence (x_k) is said to be deferred statistical convergent to L if for each $\varepsilon > 0$,

$$\lim_{n \rightarrow \infty} \frac{1}{q_n - p_n} |\{k \in \mathbb{N}: p_n < k \leq q_n, |x_k - L| \geq \varepsilon\}| = 0.$$

In this case we write $S_{p,q}\text{-}\lim x = L$ and the set of all deferred statistically convergent sequences will be denoted by $S_{p,q}$ (see [13]). Throughout the paper we will use the notation $E_{\varepsilon,p,q}$ instead of the set $\{k \in \mathbb{N}: p_n < k \leq q_n, |x_k - L| \geq \varepsilon\}$. If we choose $q_n = n$ and $p_n = 0$ for all n , then $S_{p,q}$ coincides with S .

Note that $w_{p,q} \subset S_{p,q}$ and $w_{p,q} \cap \ell_\infty = S_{p,q} \cap \ell_\infty$, also if the sequence $(\frac{p_n}{q_n - p_n})$ is bounded then $S \subset S_{p,q}$, where ℓ_∞ is the set of all bounded sequences.

Any function $f : \mathbb{R}^+ \rightarrow \mathbb{R}^+$ with the following properties is called a modulus function;

1. $f(x) = 0$ if and only if $x = 0$,
2. $f(x + y) \leq f(x) + f(y)$ for all $x, y \in \mathbb{R}^+$,
3. f is increasing,
4. f , is continuous from the right at zero [23].

$f(x) = x^p$ ($0 < p \leq 1$) and $f(x) = \frac{x}{1+x}$ are some examples of a modulus function. A modulus function can be bounded or unbounded.

Let f be any modulus function. A sequence $x = (x_k)$ is said to be f -statically convergent to L if for each $\varepsilon > 0$

$$\lim_{n \rightarrow \infty} \frac{f(|\{k \leq n: |x_k - L| \geq \varepsilon\}|)}{f(n)} = 0$$

(see, [10]). It is also known from [10] that any f -statistically convergent sequence is also statistically convergent but not conversely. We remark here that if f is bounded modulus function, then these definitions hold only for trivial cases (for empty set and constant sequences). So, throughout the paper, we only consider the unbounded modulus functions.

In [14], Gupta and Bhardwaj defined the notion of deferred f -statistical convergence and strongly deferred Cesàro convergence with respect to f as follows:

Let f be any modulus function and $x = (x_k)$ be any real sequence. Then, x is said to be deferred f -statistically convergent to L if for each $\varepsilon > 0$,

$$\lim_{n \rightarrow \infty} \frac{1}{f(q_n - p_n)} f(|\{k: p_n < k \leq q_n, |x_k - L| \geq \varepsilon\}|) = 0$$

and if

$$\lim_{n \rightarrow \infty} \frac{1}{q_n - p_n} \sum_{k=p_n+1}^{q_n} f(|x_k - L|) = 0$$

then x is said to be strongly deferred Cesàro convergent to L with respect to f . The sets of all deferred f -statistically convergent and all strongly deferred Cesàro convergent with respect to f will be denoted by $S_{p,q}^f$ and $w_{p,q}^f$, respectively. We know from [14] that the inclusion $S_{p,q}^f \subset S_{p,q}$ is strict.

Now let $A = (a_{nk})$, $n, k \in \mathbb{N}$, be any non-negative regular matrix, i.e. that transforms any convergent sequence into a convergent sequence with the same limit. Any real sequence $x = (x_k)$ is A -statistically convergent to L if

$$\lim_{n \rightarrow \infty} \sum_{k: |x_k - L| \geq \varepsilon} a_{nk} = 0$$

for each $\varepsilon > 0$. Also x is said to be A -strong convergent if

$$\lim_{n \rightarrow \infty} \sum_{k=1}^{\infty} a_{nk} |x_k - L| = 0.$$

Khan and Orhan [9] characterized A -strong convergence and A -statistical convergence through A -uniform integrable sequences. A real sequence $x = (x_k)$ is called A -uniformly integrable if

$$\limsup_{c \rightarrow \infty} \sum_{|x_k| \geq c} a_{nk} |x_k| = 0.$$

Khan and Orhan proved that a sequence is A -strongly convergent if and only if it is A -statistically convergent and A -uniformly integrable. Replacing the matrix A with $D_{p,q} := (d_{nk})$, where

$$d_{nk} = \begin{cases} \frac{1}{q_n - p_n}, & p_n < k \leq q_n, \\ 0, & \text{otherwise} \end{cases}$$

we obtain the the following result.

Theorem 2.1 [9] Let $x = (x_k)$ be a real sequence. Then the following are equivalent.

- (i) x is strongly deferred Cesàro convergent to L .
- (ii) x is deferred statistically convergent to L and $D_{p,q}$ -uniformly integrable

Main Results

In this section, we first characterize the sets $w_{p,q}^f$ and $S_{p,q}$ via deferred uniformly integrable sequences with respect to a modulus function. For this, we define the following idea motivated by [9].

Definition 3.1 Let f be any modulus function. Then a sequence (x_k) is said to be f - $D_{p,q}$ -uniformly integrable if

$$\limsup_{c \rightarrow \infty} \frac{1}{n} \sum_{k=p_n+1}^{q_n} \frac{f(|x_k|)}{f(|x_k|) \geq c} = 0.$$

Theorem 3.1 Let f be any modulus function and $x = (x_k)$ be a real sequence. Then the following are equivalent.

(i) x is strongly deferred Cesàro convergent to L with respect to f .

(ii) x is deferred statistically convergent to L and f - $D_{p,q}$ -uniformly integrable.

Proof. (i) \Rightarrow (ii). Let $x \in w_{p,q}^f$ with limit L , that is

$$\lim_{n \rightarrow \infty} \frac{1}{q_n - p_n} \sum_{k=p_n+1}^{q_n} f(|x_k - L|) = 0.$$

Let $E_{\varepsilon,p,q} = \{k: p_n < k \leq q_n, |x_k - L| \geq \varepsilon\}$ for any given $\varepsilon > 0$. Then we have

$$\begin{aligned} \frac{1}{q_n - p_n} \sum_{k=p_n+1}^{q_n} f(|x_k - L|) &\geq \frac{1}{q_n - p_n} \sum_{k \in E_{\varepsilon,p,q}} f(|x_k - L|) \\ &\geq \frac{f(\varepsilon)}{q_n - p_n} |\{k: p_n < k \leq q_n, |x_k - L| \geq \varepsilon\}|, \end{aligned}$$

since f is increasing. Letting limit for $n \rightarrow \infty$ in this inequality, we get $S_{p,q}\text{-}\lim x = L$. If we set $y_k := f(|x_k|)$, then we obtain from Theorem 2.1 that x is f - $D_{p,q}$ -uniformly integrable.

(ii) \Rightarrow (i). Assume that $S_{p,q}\text{-}\lim x = L$ and x is f - $D_{p,q}$ -uniformly integrable. Let $\varepsilon > 0$. $|x_k - L| \geq \varepsilon$ implies that $f(|x_k - L|) \geq f(\varepsilon)$. On the other hand, $\lim_{\varepsilon \rightarrow 0^+} f(\varepsilon) = 0$ since f is continuous at zero. This implies that any deferred statistically convergent sequence satisfies the condition

$$\lim_{n \rightarrow \infty} \frac{1}{q_n - p_n} |\{k: p_n < k \leq q_n, f(|x_k - L|) \geq f(\varepsilon)\}| = 0. \quad (1)$$

Thus, f - $D_{p,q}$ -uniformly integrability and (1) imply by Theorem 2.1 that x is strongly deferred Cesàro convergent to L with respect to f . This completes the proof.

Next, we define the class of f -strongly deferred Cesàro convergent sequences and display its relation with strongly deferred Cesàro convergent sequences.

Definition 3.2 Let f be a modulus function and $x = (x_k)$ be a sequence of real numbers. The sequence x is said to be f -strongly deferred Cesàro convergent to the number L if

$$\lim_{n \rightarrow \infty} \frac{1}{f(q_n - p_n)} f \left(\sum_{k=p_n+1}^{q_n} |x_k - L| \right) = 0.$$

The set of all f -strongly deferred Cesàro convergent sequences will be denoted by f - $w_{p,q}$.

Theorem 3.2 Let f be any unbounded modulus function and $x = (x_k)$ be a sequence of real numbers. If x is f -strongly deferred Cesàro convergent to L , then x is strongly deferred Cesàro convergent to L . That is f - $w_{p,q} \subset w_{p,q}$.

Proof. Assume that (x_k) is f -strongly deferred Cesàro convergent to L . Then for each $p \in \mathbb{N}$, there exists an $n_0 \in \mathbb{N}$ such that for $n \geq n_0$ we have

$$f \left(\sum_{k=p_n+1}^{q_n} |x_k - L| \right) < \frac{1}{p} f(q_n - p_n) \leq f \left(\frac{q_n - p_n}{p} \right).$$

Since f is increasing, we have

$$\sum_{k=p_n+1}^{q_n} |x_k - L| \leq \frac{1}{n} (q_n - p_n) \quad (2)$$

for all $n \geq n_0$. From this, we obtain that (x_k) is strongly deferred Cesàro convergent to L . This completes the proof.

Now recall the concept of compatible modulus function used in [11] and also in [24, 6].

Definition 3.3 [11] Let f be a modulus function. We say that f is compatible provided for any $\varepsilon > 0$ there exist $\tilde{\varepsilon} > 0$ and $n_0 = n_0(\varepsilon)$ such that $\frac{f(n\tilde{\varepsilon})}{f(n)} < \varepsilon$ for all $n \geq n_0$.

For example, $f(x) = x + \log(x + 1)$, $g(x) = \frac{x}{\sqrt{1+x}}$ and $h(x) = \frac{x}{\log x + e^2}$ are unbounded compatible modulus functions, where logarithm is to the natural base e . On the other hand the $f(x) = \log(x + 1)$ and $f(x) = \log(\log(x + e))$ are examples of modulus functions which are not compatible (For the details, see [24] and [11]).

Remark 3.1 We know from [14] that $S_{p,q}^f \subset S_{p,q}$ for any modulus function f . Now let $f(x) = \log(x + 1)$, $q_n = n^2$, $p_n = n$ and

$$x_k = \begin{cases} 1, & \text{if } k \text{ is square} \\ 0, & \text{otherwise} \end{cases}.$$

Then $S_{p,q}\text{-}\lim x = 0$ but $S_{p,q}^f\text{-}\lim x \neq 0$ (see Example 2.6 of [14]). On the other hand if we replace the modulus function with $f(x) = x + \log(x + 1)$, then we obtain that $S_{p,q}\text{-}\lim x = S_{p,q}^f\text{-}\lim x = 0$. The following result shows that this case is always valid when we use compatible modulus functions.

Theorem 3.3 Let f be a compatible modulus function. Then $S_{p,q}^f = S_{p,q}$.

Proof. When f is a compatible modulus function, it is sufficient to prove that $S_{p,q} \subset S_{p,q}^f$.

Since $S_{p,q}^f \subset S_{p,q}$ for any modulus function, it is enough to prove that $S_{p,q} \subset S_{p,q}^f$ when f is a compatible modulus function. Let f be a compatible modulus function, $x = (x_k)$ be a real sequence and $S_{p,q}\text{-lim} x = L$. Since f is compatible, for any given $\varepsilon > 0$, there exist $\tilde{\varepsilon} > 0$ and $n_0 = n_0(\varepsilon)$ such that $\frac{f(n\tilde{\varepsilon})}{f(n)} < \varepsilon$ for all $n \geq n_0$. Also the assumption $q_n - p_n \rightarrow \infty (n \rightarrow \infty)$ implies that there exists $N_0 = N_0(n_0)$ (thus $N_0 = N_0(\varepsilon)$) such that for all $n \geq N_0$ we have $q_n - p_n > n_0$. Hence, we obtain that $\frac{f((q_n - p_n)\tilde{\varepsilon})}{f(q_n - p_n)} < \varepsilon$ for all $n \geq N_0$. Now, let $\lambda > 0$ and fix $\tilde{\varepsilon}$. Since $S_{p,q}\text{-lim} x = L$, there exists N_1 such that

$$|\{k: p_n < k \leq q_n, |x_k - L| \geq \lambda\}| < (q_n - p_n)\tilde{\varepsilon}$$

for all $n \geq N_1$. Since f is increasing, we get

$$\frac{1}{f(q_n - p_n)} f(|\{k: p_n < k \leq q_n, |x_k - L| \geq \lambda\}|) < \frac{f((q_n - p_n)\tilde{\varepsilon})}{f(q_n - p_n)} < \varepsilon$$

for all $n \geq \max\{N_0, N_1\}$. Thus, $S_{p,q}^f\text{-lim} x = L$ and this completes the proof.

By using the same technic we can prove the following.

Theorem 3.4 Let f be a compatible modulus function. Then $f\text{-}w_{p,q} = w_{p,q}$.

Using the same method with Proposition 1.1 of [25], one can also obtain the following result.

Theorem 3.5 Let f be a modulus function.

(i) If all deferred statistically convergent sequences are deferred f -statistically convergent, then f must be compatible.

(ii) If all strongly deferred Cesàro convergent sequences are f -strongly deferred Cesàro convergent, then f must be compatible.

Theorem 3.6 Let $x = (x_k)$ be a real sequence and f be a compatible modulus function. Then the following are equivalent.

(i) x is f -strongly deferred Cesàro convergent to L .

(ii) x is deferred f -statistically convergent to L and $D_{p,q}$ -uniformly integrable.

Proof. (ii) \Rightarrow (i). Let x be deferred f -statistically convergent to L and $D_{p,q}$ -uniformly integrable. Since, $S_{p,q}^f \subset S_{p,q}$, Theorem 2.1, x is strongly deferred Cesàro convergent to L . Finally, since f is a compatible modulus, x is f -strongly deferred Cesàro convergent to L by Theorem 3.4.

(i) \Rightarrow (ii). Assume that x is f -strongly deferred Cesàro convergent to L . Then applying Theorem 3.2 and Theorem 2.1 we obtain that x is $D_{p,q}$ -uniformly integrable. Now prove that x is deferred f -statistically convergent to L . Let $\varepsilon > 0$ and choose any $m \in \mathbb{N}$ such that $\frac{1}{m} < \varepsilon$. Since $E_{\varepsilon,p,q} \subset E_{\frac{1}{m},p,q}$ we have

$$\frac{1}{f(q_n - p_n)} f(|\{k: p_n < k \leq q_n, |x_k - L| \geq \varepsilon\}|) \leq \frac{1}{f(q_n - p_n)} f(|\{k: p_n < k \leq q_n, |x_k - L| \geq \frac{1}{m}\}|)$$

and so it is enough to prove that

$$\lim_{n \rightarrow \infty} \frac{1}{f(q_n - p_n)} f(|\{k: p_n < k \leq q_n, |x_k - L| \geq \frac{1}{m}\}|) = 0 \quad (3)$$

for any $n \in \mathbb{N}$. Hence for any $n \in \mathbb{N}$, we can write

$$\begin{aligned} f\left(\sum_{k=p_n+1}^{q_n} |x_k - L|\right) &\geq f\left(\sum_{k \in E_{\frac{1}{m},p,q}} |x_k - L|\right) \\ &\geq f\left(\frac{1}{n} \sum_{k \in E_{\frac{1}{m},p,q}} 1\right) \\ &\geq \frac{1}{n} f\left(\sum_{k \in E_{\frac{1}{m},p,q}} 1\right) \\ &= \frac{1}{m} f(|\{k: p_n < k \leq q_n, |x_k - L| \geq \frac{1}{n}\}|) \end{aligned}$$

From this, we have

$$\frac{1}{f(q_n - p_n)} f(|\{k: p_n < k \leq q_n, |x_k - L| \geq \frac{1}{m}\}|) \leq \frac{m}{f(q_n - p_n)} f\left(\sum_{k=p_n+1}^{q_n} |x_k - L|\right).$$

Thus, by the assumption we obtain (3) and this completes the proof.

Conclusion

In this paper we have studied on deferred f -statistically convergent, strongly deferred Cesàro convergent and f -strongly deferred Cesàro convergent sequences. Some results are obtained through deferred uniformly integrable sequences and compatible modulus functions. Our results in this paper generalizes the results of [11]. For further study, similar ideas can be reformulated for double sequences.

Conflict of interests

There are no conflicts of interest in this work.

References

- [1] Fast H., Sur la convergence statistique. *Colloq. Math.*, 2 (3/4) (1951) 241–244.
- [2] Buck R. C., Generalized asymptotic density, *Amer. J. Math.*, 75 (1953) 335–346.
- [3] Schoenberg I. J., The integrability of certain functions and related summability methods, *Amer. Math. Monthly*, 66 (1959) 361–375.
- [4] Šalát T., On statistically convergent sequences of real numbers. *Math. Slovaca*, 30(2) (1980) 139-150.
- [5] Fridy J. A., On statistical convergence, *Analysis*, 5 (1985) 301–313.
- [6] Maddox I.J., Sequence spaces defined by a modulus, *Math. Proc., Cambridge Philos. Soc.*, 100 (1986) 161-166..
- [7] Connor J., On strong matrix summability with respect to a modulus and statistical convergence, *Canad. Math. Bull*, 32 (1989) 194-198.
- [8] Connor J., The statistical and strong p -Cesaro convergence of sequences, *Analysis*, 8 (1988) 47-63.
- [9] Khan M. K. and Orhan C., Matrix characterization of A -statistical convergence, *J. Math. Anal. Appl.* 335 (2007) 406–417.
- [10] Aizpuru A., Listán-García M. C., Rambla-Barreno, F., Density by moduli and statistical convergence, *Quaest. Math.*, 37 (4) (2014) 525-530.
- [11] León-Saavedra F., del Carmen Listán-García M., Fernández F. J. P., de la Rosa M. P. R. On statistical convergence and strong Cesàro convergence by moduli. *J. Inequal. Appl.*, (2019) 2019:298.
- [12] Agnew R. P., On deferred Cesàro means. *Annals of Mathematics*, (1932) 413-421.
- [13] Küçükbaşlan M. and Yılmaztürk M., On deferred statistical convergence of sequences, *Kyungpook Math. J.*, 56(2) (2016) 357-366.
- [14] Gupta S. and Bhardwaj V. K., On deferred f -statistical convergence, *Kyungpook Math.*, J. 58 (2018) 91-103.
- [15] Cinar M., Yılmaz E. and Et M. Deferred statistical convergence on time scales. *Proceedings of the Romanian Academy, Series A.*, 22 (4) (2021) 301–306.
- [16] Dagadur I. and Sezgek S., Deferred Cesàro mean and deferred statistical convergence of double sequences. *J. Inequal. Spec. Funct*, 4 (2016) 118-136.
- [17] Et M. and Yilmazer M. C., On deferred statistical convergence of sequences of sets. *AIMS Mathematics*, 5 (3) (2020) 2143-2152.
- [18] Et M., Baliarsingh P., Kandemir H. Ş. and Küçükbaşlan M., On μ -deferred statistical convergence and strongly deferred summable functions. *RACSAM*, 115 (1) (2021) 34 1-14.
- [19] Kişi Ö., Gürdal M. and Savaş E., On Deferred Statistical Convergence of Fuzzy Variables. *Applications and Applied Mathematics: An International Journal (AAM)*, 17 (2) (2022) 5.
- [20] Kişi Ö. and Gürdal M., On deferred Cesàro summability and statistical convergence for the sets of triple sequences, *Annals of Fuzzy Mathematics and Informatics*, 24(2) (2022) 115–127.
- [21] Kişi Ö. and Gürdal M., Certain aspects of deferred statistical convergence of fuzzy variables in credibility space, *The Journal of Analysis*, (2023) 1-19.
- [22] Uluşu U., and Güllü E., Deferred Cesàro summability and statistical convergence for double sequences of sets, *Journal of Intelligent & Fuzzy Systems*, 42(4) (2022) 4095-4103.
- [23] Nakano H., Concave modulars, *J. Math Soc. Japan*, 5(1) (1953) 29-49.
- [24] Belen C., Yıldırım M. and Sümbül C., On statistical and strong convergence with respect to a modulus function and a power series method. *Filomat*, 34 (12) (2020) 3981-3993.
- [25] León-Saavedra F., del Carmen Listán-García M., Fernández F. J. P., de la Rosa M. P. R. Correction to: On statistical convergence and strong Cesàro convergence by moduli. *J. Inequal. Appl.*, J Inequal Appl 2023, 110 (2023). <https://doi.org/10.1186/s13660-023-02988-0>.

New Midpoint-type Inequalities of Hermite-Hadamard Inequality with Tempered Fractional Integrals

Tuba Tunç^{1,a,*}, Ayşe Nur Altunok^{1,b}

¹ Department of Mathematics, Faculty of Science, Duzce University, Duzce, Türkiye.

*Corresponding author

Research Article

History

Received: 27/06/2023

Accepted: 01/12/2023

Copyright



©2023 Faculty of Science,
Sivas Cumhuriyet University

ABSTRACT

In this research, we get some midpoint type inequalities of Hermite-Hadamard inequality via tempered fractional integrals. For this, we first obtain an identity. After that, using this identity and with the help of modulus function, Hölder inequality, power mean inequality, ongoing research and the papers mentioned, we have reached our intended midpoint type inequalities. Also, we give the special cases of our results. We see that our special results give earlier works.

Keywords: Hermite-Hadamard-type inequalities, Midpoint-type inequalities, Convex functions, Riemann-Liouville fractional integrals, Tempered fractional integrals.

^a tubatunc03@gmail.com

^b <https://orcid.org/0000-0002-4155-9180>

^b aysenur_9200@hotmail.com

^b <https://orcid.org/0009-0002-6116-583X>

Introduction

Convex functions are an important concept that is used in mathematics, economics, engineering, statistics, and many other fields. In the field of statistics, these functions have various applications such as parameter estimation, classification, clustering, and regression. Also, in engineering, convex functions play an important role in many areas such as signal processing, control systems, data compression, optimization, and energy management. Lastly, in the realm of mathematics, convex functions find extensive applications in disciplines like analysis, differential equations, topology, geometry, and mathematical programming. Especially, they have an important place in the issue of inequalities in mathematics. The most known inequality of convex analysis is Hermite-Hadamard inequality, which was investigated by C. Hermite and J. Hadamard. The Hermite-Hadamard is a mathematical inequality states that the mean of the values of a function is an upper bound between the maximum and minimum values of the function. This can be expressed as [1,2]:

Let $f: I \subseteq \mathbb{R} \rightarrow \mathbb{R}$ be a convex function $a, b \in \mathbb{R}$ with $a < b$ then the following inequalities hold

$$f\left(\frac{a+b}{2}\right) \leq \frac{1}{b-a} \int_a^b f(x) dx \leq \frac{f(a)+f(b)}{2}. \quad (1)$$

If f is concave, both inequalities hold in the opposite direction. The left-hand side of the inequality (1) represents midpoint inequality, while the right-hand side of the inequality (1) represents trapezoid inequality.

On the other hand, fractional calculus has a long history, dating back to the correspondence between Leibniz and L'Hopital. Many mathematicians and physicists have contributed to the development of fractional calculus over the past three centuries, and there are now numerous books covering the topic. Recent theories and experiments have shown that fractional calculus is a powerful tool for describing non-classical phenomena in applied sciences and engineering [3-6]. Due to its mathematical properties, fractional calculus is commonly used to study anomalous kinetics in physics, biology, chemistry, and other complex systems [3].

Fractional calculus has two important topics that are fractional derivative and fractional integral. The first fractional integrals were described by Gottfried Wilhelm Leibniz in 1695. However, the modern theory of fractional integration was developed in the 19th century by Augustin Louis Cauchy and Liouville. Cauchy was one of the first to demonstrate that fractional integrals can be calculated analytically. On the other hand, Liouville made important studies on the theory of fractional integrals and obtained many results about fractional derivatives. The modern theory of fractional integration has been developed since the early 20th century. The general theory of fractional integrals was developed in the 1930s and 1940s, especially by Norbert Wiener and Joseph L. Doob. Besides, various types of fractional derivatives, including Riemann-Liouville, Caputo [7,8], Riesz [8], and Hilfer [6,9], have been introduced for practical applications. Fractional integrals have been discovered to be an important tool for modeling stochastic processes. Advances in this area include topics such as fractional derivatives of random

walks and fractional Brownian motions. In recent years, fractional integration and derivatives have become a topic with applications in many fields such as mathematical physics, electrotechnics, materials science, biomedical engineering, fluid dynamics, and finance. One can find the papers referenced in [10-14] about fractional calculus.

In this article, we introduce several necessary definitions to present our main results. The definition of Riemann-Liouville integral operators is as follows [15]:

Definition 1. The Riemann-Liouville integrals with $\alpha > 0$ for $f \in L_1[a, b]$ are:

$$J_{a+}^\alpha f(x) = \frac{1}{\Gamma(\alpha)} \int_a^x (x-t)^{\alpha-1} f(t) dt, \quad x > a \quad (2)$$

and

$$J_{b-}^\alpha f(x) = \frac{1}{\Gamma(\alpha)} \int_x^b (t-x)^{\alpha-1} f(t) dt, \quad x < b. \quad (3)$$

It is evident that the Riemann-Liouville integrals coincide with the classical integrals when $\alpha = 1$.

The trapezoid-type inequalities for convex functions were first established by Dragomir and Agarwal in [16], while Kırmacı was the first to prove midpoint-type inequalities for convex functions in [17]. Fractional midpoint-type inequalities and trapezoid-type inequalities for convex functions were presented by Sarıkaya et al. in [18] and by Iqbal et al. in [19], respectively. To learn more about fractional integral inequalities, see [8,20] and the references mentioned there.

$$J_{a+}^{(\alpha,\lambda)} f(x) = \frac{1}{\Gamma(\alpha)} \int_a^x (x-t)^{\alpha-1} e^{-\lambda(x-t)} f(t) dt, \quad x \in [a, b]$$

and

$$J_{b-}^{(\alpha,\lambda)} f(x) = \frac{1}{\Gamma(\alpha)} \int_x^b (t-x)^{\alpha-1} e^{-\lambda(t-x)} f(t) dt, \quad x \in [a, b]. \quad (5)$$

If $\lambda = 0$, then the fractional integrals in (4) and (5) reduce to the Riemann-Liouville fractional integrals in (2) and (3), respectively.

In [21], Mohammed et al. gave Hermite-Hadamard inequality involved λ -incomplete gamma function and tempered fractional operators as follows:

Theorem 4. Let $f: [a, b] \rightarrow \mathbb{R}$ be a convex L_1 function on $[a, b]$ with $a < b$. Then, the following inequalities hold:

$$f\left(\frac{a+b}{2}\right) \leq \frac{\Gamma(\alpha)}{2(b-a)^\alpha \Upsilon_{\lambda(b-a)}(\alpha, 1)} [J_{a+}^{(\alpha,\lambda)} f(b) + J_{b-}^{(\alpha,\lambda)} f(a)] \leq \frac{f(a) + f(b)}{2}, \quad (6)$$

for $\alpha > 0$ and $\lambda \geq 0$.

Tempered fractional calculus is considered as an extension of fractional calculus. Buschman's work [25] introduced the definitions of fractional integration with weak singular and exponential kernels which later led to the development of tempered fractional integration. Meerschaert, Samko, Srivastava [8,26,27], and other researchers have studied various definitions of tempered fractional integration. In [21], Hermite-Hadamard-type

Mohammed et al. defined new function and gave some properties of this function as follows [21]:

Definition 2. For the real numbers $\alpha > 0$ and $x, \lambda \geq 0$ the λ -incomplete gamma function is defined as follows:

$$Y_\lambda(\alpha, x) = \int_0^x t^{\alpha-1} e^{-\lambda t} dt.$$

Taking $\lambda = 1$ it turns the incomplete gamma function [22]:

$$Y(\alpha, x) := \int_0^x t^{\alpha-1} e^{-t} dt.$$

Remark 3. For real numbers $\alpha > 0$; $x, \lambda \geq 0$ and $a < b$, there are the following equalities:

$$1) Y_{\lambda(b-a)}(\alpha, x) = \int_0^1 t^{\alpha-1} e^{-\lambda(b-a)t} dt = \left(\frac{1}{b-a}\right)^\alpha Y_\lambda(\alpha, b-a),$$

$$2) \int_0^1 1) Y_{\lambda(b-a)}(\alpha, x) dx = \frac{Y_\lambda(\alpha, b-a)}{(b-a)^\alpha} - \frac{Y_\lambda(\alpha+1, b-a)}{(b-a)^{\alpha+1}}.$$

Now, we will review the basic definitions and introduce new symbols for the tempered fractional operators [23,24].

Definition 3. Let $f \in L_1[a, b]$ and $\alpha > 0$, $\lambda \geq 0$. The fractional tempered integral operators $J_{a+}^{(\alpha,\lambda)} f(x)$ and $J_{b-}^{(\alpha,\lambda)} f(x)$ are presented by

$$(4)$$

$$(5)$$

inequalities involving tempered fractional integrals were established for convex functions, extending previously published results such as Riemann integrals and Riemann-Liouville fractional integrals. The authors followed the techniques developed by Sarıkaya et al. [18,28] to establish these inequalities.

In this paper, we first obtain an identity for the midpoint side of Hermite-Hadamard inequality [21]. After that using this identity and with the help of modulus function, Hölder inequality, power mean inequality,

ongoing research and the papers mentioned above, we get number of midpoint-type inequalities that involve tempered fractional integral operators for the differentiable convex mappings. Also, we give the special cases of these inequalities.

Midpoint-Type Inequalities Involving Tempered Fractional Integrals

Using tempered fractional integrals, we build Hermite-Hadamard type inequalities through differentiable convex functions in this section. To start, we'll define the following identity for obtaining such inequalities.

Lemma 5. Consider that $f: [a, b] \rightarrow \mathbb{R}$ is a differentiable function on (a, b) such that $f', f \in L_1[a, b]$. The following equality for Tempered fractional integrals holds with $\alpha > 0, \lambda \geq 0$:

$$f\left(\frac{a+b}{2}\right) - \frac{\Gamma(\alpha)}{2(b-a)^\alpha Y_{\lambda(b-a)}(\alpha, 1)} [J_{a^+}^{(\alpha, \lambda)} f(b) + J_{b^-}^{(\alpha, \lambda)} f(a)] = \frac{b-a}{2 Y_{\lambda(b-a)}(\alpha, 1)} \sum_{k=1}^4 I_k \tag{7}$$

where

$$I_1 = \int_0^{1/2} Y_{\lambda(b-a)}(\alpha, t) f'(tb + (1-t)a) dt, \quad I_2 = \int_0^{1/2} -Y_{\lambda(b-a)}(\alpha, t) f'(ta + (1-t)b) dt,$$

$$I_3 = \int_{1/2}^1 [Y_{\lambda(b-a)}(\alpha, t) - Y_{\lambda(b-a)}(\alpha, 1)] f'(tb + (1-t)a) dt,$$

$$I_4 = \int_{1/2}^1 [Y_{\lambda(b-a)}(\alpha, 1) - Y_{\lambda(b-a)}(\alpha, t)] f'(ta + (1-t)b) dt.$$

Proof. We can obtain the following result by applying integration by parts

$$\begin{aligned} I_1 &= \int_0^{1/2} Y_{\lambda(b-a)}(\alpha, t) f'(tb + (1-t)a) dt \\ &= \left. \frac{Y_{\lambda(b-a)}(\alpha, t) f(tb + (1-t)a)}{b-a} \right|_0^{1/2} - \frac{1}{b-a} \int_0^{1/2} t^{\alpha-1} e^{-\lambda(b-a)t} f(tb + (1-t)a) dt \\ &= \frac{Y_{\lambda(b-a)}\left(\alpha, \frac{1}{2}\right)}{b-a} f\left(\frac{a+b}{2}\right) - \frac{1}{b-a} \int_0^{1/2} t^{\alpha-1} e^{-\lambda(b-a)t} f(tb + (1-t)a) dt. \end{aligned} \tag{8}$$

By computing the remaining integrals in a similar method, we arrive at

$$\begin{aligned} I_2 &= \int_0^{1/2} -Y_{\lambda(b-a)}(\alpha, t) f'(ta + (1-t)b) dt \\ &= \frac{Y_{\lambda(b-a)}\left(\alpha, \frac{1}{2}\right)}{b-a} f\left(\frac{a+b}{2}\right) - \frac{1}{b-a} \int_0^{1/2} t^{\alpha-1} e^{-\lambda(b-a)t} f(ta + (1-t)b) dt, \end{aligned} \tag{9}$$

$$\begin{aligned} I_3 &= \int_{1/2}^1 [Y_{\lambda(b-a)}(\alpha, t) - Y_{\lambda(b-a)}(\alpha, 1)] f'(tb + (1-t)a) dt \\ &= \frac{[Y_{\lambda(b-a)}(\alpha, 1) - Y_{\lambda(b-a)}\left(\alpha, \frac{1}{2}\right)]}{b-a} f\left(\frac{a+b}{2}\right) - \frac{1}{b-a} \int_{\frac{1}{2}}^1 t^{\alpha-1} e^{-\lambda(b-a)t} f(tb + (1-t)a) dt, \end{aligned} \tag{10}$$

and

$$\begin{aligned}
 I_4 &= \int_{1/2}^1 [Y_{\lambda(b-a)}(\alpha, 1) - Y_{\lambda(b-a)}(\alpha, t)] f'(ta + (1-t)b) dt \\
 &= \frac{[Y_{\lambda(b-a)}(\alpha, 1) - Y_{\lambda(b-a)}(\alpha, \frac{1}{2})]}{b-a} f\left(\frac{a+b}{2}\right) - \frac{1}{b-a} \int_{\frac{1}{2}}^1 t^{\alpha-1} e^{-\lambda(b-a)t} f'(ta + (1-t)b) dt.
 \end{aligned}
 \tag{11}$$

By summing up the inequalities (8)-(11), we conclude that

$$\begin{aligned}
 \sum_{k=1}^4 I_k &= \frac{2 Y_{\lambda(b-a)}(\alpha, 1)}{b-a} f\left(\frac{a+b}{2}\right) \\
 &\quad - \frac{1}{b-a} \left\{ \int_0^1 t^{\alpha-1} e^{-\lambda(b-a)t} f'(tb + (1-t)a) dt + \int_0^1 t^{\alpha-1} e^{-\lambda(b-a)t} f'(ta + (1-t)b) dt \right\}.
 \end{aligned}
 \tag{12}$$

When the above integrals are rewritten using the variable change $x = tb + (1-t)a$ and $x = ta + (1-t)b$, the following expressions are obtained

$$\int_0^1 t^{\alpha-1} e^{-\lambda(b-a)t} f'(tb + (1-t)a) dt = \frac{\Gamma(\alpha)}{(b-a)^\alpha} J_{a+}^{(\alpha, \lambda)} f(b),
 \tag{13}$$

$$\int_0^1 t^{\alpha-1} e^{-\lambda(b-a)t} f'(ta + (1-t)b) dt = \frac{\Gamma(\alpha)}{(b-a)^\alpha} J_{b-}^{(\alpha, \lambda)} f(a).
 \tag{14}$$

By replacing the equalities (13) and (14) in (12) and applying a multiplication operation to the resulting expression using $\frac{b-a}{2 Y_{\lambda(b-a)}(\alpha, 1)}$, we arrive at the following equality

$$\frac{b-a}{2 Y_{\lambda(b-a)}(\alpha, 1)} \sum_{k=1}^4 I_k = f\left(\frac{a+b}{2}\right) - \frac{\Gamma(\alpha)}{2 Y_{\lambda(b-a)}(\alpha, 1)(b-a)^\alpha} \{J_{a+}^{(\alpha, \lambda)} f(b) + J_{b-}^{(\alpha, \lambda)} f(a)\}.$$

This completes the demonstration of the statement.

Theorem 6. Suppose that $f: [a, b] \rightarrow \mathbb{R}$ be a differentiable function on the interval (a, b) with $f, f' \in L_1[a, b]$ and $|f'|$ is a convex function on $[a, b]$ with $a < b$. Then, we have the following inequality for $\alpha > 0, \lambda \geq 0$ and the Tempered fractional integrals

$$\left| f\left(\frac{a+b}{2}\right) - \frac{\Gamma(\alpha)}{2 (b-a)^\alpha Y_{\lambda(b-a)}(\alpha, 1)} \{J_{a+}^{(\alpha, \lambda)} f(b) + J_{b-}^{(\alpha, \lambda)} f(a)\} \right| \leq A_1^{(\alpha, \lambda)}(a, b) (|f'(a)| + |f'(b)|)
 \tag{15}$$

where

$$A_1^{(\alpha, \lambda)}(a, b) = \frac{b-a}{2 Y_{\lambda(b-a)}(\alpha, 1)} \left\{ \int_0^{1/2} Y_{\lambda(b-a)}(\alpha, t) dt + \int_{1/2}^1 [Y_{\lambda(b-a)}(\alpha, 1) - Y_{\lambda(b-a)}(\alpha, t)] dt \right\}.$$

Proof. By taking the absolute value of both sides of the equation in Lemma 5, we obtain

$$\left| f\left(\frac{a+b}{2}\right) - \frac{\Gamma(\alpha)}{2 (b-a)^\alpha Y_{\lambda(b-a)}(\alpha, 1)} \{J_{a+}^{(\alpha, \lambda)} f(b) + J_{b-}^{(\alpha, \lambda)} f(a)\} \right| \leq \frac{b-a}{2 Y_{\lambda(b-a)}(\alpha, 1)} \sum_{k=1}^4 |I_k|.$$

Using the convexity of the function $|f'|$, we get

$$|I_1| = \left| \int_0^{1/2} Y_{\lambda(b-a)}(\alpha, t) f'(tb + (1-t)a) dt \right|
 \tag{16}$$

$$\begin{aligned} &\leq \int_0^{1/2} |Y_{\lambda(b-a)}(\alpha, t)| |f'(tb + (1-t)a)| dt \\ &\leq \int_0^{1/2} Y_{\lambda(b-a)}(\alpha, t) [t|f'(b)| + (1-t)|f'(a)|] dt \\ &= |f'(a)| \int_0^{1/2} (1-t) Y_{\lambda(b-a)}(\alpha, t) dt + |f'(b)| \int_0^{1/2} t Y_{\lambda(b-a)}(\alpha, t) dt. \end{aligned}$$

Utilizing the same approach for the other integrals, the listed expressions are appeared

$$|I_2| \leq |f'(a)| \int_0^{1/2} t Y_{\lambda(b-a)}(\alpha, t) dt + |f'(b)| \int_0^{1/2} (1-t) Y_{\lambda(b-a)}(\alpha, t) dt, \tag{17}$$

$$\begin{aligned} |I_3| &\leq |f'(a)| \int_{1/2}^1 (1-t) [Y_{\lambda(b-a)}(\alpha, 1) - Y_{\lambda(b-a)}(\alpha, t)] dt \\ &\quad + |f'(b)| \int_{1/2}^1 t [Y_{\lambda(b-a)}(\alpha, 1) - Y_{\lambda(b-a)}(\alpha, t)] dt \end{aligned} \tag{18}$$

and

$$\begin{aligned} |I_4| &\leq |f'(a)| \int_{1/2}^1 t [Y_{\lambda(b-a)}(\alpha, 1) - Y_{\lambda(b-a)}(\alpha, t)] dt \\ &\quad + |f'(b)| \int_{1/2}^1 (1-t) [Y_{\lambda(b-a)}(\alpha, 1) - Y_{\lambda(b-a)}(\alpha, t)] dt. \end{aligned} \tag{19}$$

By taking the sum of the inequalities from (16) to (19) and after that multiplying the outcome of expression by $\frac{b-a}{2 Y_{\lambda(b-a)}(\alpha, 1)}$, we conclude that

$$\frac{b-a}{2 Y_{\lambda(b-a)}(\alpha, 1)} \sum_{k=1}^4 I_k = A_1^{(\alpha, \lambda)}(a, b) (|f'(a)| + |f'(b)|).$$

The proof is completed.

Remark 7. Setting $\lambda = 0$ in inequality (15) and applying the property that is $|t_1^\alpha - t_2^\alpha| \leq |t_1 - t_2|^\alpha$ for $t_1, t_2 \in [0, 1]$ and $\alpha \in (0, 1]$ to the obtained inequality, then it follows that:

$$\begin{aligned} &\left| f\left(\frac{a+b}{2}\right) - \frac{\Gamma(\alpha+1)}{2(b-a)^\alpha} \{J_{a+}^\alpha f(b) + J_{b-}^\alpha f(a)\} \right| \\ &\leq \frac{b-a}{2^{\alpha+1}(\alpha+1)} (|f'(a)| + |f'(b)|), \end{aligned}$$

which is proved by Iqbal et al. in [19].

Remark 8. Setting $\alpha = 1$ and $\lambda = 0$ in (15), we obtain

$$\left| f\left(\frac{a+b}{2}\right) - \frac{1}{b-a} \int_a^b f(x) dx \right| \leq \frac{b-a}{8} (|f'(a)| + |f'(b)|),$$

which is proved by Kırmacı in [17].

Theorem 9. Assuming that $f: [a, b] \rightarrow \mathbb{R}$ is a differentiable function on (a, b) with $f, f' \in L_1[a, b]$ and $|f'|^q, q > 1$ is a convex function on $[a, b]$, the subsequent inequality is satisfied

$$\left| f\left(\frac{a+b}{2}\right) - \frac{\Gamma(\alpha)}{2(b-a)^\alpha \Upsilon_{\lambda(b-a)}(\alpha, 1)} \left\{ J_{a^+}^{(\alpha, \lambda)} f(b) + J_{b^-}^{(\alpha, \lambda)} f(a) \right\} \right| \tag{20}$$

$$\leq A_2^{(\alpha, \lambda)}(a, b) \left\{ \left(\frac{3|f'(a)|^q + |f'(b)|^q}{8} \right)^{1/q} + \left(\frac{|f'(a)|^q + 3|f'(b)|^q}{8} \right)^{1/q} \right\}$$

where

$$A_2^{(\alpha, \lambda)}(a, b) = \frac{b-a}{2 \Upsilon_{\lambda(b-a)}(\alpha, 1)} \left\{ \left(\int_0^{1/2} [\Upsilon_{\lambda(b-a)}(\alpha, t)]^p dt \right)^{1/p} + \left(\int_{1/2}^1 [\Upsilon_{\lambda(b-a)}(\alpha, 1) - \Upsilon_{\lambda(b-a)}(\alpha, t)]^p dt \right)^{1/p} \right\}$$

and $\frac{1}{p} + \frac{1}{q} = 1$.

Proof. By utilizing the properties of the modulus function and Lemma 5, we can conclude that

$$\left| f\left(\frac{a+b}{2}\right) - \frac{\Gamma(\alpha)}{2(b-a)^\alpha \Upsilon_{\lambda(b-a)}(\alpha, 1)} \left\{ J_{a^+}^{(\alpha, \lambda)} f(b) + J_{b^-}^{(\alpha, \lambda)} f(a) \right\} \right| \leq \frac{b-a}{2 \Upsilon_{\lambda(b-a)}(\alpha, 1)} \sum_{k=1}^4 |I_k|.$$

The Hölder inequality and the convexity of $|f'|^q$ allow us to arrive the following inequality

$$|I_1| = \left| \int_0^{1/2} \Upsilon_{\lambda(b-a)}(\alpha, t) f'(tb + (1-t)a) dt \right| \tag{21}$$

$$\leq \left(\int_0^{1/2} [\Upsilon_{\lambda(b-a)}(\alpha, t)]^p dt \right)^{1/p} \left(\int_0^{1/2} |f'(tb + (1-t)a)|^q dt \right)^{1/q}$$

$$\leq \left(\int_0^{1/2} [\Upsilon_{\lambda(b-a)}(\alpha, t)]^p dt \right)^{1/p} \left(\frac{3|f'(a)|^q + |f'(b)|^q}{8} \right)^{1/q}.$$

In the same way,

$$|I_2| = \left| \int_0^{1/2} -\Upsilon_{\lambda(b-a)}(\alpha, t) f'(ta + (1-t)b) dt \right| \tag{22}$$

$$\leq \left(\int_0^{1/2} [\Upsilon_{\lambda(b-a)}(\alpha, t)]^p dt \right)^{1/p} \left(\frac{|f'(a)|^q + 3|f'(b)|^q}{8} \right)^{1/q},$$

$$|I_3| = \left| \int_{1/2}^1 [\Upsilon_{\lambda(b-a)}(\alpha, t) - \Upsilon_{\lambda(b-a)}(\alpha, 1)] f'(tb + (1-t)a) dt \right| \tag{23}$$

$$\leq \left(\int_{1/2}^1 [\Upsilon_{\lambda(b-a)}(\alpha, 1) - \Upsilon_{\lambda(b-a)}(\alpha, t)]^p dt \right)^{1/p} \left(\frac{3|f'(a)|^q + |f'(b)|^q}{8} \right)^{1/q},$$

and

$$|I_4| = \left| \int_{1/2}^1 [\Upsilon_{\lambda(b-a)}(\alpha, 1) - \Upsilon_{\lambda(b-a)}(\alpha, t)] f'(ta + (1-t)b) dt \right| \tag{24}$$

$$\leq \left(\int_{1/2}^1 [\Upsilon_{\lambda(b-a)}(\alpha, 1) - \Upsilon_{\lambda(b-a)}(\alpha, t)]^p dt \right)^{1/p} \left(\frac{|f'(a)|^q + 3|f'(b)|^q}{8} \right)^{1/q}.$$

When the inequalities are added up (21)-(24) and subsequently the result is multiplied by $\frac{b-a}{2 Y_{\lambda(b-a)}(\alpha, 1)}$, the next expression is displayed:

$$\frac{b-a}{2 Y_{\lambda(b-a)}(\alpha, 1)} \sum_{k=1}^4 |I_k| \leq A_2^{(\alpha, \lambda)}(a, b) \left[\left(\frac{3|f'(a)|^q + |f'(b)|^q}{8} \right)^{1/q} + \left(\frac{|f'(a)|^q + 3|f'(b)|^q}{8} \right)^{1/q} \right].$$

Thus, the hypothesis of the theorem is obtained.

Remark 10. The inequality can be obtained by setting $\lambda = 0$ in (20):

$$\left| f\left(\frac{a+b}{2}\right) - \frac{\Gamma(\alpha+1)}{2(b-a)^\alpha} \{J_{a+}^\alpha f(b) + J_{b-}^\alpha f(a)\} \right| \leq \frac{b-a}{2^{\alpha+1}(\alpha p+1)^{1/p}} \left[\left(\frac{3|f'(a)|^q + |f'(b)|^q}{4} \right)^{1/q} + \left(\frac{|f'(a)|^q + 3|f'(b)|^q}{4} \right)^{1/q} \right],$$

which is proved by Iqbal et al. in [19].

Remark 11. The inequality can be obtained by setting $\alpha = 1$ and $\lambda = 0$ in (20):

$$\left| \frac{1}{b-a} \int_a^b f(x) dx - f\left(\frac{a+b}{2}\right) \right| \leq \frac{b-a}{16} \left(\frac{4}{p+1}\right)^{1/p} \left\{ [3|f'(a)|^{p/(p-1)} + |f'(b)|^{p/(p-1)}]^{(p-1)/p} + [|f'(a)|^{p/(p-1)} + 3|f'(b)|^{p/(p-1)}]^{(p-1)/p} \right\},$$

which is proved by Kırmacı in [17].

Theorem 12. Let $f: [a, b] \rightarrow \mathbb{R}$ be a differentiable function on (a, b) such that $f, f' \in L_1[a, b]$. If the function $|f'|^q$ is convex on $[a, b]$ with $q \geq 1$, then the following inequality holds:

$$\left| f\left(\frac{a+b}{2}\right) - \frac{\Gamma(\alpha)}{2(b-a)^\alpha Y_{\lambda(b-a)}(\alpha, 1)} \{J_{a+}^{(\alpha, \lambda)} f(b) + J_{b-}^{(\alpha, \lambda)} f(a)\} \right| \tag{25}$$

$$\leq \frac{b-a}{2 Y_{\lambda(b-a)}(\alpha, 1)} [|f'(a)| + |f'(b)|] \left\{ A_3^{(\alpha, \lambda)}(a, b) \left(\int_0^{1/2} Y_{\lambda(b-a)}(\alpha, t) dt \right)^{1-1/q} + A_4^{(\alpha, \lambda)}(a, b) \left(\int_{1/2}^1 [Y_{\lambda(b-a)}(\alpha, 1) - Y_{\lambda(b-a)}(\alpha, t)] dt \right)^{1-1/q} \right\},$$

where

$$A_3^{(\alpha, \lambda)}(a, b) = \left(\int_0^{1/2} t Y_{\lambda(b-a)}(\alpha, t) dt \right)^{1/q} + \left(\int_0^{1/2} (1-t) Y_{\lambda(b-a)}(\alpha, t) dt \right)^{1/q},$$

$$A_4^{(\alpha, \lambda)}(a, b) = \left(\int_{1/2}^1 t [Y_{\lambda(b-a)}(\alpha, 1) - Y_{\lambda(b-a)}(\alpha, t)] dt \right)^{1/q} + \left(\int_{1/2}^1 (1-t) [Y_{\lambda(b-a)}(\alpha, 1) - Y_{\lambda(b-a)}(\alpha, t)] dt \right)^{1/q}.$$

Proof. The absolute value of Lemma 5 yields:

$$\left| f\left(\frac{a+b}{2}\right) - \frac{\Gamma(\alpha)}{2(b-a)^\alpha Y_{\lambda(b-a)}(\alpha, 1)} \{J_{a+}^{(\alpha, \lambda)} f(b) + J_{b-}^{(\alpha, \lambda)} f(a)\} \right| \leq \frac{b-a}{2 Y_{\lambda(b-a)}(\alpha, 1)} \sum_{k=1}^4 |I_k|.$$

Applying the power-mean integral inequality for $q > 1$ and using the fact that for $0 \leq r < 1$, $\sum_{i=1}^n (a_i + b_i)^r \leq \sum_{i=1}^n a_i^r + \sum_{i=1}^n b_i^r$ with $a_i, b_i \geq 0, i = 1, 2, \dots, n$, then we obtain:

$$\begin{aligned}
|I_1| &= \left| \int_0^{1/2} Y_{\lambda(b-a)}(\alpha, t) f'(tb + (1-t)a) dt \right| & (26) \\
&\leq \int_0^{1/2} |Y_{\lambda(b-a)}(\alpha, t)| |f'(tb + (1-t)a)| dt \\
&= \int_0^{1/2} [Y_{\lambda(b-a)}(\alpha, t)]^{1/p} [Y_{\lambda(b-a)}(\alpha, t)]^{1/q} |f'(tb + (1-t)a)| dt \\
&\leq \left(\int_0^{1/2} Y_{\lambda(b-a)}(\alpha, t) dt \right)^{1-1/q} \left(\int_0^{1/2} Y_{\lambda(b-a)}(\alpha, t) |f'(tb + (1-t)a)|^q dt \right)^{1/q} \\
&\leq \left(\int_0^{1/2} Y_{\lambda(b-a)}(\alpha, t) dt \right)^{1-1/q} \left(\int_0^{1/2} Y_{\lambda(b-a)}(\alpha, t) [t|f'(b)|^q + (1-t)|f'(a)|^q] dt \right)^{1/q} \\
&= \left(\int_0^{1/2} Y_{\lambda(b-a)}(\alpha, t) dt \right)^{1-1/q} \times \left(|f'(b)|^q \int_0^{1/2} t Y_{\lambda(b-a)}(\alpha, t) dt + |f'(a)|^q \int_0^{1/2} (1-t) Y_{\lambda(b-a)}(\alpha, t) dt \right)^{1/q} \\
&\leq \left(\int_0^{1/2} Y_{\lambda(b-a)}(\alpha, t) dt \right)^{1-1/q} \\
&\quad \times \left[|f'(b)| \left(\int_0^{1/2} t Y_{\lambda(b-a)}(\alpha, t) dt \right)^{1/q} + |f'(a)| \left(\int_0^{1/2} (1-t) Y_{\lambda(b-a)}(\alpha, t) dt \right)^{1/q} \right].
\end{aligned}$$

In the same way,

$$\begin{aligned}
|I_2| &= \left| \int_0^{1/2} -Y_{\lambda(b-a)}(\alpha, t) f'(ta + (1-t)b) dt \right| & (27) \\
&= \left(\int_0^{1/2} Y_{\lambda(b-a)}(\alpha, t) dt \right)^{1-1/q} \times \left(|f'(a)|^q \int_0^{1/2} t Y_{\lambda(b-a)}(\alpha, t) dt + |f'(b)|^q \int_0^{1/2} (1-t) Y_{\lambda(b-a)}(\alpha, t) dt \right)^{1/q} \\
&\leq \left(\int_0^{1/2} Y_{\lambda(b-a)}(\alpha, t) dt \right)^{1-1/q} \\
&\quad \times \left[|f'(a)| \left(\int_0^{1/2} t Y_{\lambda(b-a)}(\alpha, t) dt \right)^{1/q} + |f'(b)| \left(\int_0^{1/2} (1-t) Y_{\lambda(b-a)}(\alpha, t) dt \right)^{1/q} \right],
\end{aligned}$$

$$\begin{aligned}
|I_3| &= \left| \int_{1/2}^1 [Y_{\lambda(b-a)}(\alpha, t) - Y_{\lambda(b-a)}(\alpha, 1)] f'(tb + (1-t)a) dt \right| & (28) \\
&\leq \left(\int_{1/2}^1 [Y_{\lambda(b-a)}(\alpha, 1) - Y_{\lambda(b-a)}(\alpha, t)] dt \right)^{1-1/q} \times \left\{ |f'(b)|^q \int_{1/2}^1 t [Y_{\lambda(b-a)}(\alpha, 1) - Y_{\lambda(b-a)}(\alpha, t)] dt \right. \\
&\quad \left. + |f'(a)|^q \int_{1/2}^1 (1-t) [Y_{\lambda(b-a)}(\alpha, 1) - Y_{\lambda(b-a)}(\alpha, t)] dt \right\}^{1/q}
\end{aligned}$$

$$\leq \left(\int_{1/2}^1 [\Upsilon_{\lambda(b-a)}(\alpha, 1) - \Upsilon_{\lambda(b-a)}(\alpha, t)] dt \right)^{1-1/q} \\ \times \left\{ |f'(b)| \left(\int_{1/2}^1 t [\Upsilon_{\lambda(b-a)}(\alpha, 1) - \Upsilon_{\lambda(b-a)}(\alpha, t)] dt \right)^{1/q} \right. \\ \left. + |f'(a)| \left(\int_{1/2}^1 (1-t) [\Upsilon_{\lambda(b-a)}(\alpha, 1) - \Upsilon_{\lambda(b-a)}(\alpha, t)] dt \right)^{1/q} \right\},$$

and

$$|I_4| = \left| \int_{1/2}^1 [\Upsilon_{\lambda(b-a)}(\alpha, 1) - \Upsilon_{\lambda(b-a)}(\alpha, t)] f'(ta + (1-t)b) dt \right| \tag{29} \\ \leq \left(\int_{1/2}^1 [\Upsilon_{\lambda(b-a)}(\alpha, 1) - \Upsilon_{\lambda(b-a)}(\alpha, t)] dt \right)^{1-1/q} \\ \times \left\{ |f'(a)|^q \int_{1/2}^1 t [\Upsilon_{\lambda(b-a)}(\alpha, 1) - \Upsilon_{\lambda(b-a)}(\alpha, t)] dt \right. \\ \left. + |f'(b)|^q \int_{1/2}^1 (1-t) [\Upsilon_{\lambda(b-a)}(\alpha, 1) - \Upsilon_{\lambda(b-a)}(\alpha, t)] dt \right\}^{1/q} \\ \leq \left(\int_{1/2}^1 [\Upsilon_{\lambda(b-a)}(\alpha, 1) - \Upsilon_{\lambda(b-a)}(\alpha, t)] dt \right)^{1-1/q} \\ \times \left\{ |f'(a)| \left(\int_{1/2}^1 t [\Upsilon_{\lambda(b-a)}(\alpha, 1) - \Upsilon_{\lambda(b-a)}(\alpha, t)] dt \right)^{1/q} \right. \\ \left. + |f'(b)| \left(\int_{1/2}^1 (1-t) [\Upsilon_{\lambda(b-a)}(\alpha, 1) - \Upsilon_{\lambda(b-a)}(\alpha, t)] dt \right)^{1/q} \right\}.$$

By totaling the inequalities from (26) to (29), it follows that

$$\sum_{k=1}^4 |I_k| \leq \left(\int_0^{1/2} \Upsilon_{\lambda(b-a)}(\alpha, t) dt \right)^{1-1/q} \{A_3^{(\alpha, \lambda)}(a, b)[|f'(a)| + |f'(b)|]\} \\ + \left(\int_{1/2}^1 [\Upsilon_{\lambda(b-a)}(\alpha, 1) - \Upsilon_{\lambda(b-a)}(\alpha, t)] dt \right)^{1-1/q} \{A_4^{(\alpha, \lambda)}(a, b)[|f'(a)| + |f'(b)|]\}.$$

This completes the proof.

Remark 13. The inequality can be obtained by setting $\lambda = 0$ in (25) and using for $0 \leq r < 1$ $\sum_{i=1}^n (a_i + b_i)^r \leq \sum_{i=1}^n a_i^r + \sum_{i=1}^n b_i^r$ with $a_i, b_i \geq 0, i = 1, 2, \dots, n$

$$\left| f\left(\frac{a+b}{2}\right) - \frac{\Gamma(\alpha+1)}{2(b-a)^\alpha} \{J_{a+}^\alpha f(b) + J_{b-}^\alpha f(a)\} \right| \leq \frac{b-a}{2^{\alpha+1}(\alpha+1)} [|f'(a)| + |f'(b)|] \left\{ \frac{(\alpha+1)^{1/q} + (\alpha+3)^{1/q}}{[2(\alpha+2)]^{1/q}} \right\}$$

which is proved by Iqbal et al. in [19].

Remark 14. The inequality can be obtained by setting $\alpha = 1$ and $\lambda = 0$ in (25):

$$\left| \frac{1}{b-a} \int_a^b f(x) dx - f\left(\frac{a+b}{2}\right) \right| \leq \frac{b-a}{8} \left(\frac{1+2^{1/q}}{3^{1/q}} \right) [|f'(a)| + |f'(b)|],$$

which is proved by Kirmaci et al. in [17].

Conflict interests

The authors declare that they have no conflict interests.

References

- [1] Dragomir S.S., Pearce C.E.M., Selected topics on the Hermite-Hadamard inequalities and applications, RGMIA Monographs, Victoria University.
- [2] Hadamard J., Etude sur les proprietes des fonctions entieres et en particulier d'une fonction considree par Riemann, *Journal de Math'ematiques Pures et Appliqu'ees*, 58 (1893) 171-215.
- [3] Metzler R., Klafter J., The random walk's guide to anomalous diffusion: a fractional dynamics approach, *Physics Reports*, 339 (2000) 1-77.
- [4] Mohammed P.O., Brevik I., A new version of the Hermite-Hadamard inequality for Riemann-Liouville fractional integrals, *Symmetry*, 12(4) (2020), 1-11.
- [5] Nonlaopon K., Awan M.U., Javed M.Z., Budak H., Noor M.A., Some q-fractional estimates of trapezoid like inequalities involving Raina's function, *Fractal and Fractional*, 6(4) (2022) 1-19.
- [6] Tomovski Z., Generalized Cauchy type problems for nonlinear fractional differential equations with composite fractional derivative operator, *Nonl. Anal.*, 75(7) (2012) 3364-3384.
- [7] Podlubny I., Fractional differential equations, Academic Press, San Diego, (1999).
- [8] Samko S., Kilbas A., Marichev O., Fractional Integrals and Derivatives: Theory and Applications, Gordon and Breach, London, (1993).
- [9] Hilfer R., Applications of Fractional Calculus in Physics, World Scientific, Singapore, 2000.
- [10] Bin-Mohsin B., Awan M.U., Javed M.Z., Khan A.G., Budak H., Mihai M.V., Noor M.A., Generalized AB-fractional operator inclusions of Hermite-Hadamard's type via fractional integration, *Symmetry*, 15(5) (2023) 1-21.
- [11] Budak H., Kiliç Yildirim S., Sarikaya M.Z., Yildirim H., Some parameterized Simpson-, midpoint- and trapezoid-type inequalities for generalized fractional integrals, *J. Inequal. Appl.*, 2022(1) (2022) 1-23.
- [12] Ertuğral F., Sarikaya M.Z., Budak H., On Hermite-Hadamard type inequalities associated with the generalized fractional integrals, *Filomat*, 36(12) (2022) 3983-3995.
- [13] Jarad F., Abdeljawad T., Baleanu D., On the generalized fractional derivatives and their Caputo modification, *J. Nonlinear Sci. Appl.*, 10(5) (2017) 2607-2619.
- [14] Kirmaci U.S., Özdemir M.E., On some inequalities for differentiable mappings and applications to special means of real numbers and to midpoint formula, *Appl. Math. Comput.*, 153(2) (2004) 361-368.
- [15] Kilbas A.A., Srivastava H.M., Trujillo J.J., Theory and Applications of Fractional Differential Equations, North-Holland Mathematics Studies, 204, Elsevier Sci. B.V., Amsterdam, (2006).
- [16] Dragomir S.S., Agarwal R.P., Two inequalities for differentiable mappings and applications to special means of real numbers and to trapezoidal formula, *Appl. Math. Lett.*, 11 (5) (1998) 91-95.
- [17] Kirmaci U.S., Inequalities for differentiable mappings and applications to special means of real numbers to midpoint formula, *Appl. Math. Comput.*, 147 (5) (2004) 137-146.
- [18] Sarikaya M.Z., Set E., Yaldiz H., Basak N., Hermite-Hadamard's inequalities for fractional integrals and related fractional inequalities, *Math. Comput. Model.*, 57(9-10) (2013) 2403-2407.
- [19] Iqbal M., Iqbal B.M., Nazeer K., Generalization of inequalities analogous to Hermite-Hadamard inequality via fractional integrals, *Bull. Korean Math. Soc.*, 52(3) (2015) 707-716.
- [20] Budak H., Ertuğral F., Sarikaya M.Z., New generalization of Hermite-Hadamard type inequalities via generalized fractional integrals, *An. Univ. Craiova Ser. Mat. Inform.*, 47(2) (2020) 369-386.
- [21] Mohammed P.O., Sarikaya M.Z., Baleanu D., On the Generalized Hermite-Hadamard Inequalities via the Tempered Fractional Integrals, *Symmetry*, 12(4) (2020) 1-17.
- [22] Chaudhry M.A., Zubair S.M., Generalized incomplete gamma functions with applications, *J. Comput. Appl. Math.*, 55 (1994) 99-124.
- [23] Li C., Deng W., Zhao L., Well-posedness and numerical algorithm for the tempered fractional ordinary differential equations, *Discret. Cont. Dyn-B*, 24 (2019) 1989-2015.
- [24] Meerschaert M.M., Sabzikar F., Chen J., Tempered fractional calculus, *J. Comput. Phys.*, 293 (2015) 14-28.
- [25] Buschman R. G., Decomposition of an integral operator by use of Mikusinski calculus, *SIAM J. Math. Anal.*, 3 (1972) 83-85.
- [26] Meerschaert M.M., Sikorskii A., Stochastic Models for Fractional Calculus, *De Gruyter Studies in Mathematics* Vol. 43, (2012).
- [27] Srivastava H.M., Buschman R.G., Convolution Integral Equations with Special Function Kernels, John Wiley and Sons, New York, (1977).
- [28] Sarikaya M.Z., Yildirim H., On Hermite-Hadamard type inequalities for Riemann-Liouville fractional integrals, *Miskolc Math. Notes*, 17(2) (2017) 1049-1059.



Predictions on Flexible CdTe Solar Cell Performances by Artificial Neural Networks

Sevinj Ganbarova^{1,a}, Serkan Akkoyun^{2,b,*}, Vusal Mamedov^{1,c}, Huseyn Mamedov^{1,d}

¹ Faculty of Physics, Baku State University, Baku, Azerbaijan.

² Department of Physics, Faculty of Science, Sivas Cumhuriyet University, Sivas, Türkiye

*Corresponding author

Research Article

History

Received: 09/06/2023

Accepted: 02/10/2023

Copyright



©2023 Faculty of Science,
Sivas Cumhuriyet University

ABSTRACT

The linear structure of the Lorentz-Minkowski plane is almost the same as Euclidean plane. But, there is one different aspect. These planes have different distance functions. So, it can be interesting to study the Lorentz analogues of topics that include the distance concept in the Euclidean plane. Thus, in this study, we show that the relationship between Euclidean and Lorentz distances is given depending on the slope of the line segment. Following, we investigate Lorentz analogues of Thales' theorem, Angle Bisector theorems, Menelaus' theorem and Ceva's theorem.

Keywords: CdTe flexible solar cell, Solar cell efficiency, Artificial neural network.

^a sevinjganbarova@gmail.com

^b <https://orcid.org/0009-0004-0913-0060>

^c mammadovv@gmail.com

^d <https://orcid.org/0009-0007-8084-3436>

^e sakkoyun@cumhuriyet.edu.tr

^f <https://orcid.org/0000-0002-8996-3385>

^g mhuseyng@bsu.edu.az

^h <https://orcid.org/0000-0002-9980-9189>

Introduction

Solar energy has become one of the most essential resources of the world in the last decades, due to the restriction of resource reserves and environmental problems of fossil energy. Unlike other non-renewable resources of energy, use of solar energy does not yield any harm to the environment. The silent and clean operation, little maintenance, long life, unobtrusiveness, and direct conversion of solar energy into electricity without moving parts and without producing atmospheric emissions are the main advantages of Photovoltaic (PV) energy systems [1]. Thin-film solar-cells are lightweight and flexible as compared with modules built by traditional crystalline silicon cells. Moreover, thin-film cells may be easily molded into various shapes and sizes. The rapid development of flexible PV panels in recent years makes it the main source of energy for the future. The investigation of the performances of solar cells when flexed is important for the applications of flexible devices. CdTe solar cells which are commonly used in alternative energy source studies were introduced about 50 years ago and they have been particularly studied recently. CdTe solar cells on ultra-thin glass surfaces are advantageous because they are light and flexible. These characteristics of batteries are important in applications that require high specific power, unique form factors and low manufacturing costs. Solar modules based on CdTe are due to its remarkable qualities such as having a direct energy band gap of 1.45 eV, a high absorption coefficient ($> 1 \times 10^4 \text{ cm}^{-1}$) and excellent thermodynamic stability [2-5]. The performance of lightweight and flexible CdTe depends on flexing as well.

In recent years artificial neural network (ANN) has been used in solar energy field. Qian et al. [6] predicted the mass proportion of trichromatic colorants and acrylic substrate on the optical and thermal performance of external wall coatings by using an artificial neural network. Wang et al. [7] performed PV output prediction using artificial neural network with overlap training range. Su et al. [8] applied machine learning techniques to study the large-lattice-mismatched CdS/CdTe interface. Jaber et al. [9], predicted the performance of different pv modules using artificial neural networks. Few studies exist in the literature on the effect of flexing photovoltaic on Ultra-thin glass (see Ref. [5] and reference therein). Teloken et al. investigated experimentally the performance of CdTe flexible solar cells due to the effect of bending and time. In their work, the photovoltaic performance was measured by current density versus voltage. The measurements were performed for planar (before and after flexing) and flexed states in a bend Radius of 32 mm [5]. In this study, we have borrowed the data from their experiments and used in our present machine learning applications. From the study from which the data was obtained, solar-cell performances are available after a bending radius and different waiting times. However, determining the performance for different bending radius and waiting times is also important in terms of increasing efficiency. An alternative simpler way to make this determination is to perform machine learning with existing data to estimate performance for the desired bending radius and waiting times. This is the main motivation of our work. Thus, we can state that the main goal of the study is whether ANN method is a suitable tool

for the prediction of the performances of flexible solar cells in different conditions. According to the results obtained from the present study, seeing that the performances of the solar cells at new bending angles are accurately estimated by this method, through machine learning without the need for any extra new experiments, revealed the importance of the ANN method. Therefore, we conclude that the ANN method is highly successful in predicting the performance of flexible solar cells.

Materials and Methods

In this work, the artificial neural network (ANN) method [10] has been used for the prediction of the performance of the flexible CdTe solar cell. The data is borrowed from Teloeken et al. [4] which is available in the literature. The photovoltaic performance was measured by J-V under AM1.5G at 25 °C following a 10-minute light soak, using an ABET Technologies Sun 2000 Solar Simulator [5]. The measurements were performed when the cell was in a planar state (0F), and then when flexed to a 40 mm and subsequent 32 mm bend radius (0B). After flexion the device was relaxed and measured flat. In addition, the sample was held at a bend radius of 32 mm for 168 hours with measurement at 0, 24, 48, 120, 144 and 168 hours. Again, the sample was measured flat before (168F) and after (168B) the bending test. As a nonlinear mathematical method, ANN mimics the brain functionality and consists of several processing units which are called as neurons [11]. The neurons in different layers have connected to each other by weighted connections. Input layer neurons receive the data and the output layer neurons give the result as close as to the desired results. There is no rule for the determination of the number of hidden layers which are located between the input and output layers. In the training of the ANN, Levenberg-Marquardt algorithm and tangent hyperbolic activation function were used which give the better results [12,13].

ANN includes two main stages: training and test. The whole data belonging to the problem is separated into two different parts. One part (%75) is for the training of ANN and the second part (%25) is for the test. In the training stage, the weights between neurons are modified correctly to construct ANN for the true solution of the given problem. If weights are modified well, constructed ANN works for all similar type data that is never seen in the training stage. Training stage continues until the acceptable error level between desired and obtained outputs. The error is calculated by the mean square error (MSE) formula as given below in Eq.(1).

$$MSE = \frac{1}{n} \sum_{i=1}^n (Y_i - \hat{Y}_i)^2 \tag{1}$$

Our study consisted of three different stages performed with ANN. In the first stage, we considered the wavelength (λ) of the light on the flexible CdTe solar cells as the input of the ANN. The outputs of the ANN were before 0F, 0B, 168F and 168B external quantum

efficiencies of the solar cell. After the calculations for the number of hidden layer neurons 4, 7 and 10, the results were presented for each calculation. In Fig.1, 1-7-4 ANN topology has been presented. The total number of adjustable weights was 20, 35 and 50 for 4, 7 and 10 hidden neuron numbers.

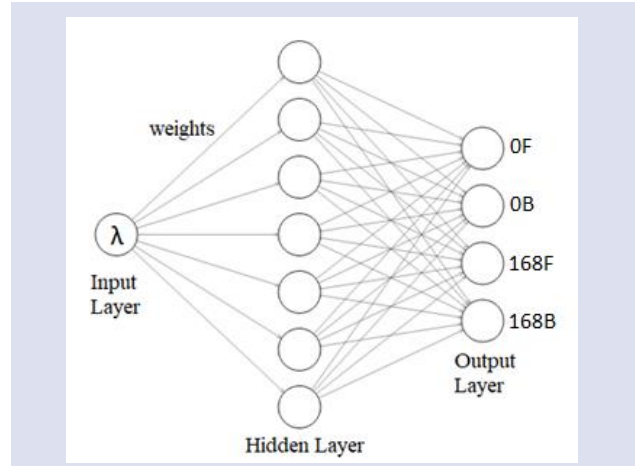


Figure 1. ANN structure (1-7-4) for the prediction of the solar cell performance.

In the second stage of the work, the inputs were the wavelength (λ) of the light on the flexible CdTe solar cells and external quantum efficiencies of 0F. The output was external quantum efficiencies of 0B. After the trials with low ($h=4$), medium ($h=7$) and high ($h=10$) neuron numbers, it was seen that the number of neurons giving the best results was 10. At this stage, we examined the effect of the bending flexible solar cells on performance. The total number of adjustable weights was 12, 21 and 30 for 4, 7 and 10 hidden neuron numbers in this stage. In Fig.2, we have shown the 2-7-1 ANN topology as an illustration

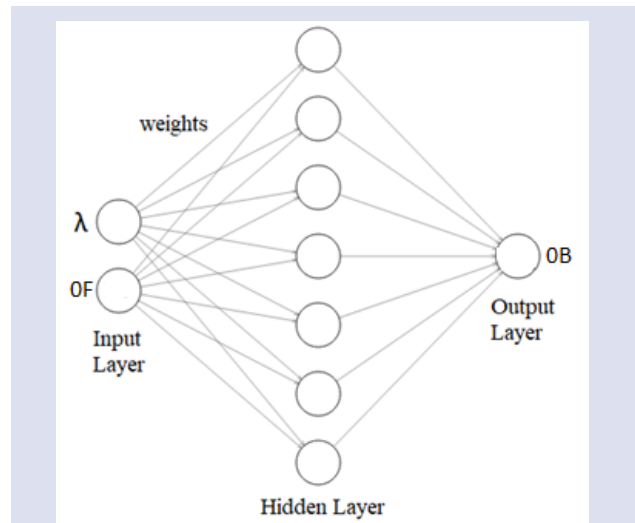


Figure 2. ANN structure (2-7-1) for the prediction of the solar cell performance by bending.

In the last stage of the work, the inputs were the wavelength (λ) of the light on the flexible CdTe solar cells and external quantum efficiencies of OF. The output was external quantum efficiencies of 168B. Again, the hidden neuron numbers were taken as 4, 7 and 10, separately. In Fig. 3, 2-7-1 ANN structure has been given with the total number of adjustable weights of 21. For the 4 and 10 hidden neuron numbers, the weights numbers were 12 and 30, respectively. In the study we carried out at this stage, we examined the effect of time on the performance of solar cells.

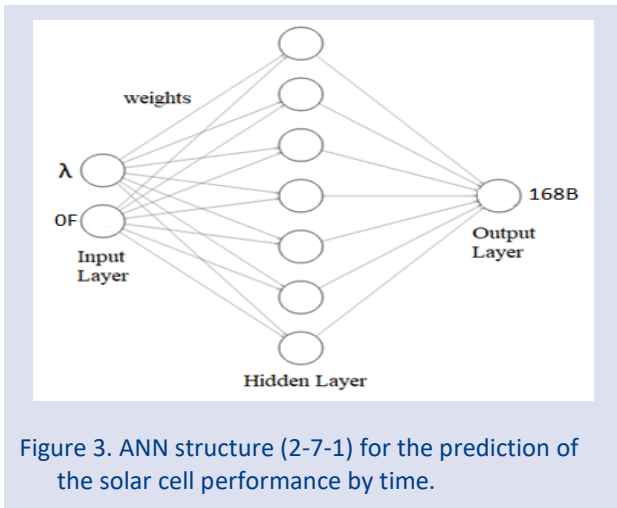


Figure 3. ANN structure (2-7-1) for the prediction of the solar cell performance by time.

Results and Discussion

For all three stages, the results of the calculations in which the number of hidden neurons is used as seven are presented in detail with their graphics. However, the statistical values of the calculations in which the number of hidden layer neurons are four and ten are also given in Table 1 in tabular form. The results obtained from the artificial neural networks (ANN) calculations carried out in the first stage of the study are shown separately on the training and test data. In Fig. 4, the results of the predictions of the ANN over the training data are presented. As can be seen from these results of calculations in which OF, OB, 168F and 168B values are estimated against wavelength, the difference between the experimental data of external quantum efficiency (%) values and the result of the ANN shows a maximum range of +4 to -4 for $h=4$ and $h=7$, +1 to -1 for $h=10$. However, it is seen that the distribution is concentrated in zero-line for $h=10$ ANN structure. It is clear from the graph that the variation is larger around the wavelength of around 400 and 800 nm for $h=4$ and $h=7$ and around 600 nm for $h=10$. For $h=10$, the RMSE values of the estimations of all wavelengths on the training data were obtained as 0.32, 0.35, 0.33 and 0.35 for OF, OB, 168F and 168B, respectively. The maximum absolute deviation of the ANN results from experimental values are 1.34, 0.80, 1.12 and 1.11 for OF, OB, 168F and 168B. For the other hidden neuron numbers, the statistical values on the results were presented in Table 1.

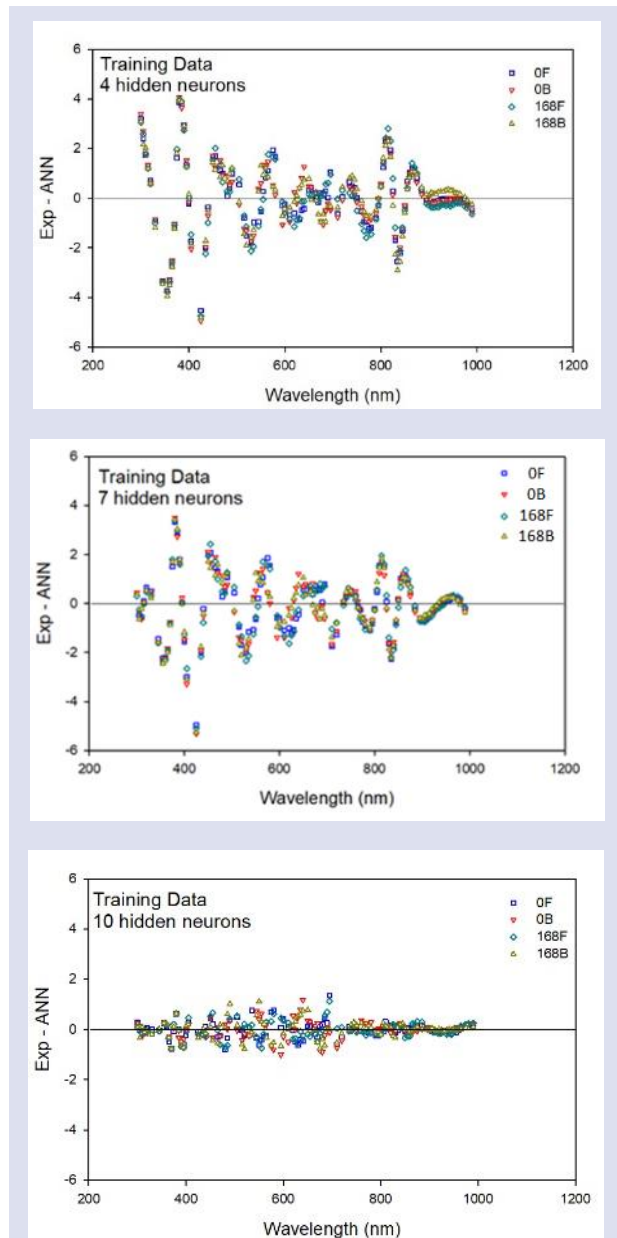


Figure 4. Difference between the experimental and ANN prediction values for external quantum efficiencies of the solar cells on training data for hidden neuron numbers 4 (top), 7 (middle) and 10 (bottom).

The results of the ANN predictions on the test data are shown in Fig. 5 for $h=4$, $h=7$ and $h=10$ ANN structures. In the graph where the ANN estimates against the experimental data are drawn, it is seen that the data points are concentrated on the diagonal line, especially for $h=10$. This indicates that the ANN structure with 10 hidden layer neurons is more successful in estimating external quantum efficiency values. For $h=10$, the RMSE values of the estimations of all wavelengths on the test data were obtained as 0.45, 0.42, 0.43 and 0.36 for OF, OB, 168F and 168B. The maximum absolute deviation of the ANN results from experimental values are 0.90, 1.00, 0.90 and 1.00 for OF, OB, 168F and 168B, respectively. For $h=4$ and $h=7$, the statistical indicators were presented in Table 1.

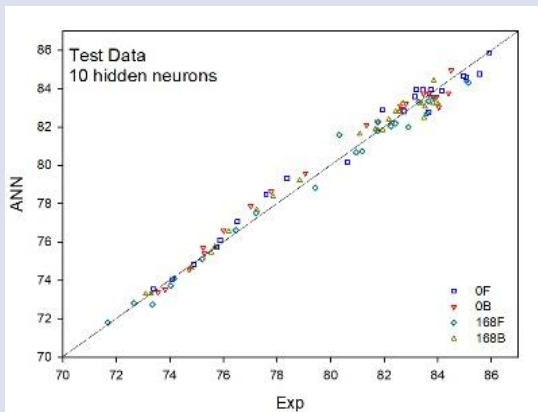
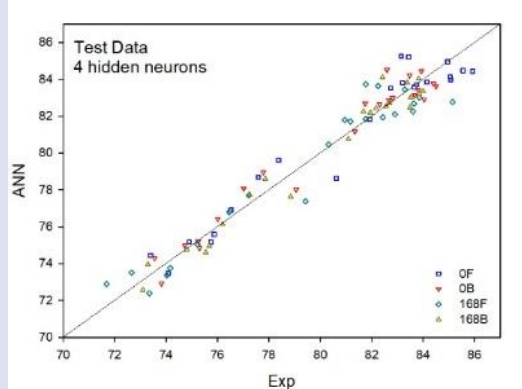
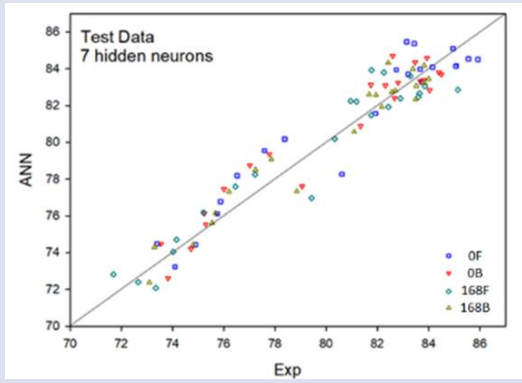


Figure 5. The experimental versus ANN prediction values for external quantum efficiencies of the solar cells on test dataset for hidden neuron numbers 4 (top), 7 (middle) and 10 (bottom).

In the second stage of our study, the wavelength and OF external quantum efficiency values were accepted as the input values of the ANN, and the OB values were estimated. As can be seen from Fig. 6, the results of the ANN predictions are also in good agreement with the experimental data in this study. In other words, it has been seen that ANN can be used as an alternative to experimental studies in examining the effects of bending on solar cell performances. According to the ANN results, it is seen that the highest efficiency is in the range of about 500 to 800 nm. For the training stage, the RMSE and maximum absolute deviation values were obtained as 0.59 and 1.42 for hidden neuron number 10. For the other hidden neuron numbers, the statistical values were

given in Table 1. These results indicate that the ANN trained for the current bending radii of the experimental data can successfully yield results for other radii. In addition, for wavelengths that are not used experimentally, if we have the external quantum efficiency information in the flat state, the bending value might be estimated by ANN. The usefulness of the method is evident from Fig. 7, where the ANN results on the test dataset are compared with the experimental data. In the graph where the results of the ANN against the experimental data are presented, it is seen that the data points are concentrated on the diagonal line. The RMSE and maximum absolute deviation values of the predictions on the test data were obtained as 0.53 and 1.34, respectively, for $h=10$. For $h=4$ and $h=7$ ANN structure, the statistical values can be seen in Table 1.

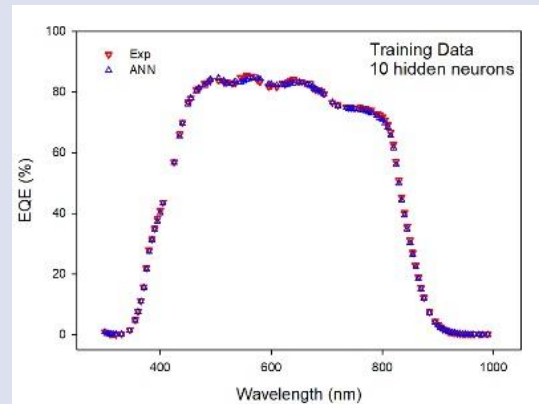
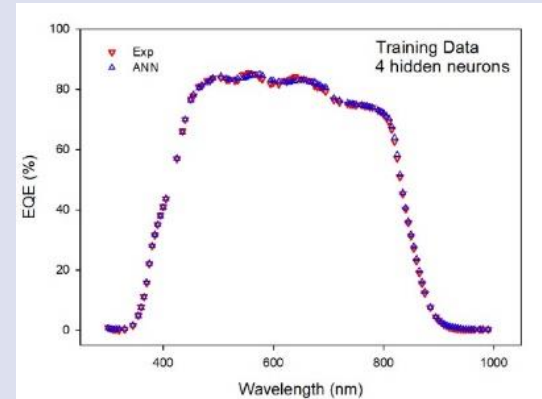
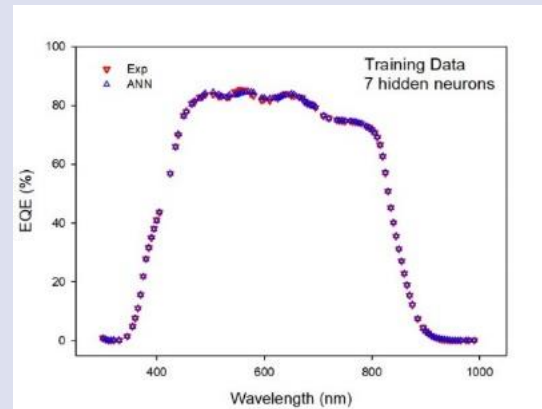


Figure 6. The experimental and ANN prediction values for OB external quantum efficiencies of the solar cells on training data for hidden neuron numbers 4 (top), 7 (middle) and 10 (bottom).

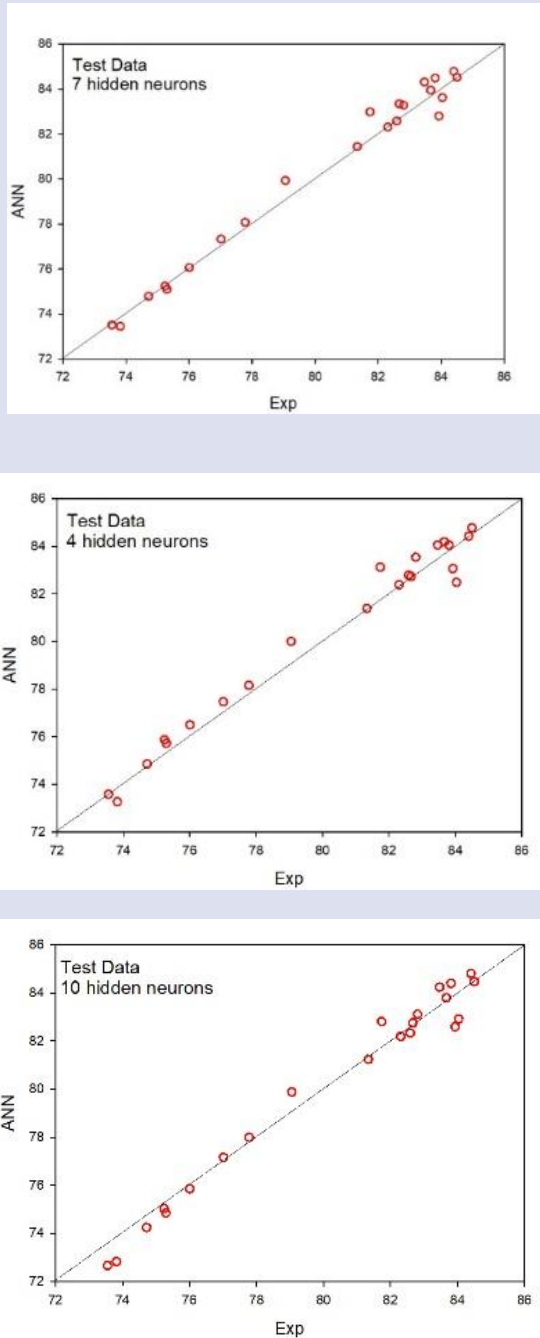


Figure 7. The experimental versus ANN prediction values for OB external quantum efficiencies of the solar cells on test dataset for hidden neuron numbers 4 (top), 7 (middle) and 10 (bottom).

In the last stage of the study, the wavelength and OF external quantum efficiency values were taken as inputs of the ANN and the 168B value was tried to be estimated. Thus, it is planned to investigate the effects of both bending and elapsed time on external quantum efficiency. In Fig. 8, the ANN predictions on the training data are presented together with the experimental data. As can be clearly seen from the figure, the ANN results are in good agreement with the experimental data. It is seen that the highest efficiency is obtained in the range of about 500 to 800 nm. For $h=10$, the RMSE and maximum absolute deviation values of the estimations on the training data

were calculated as 0.18 and 0.55. For the other ANN structures with $h=4$ and $h=7$, the results can be seen in Table 1. In Fig. 9, the results of the studies at this stage on the test data are presented. The RMSE and maximum absolute deviation values belonging to the results are 0.45 and 0.69, respectively, for hidden neuron number 10. For the other hidden neuron numbers, statistical values were presented in Table 1. It is seen that the ANN estimates against the experimental data are almost on the diagonal line in the graph. This indicates that the method is quite useful for this purpose. Knowing the external quantum efficiency value of the solar cell in its flat state at the beginning and revealing how the external quantum efficiency value will change after time and bending point out how powerful a tool the ANN is.

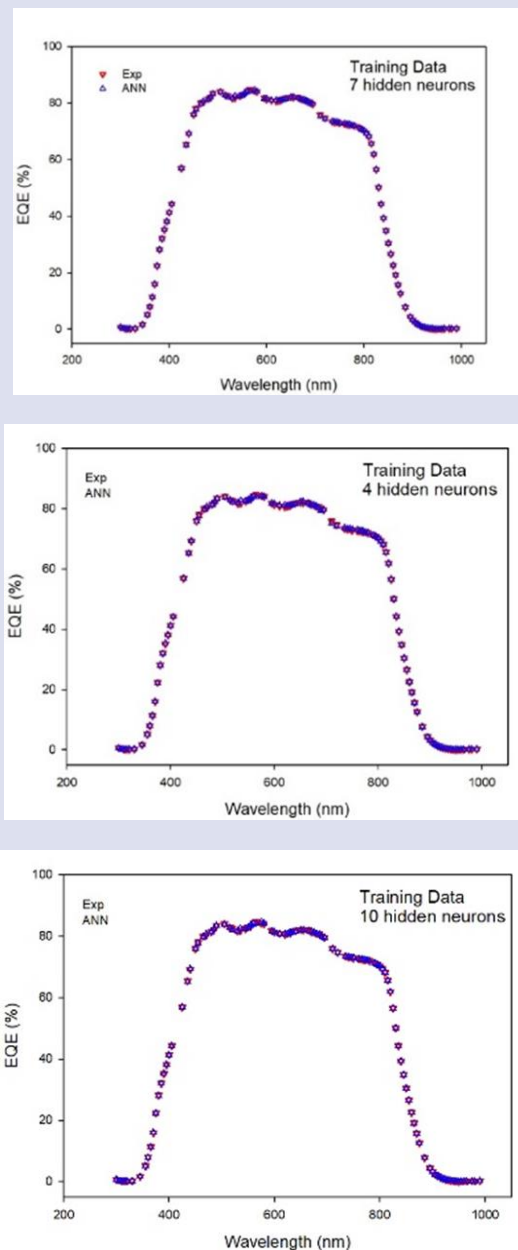


Figure 8. The experimental and ANN prediction values for 168B external quantum efficiencies of the solar cells on training data for hidden neuron numbers 4 (top), 7 (middle) and 10 (bottom).

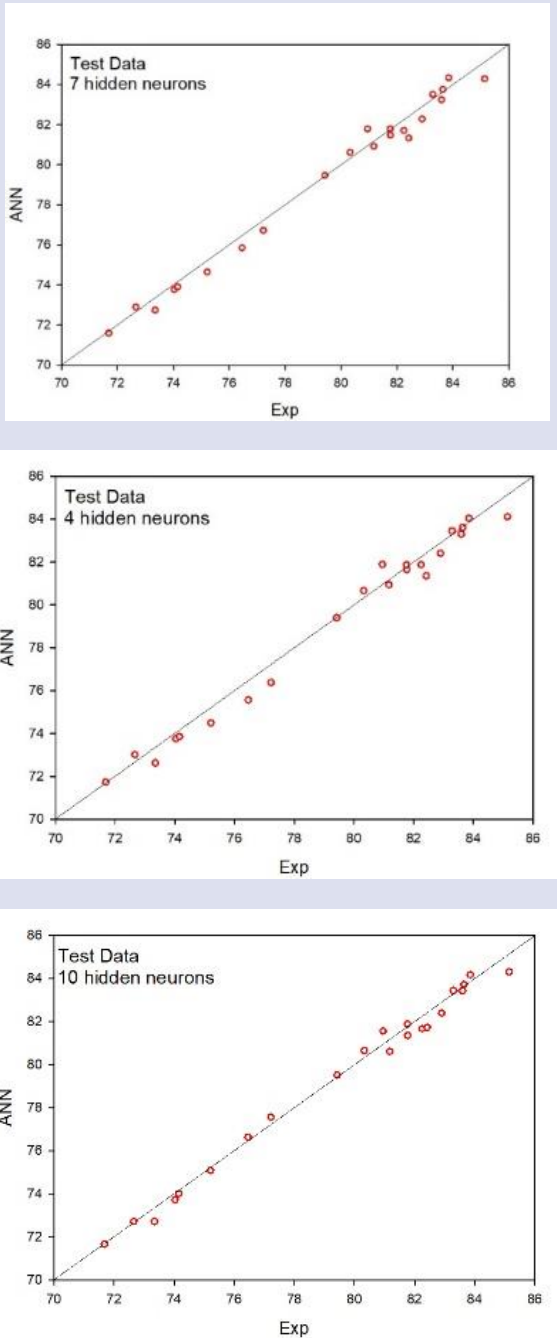


Figure 9. The experimental versus ANN prediction values for 168B external quantum efficiencies of the solar cells on test dataset for hidden neuron numbers 4 (top), 7 (middle) and 10 (bottom).

Table 1. Statistical indicators of the ANN results for hidden neuron numbers 4, 7 and 10 (RMSE: root-mean square error, MAXE: maximum absolute error).

		Training Data (h=4)		Training Data (h=7)		Training Data (h=10)	
		MAXE	RMSE	MAXE	RMSE	MAXE	RMSE
1	0F	3.87	1.43	4.97	1.24	1.34	0.32
	0B	4.07	1.43	5.32	1.23	0.80	0.35
	168F	3.97	1.49	5.09	1.27	1.12	0.33
	168B	3.94	1.46	5.28	1.22	1.11	0.35
2	0B	1.50	0.56	1.31	0.36	1.42	0.59
	168B	0.78	0.25	0.85	0.20	0.55	0.18
		Test Data (h=4)		Test Data (h=7)		Test Data (h=10)	
		MAXE	RMSE	MAXE	RMSE	MAXE	RMSE
1	0F	4.98	1.80	5.66	1.94	0.90	0.45
	0B	5.51	1.81	6.12	1.94	1.00	0.42
	168F	5.17	1.87	5.75	1.94	0.90	0.43
	168B	5.50	1.81	6.19	1.98	1.00	0.36
2	0B	1.56	0.51	1.23	0.44	1.34	0.53
	168B	1.06	0.45	1.09	0.41	0.69	0.34

Conclusion

In this study, it was investigated whether external quantum efficiency values can be predicted by the artificial neural networks (ANN) method using the data of a previous experimental study on CdTe flexible solar cells. Efficiency values in the flat state, 32 mm bent state, and after bending were estimated for different wavelengths of light. In the first stage of the study, the external quantum efficiency values in all cases were produced against the wavelength values. According to the results obtained, the RMSE value was obtained as approximately 0.40. In the second step, the effect of bending was estimated by ANN by using the untwisted efficiency value. When the results obtained at this stage were examined, it was seen that the RMSE value was around 0.50. In the last stage of the study, the efficiencies of the bent solar cell after 168 h of time were estimated from the measured efficiency value in the initial flat state. According to the results obtained, the RMSE value is around 0.45 for this stage. When the results are evaluated as a whole, it is concluded that the ANN method is an alternative powerful tool for estimating the external quantum efficiency of flexible CdTe solar cells.

The results of the study in which bending tests were carried out showed the results of using CdTe solar cells, where it is beneficial to store them in a flexible state before use, or producing curved modules without compromising performance. It has been supported in this study that CdTe solar cells do not show a significant deterioration in performance when exposed to a small bending radius. We also examined the effect of the number of hidden layer neurons in predicting the performance of flexible solar cells, it is seen that RMSE values generally decrease from $h=4$ to $h=7$ and then to $h=10$ for the training data set. After $h=10$, it increases again. However, examinations on the test data set showed that RMSE increased from $h=4$ to $h=7$, and then decreased at $h=10$. It has been observed that the optimum number of hidden layer neurons for the ANN structure may be around 7.

Conflict of interests

The authors state that did not have conflict of interests.

References

- [1] Romeo A., Artegiani E., Cdte-based thin film solar cells: Past, present and future, *Energies*, 14 (2021) 1684.
- [2] Fang, Z., Wang X.C., Wu H.C., Zhao, C.Z., Achievements and challenges of CdS/CdTe solar cells, *International Journal of Photoenergy*, (2011) 297350.
- [3] Mathew X., Thompson G.W., Singh V.P., McClure J.C., Velumani S., Mathews N.R., Sebastian P.J., Development of CdTe thin films on flexible substrates—a review, *Solar Energy Materials and Solar Cells*, 76 (2003) 293.
- [4] Kranz L., Buecheler S., Tiwari A.N., Technological status of CdTe photovoltaics, *Solar Energy Materials and Solar Cells*, 119 (2013) 278.
- [5] Teloeken A.C., Lamb D.A., Dunlop T.O., Irvine S.J.C., Effect of bending test on the performance of CdTe solar cells on flexible ultra-thin glass produced by MOCVD, *Solar Energy Materials and Solar Cells*, 211 (2020) 110552.
- [6] Qian S., Deng Y., Li X., Jin, Z., Long E., Prediction and influence of the mass proportion of trichromatic colourants and acrylic substrate on the optical and thermal performance of external wall coatings: An artificial neural network approach, *Solar Energy Materials and Solar Cells*, 236 (2022) 111551.
- [7] Wang S., Zhanga Y., Hao P., Lu H., An improved method for PV output prediction using artificial neural network with overlap training range, *Journal of Renewable and Sustainable Energy*, 13 (2021) 063502.
- [8] Su M., Yang Ji-H., Liu, Zhi-P., Gong Xin-G., Exploring Large-Lattice-Mismatched Interfaces with Neural Network Potentials: The Case of the CdS/CdTe Heterostructure, *J. Phys. Chem. C* 126 (2022) 13366.
- [9] Jaber M., Abd Hamid A.S., Sopian K., Fazliza, A., Ibrahim A., Prediction Model for the Performance of Different PV Modules Using Artificial Neural Networks, *Appl. Sci.* 12 (2022) 3349.
- [10] Haykin S., "Neural Networks: a Comprehensive Foundation" Englewood Cliffs, Prentice-Hall, New Jersey, pp.842 (1999).
- [11] Hornik K., Stinchcombe M. and White H., Neural Networks, 2 (1989) 359.
- [12] Levenberg K., A method for the solution of certain non-linear problems in least squares, *Q. Appl. Math.*, 2 (1944) 164.
- [13] Marquardt D., An algorithm for least-squares estimation of nonlinear parameters, *SIAM J. Appl. Math.*, 11 (1963) 431.

The Slab Critical Thickness Problem with Reflecting Boundary Condition for the Anlı-Güngör Scattering Function

Demet Gülderen ^{1,a}, R. Gökhan Türeci ^{2,b,*}

¹ Ankara Science High School, Center Building, Ankara, Türkiye.

² Kırıkkale University, Kırıkkale Vocational School, Kırıkkale, Türkiye.

*Corresponding author

Research Article

History

Received: 20/01/2023

Accepted: 09/10/2023

Copyright



©2023 Faculty of Science,
Sivas Cumhuriyet University

ABSTRACT

The criticality equation, which defines the relation between the secondary neutron number and the thickness of the slab, and the numerical solutions of this equation are investigated with reflecting boundary condition for the recently studied the Anlı-Güngör (AG) scattering function. The analytical calculations are performed by HN method. The numerical results are calculated with Wolfram Mathematica software for the varying secondary neutron number, the varying scattering parameter, and the varying reflection coefficient. The critical slab thickness values decrease for increasing reflection coefficient as expected.

Keywords: Legendre expansion of scattering function, Anlı-Güngör scattering function, HN method, The critical slab problem, Reflecting boundary condition.

^a cemreelif@yahoo.com

^b <https://orcid.org/0000-0001-8038-219X>

^b tureci@gmail.com

^b <https://orcid.org/0000-0002-8996-3385>

Introduction

In this study the critical slab problem is investigated with the reflecting boundary condition for the Anlı-Güngör (AG) scattering function [1] with quadratic term. The criticality equation defines the relation between the secondary neutron number and the thickness of medium.

The critical slab problem was investigated by Mitsis [2] with the Case method [3,4], Carlvik [5], Sahni and Sjöstrand [6-8], Sahni [9], Dahl and Sjöstrand [10]. It was investigated for the reflecting boundary conditions by Garis [11], Garis and Sjöstrand [12], Atalay [13], Türeci *et al.* [14]. The problem was investigated with different methods such as the Case method, C_N Method [15], F_N method [16] and H_N method [17]. The effects of the anisotropic scatterings were also investigated with İnönü's scattering function [18]. Siewert and Williams [19] searched the effect of the anisotropy for the critical slab problem. The different types of the Legendre expansion of scattering function [20] were studied by different researchers [21-26].

The AG scattering function is

$$f(\mu, \mu') = \sum_{n=0}^N t^n P_n(\mu) P_n(\mu') \quad (1)$$

where t is the scattering parameter, $P_n(\mu)$ is the Legendre polynomial with n^{th} order. Here the defining interval of the scattering parameter for all scattering situations is given as $|t| \leq 1$. The Legendre expansion of scattering function is

$$f(\mu, \mu') = \sum_{n=0}^N (2n+1) f_n P_n(\mu) P_n(\mu'), \quad (2)$$

where f_n is the scattering coefficients, and $P_n(\mu)$ is the Legendre polynomial with n^{th} order.

It is obvious that both scattering functions are the same for only linear anisotropic scattering. Although both scattering functions are similar, these functions have different properties. One of differences between the Legendre expansion of scattering function and AG anisotropic scattering function is about the scattering coefficients. t parameter in AG scattering is defined in $t \in [-1, 1]$. But the determination of the defining interval of the scattering coefficients in Legendre expansion of scattering function is a difficult job. A detailed analysis was performed by Gülderen *et al.* [27] in the Milne problem for linear-triplet Legendre expansion of scattering function. A different analysis was given by Köklü and Özer [28] for the tetra Legendre expansion of scattering function. Although the scattering parameter is defined in the interval $t \in [-1, 1]$, the parameter is defined in $t \in [-0.54, 0.54]$ for the quadratic AG scattering because of the rule that the sum of probabilities is equal to one. This result can be determined by the solving of an inequality relation of Eq.(1), which defines the rule that the sum of probabilities is equal to one.

The other difference appears for the further scattering terms. For instance, if we take $f_1 = 0$, $f_2 \neq 0$ and $f_{n \geq 3}$, then the scattering is called as pure-quadratic anisotropic scattering in Legendre expansion of scattering function. But a similar selection is not possible in the AG scattering function. If any researcher wants to study the quadratic

AG scattering as in this study, then the linear anisotropic scattering term will automatically be in the scattering function.

The AG scattering function which has been recently studied with P_N method [29] for the criticality problem. It also has been studied for half-space albedo problem [30], the Milne problem [31], slab albedo problem [32] and the criticality problem [33] for quadratic AG scattering with H_N method. Maleki [34] used the scattering function to solve

the half-space albedo and slab albedo problems with Monte Carlo method.

In this study the reflection situation is taken into account. Thus, the effect of the reflection could be investigated. The results are interesting for being closed to unity of the scattering term values for fixed c . The thickness of the medium represents the parabolic behaviour for this situation.

The Case Method Solution for the Anlı-Güngör Scattering Function

The analytical calculations are performed by H_N method. The method is based on the usage the Case method relations. Therefore, the relations of the Case method must be derived for the AG scattering function. This analysis was performed by Türeci and Bülbül [35].

First, we can start with the source-free, one-speed, time-independent, homogeneous medium and plane geometry neutron transport equation:

$$\mu \frac{\partial \psi(x, \mu)}{\partial x} + \psi(x, \mu) = \frac{c}{2} \int_{-1}^1 f(\mu, \mu') \psi(x, \mu') d\mu' \tag{3}$$

where x is the spatial variable in mfp unit, μ is the direction cosine, c is the secondary neutron number, and $f(\mu, \mu')$ is the AG scattering function. The Case eigenfunction for the AG scattering is

$$\phi(v, \mu) = \frac{cv}{2} \frac{K_n(v, \mu)}{v - \mu} \tag{4}$$

where

$$K_n(v, \mu) = \sum_{n=0}^N t^n P_n(\mu) J_n(v) \tag{5}$$

and

$$J_n(v) = \int_{-1}^1 P_n(\mu) \phi(v, \mu) d\mu \tag{6}$$

$J_n(v)$ obeys the recursion relation, and it is given by

$$J_{k+1}(v) = \frac{v}{k+1} \left[(2k+1) - ct^k \right] J_k(v) - \frac{k}{k+1} J_{k-1}(v) \tag{7}$$

$J_0(v)$ corresponds to the normalization of the Case eigenfunction. The normalization condition is

$$\int_{-1}^1 \phi(v, \mu) d\mu = 1 \tag{8}$$

If $v \notin [-1, 1]$, then the solution of the Eq. (8) gives one pair discrete eigenvalues, $\pm v_0$. If $v \in [-1, 1]$, then we have a singular point at $v = \mu$. We are interested in the quadratic AG scattering here. Therefore, the upper limit of the scattering is $N = 2$ in the expansion of Eq. (2), and the fourth and beyond terms, $N > 2$, are assumed to be small enough to be neglected. Thus, the scattering function studied in this study is

$$f(\mu, \mu') = 1 + t P_1(\mu) P_1(\mu') + t^2 P_2(\mu) P_2(\mu') \tag{9}$$

The explicit form of Eq. (5) is

$$K_2(\xi, \mu) = 1 + t\xi(1-c)\mu + \frac{t^2}{4}(3\mu^2 - 1) \left(\xi^2(1-c)(3-ct) - 1 \right), \tag{10}$$

and the Case eigenfunction is

$$\phi(v, \mu) = \frac{cv^{1+tv(1-c)\mu} + \frac{t^2}{4}(v^2(1-c)(3-ct) - 1)(3\mu^2 - 1)}{2(v - \mu)} \tag{11}$$

The normalization condition for the quadratic AG scattering given in Eq. (8) is

$$\ln\left(\frac{1+v_0}{1-v_0}\right) = \frac{2}{cv_0} \frac{1+cv_0tJ_1(v_0) + \frac{3cv_0^2}{2}t^2J_2(v_0)}{1+v_0tJ_1(v_0) + t^2J_2(v_0) - \frac{3v_0^2-1}{2}} \tag{12}$$

$$J_0(\xi) = 1, \tag{13a}$$

$$J_1(\xi) = \xi(1-c), \tag{13b}$$

$$J_2(\xi) = \frac{1}{2}(\xi^2(1-c)(3-ct) - 1) \tag{13c}$$

The discrete eigenvalues, $\pm v_0$, are the numerical solutions of Eq. (12). Equation (12) is a transcendental equation, and it can be only solved as numerical methods such as Newton-Raphson method [36, 37] or Muller’s method [36, 38]. Both methods can give real and complex roots of any function. The criticality problem is studied for $c > 1$, and Eq. (12) has complex roots, $\pm i v_0$ where $i^2 = -1$. Finally, the discrete and the continuum eigenfunctions are

$$\phi(\pm v_0, \mu) = \frac{cv_0^{1 \pm tv_0(1-c)\mu} + \frac{t^2}{4}(v_0^2(1-c)(3-ct) - 1)(3\mu^2 - 1)}{2(v_0 \mp \mu)} \tag{14}$$

$$\phi(v, \mu) = \frac{cv^{1+tv(1-c)\mu} + \frac{t^2}{4}(v^2(1-c)(3-ct) - 1)(3\mu^2 - 1)}{2} P + \lambda(v)\delta(v - \mu) \tag{15}$$

where P corresponds to the Cauchy principal value, and $\lambda(v)$ is

$$\lambda(v) = 1 - \frac{cv}{2} P \int_{-1}^1 \frac{K_n(v, \mu)}{v - \mu} d\mu \tag{16}$$

The explicit form of Eq. (16) is

$$\lambda(v) = 1 + cvtJ_1(v) + \frac{3cv^2}{2}t^2J_2(v) - cv \left[1 + tvJ_1(v) + t^2J_2(v) - \frac{3v^2-1}{2} \right] \tanh^{-1}(v) \tag{17}$$

These eigenfunctions obey the orthogonality relations:

$$\int_{-1}^1 \mu \phi(\pm v_0, \mu) \phi(\pm v_0, \mu) d\mu = M(\pm v_0), \quad M(\pm v_0) = -M(\mp v_0), \tag{18}$$

$$\int_{-1}^1 \mu \phi(\pm v_0, \mu) \phi(\mp v_0, \mu) d\mu = 0, \tag{19}$$

$$\int_{-1}^1 \mu \phi(v, \mu) \phi(v, \mu) d\mu = M(v) \tag{20}$$

Finally, the solution of Eq. (3) for the AG scattering function is

$$\psi(x, \mu) = A(v_0) \phi(v_0, \mu) e^{-x/v_0} + A(-v_0) \phi(-v_0, \mu) e^{x/v_0} + \int_{-1}^1 A(v) \phi(v, \mu) e^{-x/v} dv \tag{21}$$

where $A(\pm v_0)$ and $A(v)$ are the arbitrary expansion coefficients. The explicit form of Eq. (18) for the scattering function is

$$M(v_0) = \left(\frac{cv_0}{2}\right)^2 \frac{2}{v_0^2 - 1} \left[(\alpha_0 + v_0 \beta_0) (\alpha_0 v_0 - 2\beta_0 + 3v_0^2 \beta_0) + \frac{2}{3} \gamma_0 (-6v_0 \alpha_0 + 9v_0^3 \alpha_0 - \beta_0 (1 - 8v_0^2) + 12\beta_0 v_0^4) + \frac{v_0 \gamma_0^2}{3} (-2 - 10v_0^2 + 15v_0^4) \right] - \left(\frac{cv_0}{2}\right)^2 (\alpha_0 + \beta_0 v_0 + \gamma_0 v_0^2) (\alpha_0 + 3\beta_0 v_0 + 5\gamma_0 v_0^2) \ln\left(\frac{v_0 + 1}{v_0 - 1}\right) \tag{22}$$

where

$$\alpha_0 \equiv \alpha(v_0) = 1 - \frac{1}{2} t^2 J_2(v_0) \tag{23a}$$

$$\beta_0 \equiv \beta(v_0) = v_0^2 t(1 - c) \tag{23b}$$

$$\gamma_0 \equiv \gamma(v_0) = \frac{3}{2} t^2 J_2(v_0) \tag{23c}$$

and the explicit form of Eq. (20) is

$$M(v) = v \lambda^2(v) + \frac{c^2 \pi^2 v^3}{4} \left[1 + t J_1(v) P_1(v) + t^2 J_2(v) P_2(v) \right]^2 \tag{24}$$

where $P_1(v)$ and $P_2(v)$ are the Legendre polynomials in terms of the continuum eigenvalue, v .

The criticality equation with HN method

We are interesting a slab reactor which is placed in $x \in [-a, a]$. Thus, the thickness of the slab is $\tau = 2a$. It is assumed that the inside of the slab is the medium, and the outside is the vacuum. The interaction of the neutrons with the medium is thought as the quadratic AG scattering.

The neutron flux has a symmetry condition over the right and left walls over the boundaries of the medium. This condition implies that the outgoing fluxes are the same. The outgoing neutron fluxes are defined as a power series expansion:

$$\Psi(-a, -\mu) = \Psi(a, \mu) = \sum_{\ell=0}^G a_{\ell} \mu^{\ell}, \quad \mu \in [0, 1] \tag{25}$$

The reflection boundary condition means that there are reflected neutrons from the boundaries to the medium. The reflection is defined with the reflection coefficient. Therefore, the reflected neutron flux from the boundaries is proportional with the outgoing flux with the reflection coefficient, R , $R \in [0, 1]$. Thus, the reflection boundary conditions are

$$\Psi(a, -\mu) = R \Psi(a, \mu), \quad \mu > 0 \tag{26}$$

$$\Psi(-a, \mu) = R \Psi(-a, -\mu), \quad \mu > 0 \tag{27}$$

If the symmetry condition given in Eq. (25) is used in the solution, Eq. (21), then the arbitrary expansion coefficients in the solution of the transport equation become

$$A(v_0)=A(-v_0) \quad \text{and} \quad A(v)=A(-v). \tag{28}$$

Thus, the solution of Eq. (3) turns into

$$\Psi(x,\mu) = A(v_0) \left[\phi(v_0,\mu)e^{-x/v_0} + \phi(-v_0,\mu)e^{x/v_0} \right] + \int_0^1 A(v) \left[\phi(v,\mu)e^{-x/v} + \phi(-v,\mu)e^{x/v} \right] dv, \quad \mu \in [-1,1]. \tag{29}$$

If Eq. (29) is written for $x = a$, then we get the following equation:

$$\Psi(a,\mu) = A(v_0) \left[\phi(v_0,\mu)e^{-a/v_0} + \phi(-v_0,\mu)e^{a/v_0} \right] + \int_0^1 A(v) \left[\phi(v,\mu)e^{-a/v} + \phi(-v,\mu)e^{a/v} \right] dv, \quad \mu \in [-1,1]. \tag{30}$$

Now, the aim is to determine the arbitrary expansion coefficients in Eq. (30) by using the neutron flux definitions in Eqs. (25-27), and the orthogonality properties given in Eqs. (18-20). Since the neutron flux must go to zero when x goes to infinity, we want to eliminate the positive exponential terms in the application of the orthogonality relations. Therefore, the equation is multiplied by $\mu\phi(-v_0,\mu)$, and integrated over $\mu \in [-1,1]$. Thus, we find

$$A(v_0)M(-v_0)e^{a/v_0} = \int_{-1}^1 \mu\phi(-v_0,\mu)\Psi(a,\mu)d\mu \tag{31}$$

$$A(v_0)M(-v_0)e^{a/v_0} = \int_0^1 \mu\phi(-v_0,\mu) \underbrace{\Psi(a,\mu)}_{\sum_{\ell=0}^G a_\ell \mu^\ell} d\mu - \int_0^1 \mu\phi(-v_0,-\mu) \underbrace{\Psi(a,-\mu)}_{R \sum_{\ell=0}^G a_\ell \mu^\ell} d\mu \tag{32}$$

$$A(v_0) = -\frac{e^{-a/v_0} cv_0}{M(v_0)} \sum_{\ell} a_\ell [A_\ell(v_0) - RB_\ell(v_0)] \tag{33}$$

Similarly, if Eq. (30) is multiplied by $\mu\phi(-v,\mu)$ and integrated over $\mu \in [-1,1]$, then we find the arbitrary coefficient for the continuum part:

$$A(v) = -\frac{e^{-a/v} cv}{M(v)} \sum_{\ell} a_\ell [A_\ell(v) - RB_\ell(v)] \tag{34}$$

where $A_\ell(\xi)$ and $B_\ell(\xi)$, $\xi = v, v_0$ are the moments of Case's eigenfunctions in interval $\mu \in [0,1]$:

$$A_\ell(\xi) = \frac{2}{c\xi} \int_0^1 \mu^{\ell+1} \phi(v_0,-\mu) d\mu \tag{35}$$

$$B_\ell(\xi) = \frac{2}{c\xi} \int_0^1 \mu^{\ell+1} \phi(v_0,\mu) d\mu \tag{36}$$

$$A_0(\xi) = \alpha_\xi - \frac{\beta_\xi}{2} + \frac{\gamma_\xi}{3} - \xi \left[\alpha_\xi + \xi\beta_\xi + \xi^2\gamma_\xi \right] \ln\left(1 + \frac{1}{\xi}\right) + \xi\beta_\xi - \frac{\xi\gamma_\xi}{2} + \xi^2\gamma_\xi \tag{37}$$

$$B_0(\xi) = \frac{2}{c} \left(1 + c\xi\beta\xi + c\xi^2\gamma\xi \right) - \xi \left[\alpha\xi + \xi\beta\xi + \xi^2\gamma\xi \right] \ln \left(1 + \frac{1}{\xi} \right) - \xi\beta\xi - \xi^2\gamma\xi - \frac{\xi\gamma\xi}{2} - \alpha\xi - \frac{\beta\xi}{2} - \frac{\gamma\xi}{3}, \tag{38}$$

where α_ξ , β_ξ and γ_ξ for $\xi = \pm\nu_0, \nu$ are defined in Eqs. (23). $A_\ell(\xi)$ and $B_\ell(\xi)$ satisfy own recursion relations:

$$A_\ell(\xi) = \frac{\alpha_\xi}{\ell+1} - \frac{\beta_\xi}{\ell+2} + \frac{\gamma_\xi}{\ell+3} - \xi A_{\ell-1}(\xi) \tag{39}$$

$$B_\ell(\xi) = \xi A_{\ell-1}(\xi) - \frac{\alpha_\xi}{\ell+1} - \frac{\beta_\xi}{\ell+2} - \frac{\gamma_\xi}{\ell+3} \tag{40}$$

Now, if Eq. (25) is written for $\mu \in [0, 1]$, then we have

$$\Psi(a, \mu) = A(\nu_0) \left[\phi(\nu_0, \mu) e^{-a/\nu_0} + \phi(-\nu_0, \mu) e^{a/\nu_0} \right] + \int_0^1 A(\nu) \left[\phi(\nu, \mu) e^{-a/\nu} + \phi(-\nu, \mu) e^{a/\nu} \right] d\nu, \quad \mu \in [0, 1]. \tag{41}$$

If the expansion coefficients given in Eqs. (33, 34) are written in Eq. (41), and equation is multiplied to μ^{m+1} and integrated over $\mu \in [0, 1]$, then we get the following equation system. m is an integer number, and it takes its value from 0 to G .

$$\sum_{\ell=0}^G a_\ell \left[\frac{1}{\ell+m+2} + \left(\frac{c\nu_0}{2} \right)^2 \frac{[A_\ell(\nu_0) - RB_\ell(\nu_0)] B_m(\nu_0)}{M(\nu_0)} e^{-2a/\nu_0} + \left(\frac{c\nu_0}{2} \right)^2 \frac{[A_\ell(\nu_0) - RB_\ell(\nu_0)] A_m(\nu_0)}{M(\nu_0)} + \left(\frac{c}{2} \right)^2 \int_0^1 \nu^2 \frac{[A_\ell(\nu) - RB_\ell(\nu)] B_m(\nu)}{M(\nu)} e^{-2a/\nu} d\nu + \left(\frac{c}{2} \right)^2 \int_0^1 \nu^2 \frac{[A_\ell(\nu) - RB_\ell(\nu)] A_m(\nu)}{M(\nu)} d\nu \right] = 0. \tag{42}$$

This last equation can be written as

$$\sum_{\ell=0}^G a_\ell T_{\ell m} = 0 \tag{43}$$

Now, we can define a square matrix with the elements of $T_{\ell m}$ so that since a_ℓ can't become zero, the determinant of T matrix must be equal to zero. This defines the criticality equation:

$$\det T = 0 \tag{44}$$

Results

The tabulated results are the numerical solutions of Eq. (44) for varying c , t and R . The results are calculated with Wolfram Mathematica [39] software. Equation (42) contains two integral term and one of them, first integral term, includes the unknown slab thickness variable. Gaussian-quadrature method [37] is used to calculate the numerical value of this integral. Thus, this integral term is

written as sum relation by using the Gaussian-quadrature. The *WorkingPrecision* option in Mathematica was selected as 32. Therefore, all calculations are performed with this precision in the background.

Table 1 represents the critical thickness results, $\tau = 2a$, for varying c for varying scattering parameter and varying reflection coefficients. Figures 1-3 represent the critical thickness values for fixed secondary neutron number, varying scattering parameter and reflection

coefficient for $c = 1.1, 1.2$ and 1.5 , respectively. Figures 4-5 represent the 3D plot for fixed secondary numbers, $c = 1.1$ and 1.5 , respectively.

When the scattering parameter increases for fixed c and R , the critical thickness increases. While the critical thickness values decrease for the increasing reflection coefficient and the fixed c and t as we expected.

As a result of the calculation for the critical thickness, it is seen that for small c values the critical thickness shows a concave downward decreasing behaviour for increasing R values, but for large c values it shows a concave upward decreasing behaviour. Accordingly, it can be concluded that reflection is more dominant for small c values than for large c values.

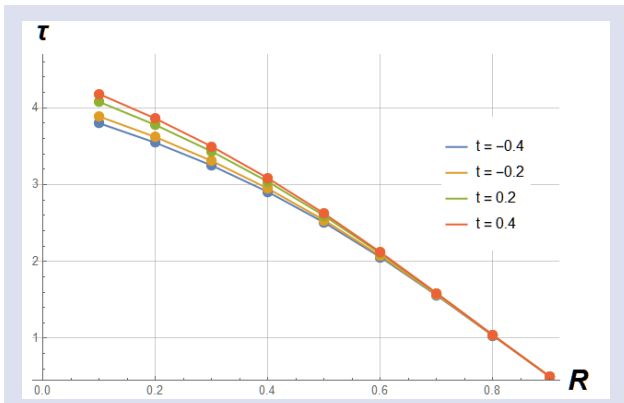


Figure 1. The critical thickness values for $c=1.1$ and varying reflection coefficient.

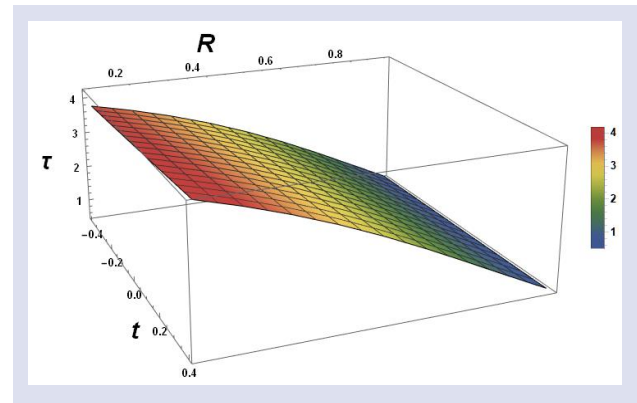


Figure 4. The critical thickness values for $c=1.1$ and varying t and R .

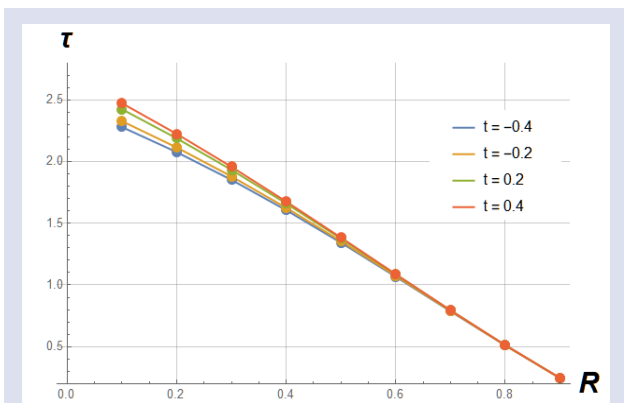


Figure 2. The critical thickness values for $c=1.2$ and varying reflection coefficient.

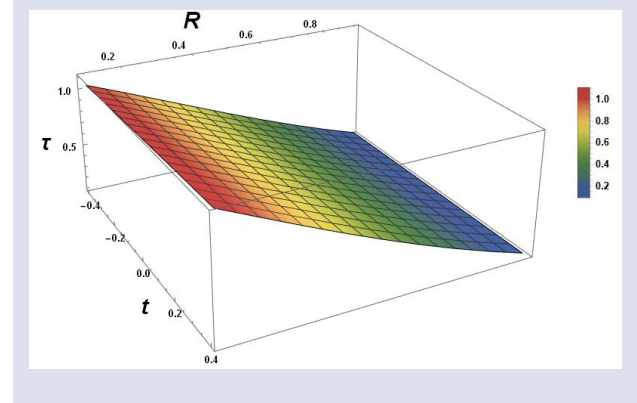


Figure 5. The critical thickness values for $c=1.5$ and varying t and R .

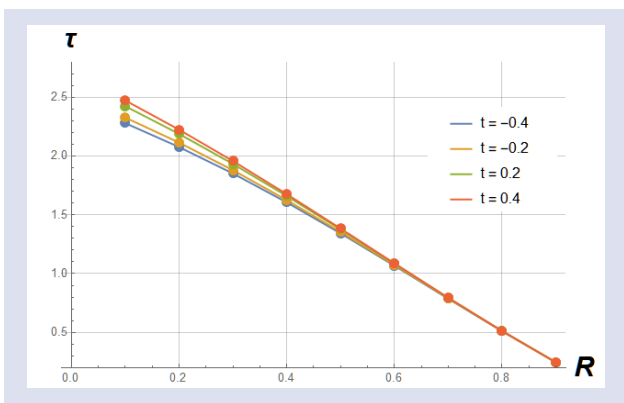


Figure 3. The critical thickness values for $c=1.5$ and varying reflection coefficient.

Table 1. The critical thickness values for varying c and for varying t and R with only 6th approximation

c	t/R	0.1	0.2	0.3	0.4	0.5	0.6	0.7	0.8	0.9
1.1	-0.40	3.80104467	3.54729782	3.25098206	2.90581248	2.50736783	2.05572136	1.55856109	1.03308608	0.50440557
	-0.20	3.88935824	3.62157117	3.31035936	2.95003729	2.53717277	2.07313449	1.56682989	1.03597076	0.50503525
	0.20	4.07880035	3.77846691	3.43336829	3.03938983	2.59543075	2.10561110	1.58109247	1.04014183	0.50552139
	0.40	4.18126050	3.86187248	3.49734950	3.08458338	2.62381989	2.12059592	1.58704169	1.04141439	0.50537625
1.2	-0.40	2.27973382	2.07674808	1.85196894	1.60639728	1.34311558	1.06755242	0.78717660	0.51053495	0.24589472
	-0.20	2.32758131	2.11439170	1.87989904	1.62563335	1.35517752	1.07428209	0.79043220	0.51186420	0.24632210
	0.20	2.42418263	2.18834355	1.93289863	1.66050297	1.37567202	1.08460617	0.79457662	0.51299478	0.24644826
	0.40	2.47299333	2.22452930	1.95777578	1.67595626	1.38397783	1.08813144	0.79543707	0.51278839	0.24614617
1.3	-0.40	1.63931760	1.47091460	1.29089088	1.10170522	0.90690300	0.71084003	0.51817916	0.33329141	0.15974203
	-0.20	1.67155373	1.49532402	1.30834922	1.11337952	0.91412681	0.71493846	0.52029633	0.33427534	0.16011436
	0.20	1.73291589	1.53997387	1.33868243	1.13229104	0.92468808	0.72002323	0.52226397	0.33479809	0.16017173
	0.40	1.76172571	1.55989287	1.35129162	1.13934326	0.92791662	0.72095630	0.52209387	0.33433148	0.15985613
1.4	-0.40	1.27709152	1.13375149	0.98435875	0.83144467	0.67799934	0.52716053	0.38186106	0.24452771	0.11690145
	-0.20	1.30110321	1.15151896	0.99683695	0.83971643	0.68315441	0.53017559	0.38351364	0.24536187	0.11724244
	0.20	1.34426557	1.18181555	1.01669268	0.85167953	0.68963288	0.53321489	0.38466629	0.24566381	0.11727524
	0.40	1.36296781	1.19397747	1.02380653	0.85520440	0.69086466	0.53319621	0.38415019	0.24512731	0.11696650
1.5	-0.40	1.04230861	0.91794640	0.79080504	0.66313873	0.53731702	0.41558037	0.29982540	0.19146657	0.09139188
	-0.20	1.06129148	0.93179758	0.80045315	0.66954117	0.54136417	0.41802057	0.30122588	0.19221184	0.09170958
	0.20	1.09357304	0.95385306	0.81453772	0.67782785	0.54576006	0.42004838	0.30198515	0.19240896	0.09173081
	0.40	1.10638080	0.96169113	0.81872881	0.67956489	0.54603061	0.41960018	0.30133060	0.19185727	0.09143383
1.6	-0.40	0.87739918	0.76788463	0.65760987	0.54849023	0.44237478	0.34087438	0.24524057	0.15631335	0.07453353
	-0.20	0.89301557	0.77918514	0.66546139	0.55373000	0.44574013	0.34295851	0.24647900	0.15699598	0.07483198
	0.20	0.91818923	0.79602579	0.67600645	0.55982647	0.44892655	0.34441107	0.24701809	0.15713506	0.07484684
	0.40	0.92725150	0.80121654	0.67847566	0.56055276	0.44867982	0.34374885	0.24630737	0.15658845	0.07456272
1.7	-0.40	0.75518926	0.65758994	0.56051625	0.46556655	0.37418030	0.28752435	0.20643193	0.13139592	0.06260446
	-0.20	0.76840801	0.66711136	0.56713665	0.47001879	0.37708444	0.28936390	0.20755425	0.13202988	0.06288625
	0.20	0.78864907	0.68042495	0.57534549	0.47470115	0.37950453	0.29045746	0.20795748	0.13213342	0.06289721
	0.40	0.79518965	0.68388960	0.57672966	0.47481501	0.37896089	0.28968475	0.20722847	0.13160027	0.06262585
1.8	-0.40	0.66105918	0.57321874	0.48673951	0.40294590	0.32295954	0.24762910	0.17750688	0.11286608	0.05374462
	-0.20	0.67249103	0.58143513	0.49246763	0.40683050	0.32552974	0.24928801	0.17853979	0.11345994	0.05401160
	0.20	0.68915399	0.59224378	0.49904953	0.41054499	0.32743291	0.25014220	0.17885320	0.11354012	0.05402001
	0.40	0.69392430	0.59453124	0.49971714	0.41027050	0.32671290	0.24931382	0.17812488	0.11302392	0.05376084
1.9	-0.40	0.58640447	0.50669193	0.42888889	0.35408971	0.28316927	0.21674402	0.15517213	0.09858288	0.04692188
	-0.20	0.59645745	0.51391331	0.43394201	0.35754548	0.28548511	0.21826234	0.15613270	0.09914250	0.04717555
	0.20	0.61043480	0.52287495	0.43934349	0.36056751	0.28702271	0.21894877	0.15638358	0.09920649	0.04718220
	0.40	0.61392240	0.52433224	0.43952170	0.36003943	0.28619690	0.21809568	0.15566593	0.09870849	0.04693448

We can also discuss the scattering functions. If we take the first two terms of these scattering functions, then we have

$$f_{Legendre}(\mu, \mu') = f_0 + 3f_1P_1(\mu)P_1(\mu'), \quad (45)$$

$$f_{AG}(\mu, \mu') = f_0 + tP_1(\mu)P_1(\mu'). \quad (46)$$

By using an analogue between Eqs. (45 and 46) we can take that $3f_1 \equiv t$. Thus, we can define a relation between the scattering coefficients. If we take the first three terms of the scattering functions, then we have

$$5f_2 = t^2 = (3f_1)^2 \Rightarrow f_2 = \frac{(3f_1)^2}{5}. \quad (47)$$

Therefore, both scattering functions will give the same result for the above condition. But the results will be different except this condition. If we go on over the scattering functions, a similar result will be valid for the triplet scattering situation. Then, we can define a condition for f_3 :

$$7f_3 = t^3 = (3f_1)^3 \Rightarrow f_3 = \frac{(3f_1)^3}{7}. \quad (48)$$

But it is important that we cannot separate the scattering terms for AG scattering function. If any researcher wants to study triplet anisotropic scattering, for instance, then the linear and the quadratic scatterings will automatically be in the scattering function, except for the Legendre expansion of scattering function.

Conclusions

In this study the critical slab problem was investigated for the reflection boundary condition. The criticality equation defines the relation between the secondary neutron number, c , and the critical thickness, $\tau = 2a$, in mfp unit. Therefore, c and the scattering parameter, t , are the independent variable, and τ is the dependent variable. But, since we take into account the reflection boundary condition, another independent variable is the reflection boundary condition, R .

The critical thickness values are investigated for varying c , t and R . The results are given in tables for only 6th approximation. The critical thickness values decrease for increasing c for certain t and R values as we expected. Similarly, the critical thickness values decrease for increasing R values.

Another result is that both Legendre expansion of scattering and AG scattering will give the same result for certain scattering situations. If the scattering is taken quadratic AG scattering; then the situations must be the same for $t = 3f_1$, and $t^2 = (3f_1)^2$. But other values of t will give different results.

Acknowledgment

This work was studied with the computer system which was collected with personal opportunities.

Conflicts of interest

The author states no conflict of interests.

References

- [1] Anli F., Güngör S., Some useful properties of Legendre polynomials and its applications to neutron transport equation in slab geometry, *Applied Mathematical Modelling*, 31 (2007) 727-733.
- [2] Mitsis G.J., Transport Solutions to the One-Dimensional Critical Problem, *Nuclear Science and Engineering*, 17 (1963) 55-64.
- [3] Case K.M., Elementary Solutions of the Transport Equation and Their Applications, *Annals of Physics*, 9 (1960) 1-23.
- [4] Case K.M., Zweifel P.F., Linear Transport Theory, Massachusetts, (1967).
- [5] Carlvik I., Monoenergetic Critical Parameters and Decay Constants for Small Homogeneous Spheres and Thin Homogeneous Slabs, *Nuclear Science and Engineering*, 31 (1968) 295-303.
- [6] Sahni D.C., Sjöstrand N.G., Criticality and Time Eigenvalues for One-Speed Neutron Transport, *Progress in Nuclear Energy*, 23 (1990) 241-289.
- [7] Sahni D.C., Some New Results Pertaining to Criticality and Time Eigenvalues of One-Speed Neutron Transport Equation, *Progress in Nuclear Energy*, 30 (1996) 305-320.
- [8] Sahni D.C., Sjöstrand N.G., Non-monotonic variation of the criticality factor with the degree of anisotropy in one-speed neutron transport, *Transport Theory and Statistical Physics*, 20 (1991) 339-349.
- [9] Sahni D.C., Sjöstrand N.G., Criticality eigenvalues of the one-speed transport equation with strong forward-backward scattering relationship with rod model, *Transport Theory and Statistical Physics*, 27 (1998) 137-158.
- [10] Dahl E.B., Sjöstrand N.G., Eigenvalue Spectrum of Multiplying Slabs and Spheres for Monoenergetic Neutrons with Anisotropic Scattering, *Nuclear Science and Engineering*, 69 (1979) 114-125.
- [11] Garis N.S., One-Speed Neutron Transport Eigenvalues for Reflected Slabs and Spheres, *Nuclear Science and Engineering*, 107 (1991) 343-358.
- [12] Garis N.S., Sjöstrand N.G., Eigenvalues for reflecting boundary conditions in one-speed neutron transport theory, *Annals of Nuclear Energy*, 21 (1994) 67-80.
- [13] Atalay M.A., The Critical Slab Problem for Reflecting Boundary Conditions in One-Speed Neutron Transport Theory, *Annals of Nuclear Energy*, 23 (1996) 183-193.
- [14] Türeci R.G., Güleçyüz M.Ç., Kaşkaş A., Tezcan C., Application of the HN Method to the Critical Slab Problem for Reflecting Boundary Conditions, *Journal of Quantitative Spectroscopy and Radiative Transfer*, 88 (2004) 499-517.
- [15] Kavenoky A., The CN Method of Solving the Transport Equation: Application to Plane Geometry, *Nuclear Science and Engineering*, 65 (1978) 209-225.
- [16] Grandjean P., Siewert C.E., The FN Method in Neutron-Transport Theory. Part II: Applications and Numerical Results, *Nuclear Science and Engineering*, 69 (1979) 161-168.

- [17] Tezcan C., Kaşkaş A., Güleçyüz M.Ç., The HN method for solving linear transport equation: Theory and applications, *Journal of Quantitative Spectroscopy and Radiative Transfer*, 78 (2003) 243-254.
- [18] İnönü E., A Theorem on anisotropic scattering, *Transport Theory and Statistical Physics*, 3 (1973) 137-146.
- [19] Siewert C.E., Williams M.M.R., The Effect of Anisotropic Scattering on the Critical Slab Problem in Neutron Transport Theory Using a Synthetic Kernel, *Journal of Physics D: Applied Physics*, 10 (1977) 2031-2040.
- [20] Mika J.R., Neutron Transport with Anisotropic Scattering, *Nuclear Science and Engineering*, 11 (1961) 415-427.
- [21] Türeci R.G., Güleçyüz M.Ç., Kaşkaş A., Tezcan C. The singular eigenfunction method: the critical slab problem for linearly anisotropic scattering, *Kerntechnik*, 70 (5-6) (2005) 322-326.
- [22] Güleçyüz M.Ç., Türeci R.G., Tezcan C., The Critical Slab Problem for Linearly Anisotropic Scattering and Reflecting Boundary Conditions with the HN Method, *Kerntechnik*, 71 (2006) 149-154.
- [23] Türeci R.G., Güleçyüz M.Ç., The Slab Albedo and Criticality Problem for the Quadratic Scattering Kernel with the H-N Method, *Kerntechnik*, 73 (2008) 171-175.
- [24] Türeci R.G., Solving the criticality problem with the reflected boundary condition for the triplet anisotropic scattering with the modified FN method, *Kerntechnik*, 80 (6) (2015) 583-591.
- [25] Türeci R.G., Türeci D. The critical slab problem for pure-triplet anisotropic scattering by singular eigenfunction method, *Kerntechnik*, 82 (6) (2017) 693-699.
- [26] Koklu H., Ozer O., Critical thickness problem for tetra-anisotropic scattering in the reflected reactor system. *Pramana - J Phys*, 95 (2021) 190
- [27] Gülderen D., Sahni D.C., Türeci R.G., Aydın A., The Milne Problem for Linear-Triplet Anisotropic Scattering with HN Method, *Journal of Computational and Theoretical Transport*, 51 (2022) 329-353.
- [28] Köklü H., Özer O., Analyzing of the Scattering Coefficients in the Neutron Transport Equation for Critical Systems, *Journal of Computational and Theoretical Transport*, 51 (2022) 112-138.
- [29] Bülbül A., Anlı F., Criticality calculations with PN approximation for certain scattering parameters of Anlı-Güngör and Henyey-Greenstein phase functions in spherical geometry, *Kerntechnik*, 80 (2015) 161-166.
- [30] Bozkır A.Z., Türeci R.G., Sahni D.C., Half-space albedo problem for the Anlı-Güngör scattering function, *Kerntechnik*, 87 (2022) 237-248.
- [31] Türeci R.G., The Milne Problem with the Anlı-Güngör Scattering. *Journal of Computational and Theoretical Transport*, 51 (6) (2022) 354-371.
- [32] Türeci R.G., The Slab Albedo Problem with the Anlı-Güngör Scattering Function. *Indian Journal of Physics*, 97 (2023) 2483-2506.
- [33] Türeci R.G., The Critical Slab Problem with The Anlı-Güngör Scattering Function. *Nuclear Engineering and Technology*, 95 (2023) 2864-2872.
- [34] Maleki B.R., Using the Monte Carlo method to solve the half-space and slab albedo problems with İnönü and Anlı-Güngör strongly anisotropic scattering functions, *Nuclear Engineering and Technology*, In Press. Available online: 27 Sep 2022.
- [35] Türeci R.G., Bülbül A., Case's Method for Anlı-Güngör Scattering Formula, *Süleyman Demirel Üniversitesi Fen Edebiyat Fakültesi Fen Dergisi*, 17 (2022) 1-8.
- [36] Türeci, R.G. Dağistanlı H., Çakır İ.T. Fizik ve Mühendislikte Python, Ankara, (2021) 210.
- [37] Türeci R.G. Fizik ve Mühendislikte Wolfram Mathematica, Ankara, (2020) 176.
- [38] Burden A., Burden R., and Faires J., Numerical Analysis, 10th Edition, Cengage, (2016).
- [39] Wolfram Research, Inc., Mathematica, Version 12.2, Champaign, IL (2023).

Study on Electrical, Thermal, Magnetic Properties and Microstructure for α -Al, θ -Al₂Cu, ω -Al₇Cu₂Fe Phases in Al-32.5 wt. % Cu-1 wt. % Fe Ternary Alloy

Canan Alper Billur ^{1,a,*}, Buket Saatçi ^{2,b}¹ Sivas Vocational School of Technical Sciences, Sivas Cumhuriyet University, Sivas, Türkiye.² Department of Physics, Erciyes University, Kayseri, Türkiye.

*Corresponding author

Research Article

History

Received: 24/08/2023

Accepted: 24/11/2023




Copyright

©2023 Faculty of Science,
Sivas Cumhuriyet University

ABSTRACT

The electrical properties of the Al-32.5 wt. % Cu-1 wt. % Fe ternary alloy were examined, it was observed that the electrical resistivity increased depending on the temperature and it was found as $6.8546 \times 10^{-8} \Omega \cdot m - 5.7780 \times 10^{-7} \Omega \cdot m$ in the temperature range of 298-810K. The thermal conductivity was calculated using electrical measurement results and it was observed that it decreased depending on the temperature. The ternary alloy (cubic α -Al, Fm-3m, 225 a = 4.0480 Å, θ -tetragonal Al₂Cu, I4mcm, 140, a=6.0654 Å c=4.8732 Å, ω -tetragonal Al₇Cu₂Fe, P4/mnc, 128, a = 6.3360 Å, m and c = 14.87 Å) phases were obtained. In this ternary alloy, phases were clearly seen in XRD studies and EDAX analyzes at room temperature. Magnetic properties such as magnetic transition temperature and magnetization curves of the alloy were determined.

Keywords: Mechanical properties, Electrical properties, Thermal properties, Magnetic properties, Intermetallic phase.

 cbillur@cumhuriyet.edu.tr <https://orcid.org/0000-0002-6888-8013> bayender@erciyes.edu.tr <https://orcid.org/0000-0002-1351-5279>

Introduction

The discovery of quasicrystals (QCs) has been one of the most intense investigations in recent decades in terms of the investigation of its structure and the determination of its properties. Studies on many systems under stable or metastable conditions were defined as QC forms. Most of these systems are based on aluminum alloying with transition metals. Although a lot of scientific knowledge about QCs has already emerged, the technological use of these materials has not yet been reached. Its use as a reinforcement phase in aluminum alloys is promising [1]. Aluminum alloys are widely used in the automotive and aerospace industries due to their light weight and satisfactory mechanical properties [2]. Al-Cu-Fe alloys, which are aluminum alloys, are typical materials in which semi-crystals appear. These alloys are interesting because of their non-toxicity, easy availability, and affordable cost of alloying elements [3] and interest in Al-Cu-Fe quasicrystals, the fact that they have an unusual combination of physics micromechanical properties [4]. Tsai *et al.* first reported a stable icosahedral quasicrystal forming composition [5]. Again, the mechanical properties of the Al-Cu-Fe ternary metallic alloy were obtained by Tsai *et al.* with the Vickers test. It has a composition around Al₆₅Cu₂₀Fe₁₅ in the Al-Cu-Fe ternary system. Besides, the equilibrium phase diagram of the Al-rich Al-Cu-Fe alloy system has been the subject of several previous studies [6–12].

Also recently, laser processing of Al-Cu-Fe alloys has become an attractive process to obtain high-quality coatings [13,14]. The change in electrical and magnetic properties of Al-Cu-Fe semi-crystals (QCs) has also been studied recently. The structure of icosahedral Al-Cu-Fe shows ferromagnetic properties. Al-Cu-Fe QCs powder was studied in detail using a vibrating sample magnetometer (VSM) [15].

In the Al-Cu-Fe system, the icosahedral quasicrystalline is stable in a certain composition range when the ψ phase is in equilibrium with the β -AlFe(Cu), λ -Al₁₃Fe₄, λ 1-Al₃ Fe, θ -Al₂ Cu, ω -Al₇Cu₂ Fe and ϕ -Al₁₀Cu₁₀Fe phases [3]. The coordination of Fe atoms in the ω phase is very similar to the icosahedral (Al₆₃Cu₂₅Fe₁₂ (at. %)) ψ phase [16].

In this study, θ -Al₂Cu, ω -Al₇Cu₂Fe intermetallic phases formed by adding Cu element to Al-Cu binary eutectic alloy were observed and mechanical, electrical, thermal and magnetic properties of the obtained ternary alloy were determined.

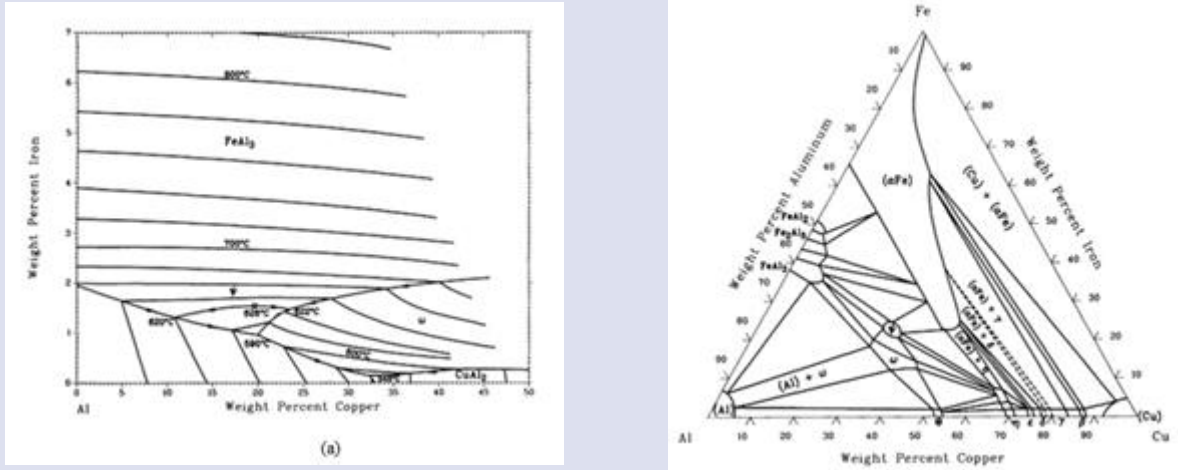


Figure 1. Al-Cu-Fe Ternary Phase diagram. Al-Cu binary, b) Al-Cu-Fe Ternary [17,18].

Experimental Method

The Al-32.5 wt. % Cu-1 wt. % 1 Fe sample was determined from the relevant phase diagram related to stoichiometric calculations as seen in Figure 1 [17-18]. After weighing the masses of the Al, Cu, Fe elements (Alfa Aesar, 4N in purity) whose composition was determined from the phase diagram, they were placed in the graphite crucible in the vacuum melting furnace according to their melting temperatures. A homogeneous alloy was obtained from the elements melted without oxidation in the vacuum melting furnace. Then the homogenized alloy was cast in the hot casting furnace without any air bubbles into 5 cylindrical graphite molds which is 200 mm height, 4 mm inner diameter and outer diameter of 6.35 mm. The samples obtained after the casting stage were cut and placed in the mold and then used for the desired purposes (for XRD, SEM, EDAX, mapping, DTA, electrical resistivity, magnetization) in this study.

Determination of the Electrical Resistivity

The conductivity and temperature resistance coefficient, which are important electrical properties of the material, determine the use of from wire to resistors, potentiometers and many more in electrical and electronic components. Electrons carry the current in metals without changing the chemical properties of metal. Electrical conductivity (EC), one of the physical properties of the material, is affected by the chemical composition of the substances and the stress of the crystal structure. For this reason, electrical conductivity is a parameter used for many purposes such as determining the appropriate heat treatment for metals, controlling heat damage in materials, as well as classifying materials.

Standard conversion method [19,20] was used in the measurement of electrical resistance and conductivity. The temperature dependence of the electrical resistivity of the sample was determined using standard DC four-point probe method (FPPM) in the temperature range of 298-810K (Figure 2). In the DC FPPM, measurement errors have been blocked due to probe resistance, spread resistance under each probe, and contact resistances between metal probes and material [21].

Electrical measurement of the sample was taken on samples with 4 mm diameter. A Keithley 2400 SourceMeter was used to provide constant current, and potential drop was measured by a Keithley 2700 Multimeter through an interface card, which was controlled by a computer in previous study. While using the known conversion rule between electrical resistivity and conductivity, voltage drop is determined by using platinum wires with 0.5 mm radius as current and potential probes [19,22]. At the same time, the electrical resistance temperature coefficient was calculated using the electrical resistance results in the temperature range of 298-810 K [21].

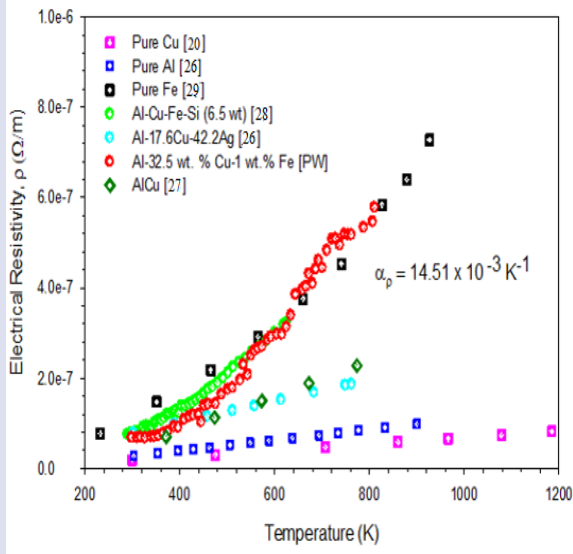


Figure 2. The graph of variation of electrical resistivity with temperature.

Calculation of Thermal Conductivity

Along with electrons, phonons also contribute to thermal conductivity. The relation between thermal conductivity and electrical resistivity is explained by the Wiedemann-Franz-Lorenz law [23].

$$\frac{\kappa}{\sigma T} = \frac{\pi^2 k^2}{3e^2} = L_0 = 2.445 \times 10^{-8} \text{ W}\Omega\text{K}^{-2} \quad (1)$$

where $\kappa, \sigma, T, k, e, L_0$ represent thermal conductivity, electrical conductivity, temperature, Boltzmann constant, electron charge, Lorenz number, respectively. The electrical conductivity and the thermal conductivity can be connected via the W-F law as follows:

$$\sigma = \frac{\kappa_s}{LT} \quad (2)$$

where σ is the electrical conductivity, κ_s is the thermal conductivity, T is temperature, and L is the Lorenz number.

In this study, thermal conductivity values for Al-32.5 wt. % Cu – 1 wt. % Fe composition of alloy was calculated from W-F equation using electrical measurement results. While the value of L is well known for pure materials, it is not well known for alloys as it depends on the property of the material. L and κ_s are required to show electrical resistivity change with temperature and composition. The Lorenz numbers for pure Al, Cu and Fe are $2.24 \times 10^{-8}, 2.49 \times 10^{-8}$ and $2.55 \times 10^{-8} \text{ W}\Omega/\text{K}^2$ [24].

$$L_{\text{alloy}} = \sum_{n=1}^2 x_n L_n \quad (3)$$

Lorenz value for Al-Cu-Fe ternary alloy was calculated from Eq. (3). x_n is the percent by weight of the n^{th} component; L_n is the percent of the Lorenz value of the n^{th} component.

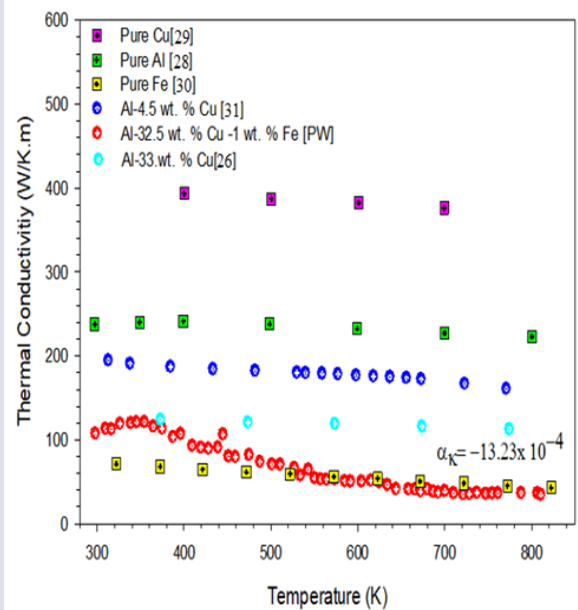


Figure 3. The graph of variation of thermal conductivity with temperature

Characterization Studies

The crystal structure analysis was carried out at room temperature using the Panalytical Empyrean Model Diffractometer. The XRD patterns of the produced samples were obtained using Cu-K α radiation at a wavelength of 1.54 Å and a scanning step of 0.02 °/sec from 10° to 90°. The X-rays scattered from distinct atomic planes were detected by the thallium-activated sodium iodide detector (NaI) scintillation counter. The Win-Index and X-Powder software programs were employed for evaluating the XRD patterns and calculating crystal structure parameters, such as crystal size. The Perkin Elmer Diamond TG & DTA device was utilized for investigating temperature-dependent thermal events such as transitions in phase and weight loss.

This system's heating rate was set at 10 °C/min in order to precisely observe endothermic or exothermic peaks on the DTA curves, suggesting a possible phase transition. The morphological features of materials were studied using Field-Emission Scanning Electron Microscopy (FE-SEM) technique by the ZEISS Gemini SEM 500 model device

Also, DTA and TGA measurements were made depending on the temperature of Al-32.5 wt. % Cu – 1 wt. % Fe alloy. During uniform heating, a shape endothermic peak is present in the DTA curves, indicating a possible phase transition. The endothermic reactions show heat entering the sample, and exothermic reactions show heat leaving the sample during the heating or cooling process [25].

After electrical measurements, XRD and DTA and TGA analysis were performed on the sample obtained in the study, the microstructure of the sample was examined. While examining the microstructure of the samples, FE-SEM images were also taken, and EDAX and Mapping analyzes were performed with FE-SEM apparatus from the same region at the same time.

Magnetic Properties

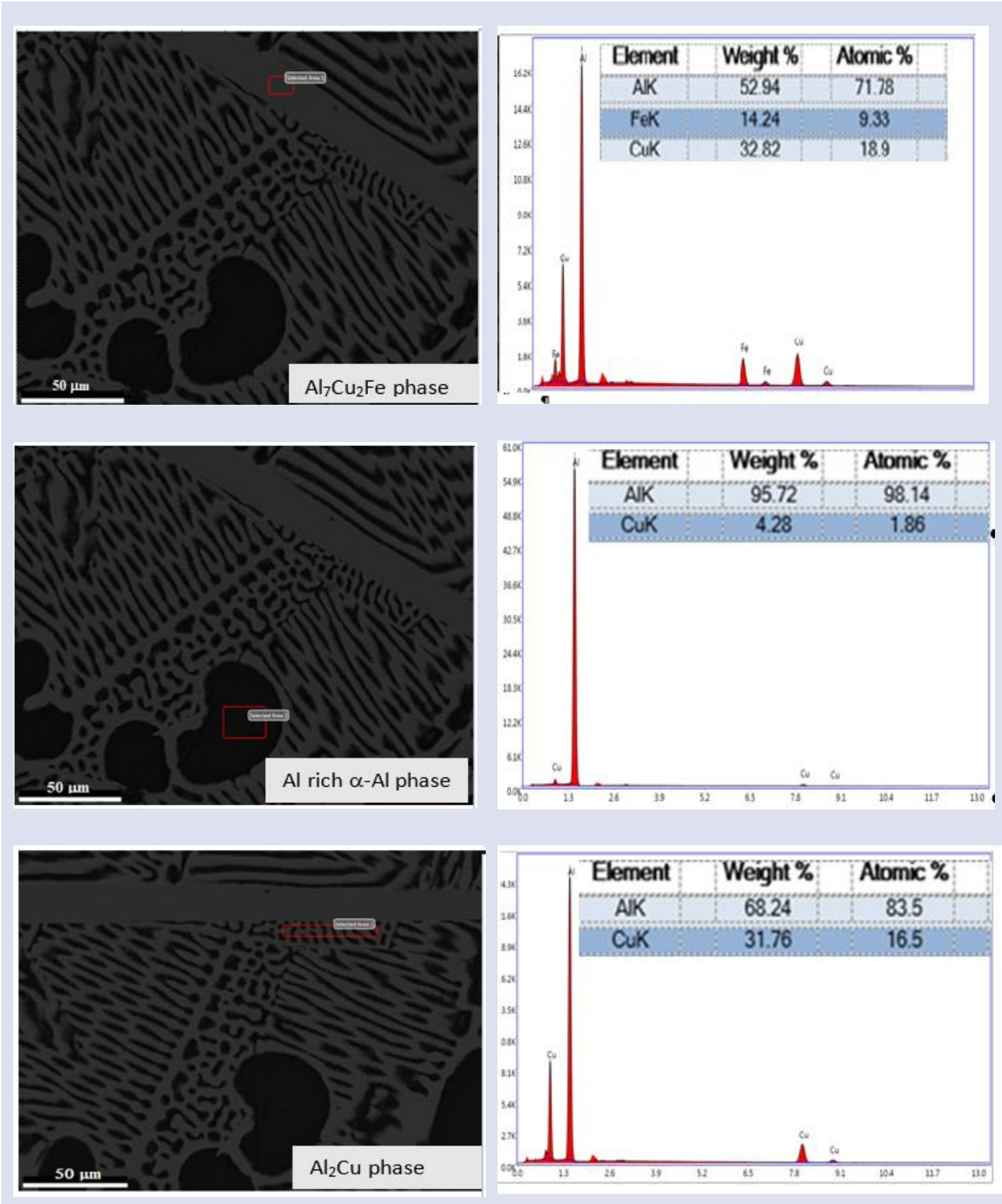
In this study, the magnetic property of the Al-Cu-Fe alloy was determined with a Quantum Design-PPMS DynaCool-9 model device, which can apply a magnetic field up to 9 T in the temperature range of 1.8-600 K. Magnetic field (M-H) and temperature-dependent magnetization (M-T) measurements were made with this device. The experimental magnetic transition temperatures (T_c) were determined by the first derivative of the magnetization curves.

Results and Discussion

Electrical resistivity of Al-Cu-Fe alloy was measured by FPPM method depending on temperature. In the measurements obtained at 298-810 K in temperature range, it was found that the resistance increased linearly with temperature.

Table 1. The elemental composition of Al-32.5 wt. % Cu-1 wt. % Fe, α -Al, θ -Al₂Cu ω -Al₇Cu₂Fe phases as determined by EDAX.

Phase	Al (at. %)	Al(wt. %)	Cu (at. %)	Cu(wt. %)	Fe (at. %)	Fe (wt. %)
α -Al	98.14	95.72	1.89	4.28
θ -Al ₂ Cu	83.5	68.24	16.5	31.76
ω -Al ₇ Cu ₂ Fe	71.78	52.94	18.19	32.82	9.33	14.24



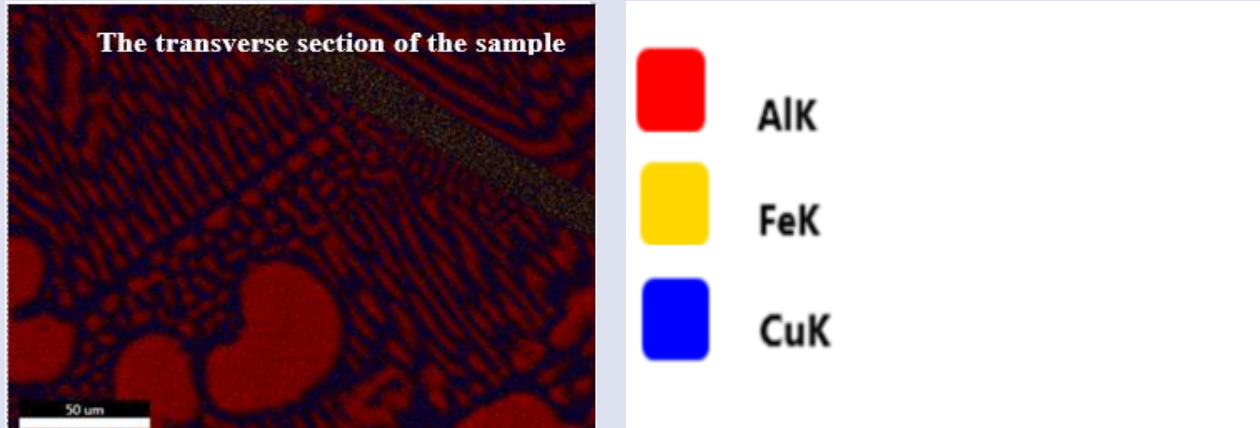


Figure 4. FE-SEM and MAPPING images of the Al-32.5 wt. % Cu- 1 wt. % Fe sample.

Increasing the temperature of the alloy will decrease the mean free path. This is due to lattice vibrations that increase with temperature. With the decrease of the mean free path, the electrical conductivity will decrease while the electrical resistivity will increase. At the same time, alloys have higher electrical resistivity than pure metals. When the electrical resistivity values of the alloy were compared with the literature results, it was determined that the electrical resistivity of the Al-Cu-Fe alloy was higher than the pure Al[26] and Cu[20], Al-Cu[27] alloy, Al-Cu-Ag[26] alloy. When compared with pure Fe[29], the amount of Fe in our Al-Cu-Fe alloy increased the electrical resistivity.

coefficient of the electrical resistance (TCR), α_p value of the alloy in the temperature range of 298-810 K was found to be $14.51 \times 10^{-3} \text{ K}^{-1}$ by using the electrical resistivity values [Figure 2].

Thermal conductivity values were calculated using W-F equation using electrical measurements results. It has been observed that the thermal conductivity values decrease depending on the temperature. This is expected because as the temperature increases, carrier electrons, holes and lattice vibrations increase. This combined situation may cause a decrease in electrical conductivity in some alloys and an increase in others. In our study, phonon-phonon and electron-phonon scattering became more prominent with the increase in lattice vibrations. This reduces the thermal conductivity. When the results were compared with the literature in Figure 3, it was seen that it was compatible with pure Al, Cu, Fe and other alloys.

The thermal conductivity value of the alloy in the temperature range of 298-810K was obtained between 107.4445 W/Km - 34.6622 W/Km. The temperature coefficient of the thermal resistance (TCTR), α_k value of the alloy in the temperature range of 298-810 K was found to be $14.51 \times 10^{-3} \text{ K}^{-1}$ by using the electrical resistivity values [Figure 3].

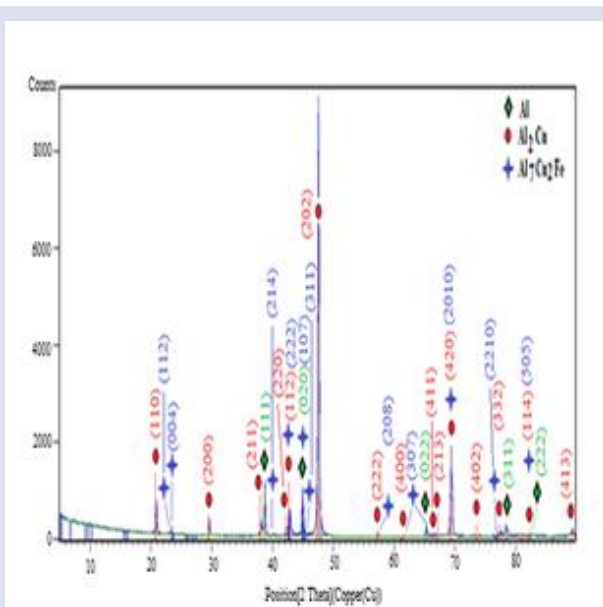


Figure 5. The graph of variation of thermal conductivity with temperature

The electrical resistivity value of the alloy in the temperature range of 298-810 K was obtained between $6.8546 \times 10^{-8} \text{ } \Omega\text{m}$ and $5.7780 \times 10^{-7} \text{ } \Omega\text{m}$. The temperature

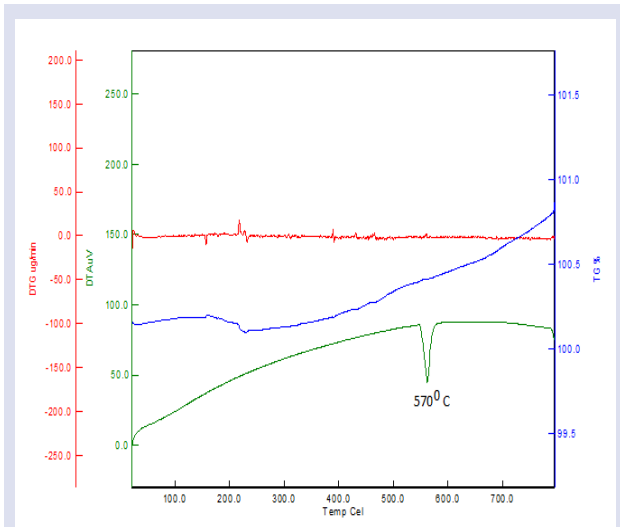


Figure 6. Thermal curves depending on temperature in the Al-32.5 wt. % Cu – 1 wt. % Fe ternary metallic alloy system.

In the ternary alloy, multiple solid phases were formed simultaneously from the liquid phase and these phases

were determined by microstructure analysis. The existence of these phases was confirmed by the phase diagram of the Al-Cu-Fe ternary alloy.

The microstructure of the alloy was visualized by FE-SEM [Figure 4]. It has been observed that the alloy has homogeneous and regular structure. No defects, gaps or cracks were observed. The phases imaged by SEM were determined by MAPPING. Cu and Fe elements in the alloy dissolved in the structure and took place as θ -Al₂Cu, ω -Al₇Cu₂Fe phases. At the same time, the α -Al phase was determined [Figure 4.]. The quantitative chemical composition of these phases determined by MAPPING are given by EDAX analysis [Table 1.]. With XRD diffraction peaks measurements, both phases were indexed and microstructure parameters such as crystal systems, space groups, cell parameters (a, b, c) of these phases were determined. When the indexed α -Al, θ -Al₂Cu, ω -Al₇Cu₂Fe phases were examined, it was observed that both the peak density and the peak intensity were in the Al₂Cu phase [Figure 5] [Table 2.].

Table 2. In the study, the crystal system and cell parameters obtained in Al-Cu-Fe ternary metallic alloy.

Component of Ternary Alloy	Al							Volume of Cell (106 pm ³)	Crystallite Size only [Å]
	Space Group	Space group Number	Crystal System	Cell parameters a(Å) b(Å) c(Å)					
Al-32.5 wt.% Cu-1 wt.% Fe	Fm-3m	225	Cubic	4.0406	4.0406	4.0406	65.97	39.8 ± 7.29	
Component of Ternary Alloy	Al ₂ Cu							Volume of Cell (106 pm ³)	Crystallite Size only [Å]
	Space Group	Space group Number	Crystal System	Cell parameters a(Å) b(Å) c(Å)					
Al-32.5 wt.% Cu-1 wt.% Fe	I4/mcm	140	Tetragonal	6.0654	6.0654	4.8732	179.28	39.00 ± 3.37	
Component of Ternary Alloy	Al ₇ Cu ₂ Fe							Volume of Cell (106 pm ³)	Crystallite Size only [Å]
	Space Group	Space group Number	Crystal System	Cell parameters a(Å) b(Å) c(Å)					
Al-32.5 wt.% Cu-1 wt.% Fe	P4mnc	128	Tetragonal	6.3360	6.3360	14.8700	596.65	47.00 ± 13.47	

Also, Figure 6 show the DTA and TGA curves for sample Al-32.5 wt. % Cu – 1 wt. % Fe, as a function of temperature. In the observed endothermic reaction, the temperature was measured as 570 °C [Figure 6]

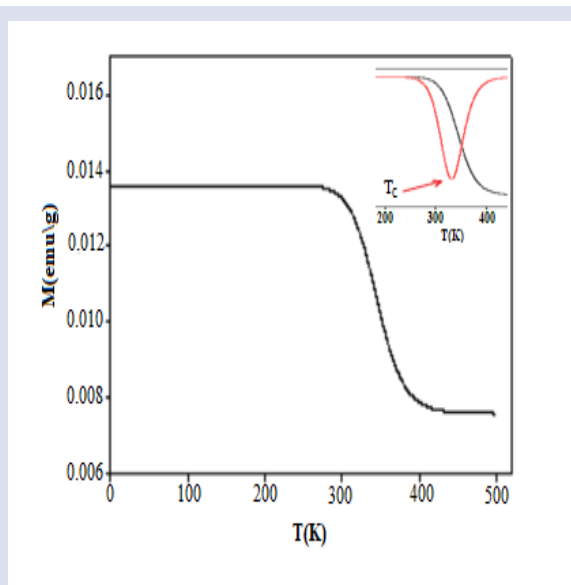


Figure 7. The temperature dependence magnetization curve of the two compositions Al-32.5 wt. % Cu- 1 wt. % Fe alloy. The inset present overlap $\partial M/\partial T$ curve as a function of temperature with M-T curve for determine to T_c

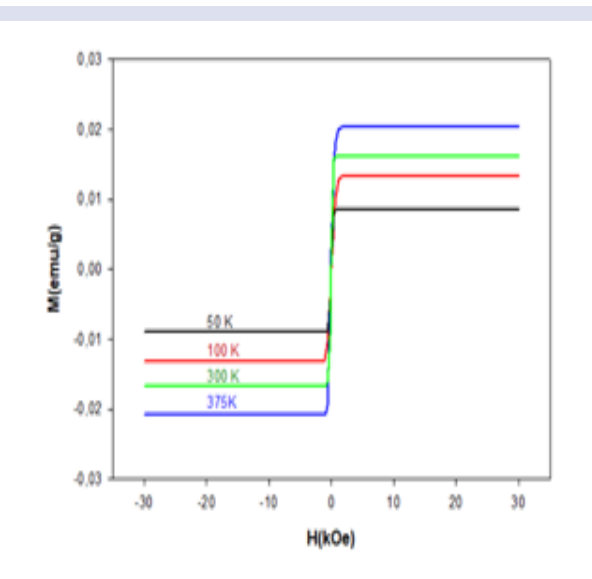


Figure 8. The magnetization as a function of applied field Al-32.5 wt. % Cu- 1 wt. % Fe alloy at 50 K, 100 K and 375 K degree temperature.

The temperature dependence of the magnetic field in the alloy was determined from the base temperature to the temperature of 500K in the 1kOe magnetic field. The Curie temperature, which is the magnetic transition temperature, was obtained from the Figure 7 graph, which gives the variation of the magnetic field with temperature. The Curie temperature (T_c) of the Al-32.5 wt. % Cu- 1 wt. % Fe alloy was found to be 343.4 K. We determined that the alloy exhibits ferromagnetic (FM)

properties from room temperature to the Curie temperature (T_c) and paramagnetic (PM) properties after T_c temperature (Figure 7). As can be seen from the magnetization hysteresis curve of the alloy in Figure 8, the magnetization curves decreased as the temperature increased. In the graph obtained for 50 K, 100 K, 300 K, 374 K temperature values, it was concluded that these were soft ferromagnetic materials with narrow hysteresis loops. For this reason, they exhibit a sigmoidal shape. Soft ferromagnetic materials have low remanence, low coercivity and low hysteresis loss. These results are compatible with the literature.[32-34].

Conclusion

Quasicrystals (QCs) which has icosahedral symmetry show the properties of heat and electrical conduction, high resistance and low expansion. In our study, an increase in electrical resistivity was observed with Fe added to the Al-Cu alloy. This supports the high resistance feature of quasicrystals (QC). At the same time, the decrease in thermal conductivity also supports heat conduction and, accordingly, expansion.

The results of the determined properties of the Al-32.5 wt. % Cu- 1 wt. % Fe alloy are given below

The electrical resistivity values increasing linearly with temperature were found in the $6.8546 \times 10^{-8} \Omega \text{m}$ - $5.7780 \times 10^{-7} \Omega \text{m}$ range.

The thermal conductivity values of the alloy calculated using the Wiedeman-Franz law are in the 107.4445 W/Km - 34.6622 W/Km range.

Phases of the Al-32.5 wt. % Cu- 1 wt. % Fe alloy were determined from FE-SEM and MAPPING images. α -Al, θ -Al₂Cu, ω -Al₇Cu₂Fe phases in Al-32.5 wt. % Cu- 1 wt. % Fe composition were determined. The composition of each phase was obtained by EDAX analysis.

Space group, crystal system and cell parameters were determined by XRD measurements of the alloy.

The magnetic properties of the alloy were determined. It was observed that alloy showed ferromagnetic properties from room temperature to the curie temperature, which is the magnetic transition temperature(T_c). When the magnetization M(H) curves were examined, it was seen that the magnetization decreased as the temperature increased.

Conflict interests

There are no conflicts of interest in this work.

References

- [1] ravessa D.N., Cardoso K.R., Wolf W., Jr. Jorge A.M., Botta W.J., The Formation of Quasicrystal Phase inn Al-Cu-Fe System by Mechanical Alloying *Materials Research*, 15 (5) (2012) 749-752.
- [2] Školáková A., Novák P., Mejzliková L., Průša F., Salvetr P., Vojtěch D., Structure and Mechanical Properties of Al-Cu-Fe-X Alloys with Excellent Thermal Stability, *Materials (Basel) NOV*, 10 (11) (2017) 1269.

- [3] Huttunen-Saarivirta E., Microstructure, fabrication and properties of quasicrystalline Al–Cu–Fe alloys: A review., *J. Alloy. Compd.*, 363 (2004) 154–178.
- [4] Biswas K., and Chattopadhyay K., Formation of w-Al₇Cu₂Fe phase during laser processing of quasicrystal-forming Al–Cu–Fe alloy, *Philosophical Magazine Letters*, 88 3 (2008) 219-230.
- [5] Tsai A.P., Inoue A. and Masumoto T., A Stable Quasicrystal in Al–Cu–Fe System, *Jap. J. appl. Phys.*, 26 (9) (1987) L1505-L1507.
- [6] Liu W. and Köster U., Decomposition of the icosahedral phase in AlCuFe alloys, *Mater. Sci. Engng A*, 133 (1991) 388-392.
- [7] Gayle F.W., Shapiro A.J., Boancaniello F.S., et al., The Al–Cu–Fe phase diagram: 0 to 25 At. pct Fe and 50 to 75 At. Pct Al – Equilibria Involving the Icosahedral Phase, *Metall. Trans. A*, 23 (1992) 2409-2417.
- [8] Gratiyas D., Calvayrac Y., Devaud-Rzepski J., et al., Phase diagram and structures of the ternary AlCuFe system in the vicinity of the icosahedral region, *J. Non-Crystalline Solids* 153–154 (1993) 482-488.
- [9] Grushko B., Wittenberg R. and Holland-Moritz D., Solidification of Al–Cu–Fe alloys forming icosahedral phase, *J. Mater. Res*, 11 (1996) 2177-2185.
- [10] Gui J., Wang J., Wang R., et al., On some discrepancies in the literature about the formation of icosahedral quasicrystal in Al–Cu–Fe alloys, *J. Mater. Res*, 16 (2001) 1037-1046.
- [11] Rosas G. and Perez R., On the transformations of the ψ -AlCuFe icosahedral phase, *Mater. Lett*, 47 (2001) 225-230.
- [12] Zhang L. and Lück R., Z., Phase diagram of the Al–Cu–Fe quasicrystal-forming alloy system, *Metallkd*, 94 (2003) 91-97.
- [13] Auderbert F., Colaço R., Viller R., et al., Laser cladding of aluminium-base quasicrystalline alloys, *Scripta Mater*, 40 (1999) 551-557.
- [14] Biswas K., Galun R., Mordike B.L., et al., Laser cladding of quasicrystal forming Al–Cu–Fe on aluminum, *J. Non-Crystalline Solids*, 334–335 (2004) 517.
- [15] Zahoor A., Nawaz Shahid R., Tariq N.H., Wahab H., Anwar S., Rafiq M.A., Ameer A., Izhar S., Ali F., Hasan B.A., Effect on electrical and magnetic behavior of Al–Cu–Fe quasicrystals during surface leaching, *Applied Physics A*, (2021) 127, 551.
- [16] Yin S, Xie Z, Bian Q, He B, Pan Z, Sun Z et al., Formation of AlCuFe icosahedral quasicrystal by mechanical alloying: XAFS and XRD studies. *Journal of Alloys and Compounds*, 455 (1-2) (2008) 314-321.
- [17] Willey L.A., Metallography, Structures and Phase Diagrams, Vol.8, Metals Handbook 8th ed., American Society for Metals, Metals Park, OH. (1973)
- [18] Prevarskiy A.P., Investigation of Fe–Cu–Al Alloys, Russ. Metall. TR:Izv.Akad. Nauk SSSR, *Metall.*, 4 (1971) 154-156.
- [19] Yuan G.C., Influence of silicon content on friction and wear characteristics of new Al–Sn–Si alloys, *Chin. J. Nonferrous Metals*, 8 (9) (1998) 101-105.
- [20] Rudnev V., Loveless D., Cook R., Black M., Handbook of Induction Heating. Markel Dekker Inc, New York, (2003) 119-120.
- [21] Ari M., Saatçi B., Gündüz M., Payveren M., Durmus S., Thermo-electrical characterization of Sn–Zn alloys, *Mater. Char.*, 59 (2008) 757-763.
- [22] Zhou D.J., Study on Al–Sn–Si–Cu bearing alloy, *J. Light Alloy Fabr. Technol.*, 28 (5) (2000) 44-46.
- [23] Yamasue, E., Susa, M., Fukuyama, H., Nagata, K., Deviation from Wiedemann–Franz law for the thermal conductivity of liquid tin and lead at elevated temperature., *Int. J. Thermophys.* 24 (2003) 713-730.
- [24] Sergeant, E.J., Krum, A., Thermal management handbook: for electronic assemblies. 1 edition, McGraw-Hill Professional: New York, (1998) 26.
- [25] Bandyopadhyay, A. Dutta, Thermal, optical and dielectric properties of phase stabilized δ – Dy–Bi₂O₃ ionic conductors, *J. Phys. Chem. Solids*, 102 (2015) 12–20.
- [26] Büyük U., Maraşlı N., Çadırılı E., Kaya H., Keşlioğlu K., Variations of microhardness with solidification parameters and electrical resistivity with temperature for Al–Cu–Ag eutectic alloy., *Current Applied Physics* 12 (2012) 7-10.
- [27] Kaya H., Dependence of electrical resistivity on temperature and composition of Al–Cu alloys, *Materials Research Innovations*, 16 (3) (2012) 224-229.
- [28] Çadırılı E., Büyük U., Engin S., Kaya H., Effect of silicon on microstructure, mechanical and electrical properties of the directionally solidified Al-based quaternary alloys, *J. Alloys and Comp.*, 694 (2017) 471-479.
- [29] Youjun Z., Mingqiang H., Guangtao L., Chengwei Z., Vitali P.B., Eran G., Yingwei F., Jung-Fu L., Reconciliation of experiments and theory on transport properties of iron and the geodynamo. *Phys. Rev. Lett* 125 (2020) 0.78501.
- [30] Touloukian Y.S., Powell R.W., Ho C.Y., Klemens P.G., Thermal Conductivity Metallic Elements and Alloys, vol. 1, New York, Washington, (1970) 60.
- [31] Choi S.W., Cho H.S., Kumai S., Effect of the precipitation of secondary phases on the thermal diffusivity and thermal conductivity of Al–4.5 Cu alloy, *J. Alloys and Comp.* 688 (2016) 897-902.
- [32] Nguyen H. V. , Do N. B. , Nguyen T. H. O. , Nguyen C. S. , Trinh V. T. , Le H. T. , Junior A. M. J., Synthesis and magnetic properties of Al–Cu–Fe quasicrystals prepared by mechanical alloying and heat treatment, *J. of Materials Research*, 38 (2023) 3 644-653.
- [33] Oanha N. T. H., Vieta N. H., Dudina D. V., Jorge Jr A. M., Kimi Ji-Soon, Structural characterization and magnetic properties of Al₈₂Fe₁₆TM₂ (TM: Ti, Ni, Cu) alloys prepared by mechanical alloying, *J. of Non-Crystalline Solids*, 468 (2017) 67-73.
- [34] Li Z., Bai H. Y., Pan M. X., Zhao De Q., Wang W. L., Wang W. H., Formation, properties, thermal characteristics, and crystallization of hard magnetic Pr–Al–Fe–Cu bulk metallic glasses, *J. Mater. Res.*, Vol. 18 (2003) 9 2208-2213.

A Study on The Optical Properties of Long-Infrared Intraband Transitions of Quadruple GaAs/Al_xGa_{1-x}As Quantum Well Under Applied Electric Field

Didem Altun^{1,a,*}¹ Sivas Vocational College, Sivas Cumhuriyet University, 58140, Sivas, Türkiye.

*Corresponding author

Research Article

History

Received: 25/08/2023

Accepted: 05/12/2023

Copyright

©2023 Faculty of Science,
Sivas Cumhuriyet University

ABSTRACT

The linear structure of the Lorentz-Minkowski plane is almost the same as Euclidean plane. But, there is one different aspect. These planes have different distance functions. So, it can be interesting to study the Lorentz analogues of topics that include the distance concept in the Euclidean plane. Thus, in this study, we show that the relationship between Euclidean and Lorentz distances is given depending on the slope of the line segment. Following, we investigate Lorentz analogues of Thales' theorem, Angle Bisector theorems, Menelaus' theorem and Ceva's theorem.

Keywords: GaAs/Al_{0.44}Ga_{0.56}As, Optical properties, Absorption coefficient, Refractive index.^a didemaltun@cumhuriyet.edu.tr  <https://orcid.org/0000-0002-1964-3538>

Introduction

Infrared light sources have been given attention in industry, health, and military applications due to the long-range transmission and high coherence of the electromagnetic source in the last couple of decades [1]. The infrared sensors have found space in target tracking, missile guiding, and night vision [2]. In addition, the infrared sensors are also widely used in telecommunication and health applications with a lower cost of production [3]. One of the most used infrared light sources is mercury-based materials but difficulties in production make working with these materials reluctant [4]. Beyond the Mercury-based materials, infrared light sources are rare, and the device performances are not the best till now. Because of that, low-dimensional GaAs-based materials are an option, and multi-quantum well structures have become very attractive for infrared devices. These material groups not only offer an option for the infrared sensor, but it has also made it possible to produce a device that emits infrared light. Due to the superior performances of the light emitting property of the GaAs-based materials, GaAs/AlGaAs multiple quantum wells have been widely used as the infrared laser source.

The electron transitions, in the quantum wells, between the bands and minibands emit/absorb infrared light [5]. For wider material selection, intra-band transition, which uses the space within the band, is used, unlike inter-band transition. An extensive study of intraband infrared transitions has been done by Hao. [6]. The wavelength of the device is set by tuning the quantum well width and barrier thicknesses. In these light sources, GaAs and AlGaAs materials are frequently used due to

negligible lattice constant difference which makes wavelength control of the device easier. Furthermore, the relatively easier growth of the GaAs materials than other materials is another advantage of these materials [7].

Beyond the advantage of the material property, the reaction of the GaAs-based low-dimensional structures to the external fields has shown superior performance. These structures are mostly used as a light sources and are mostly electrical pumped so that there is no any external light source to trigger nonlinear properties. In addition to this, importance of electric field is shown up here as a pump source. The electric field, magnetic field, temperature, pressure, and laser field have been applied to the GaAs-based quantum wells. In these studies, optical and electronic properties have been studied by many researchers [8-12]. In the study conducted by Öztürk, linear optical properties of GaAs/AlGaAs OWs were calculated depending on the applied electric field, and changes were observed in the potential profile shape, energy levels and dipole moments. This has shown that the variation of resonance peaks suitable for optical modulators and infrared optical device applications can be achieved smoothly by changing the electric field [13]. In addition; the effect of the laser field on the optical properties of the asymmetric quantum well has been analyzed [14]. Pöschl-Teller potential has been studied to analyze nonlinear optical properties [15]. The effect of the temperature and hydrostatic pressure on the optical and electronic properties has been studied by Öztürk [16]. The effects of the quantum well and barrier thicknesses have been investigated by Alaydin [17]. The electric and

magnetic field effects applied to the QW structure with increasing well widths were shown by Altun [18].

In this report, I have considered energy band structures of long-infrared emitting/absorbing GaAs/Al_xGa_{1-x}As quadruple quantum well heterojunction structures under varying EF for quantum cascade laser/detector applications. The wave functions and the corresponding energy eigenvalues have been obtained by solving the Schrödinger equation using effective mass approximation. The finite element method is used to obtain solutions. The EF intensity has been applied through positive growth direction and the intensity of the EF changes from 0 – 80 kV/cm to analyze the optical properties of the structure under real device operation conditions. The three bounded energy states are obtained and the probability density of wave functions (PDW), transitions energies, and dipole moment matrix elements (DMME) are first calculated. Then, the changes in the linear refractive indices and absorption coefficients depending on the EF are investigated to be used in long-infrared devices.

Materials and Methods

In this research, GaAs/Al_{0.44}Ga_{0.56}As quadruple quantum well heterojunction grown in z-direction is studied. QW structure is designed to obtain long-infrared transition between subbands. The details of the calculation methods are very well known in the literature and given by the references Altun, [18], Alaydin [19]. The EF is set perpendicular to the growth surface as $\vec{F} = F\hat{z}$. Hamiltonian with an external field (electric field) is defined as [17];

$$H = -\frac{\hbar^2}{2m^*} \frac{d^2}{dz^2} + V(z) + eFz \tag{1}$$

In equation (1), m^* describes the effective mass of the electron in GaAs and in this research, it is taken as $m^* = 0.067m_0$ (m_0 is the free electron mass), e is the electron charge and $V(z)$ is the confinement potential. For GaAs/Al_{0.44}Ga_{0.56}As system conduction band offset is taken as 0.6 and potential discontinuity $V(z)$ is 448 meV. $V(z)$ potential height is the same as the reference [20]. Where the second-order differential is defined as;

$$\frac{d^2}{dz^2} = [-2 \text{diag}(\text{ones}(1, N)) + \text{diag}(\text{ones}(1, N - 1), -1) + \text{diag}(\text{ones}(1, N - 1), 1)]^2 \tag{2}$$

N is the length of the matrix to define the total quantum region. After obtaining the energy levels and wave functions, linear absorption coefficient is calculated as follows [21]:

$$\beta(\omega) = w \sqrt{\frac{\mu}{\epsilon_r}} \frac{|M_{ij}|^2 \sigma_v \hbar \Gamma_{ij}}{(\Delta E_{ij} - \hbar\omega)^2 + (\hbar \Gamma_{ij})^2} \tag{3}$$

where w is the angular frequency, Γ_{ij} is the intersubband relaxation time, μ is the magnetic permeability, ϵ_r is the real part of the electrical permittivity, σ_v is the carrier number, \hbar is the reduced Planck constant and ΔE_{ij} is the energy difference between final and initial energy levels of the electron. M_{ij} is the dipole matrix element and it is defined as [22];

$$M_{ij} = \int \psi_j(z)^* |e| z \psi_i(z) dz \tag{4}$$

The linear refractive index change is expressed as [23]:

$$\frac{\Delta n(\omega)}{n_r} = \frac{|M_{ij}|^2 \sigma_v}{2n_r^2 \epsilon_0} \left[\frac{\Delta E_{ij} - \hbar\omega}{(\Delta E_{ij} - \hbar\omega)^2 + (\hbar \Gamma_{ij})^2} \right] \tag{5}$$

Results and discussion

In this study, I analyze GaAs/Al_xGa_{1-x}As quadruple QW structures to have long-infrared emission/absorption. To reach long-infrared wavelength (THz region), aluminum concentration is set to 0.44, which is the border of direct to indirect bandgap transition and Al_{0.45}Ga_{0.55}As has a direct bandgap [20]. The potential barrier height of the QW is calculated as $V_0 = 448 \text{ meV}$ and the thickness of the layer sequence of quadruple QW heterostructures is

as follows **8-2.2-1.2-2-1-4-2.3-1.2-8** nm (QB are shown bold). The effective mass approximation is used to solve the Schrödinger equation using the finite element method (FEM) and the parameters used in this study are $\mu = 4\pi \times 10^{-7} \text{ H/m}$, $\sigma = 1 \times 10^{22} \text{ cm}^{-3}$, $\tau_{21} = 0.3 \text{ ps}$, $\tau_{32} = 2.8 \text{ ps}$, and $\tau_{31} = 4 \text{ ps}$, $\Gamma_{ij} = \frac{1}{\tau_{ij}}$ and $n_r = 3.3254$.

In the calculations, I have seen that there are only three bounded states and I have considered carrier transitions in these states as shown in Figure 1.

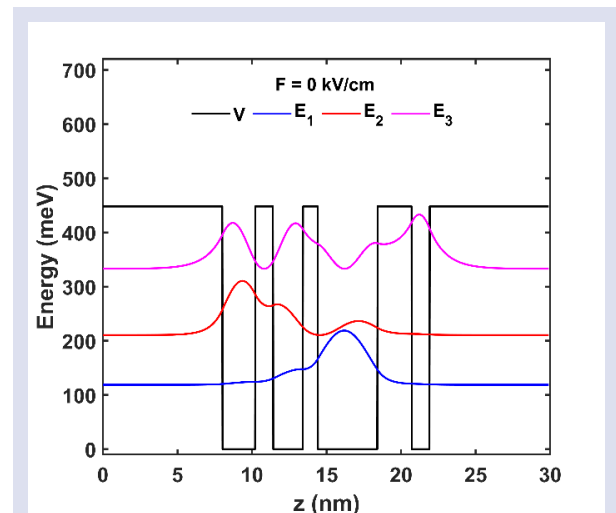


Figure 1. PDW of quadruple QW structure in the absence of EF.

In the case of zero EF, the ground state is mostly localized in the third (from left to right) QW. While the first excited state is mostly localized in the first QW, its localization has been distributed up to the end of the second QW. Apart from the ground and first excited state the second excited state's localization has been distributed between the first, second, and fourth QWs. As seen in Figure 1, energy eigenvalues of the ground, first excited, and second excited states are as follows 119 meV, 211 meV, and 333 meV. The transition energies show that long-infrared absorption/emission is obtained from the E_{32} transition as desired and the E_{21} transition has higher energy than the phonon vibrations of GaAs (0.026 eV), which is crucial for heat dissipation via phonon vibration in long infrared devices.

Figure 2 shows the PDW of the quadruple QW structure under varying EF intensities. I have obtained the wave functions and corresponding energy eigenvalues for every 5 kV/cm up to 80 kV/cm. To prevent confusion and for the sake of simplicity, we do not present every plot for different EF intensities. With the effect of EF, all three energy states are shifted up to higher energies. Localization of the ground state has also started to show up in the first and second QWs. The localization of the first excited state in the second QW is inversely proportional to EF intensity however, localization in the third QW is independent of the EF intensity. When the second excited state is localized in the fourth QW in the case of zero EF, it is mostly localized in the first and second QWs after the applied EF. In another study by Altun, wave functions and energy eigenvalues were shown for different electric fields applied to GaAs/AlGaAs QWs with periodically increasing well width. [18].

In the design, there has been no localization in the fourth QW in the case of EF but I have used the fourth QW to tune transition energies changing the QW thickness. According to the probability density functions and energy eigenvalues, 80 kV/cm is the highest EF intensity. Electron leakage has started over this value and after a bit more increase, the second excited state has higher eigen energy than barrier height, which causes stopping device operation. Here I conclude that 80 kV/cm is the highest EF, which can be applied to the device under consideration.

Even though there is a slight increase in E_{32} transition energy, the dipole matrix moment corresponding to the M_{32} is constant and independent from EF intensity as shown in Figure 3. This means the design shows stable operation over changing EF. Also, M_{32} is the most probable transition in the design till the highest EF intensity. E_{21} transition energy is inverse linearly proportional with EF intensity however dipole matrix element M_{21} is linearly proportional to EF intensity. Even with a decrease in E_{21} , it is higher than the phonon vibration energies of GaAs, which is the desired behavior for quantum cascade laser/detector applications. As a last, E_{31} transition is inversely proportional to EF intensity and M_{31} is decreasing at higher EF intensities, which supports radiative transition through E_{32} .

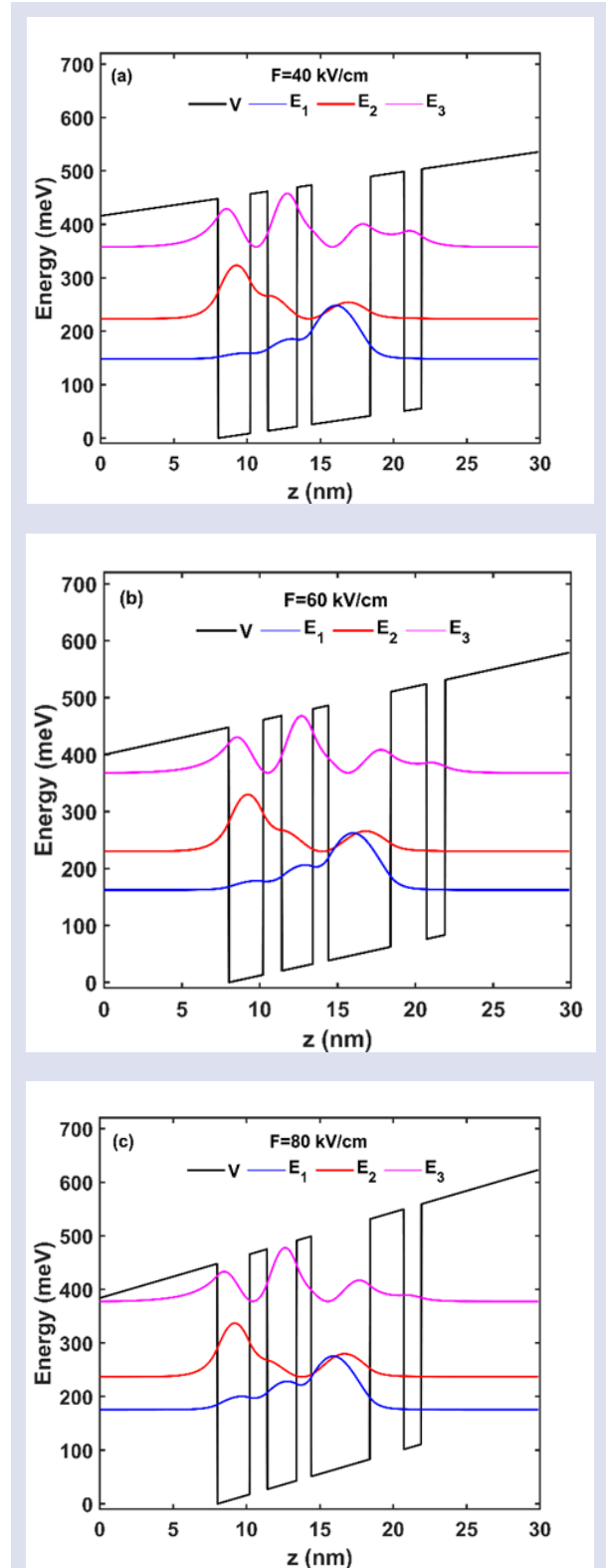


Figure 2. PDW of quadruple QW structure under varying EF intensities (a) $F = 40 \text{ kV/cm}$, (b) $F = 60 \text{ kV/cm}$, (c) $F = 80 \text{ kV/cm}$.

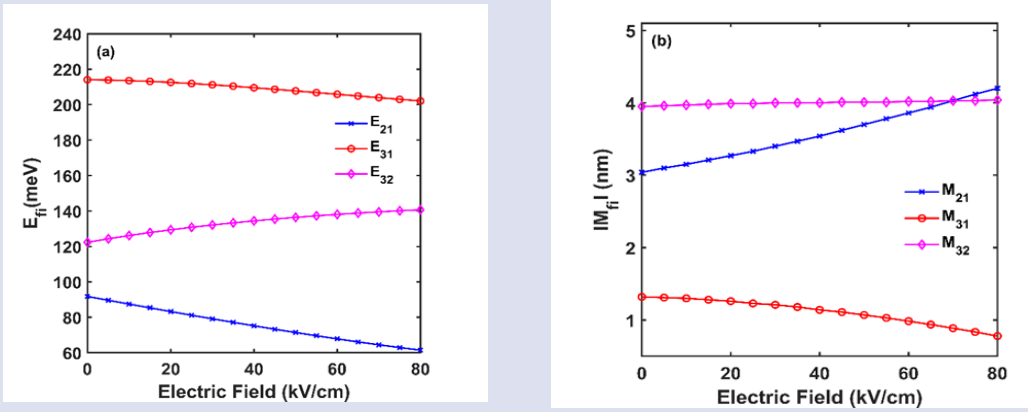


Figure 3. Transition energies and corresponding DMMEs.

In this part of the study, I have studied the effect of varying EF on absorption coefficients. In Figure 4 a-d, absorption coefficients for different EF intensities (0, 40, 60, and 80 kV/cm) and maximum values for each EF intensities are given. I have seen that the absorption coefficient of E_{21} and E_{31} transitions are factors approximately 38 and 3 lower than E_{32} when EF intensity is zero (Figure 4 a). When the EF is applied (Figure 4 a-d), the absorption coefficient of E_{21} is not changing over varying EF intensities. In total, E_{32} has shown an increasing trend while E_{31} is in a decreasing trend over EF change. This means quadruple QW structure absorbs/emits more photons under applied EF and

decreases in E_{31} is an indicator of lower heat in the structure due to less absorption/emission. At the same time, the absorption coefficient of E_{21} transition is independent of the EF intensity as given in Figure 4d. This indicates that there is a constant heating effect owing to the phonon vibrations, which is independent of the increased EF and is the desired behavior for device applications. In addition, in Figure 4-d, the y-axis where the "peak of absorption coefficient" values are given is in the range of 0-9000 cm^{-1} . Since the change of E21 is approximately in the range of 180-220 cm^{-1} , small differences in the change on this scale cannot be seen very clearly.

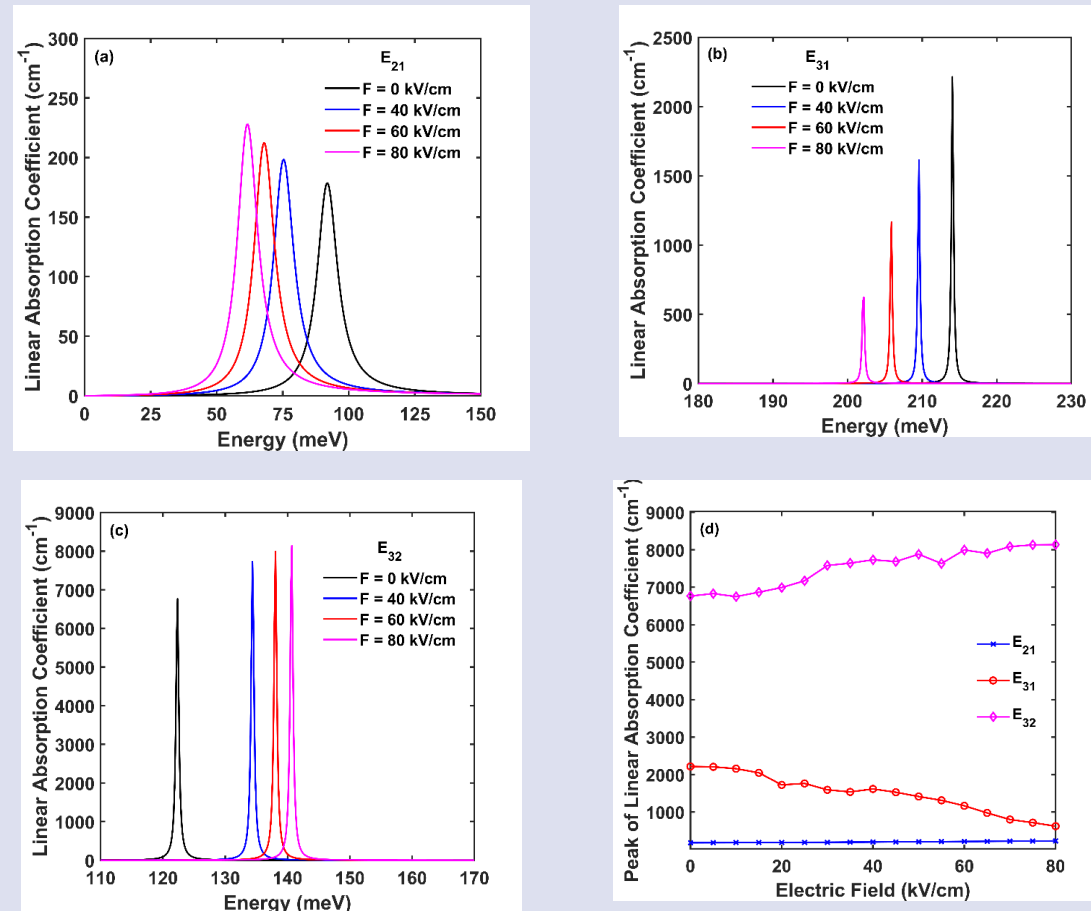


Figure 4. Absorption coefficients for F=0, F=40, F=60 and F=80 kV/cm of a) E_{21} , b) E_{31} , c) E_{32} transitions and d) maxima of absorption coefficients versus EF intensity.

In this section of the study, I have analyzed the effect of the varying EF on refractive index change. In Figure 5 a-d, refractive index change for different EF intensities (0, 40, 60, and 80 kV/cm) and maximum values for each change dependent on the EF intensities are given in Figure 5 d. The change in refractive index is inversely proportional to the EF intensity. Therefore, as seen in Figure 5 b, with the increase in EF intensity, the refractive index decreased due to dipole moments. I have observed that the linear refractive index change of E_{32} is

independent of EF intensity. This is especially crucial for laser applications otherwise change in refractive index can cause a problem with waveguide and cladding layers. However, there is an incremental change in the refractive index of E_{21} , we attribute this to a decrease in transition energies and dipole matrix moment as shown in Figure 3. In addition, there is an incremental increase in refractive index change of E_{12} , this is also related to the barely increasing dipole matrix moment of E_{12} with increasing EF intensity.

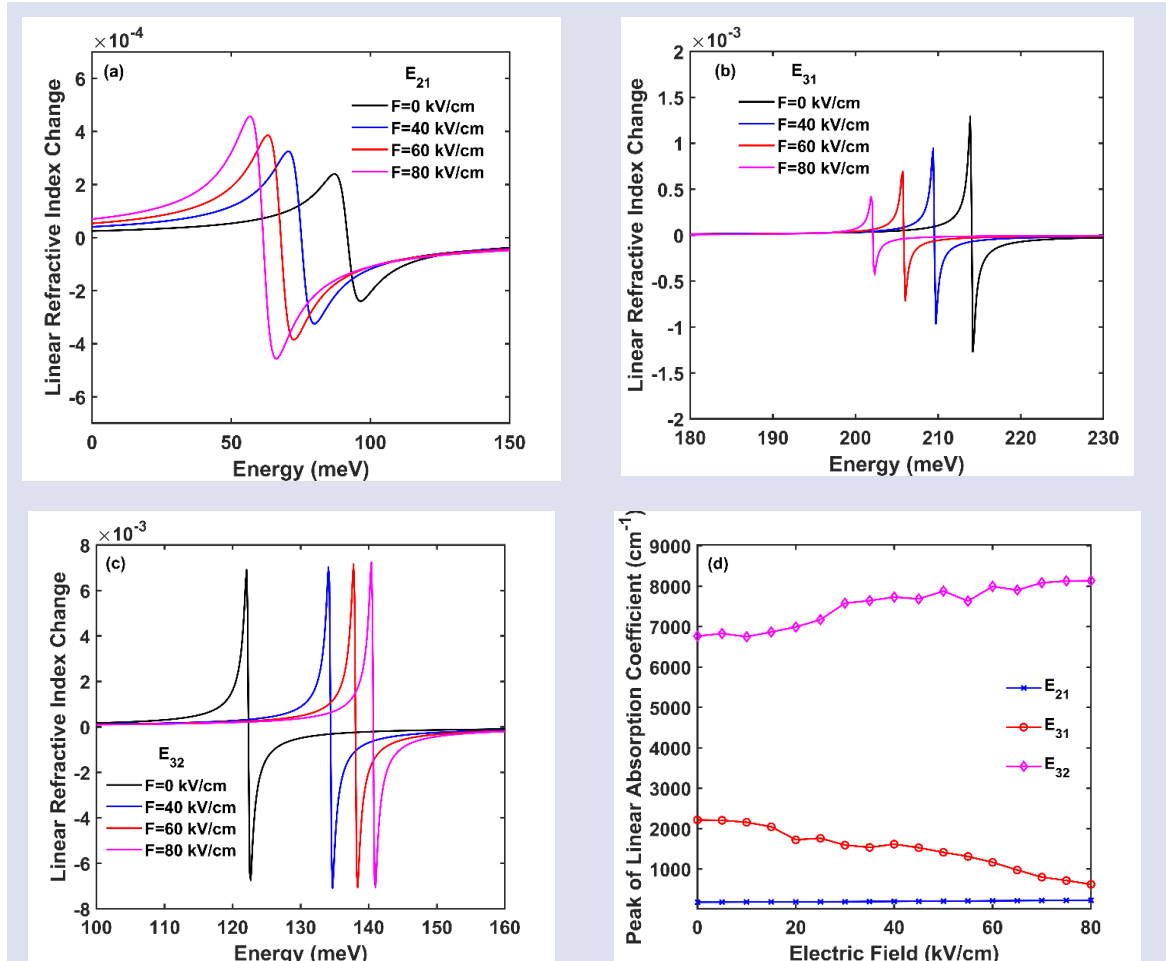


Figure 5. Linear refractive index change for F=0, F=40, F=60, and F=80 kV/cm of a) E_{21} , b) E_{31} , c) E_{32} transitions, and d) maxima of linear refractive index change versus EF intensity.

Conclusion

In the present article, I have summarized the results as follows. I have designed a quadruple QW structure to be used in long infrared devices, which emit/absorb under varying EF. To do this I have solved the Schrödinger equation using the finite element method under effective mass approximation. I have seen that long infrared emission/absorption can be obtained via E_{32} transition, which is between 120 – 140 meV. The transition energy is pretty much the same with changing EF intensities. It is observed that the overlap of the second excited state and first excited state is increasing with EF intensity due to increased localization of the second excited state in the

first and second QWs. Another important parameter is the transition energy between the ground state and the first excited state, it is higher than the phonon vibration energy of GaAs. This is crucial for devices, which is operating using intraband transitions such as quantum cascade laser/detector. Linear absorption coefficients corresponding to the E_{21} and E_{31} transitions are factors 10 and 2 lower than E_{32} when EF intensity is zero. However, E_{32} has shown an increasing trend while E_{31} is in a decreasing trend over EF change while E_{21} is constant. This means there is more absorption/emission of photons via E_{32} transition. Lastly, EF intensity has a minor effect on the refractive index change, which is in total desired for semiconductor applications during the device design.

Here I show that in the quadruple QW design, a change in EF intensity does not affect the device operations. Here, I conclude that the results I have obtained show novelty in the literature and are especially important for device designs in long infrared regions.

Conflict of interests

There are no conflicts of interest in this work.

References

- [1] Wang F., Slivken S., Razeghi M., High-Brightness LWIR Quantum Cascade Lasers, *Optics Letters*, 46 (20) (2021) 5193-5196.
- [2] Harrer A., Schwarz B., Schuler S., Reininger P., Wirthmüller A., Detz H., MacFarland D., Zederbauer T., Andrews A. M., Rothermund M., Oppermann H., Schrenk W., Strasser G., 4.3 μm Quantum Cascade Detector in Pixel Configuration, *Optics Express*, 24 (15) (2016) 17041-17049.
- [3] Vitiello M. S., Scalari G., Williams B., De Natale P., Quantum Cascade Lasers: 20 Years of Challenges, *Optics Express*, 23 (4) (2015) 5167-5182.
- [4] Hanna S., Eich D., Mahlein K. M., Fick W., Schirmacher W., Thöt R., Wendler J., Figgemeier H., MCT-Based LWIR and VLWIR 2D Focal Plane Detector Arrays for Low Dark Current Applications at AIM, *Journal of Electronic Materials*, 45 (9) (2016) 4542-4551.
- [5] Alaydin B. O., Ozturk E., Elagoz S., Interband Transitions Dependent on Indium Concentration in Ga_{1-x}In_xAs/GaAs Asymmetric Triple Quantum Wells, *International Journal of Modern Physics B*, 32 (05) (2017) 1850052.
- [6] Hao Q., Zhao X., Tang X., Chen M., The Historical Development of Infrared Photodetection Based on Intraband Transitions, *Materials*, 16 (2023) 1562.
- [7] Jiang M., Xiao H. Y., Peng S. M., Yang G. X., Liu Z. J., Zu X. T., A Comparative Study of Low Energy Radiation Response of AlAs, GaAs and GaAs/AlAs Superlattice and The Damage Effects on Their Electronic Structures, *Scientific Reports*, 8 (1) (2018) 2012.
- [8] Karabulut İ., Atav Ü., Şafak H., Tomak M., Second Harmonic Generation in an Asymmetric Rectangular Quantum Well Under Hydrostatic Pressure, *Physica B: Condensed Matter*, 393 (1) (2007) 133-138.
- [9] Karki H. D., Elagoz S., Baser P., The High Hydrostatic Pressure Effect on Shallow Donor Binding Energies in GaAs-(Ga, Al)As Cylindrical Quantum Well Wires at Selected Temperatures, *Physica B: Condensed Matter*, 406 (11) (2011) 2116-2120.
- [10] Ozturk E., Depending on The Electric and Magnetic Field of The Linear Optical Absorption and Rectification Coefficient in Triple Quantum Well, *Optical and Quantum Electronics*, 49 (8) (2017) 270.
- [11] Alaydin B. O., Effect of High Bandgap AlAs Quantum Barrier on Electronic and Optical Properties of In_{0.70}Ga_{0.30}As/Al_{0.60}In_{0.40}As Superlattice Under Applied Electric Field for Laser and Detector Applications, *International Journal of Modern Physics B*, 35 (02) (2021) 2150027.
- [12] Durmuslar A. S., Billur C. A., Turkoglu A., Ungan F., Optical Properties of a GaAs Quantum Well with a New Type of Hyperbolic Confinement Potential: Effect of Structure Parameters and Intense Laser Field, *Optics Communications*, 499 (2021) 127266.
- [13] Öztürk E., Sökmen İ., Resonant Peaks of The Linear Optical Absorption and Rectification Coefficients in GaAs/GaAlAs Quantum Well: Combined Effects of Intense Laser, Electric and Magnetic Fields, *International Journal of Modern Physics B*, 29 (05) (2015) 1550030.
- [14] Karabulut İ., Laser Field Effect on The Nonlinear Optical Properties of a Square Quantum Well Under the Applied Electric Field, *Applied Surface Science*, 256 (24) (2010) 7570-7574.
- [15] Yıldırım H., Tomak M., Nonlinear Optical Properties of a Pöschl-Teller Quantum Well, *Physical Review B*, 72(11) (2005) 115340.
- [16] Öztürk E., The Effects of Hydrostatic Pressure on The Nonlinear Intersubband Transitions and Refractive Index Changes of Different QW Shapes, *Optics Communications*, 285 (24) (2012) 5223-5228.
- [17] Alaydin B. O., Optical Properties of GaAs/AlxGa1-xAs Superlattice Under E-Field for Quantum Cascade Laser Application, *Gazi University Journal of Science*, 1: (2021) 1.
- [18] Altun D., Ozturk O., Alaydin B.O., Ozturk E., Linear and Nonlinear Optical Properties of a Superlattice with Periodically Increased Well Width Under Electric and Magnetic Fields, *Micro and Nanostructures*, 166 (2022) 207225.
- [19] Alaydin B.O., Altun D., Ozturk O., Ozturk E., High Harmonic Generations Triggered by The Intense Laser Field in GaAs/AlxGa1-xAs Honeycomb Quantum Well Wires, *Materials Today Physics*, 38 (2023) 101232.
- [20] Bai Y., Bandyopadhyay N., Tsao S., Selcuk E., Slivken S., Razeghi M., Highly Temperature Insensitive Quantum Cascade Lasers, *Appl. Phys. Lett.*, 97 (2010) 251104.
- [21] Alaydin B.O., Effect of High Bandgap AlAs Quantum Barrier on Electronic and Optical Properties of In_{0.70}Ga_{0.30}As/Al_{0.60}In_{0.40}As Superlattice Under Applied Electric Field for Laser and Detector Applications, *International Journal of Modern Physics B*, 35 (02) (2021) 2150027.
- [22] Niculescu E. C., Eseauu N., Radu A., Heterointerface Effects on The Nonlinear Optical Rectification in a Laser-Dressed Graded Quantum Well, *Optics Communications*, 294 (2013) 276-282.
- [23] Ghosh P., Mandal A., Sarkar S., Ghosh M., Influence of Position-Dependent Effective Mass on The Nonlinear Optical Properties of Impurity Doped Quantum Dots in Presence of Gaussian White Noise, *Optics Communications*, 367 (2016) 325-334.

Development of Image Processing Based Line Tracking Systems for Automated Guided Vehicles with ANFIS and Fuzzy Logic

Ahmet Gürkan Yüksek ^{1,a,*}, Ahmet Utku Elik ^{1,b}

¹ Computer Engineering, Faculty of Engineering, Sivas Cumhuriyet University, Sivas, Türkiye.

*Corresponding author

Research Article

History

Received: 25/09/2023

Accepted: 22/11/2023

Copyright





©2023 Faculty of Science,
Sivas Cumhuriyet University


ABSTRACT


Automated Guided Vehicles (AGVs) are robotic vehicles with the ability to move using mapping and navigation technologies to perform tasks assigned to them, guided by guides. Using sensor data such as laser scanners, cameras, magnetic stripes or colored stripes, they can sense their environment and move safely according to defined routes. The basic requirement of motion planning is to follow the path and route with minimum error even under different environmental factors. The key factor here is the most successful detection of the guiding structure of a system moving on its route. The proposed system is to equip a mechanical system that can produce very fast outputs and autonomous motion as a result of combining different algorithms with different hardware structures. In the line detection process, the wide perspective image from the camera is designed to be gradually reduced and converted into image information that is more concise but representative of the problem in a narrower perspective. In this way, the desired data can be extracted with faster processing over less information. In this study, the image information is divided into two parts and planned as two different sensors. The fact that the line information was taken from two different regions of the image at a certain distance enabled the detection of not only the presence of the line but also the flow direction. With the fuzzy system, the performance of the system was increased by generating PWM values on two different hardware structures, loading image capture, image processing processes and driving the motors. In order to determine the membership function parameters of the fuzzy system for each input, the ANFIS approach was used on the data set modeling the system. The outputs produced by the ANFIS model were combined into a single fuzzy system with two outputs from the system rules framework and the system was completed. The success of the algorithms was ensured by partitioning the task distribution in the hardware structure. With its structure and success in adapting different technologies together, a system that can be recommended for similar problems has been developed.

Keywords: Automated guided vehicles, Line following, Image processing, Fuzzy logic systems, ANFIS.

 aguyuksekc@cumhuriyet.edu.tr

 <https://orcid.org/0000-0001-7709-6360>

 auelik@cumhuriyet.edu.tr

 <https://orcid.org/0009-0009-0298-9944>

Introduction

Science and technology are sets of values that model human life and define its standards on an incredible scale with the changes they continually bring about. In the world's scientific development adventure, there are such processes encountered as technological leaps that tend to radically change the way of life, habits and order. Intelligent Autonomous Systems (AOS) are among the most prominent of these leaps that have the potential to trigger these trends [1]. AOSs based on artificial intelligence are defined as having the ability to make decisions and perform tasks independently by adapting to changing environmental conditions. While performing many tasks, classical systems are handed over to AOSs that have the ability to make decisions on their own, can take situations according to changing environmental conditions, develop the ability to act in accordance with the tasks they undertake, and interact with other environmental systems. They also pave the way for innovative technological revolutions or developments and can perform tasks autonomously without the need for human intervention [2, 3].

AOSs are capable of creating innovative uses in robotics, transportation, logistics, retail, healthcare, manufacturing and many more. In robotics, examples include autonomous robots for tasks such as automated assembly lines, hazardous material handling and exploration in environments unsuitable for humans. In transportation, self-driving cars and autonomous drones have the potential to improve safety, efficiency and convenience. In healthcare, smart systems can help diagnose diseases, perform surgeries and provide personalized treatments [4, 5].

Automated Guided Vehicles (AGVs) are robotic systems used to automatically move loads in a given area or to perform tasks assigned to them under guidance. AGVs usually have the ability to move using mapping and navigation technologies. Using sensor data such as laser scanners, cameras, magnetic strips or colored stripes, they can sense their environment and identify obstacles, corridors and target points. In this way, they can move with safe guides based on set routes [6] and perform a variety of tasks such as moving materials, flowing materials to storage racks or between machines,

managing inventory, or moving medical supplies in a hospital environment [7]. Grand View Research (2017), a market report forecasting the period from 2018 to 2025, focuses on the potential growth opportunities of AGVs, noting that the future growth of AGV systems is driven by the emergence of flexible manufacturing systems, increasing demand for customized AGVs, and the adoption of industrial automation by SMEs [8].

The main consideration in controlling AGVs operating indoors is orientation, which is a combination of positioning, route tracking and wayfinding [6]. Guidance is defined as the ability of the AGV to choose its route and decide on the start-finish path, and aims to find the shortest feasible route and follow the correct path to the destination. The AGV moves with the presence of navigators to guide it along its defined route. Wan. et al. summarized smart factories as a model in which production efficiency is increased through the use of digital technologies in production processes, production processes are automated, and data collection and analysis concepts are included in the processes.[9]. Smart factories use AGVs to transport materials or equipment, increasing productivity and reducing the cost of material handling. Navigation systems applied in AGV technology are usually fixed path and free range type [9]. Typically, in such structures, paths exist as physical guides on the ground and positioning is guided by sensors that detect the guide. These predefined paths are marked on the ground using marking methods such as ground painting, magnetic striping, etc., or buried in the ground using a wire. The AGV does not actually know its position in the territory map, it just stays on the path. Mobile robot guidance

based on landmarks is widely practiced worldwide and is an important sense-making for a mobile robot capable of navigating on a predefined path or towards a designated destination using a line, landmark or mark as a reference point.[10]. The focus of the present study is on the line following guide task, which is realized by using an imaging system (camera), interpreting the instantaneous images (image processing) by an expert system (fuzzy system) and completing the task.

The AGV is the main component of the structure in which it operates, for example a flexible production line, and it performs its task by moving in structures that are considered intelligent, without any human intervention other than planning. It picks up a load, an unfinished product, a piece of equipment, etc. from a defined starting point and transports it to a different point for the ongoing stages. AGV systems are available in different structures designed for different tasks [11, 12]. Four main guidance methods are commonly used in AGVs: laser signals, line tracking, magnetic dot or stripe tracking and barcode tracking guidance [13, 14]. In the line tracking method, the scenario is brief; the AGV will follow a pre-loaded path in the work area. The route is determined by drawing lines of different colors on the ground surface, drawing magnetic tape or burying a wire in the ground. The sensor system attached to the robot detects the existing or planned structures on the route and the device follows the path to reach the desired destination. Table I shows a comparison of these methods in terms of installation cost, ease of installation, complexity, flexibility, ability to deviate from the route, efficiency and ease of expansion for the system. [15].

Table I – Comparison of guidance systems.

Guidance System	Laser Signals	Line Following	Magnetic Tracking	Barcode Tracking
Installation Cost	Moderate	Low	High	Low
Ease of Installation	Moderate	High	Moderate	High
Complexity	High	Low	Moderate	Low
Flexibility	Low	High	High	High
Ability to Deviate from Path	High	Moderate	Low	Low
Efficiency	High	Moderate	High	Moderate
Ease of System Expansion	Moderate	High	High	Moderate

A project by Ishikawa et al is one of the first similar studies. A camera-mounted AGV is designed for navigation use in an industrial or factory environment

[16]. The AGV is trained to recognize and respond to different possible line shapes captured by the camera and is also equipped with obstacle detection systems in case

of collisions. Due to hardware limitations and algorithm complexity, there are significant drawbacks for such vehicles that need to operate in real time. Processing time is the most important factor for systems such as AGVs that perform their tasks in real time, and there is a very important link between the compatibility and speed of the system components. In short, the most prominent output of the hardware and software structure that make up the system is the speed, performance and compatibility of producing results together. The basic steering circuitry of a line following AGV is generally not very complex and has light computing processes. However, by selecting the appropriate sensor combinations, it should be developed with a very high efficiency line following system that can distinguish even small color changes in the sensed environment from the color of the line to be followed.. Shah M., for ROBOCON 2016 (International robotics event), talked about the process of designing a robot line following system and explained how he designed the most optimized, efficient and high performance line following system to overcome similar problems [17]. Vo Nhu Thanh presented the development of a restaurant service robot using dual line sensors in combination with a PID control approach for a system aiming at a stable speed result. They focused on hardware, software and mathematical calculations for multidimensional line tracking. They provided a comparison of the existing shortcomings over the system they developed and provided a reference for future studies. [18].

In the proposed study, a method that uses a combination of image processing, artificial intelligence and fuzzy logic technologies for guidance tracking is proposed. The PWM values of the motors that steer the AGV are generated by the fuzzy system. The input parameters of the fuzzy system are obtained instantaneously by image processing, divided into ROI fields and presented to the system as sensor data. The parameters (membership functions) of the fuzzy system are trained by ANFIS over the data set in which the routing pattern of the system is defined. The requirements of the overall system are designed to produce high performance considering the real-time operation of the AGV system. The images taken by the camera include steps such as detecting the line, extracting information about the line and generating commands for the AGV to follow the line. A fuzzy logic control system is developed to control the position and movement of the AGV on the line and evaluates various input data to determine where it is on the line and how fast it should move, and generates the appropriate outputs PWM outputs. ANFIS is trained on the dataset to determine the fuzzy logic parameters that will produce the most optimal outputs.

Material and Methods

The basic requirement of motion planning in AVG or mobile robot systems is to proceed with minimum error in path planning and route following even under different environmental factors. The key factor here is the most

successful detection of the structure that is the guide of a system moving on its route. The main problem encountered in sensing with optical or magnetic sensors is that the signals they send are reflected according to the properties of the surfaces they hit and the system works according to different situations in this reflection. For example, infrared sensors have operating principles such as Planck's law of radiation, Stephan Boltzmann's law and Wein's displacement law because they reflect part of the light incident on a colored surface. In the case of a white surface, the light is completely reflected. But if light falls on a black surface, it is completely absorbed due to the absorption of the black color. This principle is used in the design of infrared sensors. When light falls on normal or regular surfaces it bounces back to the photodiode, whereas when it falls on a black object it is absorbed; therefore, no light ray is captured by the photodiode. Difficulties in accurately detecting reflected signals with different tones or distortions, or in instantaneously determining differences in threshold values according to ambient variations, are important factors in the success of such systems. However, the most obvious advantages of these systems are their simple structure, response generation and data transmission speed. In recent years, technological and theoretical advances have offered many advantages to system developers, especially the powerful computing capacities and low cost of small-sized computers with very fast data processing capabilities. These benefits have enabled more computationally intensive algorithms to be used at low cost in systems that require fast response times. In the positioning process, an AGV is evaluated on its ability to use the image information it receives from the camera, to make intelligent decisions, to quickly evaluate situations and to see in real time.

Image processing is the combination of different methods to obtain the desired information with algorithms to be used to solve the problem determined on real-world images transferred to digital media. Image processing is also used to process the visual data taken with cameras and to produce outputs that will make decisions based on these data in a digital environment. Environment detection is an identification technology that helps a robot understand its environment. When combined with the image processing method, firstly, using a camera with a digital image capture element, the surrounding images are processed using image processing algorithms and the environment is tried to be perceived. In this way, robots can perceive their surroundings and adjust their movements accordingly. The important distinction here is that AGV or robot systems are equipped with algorithms capable of detecting image information and processing it to produce target output. In order to specialize the systems in line following processes, it may be preferable to develop the expert systems approach using fuzzy logic methods and to use this combination as the eyes of the systems in order to obtain fast results [19-20].

Fuzzy logic is a theory developed for solving problems involving uncertainty [21] and focuses on the possibility of a quantity taking values within a range, rather than on the possibility of a quantity taking exact values. Fuzzy logic is also used in expert systems. Expert systems can be used in decision-making processes using methods such as fuzzy logic.

Image Processing Basics:

An image is represented by its dimensions (height and width) based on the number of pixels. This pixel is a point on the image that receives a certain shade, opacity or color. Usually an image is represented in one of the following forms: Grayscale (a pixel is an integer with a value between 0 and 255, where 0 is all black and 255 is all white), RGB (a pixel consists of 3 integers between 0 and 255, the integers represent the intensity of red, green and blue), RGBA (an extension of RGB with an additional alpha field representing the opacity of the image).

Image processing is the process of converting an image into a digital form and performing certain operations to extract some useful information from it. The image processing system usually treats all images as 2D signals while applying certain predetermined signal processing methods [22]. There are five main types of image processing:

Visualization - Finding objects that are not visible in the image

- Recognition - Distinguish or detect objects in the image
- Sharpen and restore - Create an enhanced image from the original image
- Pattern recognition - Measuring various patterns around objects in an image
- Import - Browse and search for images from a large database of digital images that resemble the original image.

Processing steps can be listed as follows:

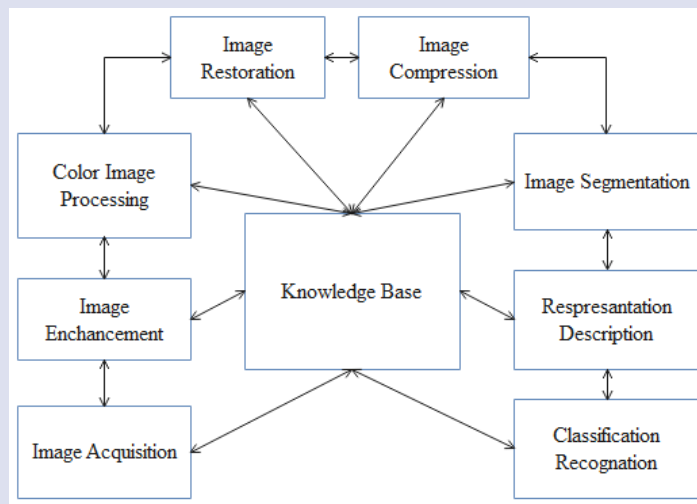


Figure 1. Image processing steps.

These steps represent a basic image processing process. However, different steps and techniques can be used depending on the application.

Fuzzy Logic(FL)

Fuzzy Logic based on multivariate logic, probability theory, genetic algorithms and artificial neural networks, it introduces the concept that deals with the degree to which events occur rather than the probability of occurrence Prof. Zadeh describes FL as "a technique close to a human with a high mechanical IQ". The initial idea of FL started with "everything is a problem of gradation" proposed by logicians in the 1920s. Jan Lukasiewicz, who worked extensively on logic in the 1920s, worked on principles showing that propositions can take fractional values between the binary values 1 and 0. In the light of this work, Lotfi A. Zadeh of the University of California published his seminal paper "Fuzzy Sets". Lotfi A. Zadeh developed an arithmetic for fuzzy sets by applying

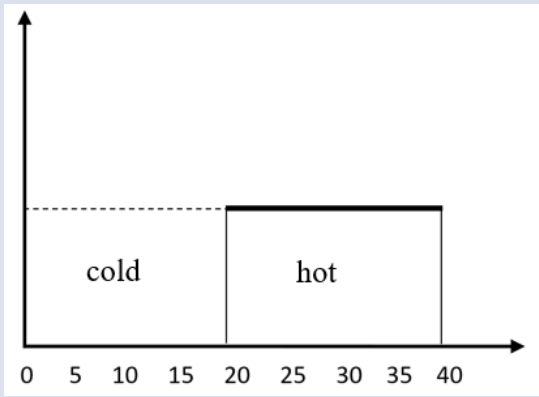
Lukasiewicz's logic improvements to all elements of a set [23]. The basic logic here is about the degree to which events occur rather than their probability. Probability and fuzziness, which seem to be close concepts, are actually quite different concepts. Probability measures the likelihood of an event occurring, while fuzziness measures the extent to which an event will occur, the extent to which a condition will exist.

Fuzzy logic, in essence, enables the realization of processes identical to human thought and helps to explain or assist in modeling uncertain and imprecise events that are frequently encountered in the real world. In classical logic, any proposition is "true" or "false". However, when modeling events in the real world, it is necessary to determine to what extent it is true or false. The fuzzy set approach performs graded data modeling by using linguistic structures such as a little, little, medium, low, low, much, more, many. Thus, it enables the production of results that are closer to natural, realistic and expressive in modeling events.

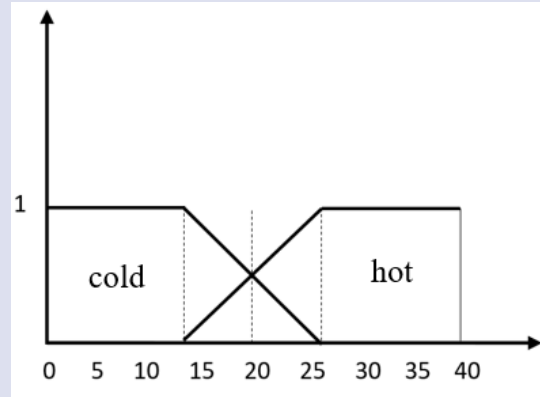
In classical binary logic, an object (element) either belongs (is a member) or does not belong (0 or 1) to a set, and such sets are called crisp. FL, on the other hand, creates a more convenient approach to logic that matches real-world data (everyday expressions) by representing the binary concepts that sharp logic restricts to precise concepts with softer determinants such as less short/less long, slightly slower/slightly slower or faster [24]. More precisely, a classical (sharp) set determines the relation of an element to itself by assigning 0 or 1 values to its elements.

In classical set theory, a set determines the relation of an element to itself by assigning a value of 1 or 0 to the

element to which it belongs. In other words, if the element takes the value 1, it belongs, and if it takes the value 0, it does not belong. As can be seen in Figure 2a, a temperature of 20 degrees is considered "hot", whereas according to binary logic and the classical set, a temperature of 19.5 degrees is considered cold. It is obvious that the boundaries of this approach are strict and lack flexibility, and it is also obvious that many real-world problems are difficult to model with this structure due to the lack of such strict boundaries.



(a)

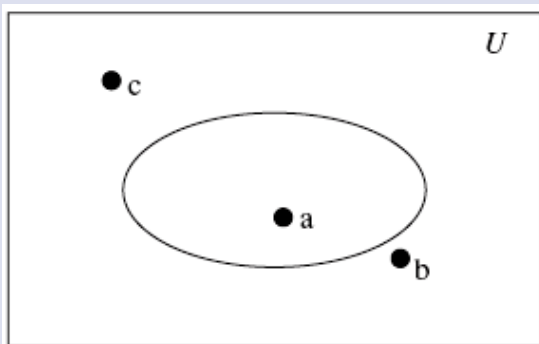


(b)

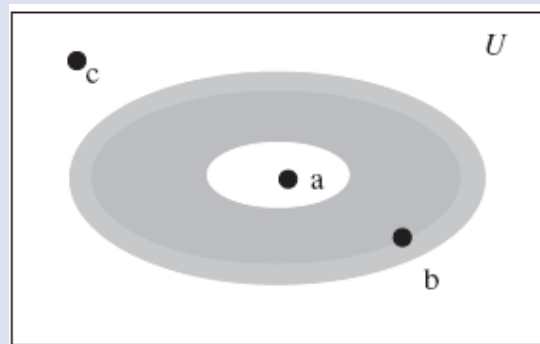
Figure 2.(a) Classical set theory, (b) Fuzzy set theory.

Classical set theory was developed by the German mathematician George CANTOR (1845-1918). In this theory, an element is either an element of the set in question or it is not (Figure 3-a). There can never be partial membership. If the membership value of the element is 1,

it is a full element of the set, and if it is 0, it is not an element. In other words, in classical sets, the membership values of the elements are {0,1}.



(a)



(b)

Figure 3.(a) Classical set boundaries, (b) Fuzzy set boundaries.

A classical set can be expressed as $A = \{x \in U \mid p(x)\}$. Here A is the classical set, P is the property of the set and U is the space to which this set belongs. The characteristic function, $\mu_A(x):U \rightarrow \{0,1\}$, is defined as '1' if x is an element of this set and '0' if it is not. In fuzzy set theory, the characteristic function, known as the membership function, represents a more generalized structure. Figure 3-b shows the expression of a fuzzy set with a venn

diagram. Here the element 'a' is the definite element of the fuzzy set. The membership degree of this element is expressed as 1. If element 'c' does not belong to the fuzzy set, its membership degree is considered as 0. The element 'b' is a member of the fuzzy set at a certain degree (level). This membership is expressed by a membership degree in the range [0,1]. The degree of membership function is important.

ANFIS-Adaptive Network-Based Fuzzy Inference System Theory and Calculation

ANFIS, It is a hybrid approach that combines the ability to learn and parallel computation, which are the most basic features of Artificial Neural Network (ANN) theories, with the ability of Fuzzy Logic (FL) models to infer inexact structures. Developed by Jang [25], this theory has been widely used in problems in different disciplines such as classification, grouping, control and time series analysis, and in particular in modeling nonlinear functions, prediction of chaotic time series [26]. In order to model the pattern hidden in the data, it uses the expert insights and experience of the UN and the learning capabilities of the ANN. Successfully models functional structures that can be expressed in different forms and converges to the functions of the structures at acceptable rates [27, 28]. The training process of ANFIS, one of the machine learning approaches, depends on the ability of the data set to represent the problem (all inputs and outputs). It learns system behavior from a data set of real measurements and is a more flexible computational tool than conventional statistical methods, especially for nonlinear functions [29]. One of the most obvious disadvantages of ANNs, which derive their power from their ability to learn, is that the learning results are presented with very large parameter sets, which makes it difficult to express the results in words. The basis of the UN is that it mimics the thinking structure of the human brain, as in natural languages. As it is known, it cannot learn the rules by itself, as a result, it needs guidance from experts. At this point, the neural fuzzy logic approach comes into play. The neural fuzzy logic approach offers the idea of combining ANN learning processes with the views of a BM expert system.

In the theoretical background of this idea, BM controllers are introduced into the system with two different adaptations: structural and variable tuning. Structural tuning consists of setting up the BM rule structures such as the number of variables to be present in the system, the number of rules and the separation of the definition spaces of each input-output parameter. The determination of the rule structure that fits the requirements must be accompanied by the determination of the controller parameters. In the variable/parameter setting part, the centers, widths and slopes of the membership functions and the weights of the BM rules are calculated [30].

The development of autonomous systems or object detection based systems based on environment analysis with camera images is the basis of many academic and theoretical studies. [31-34]. Camera images provide comprehensive visual information about the position, shape, size, color and motion of objects or environments. In particular, using this information, an automated system or artificial intelligence model can successfully analyze the environment. This detailed information can enable detailed analysis of environments and create a more comprehensive perception feedback. The real-time nature of camera images is almost the most fundamental factor in applications that require fast response. In recent years, thanks to advances in deep learning and artificial intelligence technologies, systems have been trained with large amounts of image data from camera images and more qualified identification capabilities have been developed. In the light of all these explanations, it is an accepted fact that environment detection of the autonomous line-following system, which is the subject of this study, using a camera is an appropriate method[35]. The camera can flexibly detect and process color, shape and location information of real objects in the environment in harmony with the environment. The real-time nature of the images allows the system to react quickly to instantaneous changes and information. The flow given in Figure 4-a is a visualization that briefly summarizes the theoretical structure, data flow and processing processes of the proposed work. The hardware architecture of the system is shown in Figure 4-b. The system input information is obtained by taking camera images with an SCB (Single Board Computer) that performs image processing processes on the Linux operating system. These data, which are generated as numerical values, are transferred to another SCB, which is also responsible for the movement of the motors, via the I2C [36] communication protocol. Fuzzy analysis algorithms are also operated on this second SCB to control the system operation by generating coefficients for the PWM signals required for the version control of the motors.

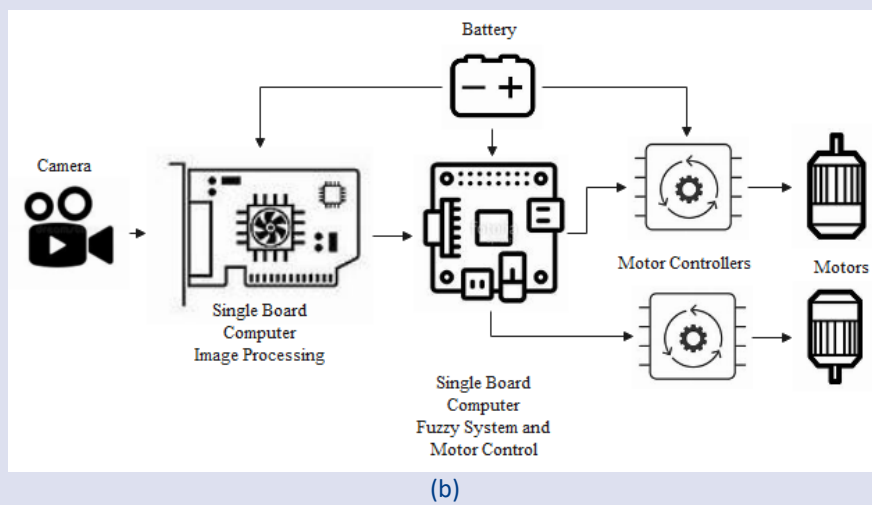
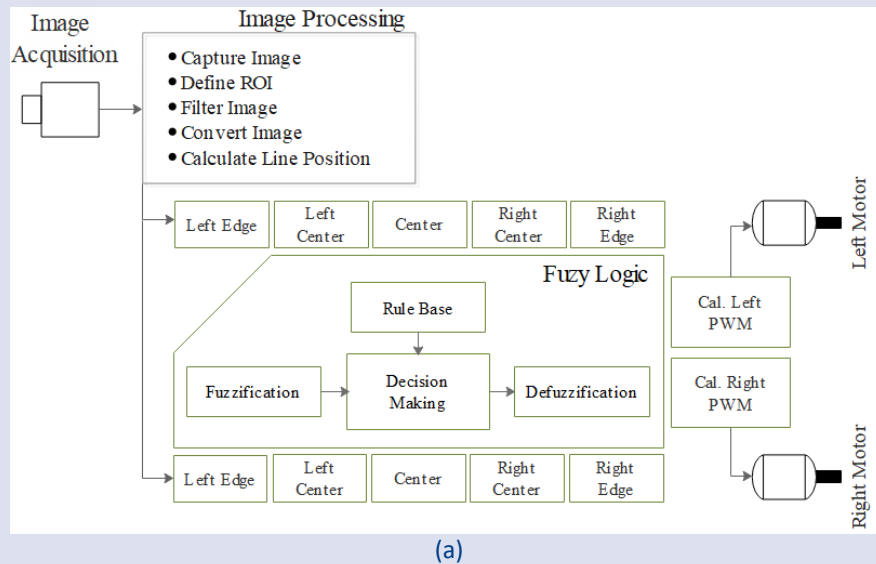


Figure 4.(a) General architecture of the system, (b) Hardware implementation of system.

The line following model of the AGV will consist of two basic steps. In the first step, the presence and position of the line with the camera image will be determined by image processing steps. In the second step, the line information will be processed by the expert system to manage the motor systems that control the vehicle's orientation Figure 4.

The key factor in the proposed system is to acquire, process and quickly transfer the image selected as a guide for route tracking to the system in a semantic way. Real-time image processing is the process of perceiving and organizing digital images with a limited and fast time constraint. It is often used in applications that require fast and accurate responses, such as digital cameras, machine vision, surveillance and biomedical imaging. Some of the key factors of real-time image processing are: computational complexity, frame processing speed, real-time hardware implementation and real-time software optimizations. These factors affect the quality and reliability of real-time image processing applications, as well as the trade-off between speed and accuracy.

Images taken at 320x240 pixel resolution from the camera placed on the front of the AGV system at a distance of approximately 20 cm from the ground and at an angle of 15° forward are divided into areas of interest as shown in Figure 5. Here, no processing is performed on the image parts corresponding to Out of Interest (OoI) areas. In this way, image processing time is significantly reduced. By detecting the presence and position of the line on the image information in the parts determined as Region of Interest (RoI), input data will be generated for the algorithms of the model that will guide the AGV system as it moves forward.

[OoI : Out of Interest , The image detected by the camera is divided into four segments horizontally (Figure 5), two of these segments are not included in the calculations and processing, this approach reduces the number of data to be processed. RoI : Region Of Interest is the image range corresponding to the segments detected and separated by the camera and all processes are performed from the data in this range].

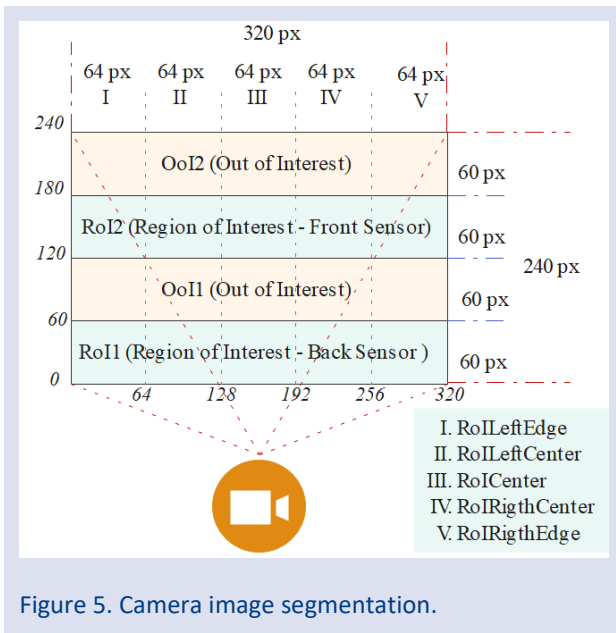


Figure 5. Camera image segmentation.

For the prototype vehicle used in the modeling of the system, the segmentation in the camera field of view is at the pixel ratios given in Figure 5. These ratios can be updated according to different designs or situations, and since the system will be dynamically configured, it is capable of responding to such update situations (from this part of the study onwards, the system will be analyzed with reference to these ratios in the explanations about the structure). The flow given in Table 2 describes how the line image will be used to generate data to be used for training expert systems.

Table 2 – Determining line input value

```

Capture camera image
Ool ( Out of Interest) extract parts from the image information
{ Ool_1 [60 pix-120 pix, 0 pix -320 pix] range
  Ool_2 [180 pix-240 pix, 0-320 pix] range }

RoI ( Region of Interest) take the parts from image information
{ Front Sensor -> RoI_1 [120-180 pix, 0-320 pix]
  Back Sensor -> RoI_2 [0-60 pix, 0-320 pix]
} define as

For Each RoI
{ Image processing, filtering
  Detect line, center_point =(First pixel + last pixel)/2
  send the point value to the expert system
}
    
```

RoI fields are actually sensors where the input values for the Fuzzy System are generated, and the system continuously scans these fields to generate the input values of the system that will control the AGV movement Figure 6.

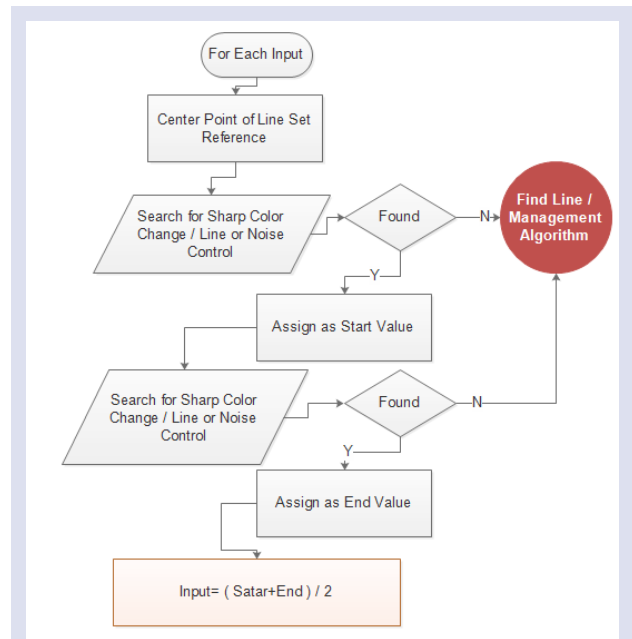


Figure 6. Determining the values of sensor1 and sensor2 variables.

With the algorithm given in Table 2, the pixel values of the approximate midpoint of the line corresponding to the RoIs are obtained. These values constitute the definition ranges of the Fuzzy Logic system as defined in Table 3.

Table 3- Input values expert system definition ranges

LeftEdge	LeftCenter	Center	RightCenter	RightEdge
0-64	64-128	128-192	192-256	256-320

In summary, the steps to be followed when developing a Fuzzy System are: creating linguistic variables, creating membership functions and creating a rule base. The system input of the line tracking algorithm is the flow of the camera image, which is two-dimensional in the non-linear RGB color space. According to the pixel values of the position of the lines perceived by the system's eye on the image, the linguistic variables for input were represented by 5 different values as "LeftEdge, LeftCenter, Center, RighthCenter, RighthEdge" and their ranges were determined as given in Table 3 . Likewise, the output linguistic expressions of the PWM values that will determine the movement rates of the right and left motors were determined with 3 different expressions as "Back1 (-1) , Constant (0), Forward1 (+1) " and the coefficient values were determined as shown in Table 4.

Table 4- Output values fuzzy definition ranges

Back1 Vel.	Constant	Forward1 Vel.
-1	0	1

Summary study of the model; The image taken as 320x240 pixels instantaneously in Figure 7 will be divided into areas of interest and subjected to image processing processes as shown in the flow given in Table 2 and Figure 6. In the developed system, the image taken at the determined resolution ratios is divided into 5 columns of 5x64 pixels and 4 rows of 4x60 pixels. The images in the 1st and 3rd rows of these rows will constitute the source for the data input of the system. RoI1 targets the pixel range (0-60 lines) and RoI2 targets the pixel range (120-180 lines). The remaining parts are excluded from the process. The 60 pixel range is chosen because of the line thickness, which should be changed for different resolutions and structures, or these parameters should be determined dynamically, as in the development of the proposed model.

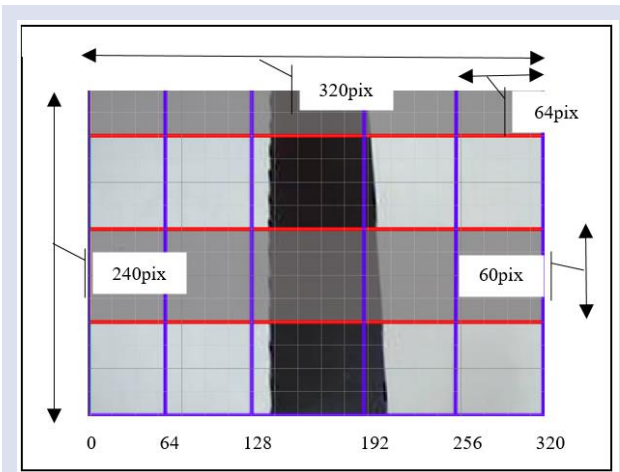


Figure 7. Camera view - identifying areas of interest.

The pixel values obtained by image processing from the snapshot taken with Figure 7 will form the inputs for the control of the Fuzzy System as given in Table 3. Figure 7 illustrates a snapshot of the screen, segmented and represented by a grid. On this sample image, the pixel value at which the line starts and the pixel value at which the line ends are instantaneously determined by the image processing programme as 132 and 200, respectively, and transferred to the relevant part of the system. The method of calculating the midpoint of these values is summarised in Table 5.

Table 5- Sample line position calculation

RoI1	
Star→132. pix.	$= (132+200)/2$
End→ 200. pix.	$= 166$
RoI2	
Start→134. pix.	$= (134+190)/2$
End→ 190. pix.	$= 162$

The width of the line will vary in proportion to the distance of the camera from the image. However, since the midpoint of the line is considered the target value, the line thickness is not a decisive factor. Given the fps (frames per second) of the camera and the speed of the car, the line will be close to its previous position in the next image. During the analysis of the search for the start and end points of the line, the presence of the line is verified by applying intermediate image processing algorithms to prevent possible noise-induced errors. The values generated by the image processing steps will feed the input values of the Fuzzy Control system shown in Figure 8.

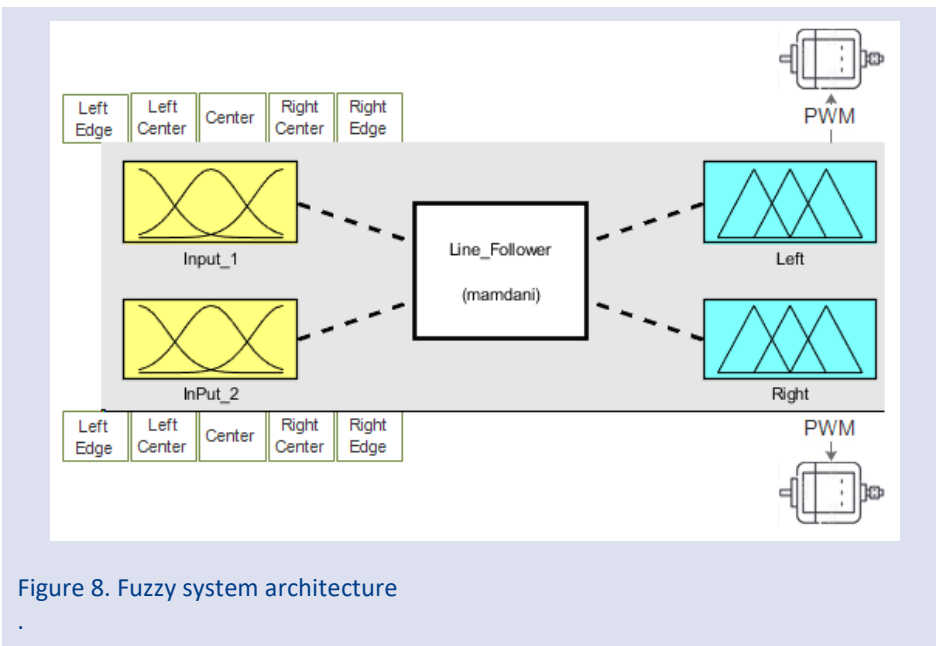


Figure 8. Fuzzy system architecture

The effective factor on the success of the systems using fuzzy logic is to determine the membership functions in a structure that will best model the accuracy and performance of the system. Membership functions indicate the degree to which an input value belongs to a set in fuzzy logic systems and are based on fuzzy set theory. Systems designed with the right membership functions can model the input values more precisely and produce more accurate results. Therefore, it is of great importance to determine the membership functions accurately [23] [37] [38]. In general, the selection of fuzzy membership functions takes into account properties such as suitability to the data, expressiveness, validity, interpretability, ease of computation, adaptability and generalization. However, each problem and application area is different and sometimes the most appropriate membership functions should be determined by trial and error methods or expert opinions. There are different structures of membership functions used in the literature [37]. The determination of the membership functions for each system input was performed using the ANFIS approach over a database containing the pattern of the motion modeling of the system. In this way, a process that requires expert behavior was identified using artificial intelligence, based on a pattern, and an intelligent system was used instead of trial and error or past experience. Sample data of the data set used for training the ANFIS system is shown in Table 6. For different input values, the PWM output parameters to be generated for the motors were determined.

Table 6- Samples data ANFIS model training

Ro11	Ro12	Left Motor	Right Motor
Sensor 1	Sensor 2		
1	1	-1	1
57	57	-1	1
182	182	0	0
185	185	0	0
206	206	0	-1
210	210	0	-1
208	272	0	-1
233	297	0	-1
311	311	1	-1
320	320	1	-1
---	---	---	---

As seen in Figure 9, the fuzzy system is planned as 2 inputs and 2 outputs. The important factor here is to determine the membership functions of the inputs. Each membership function contains a curve representing each point in the specified input section. Depending on the shape of the curve, each membership function is given a

specific name, i.e. triangular, bell-shaped, trapezoidal and Gaussian membership functions. There are different types of membership functions that are commonly used [39] (Table 7).

Table 7. Member ship functions

Membership Type	Description
'gbellmf'	Generalized bell-shaped membership function
'gaussmf'	Gaussian membership function
'gauss2mf'	Gaussian combination membership function
'trimf'	Triangular membership function
'trapmf'	Trapezoidal membership function
'dsigmf'	Difference between two sigmoidal membership functions
'pimf'	Pi-shaped membership function

In order for the ANFIS model to best represent the pattern structure of the data set it is trained on, the membership functions of the input parameters should be selected in a way that reflects the effects of the input data on the model. For this reason, ANFIS models were trained over approximately 64 different combinations by taking all combinations of eight different membership functions to produce the desired results for two inputs, and the membership functions that produce the best output from the models were determined separately for each input. At this stage, statistical measures (Mean Absolute Error (MAE), Root Mean Squared Error (RMSE), Mean Absolute Percentage Error (MAPE), R Squared (R2) [40]) were used to test the outputs produced by the ANFIS model trained using each different combination of membership functions. While these results obtained using the Training, Test and Validation Datasets are analyzed with statistics metrics, here the main criterion for selecting the most successful ANFIS model was the results of the "Test Dataset" and the R Squared (R2) value was used as the basis and values for all datasets used in ANFIS training were generated. ANFIS is an approach designed to produce a single output. However, the proposed system should be designed with two outputs for two different motors. For this reason, the ANFIS model is trained separately for each different output. Table 8 and Figure 9 shows the best value measures produced by the trained models.

Table 8-a Right motor ANFIS model statistical metric values

Inputs	RoI1 Sensor 1		RoI2 Sensor 2	
	Data Set	Training	Test	
MF	gauss2mf		gauss2mf	
MAPE	0.5838	0.5836	0.5067	
MAE	0.0516	0.0523	0.0404	
RMSE	0.1335	0.1374	0.0976	
R ²	0.96	0.97	0.97	

Table 8-b Left motor ANFIS model statistical metric values

Inputs	RoI1 Sensor 1		RoI2 Sensor 2	
	Data Set	Training	Test	
MF	gauss2mf		gauss2mf	
MAPE	0.5512	0.5648	0.5408	
MAE	0.0159	0.0158	0.0207	
RMSE	0.0661	0.0678	0.0737	
R ²	0.9881	0.9873	0.9844	

With ANFIS, the most appropriate membership functions for the inputs were determined as "gauss2mf" based on the statistics value measures. As seen in Figure 8, the Fuzzy system is designed as 2 inputs and 2 outputs. Since the single output structure of ANFIS is not sufficient to model the system, the fuzzy model of the system was designed using the membership functions determined with ANFIS as shown in Figure 8.

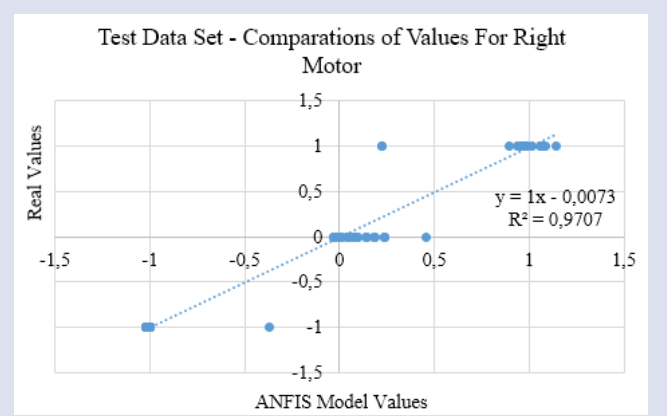


Figure 9 (a). Right motor ANFIS model comparisons of test data set values.

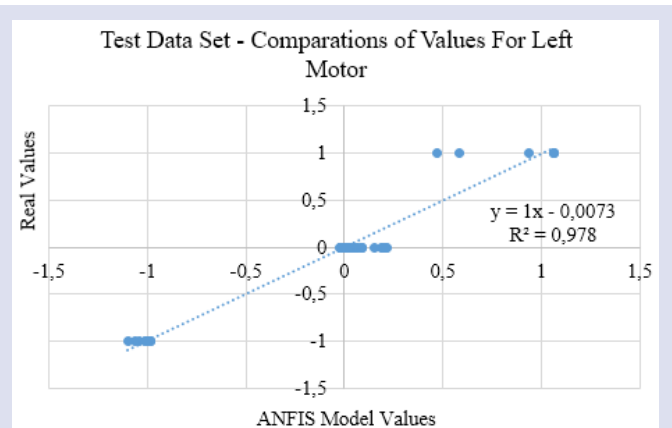
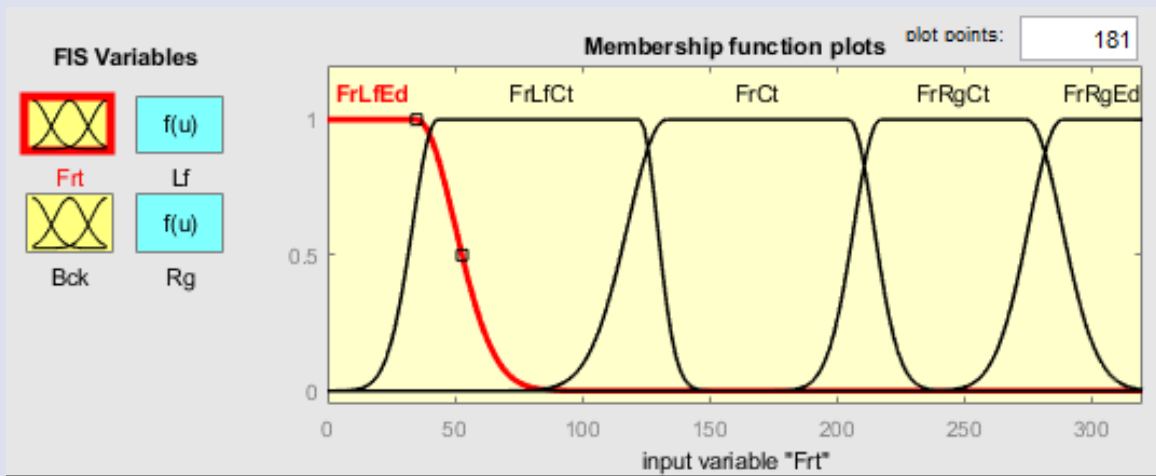


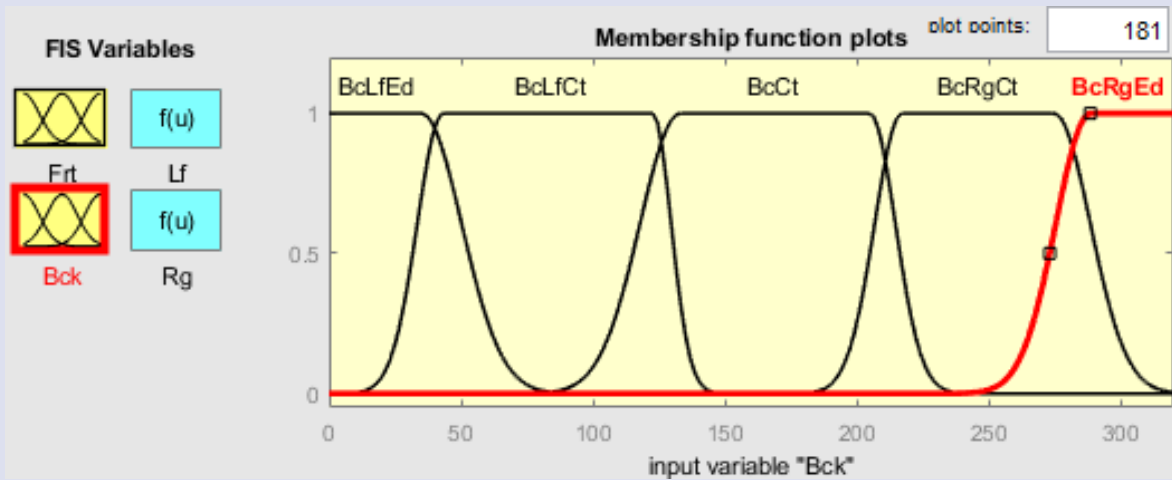
Figure 9 (b). Left motor ANFIS model comparisons of test data set values.

With the step of determining the membership functions using ANFIS, a structure to determine the right and left motor PWM coefficient values with two different models was created. By combining the parameters of these two different models in a fuzzy system, the system that will manage the motion system subject to the study has been created. In the fuzzy system, the truth table given in Table 9 was used to define the rules for the right and left motors to be controlled by the inputs defined by the membership functions determined by ANFIS. The parametric values of the membership function of this structure are defined as given in Figure 10 for Sensor1 and Sensor2.



[Sensor 1]
 Name='Frt'
 Range=[0 320]
 NumMFs=5
 MF1='FrLfEd':'gauss2mf',[13.6 -22.9 15.2 35.01]
 MF2='FrLfCt':'gauss2mf',[9.76 43.2 7 122.6]
 MF3='FrCt':'gauss2mf',[15.2 133 9.74 204.8]
 MF4='FrRgCt':'gauss2mf',[10.3 217 13.7 274.7]
 MF5='FrRgEd':'gauss2mf',[13.1 288.4 13.6 344]

Figure 10 (a). Fuzzy input for sensor 1.

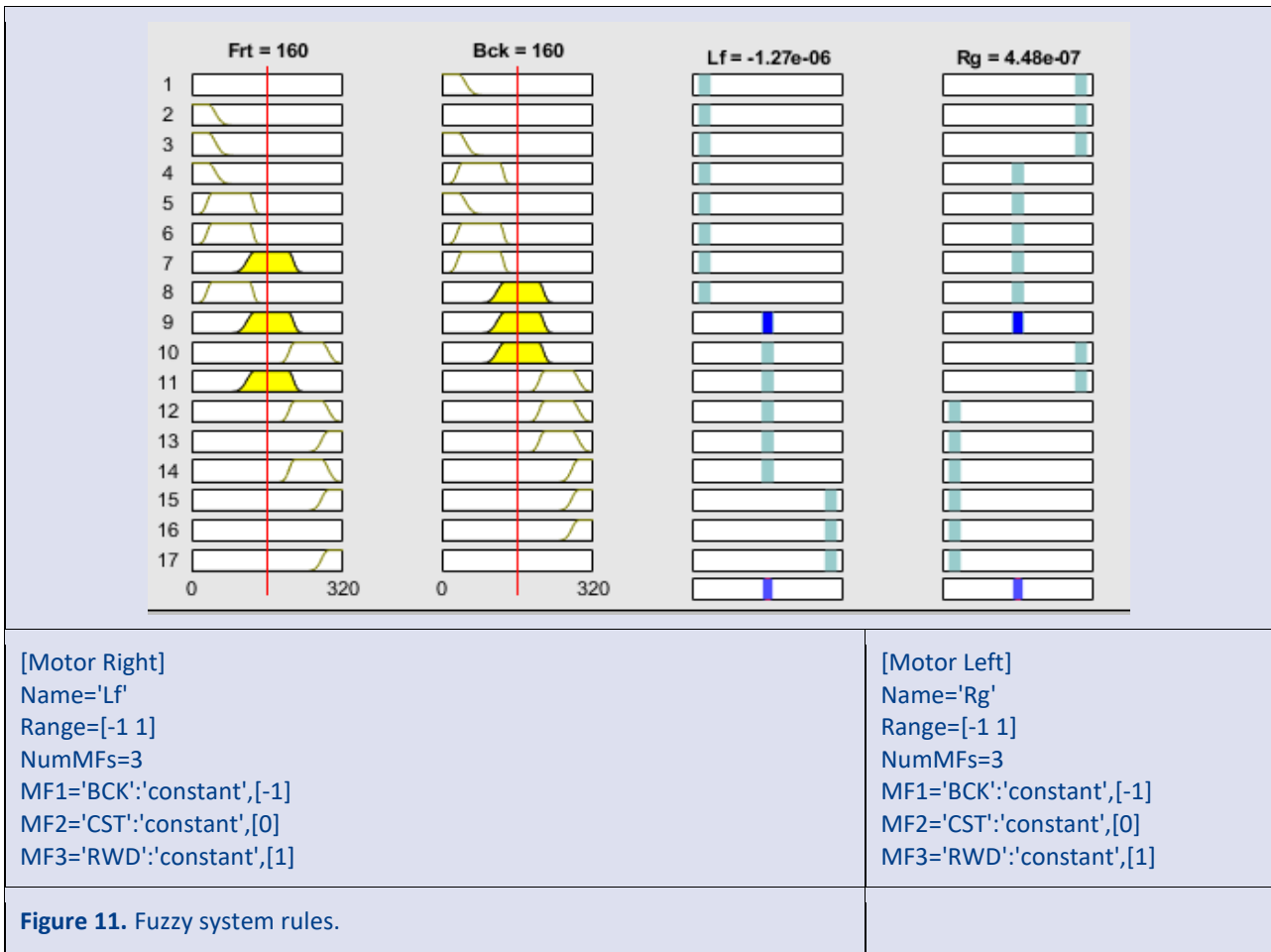


[Sensor 2]
 Name='Bck'
 Range=[0 320]
 NumMFs=5
 MF1='BcLfEd':'gauss2mf',[13.55 -22.93 15.25 26.59]
 MF2='BcLfCt':'gauss2mf',[9.691 59.55 13.82 104.8]
 MF3='BcCt':'gauss2mf',[15.11 136 4.178 181.5]
 MF4='BcRgCt':'gauss2mf',[10.91 216.4 13.69 264.4]
 MF5='BcRgEd':'gauss2mf',[13.95 295.7 13.55 343.9]

Figure 10 (b). Fuzzy input for sensor 2.

The type of membership functions and parametric settings of the membership functions were determined by training the ANFIS model. The fuzzy rules to control the motor directions with the line information (midpoint pixel

values) received from the camera were developed with the verification values given in Table 6 and Figure 11 shows the structure of the defined rules.



The comparison of the actual values produced by the developed system according to the values it receives from the inputs can be examined in Table 9 for some randomly selected values. Here, the numerical comparison of the

values produced by presenting the data used in the training of the system to the Fuzzy System is given. As can be seen from the values, the system produces outputs that are very convergent to the real values.

Table 9 – Actual values - fuzzy system generated values comparison.

RoI1 Sensor 1	RoI2 Sensor 2	Left Motor	Right Motor	Fuzzy System	Fuzzy System
1	1	-1	1	-1	1
57	57	-1	1	-1	0,88
182	182	0	0	0,00617	0,0089
185	185	0	0	0,0058	0,00157
206	206	0	-1	0,00121	-0,87
210	210	0	-1	0,0135	-0,81
208	272	0	-1	0,019	-0,79
233	297	0	-1	0,04	-0,99
311	311	1	-1	0,98	-1
320	320	1	-1	0,98	-1
...		

Discussion

The goal of the designed system is to equip a mechanical system with the ability to produce very fast outputs and autonomous movement as a result of the combination of different algorithms with different hardware structures. Therefore, this system should be able to react quickly and reliably, comply with time constraints, and work in harmony with all its components to minimize latency and meet timing requirements. Unlike similar approaches, the system is designed to gradually reduce the wide perspective image from the camera in the line detection process and convert it into a more concise image information in a narrower perspective, but more concise image information to represent the problem. In this way, the desired data can be extracted with faster processing over less information. In this study, the image information is divided into two parts and planned as two different sensors. However, the system has the dynamism to work with more partitions. The fact that the line information is taken from two different regions of the image at a distance has also added the ability to detect not only the presence of the line but also the flow direction. Similar studies are weaker at this point. The performance of the system was increased by loading the image capture, image processing processes and driving the motors by generating PWM values with the fuzzy system on two different hardware structures. The computational load of the system is designed to provide fast feedbacks by loading the computational load on two different hardware. The time between the acquisition of a snapshot and the conversion of the output of this snapshot into the control commands required for the motors was kept below 0.1 s, ensuring that the planned system is within the acceptance limits.

A library of fuzzy rules was not used on the SBC, and with the logic of directly coding and loading the algorithms needed, performance degrading reasons on the board were also prevented. Thus, efficiency is increased and the average system performance is improved in terms of processing load and computation speed.

When the literature was reviewed, no similar studies were found in which the approaches summarized below, which are parts of the study, were used together.

These sections summarize

Partitioning large amounts of camera information into smaller areas of interest and using these areas as sensor information,

Determining the rules of the fuzzy system that will generate PWM coefficients from this information with ANFIS, an Artificial Intelligence method,

ANFIS is a single output system, in this study ANFIS is designed to be trained separately for both engines (with different output values for each engine with the same data sets),

As a result, the structure of these two ANFIS models is combined into a single fuzzy system with two outputs from the system rules framework.

Partitioning the task distribution in the hardware structure

It can be given. The combination of all these processes suggests an innovative approach to solving problems similar to the literature.

Conclusion

With the membership functions determined by the ANFIS models Table 8-a,b, the Fuzzy system is designed to produce two outputs. During this design, the accuracy or expert data of the input/output values shown in Table 10 were used.

Table 10- State control evaluation for fuzzy rules.

	LeftEdge 0-64	LeftCenter 64-128	Center 128-192	RightEdge 192-256	RightCenter 256-320	Left Motor	Right Motor
Sensor2						-1	+1
Sensor1	1						
Sensor2	1					-1	+1
Sensor1							
Sensor2	1					-1	+1
Sensor1	1						
Sensor2	1					-1	0
Sensor1		1					
Sensor2		1				-1	0
Sensor1	1						
Sensor2		1				-1	0
Sensor1							
Sensor2			1			-1	0
Sensor1			1				
Sensor2			1			-1	0
Sensor1							
Sensor2				1		0	+1
Sensor1				1			
Sensor2				1		0	+1
Sensor1							
Sensor2					1	0	-1
Sensor1					1		
Sensor2					1	0	-1
Sensor1							
Sensor2						+1	-1
Sensor1							
Sensor2						+1	-1
Sensor1							
Sensor2						+1	-1
Sensor1							
Sensor2						+1	-1
Sensor1							

The designs of the Fuzzy System designed within the framework of these rules are given in Figure 10 and Figure 11. Correlation graphs showing the relationship between the data generated by ANFIS and the real data for the whole data set produced by this system are given in Figure 12-a and 12-b for the right motor. Similarly, Figure 13-a and Figure 13-b are given for the left motor.

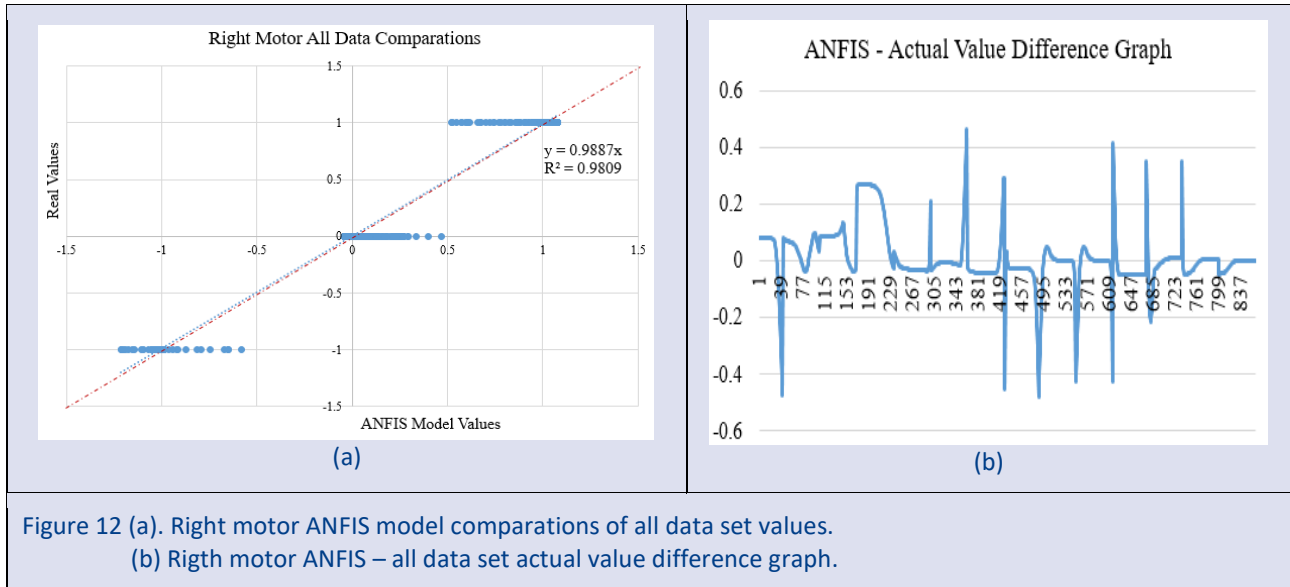


Figure 12 (a). Right motor ANFIS model comparisons of all data set values.
 (b) Right motor ANFIS – all data set actual value difference graph.

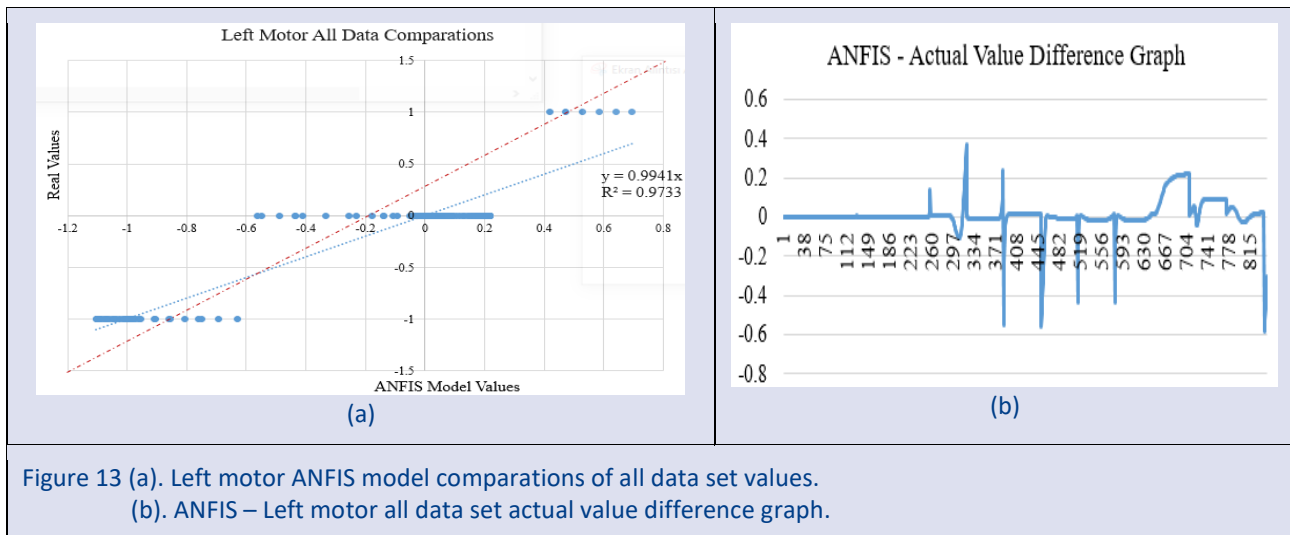


Figure 13 (a). Left motor ANFIS model comparisons of all data set values.
 (b). ANFIS – Left motor all data set actual value difference graph.

In the light of all these values and the behavior of the real autonomous system to which the model was applied, the performance of the system was accepted. Basic image processing steps were followed to keep the speed performance of the system at a higher level. It is envisaged that by using more powerful SCBs and more sensitive image processing processes, systems that are more sensitive to environmental effects can be developed with this approach.

The determination of membership functions, which is the most decisive point of fuzzy systems, was generated from the data set containing the pattern of the system with ANFIS, and thus expert opinion was made by an intelligent system. It provided an important perspective for similar control applications.

In addition, this system can be applied not only to image-based systems but also to similar systems that will follow the line using IR or magnetic information.

Conflict of interests

The authors state that did not have conflict of interests.

References

- [1] Fard N. E., Selmi R. R., Khorasani K., Public Policy Challenges, Regulations, Oversight, Technical, and Ethical Considerations for Autonomous Systems: A Survey, *IEEE Technol. Soc. Mag.*, 42 (1) (2023) 45-53.
- [2] Pratihari D. K., Jain L. C., Ed., Studies in computational intelligence, *Intelligent autonomous systems: foundations and applications*. Berlin: Springer Verlag, 275 (2010).
- [3] Li J., Cheng H., Guo H., Qiu S., Survey on Artificial Intelligence for Vehicles, *Automot. Innov.*, 1 (1) (2018) 2-14
- [4] Veres S. M., Molnar L., Lincoln N. K., Morice C. P., Autonomous vehicle control systems — a review of decision making, *Proc. Inst. Mech. Eng. Part J. Syst. Control Eng.*, 225 (2) (2011) 155-195.

- [5] Ma Y., Wang Z., Yang H., Yang L., Artificial intelligence applications in the development of autonomous vehicles: a survey, *IEEECAA J. Autom. Sin.*, 7 (2020) 315-329.
- [6] Reis W. P. N. D., Couto G. E., Junior O. M., Automated guided vehicles position control: a systematic literature review, *J. Intell. Manuf.*, 34 (4) (2023) 1483-1545.
- [7] Ryck M. D., Versteyhe M., Debrouwere F., Automated guided vehicle systems, state-of-the-art control algorithms and techniques, *J. Manuf. Syst.*, 54 (2020) 152-173.
- [8] Grand View Research, GVR Report cover Automated Guided Vehicle Market Size, Share & Trends Report Automated Guided Vehicle Market Size, Share & Trends Analysis Report By Vehicle Type, By Navigation Technology, By Application, By End-Use Industry, By Component, By Battery Type, By Region, And Segment Forecasts, 2023 - 2030. Available at : <https://www.grandviewresearch.com/industry-analysis/automated-guided-vehicle-agv-market>, Retrieved 2023.
- [9] Wan J., Tang S., Hua Q., Li D., Liu C., Lloret J., Context-Aware Cloud Robotics for Material Handling in Cognitive Industrial Internet of Things, *IEEE Internet Things J.*, 5 (4) (2018). 2272-2281.
- [10] Ismail A. H., Ramli H. R., Ahmad M. H., Marhaban M. H., Vision-based system for line following mobile robot, *2009 IEEE Symposium on Industrial Electronics & Applications*, Kuala Lumpur, Malaysia: IEEE, (2009) 642-645.
- [11] A. VehicleManufacturers, I. Savant Automation, A. Motion, A. Inc., J. Corporation, A. Eckhart and I. Ward Systems, AGV Manufacturers | AGV Suppliers. Available at : <https://www.automaticguidedvehicles.com/>, Retrieved: 2023.
- [12] Fedorko G., Honus S., Salai R., Comparison of the Traditional and Autonomous AGV Systems, *MATEC Web Conf.*, 134 (2017) 13.
- [13] Ilas C., Electronic sensing technologies for autonomous ground vehicles: A review, *2013 8TH International Symposium On Advanced Topics In Electrical Engineering (Atee)*, Bucharest, Romania: IEEE, (2013) 1-6.
- [14] Bostelman R., Hong T., Cheok G., Navigation performance evaluation for automatic guided vehicles, *2015 IEEE International Conference on Technologies for Practical Robot Applications (TePRA)*, Woburn, MA, USA: IEEE, (2015) 1-6.
- [15] Lynch L., Neue T., Clifford J., Coleman J., Walsh J., Toal D., Automated Ground Vehicle (AGV) and Sensor Technologies- A Review, *2018 12th International Conference on Sensing Technology (ICST)*, Limerick: IEEE, (2018) 347-352.
- [16] Ishikawa S., Kuwamoto H., Ozawa S., Visual navigation of an autonomous vehicle using white line recognition, *IEEE Trans. Pattern Anal. Mach. Intell.*, 10 (5) (1988) 743-749.
- [17] Shah M., Rawal V., Dalwadi J., Design Implementation of High-Performance Line Following Robot, *2017 International Conference on Transforming Engineering Education (ICTEE)*, Pune: IEEE, (2017) 1-5.
- [18] Thanh V. N., Vinh D. P., Nghi N. T., Nam L. H., Toan D. L. H., Restaurant Serving Robot with Double Line Sensors Following Approach, *2019 IEEE International Conference on Mechatronics and Automation (ICMA)*, Tianjin, China: IEEE, (2019) 235-239.
- [19] Payne S. C., Awad E. M., The systems analyst as a knowledge engineer: can the transition be successfully made?, *Proceedings of the 1990 ACM SIGBDP conference on Trends and directions in expert systems - SIGBDP '90*, Orlando, Florida, United States: ACM Press, (1990) 155-169.
- [20] La Salle A. J., Medsker L. R., The expert system life cycle: what have we learned from software engineering, *Proceedings of the 1990 ACM SIGBDP conference on Trends and directions in expert systems - SIGBDP '90*, Orlando, Florida, United States: ACM Press, (1990) 17-26.
- [21] Zadeh L. A., Soft computing and fuzzy logic, *IEEE Softw.*, 11 (6) (1994) 48-56.
- [22] Kovasznay L. G., Joseph H., Image Processing, *Proc. IRE*, 43 (5) (1955) 560-570.
- [23] Goguen J. A., Zadeh L. A., Fuzzy sets. Information and control, 8 (1965) 338-353. - Zadeh L. A., Similarity relations and fuzzy orderings. Information sciences, vol. 3 (1971) 177-200., *J. Symb. Log.*, 38 (4) (1973) 656-657.
- [24] Chen G., Pham T. T., Introduction to fuzzy sets, fuzzy logic, and fuzzy control systems. Boca Raton, FL: CRC Press, (2001).
- [25] Jang J.S. R., ANFIS: adaptive-network-based fuzzy inference system, *IEEE Trans. Syst. Man Cybern.*, 23 (3) (1993) 665-685.
- [26] Neuro-fuzzy And Soft Computing: A Computational Approach To Learning And Machine Intelligence [Books in Brief], *IEEE Trans. Neural Netw.*, 8 (5) (1997) 1219-1219.
- [27] Cybenko G., Approximation by superpositions of a sigmoidal function, *Math. Control Signals Syst.*, 2 (4) (1989) 303-314.
- [28] Multilayer feedforward networks are universal approximators - ScienceDirect. Available at : <https://www.sciencedirect.com/science/article/pii/0893608089900208>, Retrieved: (2018)
- [29] Jang J. S. R., Neuro-fuzzy and soft computing; a computational approach to learning and machine intelligence, *Prentice Hall, Upper Saddle River*, CUMINCAD, (1997). Available at : <http://papers.cumincad.org/cgi-bin/works/Show?d036>, Retrieved: (2018)
- [30] Yüksek A. G., Hava Kirliliği Tahmininde Çoklu Regresyon Analizi Ve Yapay Sinir Ağları Yönteminin Karşılaştırılması, Doktora Tez, Cumhuriyet Üniversitesi, Sivas, (2007). Available at: <https://tez.yok.gov.tr/UlusalTezMerkezi/tezSorguSonucYeni.jsp>. Retrieved : (2018).
- [31] Wu X., Li W., Hong D., Tao R., Du Q., Deep Learning for Unmanned Aerial Vehicle-Based Object Detection and Tracking: A survey, *IEEE Geosci. Remote Sens. Mag.*, 10 (1) (2022) 91-124.
- [32] Sahba R., Sahba A., Sahba F., Using a Combination of LiDAR, RADAR, and Image Data for 3D Object Detection in Autonomous Vehicles, *2020 11th IEEE Annual Information Technology, Electronics and Mobile Communication Conference (IEMCON)*, Vancouver, BC, Canada: IEEE, (2020) 0427-0431.
- [33] Pawar P. G., Devendran V., Scene Understanding: A Survey to See the World at a Single Glance, *2019 2nd International Conference on Intelligent Communication and Computational Techniques (ICCT)*, Jaipur, India: IEEE, (2019) 182-186.

- [34] Miles V., Gurr F., Giani S., Camera-Based System for the Automatic Detection of Vehicle Axle Count and Speed Using Convolutional Neural Networks, *Int. J. Intell. Transp. Syst. Res.*, 20 (3) (2022) 778-792.
- [35] Sarwade J., Shetty S., Bhavsar A., Mergu M., Talekar A., Line Following Robot Using Image Processing, *2019 3rd International Conference on Computing Methodologies and Communication (ICCMC)*, Erode, India: IEEE, (2019) 1174-1179.
- [36] Hu Z., I2C Protocol Design for Reusability, *2010 Third International Symposium on Information Processing*, Qingdao, Shandong, China: IEEE, (2010) 83-86.
- [37] Hudec M., Fuzzy Set and Fuzzy Logic Theory in Brief, *Fuzziness in Information Systems*, Cham: Springer International Publishing, (2016) 1-32.
- [38] Dubois D., Prade H., Ed., *Fundamentals of Fuzzy Sets*, The Handbooks of Fuzzy Sets Series, Boston, MA: Springer US, (2000).
- [39] Talpur N., Salleh M. N. M., Hussain K., An investigation of membership functions on performance of ANFIS for solving classification problems, *IOP Conf. Ser. Mater. Sci. Eng.*, (2017) 226.
- [40] González-Sopeña J. M., Pakrashi V., Ghosh B., An overview of performance evaluation metrics for short-term statistical wind power forecasting, *Renew. Sustain. Energy Rev.*, 138 (2021) 515.

Determining Efficiency of 15 OECD Countries Coping with Covid-19 using Data Envelopment Analysis after 2 Years of Pandemic

Esra Polat ^{1,a,*}

¹ Department of Statistics, Hacettepe University, Beytepe, 06800, Ankara, Türkiye.

*Corresponding author

Research Article

History

Received: 27/12/2022

Accepted: 03/12/2023

Copyright



©2023 Faculty of Science,
Sivas Cumhuriyet University

espolat@hacettepe.edu.tr

<https://orcid.org/0000-0001-9271-485X>

ABSTRACT

Covid-19, emerged in Wuhan, a city of China, at the date of December 2019, it spread to the entire world soon and then by the World Health Organization (WHO) accepted as a pandemic. Today, still the coping with Covid-19 is the one of the significant topics of countries. In this study, the relative efficiencies of 15 OECD countries for coping with the pandemic is analyzed with Data Envelopment Analysis (DEA). Current health expenditure (% of GDP), Nurses and midwives (per 1 thousand people), Hospital beds (per 1 thousand people), Physicians (per 1 thousand people) variables used as inputs; Number of Total Cases (per 1 million people), Number of Deaths (per 1 million people) and Number of Tests (per 1 million people) variables used as outputs. Output oriented Charnes, Cooper and Rhodes (CCR) and Banker, Charnes and Cooper (BCC) DEA models are used, scale efficiency values are determined and potential improvement suggestions are given for inefficient countries. Austria, Mexico, South Korea, Spain and Türkiye are found to be both relative technical, total and scale efficient. It is also concluded that inefficient countries must use their input variables efficiently and number of Covid-19 tests is important for a country's efficiency against Covid-19.

Keywords: Covid-19, Data envelopment analysis, Efficiency, OECD Countries.

Introduction

Covid-19 epidemic emerged in China (Wuhan city) at the date of December 2019 and surrounded the world soon [1]. Since the quick spread of the Covid-19 epidemic had an impact on all countries, it created severe situations for countries that are not prepared for the pandemic. The administrators, who were afraid of the inadequacy of the health systems, chosen to lockdowns in case of the inadequacy of the distance precautions and masks. During this period, it became clear that not only the health systems, however, also the economic and social development levels of the countries are significant for the direction of the pandemic. The health variables from the World Bank database are usually used for in the evaluation of the health systems of the countries [2]. The Ministry of Health of Türkiye announced that the first case in Türkiye was seen on March 11, 2020, on this date also the WHO announced Covid-19 as a pandemic. 13 August 2022, when this study was written, the total number of cases worldwide is 594375578 and the number of deaths is 6452554 due to the pandemic that can't be brought under control totally [3].

There are national and international studies on evaluating the efficiencies of the health systems of different country groups during the Covid-19 pandemic. Some of them summarized below.

Selamzade and Ozdemir (2020) investigate OECD countries' efficiency levels when coping with the Covid-19 pandemic. Output oriented models of CCR and BCC are used to obtain total and technical efficiency values

respectively, scale efficiency values are calculated and potential improvement suggestions are developed for inefficient countries. The percentage of health expenditures in the Gross Domestic Product, nurses and hospital beds, number of doctors per ten thousand people are inputs; the countries' Covid-19 pandemic data for the date of August 1, 2022 that number of cases and deaths per million population, number of tests are outputs. For CCR model, 8 countries, for BCC model, 11 countries are effective. Slovakia (CCR) and Iceland (BCC) are the leading ones in terms of super efficiency. Italy, USA, Spain, Northern Ireland, United Kingdom and France ranked at the bottom in terms of efficiency scores. It is concluded that fewer number of cases and deaths might be seen in countries with high level of development and number of healthcare workers, as well the number of tests performed is significant for increasing efficiency [1].

Shirouyehzad et al. (2020) evaluate the performances of most severely affected countries considering medical treatment and contagion control of Covid-19 with DEA. In the first step, the efficiency values are computed based on the situations of the countries and the number of approved cases for creating a basis for analysis for the contagion control. In the second step the performance evaluation is done regarding recovered cases, death cases and total number of confirmed cases for evaluating the efficiency of medical treatment in the countries. As a result of this study, it is found that Vietnam, Singapore and Belgium are the countries with the highest efficiency for

both viewpoints. Especially, Singapore, which has one of the highest population densities in the Southeast Asia, has the highest efficiency among these countries and it comes forefront. For Europe it is seen that Italy is the last one while Belgium is the leading one in terms of efficiency performance. For Middle East, although Egypt is the last efficient one in terms of contagion control, it is the leading efficient one in terms of medical treatment and Iran is the top efficient one in terms of contagion control [4].

Akbulut and Senol (2022) evaluate the efficiency performances of the countries, which are in high income class in the World Bank income classification, coping with the Covid-19 pandemic by both CCR and BCC DEA models. The analysis is conducted in DEAP package program. The share of GDP assignment to health services, mortality rate per 100000 live births, the number of patient beds, the number of nurses and midwives per thousand people, the number of physicians per thousand people and health expenditure per capita are used. The number of tests, the number of cases per 100000 people, the number of deaths and the total number of people recovering from Covid-19 are output variables. 15 of 48 countries are found to be efficient [5].

Bagriacik Ayranci (2021) analyzed the relative efficiency of 41 OECD and EU member countries for combating against the pandemic using DEA. It is found that 8 of 41 countries are have relative technical efficiency in fighting the pandemic. Chile is in the last order in terms of relative technical efficiency, although Ireland having a relatively low technical efficiency it is nearly efficient. Canada and USA, which are among the richest and developed countries, among the countries having worst performance combating against the pandemic. Türkiye is one of the countries that it is not succeeded in technical efficiency [6].

Bayram and Yurtsever (2021) evaluate and compare the efficiency performances of 27 European countries on spread and deaths due to Covid-19 pandemic by input-oriented DEA model. The model is carried on in two steps. In the first step, the contagion control efficiency is evaluated while in the second step the medical treatment efficiency is determined. Moreover, area chart is used for classifying the countries into the 4 zone. Results showed that Cyprus, Malta, Denmark, Montenegro, Estonia, Finland, Greece, Netherlands and Norway are found to be effective both in the contagion control and in the treatment of Covid-19 patients. Italy, Spain, Portugal and Iceland performed well in the treatment of Covid-19 patients, but are not effective in contagion control. It is also stated that North Macedonia, Luxembourg, Switzerland and Türkiye are not effective both in the contagion control and in the treatment of Covid-19 patients [7].

Erdem (2021) evaluates the performance of the Covid-19 pandemic management activities of OECD countries with DEA. As input; the number of doctors per 1 thousand people, the number of nurses, the number of patient beds and the percentage share of health expenditures in GDP are used. As output; the number of tests per million

people, the number of cases, the number of deaths and the number of Covid-19 vaccine doses implemented per 100 people are used. The input-oriented CCR model is applied using the context dependent DEA and the model is run again to the ineffective decision-making units (DMUs) each time. As a result of the 1st level analysis, 14 of 37 DMUs are found to be efficient. Of the 23 DMUs that are inefficient at level 2, 14 are found to be efficient. At the 3rd level, 5 of the 9 DMUs are efficient. At the last level, the remaining countries such as Australia, South Korea, Japan and New Zealand are seen as the most inefficient DMUs [8].

Ergulen et al. (2021) analyzed the efficiency levels of the G7 countries in coping with the Covid-19 pandemic using DEA. Number of tests, number of vaccines are used as input variables, number of deaths is used as output variable. As a result of the study, United Kingdom, Italy and USA are totally efficient; Canada, France, Germany and Japan are not totally efficient; among the inefficient countries Germany is the leading efficient country [9].

Kaman and Yucel (2021) studied on an efficiency performance analysis of healthcare workers from 9 OECD countries which are significantly affected by the epidemic. Moreover, the other target is investigating which countries are more efficient in saving healthcare workers. The input variables are the ratio of health expenditures in the GDP, the population density of the countries and the total number of healthcare workers per 1 thousand people. The number of cases and deaths per 1 million people of healthcare workers are output variables. DEA analysis results showed that countries that have total efficiency in the safety of healthcare workers are, Poland, Portugal and Czech Republic, however, Italy is the least efficient one [10].

Sel (2021) evaluates the Covid-19 performance of the health system improvements of G-20 countries. 5 health-related variables from the World Bank database are used as inputs, Covid-19-related test numbers, healed and deaths are used as outputs. The average values of 19 years (2000-2018) for health variables are used as inputs. Scale efficiency and super efficiency values are calculated by output-oriented CCR and BCC models. For CCR model USA, Brazil, China, United Kingdom, France and Türkiye are found to be efficient. For BCC model in addition to these 6 countries also India and Indonesia are found to be efficient [2].

Mourad et al. (2021) utilize the DEA methodology to explore 7 scenarios, incorporating six variables: the count of medical practitioners (doctors and nurses), conducted COVID-19 tests, hospital beds, death cases, recovered cases, and affected cases. To illuminate the relative efficiency of factors, Tobit analysis is employed. The results from the DEA indicate that less than half of the examined countries exhibit relative efficiency. Furthermore, the Tobit regression analysis demonstrates that the primary influence on efficiency scores stemmed from the quantity of recovered and affected cases. Ultimately, the outcomes of the Spearman, Kruskal-Wallis H and Mann-Whitney U tests signify the internal validity

and robustness of the selected DEA models. The results underscore the importance of adopting best practices in achieving relative efficiency by establishing a connection between healthcare system resources and the necessary outputs [11].

Perchkolaei and HosseinzadehLotfi (2021) assess the performance of member countries of OECD utilizing the network DEA technique. To achieve this goal, efficient financial and health indicators are identified. Adverse and adaptable data are recognized across different stages, leading to the presentation of a suitable model. The outcomes derived from implementing the model offered valuable insights into the financial and health policies of the mentioned countries. To assess the two-stage network, the set of indicators for inputs, the middle stage, and the outputs (three for each) are taken into account. The input variables are population density, health costs (percentage of GDP) and population. The intermediate (middle stage) variables are hospital bed density, physician density and number of hospitals. The output variables are number of deaths, number of active patients and number of improved. The results show that Australia, Japan, Iceland and Korea are efficient in the first stage and Türkiye, Belgium, United States and Sweden are efficient in the second stage [12].

Cansever and Senol (2022) evaluate the health systems of the countries in the developed country group, taking into account the World Bank classification and their secondary aim is to compare productivity results to be obtained with the performance of the countries in the fight against Covid-19. They use input-oriented CCR and BCC models from DEA models for measuring the effectiveness of health systems. While 79 countries constitute the universe of the research; the sample constitute of 36 countries whose data can be accessed. Data on health indicators of countries; covers the years 2000-2018 and annual data are used. Data on Covid-19 is obtained for the period between 01.03.2020-01.03.2022. As a result of DEA; the health systems of 6 countries (Antigua and Barbuda, Bahamas, Barbados, Oman, Trinidad and Tobago, Uruguay) are found to be effective. The overall efficiency average of the analyzed countries is determined to be 73%, and the inefficiency factors for the ineffective countries are identified. The secondary objective of the study is measuring Covid-19 performance, involves the use of testing rates, vaccination rates, and mortality rates. By comparing the findings obtained from the analysis with the Covid-19 performances; it has been observed that there is no relationship between the efficiency level of the health systems of the countries and the Covid-19 performances [13].

Pereira et al. (2022) introduced network DEA to assess the efficiencies of 55 countries that consisted of 37 OECD member countries, 6 OECD prospective members, 4 OECD key partners, and 8 additional countries. The network DEA model is structured in a general series with 5 distinct stages: population, contagion, triage, hospitalization, and intensive care unit admission. It adopts an output maximization orientation, representing a social

perspective, as well as an input minimization orientation, signifying a financial perspective. It comprises inputs associated with healthcare expenses, desirable and undesirable intermediate products linked to the utilization of personal protective equipment and the infected population, respectively. Additionally, it encompasses desirable and undesirable outputs pertaining to COVID-19 recoveries and deaths, respectively. The conclusion is New Zealand, Latvia, Netherlands, Estonia, Iceland, and Luxembourg are the countries exhibiting higher mean system efficiencies. The national COVID-19 strategies of these countries should be examined, adjusted, and adopted by nations displaying poorer performances. Furthermore, the noteworthy observation that countries with larger populations tend to exhibit lower mean efficiency scores holds statistical significance [14].

Yousfat et al. (2022) aimed to assess the efficiency of European countries using the case fatality rate (CFR) of COVID-19. A sample of 30 countries is utilized in the analysis, employing DEA. The study incorporates population density and total cases as input indicators, with CFR serving as the output indicator. Among the 30 countries examined, only six (Albania, Malta, Belgium, France, Austria, and Italy) exhibited efficiency. Inefficient countries, on average, demonstrated an efficiency score of 0.372. Among European countries, Greece attained the lowest efficiency rate when compared to others. Belgium has recorded the highest case fatality rate, while Monaco has documented the lowest case fatality rate [15].

Acar et al. (2023) aimed to assess the response of middle-income nations to the challenges posed by Covid-19, focusing on specific health indicators in accordance with the World Bank's income classification. This evaluation employed with DEA. The proportion of GDP devoted to the number of patient beds, health services, the number of nurses and midwives per thousand populations, the number of physicians per thousand populations, and lastly, the amount of health expenditure per capita are the input variables. The number of people recovering from Covid-19 disease per 100.000 people, the total number of deaths per 1 million people, the total number of cases per 1 million people and the total number of tests conducted per 1 million people are output variables of the study. The DEA input-oriented CCR model performed, and the causes of inefficiency in countries have been determined. To position these countries on the efficient frontier, the target values have been disclosed. They found that 18 countries out of 47 countries are located in the effective border. Ultimately, the causes of inefficiency among countries falling below the efficient frontier are assessed through the application of the multiple linear regression analysis method and recommendations for necessary corrections are given [16].

Kıdak et al. (2023) aimed to compare the efficiencies of 36 OECD countries in combating the COVID 19 pandemic. They used a three-stage DEA approach. The initial phase examined the pre-COVID conditions, while

the subsequent stages assessed the current COVID status of countries, focusing on medical treatment and contagion control. Within the framework of the three-stage model, a set of 8 input variables, 3 intermediate variables, and 3 output variables were employed. The efficiency analysis utilized both the output-oriented CCR model and the BCC models. Initially, efficiency analysis is conducted for all countries at each respective stage. Türkiye has demonstrated efficiency in the pre-COVID and medical treatment stages, yet inefficiency has been identified in the contagion control stage. Recommendations have been proposed by comparing countries serving as reference points for Türkiye in the contagion control stage. Subsequently, a sensitivity analysis was conducted, wherein overall efficiency scores were computed for each country by assigning varying weights to the stages. The unique of the study to be first time that a multi-stage DEA study has been conducted that computed overall efficiency scores and addressed both the pre-COVID and COVID pandemic periods together [17].

Zhu et al. (2023) aimed to quantitatively evaluate the spread of the COVID-19 pandemic. They constructed an output-oriented multi-stage super DEA model for assessing COVID-19 transmission efficiency across 117 countries. Additionally, the model was used to analyze transmission characteristics and trends in various periods in Europe, Africa, the Americas and Asia. Significant variations were identified in the spread of the pandemic across different countries that they mentioned that the United States, Brazil and the United Kingdom experiencing relatively more severe outbreaks. Nevertheless, numerous countries exhibited comparable pandemic transmission patterns, including stable or periodic transmission. Despite 14.5% of the global population being fully vaccinated as of August 1, 2021, there has been no direct observation of a vaccine effect on pandemic transmission [18].

In this study, the efficiency levels of OECD countries are analyzed in terms of their performances fighting against the pandemic. For this purpose, the Covid-19 performances of the 15 OECD countries, whose data can be accessed, are evaluated according to the literature by using the averages of health indicators between the years 2000-2018. Output-oriented Charnes, Cooper, Rhodes (CCR) and variable-scale Banker, Charnes, Cooper (BCC) models are used for Data Envelopment Analysis (DEA) efficiency analysis. Efficiency scale values are calculated with the obtained CCR and BCC values.

Data Envelopment Analysis

DEA is one of the most popular and effective methods for performance analysis. DEA is based on two main models for input and output, CCR and BCC. The CCR model based on the assumption of constant returns to scale and the BCC model based on the assumption of variable returns to scale. The CCR input-oriented model explores how the most effective input combination needed to

produce a given output combination most effectively. The BCC output-oriented model, on the other hand, investigates how much output combination can be obtained with a certain input combination. The CCR model investigates the increment in output generated by increments in inputs. The BCC model examines the more or less increment in output that might occur as a result of an increment in inputs. Moreover, according to the variety of orientation, both models have subsections named as non-oriented, output and input [2, 5, 19].

DEA is non-parametric technique used for the evaluation of the efficiency of DMUs. Farrell (1957) suggested an efficiency measurement technique with one input and one output [20]. Then Charnes et al. (1978) widened Farrell's proposition and improved a model that can measure the efficiency of DMUs with various mutual inputs and outputs [19]. These comparable existences are mentioned as DMUs which are used to transform inputs into outputs. In this technique, no assumptions for specification of the production function is made, and it is solved via optimization models. A frontier function that encompasses the internal and external factors is built using the information on the real inputs and outputs of DMUs. This boundary involves linear parts that not only discover the most efficient units but produce a basis for analysis of inefficient units. The advantage of DEA is that the "efficiency frontier" can be inferred and used as a model for organizations that are similar [4].

DEA model is one of the linear programming methods that allows measuring efficiency. When constructing the CCR model, it is assumed that if there are n DMUs, it produces s outputs $\tilde{Y}_j = (Y_{1j}, Y_{2j}, \dots, Y_{sj})^T > 0$ with m inputs $\tilde{X}_j = (X_{1j}, X_{2j}, \dots, X_{mj})^T > 0$ for each DMU $_j$ ($j=1, \dots, n$). The CCR model provides the non-negative best U_{rk} ($r=1, \dots, s$) and V_{ik} ($i=1, \dots, m$) output and input weights, respectively, to maximize the proportion of weighted outputs obtained as a result of weighted inputs

$$\text{for each DMU [2, 19]: } \theta = \frac{\sum_{r=1}^s u_r y_{rj}}{\sum_{i=1}^m v_i x_{ij}} .$$

The models are formulated in two different ways; input and output oriented. Input-oriented analysis models maintain the given output levels and aim to minimize the amount of input used in this way. Output-oriented analyzes, on the other hand, are carried out to investigate the maximization of outputs without changing the amount of inputs available. When DEA is done with the output-oriented CCR method, the numerator value is also

equal to 1 ($\sum_{r=1}^s u_r y_{rj} = 1$). In this study, Covid-19 performances of 15 OECD countries are determined with 4 input variables (health indicator averages) and 3 outputs of death, case and test numbers. In application, since the

input values are an evaluation of the past periods, the output-oriented CCR model is used that the current situation is examined. The linear programming model for efficiency analysis with the output-oriented CCR model is as in follows [2, 17, 21]:

$$\begin{aligned} & \text{Max } \theta_{CCR} \\ & \text{Constraints:} \\ & \sum_{j=1}^n \lambda_j x_{ij} - x_{i0} \leq 0; \quad \sum_{j=1}^n \lambda_j y_{rj} - \phi y_{r0} \geq 0; \quad \lambda_j \geq 0 \end{aligned}$$

In these primal and dual problems:

- x_{ij} : i^{th} input value for j^{th} DMU
- y_{rj} : r^{th} output value for j^{th} DMU
- x_{i0} : i^{th} input value for 0^{th} DMU
- y_{r0} : r^{th} output value for 0^{th} DMU
- λ_j : the weight for j^{th} DMU

While obtaining the output-oriented efficiency value as it is “ $1 / \sum_{i=1}^m v_i x_{ij}$ ”, the efficiency comments are as follows, depending on the obtained θ value:

- If $\theta = 1$ and the residuals are zero then DMU is efficient.
- If $\theta > 1$ then DMU is inefficient.

The BCC model developed by Banker, Charnes and Cooper, the convexity constraint $\left(\sum_{j=1}^n \lambda_j = 1 \right)$ is added to the CCR model. The formula for calculating efficiency using the output-oriented BCC model is as in follows [2, 22]:

$$\begin{aligned} & \text{Max } \theta_{BCC} \\ & \text{Constraints:} \\ & \sum_{j=1}^n \lambda_j x_{ij} - x_{i0} \leq 0; \quad \sum_{j=1}^n \lambda_j y_{rj} - \phi y_{r0} \geq 0; \quad \sum_{j=1}^n \lambda_j = 1; \quad \lambda_j \geq 0 \end{aligned}$$

After calculating CCR and BCC efficiencies for DMU, scale efficiencies are calculated: Scale Efficiency (SE) = $\theta_{CCR} / \theta_{BCC}$. Scale efficiency values are found in the form of CCR/BCC, and the scale efficiency of DMU equals 1 in case for both scales it has an efficiency value of 1. If a technically efficient DMU is inefficient due to scale, the relevant DMU can't be efficient in total.

Application

The scope of this study is to do a country specific efficiency evaluation of the coping with Covid-19 for 15 OECD countries, listed in Table 1, using DEA. As input variables, 4 variables related to health are considered. The

input variables are obtained from World Bank database and the average values of these variables for the years between 2000 and 2018 are used according to the literature. Since for some of the countries the values are missing only the OECD countries with available data set is included in the study. Output variables data set of related to Covid-19 is obtained from the statistics given in Worldometer website (<https://www.worldometers.info/coronavirus/>) on August 1, 2022. Since increasing cases and deaths has negative effects, these variables inverses (1/O-1) and (1/O-2) are included in the analyses. The input and output variables are given in Table 2.

Table 1. 15 OECD Countries

Austria	Israel	Mexico	Switzerland
France	Italy	Slovakia	Türkiye
Greece	South Korea	Slovenia	United Kingdom
Ireland	Lithuania	Spain	

Table 2. The Input and Output Variables

Inputs	I-1: Current health expenditure (% of GDP)
	I-2: Hospital beds (per 1 thousand people)
	I-3: Nurses and midwives (per 1 thousand people)
	I-4: Physicians (per 1 thousand people)
Outputs	O-1: Number of Total Cases (per 1 million people)
	O-2: Number of Deaths (per 1 million people)
	O-3: Number of Tests (per 1 million people)

In performance evaluation by applying DEA method, under the R programming language the “deaR” library is used. First of all, using the “install” command, the library downloaded install.packages(“deaR”) and then imported by command library(“deaR”) [23].

Table 3. CCR Model Efficiency Values, Reference Countries and Reference Values

Countries	Efficiency Value	Austria (6)	South Korea (2)	Mexico (3)	Spain (7)	Türkiye (8)
Austria	1	1	-	-	-	-
France	3.01976	0.4527	-	-	0.0579	1.222
Greece	1.44157	0.3804	-	0.0274	0.4003	0.1361
Ireland	1.86657	-	-	-	0.2129	1.3185
Israel	1.12064	-	-	-	0.3253	0.8989
Italy	2.13237	0.0471	-	0.0538	0.6406	0.4971
South Korea	1	-	1	-	-	-
Lithuania	2.28387	-	-	-	-	-
Mexico	1	-	-	1	-	-
Slovakia	3.47319	0.4257	0.3367	0.1135	-	-
Slovenia	3.61853	0.1163	0.0041	-	-	1.2202
Spain	1	-	-	-	1	-
Switzerland	2.48901	0.0236	-	-	0.2533	1.6569
Türkiye	1	-	-	-	-	1
United Kingdom	1.26669	-	-	-	0.942	0.0858

As a result of CCR model, which measures efficiency under the assumption of constant returns to scale, efficiency values and reference countries with reference values are given in Table 3. As a result of output-oriented CCR model, 5 countries are efficient while 10 countries are inefficient.

As Table 3 is examined it is clear that Austria, South Korea, Mexico, Spain and Türkiye are efficient countries in terms fighting against Covid-19 in terms of their health systems. Türkiye is the leading one that it is taken as reference for inefficient countries 8 times, while Spain 7 times, Austria 6 times, Mexico 3 times and South Korea is taken as reference only 2 times. Slovenia is the most inefficient country and Slovakia is the second inefficient one as it is clear from their efficiency values.

In Table 4 for inefficient countries the redundant values in input variables and how much the output variables should increase is shown.

From Table 4, for example, for France nurses and midwives (per 1 thousand people) 3.1027 unit and physicians (per 1 thousand people) 2.2229 unit must be used more effective. It means for these input variables there is inactive usage. For Slovenia, which is the most in efficient country, current health expenditure 1.2533 unit, hospital beds (per 1 thousand people) 0.6593 unit, nurses and midwives (per 1 thousand people) 9.6346 unit must be used more effective. For other countries similar comments could be done. For output variables Slovakia and Slovenia must increase number of tests (per 1 million people) 4564702.8753 and 70616.7246, respectively, to be efficient.

Table 4. Potential Improvement Values of Ineffective Countries for CCR Model

Countries	I-1	I-2	I-3	I-4	O-1	O-2	O-3
Austria	0.0000	0.0000	0.0000	0.0000	0.0000	0.0000	0.0000
France	0.0000	0.0000	3.1027	2.2229	0.0000	0.0000	0.0000
Greece	0.5160	0.0000	0.0000	1.9598	0.0000	0.0000	0.0000
Ireland	0.2003	0.0000	9.3756	0.4477	0.0000	0.0000	0.0000
Israel	0.1171	0.0000	2.8317	4.3886	0.0000	0.0000	0.0000
Italy	0.0000	0.0000	0.8916	4.0111	0.0000	0.0000	0.0000
South Korea	0.0000	0.0000	0.0000	0.0000	0.0000	0.0000	0.0000
Lithuania	0.0000	0.0000	0.0000	0.0000	0.0000	0.0000	0.0000
Mexico	0.0000	0.0000	0.0000	0.0000	0.0000	0.0000	0.0000
Slovakia	0.0000	0.3160	1.7794	0.2500	0.0000	0.0000	4564702.8753
Slovenia	1.2533	0.6593	9.6346	0.0000	0.0000	0.0000	70616.7246
Spain	0.0000	0.0000	0.0000	0.0000	0.0000	0.0000	0.0000
Switzerland	0.0000	0.0000	11.7000	0.3869	0.0000	0.0000	0.0000
Türkiye	0.0000	0.0000	0.0000	0.0000	0.0000	0.0000	0.0000
United Kingdom	0.8559	0.0000	5.5273	1.4933	0.0000	0.0000	0.0000

As a result of BCC model, which measures efficiency under the assumption of variable returns to scale, efficiency values and reference countries with reference values are given in Table 5. As a result of output-oriented BCC model, similar to CCR model, 5 countries are efficient while 10 countries are inefficient.

As Table 5 shows that Austria, South Korea, Mexico, Spain and Türkiye are efficient countries in terms fighting against Covid-19 in terms of their health systems. Türkiye is the leading one that it is taken as reference for inefficient countries 10 times, while Austria 9 times, Mexico 8 times, South Korea 7 times and Spain is taken as reference only 4 times. Slovakia is the most inefficient country and Slovenia is the second inefficient one as it is clear from their efficiency values.

Table 5. BCC Model Efficiency Values, Reference Countries and Reference Values

Countries	Efficiency Value	Austria (9)	South Korea (7)	Mexico (8)	Spain (4)	Türkiye (10)
Austria	1	1	-	-	-	-
France	2.42686	0.4633	0.3575	0.1359	-	0.0433
Greece	1.39001	0.451	-	0.2803	0.2207	0.048
Ireland	1.52925	0.1127	0.1623	0.0091	-	0.7159
Israel	1.01637	-	0.0978	0	0.3394	0.5628
Italy	1.91651	0.238	-	0.0832	0.1466	0.5322
South Korea	1	-	1	0	-	-
Lithuania	1.96336	0.291	-	0.0268	-	0.6822
Mexico	1	-	-	1	-	-
Slovakia	3.37545	0.3239	0.2112	0.1688	-	0.2961
Slovenia	3.30786	0.186	0.2313	0.0896	-	0.4931
Spain	1	-	-	-	1	-
Switzerland	1.86896	0.1698	0.3179	0.0176	-	0.4947
Türkiye	1	-	-	-	-	1
United Kingdom	1.25042	0.0207	0.0004	-	0.8844	0.0945

Table 6. Potential Improvement Values of Ineffective Countries for BCC Model

Countries	I-1	I-2	I-3	I-4	O-1	O-2	O-3
Austria	0.0000	0.0000	0.0000	0.0000	0.0000	0.0000	0.0000
France	3.2071	0.0000	3.8819	3.0843	0.0000	0.0000	0.0000
Greece	0.3241	0.0000	0.0000	1.4232	0.0000	0.0000	0.0000
Ireland	2.7525	0.0000	10.2266	1.3250	0.0000	0.0000	0.0000
Israel	1.0453	0.0000	3.0375	4.6990	0.0000	0.0000	0.0000
Italy	1.8917	0.0000	1.9386	4.7256	0.0000	0.0000	0.0000
South Korea	0.0000	0.0000	0.0000	0.0000	0.0000	0.0000	0.0000
Lithuania	0.0000	3.3550	4.3204	1.5140	0.0000	0.0002	0.0000
Mexico	0.0000	0.0000	0.0000	0.0000	0.0000	0.0000	0.0000
Slovakia	0.0000	1.3274	2.2517	0.2595	0.0000	0.0000	3060805.5181
Slovenia	2.2390	0.0000	9.4812	0.0754	0.0000	0.0000	663837.3943
Spain	0.0000	0.0000	0.0000	0.0000	0.0000	0.0000	0.0001
Switzerland	4.2902	0.0000	13.0044	1.8347	0.0000	0.0000	0.0000
Türkiye	0.0000	0.0000	0.0000	0.0000	0.0000	0.0000	0.0000
United Kingdom	1.0870	0.0000	5.6558	1.5892	0.0000	0.0000	0.0000

In Table 6 Potential Improvement Values of Ineffective Countries for BCC Model is shown. From Table 6, for example, for France current health expenditure (% of GDP) 3.2071 unit, nurses and midwives (per 1 thousand people) 3.8819 unit and physicians (per 1 thousand people) 3.0843 unit must be used more effective. It means for these input variables there is inactive usage. For Slovakia, which is the most inefficient country, hospital beds (per 1 thousand people) 1.3274 unit, nurses and midwives (per 1 thousand people) 2.2517 unit, physicians (per 1 thousand people) 0.2595 unit must be used more effective. For other countries similar comments could be done. For output variables Slovakia and Slovenia must increase number of tests (per 1 million people) 3060805.5181 and 663837.3943, respectively, to be efficient.

The scale efficiency values for countries are given in Table 7. For each column the value is greater than average value is showed by bold. Table 7 shows that 6 countries efficiency values are above the average for both CCR (total efficiency), BCC (technical efficiency) models and 5 countries for scale efficiency. According to the scale efficiency values as for both of CCR and BCC models the countries Austria, Mexico, South Korea, Spain and Türkiye are efficient that means they are also efficient in terms of scale efficiency. On the other hand, according to scale efficiencies, the other countries are found to be inefficient similar to results for CCR and BCC models.

Table 7. Scale Efficiency Values

Countries	CCR	BCC	Scale Efficiency Value
Austria	1	1	1
France	3.01976	2.42686	1.244307
Greece	1.44157	1.39001	1.037093
Ireland	1.86657	1.52925	1.220579
Israel	1.12064	1.01637	1.102591
Italy	2.13237	1.91651	1.112632
South Korea	1	1	1
Lithuania	2.28387	1.96336	1.163246
Mexico	1	1	1
Slovakia	3.47319	3.37545	1.028956
Slovenia	3.61853	3.30786	1.093919
Spain	1	1	1
Switzerland	2.48901	1.86896	1.331762
Türkiye	1	1	1
United Kingdom	1.26669	1.25042	1.013012
Average	1.957347	1.753433	1.102699

Conclusion

In this study, 15 OECD countries' Covid-19 performance is evaluated using average values of 19 yearly (2000-2018) data set of 4 important health variables. Only 15 of OECD countries are considered due to data availability constraint. There are 4 input variables and 3 output variables. For efficiency analysis, output-oriented CCR and BCC DEA models are used.

The results showed that Austria, Mexico, South Korea, Spain and Türkiye (5 countries) are found to be efficient for CCR, BCC models and also in terms of scale efficiency. These countries are efficient in terms of scale, technical and total efficiency. When we consider the income levels of OECD countries included in our study it is obvious that they are high or upper-middle income countries. However, as the pandemic was a sudden unexpected crisis process that these countries also suffered from the process deeply. As a result of our study Mexico and Türkiye, two upper-middle income countries are found to be efficient with the high income countries of Austria, South Korea and Spain. France, Greece, Ireland, Israel, Italy, Lithuania, Slovakia, Slovenia, Switzerland and United Kingdom are ineffective for both of CCR and BCC models. When both of CCR and BCC models results are evaluated together it is seen that both of Slovakia and Slovenia must increase the number of tests (per 1 million people) to become efficient. Moreover, as a results of both of these models, Greece uses current health expenditure (% GDP) and physicians (per 1 thousand people) inefficiently; both of Ireland, Israel and United Kingdom use current health expenditure (% GDP), nurses and midwives (per 1 thousand people), physicians (per 1 thousand people) inefficiently; Slovenia uses current health expenditure (% GDP), nurses and midwives (per 1 thousand people) inefficiently; Slovakia uses hospital beds (per 1 thousand people), nurses and midwives (per 1 thousand people), physicians (per 1 thousand people) inefficiently; both of France and Italy use nurses and midwives (per 1 thousand people) and physicians (per 1 thousand people) inefficiently. If these inefficient countries use these input variables efficiently, they become efficient.

Recently, many studies have been conducted examining the efficiencies of countries in the Covid-19 process. In these studies, different country groups, different variables, classical DEA, network DEA, different approaches and techniques were used. In these studies, in which DEA used, one or both of the input-oriented or output-oriented BCC or CCR models were used. Hence, as a result of all these causes in terms of country efficiencies different results could be obtained for different studies. When we examined literature Türkiye, our country, found to be sometimes efficient or in efficient as a result of the causes mentioned. However, we can especially emphasize that Türkiye was found to be efficient in terms of scale, technical and total efficiency in a similar study of Sel (2021) that we especially based our study at the beginning.

The restriction of this study, because of the missing values that not all OECD member countries only 15 OECD countries could be considered in the analysis. The study could be carried out and repeated in the future when data values for other countries could be obtained completely. Moreover, when the pandemic could be completely under control all over the world the study could be updated since the output variables of deaths, cases and tests will be fixed and final results could be obtained.

Conflicts of interest

There are no conflicts of interest in this work.

References

- [1] Selezade F., Ozdemir Y., COVID-19'a Karşı OECD Ülkelerinin Etkinliğinin VZA ile Değerlendirilmesi, *Turkish Studies*, 15(4) (2020) 977-991.
- [2] Sel A., Covid 19 Pandemisinde Sağlık Sistemi Gelişmelerinin Etkinliğinin Ölçülmesi: G-20 Üzerine Bir İnceleme, *Kırklareli Üniversitesi İktisadi ve İdari Bilimler Fakültesi Dergisi*, 10(2) (2021) 181-202.
- [3] Worldometer Website. Available at: <https://www.worldometers.info/coronavirus/>. Retrieved August 1, 2022.
- [4] Shirouyehzad H., Jouzdani J., Khodadadi-Karimvand M., Fight Against COVID-19: A Global Efficiency Evaluation based on Contagion Control and Medical Treatment, *J. Appl. Res. Ind. Eng.*, 7 (2) (2020) 109-120.
- [5] Akbulut F., Senol O., Üst Gelir Grubundaki Ülkelerin Covid-19 Mücadelesinin Veri Zarflama Analizi ile Değerlendirilmesi, *Gümüşhane Üniversitesi Sosyal Bilimler Dergisi*, 13(2) (2022) 679-689.
- [6] Bagriacık Ayrancı E., Covid-19 ile Mücadelede OECD ve AB Üye Ülkeleri Karşısında Türkiye'nin Etkinliğinin Değerlendirilmesi, *Erciyes Üniversitesi İktisadi ve İdari Bilimler Fakültesi Dergisi Araştırma Makalesi*, (60) (2021) 215-233.
- [7] Bayram G., Yurtsever O., Efficiency Evaluation of European Countries in Terms of COVID-19, *Int. J. Adv. Eng. Pure Sci*, 33(3) (2021) 366-375.
- [8] Erdem A. Y., Evaluation of Covid-19 Pandemi Management Activities of OECD Countries, Master Dissertation in Turkish, Bayburt University Graduate Education Institute Department of Business, 2021.
- [9] Ergülen A., Bolayır B., Unal Z., Harmankaya İ., VZA Yöntemi ile Covid-19 Pandemi Döneminde Bir Değerlendirme: G7 Ülkeleri Etkinlik Analizi, V. International Conference on Covid-19 Studies, Ankara, 2021, 255-261.
- [10] Kaman F.B., Yucel A., Covid-19'dan En Çok Etkilenen 9 OECD Ülkesinin Sağlık Çalışanlarının Etkinliğinin İncelenmesi Üzerine Bir Çalışma, *Isparta Uygulamalı Sosyal Bilimler ve Güzel Sanatlar Dergisi (SOSGÜZ)*, 3(5) (2021) 14-25.
- [11] Mourad N., Habib A.M., Tharwat A., Appraising Healthcare Systems' Efficiency in Facing Covid-19 Through Data Envelopment Analysis, *Decision Science Letters*, 10 (2021) 301-310.
- [12] Perchkolaei B.R., HosseinzadehLotfi F., Evaluating the Performance of OECD Countries in the Covid-19 Epidemic by Network Data Envelopment Analysis, *International Journal of Data Envelopment Analysis*, 9(4) (2021) 31-42.
- [13] Cansever İ.H., Senol O., Gelişmiş Ülkelerin Sağlık Sistemleri Verimlilikleri ile Covid-19 Performansları İlişkisi Üzerine bir Araştırma, *Anadolu Üniversitesi Sosyal Bilimler Dergisi*, 22(2) (2022) 611-628.
- [14] Pereira M. A., Dinis D.C., Ferreira D.C., Figueira J.R., Marques R.C., A Network Data Envelopment Analysis to Estimate Nations' Efficiency in the Fight Against SARS-Cov-2, *Expert Systems With Applications*, 210 (2022) 1-18.
- [15] Yousfat A., Bahaji K., Saws S., Efficiency Evaluation of European Countries Based on Case Fatality Rate of COVID-19 Using Data Envelopment Analysis, *International Journal*

- of Business and Social Science Research, 3(12) (2022) 15-22.
- [16] Acar E., Gokkaya D., Senol O., Efficiency Analysis of Middle-Income Countries in Terms of Health Indicators for the Covid Process. *Manas Sosyal Arařtırmalar Dergisi*, 12(ÖS) (2023) 300-317.
- [17] Kidak S.M., Arapoglu R.A., Aktar Demirtas E., Efficiency Analysis of OECD Countries During COVID-19 Pandemic Using Multi-stage DEA. *Pamukkale Üniversitesi Mühendislik Bilimleri Dergisi*, 29(5) (2023) 426-439.
- [18] Zhu Q., Zhou X., Liu S., A Multi-stage Super DEA Efficiency Evaluation Model of COVID-19 Pandemic Transmission Performance, The Twenty one Wuhan International Conference on E-Business—Healthcare service and IT management (WHICEB 2022) Proceedings 73. <https://aisel.aisnet.org/whiceb2022/73> 175-193.
- [19] Charnes A., Cooper W.W., Rhodes E., Measuring The Efficiency of Decision Making Units, *European journal of operational research*, 2(6) (1978) 429-444.
- [20] Farrell M.J., The Measurement of Productive Efficiency, *Journal of the Royal Statistical Society: Series A (General)*, 120(3) (1957) 253-290.
- [21] Cooper W.W., Seiford L.M., Zhu J., Data Envelopment Analysis: History, Models, And Interpretations. In *Handbook On Data Envelopment Analysis* (pp. 1-39). Springer, Boston, MA, (2011).
- [22] Banker R.D., Charnes A., Cooper W.W., Some Models for Estimating Technical and Scale Inefficiencies in Data Envelopment Analysis, *Management Science*, 30(9) (1984) 1078-1092.
- [23] Data Envelopment Analysis with deaR Tutorial. Available at: https://www.uv.es/dearshiny/Tutoriales_deaR/Tutorial_deaR_english.pdf. Retrieved August 1, 2022.

AUTHOR GUIDELINES

Thank you for choosing to submit your paper to Cumhuriyet Science Journal. The following instructions will ensure we have everything required so your paper can move through pre-evaluating, peer review, production and publication smoothly. Please take the time to read and follow them as closely as possible, as doing so will ensure your paper matches the journal's requirements.

Submission

Cumhuriyet Science Journal is an international, peer-reviewed, free of charge journal covering the full scope of both natural and engineering sciences. Manuscripts should be submitted by one of the authors of the manuscript as online submission after registration to the Cumhuriyet Sciences Journal. Microsoft Word (.doc, .docx, .rtf), files can be submitted. There is no page limit. If there is a problem while uploading the files of manuscript, please try to reduce their file size, especially manuscripts including embedded figures. Submissions by anyone other than one of the authors will not be accepted. The submitting author takes responsibility for the paper during submission and peer review. If for some technical reason submission through the online submission system is not possible, the author can contact csj@cumhuriyet.edu.tr for support.

Submission or processing charges

Cumhuriyet Science Journal does not charge any article submission, processing charges, and printing charge from the authors.

Terms of Submission

Papers must be submitted on the understanding that they have not been published elsewhere (except in the form of an abstract or as part of a published lecture, review, or thesis) and are not currently under consideration by another journal. The submitting author is responsible for ensuring that the article's publication has been approved by all the other coauthors. It is also the authors' responsibility to ensure that the articles emanating from a particular institution are submitted with the approval of the necessary institution. Only an acknowledgment from the editorial office officially establishes the date of receipt. Further correspondence and proofs will be sent to the author(s) before publication unless otherwise indicated. It is a condition of submission of a paper that the corresponding author permit editing of the paper for readability. All enquiries concerning the publication of accepted papers should be addressed to csj@cumhuriyet.edu.tr. Please note that Cumhuriyet Science Journal uses iThenticate software to screen papers for unoriginal material. By submitting your paper to Cumhuriyet Science Journal are agreeing to any necessary originality checks your paper may have to undergo during the peer review and production processes. Upon receiving a new manuscript, the Editorial office conducts initial pre-refereeing checks to ensure the article is legible, complete, correctly formatted, original, within the scope of the journal in question, in the style of a scientific article and written in clear English. Any article that has problems with any of the journal criteria may be rejected at this stage.

Peer Review

This journal operates a single blind review process. All contributions will be initially assessed by the editor for suitability for the journal. Papers deemed suitable are then typically sent to a minimum of two independent expert reviewer to assess the scientific quality of the paper. The author is required to upload the revised article to the system within 15 days by making the corrections suggested by the referee. The article will be rejected if there are no fixes in it. The Editor is responsible for the final decision regarding acceptance or rejection of articles. The Editor's decision is final

Title and Authorship Information

The following information should be included

Paper title

Full author names

Full institutional mailing addresses

Corresponding address

Email address

Abstract

The manuscript should contain an abstract. The researchers who are native speakers of Turkish have to add Turkish title and abstract as well. The abstract should be self-contained and citation-free and should be 250-300 words.

Keywords

Keywords of the scientific articles should be selected from the web address of www.bilimadresleri.com

Introduction

This section should be succinct, with no subheadings.

Materials and Methods

This part should contain sufficient detail so that all procedures can be repeated. It can be divided into subsections if required.

Conflicts of interest

Sample sentence if there is no conflict of interest: The authors stated that did not have conflict of interests.

Acknowledgements

Sample sentences for acknowledgements: The work was supported by grants from CUBAP (T-1111). We would like to acknowledge Prof. Mehmet Sözer, MD, for his precious technical and editorial assistance. We would like to thank

References

References to cited literature should be identified by number in the text in square brackets and grouped at the end of the paper in numerical order of appearance. Each reference must be cited in the text. Always give inclusive page numbers for references to journal articles and a page range or chapter number for books. References should be styled and punctuated according to the following examples

- [1] Karaca E., Ulusoy S., Morgül Ü., Ulusoy H.I., Development of Analytical Method for Sensitive Determination of Streptozotocin based on Solid Phase Extraction, Cumhuriyet Sci. J., 41 (4) (2020) 826-831. (sample reference for journals)
- [2] Keskin B., Ozkan A.S., Inverse Spectral Problems for Dirac Operator with Eigenvalue Dependent Boundary and Jump Conditions, Acta Math. Hungar., 130 (2011) 150-159(sample reference for journals)
- [3] Mazur M.T., Kurman R.J., Dysfunctional Uterine Bleeding. In: Mazur M.T., Kurman R.J., (Eds). Diagnosis of endometrial biopsies and curettings, A practical approach. 2nd ed. Berlin: Springer, (2005) 100-120. (sample reference for book chapters)
- [4] Mazur M.T., Kurman R.J.,Diagnosis of endometrial biopsies and curettings, A practical approach. 2nd ed. Berlin, (2005) 100-120. (sample reference for book)
- [5] National Cancer Institute, Surveillance Epidemiology and End Results. Cancer of the Corpus and Uterus, NOS. Available at: http://seer.cancer.gov/statfacts/html/corp.html?statfacts_page=corp. Retrieved March 2, 2008. (sample reference for websites)
- [6] Surname N., Title of thesis, PD or master thesis, Name of university, name of institute, year. (sample reference for thesis)
- [7] Surname N., Title of fulltext conference paper, name of conference, city, year, pages. (sample reference for Abstracts in conferences are not accepted as a valid reference except full text)

Preparation of Figures

Each figure can be integrated in the paper body or separately uploaded and should be cited in a consecutive order. Figure widths can be 4-6 inch as 300 dpi. The labels of the figures should be clear and informative. The name and the subtitles of the figures must be 9-point font.

Preparation of Tables

Tables should be cited consecutively in the text. Every table must have a descriptive title and if numerical measurements are given, the units should be included in the column heading. Tables should be simple with simple borders and text written as left text. The name and the subtitle of the tables must be 9-point font

Proofs

Corrected proofs must be returned to the publisher within 2 weeks of receipt. The publisher will do everything possible to ensure prompt publication. It will therefore be appreciated if the manuscripts and figures conform from the outset to the style of the journal.

Copyright

Open Access authors retain the copyrights of their papers, and all open access articles are distributed under the terms of the Creative Commons Attribution license, which permits unrestricted use, distribution and reproduction in any medium, provided that the original work is properly cited.

The use of general descriptive names, trade names, trademarks, and so forth in this publication, even if not specifically identified, does not imply that these names are not protected by the relevant laws and regulations.

While the advice and information in this journal are believed to be true and accurate on the date of its going to press, neither the authors, the editors, nor the publisher can accept any legal responsibility for any errors or omissions that may be made. The publisher makes no warranty, express or implied, with respect to the material contained herein.

Ethical Guidelines

New methods and ethically relevant aspects must be described in detail, bearing in mind the following:

Human Experiments. All work must be conducted in accordance with the Declaration of Helsinki (1964). Papers describing experimental work on human subjects who carry a risk of harm must include:

A statement that the experiment was conducted with the understanding and the consent of the human subject.

A statement that the responsible Ethical Committee has approved the experiments.

Animal Experiments. Papers describing experiments on living animals should provide:

A full description of any anaesthetic and surgical procedure used.

Evidence that all possible steps were taken to avoid animal suffering at each stage of the experiment. Papers describing experiments on isolated tissues must indicate precisely how the donor tissues were obtained.

Submission Preparation Checklist

As part of the submission process, authors are required to check off their submission's compliance with all of the following items, and submissions may be rejected that do not adhere to these guidelines.

The submission has not been previously published, nor is it before another journal for consideration (or an explanation has been provided in Comments to the Editor).

The submission file is in Microsoft Word document file (Times New Roman) format.

Where available, URLs for the references have been provided.

The text is single-spaced; uses a 11-point font; employs italics, rather than underlining (except with URL addresses); and all illustrations, figures, and tables are placed within the text at the appropriate points, rather than at the end.

The text adheres to the stylistic and bibliographic requirements outlined in the Author Guidelines, which is found in About the Journal.

If submitting to a peer-reviewed section of the journal, the instructions in Ensuring a Double-Blind Review have been followed.